UNIVERSITÁ DEGLI STUDI DI TRENTO

DIPARTIMENTO DI FISICA

PhilosophiæDoctor (Ph.D.)

BE ISOTOPES MEASUREMENT WITH AMS-02 TO REDUCE ASTROPHYSICAL UNCERTAINTY IN DARK MATTER MODELS

Supervisor: Prof. Paolo Zuccon
Co-Supervisor: Dr. Francesco Dimiccoli

Dottorando: Abhinandan Dass

DATE OF DISCUSSION: 14TH OF JUNE, 2024

Declaration

I hereby declare that except where specific reference is made to the work of others, the contents of this thesis are original and have not been submitted in whole or in part for consideration for any other degree or qualification in this, or any other university. This dissertation is my own work and contains nothing which is the outcome of work done in collaboration with others, except as specified in the text.

Abhinandan Dass
April 2024

Abstract

The $\bar{p}/p$ ratio published by AMS-02 shows an excess of $\bar{p}$ at rigidities above 60 GV, which can potentially be from WIMP annihilation. To that end, one has to decouple the contribution of secondary $\bar{p}$ coming from standard $p + He/H \rightarrow \bar{p} + X$ process. However models computing the latter component are affected by astrophysical and nuclear uncertainties. To reduce the former, the $\Phi_{^{10}Be}/\Phi_{^{9}Be}$ ratio is calculated by analysing 10 years of AMS-02 Be data. A set of selection criteria is developed to extract a pure sample of Be, and a fit model is constructed to extract the counts of the Be isotopes viz. ^{7}Be, ^{9}Be, and ^{10}Be. Additionally, the detector acceptance is computed using the AMS-MC datasets for Be, and the RTI information from the AMS-02 data is employed to calculate the exposure time. Using these components, the detector level fluxes are calculated for each of the isotopes which is then unfolded using a Bayesian iterative unfolding procedure to extract the particle level fluxes. These fluxes are then utilised to compute the ratios, $\Phi_{^{10}Be}/\Phi_{^{9}Be}$ and $\Phi_{^{7}Be}/\Phi_{\text{Total Be}}$. The former is compared with various theoretical models for computation of galactic halo sizes from the $\Phi_{^{10}Be}/\Phi_{^{9}Be}$ ratio; which suggests that the AMS-02 results severely challenges our understanding of halo sizes.

Furthermore, for the measurement of the $\bar{p}$ production cross-section, p beam at various energies from the CERN Super Proton Synchrotron are directed at a liquid He target within the COMPASS++/AMBER experimental hall. For this purpose, the COMPASS-RICH detector is used for $\bar{p}$ identification. As such, a Monte-Carlo simulation of the detector is developed in Geant4, and a reconstruction algorithm is written. This work is presented as an appendix to the thesis.

Acknowledgement

Enrico Fermi, one of the prominent figures of modern physics, has had a profound influence on me. He is among the rare breed of physicists who had made significant contribution to both Experimental and Theoretical physics. Inspired by his work and legacy, three years back, I made the life-changing decision to switch from Gravitational Physics to Experimental High Energy Physics. As expected, this transition posed severe challenges, but the people around me supported me in various measures, making it an enjoyable and horizon-widening experience.

Foremost, I would like to express my heartfelt gratitude to my supervisor, Prof. Paolo Zuccon, who bestowed his trust on me, and guided me through the Ph.D. journey. He helped me unlock my potential to work on multiple projects, and provided me with significant autonomy in conducting my research. I would thank him for his patience in dealing with my trivial curiosities, and engaging in discussion of results at all hours.

The succesful completion of this thesis wouldn't have been possible without the invaluable supervision of Dr. Francesco Dimiccoli. He not only guided me through the intricacies of data analysis, but also provided guidance on academic life. I am aware, I have tested his patience on many occasions, but he dealt with them calmly and clarified my concepts with utmost kindness and dedication.

I must acknowledge the significant contribution of Dr. Francesco Nozzoli for his important insights into various aspects of analysis. He was always enthusiastic in providing me with great suggestions and advise that has helped shaped my work, and thesis. I am also grateful to him for his assistance in managing the CERN missions for detector shift.

During my time at CERN, I was fortunate enough to be part of two exceptional collaborations, AMS-02 and AMBER. I extend my gratitude to the team of Engineers and Scientists who ensured the success of these experiments. In particular, I would like to acknowledge the extraordinary leadership of Prof. Samuel Ting, a Nobel laureate, and a man of inexhaustible energy and scientific rigor. I am also thankful to Dr. Mercedes Paniccia, Dr. Jiahui Wei, and Manbing Li for their scientific collaboration and insightful discussions.

Furthermore, I would like to express my gratitude to my family- Mom, Dad and my elder brother- for their constant support over video calls and heartfelt prayers for my success. My friend, Chiranjeeb, was a steadfast companions during the ups and downs of my Ph.D. journey. Additionally, Alessio, Jeevan, Ali, Revanth, Joel, Rawlings, Raktim, Preetam, Manas, Nirab, Syed, Adhiraj, Tirtha, Darpan, Partha, Himangshu, Sagar, Ayub and Manash played an invaluable part in preserving my sanity.

Words fail to describe my gratitude towards Kakoli who not only encouraged and supported me during the Ph.D but also patiently bore the brunt of my Ph.D. stress.

Contents

List of Figures

List of Tables

Chapter 1

Introduction

1.1 Overview

”Is our Universe really Dark?”

To place the above sensational comment in perspective, we need to note that unravelling the composition of our Universe is still a daunting question for Physicists. Evidence from numerous astrophysical and cosmological sources, and observations has resulted in a *Standard Model of Cosmology* wherein the ordinary matter constitutes only about 5% of the universe and the nature of the remaining 95% remains “dark” or unknown to us. Around 68% of the Universe's energy budget is in form of *Dark Energy*, which has been hypothesised to explain the current acceleration of the expanding universe. The remaining $\sim 27\%$ is in the form of *Dark Matter* (DM) which is hypothesised to be non-baryonic, non-luminous, non-relativistic form of matter that constitutes about 85% of the matter content of the universe.

Theorists have come up with several scenarios to explain the particle nature of DM. Those theories rely on going beyond the *Standard Model of Particle Physics*. The Standard Model (SM) of Particle Physics is a massively successful theory providing high-precision theoretical estimates for experimental data, and it describes the *Weak*, *Electromagnetic* and *Strong Forces*. Despite being a major breakthrough in physics, SM cannot explain the origin, existence and properties of DM. Although there has been no statistically significant results from any accelerator based experiments including the LHC, of Physics beyond SM, we have strong evidence from other experiments that SM is at best a low energy effective *Quantum Field Theory*.

We have scant knowledge about DM as a particle, however, any candidate for (most of) DM must obey the observational constraints. In cosmological terms, the relic abundance of the candidate particle should account for the observed *Cold Dark Matter* (CDM) abundance, should be non-relativistic (and hence the name cold) in nature to allow structure formation in the early universe, and among others, its lifetime should be larger than the age of the universe, or in other words, it should be cosmologically stable. Among the various candidate theories for DM, *Weakly Interacting Massive Particles* (WIMPs) are of great interest and have been widely con-

sidered theoretically which has further instigated enormous experimental endeavours to detect them. What makes WIMPs theoretically interesting is that they arise naturally in several extensions of the SM, such as the *Minimal Supersymmeteric Standard Model* (MSSM).

Efforts have been made worldwide to detect WIMPs using various methods, such as direct, indirect, and collider searches. However, there has not been a definitive WIMP detection signature thus far. The DAMA/LIBRA collaboration [74, 246] has reported a sustained annual modulation in its detector, which could be due to changes in the relative velocity between galactic WIMPs and Earth caused by Earth's rotation around the Sun. DAMA uses $NaI(Tl)$ crystals to measure WIMP scattering, and the detected signal indicates a WIMP mass of around $10\ GeV$ if the scattering from Na ions is taken into consideration. The data collected from DAMA phase 1 and phase 2 [75], which corresponds to an exposure of $2.46\ tons \times\ yr$, has a combined significance of 12.9 σ C.L. [116]. Another collaboration called CRESST [57] has also reported an excess of data that suggests WIMP masses in the range of $10 - 60\ GeV$ with a WIMP nucleon scattering cross section between 10^{-43} and $10^{-40}\ cm^2$. CoGENT [7] has observed event excesses and annual modulation similar to the DAMA experiment, with a significance of 2.8 σ C.L.. The results from the DAMA, CoGENT, and CRESST experiments are difficult to reconcile with the simplest models of DM [190, 248], and the parameter space that these models suggest for the relationship between WIMP mass and WIMP nucleon scattering cross-section seems to be inconsistent. This conflict is also apparent when comparing these positive signals to the null results from experiments such as LUX [39], XENON-1T [58], and PANDA [262], which have set the most stringent limits on WIMP nucleon spin-independent cross-sections. These limits constrain the WIMP nucleon scattering cross section to below $10^{-45}\ cm^2$ for light DM, with WIMP masses below $100\ GeV$. As a result, it is worthwhile to explore the WIMP nucleon cross-section for lighter WIMPs, using complementary techniques such as indirect detection or searches at colliders.

WIMPs can potentially be created as a result of proton-proton collisions at the LHC, alongside one or more QCD (*Quantum Chromodynamics*) jets, photons, and other detectable particles from the SM. However, the DM produced in this way would not be detected due to its very weak interaction cross-section. Therefore, experiments are looking for missing transverse energy (E_T) signals, which could indicate the presence of dark matter. Searches at the collider involve looking for E_T and specific SM particles in predicted final states, often involving searches for SUSY particles that can further decay to DM candidates. However, so far, no such signatures have been found, and results from collider searches are consistent with SM expectations. The ATLAS [4], CMS [252], and LHCb [5] experiments at the LHC have set strong limits on DM candidates. MiniBooNE experiment at Fermilab [35] also contrain Sub-GeV DM candidates. Efforts to detect DM in the sub-GeV mass range has also been actively pursued at fixed target experiments and with high intensity, low-energy colliders. In particular, Search for dark photons decaying into light DM has also been conducted at e^+e^- colliders such as BaBar (see chapter 16 of Ref. [128]). However, it's important to note that the limits set by colliders are model-dependent, and hence the interpretation of these limits should be done, taking into

consideration the underlying mechanisms that couple DM to the SM particles.

Indirect searches are often used in combination with direct detection and collider-based searches to detect DM. They involve searching for the products of the annihilation and decay of WIMPs in regions where there is a high concentration of DM, such as the center of the sun, earth, and galaxy. This can manifests as distortions in gamma-ray spectra or anomalies in rare components of *Cosmic Rays* (CRs), such as antimatter components like anti-protons, anti-deuterons, and positrons. Specifically, CR antimatter components have the potential to detect the products of DM annihilation in addition to standard astrophysical production.

$$\chi + \chi \to q\bar{q}, W^-, W^+, \ldots \to \bar{p}, \bar{d}, e^+, \gamma, \nu \quad , \tag{1.1}$$

where χ is a generic symbol for a DM candidate.

The AMS-02 experiment, which is a state-of-the art accelerator type magnetic spectrometer installed on the *International Space Station* (ISS), offers us a unique platform with its high precision results of antimatter spectrum [27] to probe the possible DM channels. In particular, the positron and antiproton channels have received attention in recent time to investigate excess over SM prediction. However, the excess of cosmic positrons observed cannot be solely attributed to DM, as it may also be caused by the emission of positrons from nearby astrophysical sources of leptons or galactic pulsars [135, 136, 202, 214, 271]. This contradicts the predictions of standard models for the production of cosmic positrons [11, 32]. The present isotropy (or anisotropy) of the cosmic positron flux cannot be relied upon to completely differentiate between the various scenarios [213]. Consequently, the anti-proton spectrum remains a privileged channel for indirectly searching for dark matter. However, to that purpose, it is crucial to assess the uncertainties related to the production and propagation of anti-protons in the galaxy.

Inelastic scattering of CRs off the ISM is responsible for the dominant part of the anti-protons in our galaxy and it sets the background against which contribution from exotic sources is investigated. AMS-02 has measured the $\bar{p}$ flux and $\bar{p}/p$ ratio with an exceptional degree of accuracy, to within a few percent. These measurements cover a broad energy range, from below $1\ GeV$ up to several hundreds GeV. The findings indicate that the $\bar{p}/p$ ratio remains steady above 60 GV rigidity, and is quite flat.

The anti-proton (secondary) component generated by CRs is expected to decrease more rapidly than the primary proton spectrum, although those theoretical predictions are affected by several uncertainties. Two major sources of uncertainties which afflict the prediction of anti-protons for indirect DM search are the astrophysical uncertainty due to propagation in the galaxy and *Heliosphere* [83–86, 90, 150, 151, 167], and the anti-proton-production cross-section [137, 140, 156, 197, 239, 278]. The AMS-02 measurements will help reduce the astrophysical one, by constraining the propagation of CRs and refining the diffusion model of CRs in

the galaxy and the *Solar System*. For the latter uncertainty, we note that, nuclei heavier than proton and helium contributes a paltry amount to the secondary production of CRs, either as projectiles or targets, and hence they play a trivial role in the production of secondary antiprotons [197]. Consequently, the dominant reactions are those involving protons and Helium ($p + p, p +^4 He,^4 He + p,^4 He +^4 He$). Approximately 40% of the $\bar{p}$ production across the entire energy spectrum involves interactions where ^4He is either the target or the projectile. To decrease uncertainty regarding the secondary $\bar{p}$ production cross section and determine if there are any indications of exotic components from DM annihilation or decay in the AMS-02 data, it is essential to conduct precise measurements of the $\bar{p}$ production cross section in both $p + p$ collisions and $p +^4 He$ collisions at energies ranging from $10\ GeV$ to a few TeV. The *Apparatus for Meson and Baryon Experimental Research* (AMBER) at the M2 beam line of *Super-Proton Synchrotron* (SPS) at CERN, offers us the possibility to explore the production cross-sections of interest. AMBER is a $60\ m$ long fixed target experiment, and is a two-staged spectrometer with numerous tracking detectors, particle identification and calorimetry. To carry out the proposed physics program, data were collected using a liquid helium (LHe) target and would be collected using a liquid hydrogen (LH_2) target in the future.

In the light of the above, there are two components to the doctoral work. The first part which serves as the primary focus of the thesis pertains to improving the CR propagation models to reduce astrophysical uncertainty. In order to achieve this objective, the Beryllium (Be) isotope analysis is performed using 10 years of AMS-02 data. Be is primarily produced in the spallation reaction of Carbon (C), Nitrogen (N), and Oxygen (O) with the ISM, and is a rare component of CRs. It has three major isotopes, $^7Be,^9 Be$, and ^{10}Be. Out of them, ^9Be is stable, while ^{10}Be is $\beta-$ radioactive, and has a relatively longer half-life ($T_{1/2} = 1.39 \times 10^6$ years). The relatively small amount of ^{10}Be, when compared to the ^9Be abundance, presents us with a radioactive clock that can be used to measure the residence time of CRs in the Galaxy. The measurement $^{10}Be/^9Be$ can also constrain the astrophysically important ratio H^2/D, where H is the *Halo Half Size*, and D is the *Diffusion Coefficient* in *Cosmic Ray Transport Equations* [153]. A discussion on the theory is done in explicit details in chapter 2 (See 2.7.1).

For completeness, the second part of the work which involves the measurement of anti-proton production cross-section is provided as an appendix to this thesis. For identification of the antiprotons, the COMPASS *Ring Imaging Cherenkov Detector* (RICH) [10], is the most important one. The RICH is a relatively large detector with a volume of $80\ m^3$, and it contains C_4F_{10} gas as a refractive medium. The mirror system of the RICH consists of two very ultra-violet (VUV) reflecting spherical surfaces, with a total area larger than $21\ m^2$. Monte Carlo (MC) simulations of the detector using the Geant4 platform was performed for the RICH detector. Furthermore, to improve the velocity reconstruction from the RICH Cherenkov Rings, the necessary physics processes calculations were implemented in C++ and visualised using ROOT classes. Along with that, both test beam with a deuteron target and actual measurements with a liquid helium target were conducted in November 2022, and in July 2023, respectively. Further data acquisition with a hydrogen and deuteron target is scheduled to be held in 2024 as of writing this

thesis. The ongoing analysis of the data would help reducing nuclear uncertainties.

Chapter 2

Cosmic Rays and Propagation Models

2.1 A brief peak into history

The beginning of the 20th century, the *de facto* golden period of modern physics, saw the parallel development of Cosmic Ray (CR) Physics and Elementary Particle Physics. In fact, in the absence of particle accelerators, CRs provided the background for the discovery of several new particles that could be observed only at high energies.

Towards the end of the 19th century, Becquerel's discovery of spontaneous radioactivity resulted in a widespread belief that ionizing radiation in the atmosphere was solely derived from radioactive elements present in the earth or their derivatives. Subsequently, a significant amount of experimental work was conducted in the early 1900s to comprehend the properties and essence of this ionizing radiation. This involved conducting experiments underground, underwater, and at high altitudes to investigate its intensity in relation to distance from the ground and its variations across different geographical locations. In 1910, Wolf [206] observed a possible radiation from outer space by measuring ionization rates with an electroscope at the top of the Eiffel Tower. The intensity of this radiation did not decrease as much as it would have if the source of the radiation was on the ground, suggesting it could have originated from extraterrestrial sources. The significant progress occurred when Victor Hess conducted experimental measurements starting in 1911, which involved multiple balloon flights at different altitudes above sea level (Fig. 2.1). Hess discovered that the rate of ionization began to increase at altitudes of around 1.5 km, leading him to conclude that a new form of radiation from outer space was causing this observed increase [178]. In 1911, Domenico Pacini [229] and, independently in the 1920s, Robert Millikan conducted underwater observations and both confirmed the existence of a new type of radiation that was originating from beyond Earth. This radiation was later identified as cosmic rays. During that period, the nature of cosmic rays was still unclear, specifically whether they were composed of charged particles or neutral photons. The debate was so intense that it even made the front page of newspapers like New York Times (2.1). Millikan initially supported the idea that cosmic rays were high-energy gamma rays with some secondary electrons produced by Compton scattering, while charged particles were considered as candidates for Compton. After the era of the electroscope, there were a few key

The New York Times

VOL. LXXXI...No. 27,370. December 31, 1932

MILLIKAN RETORTS HOTLY TO COMPTON IN COSMIC RAY CLASH

Debate of Rival Theorists Brings Drama to Session of Nation's Scientists.

THEIR DATA AT VARIANCE

New Findings of His Ex-Pupil Lead to Thrust by Millikan at 'Less Cautious' Work.

Figure 2.1: Left: Victor Hess (center) and his crew on the balloon departing from Vienna in 1911. Right: Cover page of The New York Times reporting the heated discussion between Millikan and Compton on the nature of CRs.

technical breakthroughs that greatly advanced the study of cosmic rays. These included the development of Geiger-Muller tubes, the implementation of coincidence techniques refined by Bruno Rossi [241], and the introduction of imaging devices such as bubble/cloud chambers and photographic emulsions. These advancements provided a wealth of new information about cosmic rays in the 1930s. It was discovered early on that the particles observed in cosmic rays were capable of passing through substantial amounts of material. This raised concerns about the original theory that cosmic rays were primarily composed of photons.

An important development in understanding the charged nature of cosmic rays occurred in the early 1920s, when scientists realized they could use the Earth's magnetic field to their advantage. They realized that if cosmic rays were made up of charged particles, their trajectories would be affected by the magnetic field, causing greater radiation intensity near the poles than at the equator.

Building on the earlier work of Carl Stoermer on the Earth's geomagnetic field, Rossi predicted that if CR were predominantly of one charge, an East-West flux asymmetry should be observed, with the maximum effect occurring around the geomagnetic equator. In 1934, Rossi confirmed this prediction by measuring the East-West effect [242], which was an important milestone in the understanding of cosmic rays.

In the 1940s and 1950s, a comprehensive and consistent understanding of cosmic rays was developed based on these foundations. It was discovered that the primary radiation is mainly made up of protons, with a smaller amount of heavier nuclei, and that the particles observed on the Earth's surface are secondary cosmic rays that are created through interactions between the primary cosmic rays and the atmosphere 2.3.

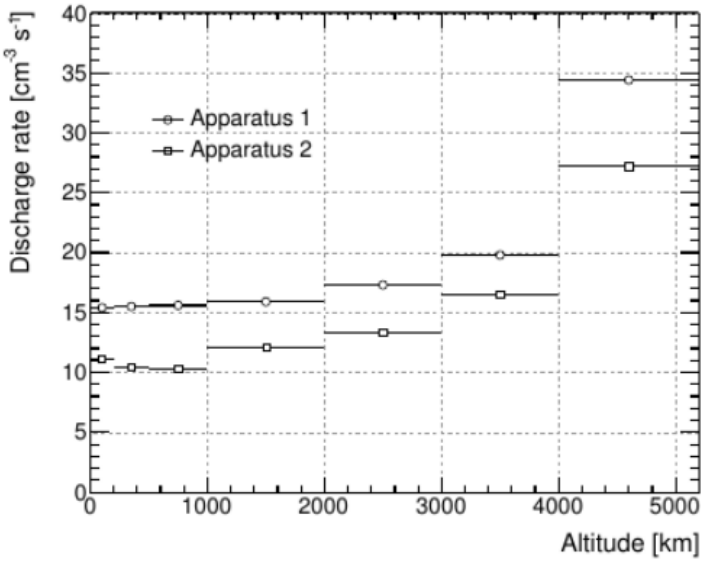

Figure 2.2: Original measurements from one of the ascents performed by Viktor Hess [178]. The increase of rate of discharge with altitude implies that the ionizing radiation responsible for it is extraterrestrial

Dirac's theory on the existence of anti-particles and Einstein's theory on the equivalence between mass and energy were both experimentally confirmed through the discovery of the positron in 1932, which was observed by Anderson while studying cosmic rays using a cloud chamber [55]. This discovery, along with the later measurement of pair conversion $\gamma \rightarrow e^{+}e^{-}$, contributed to the understanding of new interactions and particles that were postulated in the 1930s. In the 1940s, the discovery of muons [257], pions [227], and kaons [240] in cosmic rays helped to clarify this puzzle further [133]. These discoveries in the field of cosmic rays led to the creation of two complementary fields of research: high-energy elementary-particle physics and cosmic-ray astrophysics. These two fields have effectively merged today in the astroparticle domain, where fundamental physics processes are investigated using cosmic radiation as a source with high-energy physics instruments.

The launch of Sputnik I in 1957 was a significant breakthrough that marked the beginning of the space era. This allowed for advancements such as the ability to observe primary cosmic rays using satellites equipped with Geiger-Muller counters and magnetic spectrometers. One of the most notable discoveries was the existence of the Van Allen belts, which are regions around Earth with intense radiation levels due to low-energy charged particles trapped in the geomagnetic field. The *South Atlantic Anomaly*, a region where the lowest Van Allen belt is near Earth's surface, is discussed in subsequent chapters due to its impact on measurements made by the AMS-02 experiment.

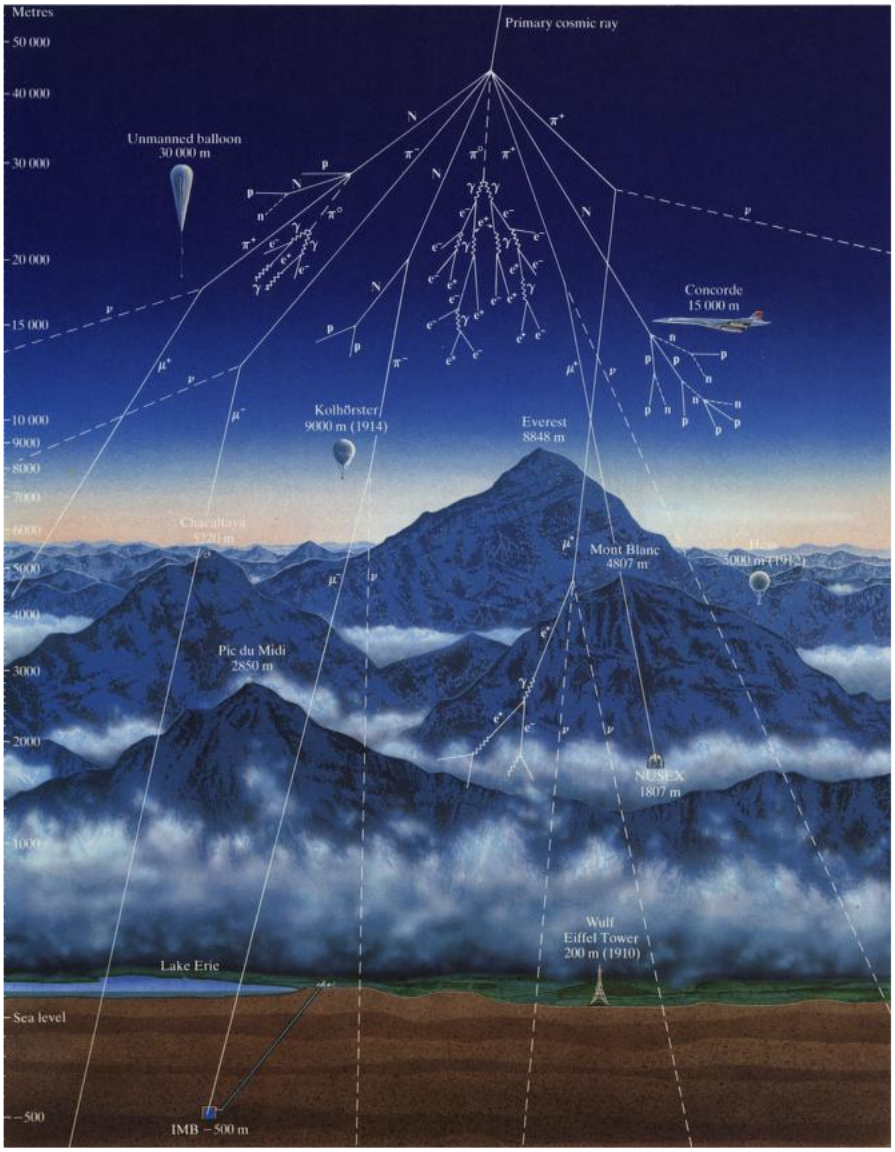

Figure 2.3: Development of a typical particle shower cascade triggered by a cosmic ray entering atsmophere

Cosmic rays have been the subject of significant study for over a century, using both ground-based and space-based detectors. Reference [218], includes more than 1000 data sets from 40 different experiments conducted across a broad range of energy levels. A number of particle detectors were flown mainly in balloons seeking to measure the cosmic ray composition with ever increasing precession. Although it is impossible to go through the details of each of the experiments. Here is a very brief review of some of them.
Some of the calorimetric and spectrometric balloon borne experiments are

- **ATIC** (Advanced Thin Ionisation Calorimeter): It's main result was an observation of an excess in electrons in the energy range of $300 - 800\ GeV$ as compared to background [101]. Although the source of this excess isn't clear, researchers points out that it might come from a nearby pulsar or some other astrophysical object. A more exotic explanation suggest that the excess comes from collision of dark matter particles, like the WIMP Kaluza-Klein particle of mass around $620\ GeV$ [212]. It also published the measurement of the relative abundances of nuclei from boron to oxygen [231], in the energy range

from 10 GeV/n to 300. And the CR nuclei flux of He, C, O, Ne, Mg, Si, and Fe in the energy range 50 GeV upto 100 TeV. [230].

- **CREAM** (Cosmic Ray Energetics and Mass): It included a Timing Charge Detector (TCD), a Cherenkov Detector (CD), a Transition Radiation Detector (TRD), a Cherenkov Camera (CherCam), a Silicon Charge Detector (SCD), scintillating fiber hodoscopes, and a calorimeter made of tungsten and scintillating fiber. It published the Boron to Carbon ratio [38], energy spectra of C, O, Ne, Mg, Si, and Fe up to $\sim 10^5$ GeV [37], the proton and Helium spectra up to $\sim 10^6$ GeV [281, 282]. After 2017, an upgraded version has been installed on the International Space Station (ISS) named ISS-CREAM. However it was switched off in 2019 because of management woes.

- **TRACER** (Transition Radiation Array For Cosmic Energetic Radiation): It consisted of two scintillators, a Cerenkov Counter, proportional tubes and plastic radiators. It measured the individual energy spectra of cosmic ray nuclei up to Fe at energies up to 10 TeV [37] and the Boron to Carbon ratio [226].

Some of the space-based detectors other than AMS-02 which would be discussed in details in later chapters, are briefly discussed below:

- **HEAO3-C2** (The Third High Energy Astrophysics Observatory): It was a spacecraft launched back in 1979, and consisted of Cerenkov counter, neon flash tube hodoscopes, and a time-of-flight system. It performed measurements of CR nuclei from Be to Ni in the energy range between 0.6 GeV to 35 GeV [148].

- **CRN** (Cosmic Ray Nuclei): It was flown as part of spacelab 2 back in 1985. It had two gas Cerenkov counter, a transition radiation detector, and two plastic scintillators. It measured the elemental composition and the energy spectra of CRs nuclei from B to Fe in the energy range between 40 GeV up to 1 TeV [219].

- **PAMELA** (Payload for Anti-Matter and Light-nuclei Astrophysics): It was a spectrometer based detector onboard a Russian satellite. Observations made by PAMELA indicated a significant increase in the fraction of positrons at energies ranging from 5 GeV to 100 GeV [16]. It was conjectured to have been due to WIMP DM annihilation. However, PAMELA surprisingly didn't find an excess in anti-protons, and this was inconsistent with most of the DM models that suggested that both the excesses should be correlated. Now it is mostly accepted that the excess might be due to pair production and subsequent acceleration due to a nearby pulsar. Additionally, PAMELA also detected a change in the spectral index of proton and helium nuclei at a rigidity of around 300 GV, which had been suggested by previous measurements using balloon-borne calorimeters but had not been detected by spectrometers until then [21]. PAMELA also measured the B/C ratio between 0.4 GeV/n and 130 GeV/n [18].

- **NUCLEON** : It's a particle detector aboard a Russian satellite. It measured the all-particle spectrum and the spectra of p, He, C, O, Ne, Mg, Si and Fe [61].

- **DAMPE** (Dark Matter Particle Explorer): It is a satellite working as a space telescope, and it was launched back in 2015. It detected a break in the cosmic electron plus positron energy spectrum at an energy of $0.9\ TeV$ [2]. It also published the proton spectrum from $40\ GeV$ to $100\ TeV$ [115].

- **CALET** (Calorimetric Electron Telescope): It was launched back in 2015 and installed on the ISS. It published data on half a million electron and positron cosmic ray events in 2017, finding a spectral index of -3.152 ± 0.016 above $30\ GeV$ [15].

2.2 Cosmic Rays

This section provides an overview of the primary features of cosmic rays, including their composition, energy distribution, and current understanding of their production and diffusion mechanisms.

2.2.1 Composition

Cosmic rays are made up mostly of protons (86 %) and helium nuclei (11%), with electrons (2%) and heavier nuclei (1%) also present, along with small amounts of antimatter (positrons and antiprotons). The composition of cosmic rays that are detected on Earth is influenced by their source and their propagation throughout the Galaxy. The chemical composition of cosmic rays has similarities with the composition of objects in the solar system, and peaks corresponding to certain elements are due to the fact that nuclei with even mass or atomic number have a higher binding energy and are less likely to fragment 2.4. Iron is the most stable nucleus and has a prominent peak in cosmic ray abundance. However, the abundance of other elements rapidly decreases, making their determination difficult. Experimental evidence qualitatively suggests the presence of every nucleus up to Uranium in cosmic rays, and measurements of the abundance of many elements have been precisely attained. Cosmic radiation also has an excess of low or rare elements, such as Li, Be, B, F, and nuclei between Si and Fe, which are generated during cosmic ray propagation and not present in cosmic ray sources. These elements can be used to trace the amount of interstellar matter through which the primary nuclei pass between acceleration and detection.

CR components are primarily divided into primary and secondary. Primary cosmic rays are particles that have traveled through the galaxy without undergoing any destructive interactions. These particles have abundances of elements that closely match the values found in the solar system, indicating that most cosmic rays come from stellar flares before undergoing acceleration. Despite the fact that the solar system formed 4.6 billion years ago and cosmic rays are much younger, the similarity in their composition can help to limit models of Galactic chemical evolution. Fig. 2.5 shows flux of primary cosmic ray nuclei from H to Fe.

Secondary cosmic ray nuclei, such as ${}^2H$, ${}^3He$, the $Li - Be - B$ group, and the sub$-Fe$ group (Sc, Ti, and V), are mainly created through the spallation of primary hydrogen, ${}^4He$, C, N, O,

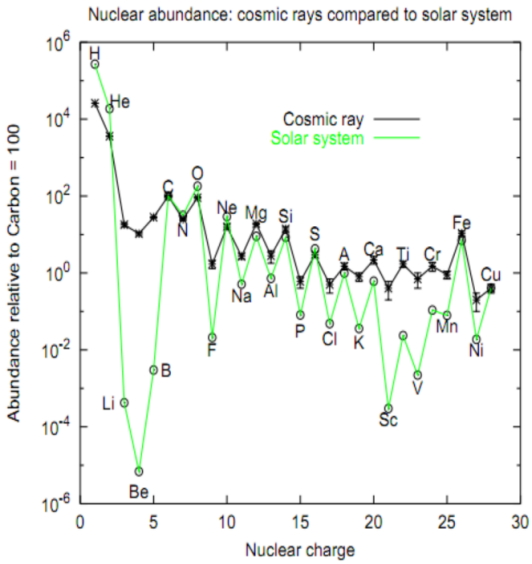

Figure 2.4: Relative abundance of elements in Cosmic Rays as compared to the Solar system

and Fe, respectively. The abundance of these secondary nuclei depends on the composition of the original primary cosmic rays and the propagation mechanism of cosmic rays throughout the galaxy. In the context of diffusion models discussed, the ratio of secondary-to-primary nuclei, such as Boron-to-Carbon and sub-Iron-to-Iron, can be used to constrain the diffusion coefficient of cosmic rays in the galaxy. An increase in the diffusion coefficient would result in faster escape of primary cosmic ray nuclei from the galaxy and a smaller amount of secondary cosmic ray nuclei being produced, and vice versa. Precise measurements of the B/C ratio across a range of energies could help to resolve the ambiguity of free parameters in different propagation models, as we will see later.

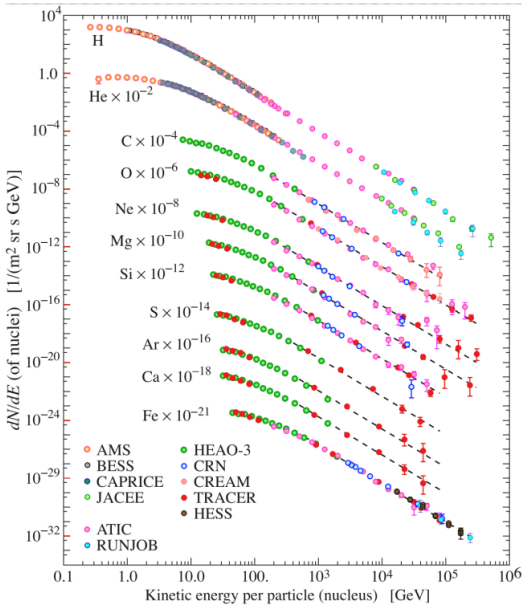

Figure 2.5: Cosmic Ray nuclei flux from different experiments [233]

The presence of antimatter components in cosmic rays is rare, but significant. Antimatter is not

found in the composition of the Solar System and is only produced in high-energy reactions. If we can properly understand and interpret these reactions, they can provide insight into the processes and components of our galaxy. For an instance, several CR detectors like PAMELA, and AMS-02 have reported an excess in the positron and antiproton fraction. Present effort, which includes the work of this thesis, involves concerted effort to understand if these excesses can be explained in terms of known physics, or requires the involvement of processes beyond SM like the annihilation of WIMP like DM candidates.

2.2.2 Energy Spectrum

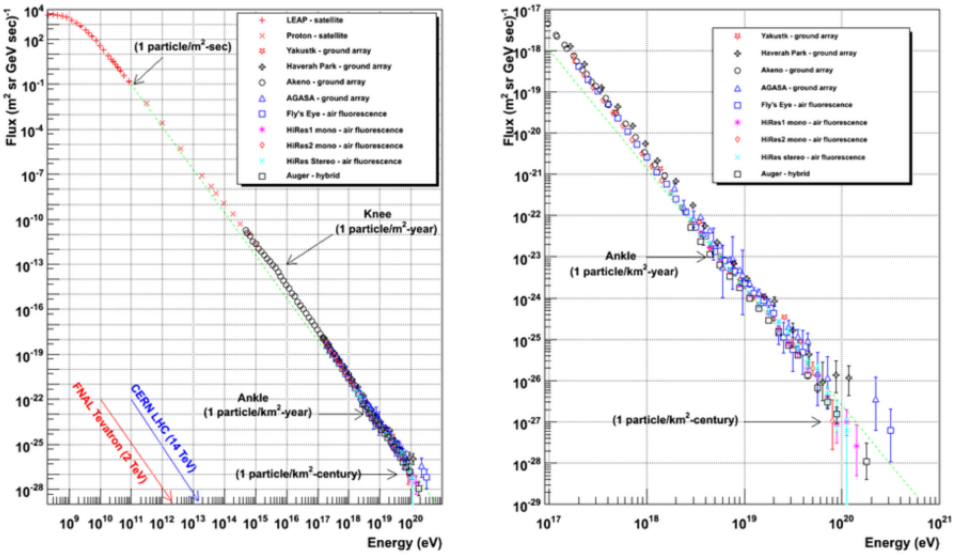

Figure 2.6: Differential energy spectra of Cosmic rays [218]

The energy spectrum for CRs can be described by a power law from 100 MeV to 1 TeV as follows:

$$N(E)dE = KE^{-\gamma}dE, \tag{2.1}$$

where $N(E)$ represents the number of CR nuclei as a function of energy (E), and γ is called the *spectral index*, and it varies from 2.5 to 3.

To explain the different features of the energy spectra in fig. 2.6, the spectra is divided into four primary zones.

- **Below** 1 **GeV/n**: A spectrum cutoff can be observed at energies below 1 GeV/n, which is caused by the interaction with the solar wind.
- **Between** 10^9 **eV and** 10^{15} **eV:** Most cosmic rays within this energy range are believed to originate from the Milky Way. The spectral index, represented by γ, ranges between 2.5 and 2.7, and the rate of occurrence at 10^9 eV is one particle per square meter per second. Primary species display less steep spectra than secondary species, which are the result of nuclear collisions between primary species. At 10^{15} eV, there is a noticeable bump in the spectra, referred to as the "knee," along with a change in slope. Galactic cosmic rays

that are below the "knee" are considered to have originated within our galaxy and were accelerated by shock waves created during supernova explosions, which are explosive events observed in most galaxies, including the Milky Way [62]. These cosmic rays then travel throughout the galaxy and are redirected many times by randomly oriented magnetic fields before eventually reaching the solar system. There are two primary factors believed to contribute to the "knee" phenomenon: the limitation of the maximum energy that cosmic accelerators can transfer and the less effective confinement of cosmic rays by galactic magnetic fields, which results in cosmic ray leakage [73].

- **Between 10^{15} eV and 10^{18} eV:** This region is considered the area where there is a transition between galactic and extragalactic phenomena. At higher energies, two breaks, a "second knee" and the "ankle", are observed in the spectrum at around 10^{17} and 10^{18} eV respectively as can be seen in fig.2.7. Beyond the "knee," the spectrum becomes steeper with a spectral index of approximately 3.2, and the rate of cosmic rays decreases to one particle per square meter per year. This range concludes with another distinctive feature in the spectrum, known as the "ankle". The "ankle" is typically understood to be a combination of two separate cosmic ray components, with a change in the abundance of the first component as it transitions to the second, which has a harder spectrum. One possible explanation for this variation in the spectrum is that charged particles with energies above the "ankle" cannot be confined within the Milky Way galaxy due to the weak strength of galactic magnetic fields. Based on estimates of the size of the galaxy (assuming a disk diameter of 20 kpc) and the strength of the magnetic fields ($1\mu G$), it is believed that the maximum energy of a relativistic particle that can be confined within the galaxy is approximately 10^18 eV. If sources within the galaxy were to produce particles with such high energies, small-scale anisotropies in the arrival directions of cosmic rays would be observed, which would pinpoint their origin. However, no such sources have been identified within the Milky Way so far, which suggests that above the "ankle," the cosmic ray flux is predominantly made up of particles from extragalactic sources [120].

- **Above 10^{18} eV:** The spectrum levels off to $\gamma = 2.5$ after the ankle, but the rate of particle detection is very low at about 1 particle per square kilometer per century, making it hard to accurately estimate the shape of the flux. The GZK (Greisen-Zatsepin-Kuzmin) limit is a theoretical cutoff point above 3×10^{19} eV [174]. According to GZK theory, CRs with energy exceeding this limit would interact with blue-shifted CMB photons, γ_{CMB}, to create pions via the Δ resonance.

$$\gamma_{CMB} + p \rightarrow \Delta^+ \rightarrow p + \pi^0$$
$$\gamma_{CMB} + p \rightarrow \Delta^+ \rightarrow n + \pi^+$$

Experimental evidence from the Telescope Array and the Pierre Auger Observatory shows that there is a notable decrease in the amount of cosmic rays with energies greater than 4×10^{19} eV [79].

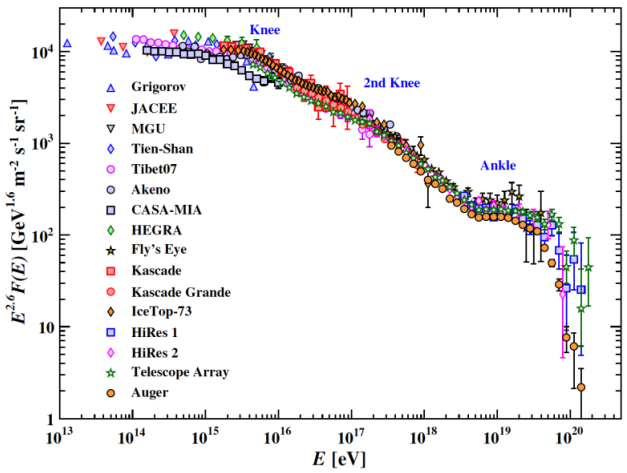

Figure 2.7: The all-particle spectrum from air shower measurements from below the knee to above the ankle. The spectra are scaled by a factor of $E^{2.6}$ [233]

.

2.3 Cosmic Ray Sources and Acceleration Mechanisms

The high energies of CRs suggest that they are generated by a very energetic astrophysical process within our galaxy. The average density of cosmic rays is approximately 1 eV/cm^3, and considering a galactic disc volume of 10^{63} cm^3, the total energy content of cosmic rays is about 10^{67} eV. The average confinement time for CRs is about 3×10^{14} s, and to maintain a stationary CR flux, approximately 5×10^{40} erg/s of energy supply is required. This energy supply must be provided by injection and acceleration of new CRs. The most likely source of CR acceleration is shock waves produced by Supernovae. Assuming a Supernova explosion rate of approximately 2 per century (equivalent to a rate of 1.5×10^{-9} Hz) and a typical yield of 10^{50} erg in fast particles, it can be estimated that the average power of this process is around 10^{41} erg/s. Pulsars and Neutron Stars in close binary systems may also be sources of CR acceleration, but the physical mechanism responsible for the acceleration of CR is still unclear.

Enrico Fermi put forward a concept of diffusive shock acceleration in 1949, which involves particles being sped up through collisions with magnetized clouds that are in motion [158]. This acceleration method was able to predict the power-law shape of CR spectrum, although with a spectral index that is less steep than the observed one. There are two variations of Fermi acceleration known as "*first-order*" (1954) and "*second-order*" (1949) acceleration, depending on whether the energy gain is proportional to $\beta = v/c$ or to β^2. A pictorial representation of both the mechanisms can be seen in fig.2.8. The former type is more effective and is thought to happen directly at the source, whereas the latter is less effective and could occur during propagation, which is why it is also referred to as "reacceleration." This mechanism can be supported by the synchrotron radiation that is observed from electrons that are being accelerated at the front of a shock wave in Supernova Remnants (SNR), as well as the π^0 lines that result from the interactions between accelerated protons and molecular clouds that are located nearby. These interactions have been observed by the Fermi experiment [12].

Acceleration of cosmic rays becomes increasingly challenging to understand once they surpass

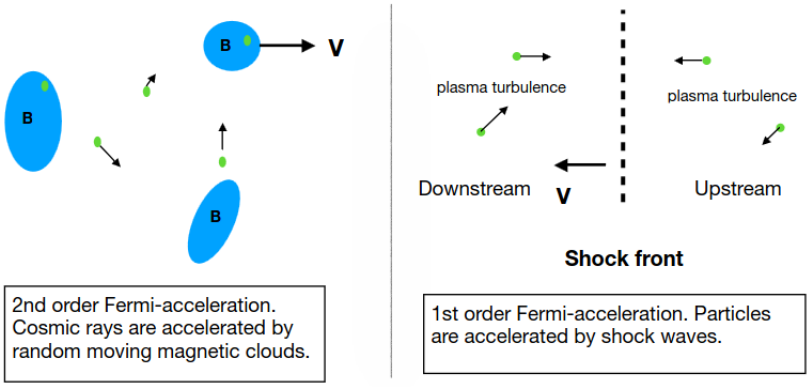

Figure 2.8: 2nd and 1st order Fermi-acceleration in astrophysical media and shock waves. Picture taken from [103]

the 10^{15} GeV threshold. At this point, various other mechanisms must be considered, such as AGN (Active Galactic Nucleus) jets, Galactic and Extragalactic halos, and Magnetars. The acceleration of CRs at energies beyond the *ankle* is still a mystery since no appropriate sources have been identified or modeled thus far. A comprehensive picture depicting the production of CR till it reaches the Earth is shown in 2.9.

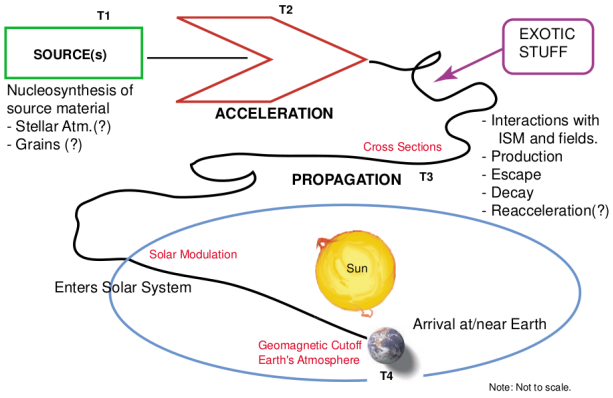

Figure 2.9: Cosmic ray journey from production site to the Earth's atmosphere. Figure from [283].

2.3.1 Second Order Fermi Acceleration

Fermi's original idea proposed that magnetic clouds that move slowly and are denser than the ISM could be responsible for the reacceleration of CRs. If the magnetic field is stationary, the particle will only reverse its direction similar to the trapped particles in the Earth's radiation belts. However, if the magnetic field is in motion, the particle can gain energy. When a fast-moving particle enters these clouds, it gets scattered by irregularities in the magnetic field, which changes its momentum. Depending on whether the particle's momentum is opposite or in the same direction as the cloud's velocity, there is either a loss or gain of energy, respectively. As frontal collision is more likely, the overall result is an energy gain for the swarm of galactic particles. Additionally, since the magnetic irregularities in the field are random, the multiple scattering process inside the cloud can be seen as a random walk as seen in fig.2.10 .

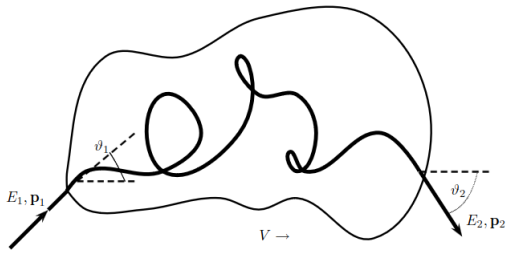

Figure 2.10: Elastic scattering of a cosmic ray in a magnetic cloud. Picture taken from [186].

We consider a relativistic particle entering a slowly moving magnetic cloud. the quantites in the cloud rest frame are denoted by a prime. As such, a simple Lorentz transformation yields [145, 186]

$$E'_{in} = \gamma E_{in}(1 - \beta \cos\theta_{in}), \tag{2.2}$$

where θ_{in} denotes the angle between the moving direction of the particle and that of the cloud, whereas, E_{in} is the energy of the particle in the lab frame, where the cloud has a speed v. Here, β, and γ are parameters pertaining to the cloud. Denoting E'_{out}, and θ'_{out}, as the energy of the particle after collision, and it's exiting angle respectively, we can perform an inverse transform back to the lab frame in the following manner

$$E_{out} = \gamma E'_{in}(1 - \beta \cos\theta'_{out}), \tag{2.3}$$

Assuming elastic scattering, we have, $E'_{out} = E'_{in}$. Using this fact in (D.21), and substituting (D.16) in it, we obtain

$$E_{out} = \gamma^2 E_{in}(1 - \beta \cos\theta_{in})(1 + \beta \cos\theta'_{out}). \tag{2.4}$$

Hence, the net relative energy gain in the original particle rest frame is

$$\frac{\Delta E}{E} = \frac{E_{out} - E_{in}}{E_{in}} = \frac{1 + \beta(\cos\theta'_{out} - \cos\theta_{in}) - \beta^2 \cos\theta'_{out}\cos\theta_{in}}{1 - \beta^2} - 1. \tag{2.5}$$

Particles scatter on the cloud randomly in all directions. As such, to obtain the average energy gain, we take the average of (D.22), with respect to both angles, θ_{in}, and θ'_{out}, in the following fashion

$$\left\langle \frac{\Delta E}{E} \right\rangle = \int_{-1}^{1} d\cos\theta_{in} \int_{-1}^{1} d\cos\theta'_{out} \frac{\Delta E}{E} P(\cos\theta_{in}) \cdot P(\cos\theta'_{out}), \tag{2.6}$$

where $P(\cos\theta)$ is the probablity distribution for the angle θ. For CRs, the collision rate with the cloud is proportional to their relative velocity given by, $(v - V\cos\theta_{in})$, but for ultra-relativistic particles, i.e., $v \to c$, we can write that, $P(\cos\theta) \propto (1 - \beta\theta)$.

Furthermore, as the CRs scatter off the magnetic irregularities numerous times in the cloud, their exit direction is random, and hence, $\langle \cos\theta'_{out} \rangle = 0$. So, we obtain

$$\langle \cos\theta_{in} \rangle = \frac{\int_{-1}^{1} \cos\theta_{in} P(\cos\theta_{in}) d\cos\theta_{in}}{\int_{-1}^{1} P(\cos\theta_{in}) d\cos\theta_{in}} \approx \frac{\int_{-1}^{1} (x - \beta x^2) dx}{\int_{1}^{-1} (1 - \beta x) dx} \approx -\frac{\beta}{3}. \tag{2.7}$$

Substituting the mean values in (D.24), and doing a Taylor expansion ($\beta^2 \ll 1$), we obtain for the average energy gain

$$\left\langle \frac{\Delta E}{E} \right\rangle \approx \frac{1 + \frac{\beta^2}{3}}{1 - \beta^2} - 1 \approx \frac{4}{3}\beta^2. \tag{2.8}$$

Although, the 2nd-order Fermi acceleration mechanism predicts a power-law spectrum, it has many shortcomings:

- The theory doesn't take in consideration energy losses by ionisation, that would compete with energy gains

- Given that the density of observed clouds is low, and their velocities are small, with a ratio of v/c approximately equal to 10^{-4}, it is expected that collisions would be infrequent, occurring only a few times per year, due to the relatively small mean free path of CR of approximately $0.1\ pc$ Consequently, the probability of gaining significant energy from such collisions would also be low

- The theory doesn't provide us the observed value of $\gamma \sim 2.7$

2.3.2 First Order Fermi Acceleration

In 1954, an improved acceleration mechanism for CRs was developed, which was further developed by Anthony Raymond Bell [70, 71]. Consider an ideal fluid with pressure P, and density ρ. Basic hydrodynamical equations tells us that the sound velocity would be $c_s = (\partial P/\partial\rho)^{1/2}$, which is the speed of density perturbations. The equation of state for a mono-atomic gas is given as $P = K\rho^\gamma$, with $\gamma = 5/3$. Hence, if an adiabatic compression with density, $\rho_1 = \epsilon\rho$ propagates, then we will have, $c_s \propto \epsilon^{(\gamma-1)/2}$. Which implies that the sound speed increases for a compression, and the dense regions overruns uncompressed region, and makes it even denser, resulting in the development of a discontinuity in some hydrodynamical variable like density, also called a "*shock*".

Let us consider a stationary fluid with density ρ_1 (up-stream region), and a perturbation zone (down-stream region) with a higher density ρ_2, moving with velocity v'_{out} as shown in fig. 2.11.

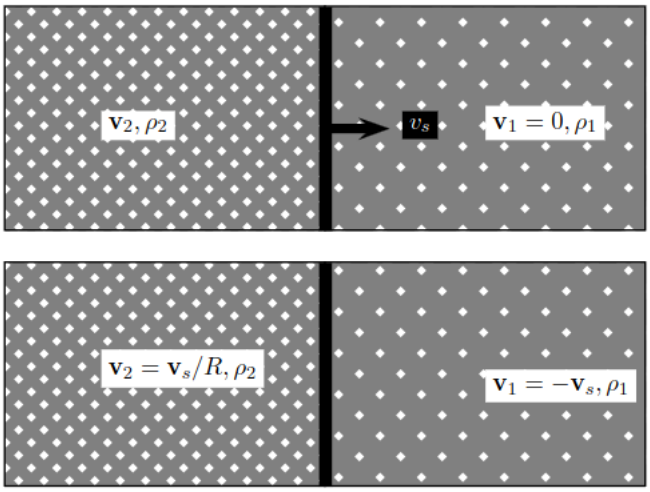

Figure 2.11: Conditions on the down-stream (left) and the up-stream (right) side of a shock in the lab system (top) and in the shock rest frame with $v_1 = -v_s$ (bottom). Here $v_2 = v_{in}$, and $v_1 = v_{out}$. Picture taken from [186].

These two regions will be separated from a shock front moving with velocity v_s. The up-stream flows with a velocity v_{in}, and the down-stream with velocity v_{out}, and we assume that the magnetic and gravitational fields can be ignored. As such, we can derive from the fluid equations in the reference frame of the shock, that the velocities in the two regions are related as

$$\frac{v_{in}}{v_{out}} = \frac{\gamma + 1}{\gamma - 1}. \tag{2.9}$$

The above relation yields a value of 4 for a monoatomic gas. It implies that irrespective of the strength of a shock, it can compress a monoatomic gas only by a factor of four. In terms of kinematics, the calculation for the 2nd-order Fermi acceleration is only distinct in the way the scattering process is arranged geometrically, leading to different average values for the cosines of the incoming and outgoing angles. The approximation here assumes a planar shock, so the crossing rate is determined by projecting a flux that is isotropic onto the planar shock

$$P(\cos\theta_{in}) = \begin{cases} 2\cos\theta_{in} & \cos\theta_{in} < 0 \\ 0 & \cos\theta_{in} \end{cases}. \tag{2.10}$$

Likewise, the outgoing probability is

$$P(\cos\theta'_{out}) = \begin{cases} 2\cos\theta'_{out} & \cos\theta'_{out} > 0 \\ 0 & \cos\theta'_{out} \end{cases}, \tag{2.11}$$

such that the averages are

$$\langle\cos\theta_{in}\rangle = \frac{2}{3}; \quad \langle\cos\theta'_{out}\rangle = -\frac{2}{3}. \tag{2.12}$$

Substituting everything in (D.16), we get

$$\left\langle \frac{\Delta E}{E} \right\rangle = \frac{4}{3}\beta = \frac{4}{3}\frac{v_{out} - v_{in}}{c}. \tag{2.13}$$

Energy Spectrum: Consider a particle that undergoes multiple scattering with the magnetic cloud. As such, its final energy after n collisions can be written as

$$E_n = E_{in}\xi^n \quad \text{where,} \quad \xi = 1 + \frac{\delta E}{E}. \tag{2.14}$$

The number of collisions required to reach the energy E_n is

$$n = \frac{\ln \frac{E_n}{E_{in}}}{\ln \xi}. \tag{2.15}$$

We now denote the probability of escaping the magnetic cloud as p_{esc}. Hence, the probability to stay in the acceleration region after n crossings is $(1-p_{esc})$. As such, the fraction of particles with energy, $E > E_n$ is given by

$$f(E_n) = \sum_{m=n}^{\infty}(1-p_{esc})^m = \frac{(1-p_{esc})^n}{p_{esc}} = \frac{1}{p_{esc}}\left(\frac{E_n}{E_{in}}\right)^{1+\gamma}, \tag{2.16}$$
$$\text{with} \quad \gamma = \frac{\ln(1-p_{esc})}{ln\xi} - 1.$$

Here (2.16) shows a power-law behaviour. It describes the integral spectrum of particles leaving the acceleration region, and has a power-law with spectral index $\gamma + 1$. Hence, the differntial spectrum would always be a power-law albeit with spectral index γ. Furthemore, as $p_{esc} < 1$, and $\xi > 1$, the spectral index of outgoing particles will be negative.

To derive the spectral index of the escaping particles, we note that

$$\xi = 1 + \frac{4}{3}\beta = \frac{4}{3}\frac{v_{out} - v_{in}}{c}. \tag{2.17}$$

As such, we have to determine the escape probability p_{esc}, to estimate the spectral index γ of the differential spectrum as a result of shock acceleration.

Making the assumption that, $v_s \ll c$, and an efficient isotropisation of CR up-stream. We can write that the particle flux Φ because of an infinite, planar shock front is related to the isotropic intensty I, and to the particle density n by

$$\Phi(E) = \pi I(E) = \frac{cn(E)}{4}. \tag{2.18}$$

In the shock rest frame, the particle flow, $\Phi_{esc} = v_{out}n(E)$, away from the shock front that would be lost by acceleration process. Hence, the p_{esc} can be expressed in terms of the ratio of

the loss and crossing flux as

$$p_{esc} = \frac{\Phi_{esc}}{\Phi} = \frac{4v_{out}}{c}. \tag{2.19}$$

Employing a Taylor expansion for γ, we get

$$\gamma \approx -1 - \frac{p_{esc}}{\xi - 1} = -1 - \frac{3}{\frac{v_{in}}{v_{out}} - 1}. \tag{2.20}$$

In the strong shock approximation, $v_{in} = 4v_{out}$. Hence,

$$\gamma \approx -2. \tag{2.21}$$

Fermi's theory suggests that the exponent anticipated at non-relativistic shock is not reliant on the shock parameters. It is in agreement, to a first-order degree, with the value required to clarify the spectrum of galactic cosmic rays. Whenever a supernova explosion happens, matter is released into the ISM, and a robust shock wave is created that expands and eliminates matter. If the diffusion mean-free-path is much smaller than the shock front curvature, then the planar shock approximation can apply, and first-order Fermi acceleration can occur. Due to these reasons, Fermi's theory of cosmic ray acceleration has gained widespread acceptance.

2.4 Galactic Propagation of Cosmic Rays

Once they depart from their source, CRs are injected into the Galaxy, where they interact with the ISM and the galactic magnetic field. These cosmic rays move in helical trajectories around the large-scale magnetic field lines and encounter its small-scale irregularities, which act as scattering centers without collisions. The Milky Way galaxy can be characterized as a spiral shape resembling a disc, with a barred central bulge that (as illustrated in fig. 2.12). The disc has a diameter of around $30\ kpc$ and a thickness ranging from $300 - 1000\ pc$. Throughout the disc, there is an average magnetic field of strength $1 - 3\ nT$, although there are random irregularities in both intensity and direction that superimpose upon it. These irregularities cause stochastic diffusion of high-energy charged particles in CRs. The turbulent galactic field has a coherence scale of approximately $10\ kpc$. The galactic magnetic field extends beyond the disk and into a larger halo that governs the region where diffusion occurs. Consequently, a CR particle traveling from the source to Earth may pass through regions with different propagation conditions. Precise knowledge of the magnetic field within the galaxy is crucial for understanding the propagation of cosmic rays.

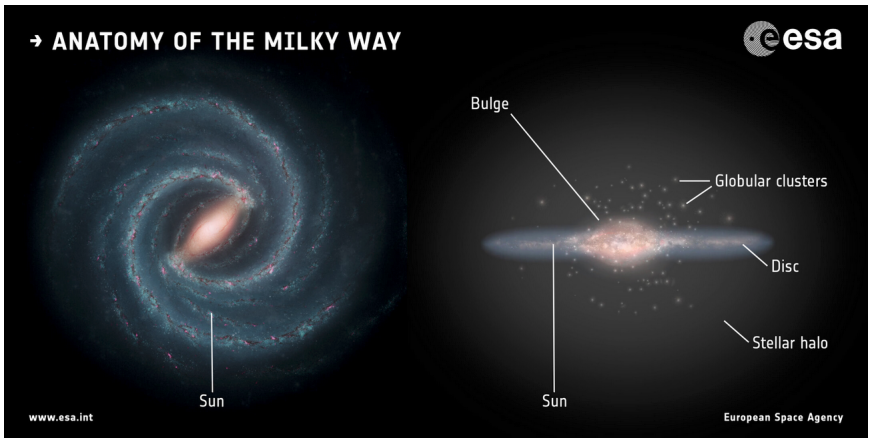

Figure 2.12: Anatomy of Milky Way Galaxy. Souce: [1]

2.4.1 Galactic Magnetic Field

In spiral, barred, irregular, and dwarf galaxies, magnetic fields play a crucial role in the ISM. They contribute significantly to the overall pressure that maintains the ISM in equilibrium against gravitational forces. Additionally, magnetic fields may impact the gas flows in various regions of the galaxy, including spiral arms, bars, and halos. The presence of magnetic fields is vital to the initiation of star formation, as they facilitate the removal of angular momentum from the protostellar cloud during its collapse. Magnetohydrodynamic (MHD) turbulence is responsible for distributing energy from supernova explosions throughout the ISM. Moreover, magnetic reconnection represents a potential source of heat for both the ISM and the halo gas. The density and distribution of CRs in the ISM are also influenced by magnetic fields. Initially, evidence of the Galactic magnetic field was obtained by analyzing the linear polarization of starlight. Subsequently, additional measurements were conducted using various methods, such as Zeeman spectral-line splitting, which involves gaseous clouds and the central region of the Galaxy, and optical polarization data, which reveals the large-scale structures of the magnetic field in the local spiral arm. Faraday rotation measurements, taken from radio continuum emissions of pulsars and extragalactic sources, represent the most dependable approach to assess large-scale magnetic field structures. Through the examination of rotation measurements, it has been determined that the Galactic magnetic field possesses a bi-symmetric spiral structure at larger scales, while it displays a turbulent nature at smaller scales, typically below several hundred parsecs. The magnitude of the large-scale magnetic field is a few microgauss and is comparable to that of the turbulent component found within the Galactic disk [69, 181, 182, 254, 260].

Consider a spherical coordinate system, with the origin at the centre of the galaxy, and the y axis oriented to the Earth. Consequently the Earth coordinates can be written as, $r = R, \theta = \pi/2, \phi = \pi/2$. Where $R = 8.5\ kpc$, i.e., the distance of the Earth from the galactic center, and θ spans from 0 to π from the north to the south galactic pole. The field strength given by this spiral model at a point defined as, $(r, \psi = \pi/2 - \phi)$, in the galactic plane of the bi-symmetric

model is

$$B(r,\phi) = B_0(r)\cos\left(\psi - \beta \ln\frac{r}{r_0}\right). \tag{2.22}$$

The radial and azimuthal components are given as

$$B_r = B_0(r,\phi)\sin p, \tag{2.23}$$

$$B_\phi = B_0(r,\phi)\cos p. \tag{2.24}$$

Here, $p = -10^\circ$ is the pitch angle, where the pitch angle determines the local regular magnetic field orientation. And, $r_0 = 9kpc$, is the galactocentric distance of the maximum field strength at galactic longitude, $l = 0^\circ$, and $B_0(r) = 3R/r$, where B is expressed in μG. The magnetic field above and below the galactic plane is an exponential function, and is given as

$$B(r,z,\phi) = B(r,\phi)\exp\left(-\frac{z}{z_0}\right), \tag{2.25}$$

where $z_0 = 1\ kpc$.

2.4.2 Deflection of Cosmic Rays by Magnetic fields

The Lorentz force on a charged particle in a magnetic field is given by

$$m_0\gamma\frac{d\vec{v}}{dt} = Ze(\vec{E} + \vec{v}\times\vec{B}), \tag{2.26}$$

where Ze is the particle charge, $\vec{v}$ is the particle velocity, γ is the Lorentz factor, $\vec{E}$, and $\vec{B}$, are the electric and magnetic fields respectively. Since, galaxies don't have $\vec{E}$, the equation of motion reduces to

$$m_0\gamma\frac{d\vec{v}}{dt} = Ze(\vec{v}\times\vec{B}). \tag{2.27}$$

We now resolve $\vec{v}$ into components parallel and perpendicular to $\vec{B}$, and denote them as $v_\parallel$, and $v_\perp$. The angle between $\vec{v}$ and $\vec{B}$, is called the pitch angle θ, and is given by $\tan\theta = v_\perp/v_\parallel$. Since, $v_\parallel$ is parallel to $\vec{B}$, (2.27) implies that $v_\parallel = constant$. Hence, the only acceleration provided is

$$m_0\gamma\frac{dv_\perp}{dt} = Zev_\perp B. \tag{2.28}$$

The above relation describes a motion in a circle. Equating it with the centripetal acceleration gives us

$$\frac{v_\perp^2}{r} = \frac{Zev_\perp B}{m_0\gamma}, \tag{2.29}$$

and hence, we get for the radius

$$r = \frac{m_0\gamma v\sin\theta}{ZeB}. \tag{2.30}$$

So, the motion is helical with a constant pitch angle θ. We can re-write the above as

$$r = \frac{m_0\gamma v}{Ze}\frac{\sin\theta}{B} = \frac{pc}{Ze}\frac{\sin\theta}{Bc}. \tag{2.31}$$

The quantity pc/Ze is called the magnetic rigidity. Particles injected with same magnetic rigidity follows the same trajectory if they have the same pitch angle.

2.4.3 Cosmic Ray Propagation equation

A system of Fokker-Planck type equations is typically used to describe the stationary state of equilibrium resulting from cosmic ray production, acceleration, diffusion on the stochastic irregularities of the galactic magnetic field, self interactions and interactions with ISM and leakage/re-absorption.

The *Transport Equation* describes the density evolution per momentum units p for the i^{th} species (ψ_i), and is given by

$$\frac{\partial\psi(\vec{r},p,t)}{\partial t} = q(\vec{r},p,t) + \vec{\nabla}\cdot\left(D_{xx}\vec{\nabla}\psi_i - \vec{V}\psi_i\right) + \frac{\partial}{\partial p}p^2 D_{pp}\frac{\partial}{\partial p}\frac{1}{p^2}\psi_i - \frac{\partial}{\partial p}\left[\dot{p}\psi_i - \frac{p}{3}\left(\vec{\nabla}\cdot\vec{V}\right)\psi_i\right] - \left(\frac{1}{\tau_{frag}} - \frac{1}{\tau_{decay}}\right)\psi_i \tag{2.32}$$

This is a system of coupled differential equations, which has to be solved simultaneously taking in consideration different astrophysical parameters, such as ISM gas density distribution, magnetic field map, source distribution, and the galactic halo shape. All the terms of the equation are briefly expounded below:

- **Source term, $q(\vec{r},p,t)$:** It denotes all the possible production mechanisms for the particles of a given species. It can be further broken down as follows:

$$q_i(\vec{r},p,t) = S_i(\vec{r},p,t) + n\sum_{j>i} v_j\sigma_{ij}\psi_j + \sum_{j>i}\frac{\psi_j}{\tau_{ij_{frag}}}. \tag{2.33}$$

  The primary term describes the astrophysical distribution, the second term describes the secondary production from spallation of all the heavier nuclei, and the third term denotes the contribution from radioactive decay of other species.

- **Diffusion terms, D_{xx}, D_{pp}:** The charged CR particles along with the stochastic variability of the galactic magnetic field causes diffusion of CR that results in an isotropic distribution of CRs.

  This variable magnetic field can be decomposed into a constant background field ($B_G \sim \mu G$) [68], that follows the matter distribution in galaxy, and a turbulent part that is depicted as a perturbation of the field, $\delta B \ll B$. The perturbations contribute to random deviations to the theoretical bending given by the B_G mean field, which results in a diffusive motion of the particles encoded by the spatial diffusion parameter D_{xx}. This is of the order of $3 - 5 \times 10^2 8\ cm^2 s^{-1}$ at $1\ GeV/n$.

Interaction of CRs with the irregular nature of the field results in further acceleration of the CRs, called "*re-acceleration*" [93], denoted by diffusion in momentum space, and encoded in the propagation equation as $D_{pp} \propto |\vec{V}^2| D_{xx}$, where, $\vec{V}$, is called the Alfvén velocity, which is the characteristic propagation speed of the stochastic fluctuations of the magnetic field.

- **Convection, $\vec{\nabla} \cdot \vec{V}\psi_i$:** This term arises from the fact that galactic winds influence the transport of CRs. These winds cause an adiabatic expansion of the galactic gas by virtue of dilution of the energy of the particles. This phenomenon is called "*adiabatic deceleration*", and results in energy loss, which is dependent on the galactic wind velocity, $V \equiv V(t, \vec{r})$.

- **Nuclear processes, $\tau_{frag}, \tau_{decay}$:** These two terms denotes the time scales for loss by fragmentation, and radioactive decay respectively. The decay of unstable nuclei has a probability per unit time given by, $\Gamma = 1/\tau_{decay}$, and results in loss rate $-\psi_i/\tau_{decay}$.

  Spallation of CRs with ISM also results in the evolution of the density of a particular species, the time scale of which is given by, $\tau_{frag} = 1/n_{ISM}\sigma_{frag}$, where, n_{ISM}, is the ISM density, and σ_{frag} is the total inelastic cross-section of the interactions. In this case, the loss rate is given by, $-\psi_i/\tau_{frag}$. Combining both the factors, the total nuclear timescale for nuclear loss is given by

$$\frac{1}{\tau} = \frac{1}{\tau_{frag}} + \frac{1}{\tau_{decay}}. \tag{2.34}$$

- **Continuous energy losses, $-\frac{\partial}{\partial p}(\dot{p}\psi_i)$:** CR while propagating through the ISM suffers continuous energy loss. Nuclei primarily lose their energy through ionisation processes, while $e^{\pm}$ lose energy mainly through synchrotron radiation, and inverse compton processes.

2.4.4 The Leaky-Box Model

The basic assumptions of the LBM model are as follows:

- The diffusion takes place rapidly
- The CR distribution is homogeneous, where the galaxy is considered as a box.
- CRs are free to propagate in the galaxy with a characteristic escape time τ_{esc}
- The CRs have a probability of undergoing inelastic nuclear interactions, i.e., fragmentation, decay, etc.

As such, the number of escaping particles per unit time is proportional to the number of particles in the box. We consider a steady-state solution, and hence, $\dfrac{\partial \psi}{\partial t} = 0$, and the spatial diffusion

term is approximated as

$$\vec{\nabla} \cdot \left(D_{xx} \vec{\nabla} \psi_i \right) = -\frac{\psi_i}{\tau_{esc}} \tag{2.35}$$

Using (D.35),(D.34), and a steady-state, along with, $1/\tau_{frag} = nv\sigma_i$, (D.29) becomes

$$\langle q_i \rangle - \frac{\psi_i}{\tau_{esc}} - \frac{\partial}{\partial p}\left(\dot{p}\psi_i\right) - \left(-\langle n \rangle v\sigma_i + \frac{1}{\tau_{i_{frag}}} \right) \psi_i + \sum_{j>i} \left(-\langle n \rangle v\sigma_{ij} + \frac{1}{\tau_{ij_{frag}}} \right) \psi_j = 0, \tag{2.36}$$

where, $\langle q_i \rangle$, and $\langle n \rangle$, represent the time and space averaged source and particle densities. The experimental input parameter from phenomenology here is the term τ_{esc}. In this simplistic description, other energy changing processes, and convection are neglected.

This model allows us a direct analysis of flux measurements as a function of three fundamental parameters:

- the escape time
- mean matter density
- source abundance

This model reproduces the main observed features of secondary to primary CR ratios quite well.

2.4.5 Numerical Solution of Transport Equation

The ever increasing power of computation over the decades has permitted physicists to modelise (D.29), and adopt numerical solutions instead of a simplistic LBM model.

The numerical model that is mostly used for CR physics is GALPROP model [258,268], which incorporates many different inputs from astrophysical, and astroparticle measurements. It performs CR propagation calculations for nuclei (isotopes of H to Ni), $\bar{p}, e^{\pm}$, $\gamma-$ rays, and synchrotron emission within the same framework. The propagation can be performed in two coordinate systems, i.e., in a 3-D grid in a cylindrical coordinate system (where r is the distance from the source, z denotes the vertical distance from the galactic plane, and p is the particle momentum), or in a 4-D Cartesian grid (where x, y, z are the spatial coordinates, and p is the momentum). In both the cases, the integration steps can be chosen either in the spatial, or the momentum coordinates.

In GALPROP, the galaxy is considered as a dense central disk with thickness $2h$, surrounded by a cylindrical halo, with CR trapped because of the galactic magnetic field. The CR sources originates in the central disk, and is the only place where matter-CR interactions take place. The halo half size is one of the most important parameter that has to be given by the user (ranges from few kpc to $\sim 20\ kpc$, as indicated by radioactive nuclei studies and synchrotron radiation distribution), whereas, the radial halo extension is fixed to $30\ kpc$. Outside the cylindrical halo,

CR are assumed to be free to escape, whereas, diffusion and reacceleration are considered to be the main propagation mechanisms inside.

Accurate modelisation of the ISM is of prime importance, for secondary CR production, and estimating energy losses. It's considered to be primarily composed of hydrogen in three forms: atomic hydrogen HI, molecular hydrogen H_2, and ionised hydrogen HII. The second abundant element in ISM is He, with a ratio to H of, $He/H = 0.10 \pm 0.08$.

Analysis of scattering of particles by random weak-MHD waves, suggests a spatial diffusion coefficient of the form:

$$D_{xx} = \beta D_0 \left(\frac{R}{R_0}\right)^{\delta}, \tag{2.37}$$

where, δ is the spectral index. In diffusive reacceleration, D_{pp}, and D_{xx}, are related as

$$D_{pp}D_{xx} = \frac{4p^2 v_A^2}{3\delta\,(4-\delta^2)\,(4-\delta)w}, \tag{2.38}$$

where, v_A is the Alfvén speed in the plasma, and w encodes the MHD wave turbulence.

After defining the spatial distribution of the source, the CR energy spectrum, and composition at the source, the transport equation is solved initiating from the heaviest nuclei (which is generally, ^{64}Ni), and then computing all the intermediate resulting secondary source functions, and progressively proceeding towards the nuclei with mass, $A-1$. An iterative process continues the procedue till it reaches, $A = 1$.

2.5 Heliosphere and Solar Modulation

Our Sun is located in the spiral arm of Milky Way, at a distance of $\sim 8.5\ kpc$ from the center, while it is at $1\ AU$ from the Earth. The electric currents in the interior of the sun, along with high conductivity give rise to a structure which is regarded as a MHD dynamo, that generates the magnetic field of the Sun. The rotation of the Sun further enhances the magnetic field in a self-exciting fashion. The field inverts its polarity with a period of 11 years, and hence takes in total 22 years to return to a previous configuration. The periodicity of 11 years is called the "*Solar Activity Cyle*". Although the exact mechanism is still a debatable topic, it is well established that the sunspot number and the periodicity is a direct consequence of the ropes of magnetic field lines emerging onto the Sun's Photosphere. Interestingly, the Sun doesn't behave like a rigid body, and possesses differential rotation, as the equator rotates with a higher angular velocity than the poles. As such, the resulting magnetic field is distorted and twisted over time. These twisted field lines, eventually emerges onto the Photopshere, and manifests as sunspots.

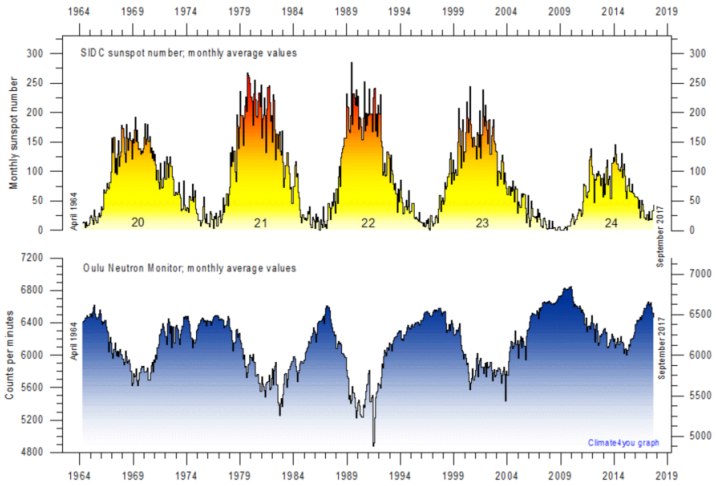

Figure 2.13: Comparison between sunspot numbers, and neutron monitor counters. High sunspot activity has a negative correlation with CR intensity. Source: https://www.sidc.be/

The sunspot number has a positive correlation with the solar activity 2.13, whereas, there is an anti-correlation between CR intensity and solar activity, as measured by ground-based neutron monitors. The latter is a very stable counter, that measures the total neutron and muon flux, produced by the CR interactions with atmospheric nuclei.

The magnetic field behaves as a dipolar one, during a solar minimum, with its axis almost aligning with the solar rotation axis, whereas, the dipole is tilted during a maximum. The angle between the rotation and magnetic axis is called the tilt angle α. The dipole term of the magnetic field dominates, however, as the solar maximum approaches, the dipolarity distorts. The solar magnetic epoch is referred to as $A > 0$, or $A < 0$, depending on whether the dipole is oriented parallel or anti-parallel to the rotation axis, as shown in fig. 2.14

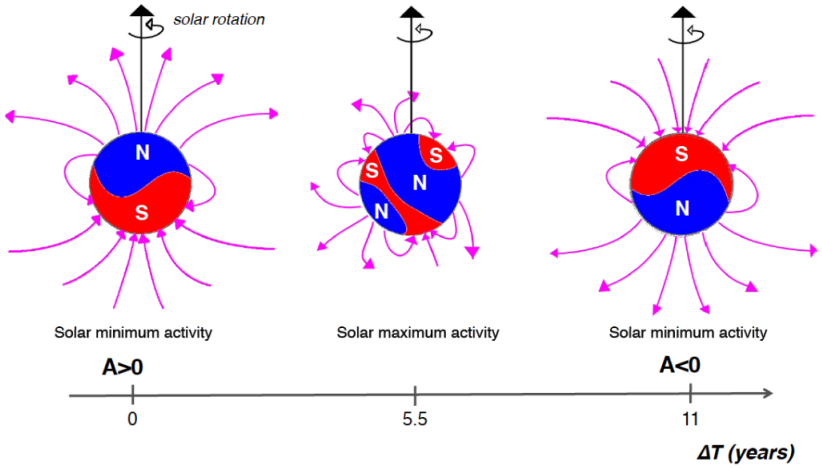

Figure 2.14: Solar periodicity starting from a solar minimum of positive polarity ($A > 0$), to that of a solar minimum of a negative polarity ($A < 0$).

As a result of the high temperature of the ionised gas inside Sun's Corona, it isn't gravitationally bounded well, and constantly blows away from the Sun's surface to establish hydrostatic equilibrium. This supersonic solar plasma expanding into space is known as the "*Solar Wind*",

which consists of a stream of $1-10\ keV\ e, p$, and He nuclei that travel through the solar system with a velocity $v \sim 400\ km/s$.

The solar wind can be regarded as an ideal plasma with zero resistivity. This leads to the condition of magnetic flux freezing, i.e., the magnetic flux through any closed contour in the plasma is a conserve quantity, given that each element of the plasma within the contour, moves with the local plasma velocity. Phenomenologically, this means that the magnetic field lines originating at the Sun's surface are carried away by the solar wind, as it expands into the interplanetary space. This results in the formation of a volume of space called the "*Heliosphere*" 2.15.

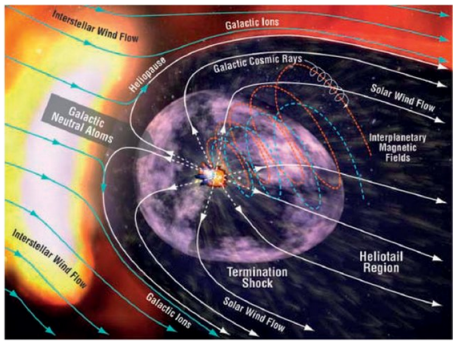

Figure 2.15: Schematic representation of the Heliosphere. Picture taken from [259]

At the Heliopause, the plasma pressure of the solar winds reaches an equilibrium with the ISM. The solar wind slows down and becomes subsonic beyond the Termination Shock (TS). On the other side, the point where the ISM travelling in the opposite direction becomes subsonic as a consequence of collision with the Heliosphere is called the *Bow Shock*.

The magnetic structure inside the Heliosphere (HMF), is described by a spiral structure of the form

$$\vec{B} = \frac{A}{r^2}\left(\vec{e}_r - \tan\psi\vec{e}_\psi\right)\left[1 - 2\mathcal{H}\left(\theta - \frac{\pi}{2}\right)\right], \tag{2.39}$$

where, $\vec{e}_r$, and $\vec{e}_\psi$ are the radial and azimuthal unit vectors, ψ is the local angle of the HMF field, $\mathcal{H}$ is a Heaviside step function, and A is some constant. The Heliospheric Current Sheet (HCS), a flat surface ($\theta = \pi/2$), separates the two heliospheric hemispheres. This is effectively the extension of the solar magnetic equator into the solar wind. Across the HCS, the polarity of the HMF changes. Above $\pi/2$, the field points in one direction, and below $\pi/2$, the field reverses the direction. This formula is valid only during a solar minimum, i.e., when the dipole and rotation axis aligns. When this condition is not met, the flat HCS assumes a wavy form. The tilt angle α is proportional to the latitudinal extent of the HCS. As such, large tilt angles correspond to a more undulated HCS.

During periods of negative polarity ($A < 0$), as depicted in fig. 2.16, positive CR particles move towards the inner Solar System, mostly through the regions near the Solar System plane, and the movement is dominated by drift along the HCS. Whereas, during periods of positive polarity ($A > 0$), charged particles originating from the polar regions of the Heliopause, propagates

towards the Earth effectively suffering minimal energy losses in the propagation. In such cases, the propagation is expected to be independent of α, whereas, for propagation through the HCS, the incurred energy losses is proportional to α.

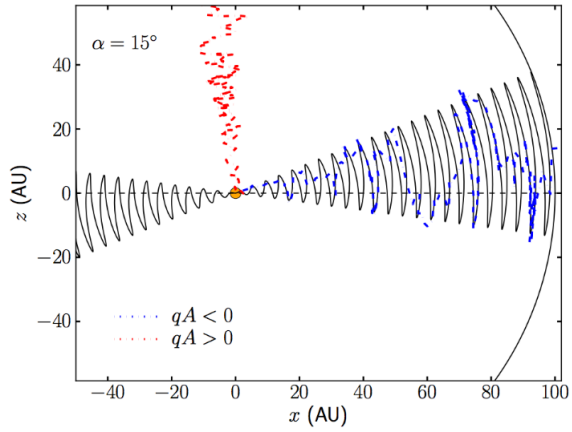

Figure 2.16: CR propagation through the Solar System [109]. Depending on the polarity of the HMF, CRs follow different trajectories to reach the Earth. During negative polarity ($A < 0$), positively charged CRs drift along the HCS, which is shown as the periodic solid line, and propagates across layers of HCS via diffusion. Whereas, particles diffuse more directly in efficient manner with minimal energy losses during periods of positive polarity ($A > 0$). The Heliospause is represented by the curved line here.

The propagation of CRs through the HMF was derived by Parker [232], assuming that galactic CRs reach the Heliosphere isotropically, and is given by

$$\frac{\partial \psi}{\partial t} = -\left(\vec{V} + \langle \vec{v}_D \rangle\right) \nabla \psi + \nabla \left(\hat{D} \nabla \psi\right) + \frac{1}{3} \left(\nabla \vec{V}\right) \frac{\partial \psi}{\partial \ln p} + J_{sources}, \tag{2.40}$$

where, ψ represents the CR space density, $\vec{V}$ is the Solar Wind velocity, $\vec{v}_D$ is the average drift velocity, $\hat{D}$ is the diffusion tensor, and J_{source} is the source term that encodes the the production sources of CRs within the Heliosphere, for an instance, the Jovian electrons, or pick-up ions. The equation, 2.40, can be broken down into five phenomena:

- **Convection and Drift :** $\frac{\partial \psi}{\partial t} = -\left(\vec{V} + \langle \vec{v}_D \rangle\right) \nabla \psi$
- **Diffusion :** $\nabla \left(\hat{D} \nabla \psi\right)$
- **Adiabatic Energy losses :** $\frac{1}{3} \left(\nabla \vec{V}\right) \frac{\partial \psi}{\partial \ln p}$
- **CR sources :** $J_{sources}$

The source term can be ignored without any consequences for CRs with $R > 0.5\ GV$, given the range of magnetic fields observed at the Earth. Also, even though, the reacceleration of CRs at the Heliosheath are important for CRs with $R < 0.2\ GV$, adiabatic energy losses dominate in the case of high energy CRs. The average drift velocity as a result of HMF gradients, and curvature is given by

$$\langle \vec{v}_D \rangle = \frac{qv}{3} \nabla \times \left(\lambda_d \hat{e}_B\right), \tag{2.41}$$

where, q,v, $\hat{e}_B$, are the charge, speed, and the unit vector in the direction of magnetic field respectively, and, λ_d is the drift scale given by

$$\lambda_d = r_{Larmor} \frac{\left(\frac{R}{R_0}\right)^2}{1 + \left(\frac{R}{R_0}\right)^2}; \tag{2.42}$$

where, r_{Larmor} is the particle Larmor radius. The Larmor radius at lower rigidities, is much lower than the HMF curvature, and hence, the particles obey the trajectory dictated by the local magnetic field configuration, suppressing the drift velocity (along with any perpendicular diffusion to the HMF lines). In contrast, CRs of high rigidities aren't affected by the HMF small-scale structures, and instead can be described by the average HMF configuration, and intensity ($\lambda_d \sim r_{Larmor}$). $R_0 \sim \mathcal{O}(1)\ GV$ is the reference rigidity, and is a free paramter that sets the scale at which the transition between the two limiting regions take place. From (D.37), and (D.38), we can estimate the timescale for CR drift to be of the following order

$$\tau_D \propto \frac{1}{|\langle \vec{v}_D \rangle|} \propto B(t) \frac{1 + (R/R_0)^2}{\beta\,(R/R_0)^3}, \tag{2.43}$$

where, $\beta = v/c$. Hence, the drift timescale is expected to have the same time-dependence as that of the HMF. This allows us to differentiate the effects of Solar modulation from those associated with propagation through the ISM. The CR flux is influenced by the Solar modulation upto $30\ GV$, such that the resulting CR spectrum is not representative of the true Galactic CR spectrum, as seen in fig. 2.17.

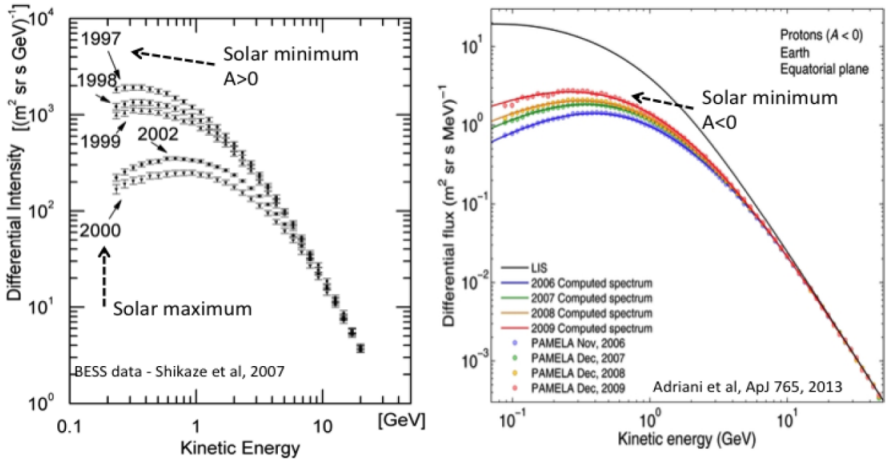

Figure 2.17: Solar modulation of the galactic p spectrum, as measured in different epochs by the BESS [220], and PAMELA [17] experiments.

2.5.1 The Force-Field approximation

The galactic CR modulation can be modelled by a spherically symmetric model, in which particles undergo convection, diffusion, and energy changes resulting from the Solar Wind expansion as a function of the radial distance r from the Sun. The force-field approximation model [170] considers the Solar Wind as a radial field with a potential ϕ. With this assumption,

the density evolution can be written as

$$k\frac{\partial N}{\partial r} + \frac{V}{3}\left[T^2 - \left(mc^2\right)^2\right]^{3/2}\frac{\partial N}{\partial T}\left[\frac{N}{T\left[T^2 - (mc^2)^2\right]^{1/2}}\right] = 0, \tag{2.44}$$

where, $N(r,T)$ is the differential density, $V(r,T)$ is the Solar Wind speed, k is the diffusion coefficient, which is assumed to be constant, T is the kinetic energy, and m is the particle mass. This equation is then integrated taking in appropriate boundary conditions. This results in a cosmic ray flux, $\Phi = \frac{\nu}{4\pi}N(E)$ as

$$\Phi_{\odot}(E) = \frac{E^2 - m^2c^4}{(E + Ze\phi)^2 - m^2c^4}\Phi_{IS}(E + Ze\phi), \tag{2.45}$$

where, $\phi_{\odot}$ is the differential particle intensity at energy E in the Heliosphere, and is related to the interstellar differential intensity Φ_{IS}, i.e., beyond the termination of the Solar Wind. The proportionality factor between the two parameters, is the ratio of two corresponding squared momenta, $p_{\odot}^2/p_{IS}^2$. Here, ϕ is the modulation parameter, and depicts the energy loss experienced by the particle as it approaches the Earth from infinity as

$$\phi = \int_r^{\infty}\frac{V}{3K}dr. \tag{2.46}$$

The characteristic energy loss experienced by a particle of charge Z, in the Heliosphere, is given by $\delta E = Ze\phi$. This parameter is used to denote the Solar activity level that modulates a measured differential CR intensity.

2.6 Magnetosphere and Rigidity Cutoff

Cosmic Rays arriving on the Earth has to endure the GeoMagnetic Field (GMF), before being detected, and this field modulates the low-energy part of the observed spectra ($\lesssim 10\ GeV/n$). If we take a first order approximation, the GMF field is a dipole that is offset and tilted with respect to the Earth's rotational axis. The GMF dipole field has a moment of, $M = 8.1 \times 10^{25}$ Gcm^3, with an inclination of 11° with respect to the Earth's rotational axis, and is displaced by $400\ km$ from the Earth's center. The GMF field is particularly weak in a certain region of the South Atlantic Ocean. This region serves as a mirror point for the trapped particles in the inner Van Allen Belt. Because of the weak GMF here, charged particles penetrate deeper into the atmosphere giving rise to stronger radiation and particle fluxes. This high radiation phenomenon is named as the *South Atlantic Anomaly (SAA)*.

To efficiently measure the Galactic CR flux, it is essential to identify, and reject the component of particle flux that isn't coming from outer space, but indeed is trapped within the GMF. The components can be decomposed by knowing the the GMF strength at the detector location, and by noting down the particle energy and arrival direction. In fig.2.18, we can observe the energy spectrum of *downgoing*, and *upgoing* protons as measured by AMS-01 [160] at different lati-

tudes. Here, we can observe two components in the downgoing population of protons, i.e., the lower energy component has an energy spectrum that overlaps with the spectrum of upgoing protons. This means, these component of the spectrum has protons which are trapped in the GMF. Rest of the higher energy part of the spectrum is of Galactic origin.

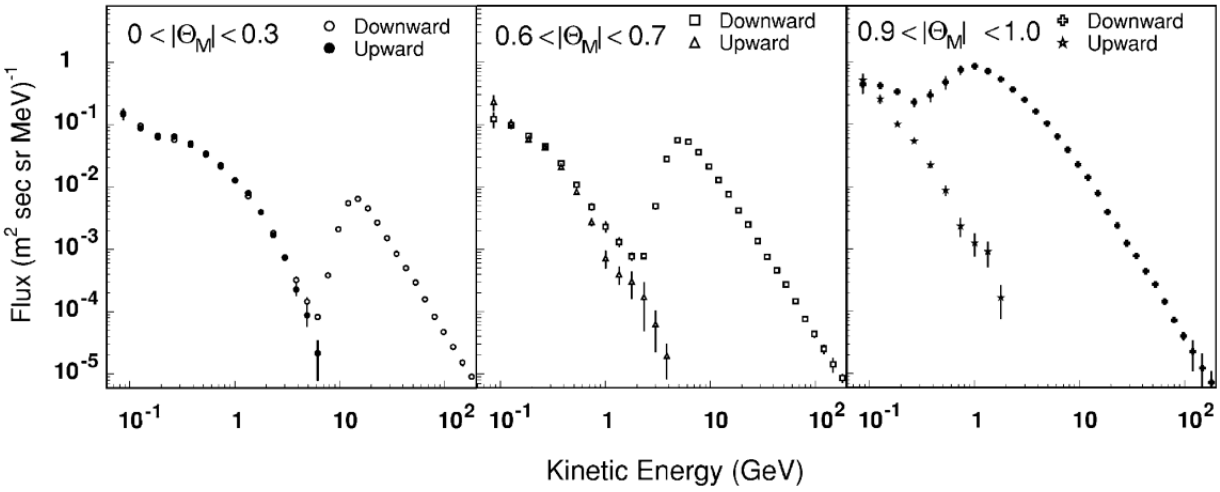

Figure 2.18: Downgoing and Upgoing proton spectrum at different geomagnetic latitudes from AMS-01 [160]. We can observe a part of the downgoing spectrum matching with the upgoing spectrum. These are the trapped proton population.

The GMF has a source potential ϕ. Hence, the magnetic field can be obtained using, $\vec{B} = -\nabla\phi$. The potential has a multipole expansion of the form given by [228]

$$\phi = R_{\oplus} \sum_{n=0}^{\infty} \left(\frac{R_{\oplus}}{r}\right)^{n+1} \sum_{m=0}^{n} P_n^m(\cos\theta) \left(g_n^m \cos(m\psi) + h_n^m \sin(m\psi)\right), \tag{2.47}$$

where, $R_{\oplus} = 6321.2\ km$ is the mean Earth radius, r is the geocentric radius, θ is the geographic latitude, and ψ is defined as the East longitude from Greenwich. Whereas, $P_n^m(\cos\theta)$ are the *Legendre* polynomials, h_n^m, and g_n^m are the Gaussian coefficients that describes the GMF, and are experimental input parameters. Because the potential has a $(r^{-(n+1)})$ dependence, the higher order terms are rapidly suppressed with distance from the Earth. As such, we can develop the theory of trapped radiation based on the dominant, $n = 1$, dipole term.

This model of the GMF is called the *International Geomagnetic Reference Field* (IGRF) [264]. The Gaussian coefficients are estimated upto the order $n = 13$, every five years and linearly interpolated between one estimate and the next one, by the International Association of Geomagnetism and Aeronomy (IAGA). The latest measurements were done in December 2019 and can be referred in https://www.ngdc.noaa.gov/IAGA/vmod/igrf.html.

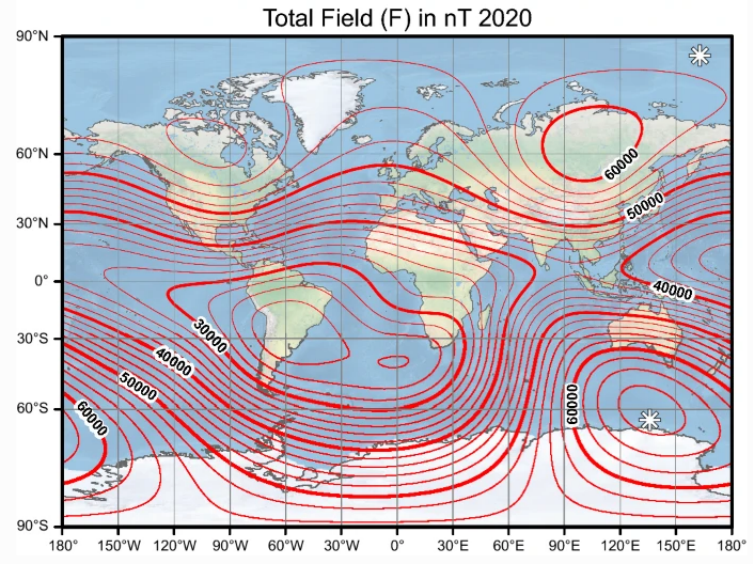

Figure 2.19: Total Geomagnetic field intensity at the WGS84 ellipsoid surface for epoch 2020 [48].

For any kind of CR measurement, we need to know the Geomagnetic cut-off. The Lorentz force experienced by a charged particle in the GMF bends its trajectory. CRs can thus suffer deviation in such a manner, depending on the their rigidity, and incoming direction, that they aren't measured by a particle detector. In the case of the Earth, this selection is configured by three parameters: The rigidity of the particle, the detector location, and the incoming direction of the particle with respect to the GMF. In other words, for a given arrival direction, and detector location, there exists, a minumum value of the particle rigidity denoted by R_C for which galactic CRs are allowed to penetrate the magnetosphere and then get detected. A formula derived for R_C by Stoermer [256] in a dipolar field geometry is given as

$$R_C = \frac{M \cos^4 \lambda}{r^2 \left[1 + (1 - \sin\epsilon \sin\xi \cos^3 \lambda)^{1/2}\right]^2}, \tag{2.48}$$

where, M is the dipole moment magnitude expressed in Gcm^3. The arrival direction is dictated by the two angles ϵ, and ξ. To understand them, we have to construct a hemisphere with the point where the particle arrives on the dipole as the center, and the plane of this hemisphere is the tangent plane at this point; ϵ is then the angle from the zenith direction and ξ is the azimuthal angle measured clockwise from the direction to the north magnetic pole. The arrival location is defined by the geomagnetic coordinates (d, λ), where, d is the distance from the dipole center, usually expressed in Earth radii units, and λ is the latitude of the dipole.

The *Stoermer* equation is enough for many practical measurements. However, for precise and sensitive measurements, a method called *Back-Tracing* is utilised. It is based on the construction of the CR trajectory in the GMF, back in time, and reversing their incoming direction. This is a computationally intensive method, and hence uses a lot of approximations. This involves the tracing of particles from a well-known position untill they reach the boundaries of the magnetosphere (allowed trajectories), or they reach the Earth (forbidden trajectories) [144]. The

first ones are allowed because it identifies a particle coming from the outer space, while the latter ones are forbidden because it identifies a trapped particle. At each position, there exists a *Upper Cutoff Rigidity* R_U, above which all charged particles are allowed, and a *Lower Cutoff Rigidity* R_L, below which all charged particles are disallowed. However, in most of the cases, the charged particle transmission diminishes from fully allowed to totally forbidden over a discrete range of charged particle rigidities. The region between the totally allowed, and totally forbidden trajectories is called *Cosmic Ray Penumbra*. Usually, the mean value of R_U, and R_L is taken as the effective geomagnetic cutoff R_C.

2.7 Cosmic Ray Composition as a Tool for Astrophysics

The diffusion-convection equations used to describe CR transport depends on a lot of microphysical factors. However, all such complexities are typically averaged out, such that CR transport equations are simplified, and depends on a few phenomenological input parameters. Two of those important parameters of interest are the $H/D(E)$, and $H^2/D(E)$, where H is so called the *Galactic Halo Half Size* as seen in fig. 2.20 , and $D(E)$ is the diffusion coefficient used in the CR transport equations. Galactic Halo is a roughly spherical envelope around the visible component of the Galaxy (can be composed of Stellar, Galactic Corona, and Dark Matter components) as seen in fig. 2.20.

The measurement of secondary-to-primary ratios of CR nuclei for example, B/C is proportional to the $H/D(E)$ ratio. However, this leaves the ratio $H^2/D(E)$, which also denotes the confinement time of galactic CRs within the Galactic Halo, weakly constrained or in other words degenerate. By which it means that, the same ratio could be obtained with a smaller Halo size, and consequently a smaller diffusion coefficient, or both quantities larger by the same amount. However, the ratio of unstable secondary over stable secondary species is sensitive to the $H^2/D(E)$ ratio. For example, ratios such as, $^{10}Be/B$, or $^{10}Be/^{9}Be$, will offer us sensitivity to this ratio. Hence, such a measurement becomes essential, along with already existing measurements of primary-to-secondary (and hence, H/D), we can decouple the parameters, H, and D.

Although AMS-02 wasn't designed to do isotopic composition analysis, thanks to the unprecedented data collection, we can perform ingenious fitting techniques taking in consideration the underlying chemistry of Be, and its isotopic composition to perform the, $^{10}Be/^{9}Be$ analysis. This analysis forms one of the major component of this thesis. This measurement would not only help us improve galactic CR transport models, but the updated parameters would also be helpful to understand if the excess observed by PAMELA, and AMS-02 in the antiproton-to-proton spectrum requires the introduction of exotic physics (read WIMP like Dark Matter) or it could be explained with standard physical mechanisms.

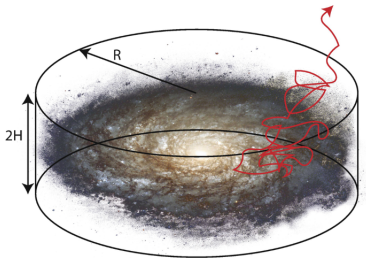

Figure 2.20: Model of our Galaxy with the Galactic Halo. Here, H is the Galactic Halo Half Size. The red zig-zag line denotes the diffusion of a CR species. Figure taken from [267]

2.7.1 Unstable Secondary to Stable Secondary Ratio

The model outlined here is based on the diffusive halo model, developed by Evoli *et al* in [153], based on a modified version of the weighted slab technique [51, 52, 150, 185]. In this model, the CR sources are assumed to be located in a thin disc with half width $h \ll H$, where H is the half thickness of the Galactic Halo. The CR interactions take place in the ISM gas, which is assumed to be confined within the thin disc, having a surface density, $\mu = 2.3\ mg/cm^2$ [159]. It is assumed that the decay of unstable nuclei taks places outside the thickness h of the disc. The relevant time scales for CR transport in the disc are the diffusion time scale $h^2/D(R)$, and the advection timescale h/v_A, where, v_A is the Alfvén speed. We also assume that the decay of the unstable nuclei takes place within the Halo

$$\gamma\tau_d \gg Min\left[\frac{h^2}{2D}, \frac{h}{v_A}\right], \tag{2.49}$$

where, τ_d is the radioactive decay time, and in the case of ^{10}Be is $\tau_d = t_{1/2}/ln2 \sim 2\ Myr$, γ is the Lorentz factor, and $D(R)$ is the rigidity-dependent diffusion coefficient. A spatially constant diffusion coefficient is assumed with sole dependence on the particle rigidity R:

$$D(R) = 2v_A H + \beta D_0 \frac{(R/GV)^\delta}{[1 + (R/R_b)^{\Delta\delta/s}]^s}, \tag{2.50}$$

where, D_0, and δ are experimental input parameters fitted from data, typically from B/C, and $B/0$ ratios as functions of energy. Whereas, $s = 0.1$, $\Delta\delta = 0.2$, and $R_b = 312\ GV$ are fixed from observations of primary nuclei [150]. The τ_d for the ^{10}Be isotope becomes longer than the CR escape time from the Galactic Halo for rigidity above $10 - 100\ GV$, depending on the Halo half size H. This is the reason why the flux of ^{10}Be is sensitive to the parameter H.

In the context of modified weighted slab approach, the CR transport equations are given as:

$$-\frac{\partial}{\partial z}\left[D_a\frac{\partial f_a}{\partial z}\right] + v_a\frac{\partial f_a}{\partial z} - \frac{dv_A}{dz}\frac{p}{3}\frac{\partial f_a}{\partial p} + \frac{1}{p^2}\frac{\partial}{\partial p}\left[p^2\left(\frac{dp}{dt}\right)_{a,ion} f_a\right] + \frac{\mu v(p)\sigma_a}{m}\delta(z)f_a + \frac{f_a}{\hat{\tau}_{d,a}} \tag{2.51}$$

$$= 2h_d q_{0,a}(p)\delta(z) + \sum_{a'>a}\frac{\mu v(p)\sigma_{a'\to a}}{m}\delta(z)f_{a'} + \sum_{a'>a}\frac{f_{a'}}{\hat{\tau}_{d,a'}},$$

where $f_a(p,z)$ denotes the distribution function of species a in phase space, $v(p) = \beta(p)c$ is the particles' velocity, and μ is the surface density of the disk. While the quantities, $\hat{\tau}_{d,a} = \gamma\tau_{d,a}$ define the Lorentz boosted decay times of unstable elements.

The particle advection is accounted by the second term in the left-hand side of (2.51) with velocity v_A. In this case, we adopt a simplistic picture where the advection speed is constant in z, which implies $dv_A/dz = 2v_A\delta(z)$. Here, $q_{0,A}(p)$ describes the injection of primary CR nuclei of type a in the infinitely thin disc. This injection function is assumed to have a power law behaviour in momentum with a corresponding slope γ_{inj}, and it depends weakly on the type of primary nucleus [150]. Also, h_d is the half-thickness of the Galactic Disk. The second terms on right-hand side of (2.51) accounts for the production of secondary CRs through spallation, while the third term describes the production of secondaries through radioactive decays of secondaries, such as production of ^{10}B by the decay of ^{10}Be.

In (2.51), we now consider it for $z \neq 0$. So, all terms proportional to $\delta(z)$ vanishes, and we are left with

$$-\frac{\partial}{\partial z}\left[D_a(p)\frac{\partial f_a}{\partial z}\right] + v_A\frac{\partial f_a}{\partial z} + \frac{f_a}{\tau_{d,a}} = 0 \tag{2.52}$$

The solution of the above equation is of the form

$$f_a = A\exp(\alpha_+ z) + B\exp(\alpha_- z), \tag{2.53}$$

where $\alpha_\pm$ are the solution of the quadratic equation, $D_a\alpha^2 - v_A\alpha - 1/\tau_{d,a} = 0$. Hence they are given by:

$$\alpha_\pm = \frac{v_A}{2D_a}\left[1 \pm \sqrt{1 + \frac{4D_a}{v_A^2\tau_{d,a}}}\right] \equiv \frac{v_A}{2D_a}\left[1 \pm \Delta_a\right]. \tag{2.54}$$

Here, Δ_a is a dimensionless quantity, and can be written in a convenient fashion in terms of the timescales involved (τ_{adv},τ_{diff}, and τ_d) in CR propagation as:

$$\Delta_a = \sqrt{1 + \frac{2\tau_{adv}^2}{(\tau_{diff,a})(\tau_{d,a})}}, \tag{2.55}$$

where

$$\tau_{diff,a} = \frac{H^2}{2D_a}, \quad \text{and} \quad \tau_{adv} = \frac{H}{v_A}. \tag{2.56}$$

The constants of the solution (2.53), can be derived by imposing the boundary conditions pertaining to the Galactic disc, and at the edge of the halo, i.e.,

$$f_a(p,z) = f_{0,a}(p), \quad \text{and} \quad f_a(p, z = H) = 0, \tag{2.57}$$

to obtain

$$f_a(z,p) = f_{0,a}(p)\frac{\exp(\alpha_- z) - \exp(\alpha_+ z + (\alpha_- - \alpha_+)H)}{1 - \exp(\alpha_- - \alpha_+)H}. \tag{2.58}$$

The value of the distribution function inside the disc, i.e., $f_{0,a}(p)$, can be derived by integrating

(2.51) between the limits 0^- and 0^+ to give,

$$-2D_a(p)\left(\frac{\partial f_a}{\partial z}\right)_{z=0^+} - \frac{2}{3}v_A p\frac{\partial f_{0,a}}{\partial p} + \frac{\mu v(p)\sigma_a}{m}f_{0,a} + \frac{2h}{p^2}\frac{\partial}{\partial p}\left[p^2 b_{0,a}(p) f_{0,a}\right] = 2h_d q_{0,a}(p) + \sum_{a'>a}\frac{\mu v(p)\sigma_{a'\to a}}{m}f_{0,a'}. \tag{2.59}$$

Here, $D_a \left.\dfrac{\partial f_a}{\partial z}\right|_{0^+}$ represents the diffusive flux at the disc position, and can be derived by differentating (2.58) with respect to z to give:

$$\left[D_a\frac{\partial f_a}{\partial z}\right]_{z=0} = -\frac{v_A}{2}\xi(p) f_{0,a}, \tag{2.60}$$

where

$$\xi(p) = -\frac{(1-\Delta_a) - (1-\Delta_a)\exp\left(-\frac{v_A\Delta_a H}{D_a}\right)}{1-\exp\left(-\frac{v_A\Delta_a H}{D_a}\right)}. \tag{2.61}$$

The meaning of ξ can be realised by analysing it for stable elements, i.e., when $\Delta = 1$, which gives

$$\xi_{stable} = \frac{2}{1-\exp\left(\frac{v_A H}{D_a}\right)}.$$

In the limit of diffusion, i.e., $D_a \gg v_A H$, we get

$$\xi_{stable,diff} \to \frac{2D_a}{v_A H},$$

while in advection case, i.e., $D_a \ll v_A H$, we get

$$\xi_{stable,adv} \to 2.$$

While in case of unstable elements, with $\tau_d \ll \dfrac{4D_a}{v_A^2}$, we get

$$\xi_{unstable} \to \Delta \simeq \sqrt{\frac{4D_a}{v_A^2\tau_d}}.$$

Hence, we can write the diffusive flux as

$$\left[D_a\frac{\partial f_a}{\partial z}\right]_{z=0} \simeq -f_{0,a}\frac{D_a}{L_a}, \tag{2.62}$$

where L_a denotes the maximum propagation distance, i.e.,

$$L_a = \begin{cases} \text{Stable elements} \to \begin{cases} H, & D_a \gg v_A H \\ \infty & D_a \ll v_A H \end{cases} \\ \\ \text{Unstable elements} \to \sqrt{D_a\tau_{d,a}}, \quad \tau_d \ll \frac{4D_a}{v_A^2}. \end{cases} \tag{2.63}$$

In accordance to the procedure outlined in [150, 153, 185], we can rewrite the CR transport equations as function of kinetic energy per nucleon, $I_a = A_a p^2 f_{0,a}$, where A_a is the atomic mass number of the nucleus:

$$\frac{I_a(E)}{X_a(E)} + \frac{d}{dE}\left\{\left[\left(\frac{dE}{dx}\right)_{ad} + \left(\frac{dE}{dx}\right)_{ion,a}\right] I_a(E)\right\} + \frac{\sigma_a I_a(E)}{m} = Q_a(E), \tag{2.64}$$

where

$$X(E) = \left(\frac{\mu v}{2 v_A}\right) \frac{2\left(1 - \exp\left(-\frac{v_A H}{D_a}\right)\right)}{(1+\Delta) - (1-\Delta)\exp\left(-\frac{v_A \Delta_a H}{D_a}\right)}, \tag{2.65}$$

is the *grammage* for nuclei with kinetic energy per nucleon E.

$$\left(\frac{dE}{dx}\right)_{ad} = -\frac{2 v_A}{3 \mu c}\sqrt{E\,(E + m_p c^2)}, \tag{2.66}$$

is the rate of adiabatic energy losses due to advection and

$$Q_a(E) = 2h_d \frac{A_a p^2 q_{0,a}(p)}{\mu v} + \sum_{a'>a} \frac{I_a(E)}{m} \sigma_{a' \to a}, \tag{2.67}$$

is the source term. The solution of (2.64) can be found using the procedure outlined in [150] for stable species with the grammage expression given by (2.65)

Now, let us analyse the asymptotic behaviour of the grammage (2.65)

$$X = \begin{cases} \dfrac{\mu v}{2 v_A} & \text{when,} \quad \tau_{adv} \ll \tau_{diff}, \tau_d \quad \text{(advection-dominated)} \\ \dfrac{\mu v H}{2D} & \text{when,} \quad \tau_{diff} \ll \tau_{adv}, \tau_d \quad \text{(diffusion-dominated)} \\ \dfrac{\mu v}{2}\dfrac{\tau_d}{\sqrt{D \tau_d}} & \text{when,} \quad \tau_d \ll \tau_{diff}, \tau_{adv} \quad \text{(decay-dominated)} \end{cases} \tag{2.68}$$

This exercise hence shows us that a measurement of secondary/primary that constrains H/D, and a measurement of unstable/stable secondary that constrains $H/\sqrt{D}$ together can allow us to decouple H and D, and have independent values for them, albeit with the systematic uncertainties coming from experimental data and spallation cross-sections.

2.7.2 Back of the envelope thumb rules for CR transport

To summarise CR transport parameters for quick calculations, we can follow the following generic rules [149]

- **Generic rule of thumb**:

$$Intensity \sim \text{Injection Rate} \times \frac{\text{Relevant lifetime}}{\text{Relevant Volume}} \tag{2.69}$$

- **Primary species** equilibrium spectrum:

$$I_p(T) \propto Q(T)\frac{\tau_{esc}(T)}{H} \tag{2.70}$$

where $\tau_{esc} \sim H^2/D$.

- **Secondary stable species** equilibrium spectrum:

$$I_s(T) \propto I_p(T)\sigma v n_d h_d \frac{\tau_{esc}}{H}, \tag{2.71}$$

where σ, v, n_d, h_d, are the cross-section of CR interaction, advection velocity, CR species density, and half-thickness of Galactic Disk respectively.

- **Secondary unstable(*) species** equilibrium spectrum:

$$I_s^*(T) \propto I_p(T)\sigma v n_d h_d \frac{\tau_d(T)}{\sqrt{\tau_d(T)D(T)}} \tag{2.72}$$

- **Stable secondary over primary** ratio:

$$\frac{I_s(T)}{I_p(T)} \propto \chi(T) \propto \frac{H}{D(T)}, \tag{2.73}$$

where D, H are the diffusion coefficient of CR transport equations, and Galactic Halo Half Size respectively, and $\chi(T) = \int \rho(l)dl$ (where ρ is the material density, and l is the path length traversed) is the grammage, i.e., the amount of material that a CR go through along propagation.

- **Unstable secondary over stable secondary** ratio:

$$\frac{I^*(T)}{I_s(T)} \propto \frac{\sqrt{D(T)}}{H} \tag{2.74}$$

2.7.3 Beryllium in Cosmic Rays

It is hypothesised that most of the stable Beryllium (Be) in our Universe emerges from the CR induced fission of heavier nuclei in the ISM. Although, both stable and unstable isotopes are synthesised in stars, they do not last long. Be is a relatively rare component of CRs as can be seen in fig.2.21. It is primarily produced by the spallation reaction of C, N, and O with the ISM. The main isotopes of Be are four, i.e., ^7Be,^{8} Be,^{9} Be, and ^{10}Be. However, ^8Be has a very short life-time ($\sim 8 \times 10^{-7}s$), and disintegrates by $\alpha-$decay into ^4He. This is also responsible for the bottleneck in Big Bang Nucleosynthesis, that necessitates Stellar Nucleosynthesis to produce elements heavier than Be.

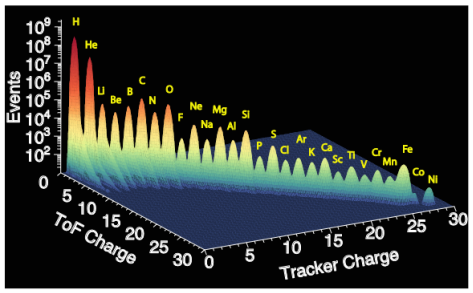

Figure 2.21: Charge measurement of the Time-of-flight counter and Tracker of AMS-02. Figure from [33]

As such, Be has three main isotopes in the CR spectra:

- ^7Be**:** It is stable as a bare nucleus in CR. When it is not fully ionised, it decays by L-electron capture (see fig. 2.22) to ^7Li ($T_{1/2} = 53.2$ days).
- ^9Be**:** It is the only stable isotope.
- ^{10}Be**:** It is produced by the CR spallation of O. It decays via β^- process (see fig.2.23) to ^{10}B, where the atomic number increases by unity along with the emission of an electron e^-, and an electron antineutrino $\bar{\nu}_e$. It has a relatively longer half life of $T_{1/2} = 1.39 \times 10^6$ years. ^{10}Be is often used as a Solar activity proxy, as the production of it is inversely proportional to the Solar activity, because increased Solar winds during periods of high Solar activity reduces the galactic CR flux (see fig. 2.24)

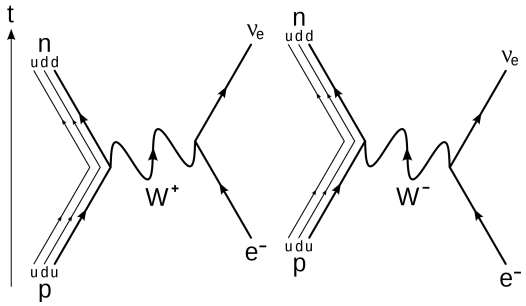

Figure 2.22: Leading-order Feynman diagrams for electron capture decay. An electron interacts with an up quark in the nucleus via a W boson to create a down quark and electron neutrino.

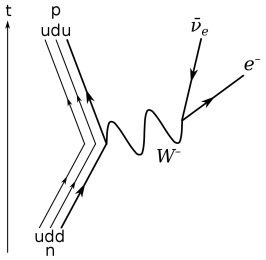

Figure 2.23: Leading-order Feynman diagram for β^- decay of a neutron into a proton, electron, and electron antineutrino via an intermediate W^- boson

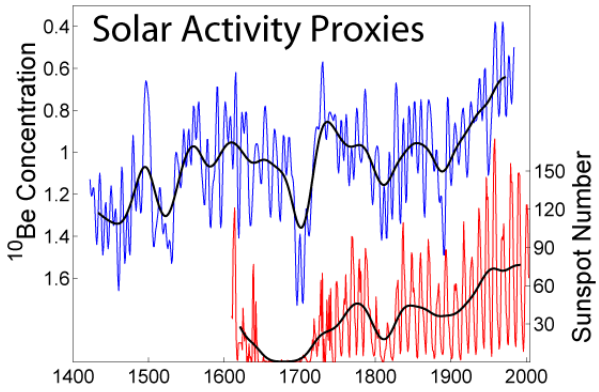

Figure 2.24: Variations in Solar activity, along with variation in sunspot number (red) and ^{10}Be concentration (blue). Note that the Be scale is inverted, so increases on this scale indicate lower ^{10}Be level. Source: wikipedia

Since the isotope ^{7}Be decays by electron-capture, it is absent on Earth. The large abundance of it in CR flux points towards the evidence of lack of atomic electrons bounded to CR nuclei. As discussed in previous section, the relatively small abundance of ^{10}Be as compared to the stable ^{9}Be offers us a radioactive clock, by virtue of which, we can measure the residence time of CR in galaxy. As already discussed in the previous section, the parameters H and D aren't decoupled and hence there exists degeneracy in the estimated H/D values. For an instance, GALPROP (refer subsection 2.4.5 for details) estimates for those parameters are degenerate and gives us a linear correlations between the *Halo-half Size* and *Diffusion Coefficient*. In fig. 2.25, you can see the GALPROP propagation parameters as a triangle plot for spectral index (δ) of the injection spectrum, alfvén velocity (v_A) of the magnetic waves, convection velocity ($v_{0,c}$), diffusion coefficient (D_0), and the Halo-half size (z_h). In this particular fit, they had eleven parameters (refer [196] for the full triangle plot of the parameters).

Three fits are considered in [196]: using only proton data (P), proton and helium data (PHe), and proton, helium and antiproton data ($main$). Fig. 2.25 shows how the propagation parameter space successively constricts by going from data set (P) to ($main$). As anticipated, because of the large degeneracy of the parameters in case of (P) almost the whole sampled parameter space is allowed. Adding He data results, a preference towards large values for the convection velocity $v_{c,0} \gtrsim 50\ km/s$, and a diffusive halo height $z_h \gtrsim 4kpc$ is seen. Nonetheless, the constraints are not extremely strong, and at the $\sim 3\sigma$ level again, almost the whole parameter space is allowed.

Fig. 2.25(b) shows the comparison between (PHe) and ($main$) results. As one would expect, the secondary antiprotons give tight constraints on the rigidity dependence of diffusion $\delta \sim 0.3$, while the usual degeneracy in $D_0 - z_h$ appears, and no constraints on z_h can be inferred. This is an expected feature as strong constraints on z_h can be achieved only using precise data on radioactive clocks like $^{10}Be/^{9}Be$, which is the prime focus of the present thesis. In the plot 2.25, the existing measurement of $^{10}Be/^{9}Be$ are compared with theoretical expectations coming from different cross-section parametrisation, i.e., GALPROP, Webber(WNEW [274, 275] and YIELDX [250, 265] combined), and DRAGON2 [152], and cross-sections derived

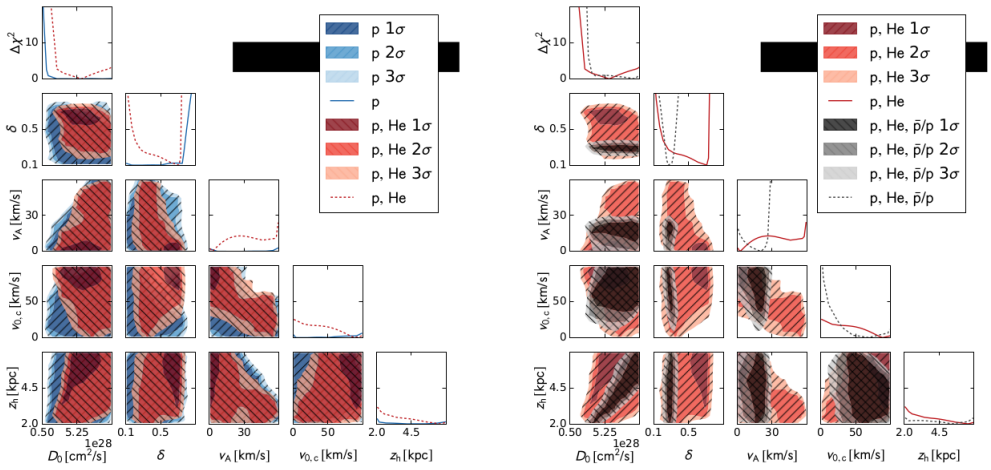

(a) (P) vs. (PHe)

(b) (PHe) vs. (main)

Figure 2.25: Comparison of fit results for three data sets (P), (PHe), and (main) in the main fit framework (11 parameters) for a selected set of propagation parameters. [196]

from fitting CR secondary/secondary flux ratios). However, due to the large error of the existing measurements and smaller kinetic energy window explored, the existing measurements for $^{10}Be/^{9}Be$ are unable to provide strong constraints on the possible H values. The relative increase in the amount of ^{10}Be at high energies is because of relativistic time dilation effect.

In theory, it is possible to infer the ratio of $^{10}Be/^{9}Be$ from measurements of elemental flux ratios of $Be/C, B/C, Be/O, B/O, C/O$ and Be/B; as well as, from absolute fluxes of C, N and O. This has been accomplished in [276] using the published $Li/C, B/C$ and Be/B fluxes of AMS-02 [28, 30, 31] as can be seen in fig. 2.27.

The summary of Galactic halo sizes fitted to the existing $^{10}Be/^{9}Be$ using various CR propagation codes can be seen in fig. 2.27. An accurate and precise measurement of $^{10}Be/^{9}Be$ using AMS-02 data, which has allowed us to explore a much wider kinetic energy per nucleon range $\sim 10GeV/n$ in this thesis, will further help us to improve the Galactic halo size estimates in the future.

2.8 Antimatter in Cosmic Rays

The dominant source of antimatter in CR spectra is the interaction of primary protons and nuclei with the ISM, as well as, the subsequent production and decay of secondary hadrons. Among others, antimatter could in principle be produced and accelerated by galactic CR sources like Pulsars, or they could arrive from more exotic regions like antimatter domains. Positrons and antiprotons can be produced as secondaries as result of CR propagation in the Galaxy, and represent a natural background for the search of extragalactic antimatter.

Following secondary particles (primarily mesons) are produced in energetic inelastic scattering between protons, or a proton with a nucleus (see fig.2.28 for full range of $pp-$interaction

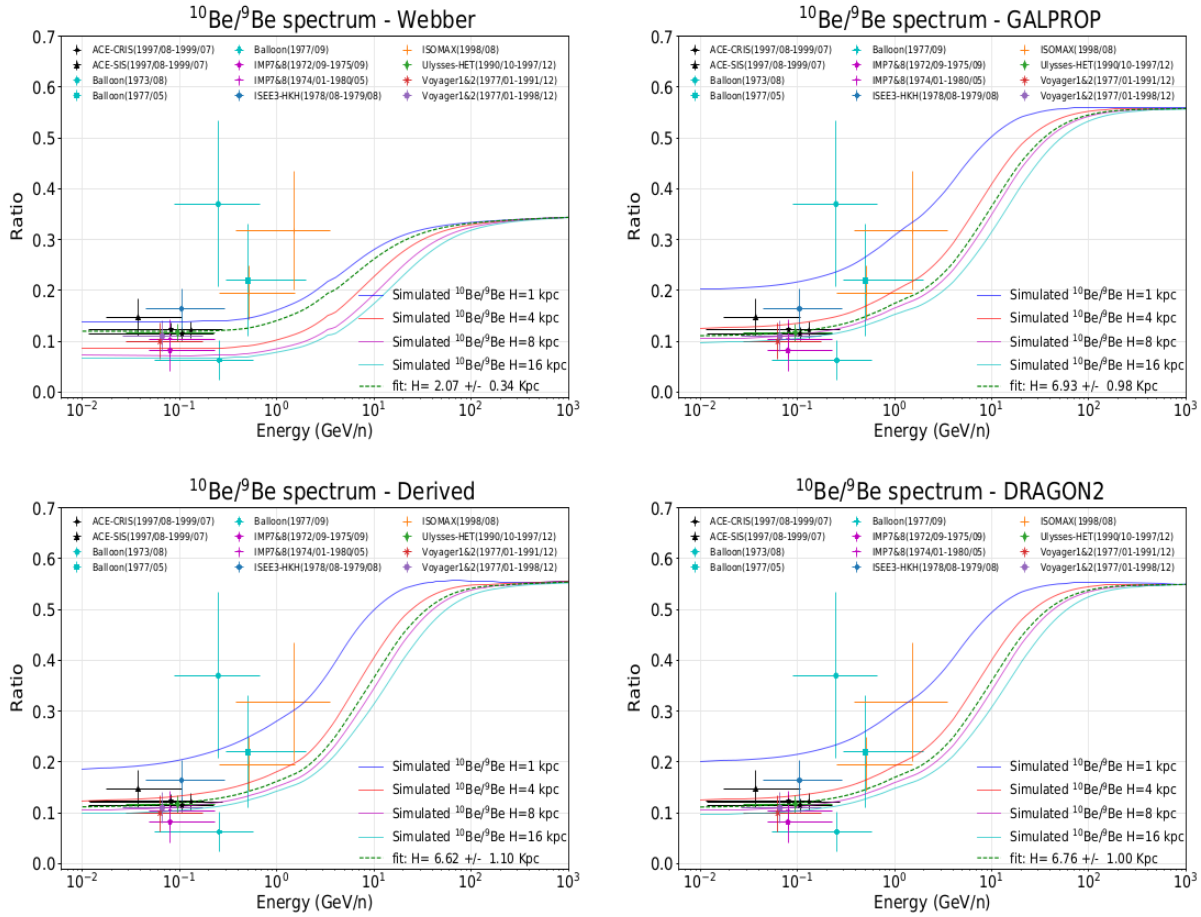

Figure 2.26: $^{10}Be/^{9}Be$ predicted flux ratios compared against all experimental data available and for every cross section parametrisation studied in [211]. For each parametrisation, various simulations with different halo sizes are provided, alongside the simulation yielding the best fit value. Plot taken from [211]

products):

$$p + p \rightarrow \pi^{\pm,0}, k^{\pm,0}, \bar{p} + \dots \tag{2.75}$$

$$p + {}^{A}_{Z}X \rightarrow \pi^{\pm,0}, k^{\pm,0}, \bar{p} + \dots \quad . \tag{2.76}$$

Furthermore the following decay of the secondaries can occur

$$\pi^{0} \rightarrow \gamma + \gamma \tag{2.77}$$

$$\pi^{\pm} \rightarrow \mu^{\pm} + \nu_{\mu}/\bar{\nu}_{\mu}. \tag{2.78}$$

Further decay of muons take place:

$$\mu^{\pm} \rightarrow e^{\pm} + \nu_{e}/\bar{\nu}_{e} + \bar{\nu}_{\mu}/\nu_{\mu} \tag{2.79}$$

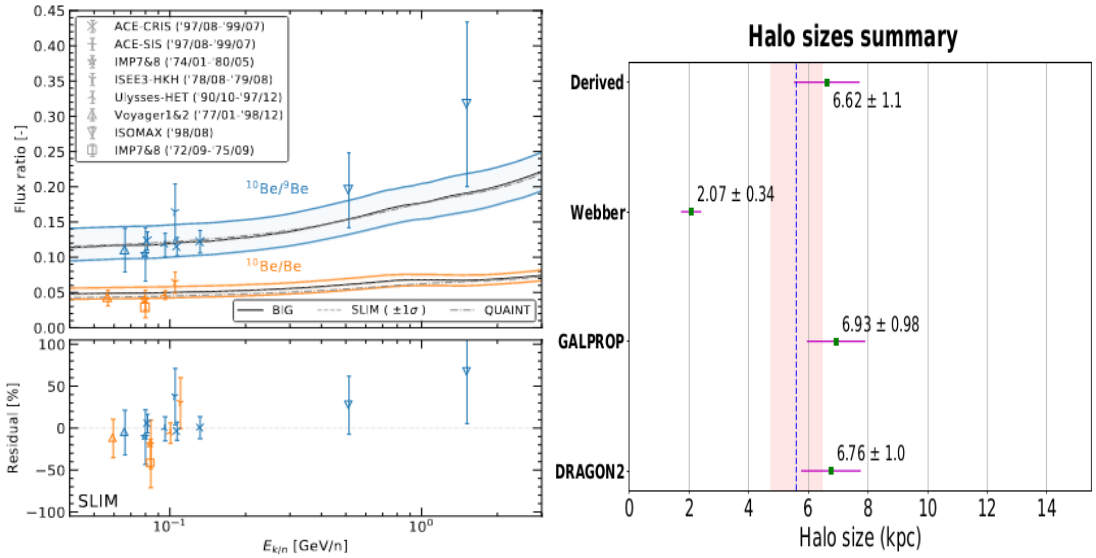

Figure 2.27: Left:Expected ratio of $^{10}Be/^{9}Be$ by fitting elemental flux ratios of $Li/C, B/C,$ and Be/B published by AMS-02. [276]. Right: Summary of the results obtained by fitting experimental data of $^{10}Be/^{9}Be$. The error bars here have statistical origin, and the blue dashed line denotes the mean of all the halo sizes obtained by different methods, and the red band represent 1σ uncertainty about the mean [211].

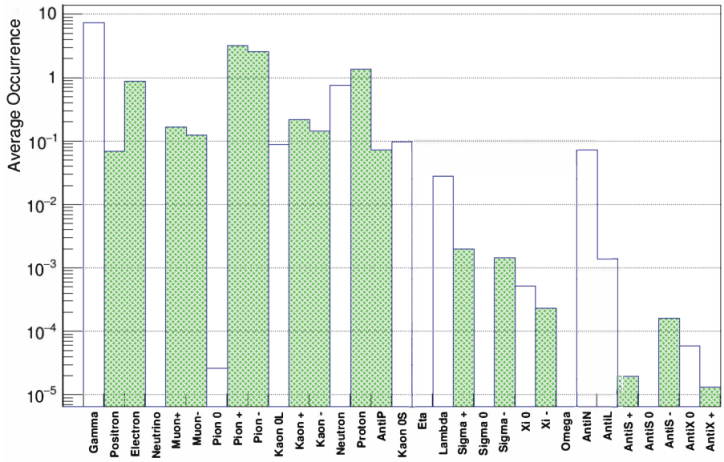

Figure 2.28: Particle type abundance in p + p interactions at 190 GeV/c. [13]

Similar to electrons e, positrons e^+ suffer heavy propagation energy losses in ISM. Hence, theoretically, we can expect the e^+ flux to have a harder spectrum than the e flux, also as a consequence of the power law nature of the primary progenitor protons. In principle, primary high-energy positrons could be produced from a Pulsar source, but it must be relatively close to Earth for detection.

However, the published AMS-02 results (see fig. 2.29) for the e^+ fraction $(e^+/(e^+ + e^-))$ shows an increase above $\sim 5\ GeV$. This is marked departure from the theoretical expectation because assuming e and e^+ are of both primary and secondary origin, one expects that the e^+ should drop monotonically as function of energy above few GeV. There are several hypotheses to test for the rising e^+ fraction. The natural one is to assume the existence of a primary high-energy e^+ source like Pulsar nearby. Pulsars can produce (e^+e^-) pairs in their highly

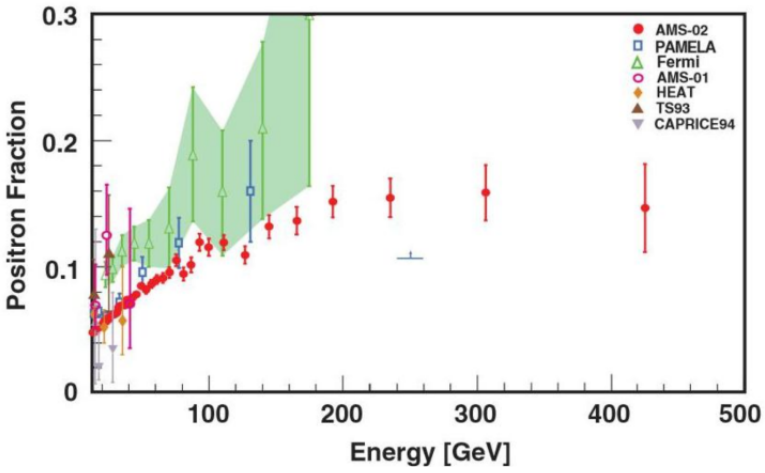

Figure 2.29: The e^+ fraction measured by AMS-02 with comparison to other experiments

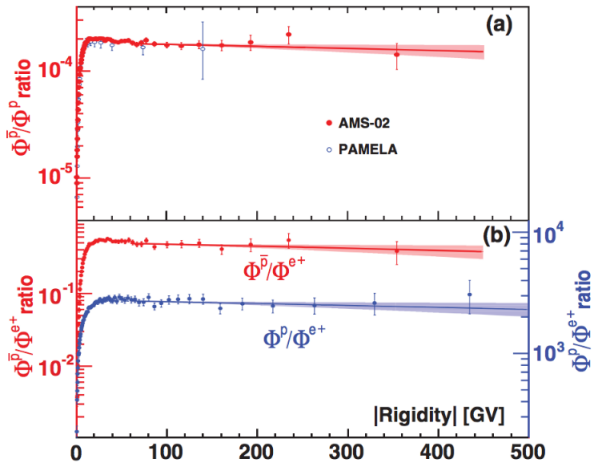

Figure 2.30: a) The measured $\bar{p}/p$ flux ratio of AMS-02 as a function of rigidity compared with PAMELA. b) $\bar{P}/e^+$ (red, left axis) and p/e^+ (blue, right axis) flux ratios [27]

magnetised and rapidly spinning magnetosphere. Earlier the Pulsar named *Geminga* was stated to be the source [280] but with the recent *FERMI*-LAT observations of GeV $\gamma-$ ray flux, now, PSR B1055-52 is the most promising source of the positron excess, and can well reproduce both the intensity and the high-energy cut off of the AMS-02 positron spectrum [154]. More recently, in [201], a total of 20 pulsar's contribution was used to fit the AMS-02 data very well. The other exotic explanation is that of new physics, viz. Dark Matter interpretation (for some references, see [63, 104, 155]). Although the jury is still out, the DM scenario doesn't seem promising as compared to the Pulsar interpretation.

In contrast, the published AMS-02 data for the $\bar{p}/p$ spectrum [27] also shows a flat lining above 60 GV rigidity (see fig. 2.30). This is in disparity with theoretical expectations, which predicts that the ratio should fall at higher rigidites due to power law nature of progenitor protons. The observed excess of anti-protons can't be fitted with any known astrophysical sources. Therefore, it remains a privileged channel to investigate Dark Matter Scenarios. In fact, the prime motive of the present thesis is to work towards finding DM explanation for the anti-proton excess.

Chapter 3

The AMS-02 Experiment

3.1 Introduction

The Alpha Magnetic Spectrometer (AMS-02) is a state-of-the art precision particle physics detector mounted aboard the International Space Station (ISS). It was launched by the space shuttle *Endeavour* in May 2011 to undertake a long-term mission of fundamental physics research with never before reached precision. The physics objectives of the experimental module ranges from indirect dark matter, and primordial anti-matter searches; CR composition studies, as well as space physics research. The AMS-02 collaboration is composed of various institutions across continents of America, Europe, and Asia.

The proposal to built a large acceptance spectrometer to be installed as a satellite or space station was put forth under the AMS project in 1994 [36]. The pioneering design was tested as a pathfinder, AMS-01, which was flown by the space shuttle *Discovery* in June 1998 for a 10-day mission. The purpose was to demonstrate the viability of a space based magnetic spectrometer. The pathfinder mission successfully collected around 8.0×10^7 CR events and provided important physics results [23–26, 42–46].

The development of AMS-02 commenced following the completion of the AMS-01 mission. Various institutions within the collaboration constructed the sub-detectors, which were eventually brought together and assembled at CERN. Unfortunately, the space shuttle program, including the planned launch of AMS-02 to the ISS, was put on hold after the Shuttle *Columbia* accident on February 1, 2003. However, a positive turn of events occurred on October 15, 2009, when NASA received authorization to add an additional apace shuttle flight dedicated to transporting AMS-02 to the ISS. On May 16, 2011, the launch successfully took place aboard the space shuttle Endeavour (see left panel of 3.1). Shortly after, the detector was installed by the crew at the *Upper Payload Attach Point* on the *ISS S3 Truss* (see right panel of 3.1). From that point onward, AMS-02 has been actively collecting data at a rate of approximately 16×10^9 events per year and is projected to continue its operations until the scheduled end of the ISS in 2028. AMS-02 mounted on the ISS can be seen in figure 3.2.

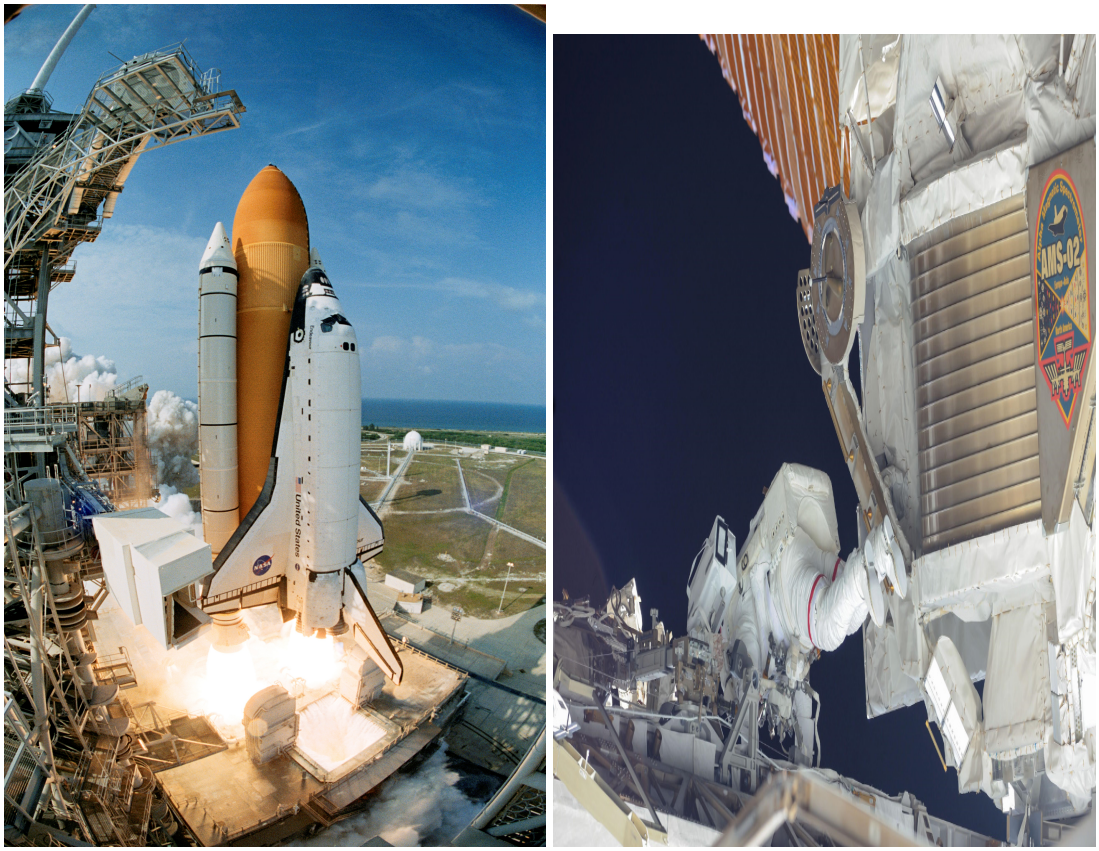

Figure 3.1: Left: Space Shuttle Endeavour. Right: AMS-02 installation on ISS by STS-134 crew. Photo copyright- NASA

3.2 The AMS-02 Detector

The AMS-02 detector is a magnetic spectrometer with acceptance of $0.5\ m^2sr$, intended for conducting accurate assessments of charged cosmic rays originating from the galaxy. It is situated on the ISS at an inclination of 12° relative to the zenith of the station. The ISS orbits the Earth at an altitude that varies between 370 and 460 km, maintaining an orbital inclination of 51.6°. Its velocity ranges from 7.6 to 7.7 km/s, resulting in a period of approximately 93 minutes [194].

The specifications for the dimensions, weight, and power consumption of AMS-02 were established to meet the necessary criteria for launch aboard the space shuttle and installation on the ISS. Specifically, AMS-02 weighs 7.5 tons, has dimensions of $3 \times 4 \times 5\ m^3$ $(height \times width \times length)$, and operates with a power budget of 2 kW supplied by the ISS.

To achieve its scientific goals, the detector was created with the aim of accurately identifying particles and specifically discerning between matter and antimatter. AMS-02 consists of a permanent magnet and six sub-detectors, which work together to redundantly measure the velocity $\beta = v/c$, momentum p, and charge Z of incoming particles. The arrangement of the detector can be observed in fig.3.3.

- **The Permanent Magnet:** It has a magnetic field of 0.15 T which bestows AMS-02 with spectrometric capabilities.

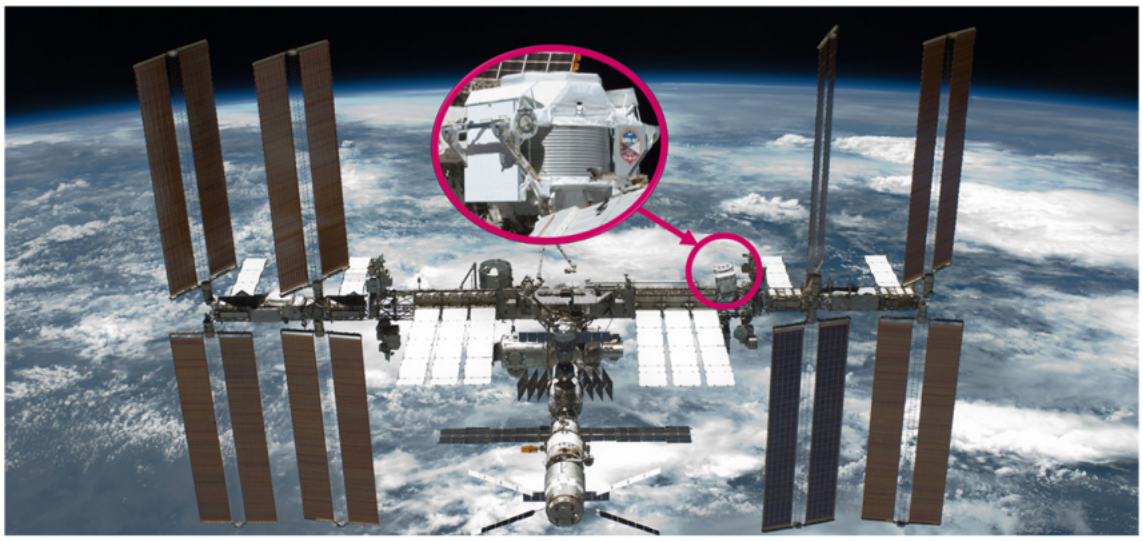

Figure 3.2: AMS-02 mounted on the ISS with a 12 degree angle to the zenith in order to prevent the interference of rotating ISS solar arrays with the AMS field of view.

- **The Silicon Tracker Detector (STD):** It consists of a total of nine high precision silicon tracker layers, labeled as L1 to L9. These layers are positioned both within and around the magnet. As particles move through the magnetic field, their trajectories are curved, and the STD plays a crucial role in reconstructing and measuring the momentum and charge, including the sign, of these particles.

- **The Transition Radiation Detector (TRD):** It is based on the principle of transition radiation and is used to differentiate between protons and positrons. It is located at the top of the AMS.

- **The Time Of Flight (TOF):** It comprises two sets of two planes positioned in orthogonal directions, situated both above and below the magnet bore. These two components, namely the upper TOF and the lower TOF, serve two purposes. Firstly, they enable the measurement of the velocity $\beta = v/c$ of particles, allowing for precise velocity determination. Additionally, they play a critical role in triggering the experiment.

- **The Anti-Coincidence Counter (ACC):** It surrounds the tracker within the magnet bore, and vetoes particles traversing laterally with respect to the detector.

- **The Ring Imaging Cherenkov Detector (RICH):** It is based on principle of Cherenkov Radiation, and is primarily used for velocity measurement in high energy regions. It is placed below the lower TOF.

- **The Electromagnetic Calorimeter (ECAL):** It is used to measure the energy of particles through electromagnetic shower, and is placed below the RICH.

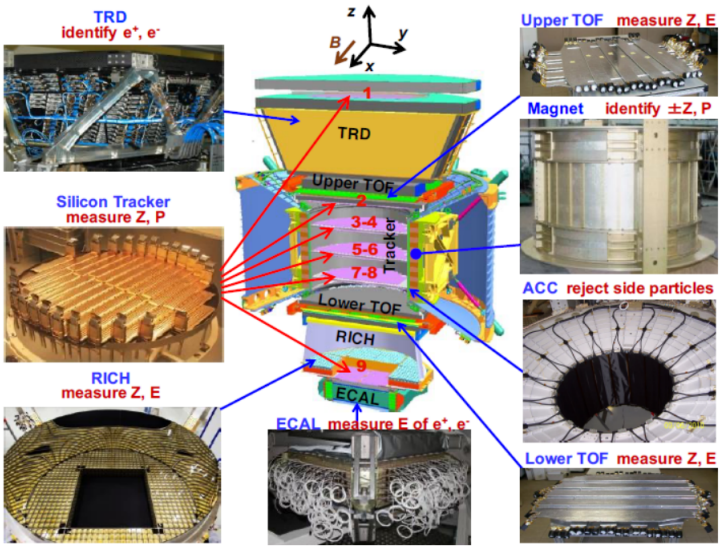

Figure 3.3: Schematic view of the AMS-02 detector.

3.3 The Permanent Magnet

The magnet employed in the AMS-02 detector is constructed using 64 high-quality $Nd\text{-}Fe\text{-}B$ sectors. Each sector comprises 100 blocks measuring $5.08 \times 5.08 \times 2.54\ cm^3$. This particular design generates a consistent magnetic field of 1.5 kG (0.15 T) in the X direction precisely at the magnet's center as shown in the right panel of fig. 3.4. It is located at the central part of AMS-02, and is assembled in a cylindrical shell structure of 0.8 m height, and with an inner and outer diameter of 1.1 m and 1.29 m respectively. [105, 207].

Within the magnet, the AMS local reference system is established, where the Y direction aligns with the bending plane. The dipole moment and the fringe field outside the magnet are intentionally kept insignificant. This approach aims to eliminate any torque effects on the ISS caused by its interaction with the Earth's magnetic field. Such measures ensure the safety of the astronauts operating in proximity to the magnet.

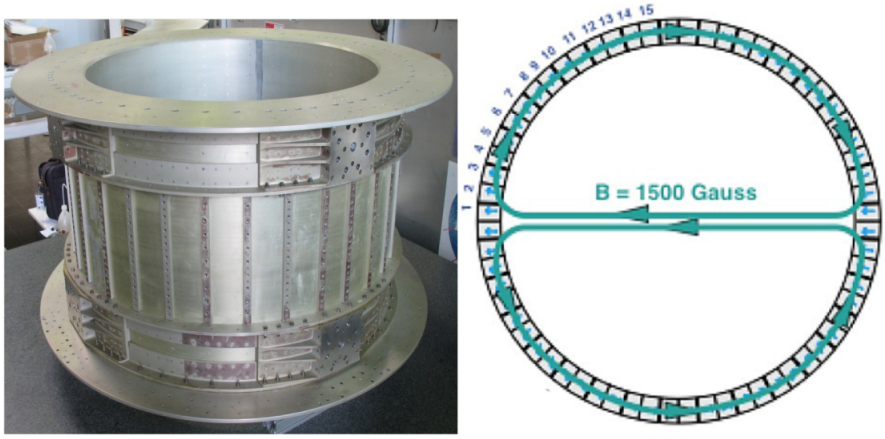

Figure 3.4: Left: The Permanent magnet. Right: The magnetic field configuration showing the field direction of the 64 permanent magnet sectors with negligible dipole moment and field leakage outside the magnet.

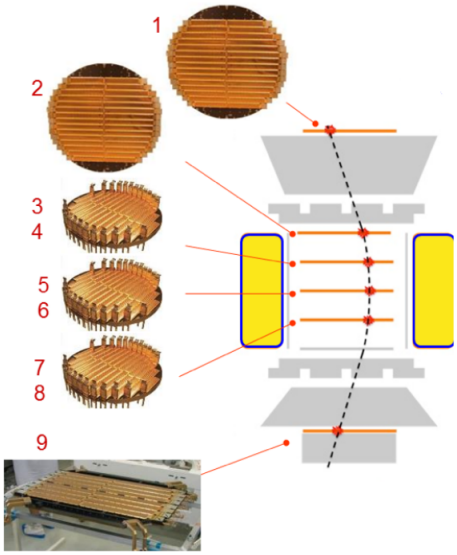

Figure 3.5: The silicon tracker detector consists of total of nine layers, each situated at different locations within the detector. Among these layers, three of the planes (L3-L8) are equipped with layers on both sides, while the remaining layers (L1, L2, and L9) are equipped with a single layer.

3.4 Silicon Tracker Detector

The Silicon Tracker Detector (STD) consists of nine layers, denoted as L1 to L9, which are arranged in six planes along the Z-axis. The first layer (L1) is positioned at the top of the detector, followed by the second layer (L2) just above the magnet. The remaining layers, L3 to L8, are situated within the magnet bore, while the final layer (L9) is positioned just above the ECAL (refer to fig. 3.5). Among these layers, three planes (L3-L8) have layers on both sides, as depicted in fig. 3.5. To maintain stability, these planes are securely held in place by a specialized honeycomb carbon fiber structure designed to match the magnet's shape. The STD incorporates a total of 2,264 double-sided microstrip silicon sensors. These sensors are assembled into 192 readout units known as ladders, resulting in approximately 200,000 readout channels. The overall length of the tracker, spanning from L1 to L9, is 3 m, providing a substantial lever arm for precise tracking measurements.

The combination of the tracker and magnet enables precise determination of the particle's trajectory through multiple coordinate measurements. Each layer of the tracker achieves a resolution better than 10 μm in the bending direction (Y) and 30 μm in the non-bending direction (X) [54]. The bending of trajectories induced by the magnet allows for the calculation of the particle's rigidity, denoted as R. Moreover, the tracker measures the energy losses, which provide the absolute value of the charge. This information is then utilized to determine the momentum, defined as $p = RZ$.

While maintaining excellent spatial resolution, it is crucial to ensure that the alignment of the different layers does not introduce any compromise. However, even small shifts in the layer positions can lead to an inherent bias in rigidity measurement, particularly at high rigidities. To

address this, the external layers (L1 and L9) undergo dynamic alignment every 2 minutes. This alignment is achieved by extrapolating the tracks from the inner tracker, with a precision better than 5 μm for both layers. Once the dynamic alignment of the external layers is complete, the precision of the rigidity bias is primarily influenced by the inner tracker layers. Overall, the accuracy of the rigidity scale bias is within 0.034 TV^{-1} or 3% at 1 TV. This level of accuracy corresponds to displacements of the layers L2-L8 of less than 0.2 μm [72].

The silicon tracker detector measures the trajectory of particles using a track-finding algorithm. Initially, this algorithm identifies various track segments within the inner tracker. From these segments, it reconstructs a single track by utilizing a track quality estimator similar to a χ^2 test. Subsequently, the track is extrapolated to the outer layers, and if additional hits are found, the track is extended to include these hits [284]. This track-finding algorithm plays a critical role, particularly in events involving heavy nuclei. In such cases, there are often additional hits or track segments due to the generation of delta-rays and interactions between the nuclei and the tracker materials [33].

The track-finding algorithm results in four different tracker patterns:

- **Inner:** No hits in the external layer. The aperture with respect to AMS zenith direction is $40°$ (fig.3.6 (a)).
- **L1+ Inner:** Hit on L1 but no hit on L9. The aperture with respect to AMS zenith direction is $30°$ (fig.3.6 (b)).
- **Inner+L9:** Hit on L9 but no hit on L1. The aperture with respect to AMS zenith direction is $35°$ (fig.3.6 (c)).
- **L1+Inner+L9 (Full Span):** Hits on L1 as well as L9. The aperture with respect to AMS zenith direction is $25°$ (fig.3.6 (d)).

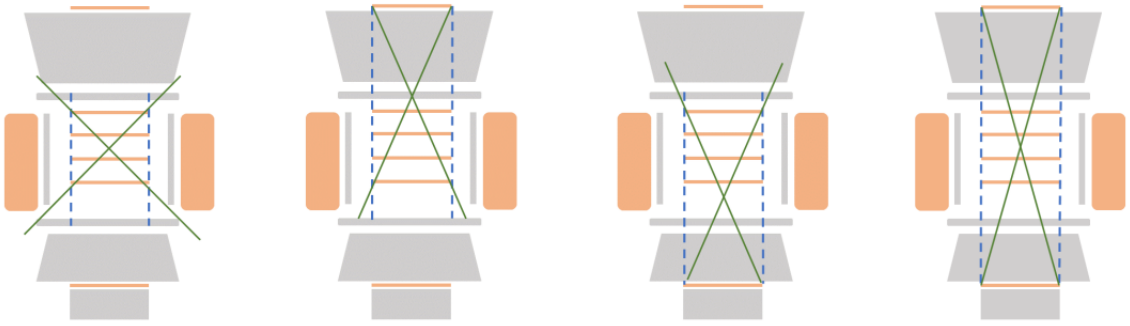

(a) Inner (b) L1+Inner (c) Inner+L9 (d) L1+Inner+L9

Figure 3.6: The four tracker patterns of the AMS-02 Silicon Tracker: (a) Inner (b) L1+Inner (c) Inner+L9, and (d) L1+Inner+L9 (Full Span).

The determination of rigidity is achieved through the utilization of a track-fitting algorithm that analyzes the particle trajectory within the AMS-02 magnet. This algorithm takes into consideration factors such as the multiple scattering of charged particles and the energy losses that

occur within the detector [179]. The resolution of rigidity, $\Delta R/R$, can be approximated using Monte Carlo (MC) simulations. It reaches 100% at the so-called Maximum Detectable Rigidity (MDR), primarily influenced by the various patterns observed in the tracker.

The nine tracker layers are able to provide independent precise measurements of the charge Z of cosmic rays since the energy deposition in the silicon is proportional to the square of the charge Z of the particle according to the *Bethe* formula, $dE/dx \propto Z^2$ [184]. The charge resolution $\Delta Z/Z$ of the inner tracker (L2-L8) allows particle identification till nickel ($Z = 28$) as can be seen in fig. 3.7. Furthermore, the measurement of the trajectory inside the magnet allows to determine the direction of the curvature and therefore the sign of the charge. All this information provides the precise tools to distinguish matter from antimatter.

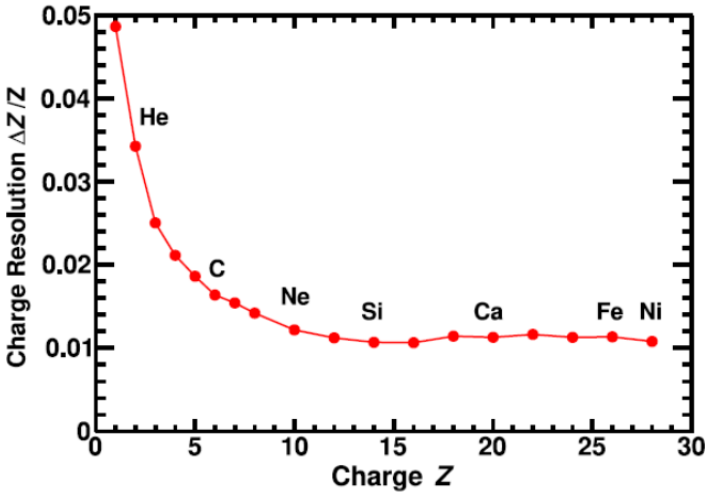

Figure 3.7: Inner tracker charge resolution $\Delta Z/Z$.

3.5 The Transition Radiation Detector (TRD)

The Transition Radiation Detector (TRD) is positioned between the L1 and upper TOF sections of the AMS [33,139,192,193]. It is constructed out of 328 modules arranged in 20 layers. Each module consists of 16 tubes with a diameter of 6 mm and a maximum length of 2 m. Fig.3.8 (a) illustrates that each layer is intertwined with a fiber fleece radiator, LRP375BK, which is 20 mm thick and has a density of 0.06 g/cm^3. To minimize the relative movement of TRD components caused by temperature changes, the layers are supported by an octagonal carbon fiber structure with an exceptionally low coefficient of thermal expansion (as depicted in Fig. 3.8 (b). The TRD is composed of 12 layers along the Y-axis, situated in the middle, and the remaining layers are positioned along the X-axis, with four layers at both the top and bottom. The tubes are filled with a gas mixture of 90% Xenon (Xe) and 10% Carbon Dioxide (CO_2). Xenon captures the X-rays produced by the transition radiation in the radiator, while CO_2 ensures the stable functioning of the tubes. The ionization signal is detected by an anode wire within each tube (see Fig. 3.8 (c).

The gas in the tubes is supplied from two tanks of 49 kg of Xe and 5 kg of CO_2 , which ensures

a livetime of more than 30 years in the space. The measured leak rate is dominated by the CO_2 and amounts to 0.47 g/day on average.

The primary objective of the TRD is to effectively detect electrons and positrons amidst a background of protons. This detection method relies on the phenomenon of electromagnetic transition radiation (TR) emitted when a charged particle crosses the boundary between two distinct materials. In the TRD, the Xe gas in the tubes efficiently absorbs this radiation. Consequently, the total energy loss experienced is directly related to the Lorentz Factor $\gamma = E/m$, enabling the differentiation of particles with varying masses, specifically electrons and positrons from protons [56, 107, 108]. Fig. 3.9 (a) illustrates the contrasting energy deposition per tube for electrons and positrons, with electrons emitting TR due to their high Lorentz factor.

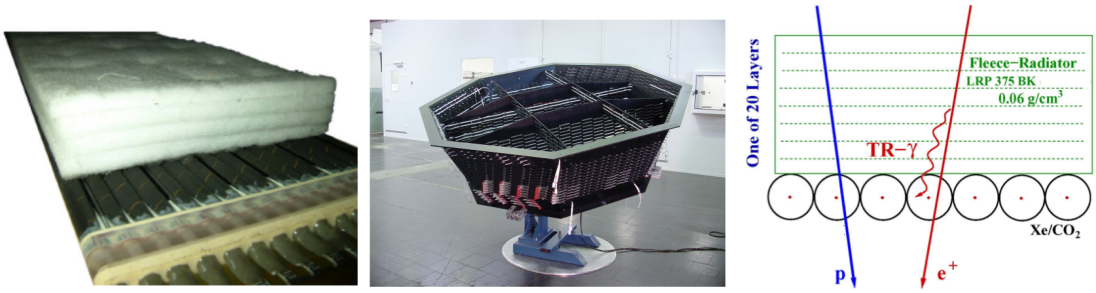

(a) (b) (c)

Figure 3.8: (a) TRD Module prototype along with the fiber fleece radiator on top of the layer, (b) TRD Support Structure, and (c) Detection Scheme: Detection of ionisation due to charged particles, here p (in blue) are compared to e^+ (in red), transition radiation photons (curved red arrow, TR-γ) are emitted as the e^+ traverses the radiator.

To differentiate between electrons/positrons $(e^{\pm})$ and protons p, the signals from the 20 layers are combined using a statistical estimator called TRD_{Lkh}. This estimator calculates the ratio of probabilities for the $e^{\pm}$ hypothesis and the p hypothesis [166]. Fig. 3.9 (b) displays the distribution of TRD_{Lkh} from 10-100 GeV, alongside the MC simulation [238], which accurately reproduces the data across six orders of magnitude. Electrons/positrons exhibit a peak at $TRD_{Lkh} = 0.35$, while protons peak at $TRD_{Lkh} = 1$. Consequently, protons can be efficiently rejected. For instance, implementing a cut-off value of 0.6 in the TRD estimator would result in a 90% efficiency in detecting electron signals and proton rejection of over 10^3 up to 200 GeV (as shown in fig. 3.9 (c)). By further tightening the cut-off in the TRD estimator, the rejection of protons can be increased in the high-energy range, albeit at the cost of reducing electron efficiency (fig. 3.9 (c)).

Furthermore, the TRD offers an autonomous particle tracking functionality through the arrangement of layers along the X and Y axes. This configuration allows for the determination of the charge of atomic nuclei by measuring their energy loss rate (dE/dx).

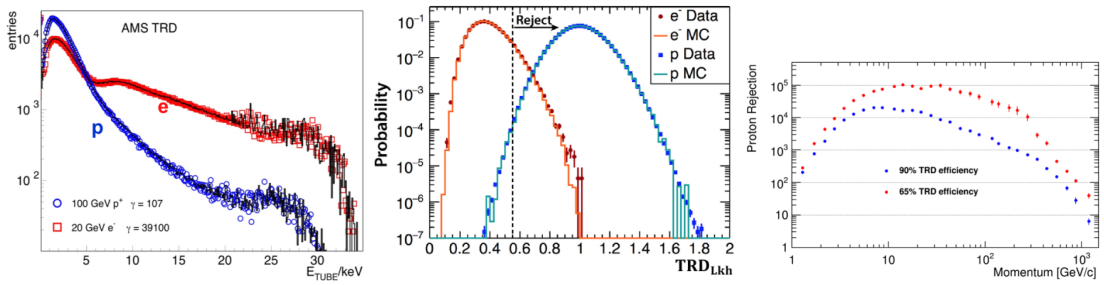

(a) (b) (c)

Figure 3.9: (a) The energy distribution of p (represented by blue points) and e^- (represented by red points) exhibits a noticeable distinction in shape. This distinction is leveraged within the likelihood function to effectively discriminate between these two species of CRs. (b) The distributions of TRD_{Lkh} for p (depicted in blue) and e^- (depicted in red) within the energy range of 10-100 GeV are displayed, along with the MC simulation that accurately represents the data across a vast range. The vertical dashed line indicates the location of the cut-off point associated with a 90% efficiency in detecting electron signals. It is possible to enhance the purity of the electron signal by tightening this cut-off, albeit at the expense of reducing the efficiency of detecting the e^- signal [33].(c) The proton rejection corresponding to a 65 % and 90 % efficiency in the TRD estimator signals [33].

3.6 The Time-Of-Flight (TOF)

The Time Of Flight (TOF) system is composed of four layers of scintillation counters, organized into two planes: the upper TOF located above the magnet bore and the lower TOF positioned beneath it [65, 80, 81]. Each layer comprises 8 or 10 scintillating paddles with a thickness of 1 cm and varying lengths (ranging from 117 to 134 cm). The paddles are alternately oriented in the X and Y directions, with inner paddles having a rectangular shape (approximately 12 cm wide) and outer paddles having a trapezoidal shape (width ranging from 18 to 26 cm) to maximize the geometric acceptance. Each paddle is equipped with 2 or 3 PhotoMultiplier Tubes (PMTs) at both ends to detect the light emitted by the scintillator. The PMTs are connected to the scintillators through plexiglass light guides. In total, there are 144 PMTs that collect light from 34 paddles distributed between the upper and lower TOF sections. Fig.3.10 provides a visual representation of the upper and lower TOF, along with a schematic illustration of one of the paddles.

Figure 3.10: Upper and Lower TOF along with a scheme of one of the paddles.

The TOF system serves as a trigger for charged particles by requiring a coincidence of signals from all four planes. Additionally, the particle's velocity ($\beta = \Delta s/c\Delta t$) can be determined by measuring the time of flight (Δt) between the upper and lower TOF, along with the particle's trajectory (Δs). The velocity resolution ($\Delta\beta/\beta$) has been measured to be 4% for $Z = 1$, decreasing to 1.2% for $Z \geq 6$, corresponding to a time resolution of 48 ps (as shown in left panel of fig. 3.11). This precise velocity measurement enables the differentiation of downward-going and upward-going particles at an exceptional level of 10^{-9} (right panel of fig. 3.11).

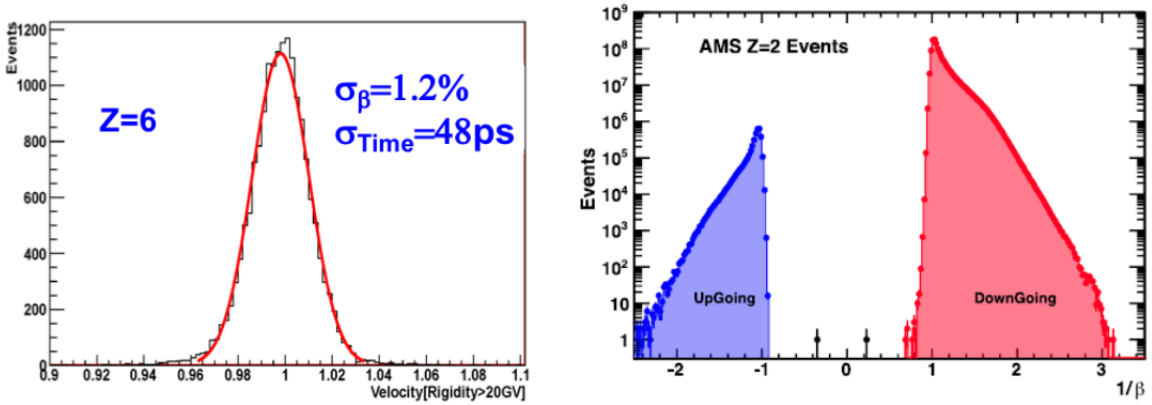

Figure 3.11: Left: The measured TOF velocity distribution for $Z = 6$ (C) with a $\sigma = 1.2\%$ from a Gaussian fit, which gives a time resolution of 48 ps [82]. Right: The inverse velocity distribution of the TOF for $Z - 2$ (He), illustrating a confusion probability of about 10^{-9} from downward-going and upward-going particles [33].

Furthermore, the TOF system is capable of determining the charge of a charged particle by measuring the energy deposited (dE/dx) which is proportional to Z^2. The signals from the PMTs on the anodes and dynodes are utilized in different ranges: anodes for $1 \leq Z \leq 3$, anodes and dynodes for $4 \leq Z \leq 8$, and dynodes for $8 \leq Z \leq 30$ (fig. 3.12), due to their distinct dynamic ranges.

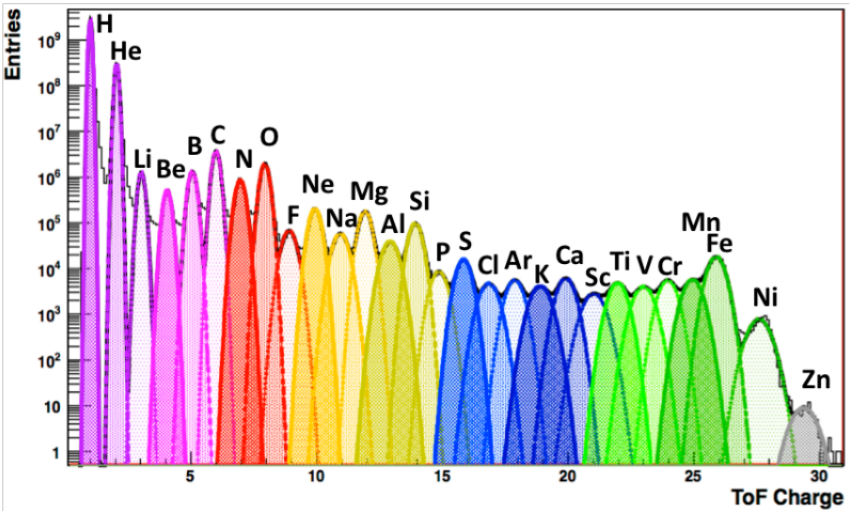

Figure 3.12: TOF charge distribution from $Z = 1$ (p) to $Z = 30$ (Zn) [82].

Finally, the signals from the anode are compared to three different thresholds, which are utilised in the level-1 trigger:

- **Low Threshold (LT):** It is used for time measurements and corresponds to around 20% of the *Minimum Ionising Particle* (MIP) signal.

- **High Threshold (HT):** It is used for the charged particle trigger ($Z \geq 1$) and corresponds to around 60 % of the MIP signal.

- **Super-High Threshold (SHT):** It is used for the ions trigger ($Z \geq 2$) and corresponds to around 400 % of the MIP signal.

3.7 Anti-Coincidence Counter (ACC)

The Anti-Coincidence Counter (ACC), also known as the veto counter, encompasses the inner tracker within the magnet bore [92, 269, 270]. It consists of 16 scintillator panels, each measuring $826 \times 826 \times 8\ mm$, arranged in a cylindrical structure spanning 1.1 m (as depicted in left panel of fig. 3.13). The scintillation panels emit light, which is then absorbed by wavelength shifter fibers with a diameter of 1 mm. These fibers guide the light to 16 PMTs located at the top and bottom (as shown in right panel of fig. 3.13). The inefficiency of the veto counter has been measured to be less than 10^{-5}.

The primary purpose of the ACC is to detect particles that enter the detector from the side or events generated by interactions with the detector material. It also serves to reduce the trigger rate during periods of high particle flux, such as in the South Atlantic Anomaly (SAA). Consequently, the ACC functions as a rapid veto trigger and is integrated into the trigger logic.

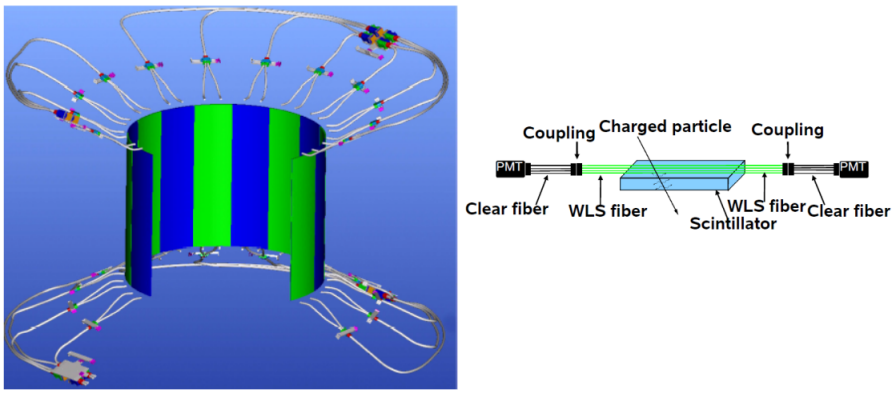

Figure 3.13: Left: The ACC counters (blue and green coloured panels) along with the collection system [269]. Right: Scheme of the ACC system.

3.8 The Ring Imaging Cherenkov Detector (RICH)

The Ring Imaging Cherenkov device is positioned between the lower TOF and the ECAL (Electromagnetic Calorimeter) [205, 234]. It consists of three primary components: a radiator, an expansion volume, and a photo-detection plane. The radiator comprises two different materials. The central part is constructed from 16 sodium fluoride (NaF) tiles, each measuring $85 \times 85 \times 3\ mm^3$, with a refractive index of 1.33. Surrounding the NaF tiles is another material composed of 92 silica aerogel tiles, each measuring $113 \times 113 \times 25\ mm^3$, and possessing a refractive index of 1.05.

The expansion volume spans a length of 470 mm and is enclosed by a conical reflector. Lastly, the photo-detection plane is composed of a matrix of 680 PMTs with sixteen pixels each. These PMTs are organized into four rectangular grids and four triangular grids, forming an octagonal configuration. The photo-detection plane features an empty area at its center, measuring 64×64 cm^2, corresponding to the size of the ECAL. This design ensures that particles can reach the ECAL without any interference. Fig. 3.14 provides an illustration of the three components of the RICH device.

The primary objective of the RICH system is to ascertain the velocity and charge of particles by detecting and measuring the Cherenkov radiation they emit (a detailed description of the RICH is given in chapter 5). Cherenkov radiation is typically generated when a charged particle passes through a dielectric medium with a refractive index (n) and a velocity (β) greater than the phase velocity of light in that medium. This condition is referred to as the Cherenkov threshold ($\beta_{th} > 1/n$) [98]. The emitted radiation takes the form of a cone, with an aperture angle (θ_c) determined by $\cos(\theta_c) = 1/n\beta$.

Within the RICH system, the emission of Cherenkov radiation occurs within one of the two radiators, namely NaF and aerogel. The NaF radiator is capable of detecting particles with a velocity (β) greater than 0.75, while the aerogel can detect particles with β values exceeding 0.953. By utilizing both materials, the detection efficiency is optimized. NaF produces

radiation with a larger aperture angle (θ_c), enabling the detection of particles that fall within the ECAL region. The emitted photons in the radiator are captured by the PMTs located in the photo-detection plane, allowing for the reconstruction of the Cherenkov cone. To enhance the efficiency of this process, a reflector within the expansion volume is employed, redirecting photons that fall outside the photo-detection plane (as depicted in left panel of fig.3.15).

Lastly, the particle velocity (β) is determined by measuring the angle (θ_c) of the Cherenkov cone. By possessing accurate information regarding the refractive indices of the radiators [168], a velocity resolution of approximately $\sigma_\beta \sim 0.8 \times 10^{-3}$ is achieved for $Z = 2$. This resolution further improves to around $\sigma_\beta \sim 0.5 \times 10^{-3}$ for higher Z values [169] (See right panel of fig. 3.15).

Additionally, the precise measurement of the velocity allows us to obtain the mass of the particle as

$$m = RZ\frac{\sqrt{1-\beta^2}}{\beta}. \tag{3.1}$$

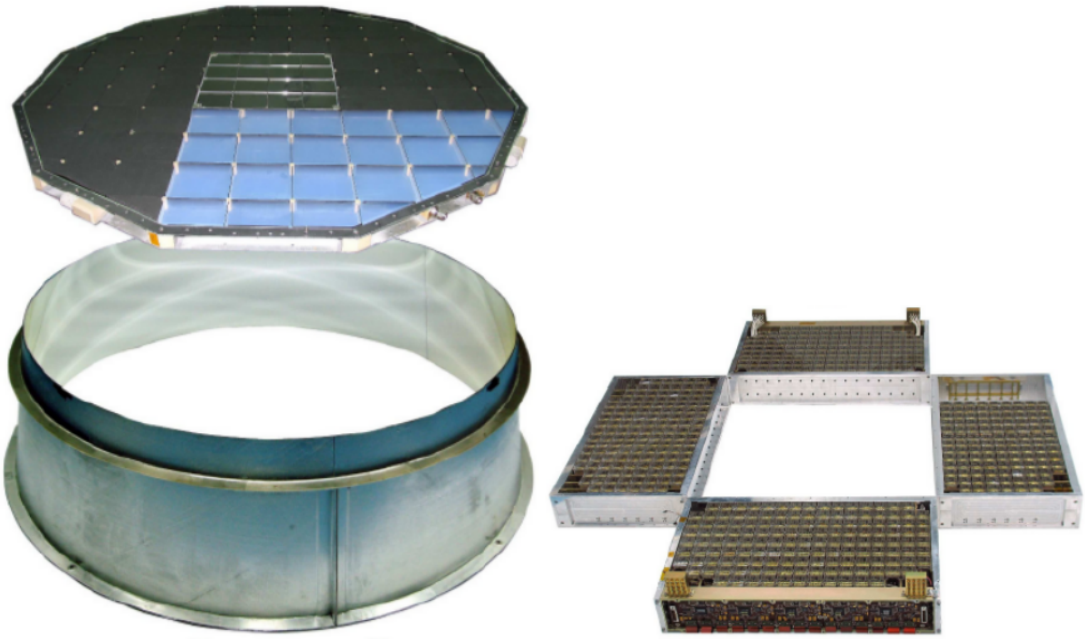

Figure 3.14: Left: RICH radiator with its expansion volume and conical reflector. Right: RICH photo-detection plane.

and thereby helps in separation of light CR isotopes. This principle is followed in the $^{10}Be/^{9}Be$ ratio determination which forms one of the major component of the present thesis.

Along with that, the *Frank-Tamm formula*, $N \propto Z^2 \sin^2(\theta_c)$ helps us to measure the charge of the particle by counting the number of photons, N [261].

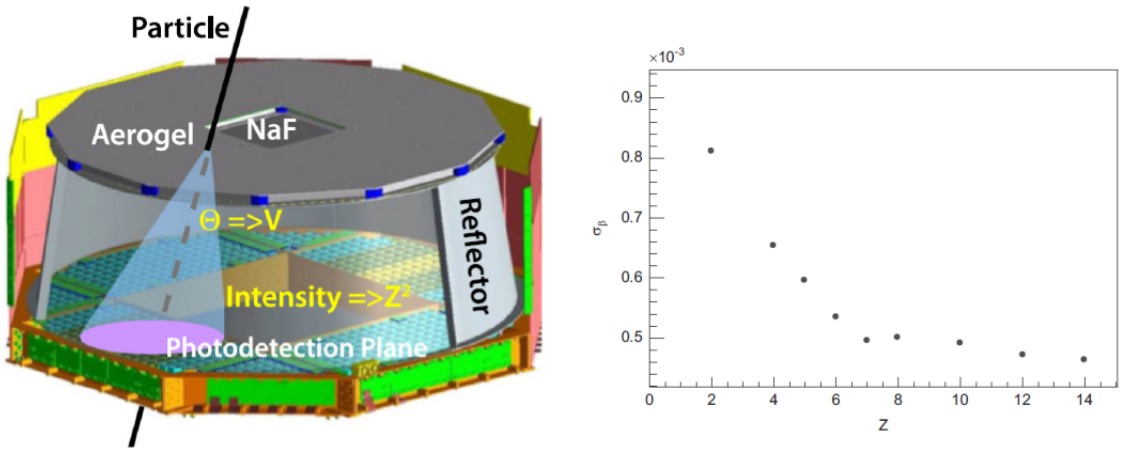

Figure 3.15: Left: RICH detection system scheme. Right: The velocity resolution as a function of the charge Z [169].

3.9 Electromagnetic Calorimeter (ECAL)

The Electromagnetic Calorimeter (ECAL) is situated at the lower part of AMS [14, 266]. It possesses an operational area measuring $648 \times 648\ mm^2$, a thickness of 166.5 mm, and an overall weight of 648 kg, inclusive of the mechanical structure and the readout cables (see fig. 3.16 (a)). This calorimeter consists of 9 modules referred to as superlayers, each with a thickness of 18.5 mm. Each superlayer comprises 11 grooved lead foils that are 1 mm thick, interleaved with 10 layers of scintillating fibers measuring 1 mm in diameter. The fibers are oriented in a single direction, resulting in the stacking of the 9 superlayers with alternating fiber orientations, parallel to the X direction (5 superlayers) and the Y direction (4 superlayers). This configuration allows for the creation of a three-dimensional representation of the electromagnetic showers (see fig. 3.16 (b)).

To prevent any inactive regions, each superlayer of the ECAL is equipped with 36 four-anode PMTs that are placed alternately at the two opposing ends. In total, there are 324 PMTs, amounting to 1296 anodes, responsible for the readout of the ECAL. Each anode covers a 9×9 mm^2 area and is composed of 35 fibers, referred to as cells. In fig. 3.16 (c), one of the superlayers is depicted, illustrating the footprint of the PMTs and one of the cells overlaid. The 1296 cells are divided into 18 longitudinal layers (2 per superlayer), with each layer containing 72 cells in the transverse direction. This segmentation provides a high level of detail, enabling precise sampling.

The primary objective of the ECAL is to accurately measure the energy deposited by electromagnetic particles. When charged particles enter the ECAL, they generate showers. These showers are more contained for electromagnetic particles like electrons and positrons due to their high number of electromagnetic interaction lengths, approximately $17X_0$. In contrast, the ECAL design (as described in references [95, 100]) ensures a significantly smaller number of nuclear interaction lengths, approximately 0.7λ. As a result, while electromagnetic showers are well-contained for electron and positron energies up to a few TeV, there is some energy

leakage for protons, indicating partial containment [199].

The energy of the incoming particle is calculated by incorporating adjustments that account for the energy leakage at the rear and lateral sides. These corrections are implemented to achieve energy linearity within a margin of less than 1% up to 300 GeV. The calorimeter's energy resolution, denoted as $\sigma(E)/E$, was determined through measurements conducted during the test beam [162] (see left panel of fig. 3.17), and is well parametrised by

$$\frac{\sigma(E)}{E} = \sqrt{\frac{(0.104)^2}{E} + (0.014)^2}. \tag{3.2}$$

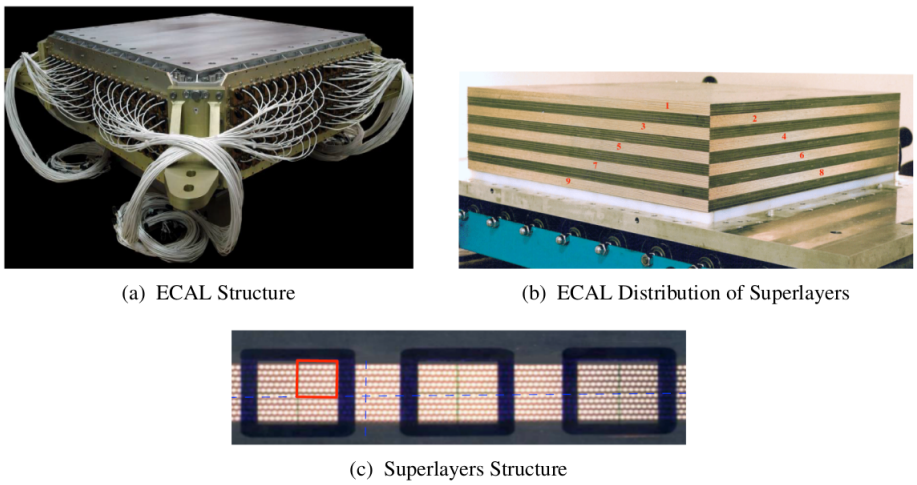

(a) ECAL Structure

(b) ECAL Distribution of Superlayers

(c) Superlayers Structure

Figure 3.16: (a) The ECAL structure. (b)The 9 superlayer distribution with the fibres stacked in an alternating fashion. (c) One of the 9 superlayers with the PMT footprint with a single cell superimposed on it.

The ECAL also plays a crucial role in effectively distinguishing between p and $e^{\pm}$ particles. Specifically, the shower's shape enables the creation of an ECAL estimator, known as $ECAL_{BDT}$, which utilizes a multivariate method based on a *Boosted Decision Tree* (BDT). Additionally, discrimination between protons and leptons is achieved by analyzing the ratio of the energy measured by the ECAL to the momentum determined by the tracker, denoted as E/p. This distinction arises because proton showers are only partially contained within the calorimeter, resulting in an E/p ratio smaller than 1. On the other hand, $e^{\pm}$ particles are almost fully contained, leading to an E/p ratio close to 1.

The right panel of fig. 3.17 demonstrates the effectiveness of using the ECAL estimator and applying a threshold of $E/p > 0.7$ to reject protons. It is evident that by implementing a more stringent cut in the estimator, the rejection of protons can be enhanced. However, this comes at the expense of reducing the selection efficiency.

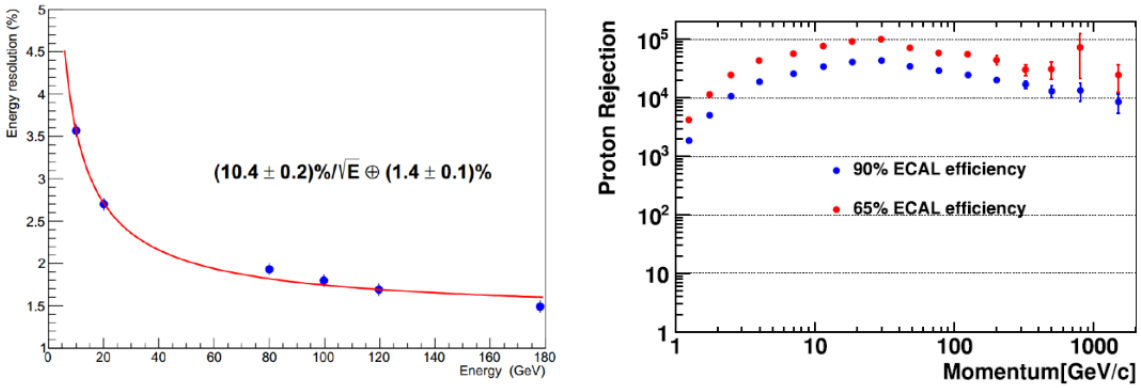

Figure 3.17: Left: The ECAL energy resolution measured using e^- test beams for perpendicularly incident particles [162]. Right: The measured proton rejection for two different $e^{\pm}$ selection efficiencies, namely 90% (represented by blue data points) and 65% (represented by red data points), is compared. It is observed that implementing a stricter cut in the ECAL estimator leads to a reduction in the proton background by approximately a factor of 3 [33]. This improvement in proton rejection is independent of the rejection capability of the TRD, as depicted in fig. 3.9 (c).

3.10 Trigger Logic and Data Acquistion System

3.10.1 The Trigger Logic

The primary objective of the trigger system in AMS-02 is to capture and record events that pass through the detector's fiducial volume, while discarding all other events. It is crucial for the decision-making process to be rapid in order to minimize detector dead-time, which refers to the period during which the detector is occupied and unable to collect events. To achieve this, the trigger logic is divided into two stages: the Fast Trigger (FT) and the level-1 trigger.

The Fast Trigger (FT) offers an exceptionally swift response by utilizing the combined information derived from the TOF and ECAL components. Specifically, the FT is triggered when any of the following signals are generated:

- **FTC:** When there is a simultaneous occurrence, within a time window of 240 ns, of signals in any three out of the four TOF planes, each exhibiting a pulse height greater than 0.5 times that of a $Z = 1$ MIP deposit. This criterion is applied to all CRs.
- **FTE:** When the energy deposited in the ECAL is indicative of an electromagnetic particle with an energy surpassing 1 GeV. This criterion is specifically applied to $e^{\pm}$, and γ.
- **FTZ:** When there is a coincidence of signals from four TOF planes within 640 ns, each with a pulse height greater than 3.5 times a MIP. This criterion is used for slow particles.

After the FT signal is produces, the level-1 trigger evaluation commences. In this stage, the information from the TOF, ECAL, and ACC is combined to generate seven sub-triggers:

- **Single Charge ($Z = 1$):** $4/4$ TOF planes passing the High-Threshold (HT) and no ACC hits.

- **Normal Ions ($Z \geq 2$):** $4/4$ TOF planes passing the Super High-Threshold (SHT) and less than 5 ACC hits.

- **Slow Ions:** $4/4$ TOF planes passing the SHT in an extended time window.

- **Electrons:** $4/4$ TOF planes passing the HT and energy deposited in the ECAL above a threshold in both projections. The ACC is disabled, once the ECAL trigger is fired.

- **Photons:** Energy deposited in the ECAL above a threshold in both projections and a shower angle in the geometric acceptance.

- **Unbiased Charged:** $3/4$ TOF planes passing the HT. As a result of high rate of signals, the events are prescaled by a factor of 100.

- **Unbiased ECAL:** Energy deposited in the ECAL above a threshold. In this case, events are prescaled by an even higher factor of 1000.

3.10.2 Data Acquisition System (DAQ)

Each sub-detector within AMS-02 is equipped with dedicated Front-End (FE) electronics that have a maximum readout time of 90 μs. The DAQ [96, 244] has been designed to collect and process signals originating from $300k$ FE channels. The system's architecture is based on a tree-like structure, comprising approximately 300 computational nodes, as depicted in fig. 3.18. Among these nodes, 264 are specifically dedicated to gathering signals from the FE electronics of each sub-detector and performing initial data reduction. They are denoted as xDR (where DR represents Data Reduction and x represents the respective sub-detector abbreviation: E for ECAL, R for RICH, T for Tracker, S for TOF and ACC, and U for TRD). The signals from the xDRs are then collected by 14 Low Level DAQ computers (JINF) with double redundancy. Simultaneously, trigger signals from the TOF and ACC are gathered in 8 SDR nodes and transmitted to the JLV1 nodes, which are also double redundant, where the Level-1 trigger is generated. Finally, the High Level DAQ computers (JINJ), which are quadruple redundant, receive all the signals from the JINF, SDR, and JLV1. They transfer the data to the main computer of AMS (JMDC), which is also quadruple redundant. The JMDC consolidates all the event information and determines whether it is of interest or not [198]. This additional level of software trigger constitutes an essential component of the system.

The interconnection of the DAQ system relies on a serial wired link protocol called AMSWire. This protocol is specifically designed to ensure low latency, low power consumption, and a transfer rate of 100 $Mbits/s$. To minimize dead-time, all event-related information is stored in internal buffers within each DAQ chain. Notably, the JMDCs possess a larger buffer known as JBUX, which can store data for approximately one day. This buffer is utilized during periods when communication between the ISS and the ground is interrupted, allowing for continuous data storage.

The DAQ system operates in runs lasting 23 minutes each, resulting in a total of 4 runs per orbit of the ISS. As part of the operational cycle, a comprehensive calibration of the sub-detectors is conducted every 2 runs while the ISS is positioned at Earth's equatorial latitudes.

Data transmission from the International Space Station (ISS) to the ground is facilitated through the utilization of NASA Tracking and Data Relay Satellites (TDRS). These satellites transmit the data to the satellite reception dishes located at NASA's *White Sands Test Facility* in New Mexico. Subsequently, the data is transferred from there to NASA's Payload Operations Integration Center (POIC) at the Marshall Space Flight Center (MSFC) in Alabama. This center houses the AMS Ground Support Computers. Eventually, all the data is sent to the AMS Payload Operations Control Center (POCC) at CERN and the Taiwan control center. The payload's status and data collection process are continuously monitored in both centers, with 8-hour shifts being employed for this purpose.

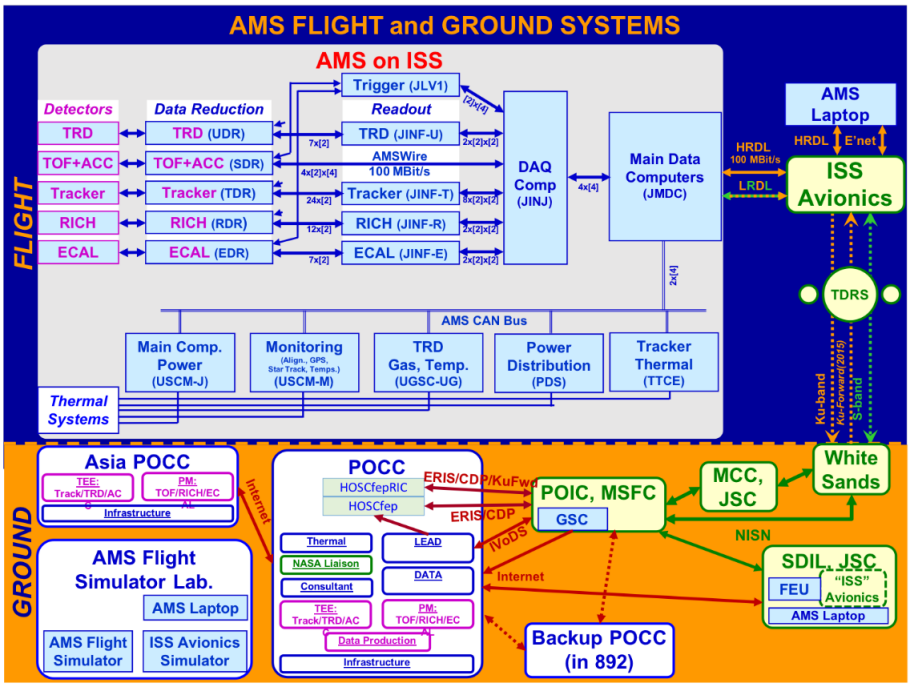

Figure 3.18: The diagram illustrates the configuration of the DAQ system within AMS-02. The process commences with the Data Reduction Boards responsible for each sub-detector. The signals originating from these boards are subsequently transmitted to the Low Level DAQ computers, JINF, where they are collected. Finally, the High Level DAQ computer, JINJ, gathers the data from the JINF computers. The main computer, JMDC, consolidates all the event information and transmits it to the ground [185].

3.10.3 Livetime

The preceding steps described in DAQ introduce a period of dead-time during which the detector is unable to collect new data. Specifically, the level-1 trigger process, data reduction, and transmission together consume approximately 220 μs. The status of the DAQ system is evaluated in samples of 20 ns. As a result, the livetime is calculated on a per-second basis as the ratio of samples where the detector was not busy to the total number of samples. In essence,

the livetime represents the efficiency of the DAQ, reflecting the fraction of time in which the detector is actively collecting data.

As discussed in chapter 2, CRs can only traverse Earth's magnetic field above a certain rigidity threshold. Consequently, the lowest energy CRs are only observable at high geomagnetic latitudes. The distribution of CR fluxes is skewed towards lower energies, resulting in a higher trigger rate in regions where a large number of particles pass through the detector, as depicted in left panel of fig. 3.19. This elevated trigger rate leads to increased dead time in the detector electronics and a reduction in livetime, as illustrated in right panel of fig. 3.19.

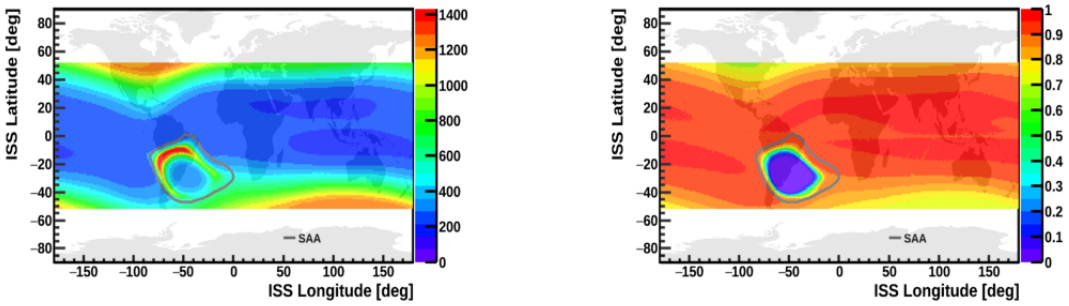

Figure 3.19: Left: Mean trigger rate. Right: Mean livetime. Near higher latitudes, higher trigger rates results in DAQ saturation, and consequently lower livetime.

3.11 Data Taking

Various factors can impact the data collection process of the AMS-02 detector and potentially affect data quality. To ensure optimal analysis, a set of criteria is established to determine which periods of time are suitable for analysis while discarding the remaining data.

As a first step, a few basic general checks are done. This assessment excludes specific periods such as the initial commissioning phase, times during detector operations (such as calibrations or TRD gas refills), and periods of ISS operations that may interfere with AMS, such as movements of solar arrays or the robotic arm within the field of view of AMS-02.

Additional conditions are imposed based on the ISS orbit and AMS-02 DAQ parameters, evaluated on a per-second basis. To facilitate this assessment, all relevant ISS orbit and DAQ parameters are stored in a Real-Time Information (RTI) database. Only seconds outside the South Atlantic Anomaly (SAA) region are considered as the particle rates are high here (refer chapter 2), along with those seconds exhibiting a livetime exceeding 0.5 s. This selection criterion aims to exclude saturated detector seconds, ensuring that the data chosen for analysis is of higher quality.

In order to ensure accurate measurement of directionality, it is crucial to have a precise understanding of the detector's behavior. To enhance the data quality, additional cuts are applied. This involves excluding seconds where the angle (α) between the AMS pointing direction and

the ISS zenith is too large, specifically within the range of $10^\circ < \alpha < 14^\circ$. This selection removes time periods when the station undergoes non-horizontal configurations, such as during docking or undocking of the *Soyuz spacecraft* or during *Extra-Vehicular Activities* (EVAs) performed by astronauts. Additionally, it is necessary to have a normal occupancy in the TRD to avoid seconds where this particular sub-detector becomes saturated.

As an example, fig. 3.20 illustrates the long-term stability of the AMS DAQ system over a period of 8.5 years, which corresponds to the duration of the data collection phase also analysed in this study. The light gray region represents the total time spent in orbit, while the red portion represents the time during which the DAQ system was actively acquiring data, accounting for approximately 99% of the total time. The cyan color indicates the fraction of seconds selected for analysis, taking into account the predetermined conditions and the livetime of the detector. This fraction represents approximately 83% of the entire time spent in orbit, and it also accounts for the time spent in the SAA, which amounts to 7% of the total time in orbit. The corresponding total exposure time amounts to $1.83 \times 10^8\ s$.

In general, the AMS DAQ system maintains a high level of stability throughout the entire duration, with only a few exceptions. The initial gap, as seen in fig. 3.20, corresponds to the commissioning period spanning from May 19th to June 5th, 2011. The subsequent gap from October to November 2014 occurred due to detector operations aimed at testing the thermal control system of the tracker. The intermittent and minor gaps observed between August 2018 and November 2019 were a result of non-standard configurations of the tracker caused by issues with the thermal control system. These problems were resolved by installing the Upgraded Tracker Thermal Pump System (UTTPS) during four EVAs conducted between November 2019 and January 2020.

3.12 Data Processing and Event Reconstuction

The events recorded by the DAQ of AMS-02, which contain raw data from the various subdetectors, are organized into time intervals called ”runs.” These runs have a duration of approximately 23 minutes, equivalent to one-fourth of an orbit around the ISS. On average, each run consists of around 7×10^5 events. However, the raw data alone is insufficient for conducting meaningful physical analysis. Therefore, a reconstruction software is employed to convert the detector readouts into events that carry relevant physical information.

To achieve these goals, a specialized software called the AMS Offline Software was created, serving two primary purposes: data reconstruction and detector response simulation [111, 112]. The data reconstruction process involves extracting meaningful physical quantities from the raw event data, which will be utilized in subsequent physics analyses. On the other hand, the simulation aspect involves assessing the performance of the detector by generating simulated events that accurately replicate the AMS geometry and incorporate all pertinent physics processes for individual CR species.

The reconstructed data format of AMS follows the structure provided by the CERN ROOT package. Each reconstructed event is stored as a ROOT tree object, which encapsulates essential high-level information required for the subsequent physical analysis.

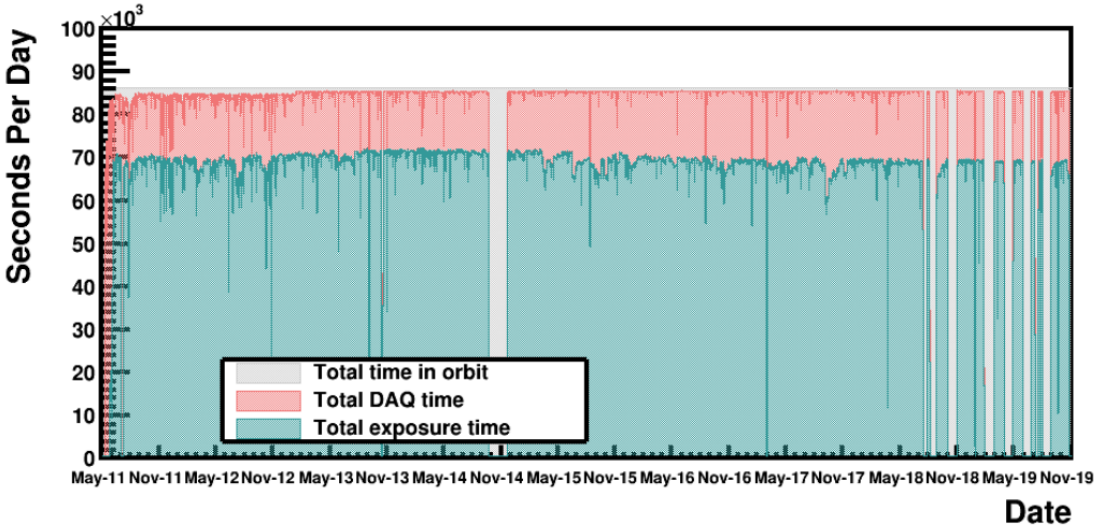

Figure 3.20: Time stability of data taking in s/day. The light gray, red and cyan represents AMS-02 orbit time, DAQ collection time, and the exposure time respectively. Plot taken from the analysis in [221].

3.13 AMS-02 Monte Carlo Simulation

The AMS Offline Software, is utilized for both data reconstruction and MC event simulation. The simulation process employs the same reconstruction procedure used for the actual data, and it relies on the Geant4 package [49, 50]. The simulation incorporates a comprehensive representation of the detector, including its geometry, material composition, and the various physical processes that occur when particles interact within the detector (such as elastic and inelastic interactions). The information from the simulated events is stored in a ROOT tree object, similar to how data is stored.

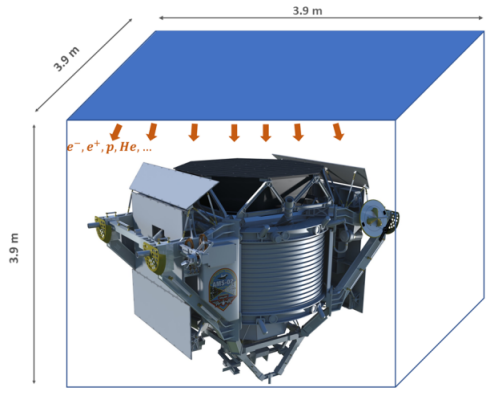

Figure 3.21: Scheme for the MC event generation in the AMS-02 Geant4 simulation.

The simulated particles are generated in an isotropic manner from the upper plane of a cube

measuring $3.9 \times 3.9 \times 3.9\ m^3$, which surrounds the AMS detector (as depicted in fig. 3.21). The generated particles have a specified momentum (p) or rigidity (R). The distribution of generated events follows a spectral shape that is proportional to the inverse of the momentum (p^{-1}) or the rigidity (R^{-1}). Consequently, the number of events (N) is uniformly distributed as a function of rigidity, according to the following relationship:

$$\frac{dN}{dR} = kR^{-1} = N(R, R + \Delta R) = k \int_{R}^{R+\Delta R} R^{-1} dR = k\Delta \ln(R), \tag{3.3}$$

where k is a constant.

The motivation behind generating events with a steeper distribution is to ensure an adequate amount of statistical data at high rigidities while avoiding an excessively large number of low rigidity events that would be challenging to handle. However, it is important to note that the generated spectrum does not reflect the natural CR spectrum. As a result, it is common practice to apply reweighting techniques in order to reproduce the observed variations in the distribution of different CR species.

Chapter 4

AMS-02 Be Isotope Data Analysis

The primary goal of this analysis is the measurement of the isotopic fraction of Beryllium in the CR flux, and in particular the flux ratio, $\Phi_{^{10}Be}/\Phi_{^{9}Be}$ as a function of the kinetic energy per nucleon, E_k/n. For relevant literature on the importance of this ratio, one can refer to the section of 2.7.3 in Chapter 2 of the present thesis.

In the following chapter, we discuss the procedure of obtaining a highly pure sample of Be, followed by a discussion on the requirements for isotopic distinctions in AMS-02 and the energy ranges where it is possible to do so. Then we demonstrate how to measure the fractional contribution of each isotopes. The chapter concludes with the computation of the the isotopic fluxes and the isotope flux ratio of interest with a brief discussion of its consequence on the Halo size of the galaxy.

4.1 Data Reconstruction

4.1.1 Data Reduction (Trigger)

In order to perform the analysis, we need to extract a pure sample of Be events from the AMS CR data. For that purpose, we take advantage of the excellent charge resolution provided by AMS-02, and hence request the distribution of events in various sub-detectors compatible with charge, $Z = 4$. Also, AMS-02 requires pre-processing of events which are subsequently saved by the electronics as discussed in chapter 3. In particular, only events passing the physical trigger (LVL1 trigger) are considered for this analysis.

To identify Be events, we need to select events with well measured rigidity and velocity. Each selection criterion influences a particular variable, setting threshold intended to select the events with the best reconstruction of physical quantities and to reject badly reconstructed events. The resulting inefficiencies has to be carefully evaluated and taken into account in producing the final fluxes of the isotopes.

An *event* is registered when a particle traverses the AMS-02 4/4 TOF layers without being rejected by the ACC system (i.e., ACC Hits < 8). A certain amount of information associated

with the event encoding the interaction parameters of the particle with the sub-detector is stored. Events are classified into $TTree$ ROOT classes named as $ntuple$.

4.1.2 Geomagnetic Environment and timestamp (RTI)

AMS-02 is installed on the ISS, and as such it has to endure the geomagnetic field of earth, the consequences of which have been extensively discussed in Chapter 2 and 3. The geomagnetic field results in chemical species to be trapped in its influence, which necessitates the decoupling of particles of cosmic origins from the former. In this regard, a quantity called the geomagnetic rigidity cutoff, denoted as R_c, which relies on latitude, longitude, and pointing information comes handy. It signifies the minimum rigidity required for a particle to be confidently identified as of cosmic origin. Particles below this cutoff may be confined to closed trajectories around the Earth, having been generated through interactions of cosmic rays with the Earth's atmosphere.

Furthermore, temporal data pertaining to the location of AMS and detector conditions is stored on a per-second basis using a distinct data format. This data, referred to as real-time information or RTI, is organized with integer Unix time in seconds as its indexing system. By utilizing the Unix timestamp associated with a stored event, one can easily access the corresponding RTI.

RTI contains various data, including ISS latitude & longitude, solar beta angle, AMS pointing direction, livetime fraction, and the number of triggers occurring in each second. The positional and pointing information within RTI enables us to perform selections based on the location. Specifically, this data is instrumental in calculating the geomagnetic rigidity cutoff.

4.1.3 AMS-02 Monte-Carlo Simulations

The AMS-02 collaboration produced a series of officially sanctioned Monte Carlo (MC) datasets utilising a simulation toolkit rooted in the Geant4 package.

The particle's trajectory through various sub-detectors is segmented into small steps, and at each step, interactions and energy losses are randomly generated based on their respective probabilities.

The event reconstruction process is similar to that of real data, resulting in benchmarks that may be utilised to build selection criteria and particle identification algorithms. We will use the same analysis protocols and selection criteria for both the MC and data in the subsequent sections. In particular, we use the simulations of ^{7}Be, ^{9}Be, and ^{10}Be for the signal, and the simulations of ^{10}B, ^{11}B, C, ^{14}N, ^{15}N, and O for the background.

4.1.4 General Quality Selections

4.1.4.1 Time and Location Based cuts

The initial stage of event selection involves a rapid process that doesn't involve analysing detector signals on a per-event basis. Instead, it relies on promptly implementing certain criteria using only the run or event timestamp. As a result of specific abnormal conditions on ISS or AMS, certain runs may be entirely excluded from further processing:

- **Commissioning Period:** After the installation of AMS, a specific timeframe was allocated to ensure the optimal performance of all systems, conduct calibrations, and establish standard operating procedures. This particular period is not taken into account during the analysis.

- **ISS hardware in AMS Field of View:** At times, ISS operations necessitate the movement of the Space Station Remote Manipulator System, a robotic arm, which, in turn, passes through the AMS field of view. Consequently, CRs experience additional material interaction before reaching AMS, resulting in energy loss and secondary production that cannot be accurately predicted through modeling. NASA provides information about the scheduled operations, allowing us to identify and tag all affected runs.

The subsequent selections are conducted using the information provided by RTI:

- **Hardware Error Checks:** It excludes the seconds in which the data errors are more than 1% the trigger count.

- **Lost Events:** It ensures that the number of stored events for a second is at least 99% of the trigger count. Anamolous large events losses during a period could allude to underlying temporary problems with the DAQ operation.

- **Livetime:** The AMS-02 electronics sends a ping every 20 ns and checks if the detector state is "busy" or "free", associating with the boolean value 0 or 1. After which, the AMS-02 event reconstruction software associates to every event the value of this variable, averaged over the last second of the AMS-02 intenal clock (which is out of phase by 0.5 s with respect to the standard UNIX time). Within a good approximation, this average gives the fraction of every second in which the experiment was ready to accept a CR event, which is the *live* fraction of each second of the measurement time which is known as the Live-Time fraction.

  The live fraction is clearly lower when the event rate is high. The geomagnetic field is not constant, and it is particularly weak over the poles and in the SAA. In such zones, the event rate is consequently high, because of weak geomagnetic shielding. As such, the averaged live time along the ISS orbit varies from a minimum of 0.5 to a maximum of 0.9, and has a mean value of 0.85 as can be seen in fig. 4.1.

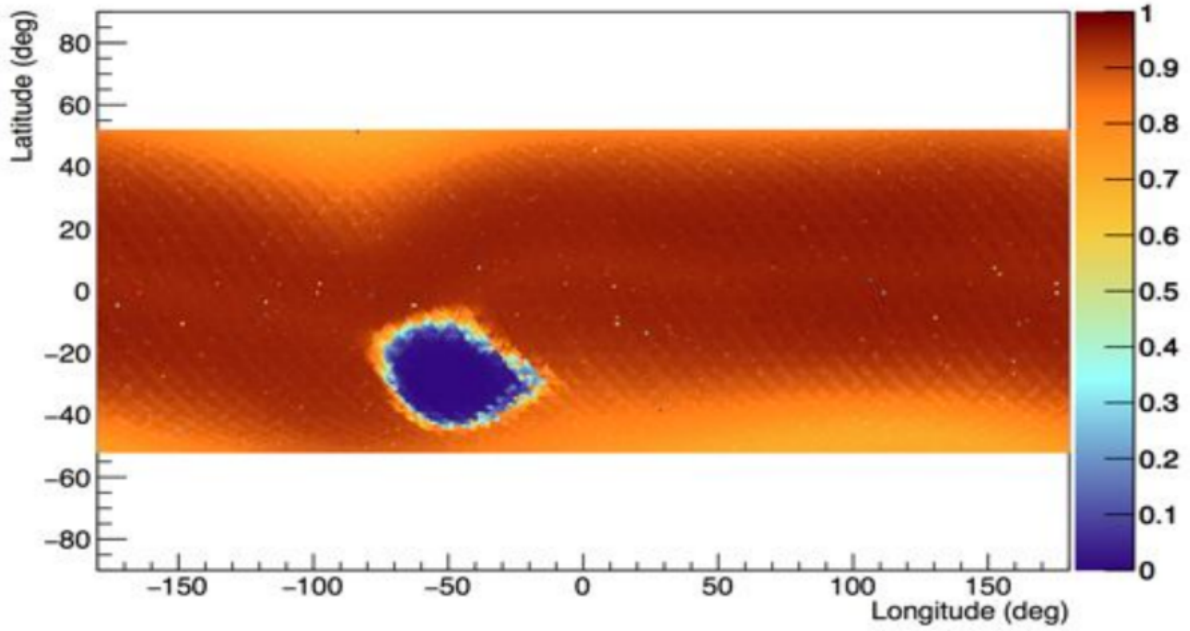

Figure 4.1: The live time fraction values along the AMS-02 orbit. The SAA position is the one where there is a drop to < 0.4.

We exclude the seconds in which the livetime is under 70 %. There are certain periods when the event rate is so high that AMS is unable to accept new triggers for a good fraction of time, and this cut helps eliminate it.

- **South Atlantic Anomaly (SAA):** The livetime cut efficiently removes a significant portion of the time spent within the SAA region (the region where we observe a livetime drop to ~ 0.4 in fig. 4.1), where the geomagnetic field's configuration causes a notable surge in CR fluxes at ISS altitude, causing saturation in the AMS detector. To ensure thorough exclusion, the SAA region is also geographically removed by applying a cut that encloses a specific polygon in latitude-longitude space.

- **Zenith Pointing:** AMS is rigidly affixed to the ISS at a constant angular orientation, typically pointing at a position of $\sim 12^{\circ}$ degrees from the zenith during regular operations. However, certain procedures like vehicle docking may necessitate adjustments in the ISS attitude, causing the AMS to deviate significantly from its zenith direction or even point towards Earth. In such cases, runs where the AMS is pointing more than 40 degrees away from the zenith are omitted from the analysis.

4.1.4.2 Event Geometry and Reconstruction Selections

In order to reduce or eliminate spurious events of non-cosmic origin, we can exploit the event geometry and outcomes from AMS reconstruction software. In particular, we use the following selections:

- **Downgoing Particle:** Only accept events measured with positive time interval, $\Delta t > 0$, between upper and lower ToF signals. The time resolution σ_T is of the order of $\sim 160\, ps$ while $\Delta t \sim 4\, ns$. As such, the excellent time resolution helps us to unambiguously and

efficiently distinguish downgoing particles, allowing us to neglect contamination from upgoing events. We employ the selection $\beta_{ToF} > 0.3$ for this purpose.

- **Single Track:** Only consider events that have only one track successfully reconstructed in the tracker and a single, high-level particle object reconstructed. Additional tracks and particle objects often arise from interactions of the incoming particle with AMS, causing other particles to be set into motion. In some cases, an extra object may be reconstructed due to detector noise. By implementing this selection, the quality of the sample is improved as it removes events where the incoming particle interacts, potentially experiencing energy loss, angular deflection, or fragmentation. Additionally, it eliminates events where inaccurately reconstructed objects could lead to misleading measurements.

4.2 Identification of Beryllium Events

The primary step in our analysis is to have a pure sample of Be. For this purpose, we employ the different sub-detectors of AMS which are capable of giving independent charge measurements as explained in Chapter 3, viz. the 9 tracker layers, and the Time-of-Flight (ToF) detectors. The following section describes the primary charge selections used to obtain our Be sample, and also the selections used to reduce contamination from heavier nuclei.

4.2.1 Principal Signal Purification with Charge (Inner Tracker)

The charge of the particle, provides the most effective way of selecting a good sample of Be (or for that matter, any element from AMS data). The best performing sub-detector in AMS-02 for charge selection is the Silicon Tracker . As already explained in chapter 3, it consist of 9 layers which are all capable of providing independent charge estimation. The excellent inner tracker charge resolution can be visualised from the fig. 4.2. In our analysis, the inner tracker charge is defined as the truncated average of the independent charge estimations of each of the inner tracker layers.

In AMS-02, a particle traversing the detector planes deposit energy by ionisation in the detector material. The Bethe-Block equation tells us that the average energy deposited by ionisation is proportional to the squared value of its electric charge. Particle with $\beta\gamma \sim 3$ deposits a constant average ionisation energy (m.i.p), while the slower particles deposit energy proportional to Z^2/β^2.

The information pertaining to the energy deposition in the ToF paddles and in the Tracker layers is recorded in the reconstructed data. In the reconstruction of the charge, the algorithm applies appropriate correction for the β dependence, and then the square root is taken, and hence, the reconstructed quantity gives us a linear output of particle charge.

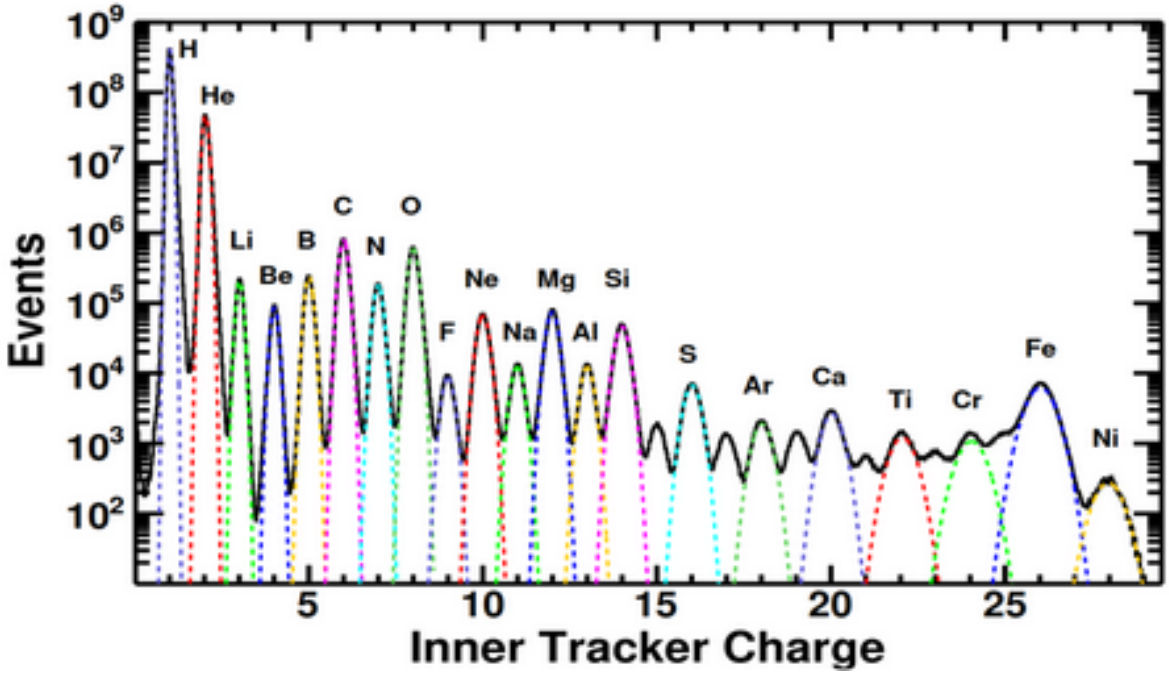

Figure 4.2: The Inner Tracker Charge distribution. We can interpret that AMS-02 has excellent charge resolution, which allows us to select a very pure Be sample ($\sigma \sim 0.23$).

As is evident from fig. 4.2, the inner tracker already assists us to select a highly pure sample of Be. In order to find the charge selection window to obtain the best sample of events of Be, we follow the following procedure:

1. With the pre-selections, we plot the charge distribution for the three variables described above

2. Since we are interested in the Be events, the possible contamination influencing the Be distribution are the ones from Lithium (Li) and Boron (B). We fit the three with Gaussian fits as shown in fig. 4.3.

3. Then we make a compromise between the efficiency of Be events and the contamination coming from Li and B distribution at greater than 90 % efficiency and less than 1 % contamination. In order to achieve this, we consider the integral (efficiency) of the Be distribution within 3 σ limits $[\mu_{Be} - 3\sigma_{Be}, \mu_{Be} + 3\sigma_{Be}]$; and the contamination of Li by considering the integral of the Li distribution within the limits $[\mu_{Be} - 3\sigma_{Be}, \infty]$, and the integral of B distribution within the limits $[-\infty, \mu_{Be} + 3\sigma_{Be}]$. The Be fit integral is iteratively reduced with a 0.05 step length in each iterations, and the contamination integrals are broadened by the same step length in each subsequent iterations. Finally, we plot the efficiency and contamination versus the number of steps. The step that corresponds to the best compromise between efficiency and contamination ($>$90 % efficiency and $<$ 1 % contamination) is then considered for the selection window (See fig. 4.4).

The procedure outlined above for Inner Tracker charge, can be repeated for the rest of the sub-detectors of interest.

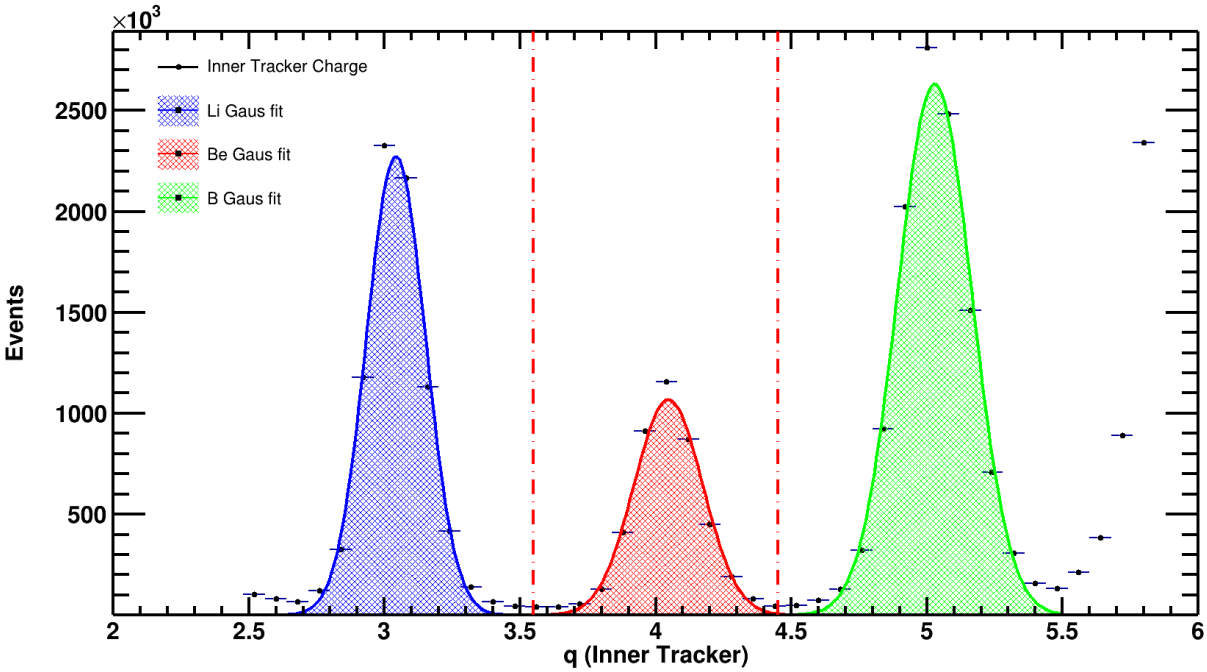

Figure 4.3: The Inner Tracker Charge distributions with pre-selections. The Li, Be, and B distributions are fitted with Gaussians. The selection window defined by the dashed red lines has a width of 0.90.

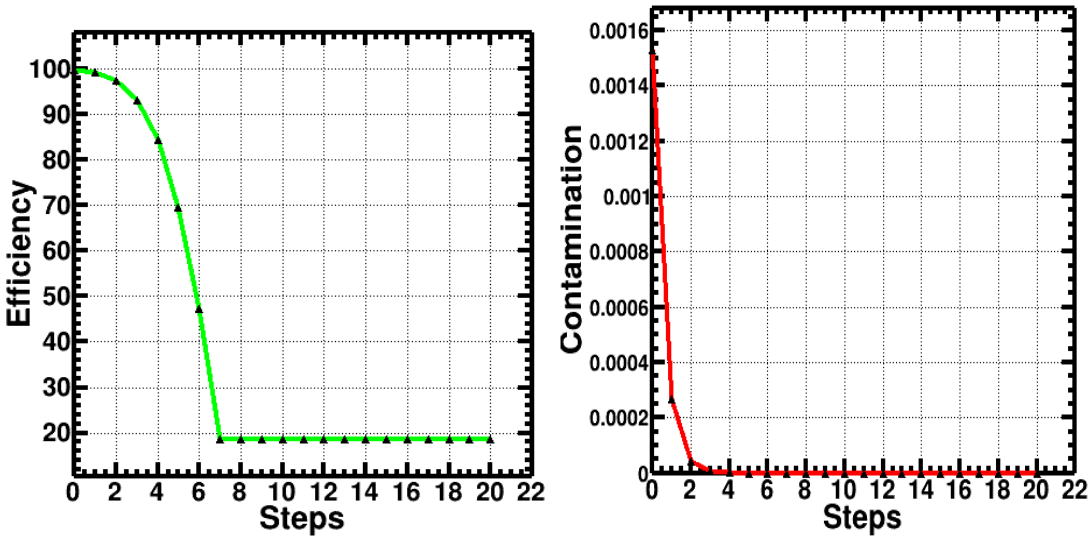

(a) Efficiency (b) Contamination

Figure 4.4: The (a) Efficiency and (b) Contamination as a function of the steps for the Inner Tracker charge. We make a compromise between the two; in this particular case, the compromise is achieved at the 1st step which translates to a selection window of $[3.55,\ 4.45]$ (the selection window is plotted in fig. 4.3).

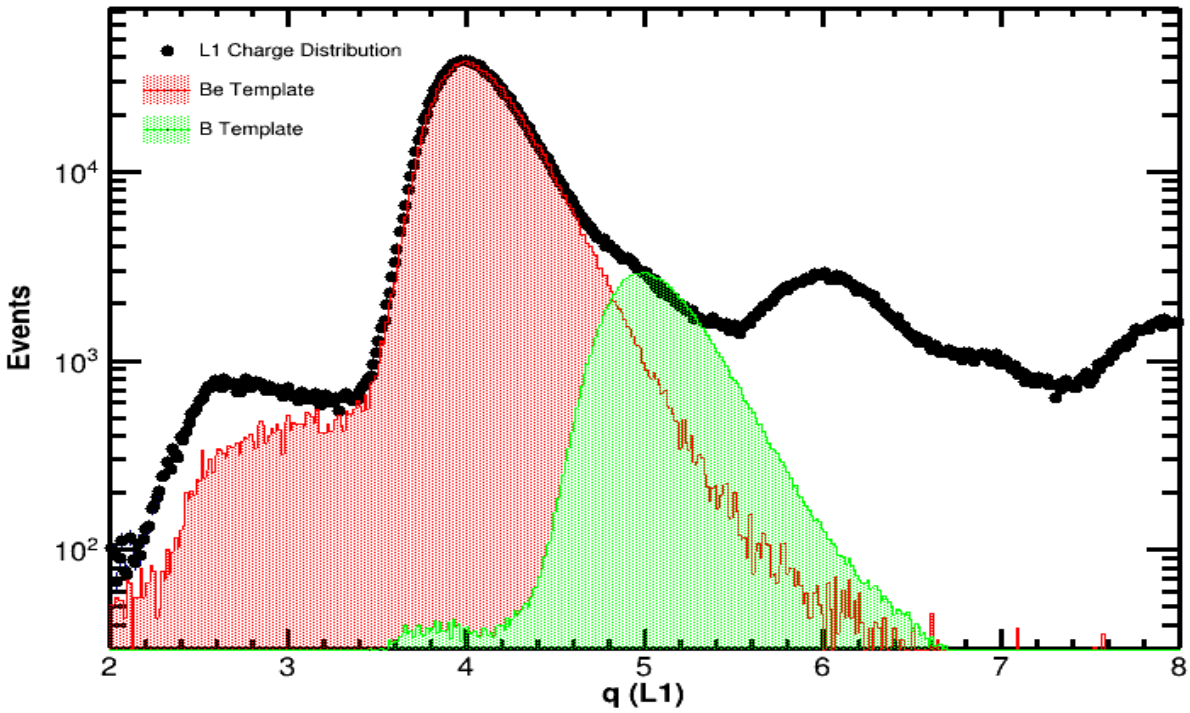

Figure 4.5: Charge distribution of L1 after applying a charge selection on the Inner Tracker, with Be and B templates from L2.

4.2.2 Background from Heavy Nuclei Fragmentation

The effect of inner tracker charge selections can be appreciated from fig. 4.5 showing the L1 charge distribution. After the application of a selection window on the inner tracker charge, the Li peak disappears in the charge distribution of Tracker Layer 1. However, we will see that we still have contamination coming from the fragmentation of heavier nuclei that are reconstructed as Be events. This motivates the deployment of further selections particularly on the ToF to reduce this fragmentation background.

Furthermore, just from the L1 charge distribution we can appreciate the amount of contamination of Li and B on the Be signal. For this purpose, we can plot the charge distribution of Tracker Layer 1 after applying a selection on it around $Z = 4$. We observe that heavier elements such as Boron, Carbon and Oxygen are also reconstructed as Be. Fitting this distribution with templates of Li, Be and B charge distributions from Tracker Layer 2 (the templates are obtained by applying selections on tracker layer 1, upper ToF, and Inner Tracker without the layer 2) shows us the contamination on the Be signal. The resulting plot is shown in fig.4.6.

4.2.3 Reduction of Fragmentation Background

The contamination from heavier species such as Carbon (C) and Oxygen (O) can be reduced by the application of a charge selection on the upper ToF. The subsequent upper ToF charge distribution for the selected Be sample is shown in fig. 4.7 . In the distributions only the Be peak is visible, except for the presence of a long tail. This tail is the result of anomalous energy

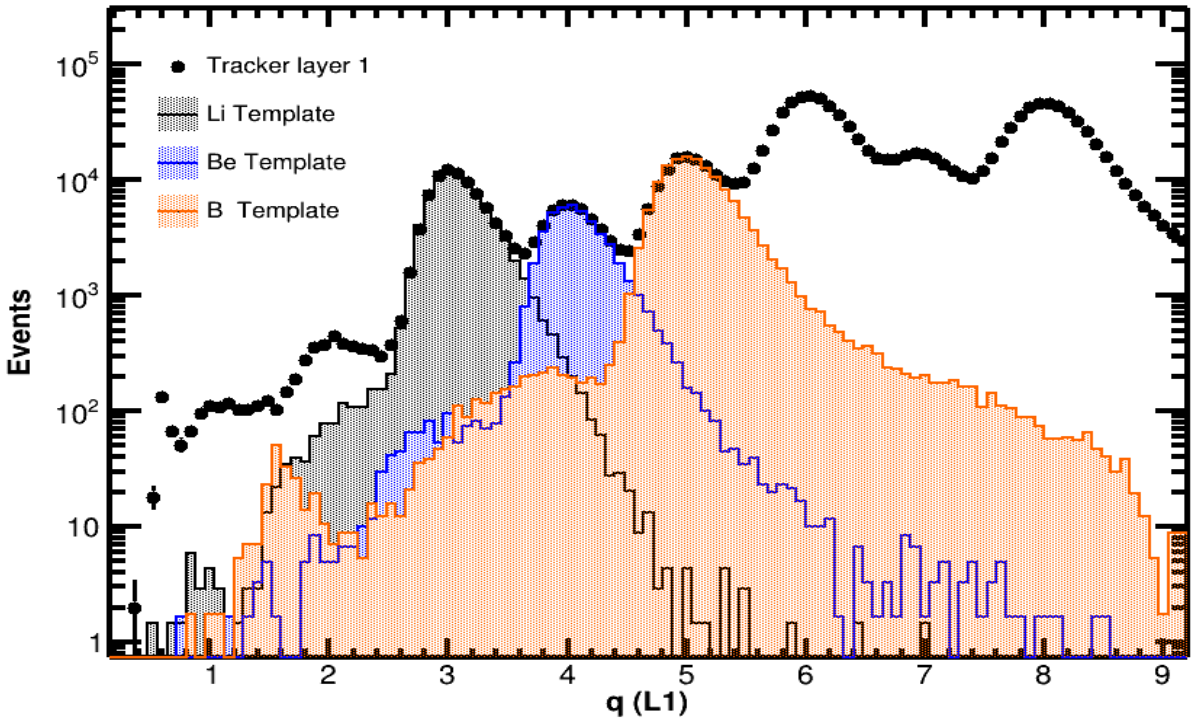

Figure 4.6: The charge distribution of Tracker Layer 1, with Li, Be, and B templates from Tracker Layer 2.

deposit in events affected by γ rays or fragmentation, where two or more like-charged particles deposits energy in the same ToF hit. The latter fact has been confirmed through MC simulation that these tails are mostly related to events where a nuclear interaction occurs within the AMS volume. A selection requesting a single track to be constructed, and a selection to cut the tail eliminate these interaction events.

The effect of the selections can be seen from the fig. 4.8, the distribution in red corresponds to the L1 charge distribution after application of a charge selection on the inner tracker and shows contamination from heavier species like C and O. After application of charge selection on the upper ToF, these $Z > 4$ events go away leaving us with a cleaner sample of Be. There might be still some spurious Li events falsely reconstructed as Be because of failure in scintillation paddles. In summary, the following two selections for remove the fragmentation background:

1. **Charge Selection on Upper Time-of-Flight (ToF)**

2. **Requesting a single track to be reconstructed in the tracker**

Since, we already have a pure Be sample from the selections on inner tracker and upper ToF charge, we can have the liberty of selecting a wider window on the charge on the tracker layer 1 as depicted in fig. 4.8. This selection further eliminates some of the B events reconstructed as Be at the cost of losing some true Be events. Cumulatively, the combined effect of charge selections on inner tracker, upper ToF, and L1 is such that we get a pure sample of Be events, however, with the possibility of heavier nuclei fragmentation to produce a Be track.

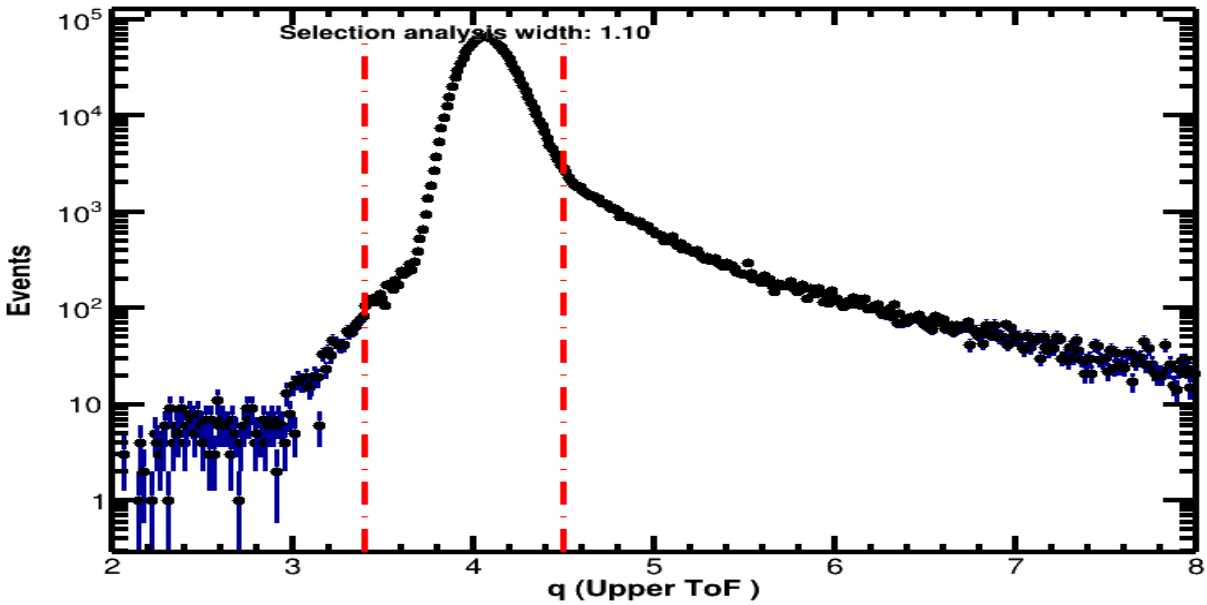

Figure 4.7: The Upper ToF charge distribution after the application of selection windows on L1 and Inner Tracker. The vertical lines represent the selection window on this quantity.

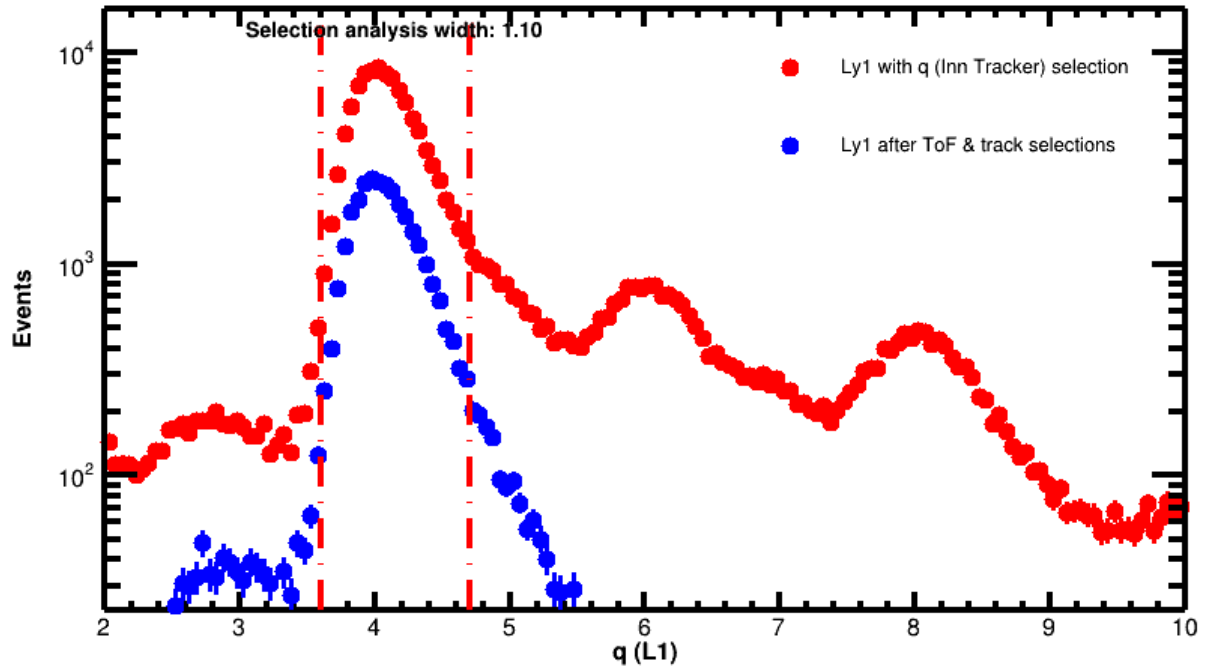

Figure 4.8: Charge distribution of L1 after application of charge selection only on the Inner Tracker shown in red shows that we have contamination from heavier species such as C and O. Application of charge selections on the upper ToF detector, and requesting a single track almost eliminates the background.

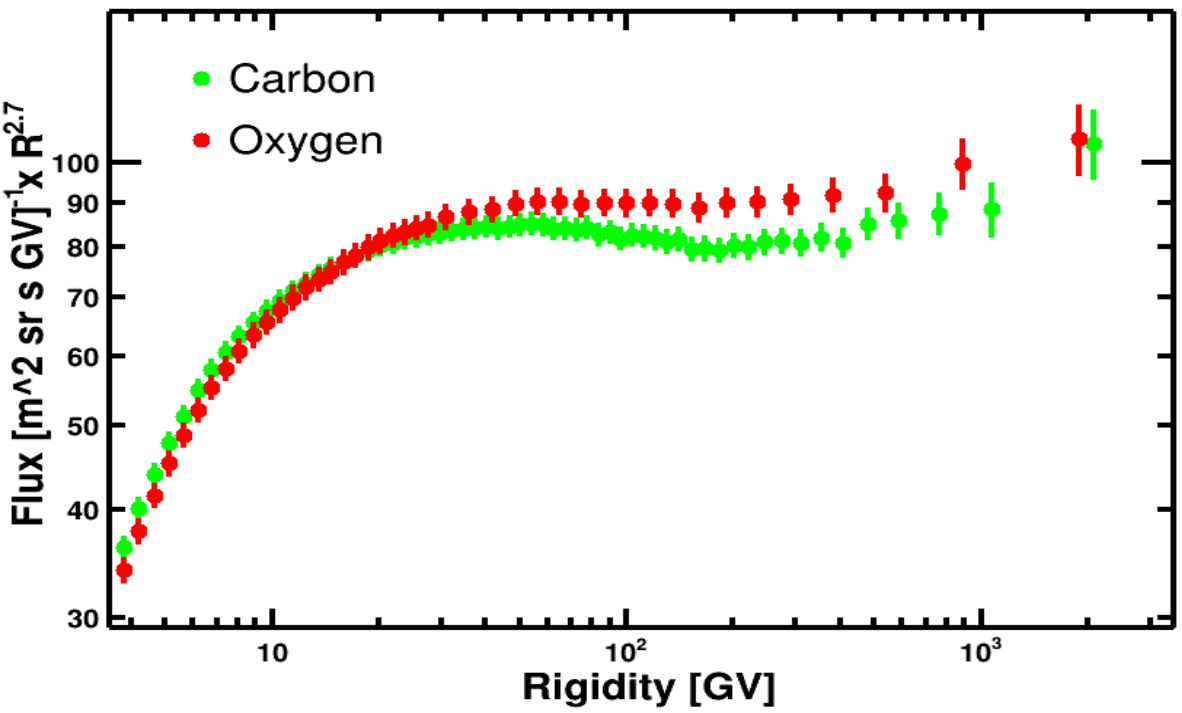

Figure 4.9: Fluxes of Carbon, and Oxygen used for estimating the contamination in Be measurement by AMS-02. These fluxes have been re-weighted according to the ones measured by the AMS-02 collaboration [29].

In addition to the above detectors, the particle charge can also be extracted from the RICH detector, as the number of collected Cherenkov photons is proportional to z^2. This can be particularly instrumental in estimating the small amount of fragmentation nuclei produced by Be nuclei interaction below Lower ToF and above/within the RICH radiators. However, this effect is estimated to be very small, and the ensuing acceptance loss shall vanish in the Be isotopic ratios. As such, we do a loose selection on the RICH charge as discussed in a later section.

4.2.4 Contamination from Interacting Heavier Nuclei

The Be measured by the AMS detectors have two source components: One from the CRs, and another contribution comes from the fragmentation of heavier nuclei interacting primarily within the AMS-02 material above the first Tracker layer. The nuclei that have potential to produce Be isotopes by fragmentation are Boron, Carbon, Nitrogen, and Oxygen. Heavier nuclei can neglected since the combination of their absolute flux and probability to generate Be, contributes negligibly to the Be isotopes measured by AMS-02 detectors.

Since Carbon and Oxygen nuclei are expected to provide the highest contamination, in order to estimate the amount of Be coming from interactions, we use a combined set of MC simulation of Carbon and Oxygen nuclei as shown in fig. 4.9 . All these MC sets have been re-weighted according to their cosmic abundance and to the corresponding spectrum as a function of rigidity measured by AMS-02 [29].

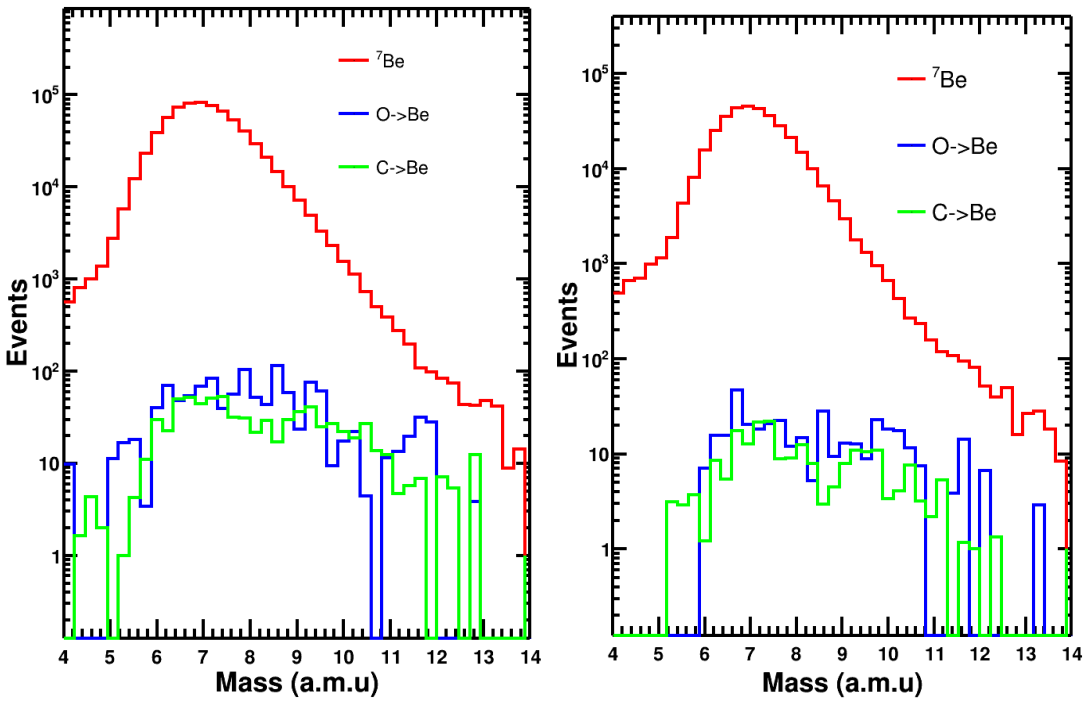

(a) ToF (b) RICH-Agl

Figure 4.10: The mass distributions for the ToF and RICH-Agl sub-detectors. The red histogram denotes the ^7Be mass distribution from AMS-MC. The blue histogram and green denotes the amount of contamination due to fragmentation from Oxygen and Carbon respectively. The contamination from Carbon is estimated to be $\sim 0.1\%$ and $\sim 0.05\%$ for ToF AND RICH-Agl respectively. Meanwhile, the contamination from Oxygen is estimated to be $\sim 0.2\%$ and $\sim 0.1\%$ for ToF AND RICH-Agl respectively.

This combined MC simulation helps to study the contribution of each of these species to the measured Be isotopes. The most abundant species in CR, i.e., Carbon & Oxygen give the highest contribution. In fig. 4.10 , the contamination from heavier nuclei to Be can be visualised for the ToF and the RICH-Agl detectors. The contamination from Carbon is estimated to be $\sim 0.1\%$ and $\sim 0.05\%$ for ToF AND RICH-Agl respectively. Meanwhile, the contamination from Oxygen is estimated to be $\sim 0.2\%$ and $\sim 0.1\%$ for ToF AND RICH-Agl respectively. The decrease in contamination from ToF to RICH-Agl is in accordance with theoretical expectations because the cross-section of interaction decreases as a function of energy.

Therfore, the contamination from heavier nuclei in our Be sample is negligible. Morever, we assume that the contamination from fragmentation is taken into account by the effective acceptance (see later section) calculated from the AMS-MC data. Hence, we wouldn't correct for it in the final results. The contamination from heavy nuclei to Be is tabulated in 4.1.

4.3 Isotopic Distinction with AMS-02

In the previous section we saw how charge measurement helps us to obtain a pure sample of Be. However, we are interested in the isotopes of Be for which we need a quantity that

Contamination % From Heavy Nuclei Fragmentation	
C $\rightarrow$ Be	$\sim 0.1\%$ (ToF) $\sim 0.05\%$ (RICH-Agl)
O $\rightarrow$ Be	$\sim 0.2\%$ (ToF), $\sim 0.1\%$ (RICH-Agl)

Table 4.1: The amount of contamination coming from fragmentation of heavy nuclei within the AMS detector volume calculated from AMS-MC.

can be employed to distinguish isotopes. The mass of the isotopes turn out to be an efficient discriminator which is directly related to the velocity and Rigidity of the CR species. In the following section, we will establish the latter relationship and describe the selection criteria developed for each sub-detectors of interest.

4.3.1 The Mass Formula

The momentum of a relativistic particle is given by $\vec{p} = m\vec{\beta}\gamma$. Hence the mass can be written as (omitting the vector notations):

$$m = \frac{p}{\beta\gamma} = \frac{p}{\beta}\sqrt{1-\beta^2}; \tag{4.1}$$

When utilising magnetic spectrometers, it is convenient to use magnetic rigidity rather than momentum. Qualitatively, the rigidity is the resistance that a constant magnetic field provides towards bending a charged particle trajectory, and it is related to the magnetic field by, $R = Br$, where B is the intensity of the magnetic field, and r is the gyro radius. Also, r is given by, $r = p/BZ$, where Z is the charge of the particle. Hence, we also get that, $R = p/Z$. In conclusion, the simultaneous measurements of the rigidity R, charge Z, and velocity β, allow to obtain the particle mass, m using the relation:

$$m = \frac{RZ}{\beta\gamma} \tag{4.2}$$

where γ is the Lorentz factor of special relativity.

Fixing a particular mass in 4.2, we can define characteristic curves of every isotopes in the $\beta - R$ phase space, around which the experimental points scatter according to R and β measurement resolution. The mass curves for ^{7}Be, ^{9}Be, and ^{10}Be are shown in fig. 4.11.

As seen in 4.11, the mass curves have very similar behaviour throughout the rigidity range. As such, it sets demanding requests on the resolution of the rigidity and β measurements to isolate the isotopes.

4.3.2 Rigidity (R)

As already mentioned in Chapter 3, when a charged particle traverses a magnetic spectrometer, the trajectory is bent. The curvature of this bending is inversely proportional to a quantity called *Magnetic Rigidity* denoted as R. It is defined as the particle momentum over its electrical

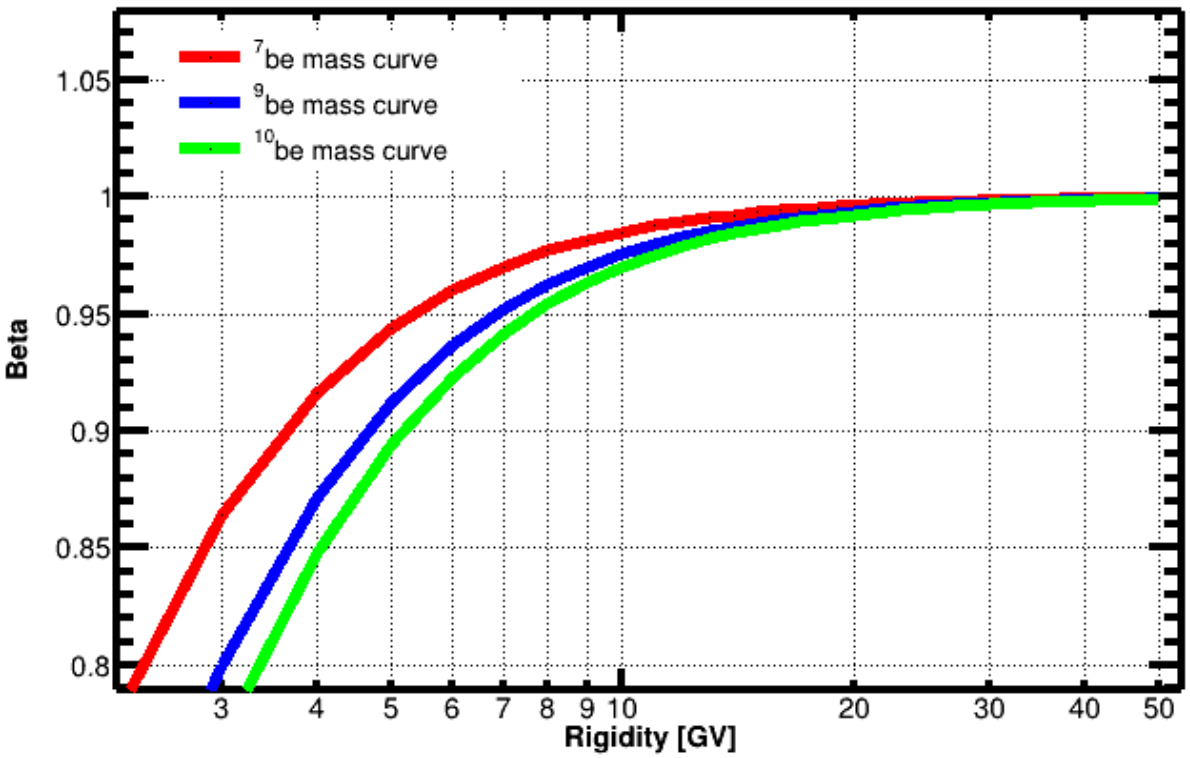

Figure 4.11: Comparison between the theoretical mass curves for ^{7}Be, ^{9}Be, and ^{10}Be isotopes.

charge, $R = p/Z$, and its unit is GV.

4.3.2.1 Measuring Rigidity

As we have seen earlier in chapter 3, that the AMS-02 Silicon Tracker has 9 layers, out of which, 7 of them are in the magnetic volume. The two external layers provides the entering and exiting direction with respect to magnetic field volume, thereby allowing to extend the rigidity measurement to the TV region. However, the latter comes at the expense of a reduction in overall geometric acceptance.

In this particular work, we are interested in particles with rigidities up to few tens of GV, where the only dominant phenomenon affecting the rigidity measurement is the *Multiple Coulomb Scattering*. As such, for these rigidites, the resolution improvement by the inclusion of external tracker layers is negligible as can be seen from fig. 4.12. As such, for our purpose, the R measurements are taken only from the Inner Tracker layers. The L1 hit is used to ensure that a particle consistent with $Z = 4$, i.e., a Be is entering the detector. A residual background from heavier nuclei fragmenting before L1 is expected.

4.3.2.2 Track Quality Selections: Improving the R Resolution

To improve R resolution, we request that the track possess an hit on L1 and L2, and at least one hit on each pair of layers placed within the magnet bore ([Ly3 — Ly4] & [Ly5 — Ly6] & [Ly7 — Ly8]). This ensures at least 5 hits to for the track reconstruction without sizeable loss

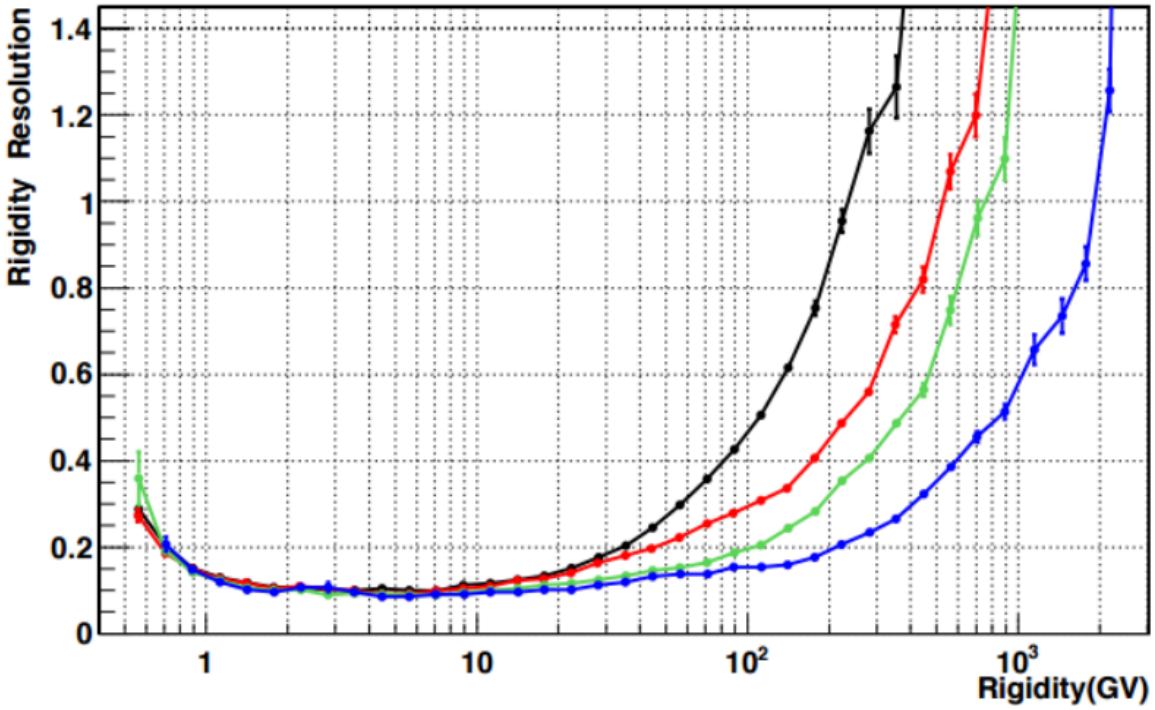

Figure 4.12: Tracker rigidity resolution for different tracker spans, evaluated by proton MC simulation. Black: Inner Tracker, Red: L1, Green: L9, and Blue: L1 & L9. Figure from [53]

in statistics.

A selection on the track $\chi^2_y/d.o.f < 10$ has been applied. In fig. 4.14 , we can see for MC events, the $log_{10}(\chi^2/d.o.f)$ distribution of events with bad R reconstruction (i.e., when MC generated rigidity, $R_{gen} > 2\,GV$ & MC measured rigidity, $R_{meas} < 1.2\,GV$), juxtaposed against the distribution for the whole MC sample.

After the application of those selections to select a clean sample of Be on the MC simulated events, we can look at the Rigidity Migration Matrix, i.e., the relation between true and measured rigidity. Fig. 4.15 displays the MC migration matrix before and after the selections.

4.3.2.3 Final Rigidity Resolution

The resolution of the velocity and rigidity can be estimated from the Monte Carlo data, where we know the true/generated momentum. We calculate the expected value of rigidity and β, and compare them with the measured ones, and extract the resolution from the fit.

There is strong energy dependence in both rigidity and β, and hence the choice of a proper binning is important. Studying the inverse value of these two variables curtails the Landau-shaped tails in the distribution and provides us with more Gaussian shapes.

To extract the rigidity resolution function, the rigidity range 1-50 GV was divided into 24 logarithmic bins and the $|1/R - 1/R_{gen}|$ distribution was obtained. The inverse of the rigidity is

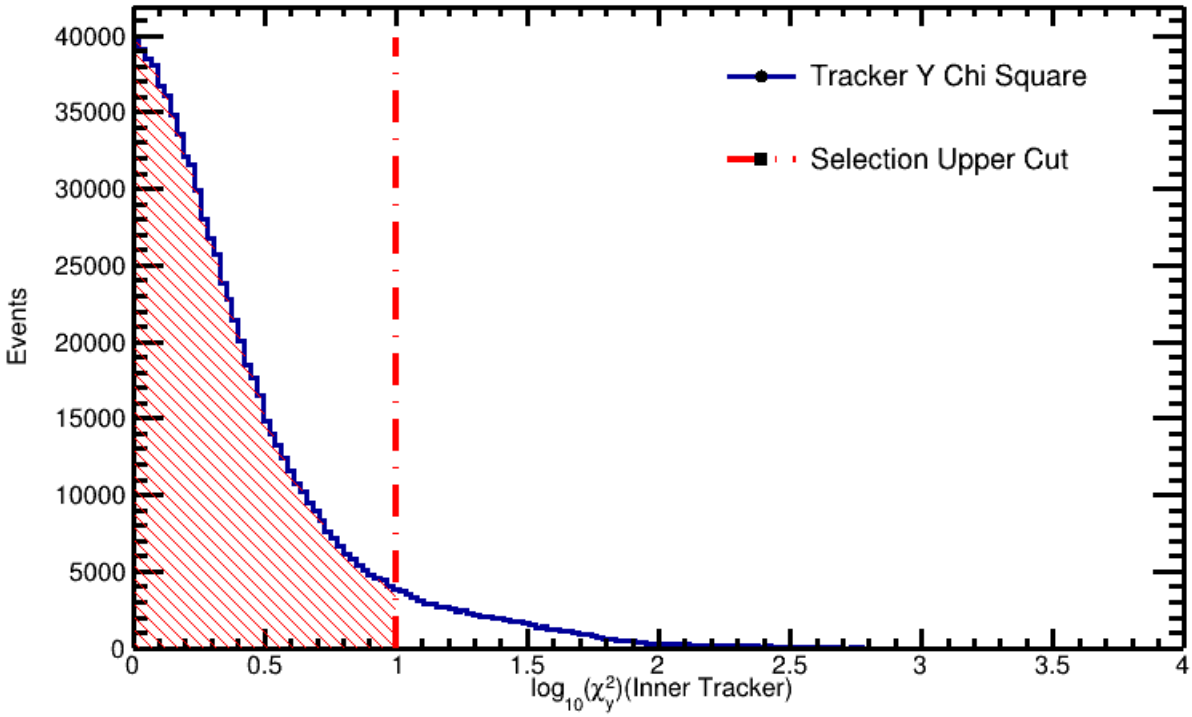

Figure 4.13: Distribution of the Tracker $\chi^2_y/d.o.f$ from ISS data. Vertical line denotes the selection upper cut on this variable.

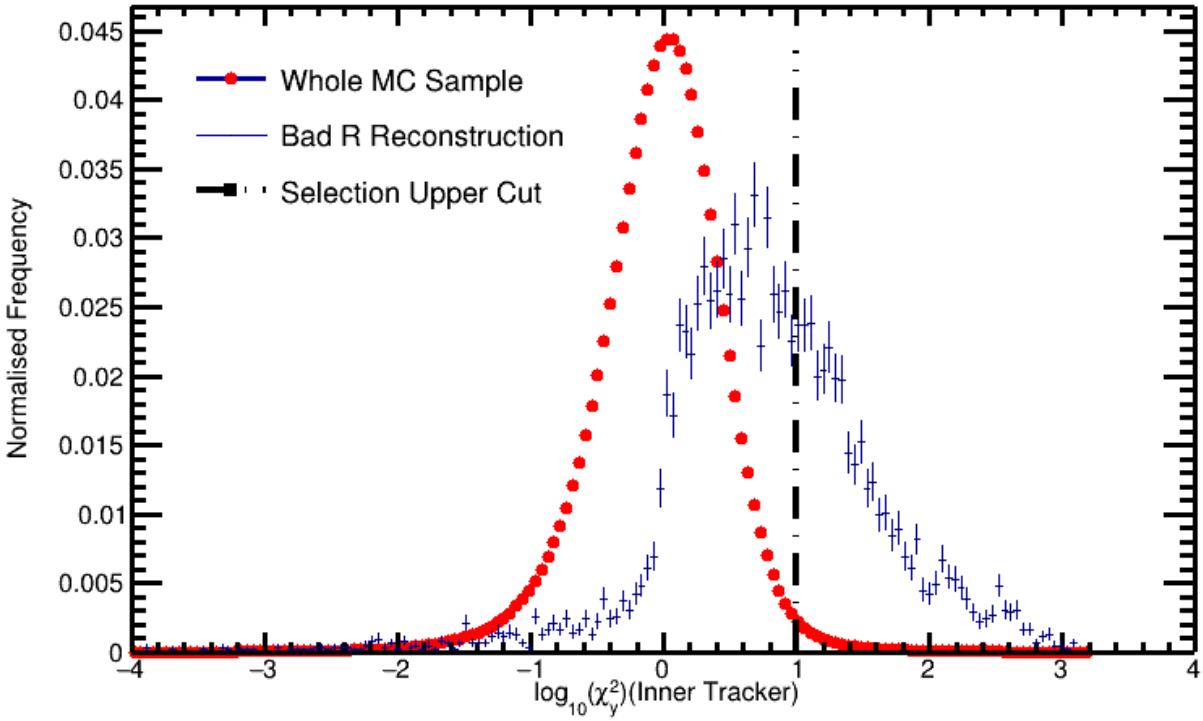

Figure 4.14: Tracker $\chi^2_y/d.o.f$ distribution of the whole MC sample (red points) and badly reconstructed rigidities blue points

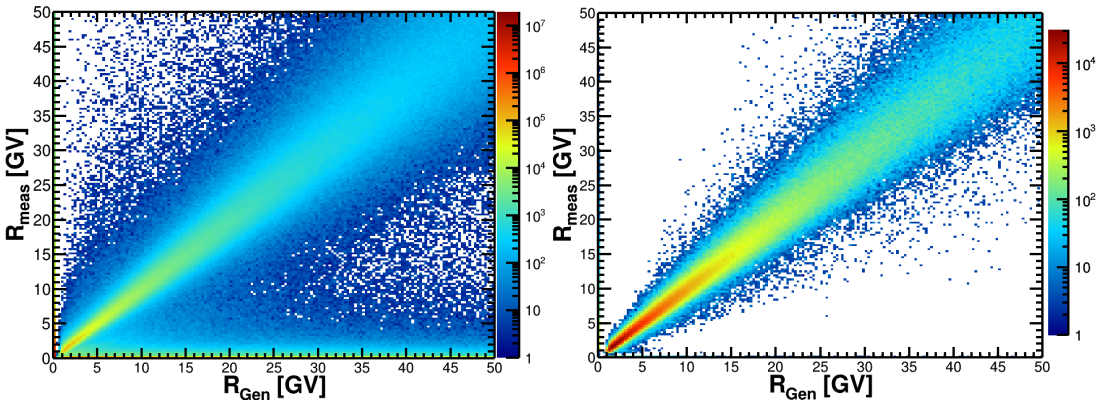

(a) (b)

Figure 4.15: The Rigidity Migration Matrix before (a) and after (b) application of charge and track quality selections.

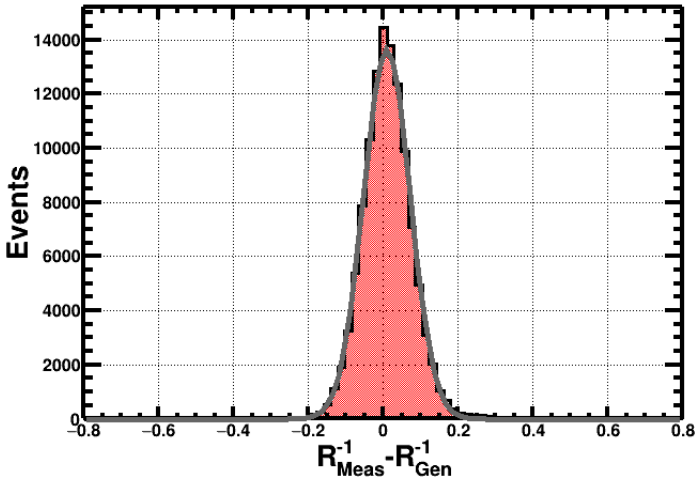

Figure 4.16: Inverse reconstructed rigidity residual distribution for MC Be events for one of the generated (true) rigidity bins. The red line is the Gaussian fit used to extract the rigidity resolution.

taken because this is the quantity that is measured by the tracker and hence approximates the Gaussian shape the most. The distributions turns out to be Gaussian at the first order. However, the behaviour of extreme tails deviates from the Gaussian character. For advanced analysis (for e.g., unfolding on resolution effect), these tails are often modeled with double Gaussians or Christal-ball functions, but for bulk resolution estimation, a Gaussian fit is sufficient, as shown in fig. 4.16.

From the fit results, the inverse rigidity standard deviation $\sigma_{1/R}$ can be obtained. Then using the following formula from error propagation, we can extract σ_R as

$$\begin{aligned} \sigma_R &= \left| \frac{d(1/R)}{dR} \right| \sigma_{1/R} \\ &= R^2 \sigma_{1/R}. \end{aligned} \tag{4.3}$$

And from the above, we can define the resolution as $R_{res} = \sigma_R / R$. Results extracted following this procedure are depicted in fig. 4.17.

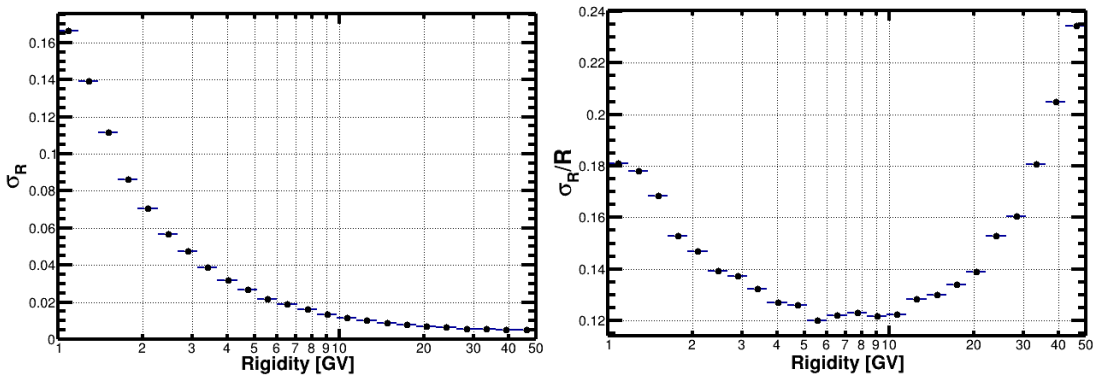

(a) (b)

Figure 4.17: (a) Rigidity standard deviation as a function of generated momentum in log scale. (b) Rigidity resolution as a function of generated momentum in log scale.

The measured resolution at low energy ($R < 10\ GV$) is consistent with a multiple scattering dominated picture [64], while at higher energy, the gradual degradation of the resolution is theoretically expected. The rigidity resolution is however higher than the one needs for isotopic distinction from inverse masses of the isotopes. This fact would become clearer in subsequent sections.

4.3.3 Velocity β

AMS-02 is equipped with three sub-detectors to measure particle velocity independently. For velocities below $\beta \lesssim 0.93$, the ToF helps us to measure the velocity between the upper and lower paddles of it. For higher velocities, we can resort to the RICH detector with the NaF or the Aerogel radiators, that have the nominal thresholds of $\beta = 0.75$ and $\beta = 0.953$ respectively. The upper threshold is however dictated by the velocity measurement resolution of each radiator.

4.3.3.1 Velocity Measurement

The energy per unit nucleon can be derived from a simple calculation starting from relativistic kinetic energy equation, $E_k = \gamma mc^2$, and approximating the mass of nucleon as following:

$$\text{Mass} = Zm_p + Nm_n - E_b \approx Am_p; \tag{4.4}$$

where m_p, and m_n are masses of protons and neutrons respectively, Z is the atomic number, N is the number of neutrons, and E_b is the binding energy. Since E_b is very small, and masses of proton and neutron are similar ($\sim 0.931\ GeV$), the equation can be approximated as Am_p where A is the mass number. After some algebraic manipulation, one can derive the following

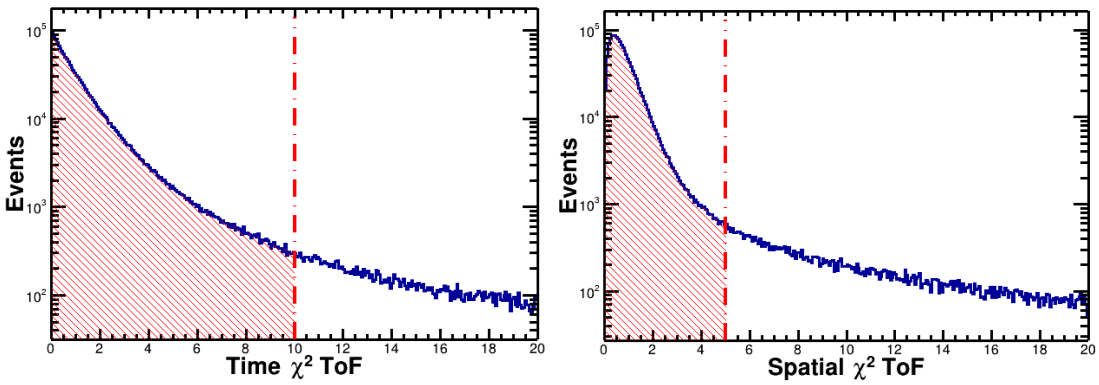

(a) (b)

Figure 4.18: Distribution of ToF (a) $\chi^2/d.of$ time of flight, and (b) spatial $\chi^2/d.o.f$ from ISS data. Vertical line represents the selection upper cut on this variable.

formula for kinetic energy per unit nucleon:

$$E_k/n = 0.931\sqrt{\frac{\beta^2}{1-\beta^2}+1} - 0.931\ GeV = 0.931(\gamma - 1)\ GeV; \tag{4.5}$$

where $E_k/n = E_k/A$, where E_k is the total kinetic energy of the particle.

4.3.3.2 ToF β Measurement and ToF β Resolution

The ToF velocity is measured by using the time of passage information from each of the 4 layers of the ToF combined with the track length obtained from the track fitted from Silicon Tracker hits. For improving the beta resolution, we take in consideration the *Spatial* χ^2_S, which is the χ^2 coming from the match between the ToF hit and the extrapolated track position of the Silicon Tracker. The ToF hit is as large as the ToF scintillation paddle (12 cm) in the orthogonal direction, while in the longitudinal direction, i.e along the scintillator paddle, it has a position and a size that depends on the accuracy of time determination at the two scintillator paddle ends. If we request a good match between the ToF hits, and the track, we get an implicit cut on the time measurement accuracy on each ToF layer.

After acquiring the time determination for each layer, and a corresponding distance along the track, we can plot four "distance-time" coordinates in a plane, with their corresponding uncertainties. After that, we can perform a linear fit, which would give us the slope of the fit as a value of the β. Consequently, we can also calculate the corresponding *time* χ^2_T.

In order to obtain a good time estimation from the ToF, we apply a suitable cut on both χ^2_S. and χ^2_T as can be seen in fig. 4.18.

The average time resolution for each ToF paddle is expected to be 160 ps for $Z = 1$, and the overall velocity resolution has been measured to be 3% for proton MIPs. Since the scinitllation photons increase with nuclear charge, the time resolution consequently improve up to $\Delta t \sim 60\ ps$ and $\Delta\beta/\beta \sim 1\%$ for $Z \geq 4$.

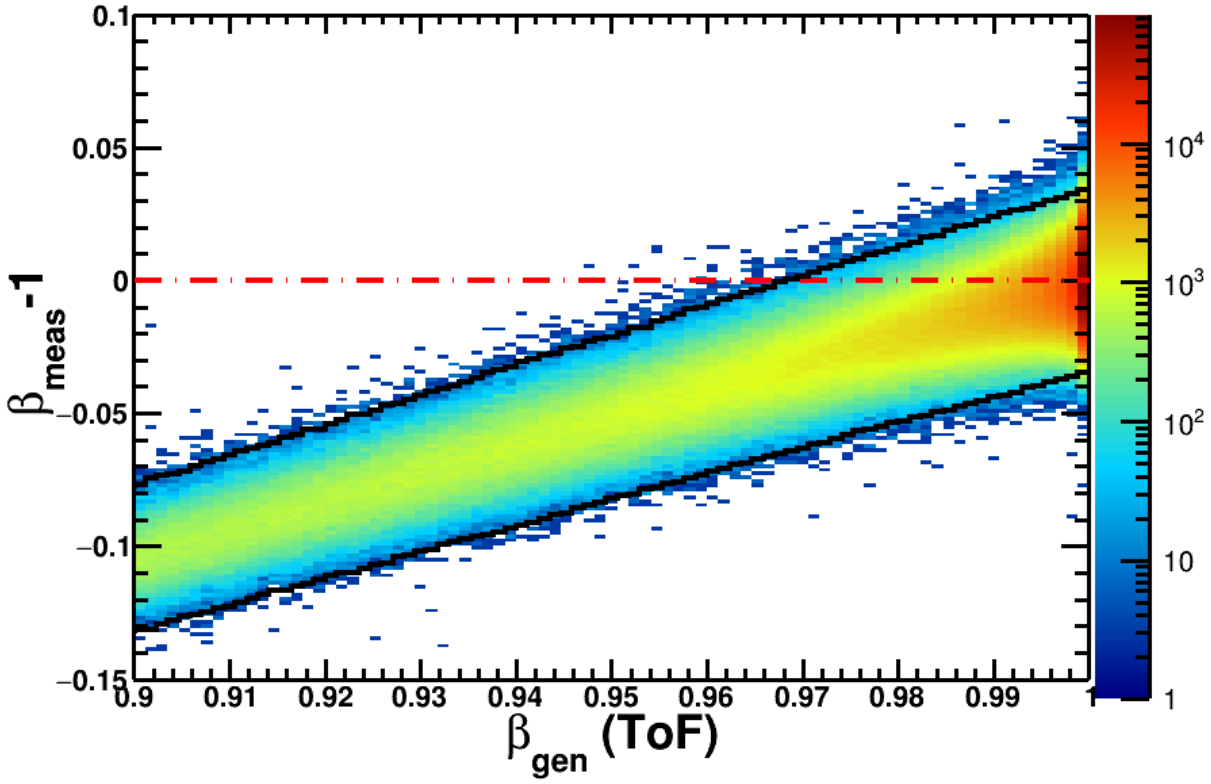

Figure 4.19: β migration matrix measured for the ToF detector. See text for explanation.

Fig. 4.19 demonstrates the velocity migration matrix for the ToF detector. The x-axis contains the MC generated β, and the y-axis contains the MC measured β subtracted by unity so that it is centered around 0. When the band meet the $y = 0$ line, it means that we are no longer able to distinguish subluminal particles from massless particles. The solid line corresponds to a 3σ quarantile alluding to the fact that the upper limit where the ToF measurement is reliable is $\beta \sim 0.97$. On the flip side, a measurement below $\beta = 0.5$ is quite difficult as it would necessitate stringent corrections pertaining to particle energy loss (also, the probability to have four hits in the four paddles of the ToF diminishes, as the particle stopping in intermediate layers would cause a drop in acceptance at lower energy).

Similar to the procedure of finding rigidity resolution, the residuals of the ToF β can be described well by a Gaussian in the core. Hence, we use a similar method to quantify β resolution as a function of an appropriate kinematic variable. As a result of the asymptotic behaviour of β, plotting the resolution against it doesn't offer a lucid visual representation. As such, we resort to the Lorentz factor $\gamma = (1 - \beta^2)^{-1/2}$, which is a strictly increasing function on the required domain $\beta \in [0, 1)$. Furthermore, energy per unit nucleon is directly proportional to $(\gamma - 1)$, and hence we use the same as the kinematical parameter. The residual that we use has the form:

$$\text{Residual} = \frac{\beta_{Meas} - \beta_{Gen}}{\beta_{Gen}}, \tag{4.6}$$

where β_{Gen} is the generated beta extraxted from AMS-MC at the point of entering the ToF detector, and β_{Meas} is the measured beta from the ToF beta reconstruction. Fig. 4.20 demon-

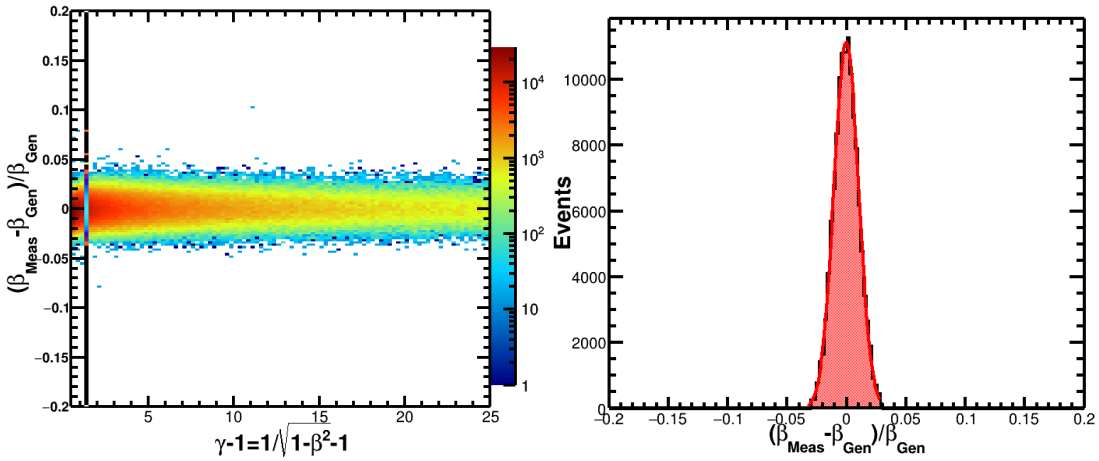

(a) (b)

Figure 4.20: (a) Two-dimensional histogram of ToF β residuals after all selections. Only AMS-MC ^{7}Be events passing through the ToF detector planes are included here. (b) Projection of the shaded vertical slice from the plot on the left. A Gaussian fit describes the core of the distribution well.

strates the beta residuals from ^{7}Be events passing through the ToF detector planes for a wide kinematic range. The shaded band of the plot is shown in projection on the right side of the plot, with a Gaussian fit on it. The Gaussian fit is performed for the bins which have values higher than 10 % of the maximum bin value. This procedure can be repeated for ^{9}Be and ^{10}Be.

The standard deviation of the Gaussian fits is used to quantify the β resolution of the ToF as shown in fig.4.21. The resolution for each of the three isotopes is similar and largely constant across the appropriate kinematical range.

4.3.3.3 RICH β Measurement and RICH β resolution

RICH detector possess a resolution that is an order of magnitude better than ToF. The two radiators, NaF and Agl have refractive index, $n = 1.33$, and $n = 1.05$ respectively. Which implies nominal velocity thresholds of $\beta > 0.75$ and $\beta > 0.953$ for NaF and Agl respectively.

Typical velocity resolution for $Z = 4$ particles is 0.3 % for NaF and 0.06% for Agl (See fig. 4.22). To ensure a good quality of RICH velocity reconstruction, a list of selections needs to be applied.

In order to enhance the ring reconstruction, we apply a selection on the minimum number of PMTs required for the ring, for the NaF and Agl radiator, as shown in fig. 4.23.

Furthermore, we require a good enough ratio for total number of PhotoElectrons collected in the ring to that of the total number of PhotoElectrons detected, for both the radiators NaF an Agl as shown in fig. 4.24.

A selection for a not excessively small probability for the *Kolmogorov-Smirnov* test of an

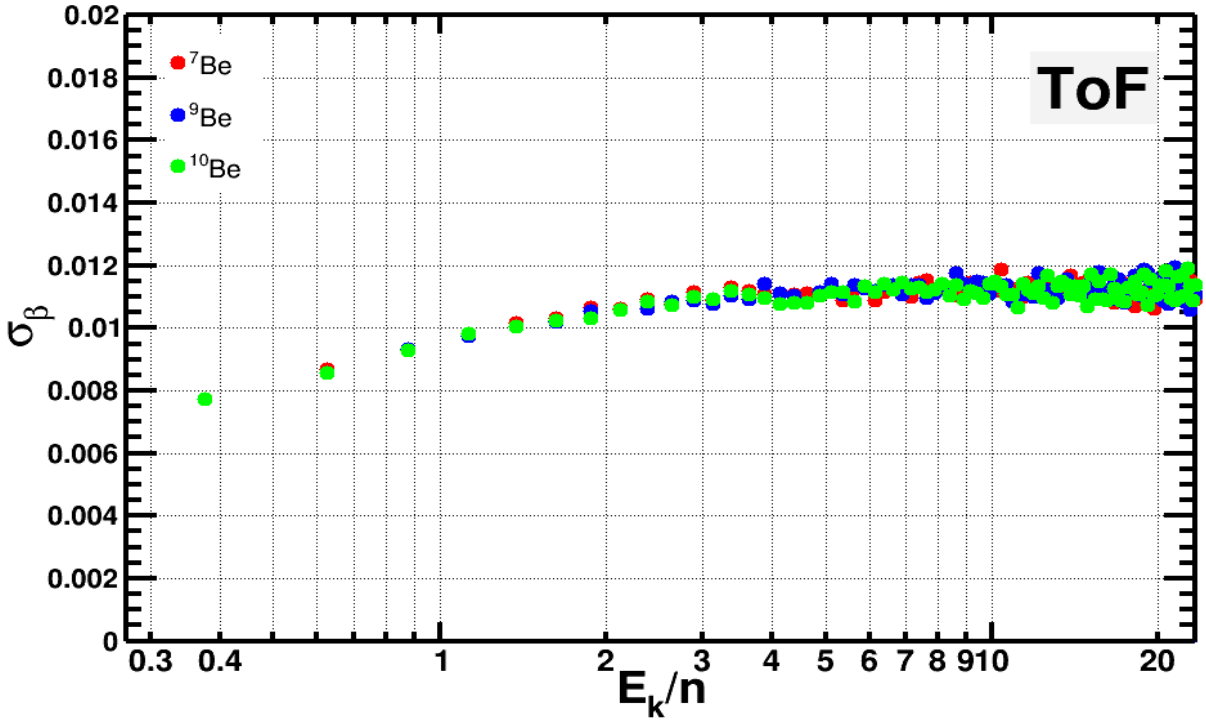

Figure 4.21: Magnitude of the resolution on β for ^{7}Be, ^{9}Be and ^{10}Be ions in the ToF, as determined by the AMS MC. The resolution for each isotope is similar. Refer to the text for further explanation.

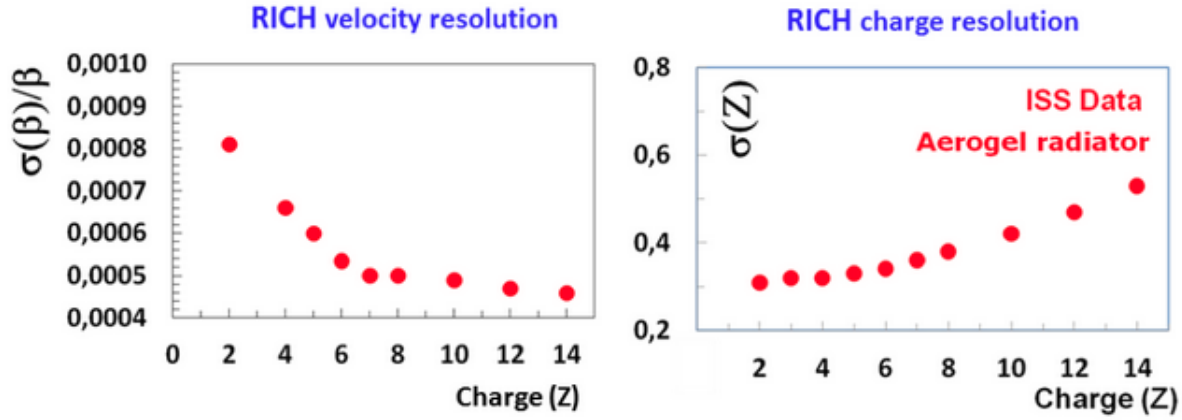

Figure 4.22: The β resolution against the Charge, Z, for the RICH Agl. Figure taken from AMS-02 website.

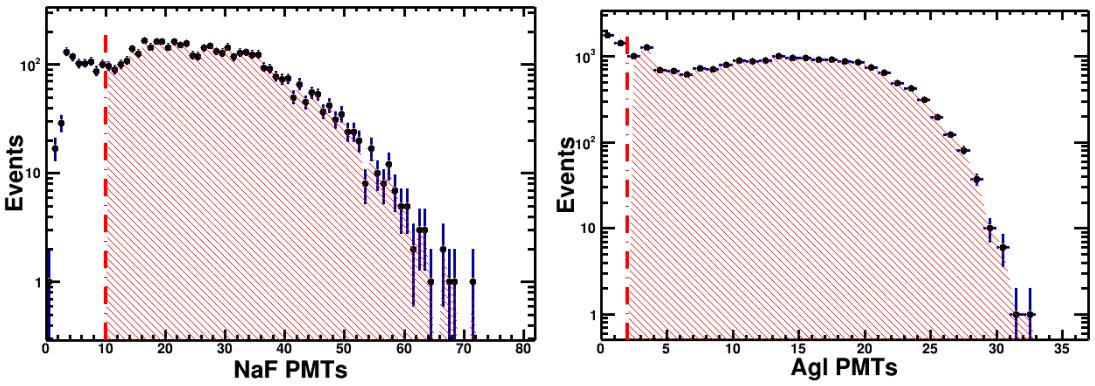

(a) (b)

Figure 4.23: Distribution for the number of PMTs for NaF (a) and Agl (b) radiators of the RICH. The vertical lines represent the selection lower-cut on these variables.

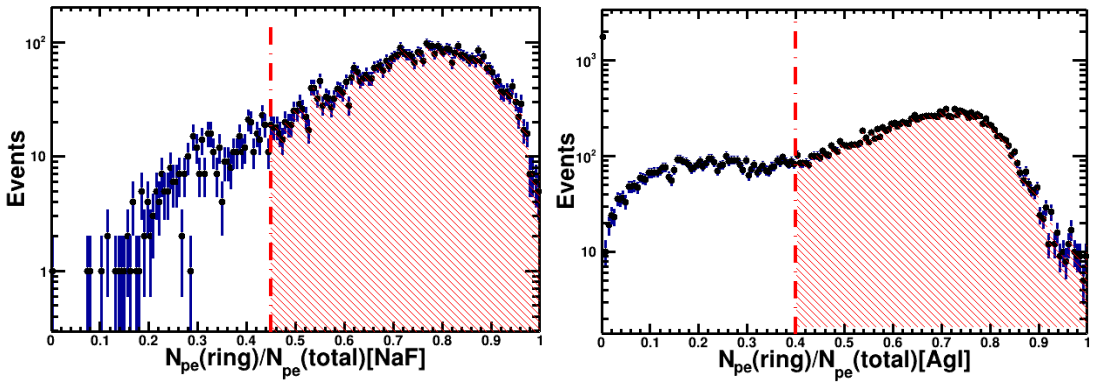

(a) (b)

Figure 4.24: The distribution for total number of PhotoElectrons collected in the RICH ring to that of the total number of collected PhotoElectrons; (a) For NaF radiator, (b) For Agl radiator. The vertical lines denotes the selection lower-cut applied on this variables.

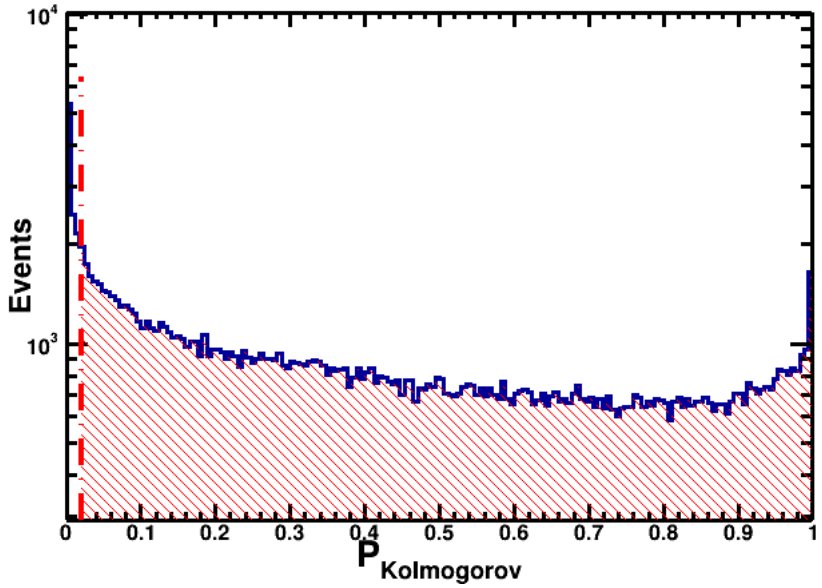

Figure 4.25: The Kolmogorov distribution for Photoelectrons along a RICH ring. The vertical line represents the selection lower-cut on this variable.

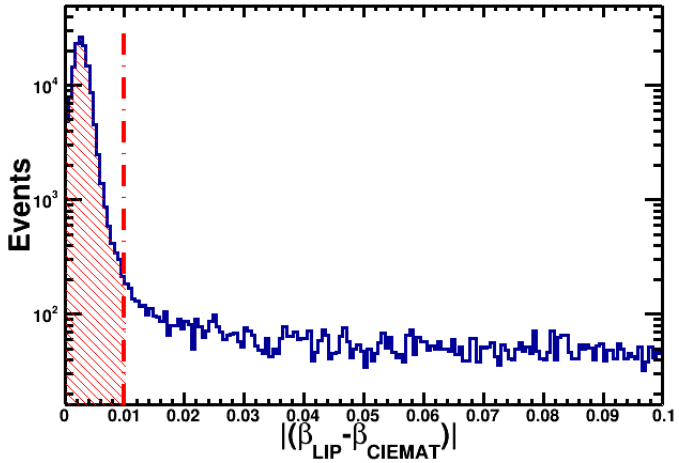

Figure 4.26: Distribution for the difference in β measured by two different reconstruction algorithm (developed by LIP and CIEMAT groups of AMS-02). The vertical line represents the selection upper-cut on this variable.

unifrom PhotoElecton distribution along the ring is required as shown in fig. 4.25.

Along with that, the compatibility of RICH velocity reconstruction using two different algorithm (developed by CIEMAT and LIP colleagues in AMS-02) is requested, as shown in fig. 4.26.

In order to be consistent across the sub-detectors, viz., the ToF and RICH; we implement a selection on the difference between the β measured by the ToF and RICH to not be excessively different, as shown in fig. 4.27.

Fig. 4.28 and fig. 4.29 demonstrates the velocity migration matrix for the NaF and Agl radiators of the RICH detector respectively. The solid line corresponds to a 3σ quarantile alluding

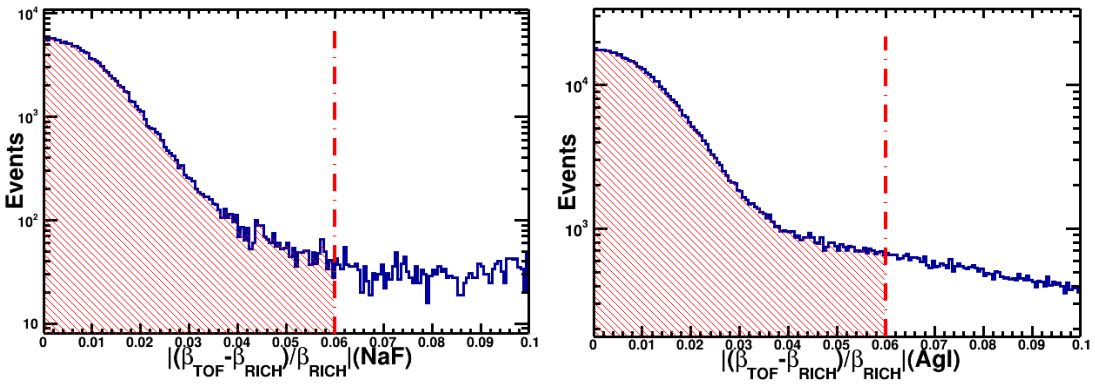

(a) (b)

Figure 4.27: Distribution for the difference between the value of β obtained from the ToF and RICH (NaF (a), Agl (b)). The vertical lines represents the selection upper-cut on these variables.

to the fact that the upper limit where the NaF measurement is reliable is around $\beta \sim 0.994$, and $\beta \sim 0.998$ for the Agl radiator. On the flip side, a measurement below $\beta = 0.75$ and $\beta = 0.953$ is impossible for the NaF and Agl respectively, because of the Cherenkov emission thresholds.

Similar to the procedure followed for the ToF detector, we can quantify the β resolution of the RICH-NaF and the RICH-Agl detector for the three isotopes by calculating the residual, and extracting the standard deviation of the Gaussian fits. The resulting resolution plots for both the detectors are shown in fig. 4.30

4.3.3.4 RICH Charge Measurement

The total number of emitted PhotoElectrons is related to the square of the crossing particle charge by the Frank-Tamm formula as described in Appendix B. As such, concluding the selection list for the RICH, we do a loose selection for the charge measured by both the NaF and Agl radiators, as shown in fig. 4.31. As the number of PhotoElectrons is directly proportional to square of the charge, this selection further helps reduce the PhotoElectrons background coming from the number of photons released by particle of charge $Z < 4$ and $Z > 4$.

4.3.4 Beta and Energy per Nucleon Range for the Analysis

Coming up with a proper binning choice is one of the fundamental aspect of particle data analysis, in order to minimise systematic errors cropping from bin-to-bin migrations as a result of the finite resolution in measuring the fundamental physical quantities.

As already stated before, the variable used in isotopic distinction in our analysis is *Kinetic Energy per nucleon* (E_k/n). This is due to the fact that as a first-order approximation of hadronic interactions, a nucleus with mass number A and kinetic energy E_k behaves to a large extent, as the superposition of A nucleons with kinetic energy E_k/A. Hence, kinetic energy per nucleon

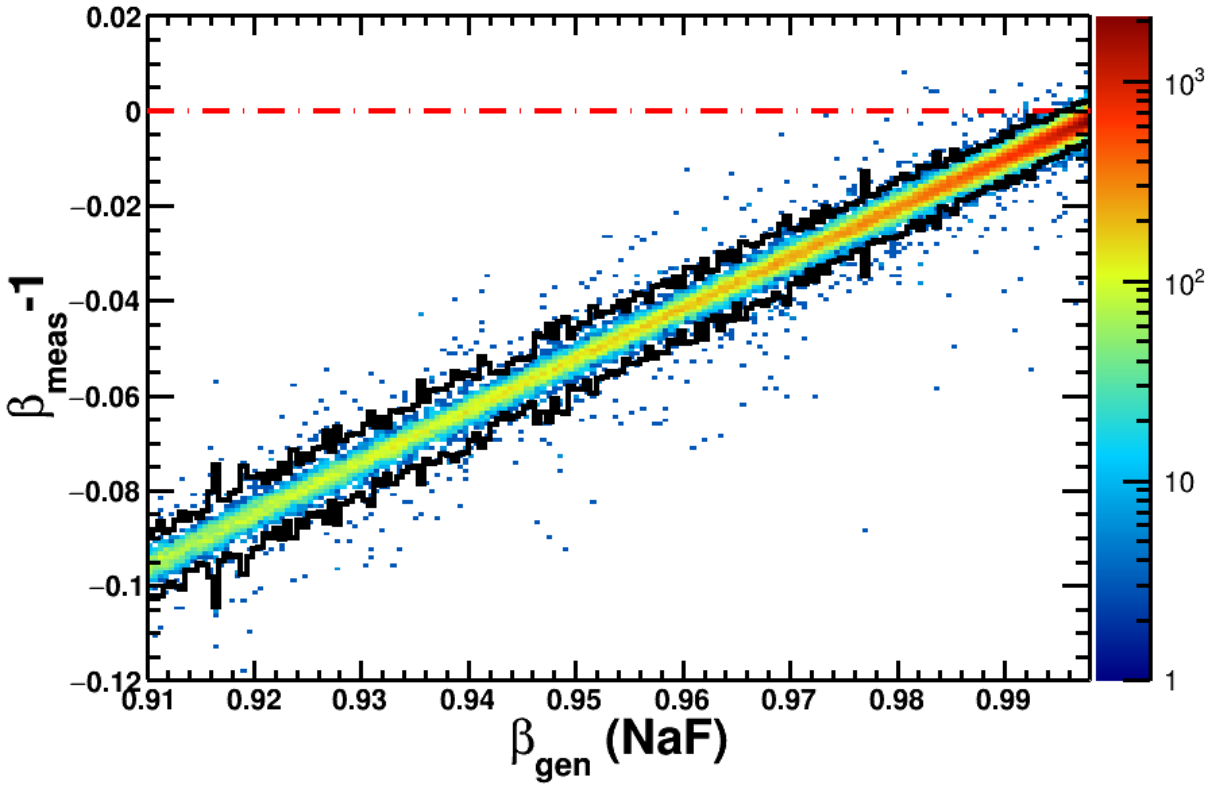

Figure 4.28: β migration matrix the NaF radiator of the RICH.

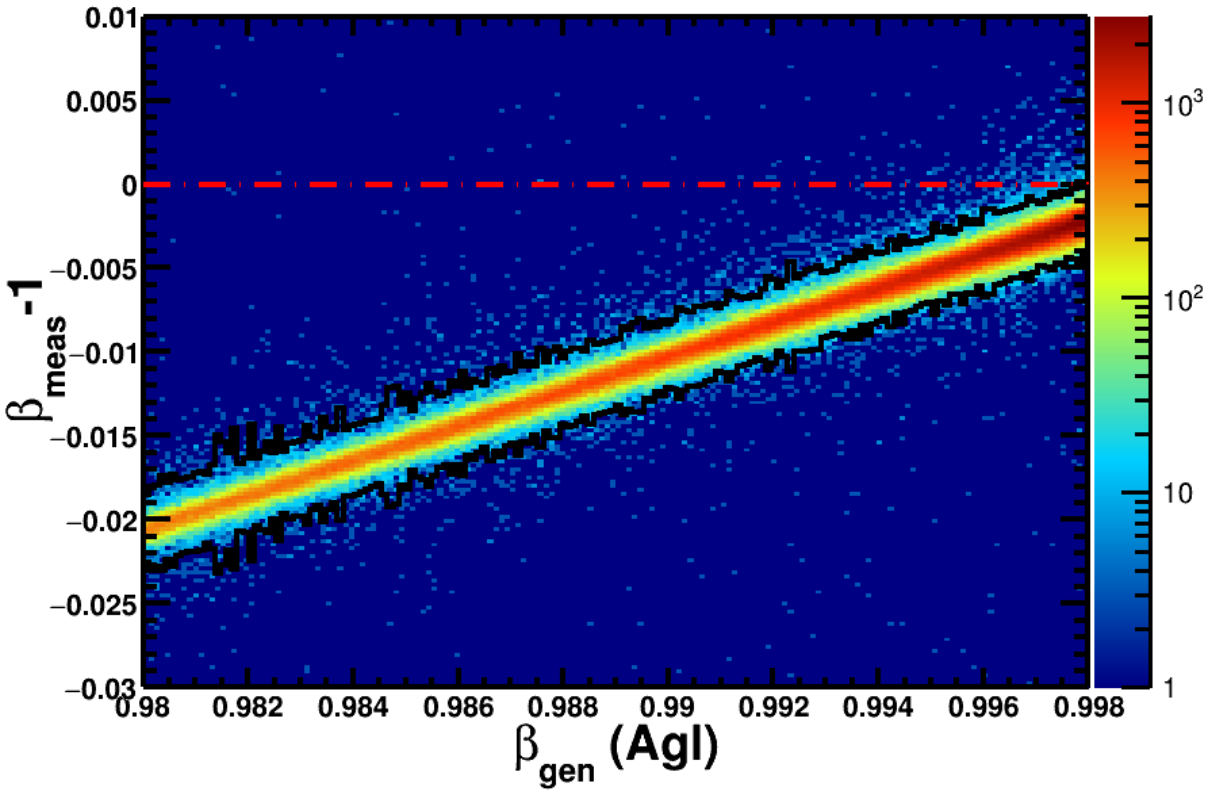

Figure 4.29: β migration matrix of the Agl radiator of the RICH.

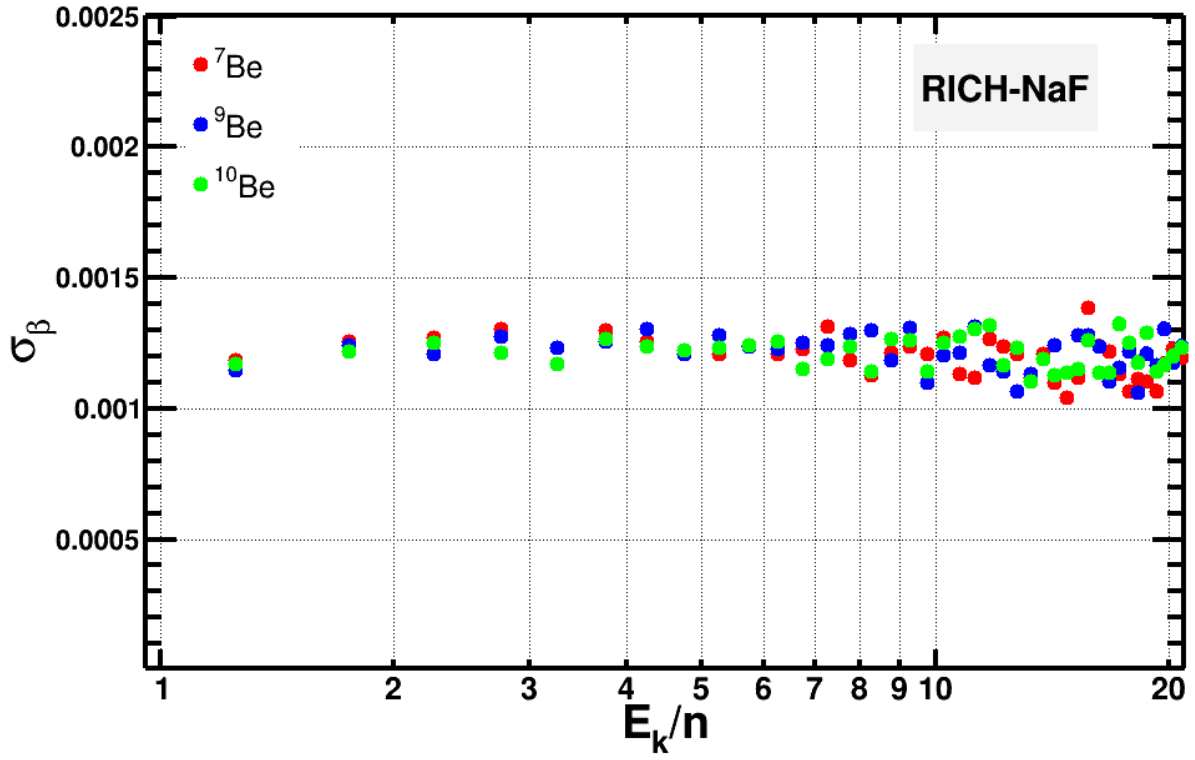

(a)

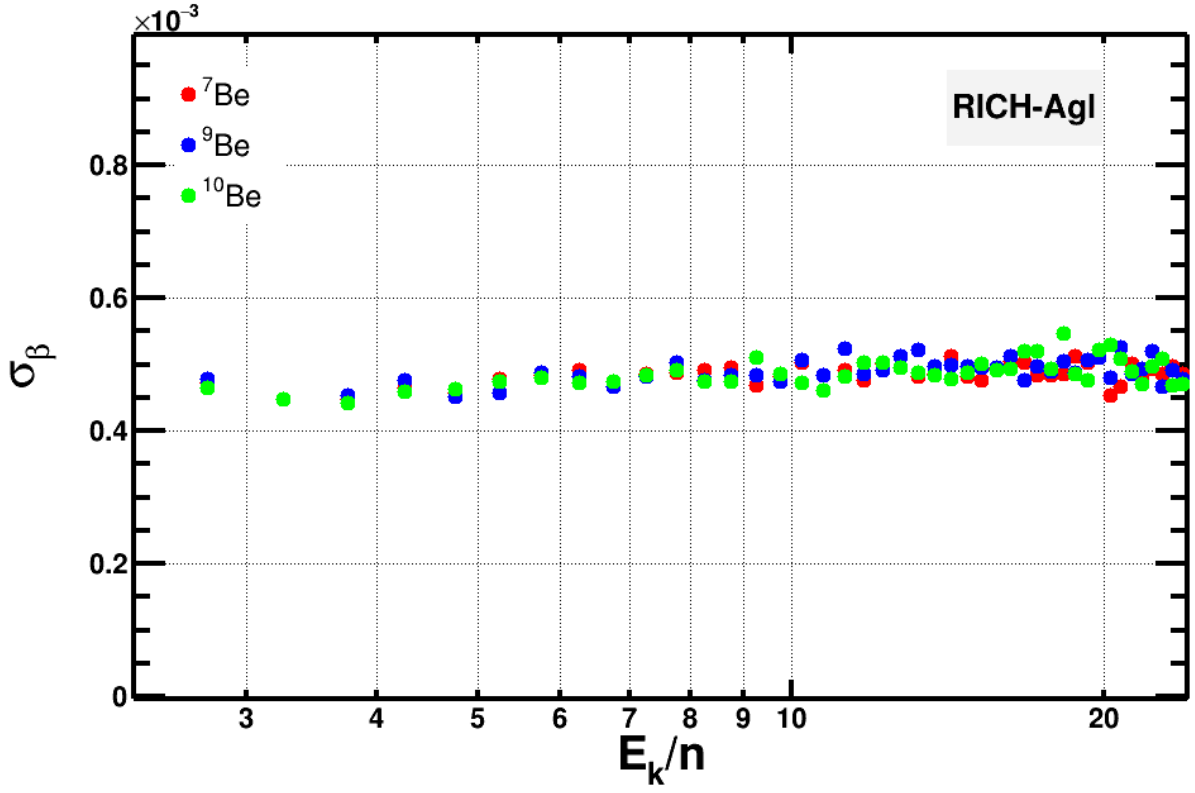

(b)

Figure 4.30: Magnitude of the resolution on β for ^{7}Be, ^{9}Be and ^{10}Be ions in the RICH-Naf (a) and RICH-Agl (b), as determined by the AMS MC. The resolution for each isotope is similar. Refer to the text for further explanation

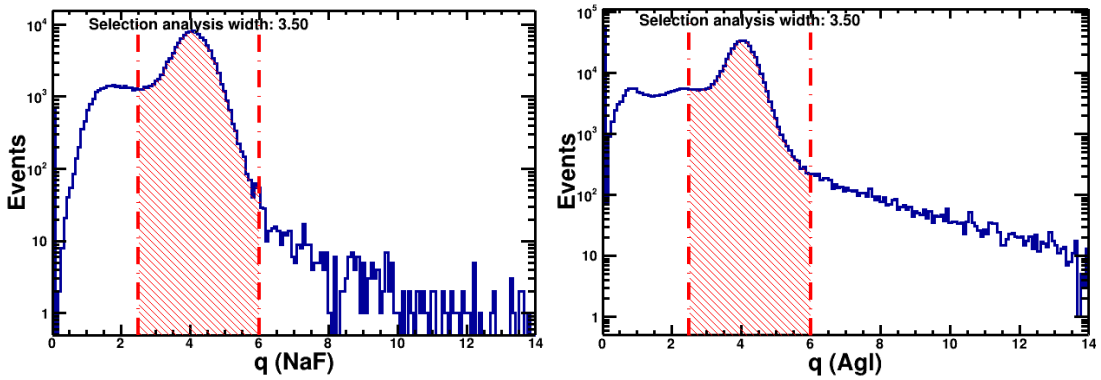

(a) (b)

Figure 4.31: RICH Charge distribution (a) NaF radiator, and (b) Agl radiator. The vertical lines represent the selection window.

is conserved in spallation reactions, which is how most of the Be is produced in CRs. Furthemore, kinetic energy per nucleon determines whether a nucleus is relativistic or not, and hence is intricately related to β.

The above consideration leads to identifying kinetic energy per nucleon as the natural independent variable also for the Be analysis. We did a dedicated MC study using the selection described above for the three Beryllium isotopes, i.e., ^{7}Be, ^{9}Be, and ^{10}Be for the three sub-detectors (ToF, NaF-RICH, and Agl-RICH) to select the analysis range. In fig. 4.32, 4.33, the mass vs R scatter-plot for the three sub-detectors are shown. In particular, it shows that it is possible to analyse the Be isotopic composition between 2-35 GV rigidity or consequently between 0.5-12.2 GeV/n kinetic energy per nucleon. After due discussion with other AMS collaborators, velocity (β) ranges for each sub-detectors were agreed to be analysed, and they are tabulated in table 4.2.

The three kinetic energy ranges defined to match corresponding β ranges, is divided into 7, 7 and 13 bins for ToF, NaF, and Agl respectively, granting the width in β to be bigger than the varying β resolution. This helps to minimise bin-to-bin migration effect due to misconstructed β, specially in ToF energy range.

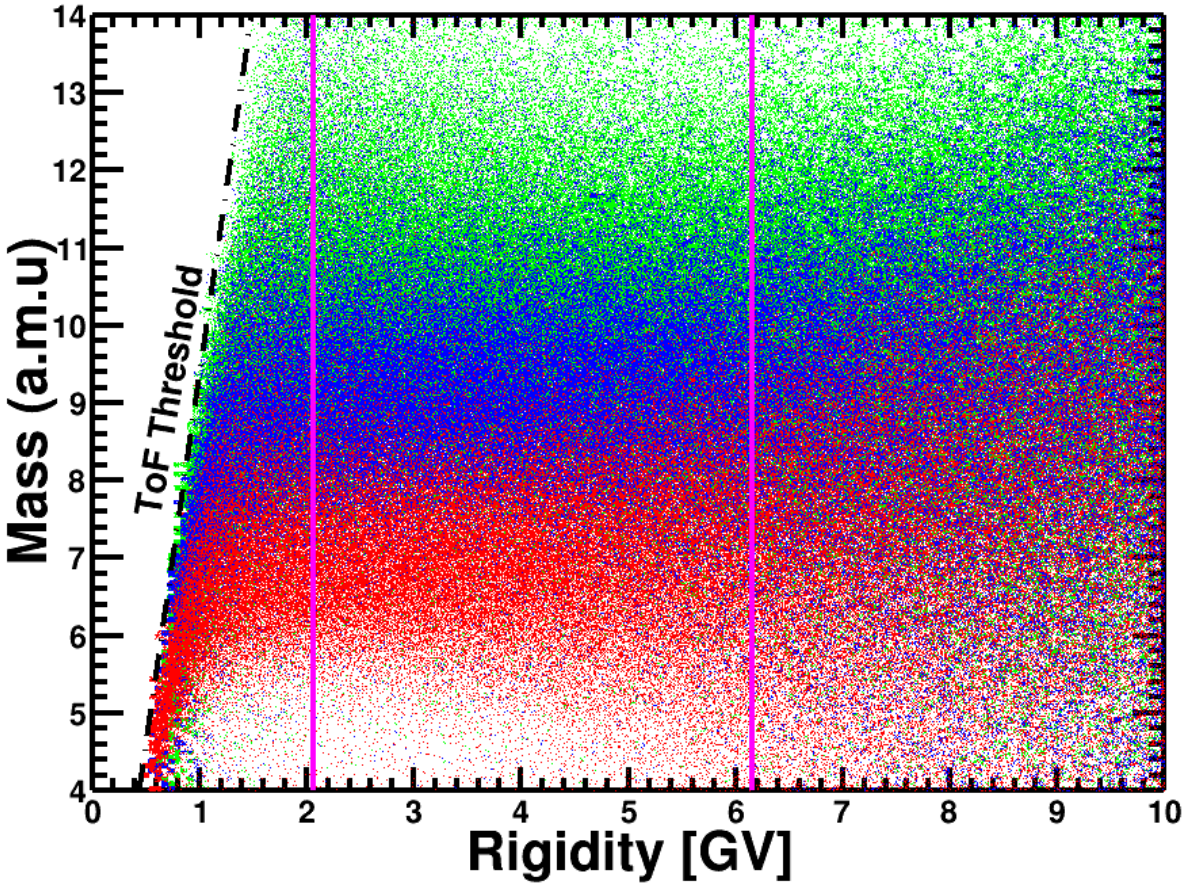

Figure 4.32: The two-dimensional histogram demonstrates the mass vs rigidity scatter plot for the ToF detector for three isotopes ^{7}Be, ^{9}Be and ^{10}Be from AMS MC. The black dashed line denotes the lower threshold for the detector, and the magneta lines denotes the analysis range selected.

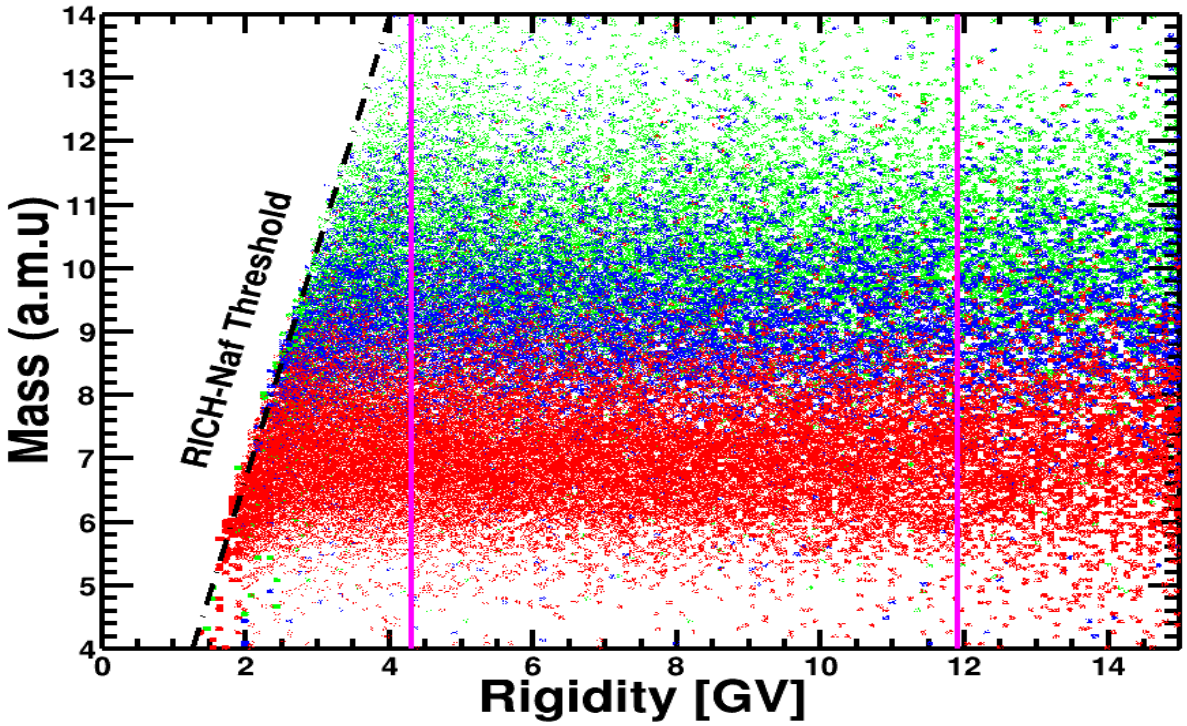

(a) NaF

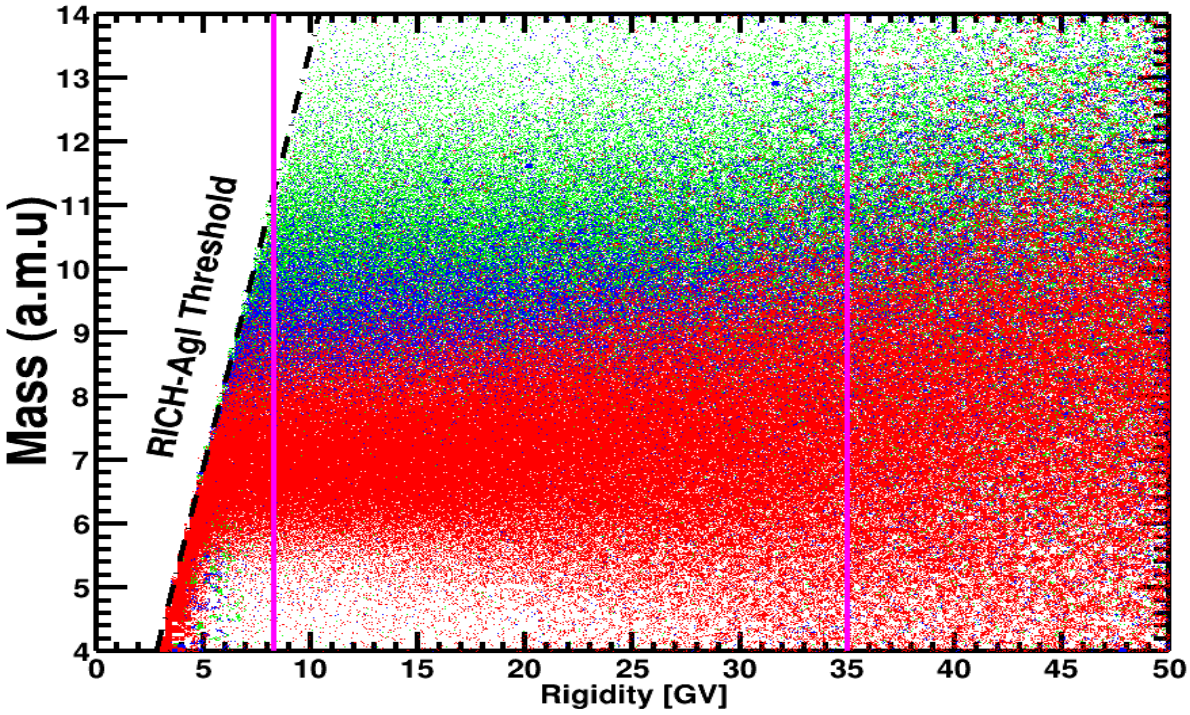

(b) Agl

Figure 4.33: The two-dimensional histogram demonstrates the mass vs rigidity scatter plot for the (a) RICH-NaF and (b) RICH-Agl detector for three isotopes ^{7}Be, ^{9}Be and ^{10}Be from AMS MC. The black dashed line denotes the lower threshold for the detector, and the magneta lines denotes the analysis range selected.

Common Ntuple Selections: Reduce Data Size	
C1	ISS is not in the SAA
C2	Down-going events $\beta > 0$
C3	Inner Tracker $Z > 2$
Charge Selections: Identify Be and remove fragmentations	
C4	$3.6 < Q_{L1} < 4.7$
C5	$3.4 < Q_{UToF} < 4.5$
C6	$3.65 < Q_{Inner} < 4.45$
Track Quality Selections: Improve R resolution	
C8	L1 & L2 & (L3 || L4) & (L5 || L6) & (L7 || L8)
C9	$\chi^2_y/d.o.f < 10$
C10	N trak==1 or bad second trk or R 2nd < 0.5
ToF Quality Selections: Improve β_{ToF} Resolution	
C11	$\chi^2_s < 5$ and $\chi^2_t < 10$
RICH NaF Quality Selections: Improve β_{RICH}(NaF) Resolution	
C12	$N_{PMT} > 10$
C13	$N_{pe}(ring)/N_{pe}(total) > 0.45$
C14	$P_{Kolmogorov} > 0.02$
C15	$2.5Q_{RICH} < 6.0$
C16	$\|\beta_{ToF} - \beta_{RICH}\|/\beta_{RICH} < 0.06$
C17	$\|\beta_{LIP} - \beta_{CIEMAT}\| < 0.01$
RICH Agl Quality Selections: Improve β_{RICH}(Agl) Resolution	
C18	$N_{PMT} > 2$
C19	$N_{pe}(ring)/N_{pe}(total) > 0.40$
C20	$2.5 < Q_{RICH} < 6.0$
C21	$\|\beta_{ToF} - \beta_{RICH}\|/\beta_{RICH} < 0.06$

Table 4.3: List of Selections used in the Analysis

	ToF	**NaF**	**Agl**
β	0.762-0.926	0.926-0.978	0.978-0.997
$E_{k/n}$ (GeV/n)	0.51-1.55	1.55-3.61	3.61-12.18

Table 4.2: Table of ranges in velocity and kinetic energy per nucleon chosen for the analysis

4.4 Data Selection Summary and Final Mass Distributions

Table 4.3 summarises the selection windows and cuts used to obtain a pure sample of Be events with a good measurement of rigidity and velocity.

Fig. 4.34 shows examples of mass distribution plot for the three detectors: ToF, RICH-NaF and RICH-Agl. A priori, we can say that the mass resolution doesn't permit to do an event-by-event identification of Be isotopes. Therefore we resort to a model to fit the distributions and extract the counts of each isotopes which will be discussed in the next section.

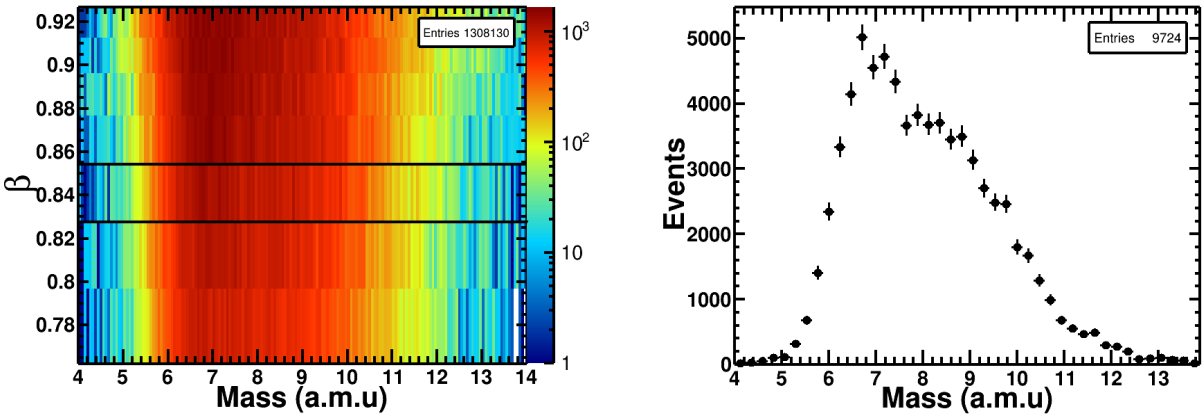

(a) ToF $<$ Mass vs β $>$

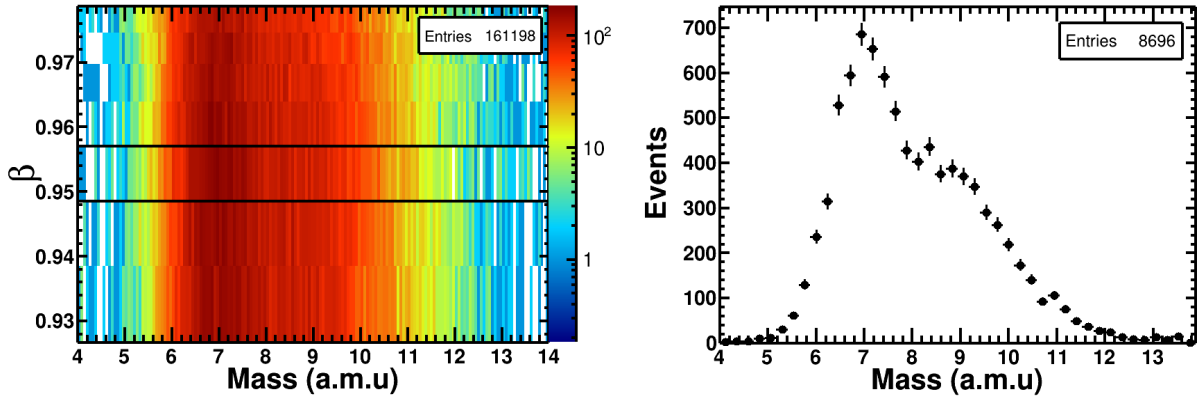

(b) RICH-NaF $<$ Mass vs β $>$

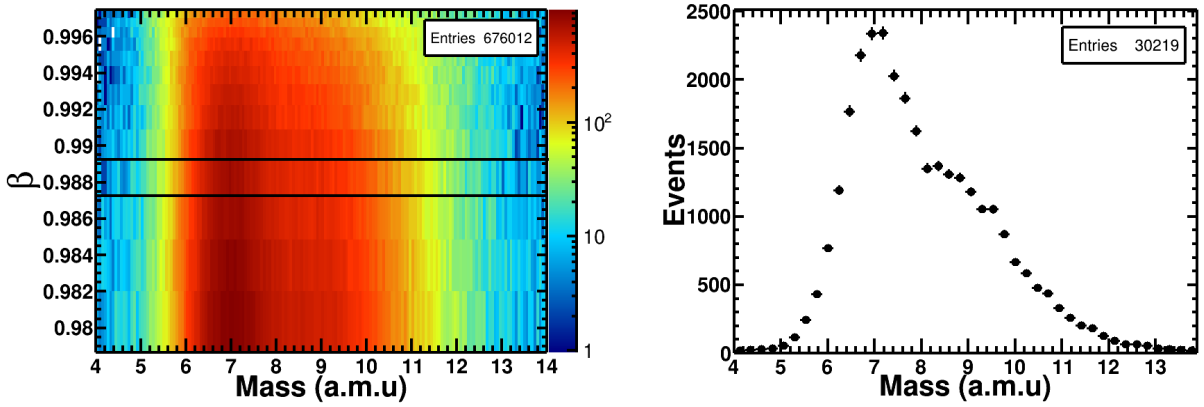

(c) RICH-Agl $<$ Mass vs β $>$

Figure 4.34: Left: The $<$ Mass vs β scatter plot. Right: Mass distribution for the highlighted bin on the left for ToF, RICH-NaF, and RICH-Agl respectively.

4.5 Fit on Be Mass Distribution

The selection described in the previous section leaves us with a collection of well-reconstructed CR Beryllium events with quality measurements of Charge (Z), Rigidity (R), and Velocity (β). We can use this events to measure the relative proportion of the isotopes, and in particular the important isotope ratio, $\Phi_{^{10}Be}/\Phi_{^{9}Be}$ as highlighted in the chapter 2.

As would be evident from the text, wherever indicated, ^{7}Be, ^{9}Be, and ^{10}Be will be indicated by Red, Blue, and Green respectively. A similar scheme would be followed for the sub-detectors **ToF (Red)**, **NaF (Blue)**, and **Agl (Green)**. It is emphasised that there is no correlation between the isotopes' and the sub-detector's colour representation.

4.5.1 Fit Method

4.5.1.1 Measurement Principle

Through a series of careful selections, we have arrived at a clean sample of $Z = 4$ CR species, which is composed of Be isotopes. We would like to determine the relative composition of this sample, in particular, the astrophysically important $^{10}Be/^{9}Be$ ratio. As the two isotopes differ in mass, the measurement of mass is the distinguishing feature of our analysis. As already discussed, the mass is calculated using the charge, rigidity, and the velocity from different sub-detectors with the expression which have been repeated here for completeness:

$$m = \frac{RZ}{\beta\gamma}. \tag{4.7}$$

As already discussed, the high precession on β measurement $(\sim 0.1\%)$ with respect to R measurement $(\sim 10\%)$ makes the former a more efficient choice from analysis perspective. Fig. 4.35 shows the distribution of measured mass for one bin, superimposed with the theoretical values of the Be isotope masses.

The fig. 4.35 exhibits significant overlap of the isotope distributions. This overlap renders event-by-event isotope identification impossible. However, it is still possible to count the overall number of each isotope, in a bin. We leverage the following two factors to our advantage:

- **Monte Carlo Accuracy:** The AMS-MC is a precise, and well-tuned tool for simulating particles traversing and interacting with the detector components.
- **Similar Physics of Be isotopes:** The behaviour of isotopes ^{7}Be, ^{9}Be, and ^{10}Be is more or less similar within the ambit of AMS measurement, with differences that could be deciphered by considering the kinematic quantity pertinent to each process or measurment. This means, we can exploit the knowledge of one isotope's resolution distribution and apply it to the others.

Taking this in consideration, we can tackle the problem of measuring the isotopes through three orthogonal methods:

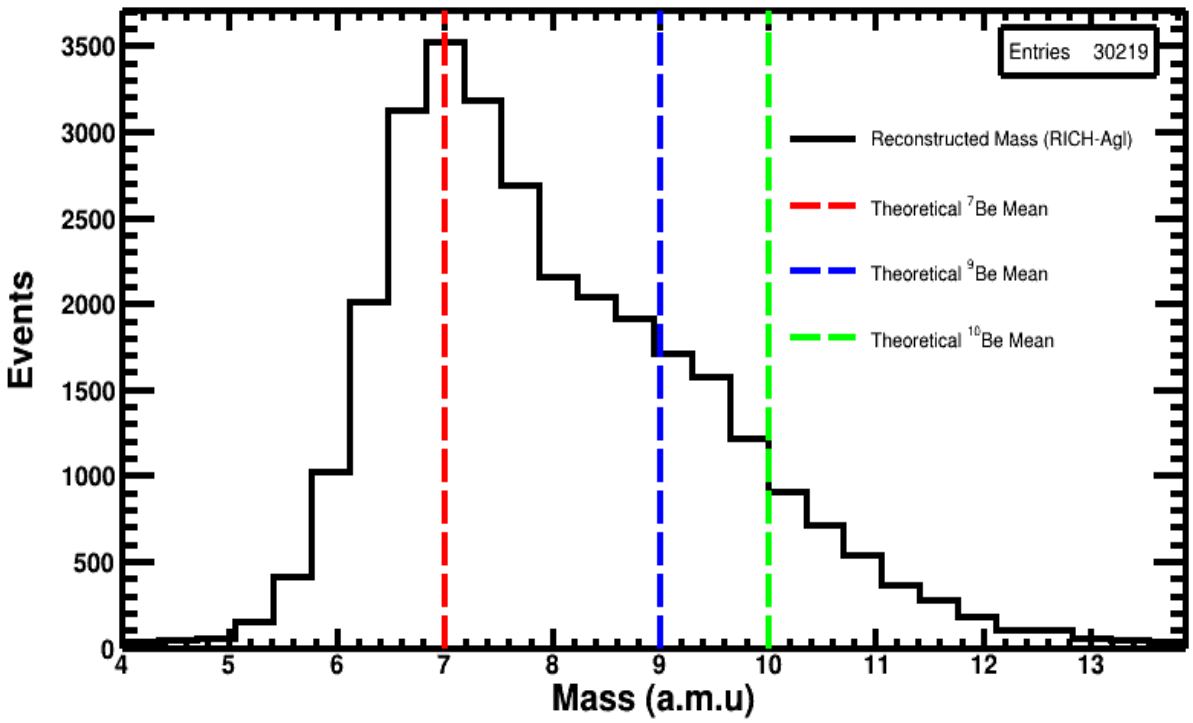

Figure 4.35: Reconstructed mass distribution for a particular β bin from RICH-Agl. The vertical lines represent the theoretical mean value for the three isotopes as indicated.

1. **Functional Parametrisation Based on Mass Resolution:** A parametrised functional form based on the shape of $1/m$ distribution is used to fit both single (AMS-MC), and triple-isotope distributions of reconstructed $1/m$. This method forms the basis of our work, and would be discussed extensively in the following sections.

2. **MC Template Fit:** For each E_k/n bin (corresponding to a β bin), MC data is selected for each of the isotopes using the same selections as that of data. This provides us MC template for each of the three isotopes. Fitting this MC templates to reconstructed mass supplies us with the isotope ratio. In the first iteration of the analysis, we used an old production version of the AMS and AMS-MC data, where we achieved a great fit result across different energy bins with a good χ^2, modulo a constant systematic normalisation shift with respect to method 1 discussed above. However, moving to new production, made us realise that we require better tuning of the MC templates. Due to paucity of time, it was decided to concentrate on method 1. However, work on this method would be done in the future as an independent cross-check of method 1.

3. **Data-Driven Templates:** This method is similar to method 2, however, the templates here are directly obtained from data. With knowledge of the true values of Be isotopes' masses and a physically motivated scaling of the mass resolution for the three beryllium isotopes, the shapes of the isotope mass distributions can be self-consistently retrieved solely from the measured data. This method has been discussed for the $\Phi_{^{10}Be}/\Phi_{^{9}Be}$ ratio in [99]. This method has not been implemented in the present analysis.

Within the context of method 1, we analyse 10 years of AMS-02 data, and incorporate the following algorithm in our analysis:

1. Scatter plots of the reconstructed mass (x-axis) vs the β (y-axis) for each of the sub-detectors, viz., **ToF**, **NaF**, and **Agl**, taking in consideration the β as described in the preceding sections, and the mass range from 4 to 14 with 170 linear bins.

2. Obtain the mass distribution for each β bins for each sub-detector by projecting the x-axis for each β bins.

3. Since the reconstructed inverse mass shape can be effectively modelled with a double-Gaussian (one peaked Gaussian, and one diffused Gaussian), we model the individual isotope mass distribution with a double-Gaussian template.

4. As a first order approximation, parametrise the shape of the single isotope template with the help of ^{7}Be reconstructed inverse mass distribution.

5. Take three such templates for the three isotopes. Taking advantage of the fact that the ^{7}Be peak is clearly visible in the Mass distribution as shown in fig. 4.35, scale the shape of the ^{9}Be, and ^{10}Be with respect to the ^{7}Be template.

6. With the help of *ROOT* framework, *TMinuit* χ^2 minimisation, perform a carefully crafted fit procedure.

7. After performing the first fit iteration, extract energy dependence trends for the shape parameters, and do a 2nd order polynomial fit of the shape parameters which would be the prior parameter estimation of our next fit iteration. In the second iteration of the global fit, let the shape parameters constrained around the 2nd order polynomials with a 10% degree of freedom around it with equal probability.

8. Integrate out the number of counts of each isotopes from the isotope templates and extract the desired ratio.

4.5.1.2 Parametrisation on Single-Isotope Template MC

The relative uncertainty on the tracker measurement of R is about one or two orders of magnitude worse than the β measurement. This suggests the well-characterised inner tracker resolution as a natural starting point for deciphering the mass resolution. Since, the tracker measures the quantity, $1/R$, it has the favourable property of Gaussian-like core distribution, which is not the case for R. Thus, for modelling the templates, inverse mass offers a much more mathematically and computationally easier starting point:

$$\frac{1}{m} = \frac{\beta\gamma}{ZR}. \tag{4.8}$$

Fig. 4.36 compares m and $1/m$ distributions from a MC sample of pure ^{7}Be from the Agl detector. The inverse mass distribution is more symmetrical about the expected value than the mass distribution, particularly if the core of the distribution is considered.

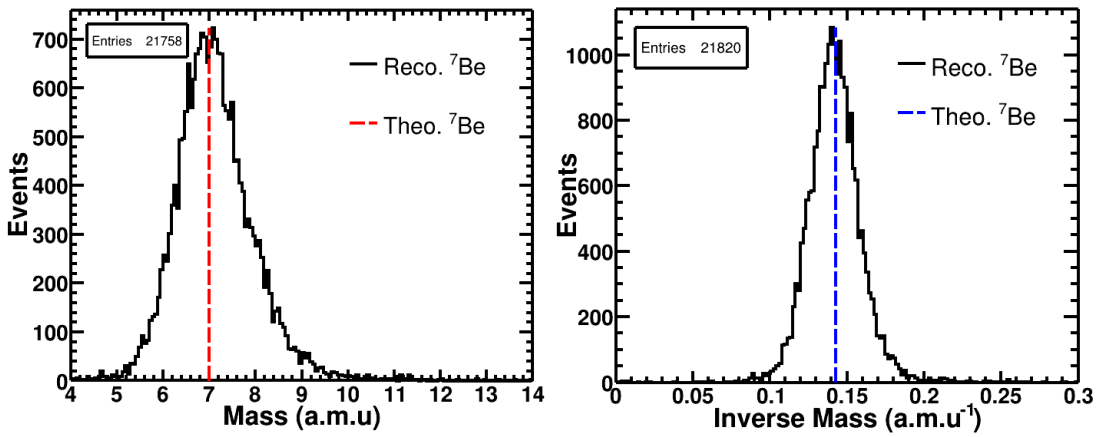

(a) Mass (b) Inverse Mass

Figure 4.36: Distribution of m (a) and $1/m$ (b) in a.m.u for a particular β bin from the RICH-Agl. The red and blue dashed lines represent the theoretical ^7Be mean location for the mass and inverse mass respectively. Inverse mass distribution is symmetric and has a Gaussian core due to it being proportional to $1/R$, which guarantees same properties in its error distribution.

A simple, first-order propagation of uncertainty provides us the basic scaling:

$$\sigma_u^2 = \left(\frac{\partial u}{\partial(1/R)}\right)^2 \sigma_{1/R}^2 + \left(\frac{\partial u}{\partial \beta}\right) \sigma_\beta^2, \tag{4.9}$$

where the covariance term yield zero as β and $1/R$ measurements are independent. The partial derivative with respect to $1/R$ yields:

$$\frac{\partial u}{\partial(1/R)} = uR = \frac{u}{(1/R)}, \tag{4.10}$$

and with respect to β yields:

$$\begin{aligned} \frac{\partial u}{\partial \beta} &= \frac{\partial}{\partial \beta}\left(\frac{m\beta}{ZR\sqrt{1-\beta^2}}\right), \\ &= \frac{m}{ZR}\left[\frac{1}{\sqrt{1-\beta^2}} + \frac{\beta^2}{(1-\beta^2)^{3/2}}\right], \\ &= u\left[\frac{1}{\beta} + \frac{\beta}{1-\beta^2}\right], \\ &= \gamma^2 \frac{u}{\beta}. \end{aligned} \tag{4.11}$$

Hence, the total relative error on u, which describes the template width, is a quadratic sum of the above two terms and given as:

$$\frac{\sigma_u}{u} = \sqrt{\left(\frac{\sigma_{1/R}}{1/R}\right)^2 + \left(\gamma^2 \frac{\sigma_\beta}{\beta}\right)^2}. \tag{4.12}$$

One can note from equation (4.8) that a characteristic width σ_u for a single-isotope distribution will depend on the tracker rigidity and β measurement resolutions, $\sigma_{1/R}$ and σ_β, with R playing a prominent role in the lower edge of every range and β in the higher. To better cope with

this joint effect, we chose to model directly the inverse mass instead of attempting a separate parametrisation of the two variables.

Furthermore, in order to validate our assumption, we produced scatter plots of inverse mass of ^7Be distribution vs the generated momentum instead of measured momentum. The resulting inverse mass ^7Be distribution could be well fitted with our single isotope template based on $1/R$ parametrisation. This confirmed the fact that we have to take in consideration the effect of measured β. That's why, a decision was made to directly parametrise the single-isotope mass template from the reconstructed $1/m$ distribution. In order to keep the thesis concise, an extensive discussion on this analysis is not done in the thesis.

The core of the reconstructed inverse mass distribution can be described with a Gaussian form. Further from the mean, additional tails are observed, which can be described by a second, concentric (i.e., similar peak position) Gaussian with a larger width. We call the former, **Core** Gaussian and the latter, **Residual** diffused Gaussian. The standard Normalised Gaussian form scaled by an amplitude which we used in our work is denoted as $\mathcal{N}(u)$, and given as:

$$\mathcal{N}(u; A, \mu, \sigma) \equiv \frac{A}{\sqrt{2\pi}\sigma} \exp\left[-\frac{1}{2}\left(\frac{u-\mu}{\sigma}\right)^2\right] \tag{4.13}$$

The above form has three free parameters (A, μ, σ) which are called the **Norm**, **Mean**, and the **Standard Deviation(std)** respectively. The advantage of the above form is that the integral of (4.13) yields the value of the amplitude or the Norm, A.

Hence, the function that is used to fit the reconstructed inverse mass distribution of the single isotope from Monte Carlo is:

$$f(u; A_{core}, A_{res}, \mu, \sigma_{core}, \sigma_{res}) = \mathcal{N}_{core}(u; A_{core}, \mu, \sigma_{core}) + \mathcal{N}_{res}(u; A_{res}, \mu, \sigma_{res}) \tag{4.14}$$

where $u \equiv 1/m$. The above function has 5 free parameters i.e., $\langle A_{core}, A_{res}, \mu, \sigma_{core}, \text{and } \sigma_{res}\rangle$. To avoid correlations between the free parameter, and hence to offer a reliable error, we indeed parameterise the function (4.14) as

1. $\mathbf{A_{core}}$: Norm of the Core Gaussian.
2. μ : Mean of the Core and the Residual Gaussian.
3. $\sigma_{\mathbf{core}}$: Standard Deviation of the Core Gaussian.
4. $\dfrac{\mathbf{A_{res}}}{\mathbf{A_{core}}}$: Ratio of the Norms of the two Gaussians.
5. $\dfrac{\sigma_{\mathbf{res}}}{\sigma_{\mathbf{core}}}$: Ratio of the Standard Deviations of the two Gaussians.

So, the function (4.14) can be modified as

$$f(u; \vec{P}) = \mathcal{N}_{core}(u; A_{core}, \mu, \sigma_{core}) + \mathcal{N}_{res}(u; (A_{res}/A_{core})\cdot A_{core}, \mu, (\sigma_{res}/\sigma_{core})\cdot\sigma_{core}) \tag{4.15}$$

where the parameters of the diffused Gaussian are obtained by multiplying the parameter 4. and 5. with that of 1. and 2. respectively, whereas the mean remains unchanged. Vector $\vec{P}$ includes all the free parameters, 5 in total: $\langle A_{core}, \mu, \sigma_{core}, A_{res}/A_{core}, \sigma_{res}/\sigma_{core} \rangle$.

One could in principle, allow for a degree of asymmetry in the diffused Gaussian by allowing different values for the standard deviation on the two sides of the peak through the asymmetric Gaussian function:

$$A(u; \mu, \sigma, \xi) = \left\{ \begin{array}{ll} \mathcal{N}(u; \mu, \sigma/\xi), & \text{if } u \leq \mu \\ \mathcal{N}(u; \mu, \sigma), & \text{if } u > \mu \end{array} \right\} \tag{4.16}$$

where, ξ is an asymmetry parameter. This would increase the number of parameters to 6, which is not convenient for the fitting procedure. Furthermore, given the expected ratio of components in the fit, the precision of a basic model is considered sufficient in this particular analysis, which would be further corroborated with a good chi-square statistics in the final fit as we see later in the subsequent sections. As such, including asymmetry in the ^7Be template is considered unnecessary keeping in mind the necessity to have fewer dimensions in the parameter space.

4.5.1.3 Fit Results and Template Verification

Fig.4.37 shows example fits of the function (4.15) to histograms of ^7Be Monte Carlo, along with the component functions that are summed to arrive at the final template.

One would expect the single-isotope peak corresponding to a particular mass to be distributed around $u = 1/m$. The mean is extracted with the estimated parameter errors from MINUIT. As seen in fig. 4.38, we can see that there is very good agreement across the energy range for all sub-detectors used in the analysis.

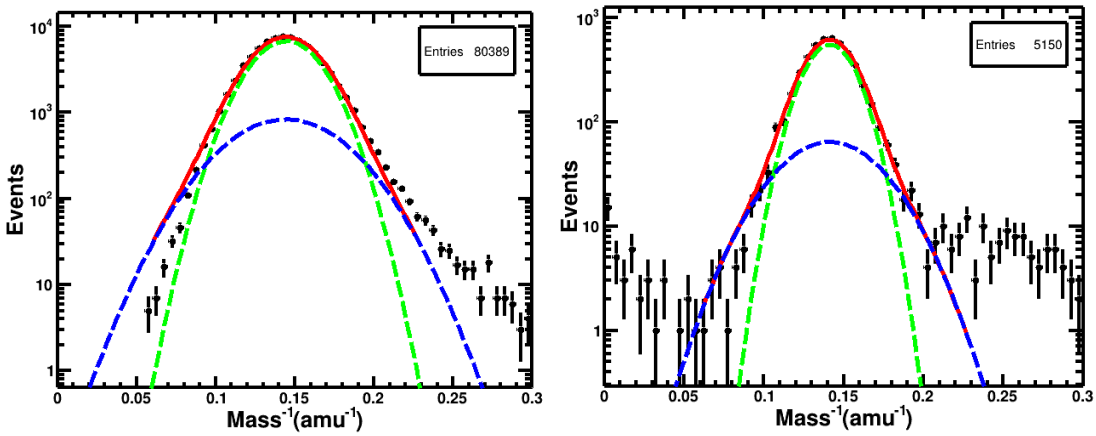

(a) ToF

(b) NaF

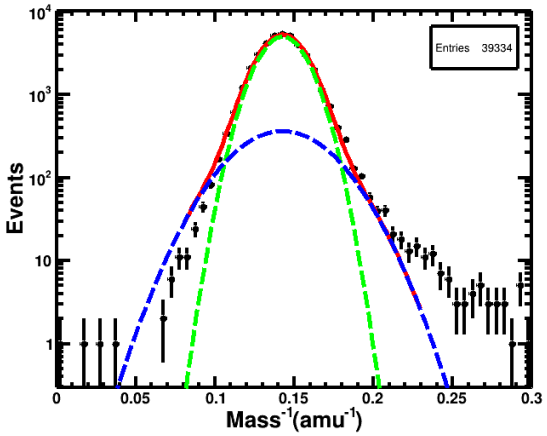

(c) Agl

Figure 4.37: Example template fits to $u = 1/m$ distribution from ^7Be AMS-Monte Carlo for the ToF, RICH-NaF and RICH-Agl sub-detectors. The green dashed line denotes the core gaussian, and the blue dashed line denotes the residual Gaussian. The red continous lines represents the summation of the two Gaussians and the overall fit.

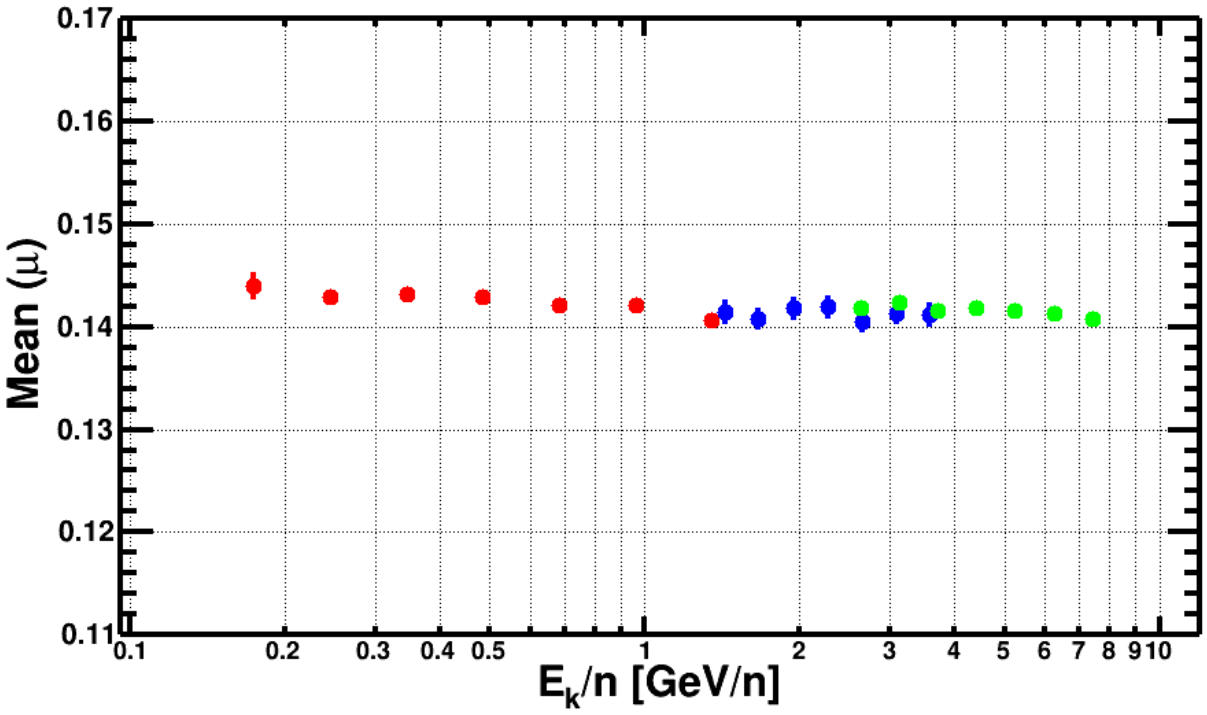

Figure 4.38: Location of the ^7Be peak μ from single-isotope template fits. We see there is good agreement with the theoretical value 0.143 amu^{-1} across the energy-range.

4.5.1.4 Full Mass-Distribution Model (The Three-Isotope Template)

The next step in our model construction is to extend the preceding model to that of three isotopes; and it is rather straightforward and necessitates minimal model complexity. The templates for ^9Be, and ^{10}Be is build up by scaling with respect to the ^7Be template. As stated before and repeated here for brevity, the isotopes templates are scaled with respect to ^7Be, as it has a clearly visible peak in the mass distribution owing to its higher abundance. The sum of the three isotopes can then be fitted to ISS data containing the Be events.

The mass templates at the first order of approximation are expected to be similar. We have directly built our single isotope template based on the mass resolution which is expected to be similar for the three isotopes too. So, we can scale the template width with the help of the theoretical mass ratios. Take for example, for species *a*, and species *b*, considering they have similar mass resolution, we have the trivial relation

$$\begin{aligned} \frac{\sigma_a}{1/m_a} &= \frac{\sigma_b}{1/m_b}, \\ \sigma_b &= \frac{m_a}{m_b}\sigma_a, \end{aligned} \tag{4.17}$$

where m_a, and m_b are masses of the respective species. As such, we can scale the template width of ^9Be, and ^{10}Be with the linear mapping:

$$\mathcal{L}(z) = \begin{cases} \frac{7}{9}z \;\forall\; z \in \{\sigma_{^9Be}, \mu_{^9Be}\} \\ \frac{7}{10}z \;\forall\; z \in \{\sigma_{^{10}Be}, \mu_{^{10}Be}\} \end{cases} \tag{4.18}$$

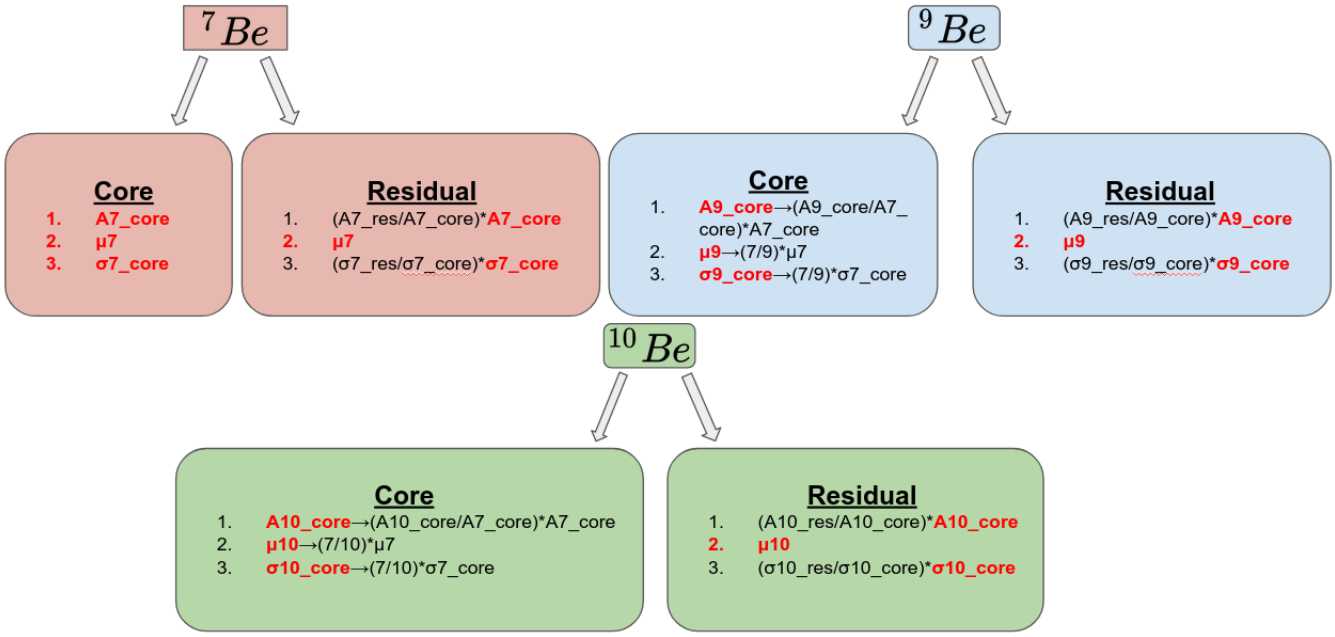

Figure 4.39: The analytical Gaussian model to fit the Be data is represented pictorially.

Hence, the three isotope templates can be written as (where c: core & r: residual):

- **^{7}Be**

$$f_7 \equiv f_7(u;\vec{P}) = {}^{7}\mathcal{N}^c(u;A_7^c,\mu_7,\sigma_7^c) + {}^{7}\mathcal{N}^r(u;(A_7^r/A_7^c)\cdot A_7^c,\mu_7,(\sigma_7^r/\sigma_7^c)\cdot\sigma_7^c), \quad (4.19)$$

- **^{9}Be**

$$\begin{aligned} f_9 \equiv f_9(u;\vec{P}) = {}^{9}\mathcal{N}^c(u;(A_9^c/A_7^c)\cdot A_7^c,(7/9)\mu_7,(7/9)\sigma_7^c) + \\ {}^{9}\mathcal{N}^r(u;(A_9^r/A_9^c)\cdot A_9^c,\mu_9,(\sigma_9^r/\sigma_9^c)\cdot\sigma_9^c), \end{aligned} \quad (4.20)$$

- **^{10}Be**

$$\begin{aligned} f_{10} \equiv f_{10}(u;\vec{P}) = {}^{10}\mathcal{N}^c(u;(A_{10}^c/A_7^c)\cdot A_7^c,(7/10)\mu_7,(7/10)\sigma_7^c) + \\ {}^{10}\mathcal{N}^r(u;(A_{10}^r/A_{10}^c)\cdot A_{10}^c,\mu_{10},(\sigma_{10}^r/\sigma_{10}^c)\cdot\sigma_{10}^c), \end{aligned} \quad (4.21)$$

where $\vec{P}$ contains all the parameters; 5 free parameters, and 2 shape parameters; and in total 7 parameters: $\langle A_7^c, \mu_7, \sigma_7, A_7^c/A_9^c, A_7^c/A_{10}^c, A^r/A^c, \sigma^r/\sigma^c\rangle$. We can add the three templates to get the full model: $f_{tot}(u;\vec{P}_{tot}) = f_7 + f_9 + f_{10}$. The full model is represented pictorially in fig. 4.39 for a better understanding. Finally, we use the three-isotope template model to fit mass distributions instead of inverse mass distribution. For this purpose, we demand that for every mass distribution, $m(z)$, the three-isotope mass template $f_{tot}(u;\vec{P}_{tot})$ assigns $u = 1/z\ \forall\ u \in m(z)$.

As compared to the single-isotope model, we have two more parameters. The mean of the ^{9}Be and ^{10}Be (i.e., the respective means) have been fixed with respect to the ^{7}Be peak because the degree of overlap does not leave sensitivity to accurately fit this parameter. However, the mean of the most prominent peak i.e., μ_7 is left as a free parameter. The value of this parameter

output from the fit acts as a check on the fit, similar to single-isotope case.

4.5.2 Monte-Carlo validation of the Fit-Model

An useful tool of AMS-MC is that we can configure the spectrum of the injected Be isotopes, which in return serves as a valuable template validation tool. In principle, we can inject different isotope mixture in the simulation and check the robustness of our analysis models over a wide range of isotopic composition. Therefore, we exploit this feature for validation of our fit model on the MC data.

4.5.2.1 Realistic Mixture of Isotopes in MC (Tuning the Spectrum)

We inject three different mixtures of ^{10}Be spectrum which varies from each other at 30 % level. We call one of them the **(1) Default Spectrum**, then the one containing 30% higher ^{10}Be is denoted a **(2) High Spectrum**, and the one with 30% lower ^{10}Be is denoted as **(3) Low Spectrum**. Examples arising from RICH-Agl mass distributions for the three different cases are depicted in fig. 4.40. If one can reproduce the injected spectrum by calculating the final Be isotope counts from the template fitting procedure, one can be confident about the validity of the model across different isotopic composition. It is highlighted that the point of this exercise is a first order validation of the model to have comparable normalisation within error bars, and that one isn't interested in reproducing the injected spectrum exactly. A highly involved fit is only done for real AMS data.

4.5.2.2 Fit on Monte-Carlo Distributions

The three-isotope template can be now fitted to MC data with a composition of the isotopes that we decide, and then we can determine the raw isotope fractions. We are interested in two isotope fractions, one is $^{10}Be/^{9}Be$ fraction, and the other is $^{7}Be/$Total Be. Fig. 4.41 shows examples of fits in a certain energy bin of each of the sub-detectors for three different injected isotopic composition. To simplify the presentation, only a single curve has been used for each of the single-isotope template. Similar to the single-isotope case, a shape dominated by a roughly Gaussian core with a diffused residual Gaussian arises from the fit. Validation of the template fit can be done by looking at the fit parameter μ_7 which should agree with the theoretical value $1/7$ within 0.1 % for all the bins across the three sub-detectors. Fig. 4.42a shows the value of this parameter. The slight decrease from ToF to RICH detector is a result of energy loss which doesn't seem significant within the ambit of the analysis.

Goodness of fit serves as another check on the apropriatness of our template for the three-isotope. Fig. 4.42b shows the reduced chi-squared statistics versus energy per unit nuleon for the three sub-detectors. The value is $\chi^2 \lesssim 2$ for all the bins across the sub-detectors and across the energy-range.

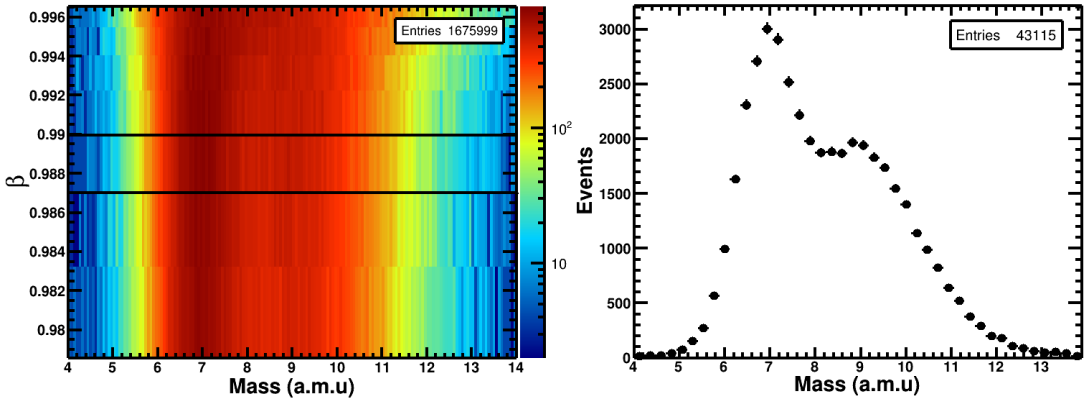

(a) MC Agl (Default)< Mass vs β >

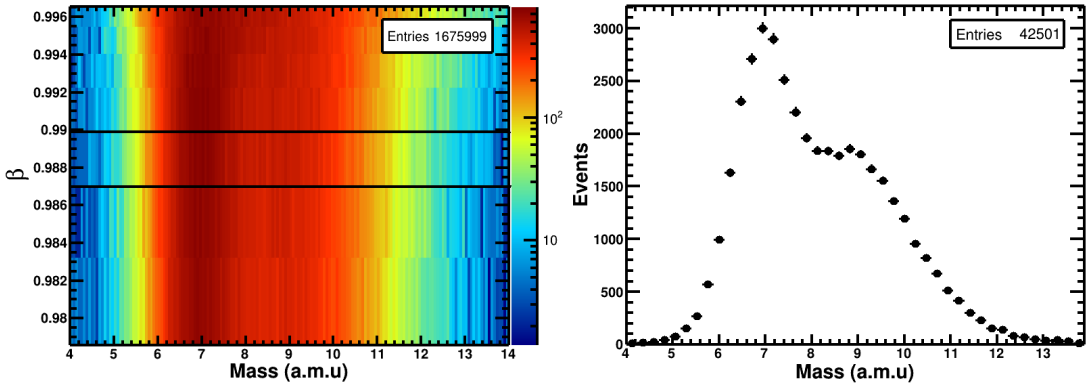

(b) MC Agl (Low ^{10}Be) < Mass vs β >

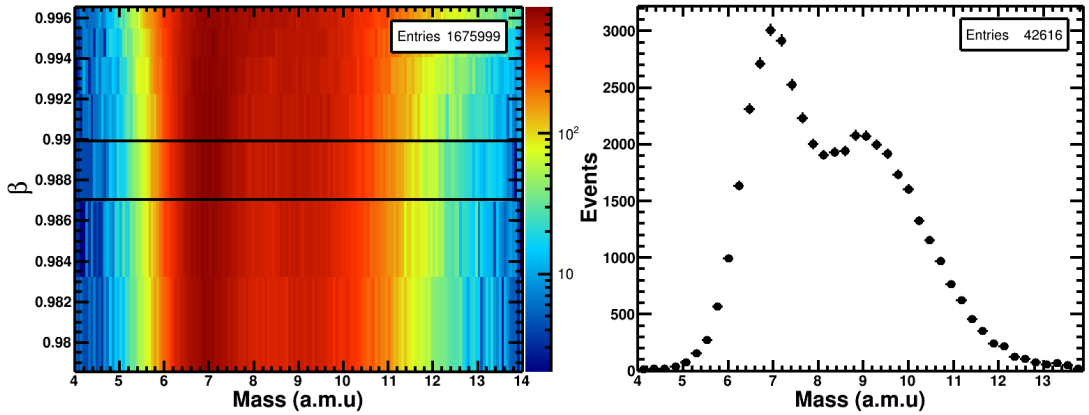

(c) MC Agl (High ^{10}Be) < Mass vs β >

Figure 4.40: Left: The < Mass vs β > scatter plot. Right: Mass distribution for the highlighted bin on the left for RICH-Agl for three different mixtures of Be isotopes in AMS-MC respectively.

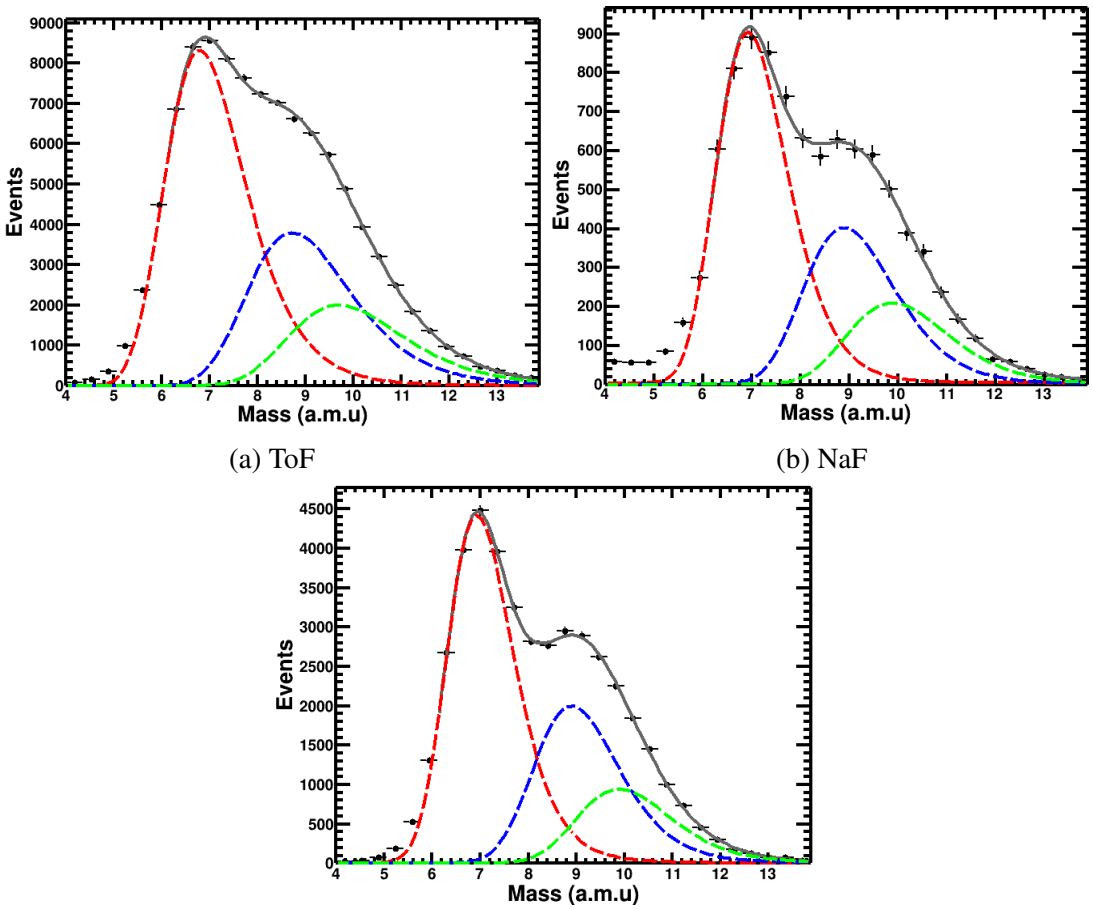

(a) ToF

(b) NaF

(c) Agl

Figure 4.41: Example of template fits to mass distribution from Be AMS-Monte Carlo for the ToF, RICH-NaF and RICH-Agl sub-detectors for the default isotope composition. The red dashed line denotes the ^{7}Be template Gaussian, and the blue dashed line denotes the ^{9}Be template Gaussian, and the green dashed line denotes the ^{10}Be template Gaussian. The red continous lines represents the summation of the three Gaussian templates and the overall fit.

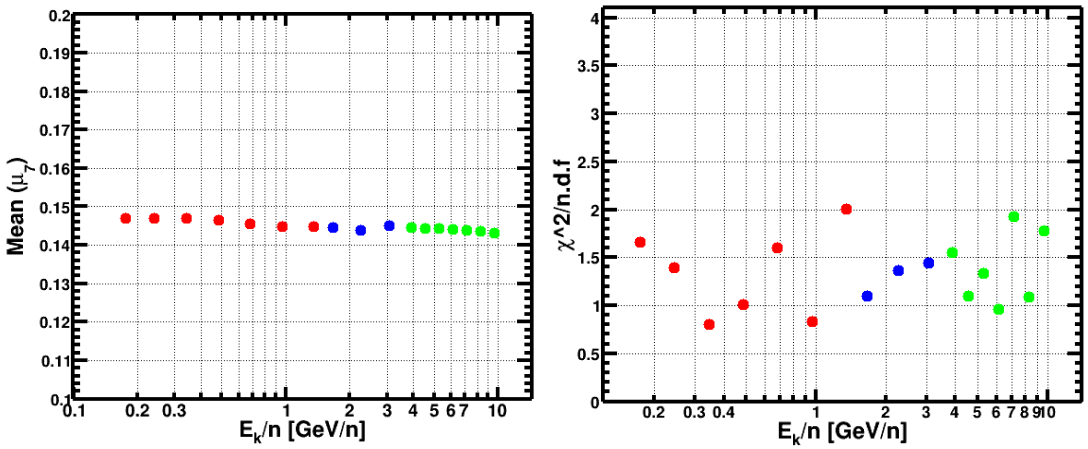

(a) $\mu 7$ (b) χ^2/ndf

Figure 4.42: a) Mean of the ^7Be peak from three-isotope template. We see that there is good agreement with the theoretical value within 0.1 %. b) The χ^2 statistic for the three sub-detectors across the enery range. The value is well within $\chi^2/ndf \lesssim 2$ for all bins.

The number of isotope counts N for a mass distribution $f(m)$ can be figured out in the following way:

$$N = \frac{\sum f(m)\Delta m}{\Delta m} \equiv \frac{\int f(m)dm}{\Delta m} \tag{4.22}$$

The division of counts for each isotopes should provide us the required isotopic fraction. In fig. 4.43, the ratio of the measured by expected isotopic fraction viz., $^{10}Be/^9Be$, and ^7Be/Total Be is plotted. It is observed that it closely follows the injected spectrum which validates our three-isotope template fit model for MC.

Now, we follow the thee-isotope template fit method where ^{10}Be is purposely injected 0.3 times lower than the default composition, and when ^{10}Be is injected 1.3 times higher than the default composition. Fig. 4.44 and Fig. 4.45 show typical fit results for three particular bins for each sub-detector. The former refers to case where the ^{10}Be composition is lower, and the latter to the case where it is higher. Similarly like before, we can verify the template fitting as seen in fig. 4.46. If we observe here, the parameter μ_7, and the chi-squared statistics are exactly similar for three different isotopic composition mixture, which offers a further validation of our model. Finally, fig. 4.47 shows the ratios of the measured by expected isotopic fraction of interest. Following this exercise, we can be confident enough that our three-isotope template model based on bi-Gaussian distribution is valid over a wide range of isotopic composition mixture, and hence offers us a robust model to apply the fit to real AMS data.

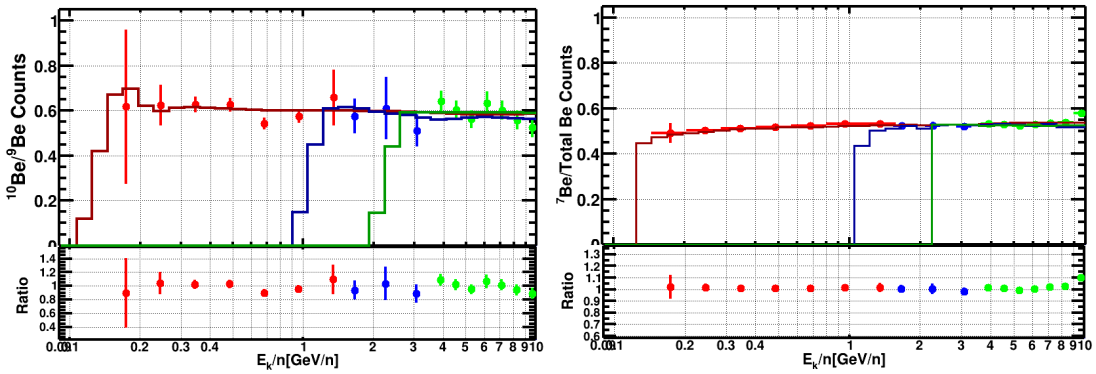

(a) $^{10}Be/^{9}Be$ ratio (b) $^{7}Be/$Total Be ratio

Figure 4.43: Top Panel: The isotopic fraction (a) $^{10}Be/^{9}Be$, and (b) $^{7}Be/$Total Be for the default composition in AMS-MC. Here, the points represent the fraction elicited from the fit model, and the histograms represent the injected spectrum into the AMS-MC. Bottom Panel: The ratio of the measured by expected isotopic fraction (a) $^{10}Be/^{9}Be$, and (b) $^{7}Be/$Total Be for the default composition in AMS-MC. We see that the extracted isotopic fraction closely follows the injected spectrum, validating our model for the default MC composition.

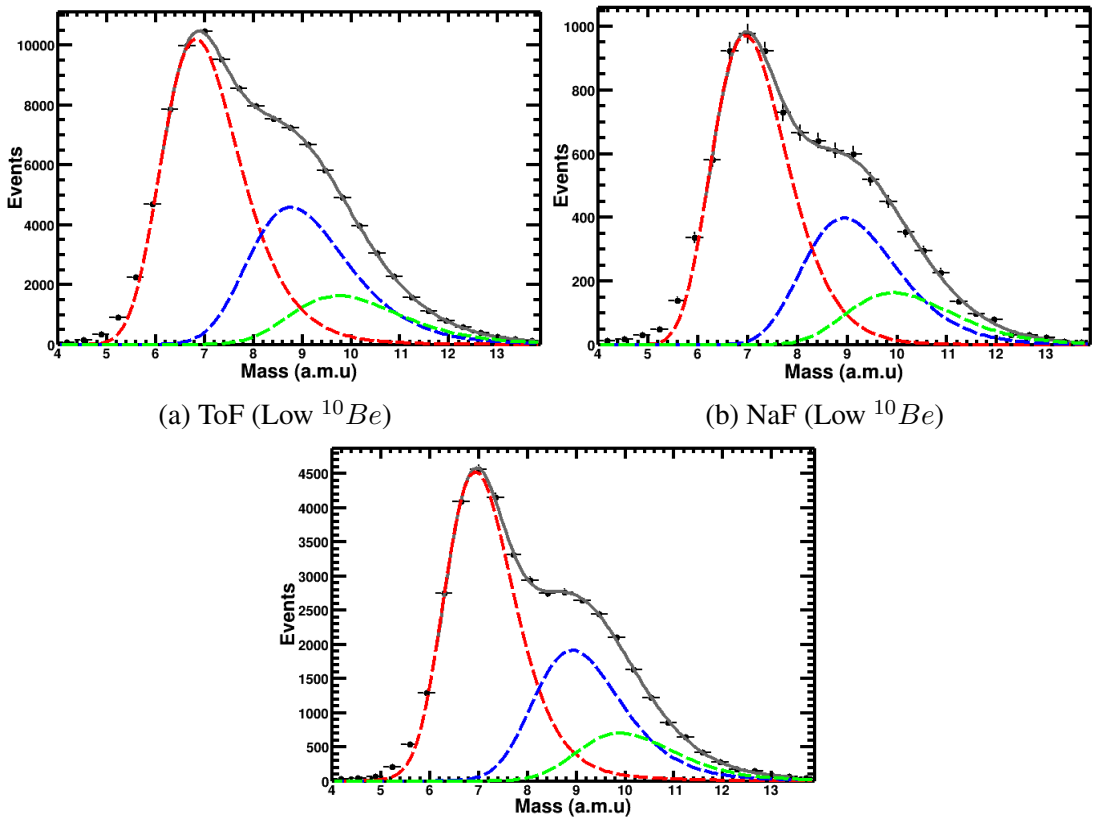

(a) ToF (Low ^{10}Be) (b) NaF (Low ^{10}Be)

(c) Agl (Low ^{10}Be)

Figure 4.44: Example of template fits to mass distribution from Be AMS-Monte Carlo for the ToF, RICH-NaF and RICH-Agl sub-detectors for the isotope composition where ^{10}Be is purposely injected 0.3 times lower than the default composition. The red dashed line denotes the ^{7}Be template Gaussian, and the blue dashed line denotes the ^{9}Be template Gaussian, and the green dashed line denotes the ^{10}Be template Gaussian. The red continuous lines represents the summation of the three Gaussian templates and the overall fit.

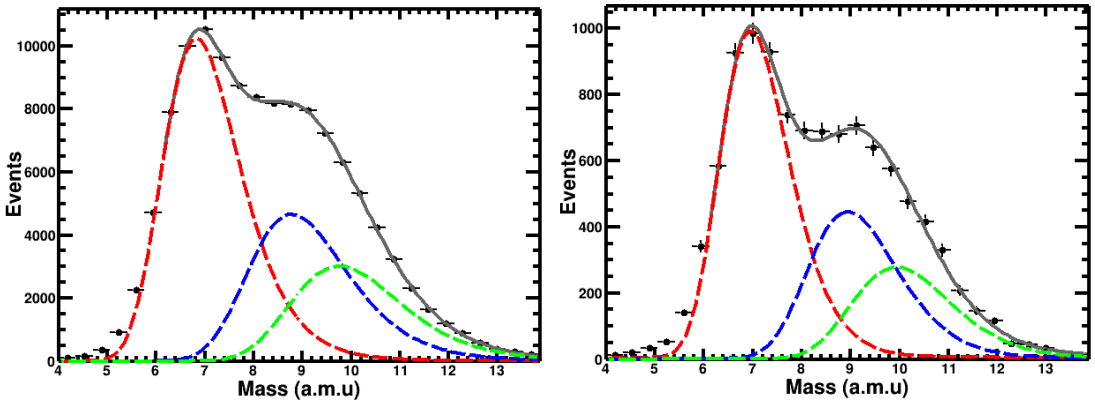

(a) ToF (High ^{10}Be)

(b) NaF (High ^{10}Be)

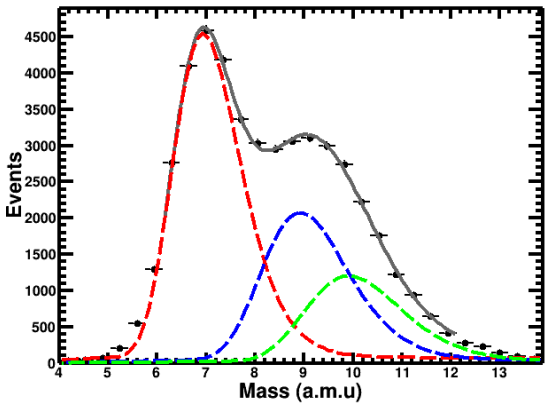

(c) Agl (High ^{10}Be)

Figure 4.45: Example of template fits to mass distribution from Be AMS-Monte Carlo for the ToF, RICH-NaF and RICH-Agl sub-detectors for the isotope composition when ^{10}Be is injected 1.3 times higher than the default composition. The red dashed line denotes the ^{7}Be template Gaussian, and the blue dashed line denotes the ^{9}Be template Gaussian, and the green dashed line denotes the ^{10}Be template Gaussian. The red continous lines represents the summation of the three Gaussian templates and the overall fit.

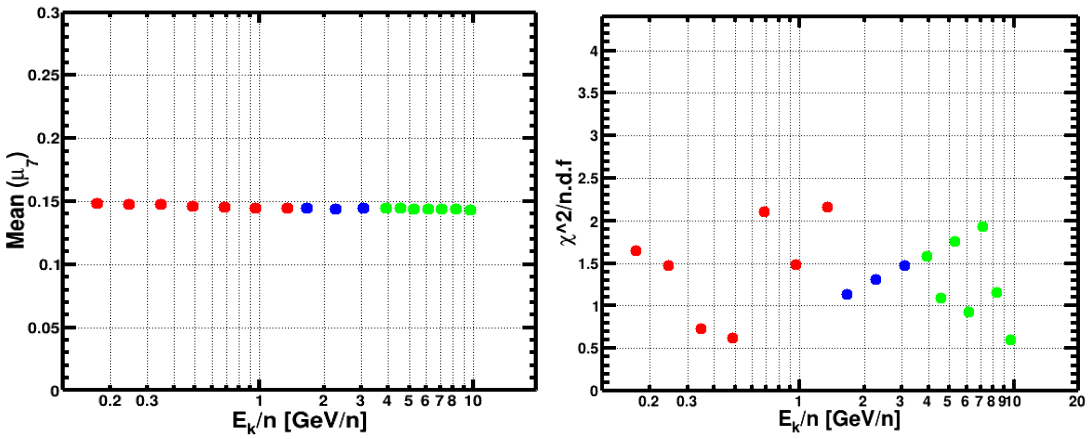

(a) μ_7 (Low ^{10}Be)

(b) χ^2/ndf (Low ^{10}Be)

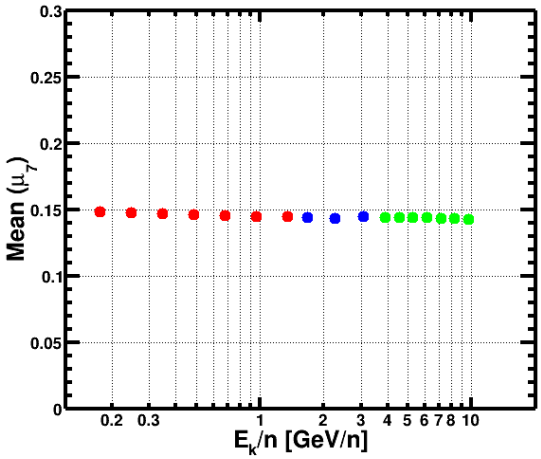

(c) μ_7 (High ^{10}Be)

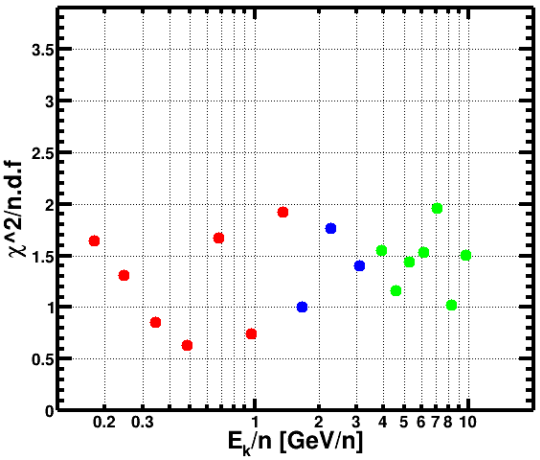

(d) χ^2/ndf (High ^{10}Be)

Figure 4.46: a) & c) Location of the ^7Be peak from three-isotope template where ^{10}Be is purposely injected 0.3 times lower than the default composition, and when ^{10}Be is injected 1.3 times higher than the default composition. We see that there is good agreement with the theoretical value within 0.1 %. b) & d) The chi-squares statistic for the three sub-detectors across the enery range. The value is well within $\chi^2/ndf \lesssim 2$ for all bins.

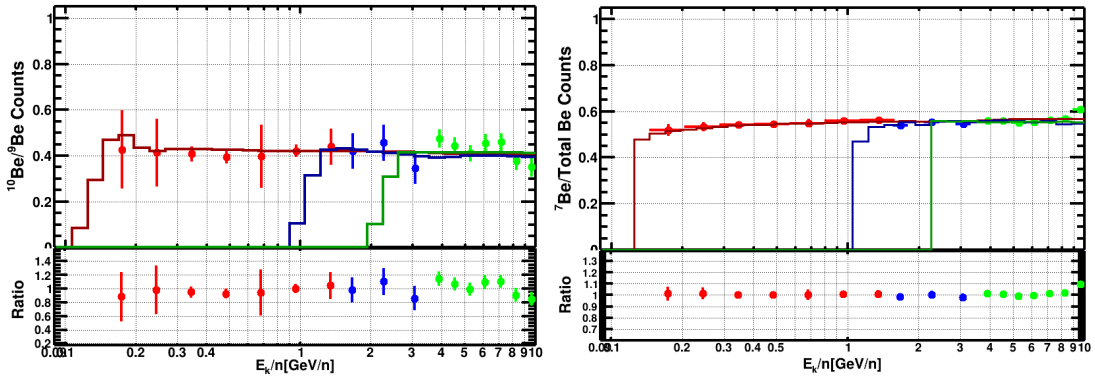

(a) $^{10}Be/^{9}Be$ ratio (Low ^{10}Be)

(b) $^{7}Be/Total\ Be$ ratio (Low ^{10}Be)

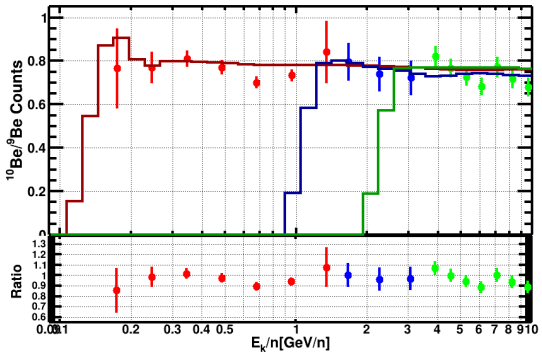

(c) $^{10}Be/^{9}Be$ ratio (High ^{10}Be)

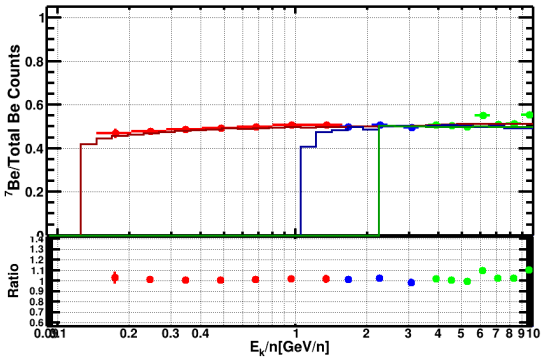

(d) $^{7}Be/Total\ Be$ ratio (High ^{10}Be)

Figure 4.47: Top Panel: (a) & (b) The isotopic fraction $^{10}Be/^{9}Be$, and $^{7}Be/$Total Be where ^{10}Be is purposely injected 0.3 times lower than the default composition, and (c) & (d) where ^{10}Be is injected 1.3 times higher than the default composition. Here, the points represent the fraction elicited from the fit model, and the histograms represent the injected spectrum into the AMS-MC. Bottom Panel: (a) & (b) The ratio of the measured by expected isotopic fraction $^{10}Be/^{9}Be$, and $^{7}Be/$Total Be where ^{10}Be is purposely injected 0.3 times lower than the default composition, and (c) & (d) when ^{10}Be is injected 1.3 times higher than the default composition. We see that the extracted isotopic fraction closely follows the injected spectrum, validating our model for the MC composition mixture employed here.

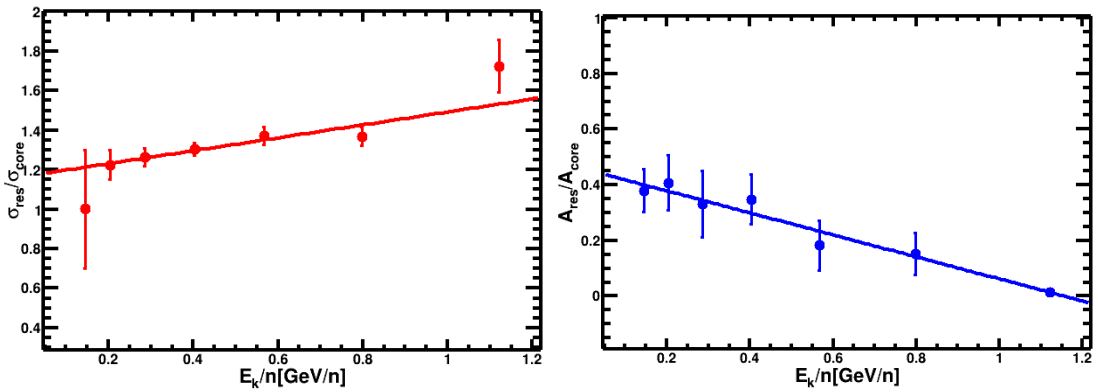

Figure 4.48: The energy per unit nucleon dependence of the shape parameters as explained in the text for ^7Be Monte-Carlo inverse mass distributions for the ToF detector. The solid red line shows the linear fit on the points.

4.6 Measured Be Isotopic Fraction on Data

4.6.1 Fit Procedure on Data

Before proceeding, for the sake of completeness, the 7 parameters of the three-isotope template model are listed below.

- **"Free" Parameters of the Model**

  1. $\mathbf{A_{7,core}}$: Norm of the ^7Be Core Gaussian.
  2. μ_7 : Mean of the Core and the Residual ^7Be Gaussian.
  3. $\sigma_{7,\mathrm{core}}$: Standard Deviation of the ^7Be Core Gaussian.
  4. $\dfrac{\mathbf{A_{9,core}}}{\mathbf{A_{7,core}}}$: Ratio of the Norms of ^9Be and ^7Be Core Gaussians.
  5. $\dfrac{\mathbf{A_{10,core}}}{\mathbf{A_{7,core}}}$: Ratio of the Standard Deviations of the ^{10}Be and ^7Be Core Gaussians.

- **"Shape" Parameters (Studied from ^7Be Monte-Carlo)**

  1. $\mathbf{A_{res}/A_{core}}$: Ratio of the Norms of the Residual and Core Gaussians.
  2. $\sigma_{\mathrm{res}}/\sigma_{\mathrm{core}}$: Ratio of the Standard Deviations of the Residual and Core Gaussians.

As a starting point for the fit, the ^7Be MC distributions were fitted with the single-isotope template as explained in the preceding section. The shape parameters, A_{res}/A_{core}, and $\sigma_{res}/\sigma_{core}$ were plotted with respect to energy per unit nucleon for each of the sub-detectors. For e.g., the two parameters for the ToF detector is shown in fig. 4.48. After which, they are fitted with linear functions, which are then used as a starting point of the fit procedure.

The fit procedure is performed in two steps. In the first attempt, the free parameters of the model are constrained very loosely, and the shape parameters are constrained around the MC parametrised values within a 10% band. Once, the fit is executed, trends of the free parameter with respect to energy for all the sub-detectors are extracted, for e.g., the trend of the μ_7,

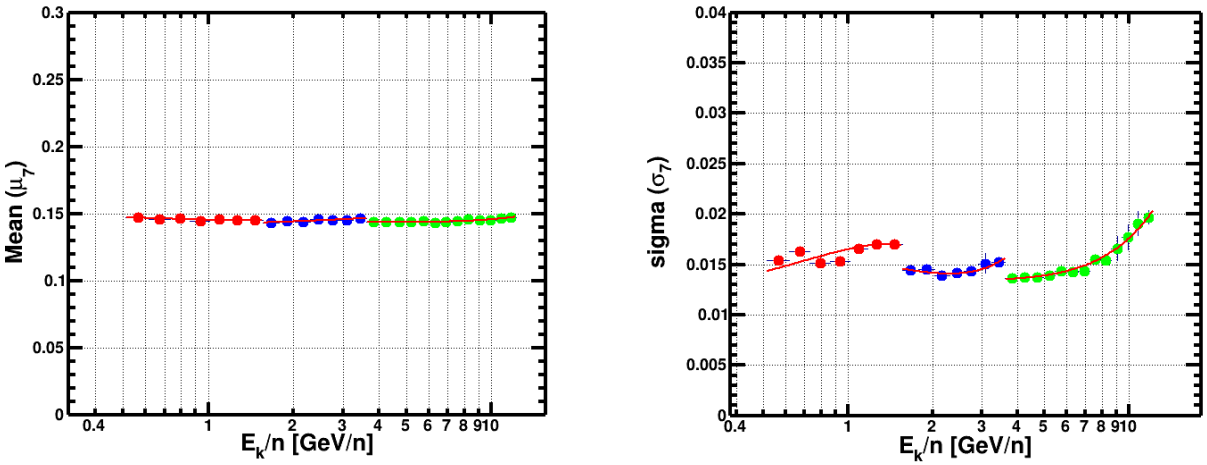

Figure 4.49: The energy-dependent trends of the free paramter μ_7 and σ_7 respectively. They are fitted with second-degree polynomials for each sub-detector range separately. The energy dependent polynomial values are used as a starting point for the second step of the fit for the free parameters.

and the σ_7 parameter is shown in fig.4.49. Those free parameter trends are then fitted with a second-order polynomial. The second fit is done, by constraining the free parameters around those polynomial values with a 10 % equi-probable band around the values.

An example of the fits to the ToF, RICH-NaF, and RICH-agl is shown in fig. 4.50, 4.51, & 4.52. For clarity, the components of the single-isotope templates are not shown. However, each of them can be resolved into its individual components as shown in fig. 4.53.

For template verification, the energy-dependent trend of the location of ^7Be is shown in fig. 4.54 . We see that the location of the peak of ^7Be traces the theoretical value well. The chi-squared statistics of all the bins across the energy range for each sub-detector is show in fig. 4.55., and it is well within, $\chi^2 \lesssim 2$. The fit on the data enables us to extract the counts of each isotopes as explained earlier. The ratio of the counts of interest, i.e., $^{10}Be/^9Be$ and $^7Be/$Total Be along with it's associated relative error is shown in fig. 4.56 and fig. 4.57 respectively. It is to be noted that the ratio of counts is only a proxy of the true isotope flux ratio since the difference in the isotope acceptance has not been accounted yet.

4.6.2 A note on the Energy Binning

The binning choice is a compromise between measurement granularity and precision. Narrow bins helps us to have a higher density of measured energy values in an energy interval, helping us to unravel fine structures that gets obscured in wider binning, at the cost of lower statistics leading to higher statistical uncertainties. In general, CR fluxes obey a decaying power-law spectrum with energy. The latter necessitates widening of bins at higher energies to have sufficient statistics. Keeping that in mind, one sound choice is a binning uniform in $\log E_{k/n}$. Which means that for n energy bins covering an energy interval $\in [E_0, E_n)$, we have the bin

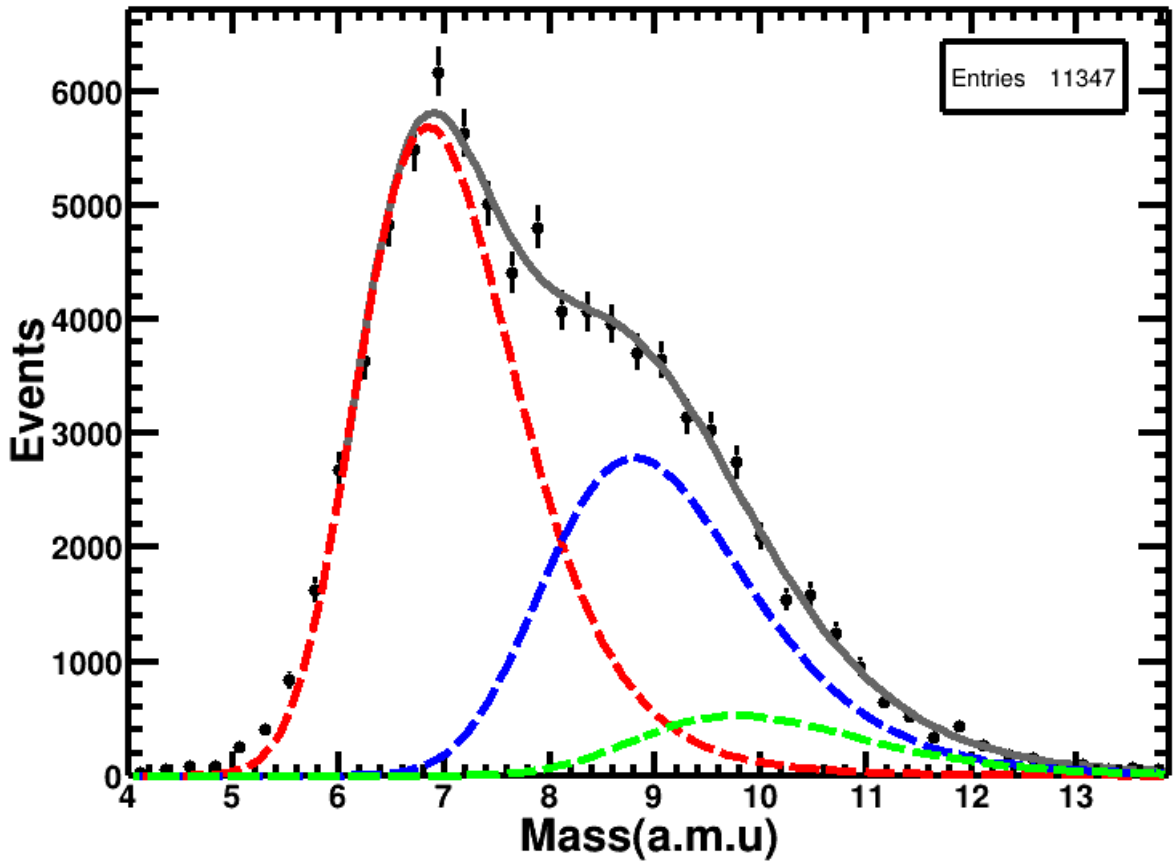

Figure 4.50: Fit on one of the ToF bin. The dashed red represents the ^{7}Be bi-Gaussian, dashed blue represents the ^{9}Be bi-Gaussian, and the green represents the ^{10}Be bi-gaussian. The thick red line denotes the sum of the three bi-Gaussians.

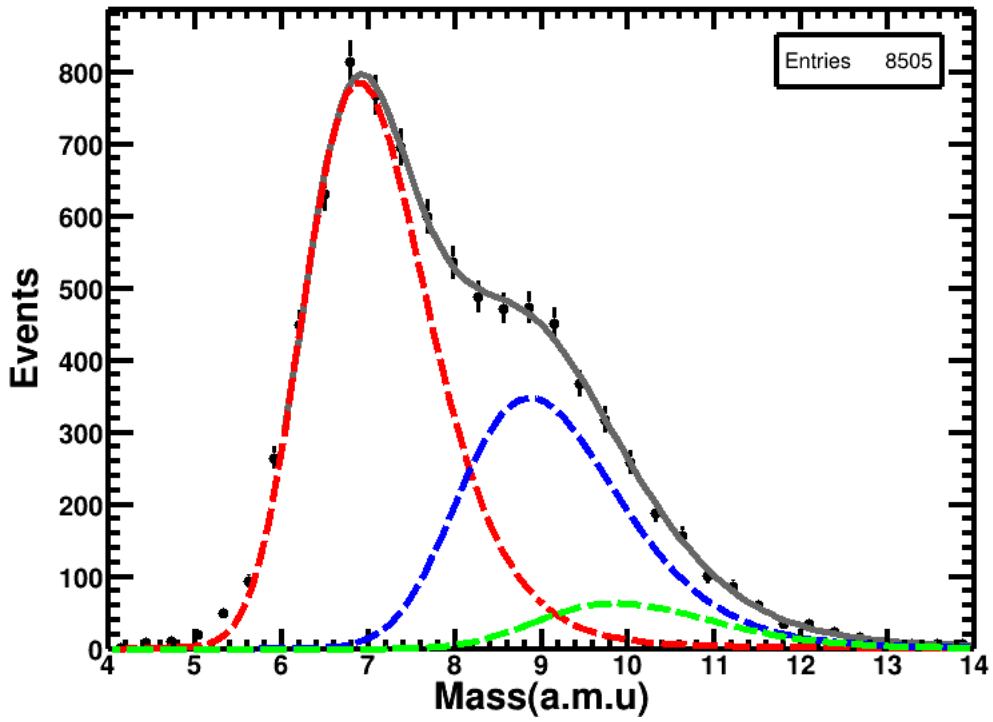

Figure 4.51: Fit on one of the RICH-NaF bin. The dashed red represents the ^{7}Be bi-Gaussian, dashed blue represents the ^{9}Be bi-Gaussian, and the green represents the ^{10}Be bi-gaussian. The thick red line denotes the sum of the three bi-Gaussians.

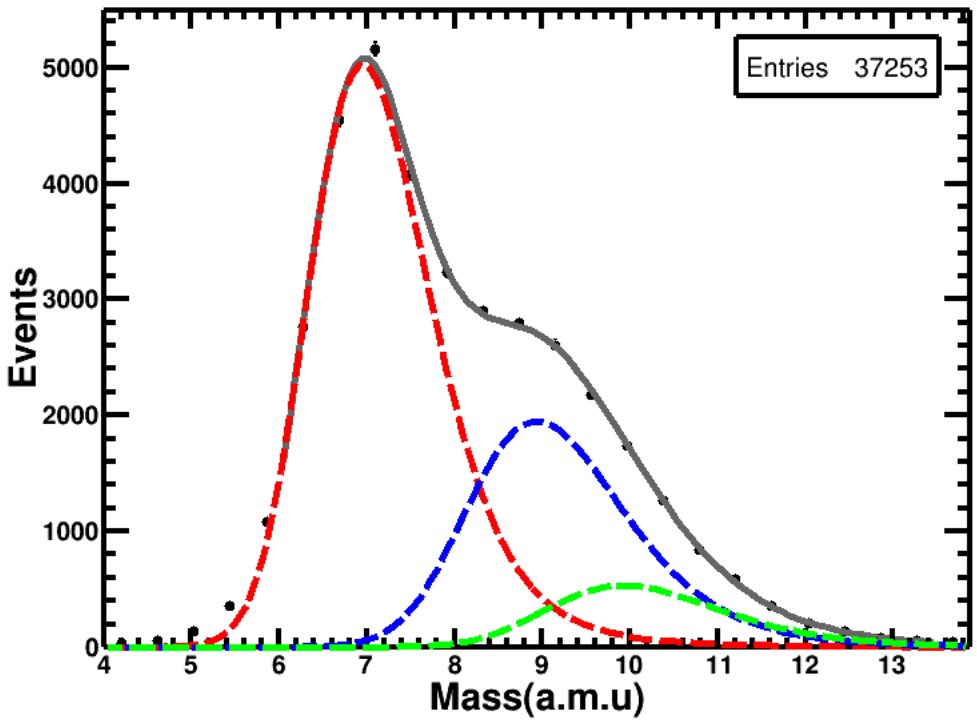

Figure 4.52: Fit on one of the RICH-agl bin. The dashed red represents the ^{7}Be bi-Gaussian, dashed blue represents the ^{9}Be bi-Gaussian, and the green represents the ^{10}Be bi-gaussian. The thick red line denotes the sum of the three bi-Gaussians.

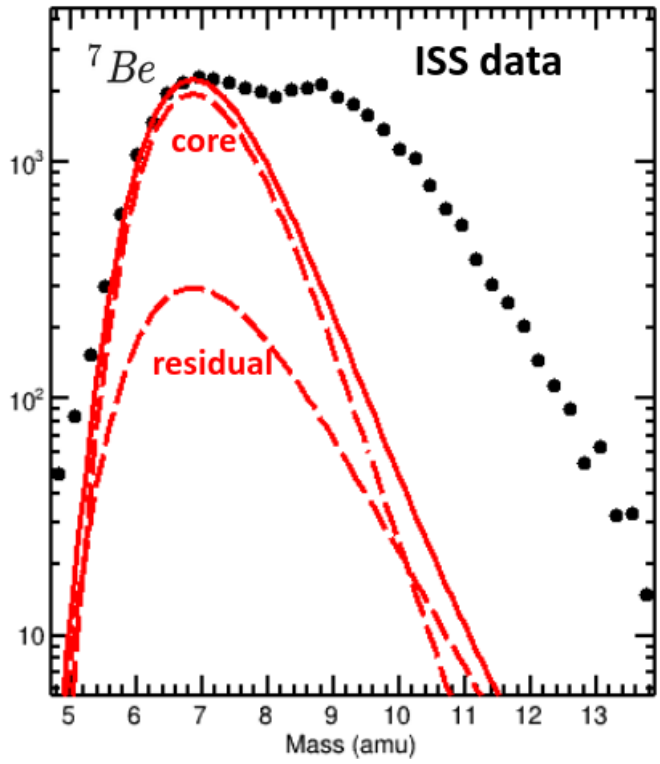

Figure 4.53: Fit on one of the bins. The dashed red represents the ^{7}Be core and residual Gaussians, while the the continous red line denotes the sum of the two Gaussians.

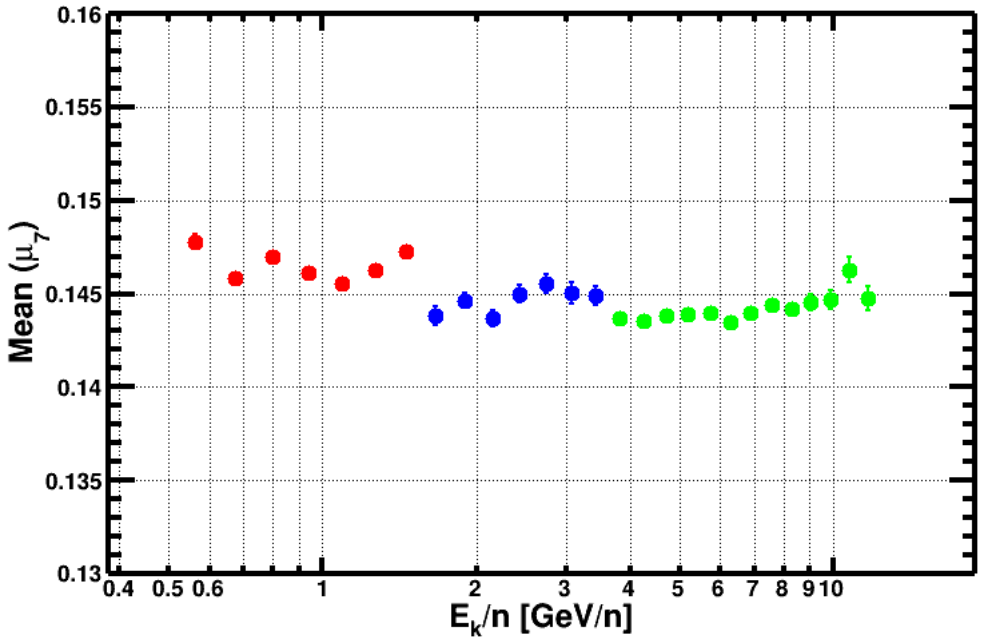

Figure 4.54: The location of the ^7Be peak with respect to energy per unit nucleon for all the sub-detectors. The location is consistent with the theoretical value of the peak ≈ 0.1423, and all points are within $\approx 0.5\%$ of the theoretical value.

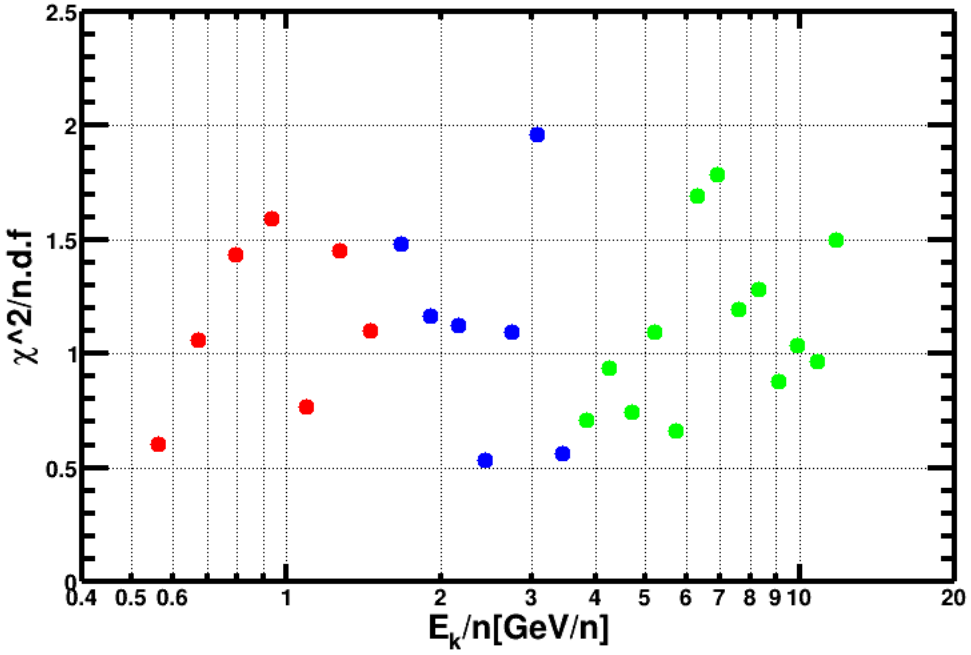

Figure 4.55: The chi-squares statistic for the three sub-detectors across the energy range. The value is well within $\chi^2/ndf \leq 2$ for all bins.

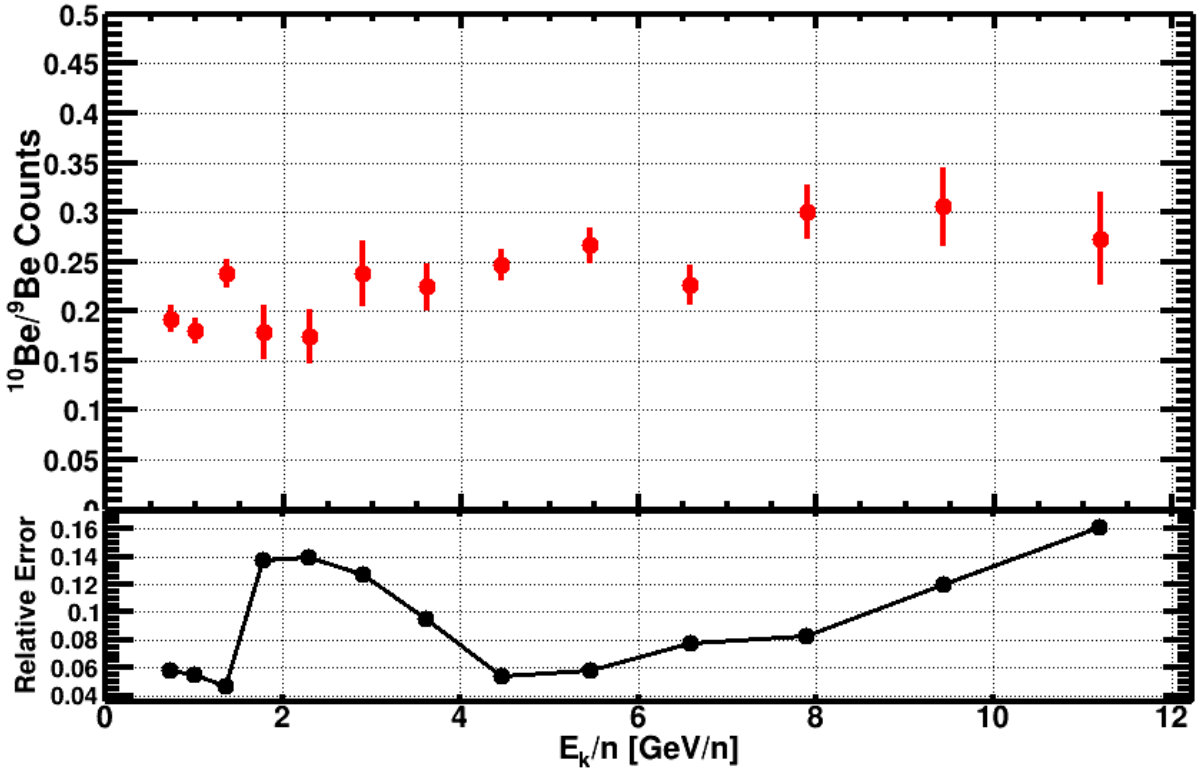

Figure 4.56: The counts ratio of $^{10}Be/^{9}Be$ along with its associated relative error. The bins have been merged to reduce statistical error and fluctuations, as well as for comparison with other analysis groups within the AMS collaboration.

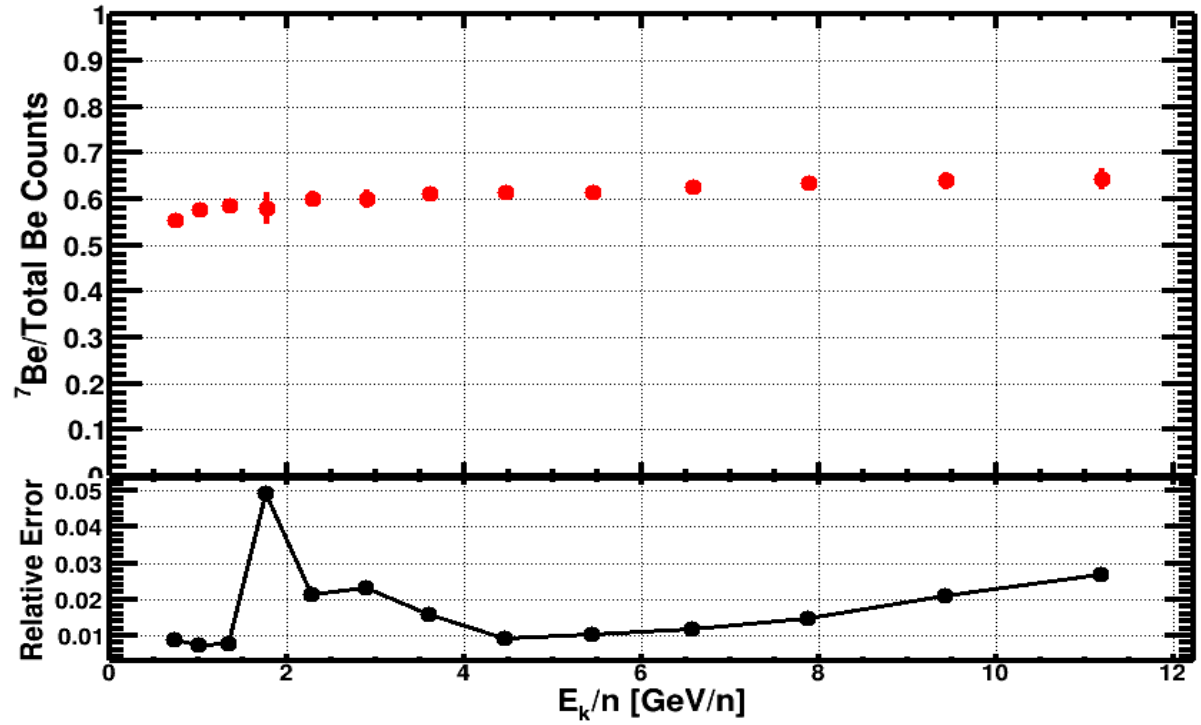

Figure 4.57: The counts ratio of $^{7}Be/$Total Be along with its associated relative error. The bins have been merged to reduce statistical error and fluctuations, as well as for comparison with other analysis groups within the AMS collaboration.

width, W_k defined as:

$$W_k \equiv \left[\exp\left(\frac{(k-1)\log\left(\frac{E_n}{E_0}\right)}{n} \right) E_0, \exp\left(\frac{k\log\left(\frac{E_n}{E_0}\right)}{n} \right) E_0 \right) , k \in \{1, 2, \cdots, n\} \tag{4.23}$$

Along with the above, another consideration stems from *bin migration*. An experimentally measured β value will always have an inherent error with respect to the true value, which translated to an error in $E_{k/n}$. This means, the measured energy per unit nucleon, $E^{meas}_{k/n}$ is:

$$E^{meas}_{k/n} = E^{true}_{k/n} + \delta E; \tag{4.24}$$

where δE is the error. Based on the sign of δE, events can either migrate to higher bins or lower bins. The cumulative effect of bin migrations on a measurement is contingent on both the δE, and the shape of the measured quantity. Bin migration is impossible to avoid altogether, as there will always be a measurement error, and some events near the bin edges. However, one can limit the migration of events from their true bins by using the criteria that the bin width shouldn't be smaller than the resolution on the binning quantity. With the bin width defined as in (4.23), we widen the upper bins, as $E_{k/n}$ (or β resolution) degrades as $\beta \to 1$.

4.6.3 A note on Template Fitting Procedure

Fitting a parametrised function to data is a complicated procedure, and the complexity increases with the dimension of the parameter space. If the variable space is one-dimensional, a parametrised function, $f(x; p_1, p_2, \cdots, p_n)$ with n-dimensional fit parameter space can be fitted to a series of m points $(x_i, y_i \pm \sigma_i)$, where σ_i is uncertainty, and $i \in \{1, 2, \cdots, m\}$; with the help of χ^2-squared statistics:

$$\chi^2 = \sum_{i=1}^{m} \left(\frac{y_i - f(x_i)}{\sigma_i} \right)^2 . \tag{4.25}$$

The aim is to minimise the χ^2 over the n-dimensional parameter space, $\{p_1, p_2, \cdot, p_n\} \in \mathcal{R}^n$. To help the minimisation process, physical or other constraints can limit the meaningful search space for the individual parameters. Such a minimisation procedure is impossible to be achieved without the aid of computational power, and hence dedicated packaged to achieve such minimisation is generally used. The minimisation procedure's complexity scales with the absolute value of n, and hence it is necessary to implement necessary dimensional reduction schemes from physical consideration to help the program. This is because, in general, the minimisation programs cannot absolutely be certain, whether it has found a local minimum or the true minimum, i.e., the global minimum.

For our template fitting, we used the robust suite of ROOT toolkit's MINUIT minimsation program. Despite it's efficiency, it is subject to several limitations, and hence user input is necessary to achieve the desired results. The fitting of our bi-Gaussian template to the Be mass distributions consisting of three isotopes, and poor mass resolution is a complex, and high-dimensional problem. A physically thoughtful process, and a great deal of trail-and-error was

neccessary to find a reliable solution.

4.6.4 A note on the Nature of the Data

The χ^2 statistic is computed as sum over (x, y) data points as can be seen from (4.25). However, we employ this method to a histogram of many measured values $\{X_1, X_2, \cdots, X_n$ which are samples of some underlying random variable. The x-axis including most of the measured values, X_k is selected, and divided into a sequence of m subintervals or bins, $[b_0, b_1), [b_1, b_2), \cdots, [b_{m-1}, b_m)$. In order to form ordered pairs, the bin center is typical taken as the x-value: $x_i = (b_{i-1} + b_i)/2$. As such, the corresponding y-value is the number of measurements X_k that lies within this bin. The uncertainty is assigned to be the square root of the y-value, which is an approximation of the standard deviation: $\sigma_i \approx \sqrt{y_i}$. This assumption relies on the approximation of Poisson errors as Gaussian for sufficiently large values of y.

As such, we get a set of m points, $(x_i, y_i \pm \sqrt{y_i})$ to which we fit our parametrised function. We say that we have a good fit results when the χ^2-squared statistic is near unity, where the number of degrees of freedom (ν) is taken to be the number of data points (non-empty bins) in the fit range minus the number of fit parameters,i.e., $\nu = m - n$. The fitted function then approximates the distribution of the underlying random variable, except for some normalisation factor. Along with that, the integral of the function over the binned range approximates the number of measurements in the range.

Chapter 5

Isotope Fluxes and Experimental Results

This chapter illustrates the important ingredients required for the calculation of fluxes, viz., the counts extracted from the fit, the acceptance of the detector corrected by efficiency losses, the exposure time of the detector, and the unfolding applied on the detector-level spectra. The chapter finally culminates with the results of final isotopic fluxes and ratios of interests, and a short note on it's theoretical implication.

5.1 Flux of Cosmic ray species

The differential flux of CR species (Φ) can be defined as the number of particles hitting a surface per unit of energy E, area, solid angle, and time t. In general, it is dependent on E, t, and the spatial coordinate $\vec{x}$, along with the arrival direction in the solid angle ω, and it is written as:

$$\Phi(E, t, \vec{x}, \omega) = \frac{dN(E, t, \vec{x}, \omega)}{dt dE d\sigma d\omega}, \tag{5.1}$$

where N is the number of incident particles, $d\sigma$ and $d\omega = d\phi d\cos\theta$ are the infinitesimal elements of area and solid angle respectively. If the flux is isotropic, $\Phi(E, t, \vec{x}, \omega)$ can be factorised as:

$$\Phi(E, t, \vec{x}, \omega) = \Phi(E, t) F(E, t, \vec{x}, \omega). \tag{5.2}$$

In our analysis, $\Phi(E, t)$ is the physical quantity of interest that we want to measure, while $F(E, t, \vec{x}, \omega)$ is a geometrical detector-dependent factor. As a consequence, the number of counts experimentally detected is given by:

$$N(\Delta E, \Delta T) = \int_S \int_{\Delta E} \int_{\Delta t} \int_\Omega \Phi(E, t) F(E, t, \vec{x}, \omega) \hat{r} \cdot d\vec{\sigma} dE dt d\omega, \tag{5.3}$$

where S is the area of the detector and Ω is the total field of view. In particular, the $F(E, t, \vec{x}, \omega)$ factor can be factorised as:

$$F(E, t, \vec{x}, \omega) = L \epsilon_{cutoff}(E, \omega, t) \epsilon(E, \omega, t, \vec{x}), \tag{5.4}$$

where

- L is the fraction of time in which the instrument effectively accepts the events.

- ϵ_{cutoff} is the factor that measures the effective time in which the detector is in appropriate spatial location such that the rigidity cutoff is lower than the rigidity corresponding to the energy E.

- $\epsilon(E, \omega, t, \vec{x})$ is the detector response function

The integral of $\epsilon(E, \omega, t, \vec{x})$ over the whole physical dimensions of the detector is the effective corrected acceptance, $A_{corr}(E, t)$.

Grouping together $\tau(E, \omega, t) = L\epsilon_{cutoff}(E, \omega, t)$, and considering a measurement time interval, Δt, and energy interval, ΔE, we obtain:

$$\begin{aligned} N(\Delta E, \Delta t) &= \int_{\Delta t} \int_{\Delta E} \int_{\Omega} \Phi(E, t)\tau(E, \omega, t)A_{corr}(E, t)dEd\omega \\ &\approx \Phi(E, t)T_{exp}(\Delta E, \Delta t)A_{corr}(\Delta E, \Delta t)\Delta E, \end{aligned} \tag{5.5}$$

where we assume constant flux in the bins of ΔE, and Δt. As such, we finally obtain the expression:

$$\Phi(E, t) = \frac{N(\Delta E, \Delta t)}{T_{exp}(\Delta E.\Delta t)A_{corr}(\Delta E, \Delta t)\Delta E}, \tag{5.6}$$

where, $T_{exp}(\Delta E, \Delta t) = \int_{\Omega} \tau(E, \omega, t)d\omega$ is the expsoure time for the energy bins ΔE above the rigidity cutoff. In the next few sections, we will discuss the methodologies to extract the $A_{corr}(\Delta E, \Delta t)$, $T_{exp}(\Delta E, \Delta t)$ and $N(\Delta E, \Delta t)$ values.

5.1.1 The Exposure Time

The exposure time measures the amount of time the detector was effectively exposed to cosmic rays. Computation of the exposure time in AMS is not straightforward, as it traverses the geomagnetic field of earth by virtue of being installed on the ISS. The following section illustrates the methodology employed to arrive at the exposure time by exploiting the rigidity cut-off value at each latitude.

5.1.1.1 Avoiding Bias to the Isotope Ratio

In the current analysis, our focus is solely on galactic CRs, which originate from beyond Earth's magnetosphere. To distinguish these particles from those potentially trapped within the magnetosphere, we utilize the geomagnetic rigidity cutoff. However, it is essential to apply this cutoff in a manner that ensures the measurement remains unbiased.

When employing rigidity as the independent kinematic variable for binning in the analysis, it becomes straightforward to exclude events below the cutoff. Only events with $R_{measured} > \alpha_{sf}R_{cutoff}$ are considered for the analysis. The flux can then be determined by correcting for the exposure time within each bin, denoted as $\Delta t(R_{measured} > \alpha_{sf}R_{cutoff})$.

However, application of the rigidity cut-off to the isotope analysis binned in β warrants a different treatment to avoid biasing the measurement. We would like to use the same β measurement for the rigidity cut-off selection as we use for binning. Similar to above, we apply a safety factor to the calculated rigidity cut-off. However since the rigidity is directly proportional to the mass, we see that for the same measured β, $R(^7Be) < R(^9Be) < R(^{10}Be)$. This means that for a fixed value of measured β, a given second of data-taking falls into one of the following four categories:

1. $R(^7Be) < R(^9Be) < R(^{10}Be) < R_{cutoff}$
2. $R(^7Be) < R(^9Be) < R_{cutoff} < R(^{10}Be)$
3. $R(^7Be) < R_{cutoff} < R(^9Be) < R(^{10}Be)$
4. $R_{cutoff} < R(^7Be) < R(^9Be) < R(^{10}Be)$

Clearly category **(1)** contains under-cut-off events and should be excluded from the analysis. Meanwhile, events satisfying **(4)** have free, unbound trajetories irrespective of the isotope, and hence these events are included in the sample. However, the events falling in either category **(2)** or **(3)** between the cut-off value of the three isotopes have no analog in the rigidity binned analysis. The events should be excluded altogether so that the sample do not admit any under cut-off ^9Be and ^{10}Be, which cannot be distinguished *a priori*. This choice maintains the same expsoure time at each measured β for the three isotopes, so that this quantity cancels out in the flux ratios. Hence. the rigidity cut-off selection applied n all cases uses the rigidity corresponding to the measured β under the hypothesis of ^7Be, i.e., $R(^7Be) > \alpha_{sf} R_{cutoff}$. The criteria for a CR particle to be of primary origin and not coming from secondary interactions with the atmosphere is that its rigidity should be higher than the estimated rigidity cutoff value at that particular position.

To understand the "cutoff" phenomenon, we can consider the scenario of a pure dipole magnetic field without any physical barrier at Earth's surface. In this ideal case, a strict cutoff occurs, with only bound orbits below the cutoff and only unbound orbits above it. (Unbound orbits are those extending to infinite distance from the dipole, indicating cosmic origin.) Although the Earth's magnetic field structure is more intricate, resulting in a transitional range of rigidities where both bound and unbound orbits coexist, the fundamental principle remains the same in the analytical theory: there exists a rigidity at the upper limit of this transition range, beyond which only unbound orbits are present. More details of how it is done can be found in Chapter 2.

The process of determining R_c involves retracing the motion of particles backward in time for a wide range of rigidities. This backtracing starts from a selected latitude-longitude position at the altitude of the ISS and follows the direction of particle motion. During this procedure, the particles experience the influence of the geomagnetic field, as described by the IGRF model. Based on whether the particles reach a distance of 50 Earth radii or remain in the vicinity of Earth for an extended period, their orbits are classified as either free or trapped, respectively.

The cutoff rigidity for the chosen position and pointing is then determined as the rigidity above which no trapped particles are found. To obtain the maximum cutoff value for particle trajectory angles within 40 degrees of the zenith, a fine grid of latitude-longitude positions is considered. To be cautious in light of uncertainties surrounding the local magnetic field, particularly its interaction with the variable solar wind, a "*safety factor*" of 1.1 (denoted as α_{sf}) is applied during the selection process.

The AMS-02 analysis software has an estimation of the rigidity cutoff $R_c(\theta, \phi)$, which is calculated taking advantage of the Stoermer cutoff formula, and using the IGRF measurements of the geomagnetic field (See Chapter 2 for details).

In the case of AMS-02, owing to its finite field of view of 40°, a corresponding maximum value of rigidity cutoff is considered given by:

$$R_c^{max} = max\{R_{cutoff}(\theta, \phi)\}, \text{ where } \theta, \phi \in \Omega_{40^\circ}^{AMS_{FoV}} \tag{5.7}$$

Given the approximations of the Stoermer formula, a conservative approach has been employed, i.e., the albedo particles trapped in the geomagnetic field lines were excluded by considering the ones in which the measured rigidity is above R_c^{max}, with a safety factor of 10%, i.e., a particle is tagged primary if it satisfies the following condition:

$$R > 1.1 \cdot R_c^{max}. \tag{5.8}$$

As can be seen in fig. 5.1, the value of R_c^{max} is plotted for the different values of geomagnetic latitudes and longitudes, with a simplified map of the Earth surface. As can be seen, it reaches values of $\sim 30\ GV$ at equatorial regions, while events with rigidities $\lesssim 5\ GV$ are allowed only in the extremely polar regions. Such values show that the whole energy range in which the Beryllium measurement is possible, with AMS-02, is influenced by the geomagnetic field.

5.1.1.2 Live-time Fraction and Exposure Time

As expounded before in the previous section, $T_{exp}(\Delta E, \Delta t)$ is a convolution of the AMS-02 *Live Time* L and the exposure due to the geomagnetic rigidity cutoff $\epsilon_{cutoff}(E, \omega, t)$, which have to be measured simultaneously due to the way in which AMS-02 measures its dead time. The instrument dead time normally associated to the processing of every CR is on an average 200 μs, and it is slightly variable due to different complexity of events.

As explained in section 4.1.2 direct evaluation of the Δt adding all the live fractions of each second would be incorrect, as it wouldn't take in consideration the rigidity cutoff. Since the rigidity cutoff varies with latitude, if one is interested only in the primary (over cutoff) flux, for every ΔE energy bin and independent live time count is necessary, i.e., to consider only the effective time in which the energy bin was observed above the cutoff.

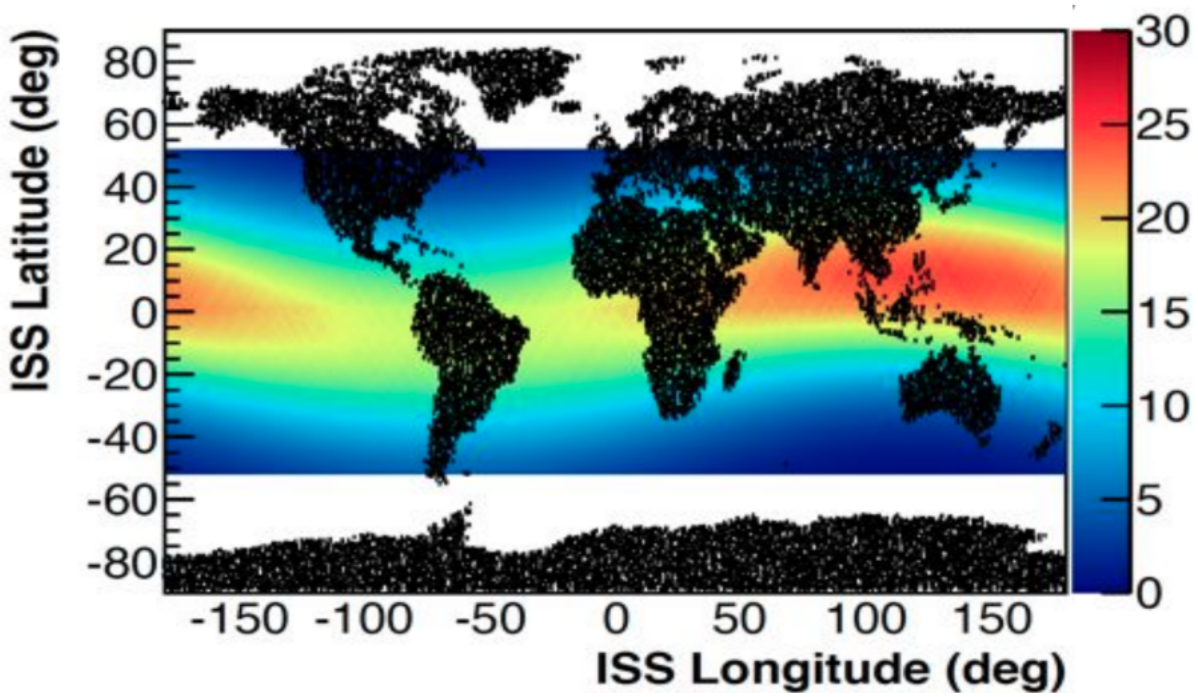

Figure 5.1: Values of R_c^{max} in GV along the AMS-02 orbit

As the rigidity cutoff value R_c^{max} depends only on the ISS geographical position, and given the ISS speed during its orbit, its value can be considered constant during each second. As such, to obtain the correct over cutoff expsoure time, it is sufficient to add the average live time only for seconds in which the R_c^{max} is lower than the lower rigidity edge of the energy bin considered. Performing this procedure yields the appproximation of $T_{exp}(\Delta E, \Delta t)$ used in this analysis. The total result for the duration of the present analysis is shown for the three different isotopes in fig 5.2.

5.1.2 Acceptance

Similar to telescopes, AMS-02 has a preferential direction of observation (from top to bottom of the instrument), along with a finite field of view contingent on its geometry. As such, the flux observed by the instrument in Monte-Carlo simulations doesn't reflect the real flux of incoming particles. The flux in general is also a function of the direction and distance from the source.

5.1.2.1 Geometric Acceptance

The Monte Carlo simulated flux is generated only from the top of the instrument, with an angular range of 45°. Whereas, actual CR fluxes are isotropic in earth's vicinity, and hence particles have equi-probability of coming from all the directions. As such, the event reconstruction efficiency needs a correction for this geometrical limitation, called the *Geometric Acceptance factor*, A_0. This quantity can be calculated by considering all possible directions in which the events are randomly generated.

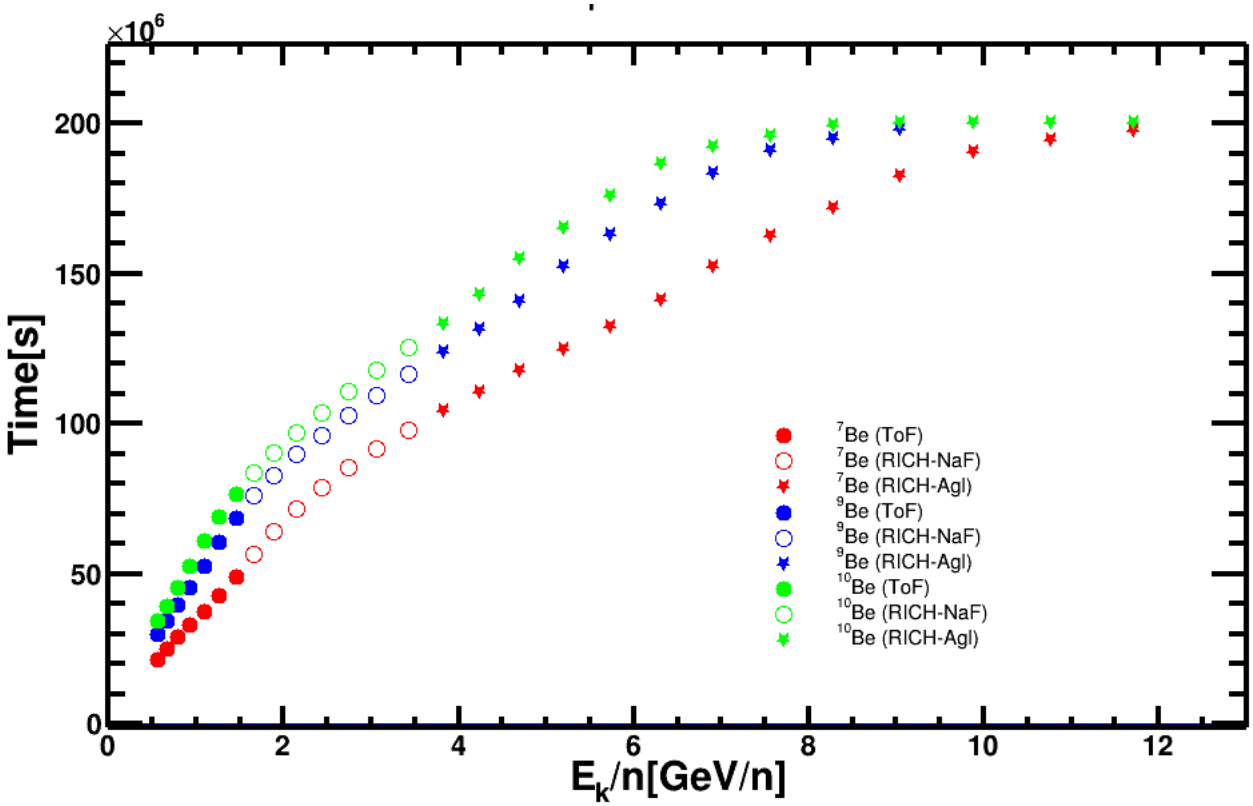

Figure 5.2: Values of the exposure time $T_{exp}(\Delta E, \Delta t)$ obtained for the bins of the three different energy ranges of the analysis.

In the case, where events are generated from source points on the top of the cube used in Monte Carlo simulations, this factor assumes the form:

$$A_0 = \int_\Omega d\omega \int_S d\sigma r = \int_\Omega \int_S \cos\theta d\sigma d\omega, \tag{5.9}$$

where $d\sigma$ is the differential surface element of S, and $d\omega = d\phi d\cos\theta$ is the differential solid angle element of Ω, with θ and ϕ being the polar and azimuthal angles respectively. The above yields:

$$A_0 = 2\pi S \int_0^{45^\circ} \cos\theta d\theta = \pi S. \tag{5.10}$$

Substituting the values of generation surface, $S = l^2 = 3.9 \times 3.9\ m^2$, the geometrical acceptance factor becomes, $A_0 = \pi l^2 = 47.78\ m^2 Sr$.

5.1.2.2 Monte Carlo Acceptance

In Monte Carlo simulations, it is possible to simulate events according to a power-law energy spectra similar to that of CRs to have maximal similarity to that of real data. However, considering a power-law would lead to a flux which is several orders of magnitude bigger at low energy, and would be computationally expensive, and storage intensive. So, in general, we opt for a flatter spectrum for Monte Carlo generation.

The generated momenta P_{gen} distribution is given by

$$\begin{aligned} p_{gen} &= 0.5 \exp\left(\log\left(\frac{p_{max}}{p_{min}}\right) RAND[0,1]\right) \\ &= 0.5 \log\left(\frac{p_{max}}{p_{min}}\right)^{RAND[0,1]}, \end{aligned} \tag{5.11}$$

where p_{max} & p_{min} are the limits of the generated momenta, and $RAND : \{\phi\} \rightarrow [0,1]$ is a random number generator.

The generated spectrum, i.e the Probability Distribution Function (PDF) can be extracted from the Cumulative Distribution Function (CDF($\tilde{P}$)), i.e., the probability for a random variable to have a value lower than a real value $\tilde{p}$:

$$\begin{aligned} CDF(\tilde{p}) = P(p_{gen} < \tilde{p}) = P(0.5 \log\left(\frac{p_{max}}{p_{min}}\right)^{RAND[0,1]} < \tilde{p}) \\ P(RAND[0,1] \log K < \log \tilde{p}) = P(RAND[0,1] < \log_K(\tilde{p})) = \log_K(\tilde{p}), \end{aligned} \tag{5.12}$$

where, $K = 0.5 \log\left(\frac{p_{max}}{p_{min}}\right)$. The PDF can be the derived as

$$PDF(\tilde{p}) = \frac{d(CDF(\tilde{p}))}{d\tilde{p}} = \frac{d(\log_k(\tilde{p}))}{d\tilde{p}} \propto \frac{1}{\tilde{p}}. \tag{5.13}$$

Identifying the $\tilde{p}$ variable with the momentum p, a generation spectrum of MC datasets proportional to p^{-1} or R^{-1} can be obtained.

Generating such a spectrum also have the advantage that spectral measurements in CR physics are generally performed in logarithmic bins, due to the large span of the energy range. This kind of spectrum has the property to be completely flat when binned in log bins as can be seen from:

$$N_{gen}(p_1, p_1) = \int_{p_1}^{p_2} \frac{dp}{p} = \Delta \log(p), \tag{5.14}$$

but if log bins are used, then

$$\Delta \log(p) = \text{constant}. \tag{5.15}$$

As such,

$$N_{gen}(p_1, p_2) = \text{constant} \tag{5.16}$$

Since, $R \propto p$, (5.14) can be also written as

$$N_{gen}(R_{min}, R_{max}) = \int_{R_{min}}^{R_{max}} \frac{dR}{R} = \log\left(\frac{R_{max}}{R_{min}}\right). \tag{5.17}$$

From the above, we can obtain the relation formula for the ith rigidity bins:

$$\frac{\text{Total Generated Events (T)}}{\log\left(\frac{R_{max}}{R_{min}}\right)} = \frac{\text{Number of Generated Events in each bin } (g_i)}{\log\left(\frac{R_{max}}{R_{min}}\right)_i} \tag{5.18}$$

So, we obtain the number of generated events in each bin, g_i to be:

$$g_i = \frac{T \times \log\left(\frac{R_{max}}{R_{min}}\right)_i}{\log\left(\frac{R_{max}}{R_{min}}\right)}. \tag{5.19}$$

Since the minimum rigidity used by AMS MC is ~ 4 and the highest rigidity used is ~ 8000, the factor in the denominator becomes $\log 2000$.

The Monte Carlo acceptance is given by:

$$A_{MC} = \frac{\text{Number of events that survives the selections in each bin } (\#survived)}{\text{Number of events generated by MC in each bin}} \tag{5.20}$$

Using (5.19) above, (5.20) becomes:

$$A_{MC} = \frac{\#survived}{\frac{T\times\log\left(\frac{R_{max}}{R_{min}}\right)_i}{\log\left(\frac{R_{max}}{R_{min}}\right)}} = \frac{\#survived}{\frac{T\times\log\left(\frac{R_{max}}{R_{min}}\right)_i}{\log 2000}} \tag{5.21}$$

For storage issues, only a number of generated events are saved. The generated events are scaled by a more or less constant factor which we name "MC Trigger Ratio"(ϵ_{trig}). As such, to get the total number of generated events, T, we have the relation

$$T = \frac{\text{Total Saved Events } (S)}{\epsilon_{trig}} \tag{5.22}$$

So, finally the Monte Carlo acceptance (5.23) becomes:

$$A_{MC} = \frac{\#survived}{\frac{\log\left(\frac{R_{max}}{R_{min}}\right)_i}{\log 2000} \times \frac{S}{\epsilon_{trig}}} \tag{5.23}$$

The final MC Acceptance, A shown in fig. 5.3 is obtained by multiplying with the geometric acceptance $A_0 = 47.78\ m^2 sr$. Hence, we get

$$\begin{aligned} A &= A_{MC} \times A_0 \\ A &= \frac{\#survived}{\frac{\log\left(\frac{R_{max}}{R_{min}}\right)_i}{\log 2000} \times \frac{S}{\epsilon_{trig}}} \times 47.78 \end{aligned} \tag{5.24}$$

5.1.2.3 Data Driven Efficiency Corrections

The cost one pays of having a clean sample of events comes with efficiency losses. As such, one has to take those efficiency losses in consideration, and correct for those losses in the acceptance to get the final fluxes.

For this purpose, a set of efficiency corrections to be performed are identified. Then a number

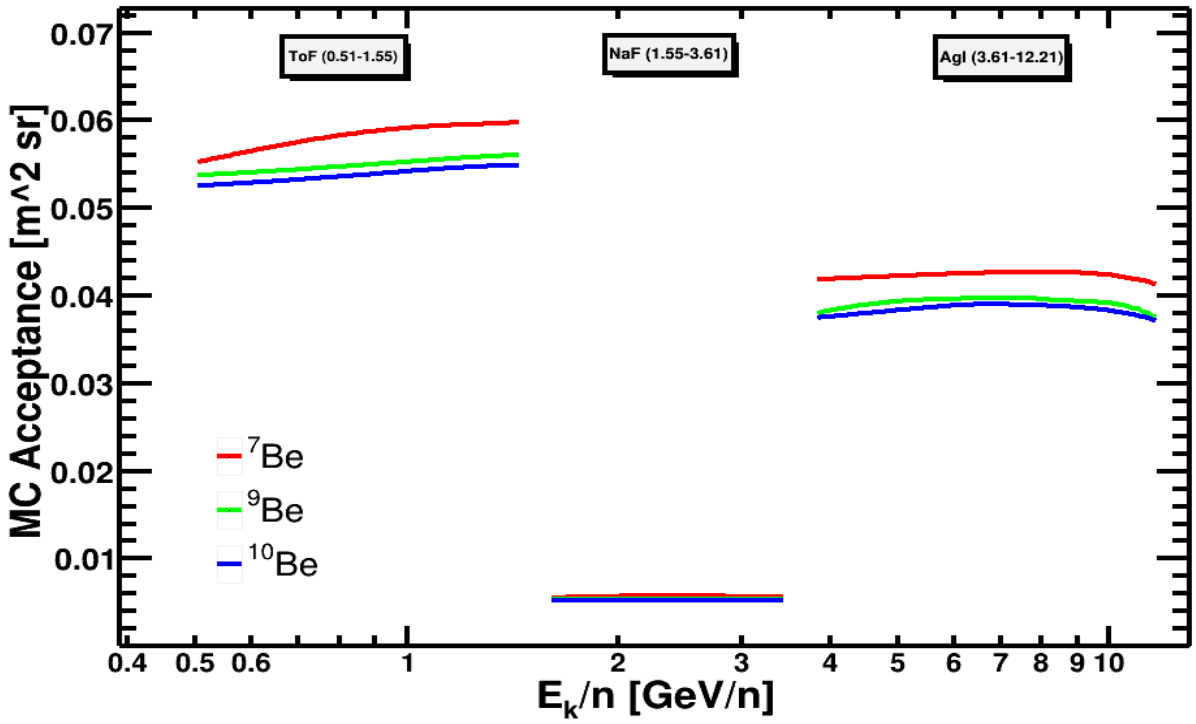

Figure 5.3: The Monte-Carlo acceptance for the three isotopes as indicated. In the RICH-NaF region, the markers for ^{9}Be aren't visible because of similar acceptance of ^{9}Be and ^{10}Be and the nature of the scale.

of events of Be from data are sampled with selections that are maximally independent from the selections that are used for the analysis. This form the sample events, N_{sample}, against which we study the effect of efficiency loss caused by the selections in question, N_{sel}. The efficiency is then given by:

$$Eff_{data} = \frac{N_{sel}}{N_{sample}}. \tag{5.25}$$

The procedure is repeated for AMS-MC data with the same set of selections to give us, Eff_{MC}. After which, the efficiency correction, Eff_{corr} to be applied to the acceptance is obtained by:

$$Eff_{corr} = \frac{Eff_{data}}{Eff_{MC}}. \tag{5.26}$$

Then, Eff_{corr} are fitted with a linear function with 1σ confidence interval as the error on the trend. These fitted linear functions are then mulitplied to the acceptance to obtain the effective acceptance.

We identify the following class of corrections:

1. **L1 pickup Efficiency (Eff_{pickup}):** Efficiency loss after application of charge and quality selections on the layer 1 of the tracker as shown in fig. 5.4a & fig. 5.4b

2. **Tracking Efficiency (Eff_{track}):** Efficiency loss as a result of applying selections for good tracker reconstruction of the rigidity and charge as shown in fig. 5.4c & fig. 5.4d.

3. **Against Interactions Efficiency (Eff_{int}):** Efficiency loss as a result of demanding

single track in the tracker and a strict charge selection on the upper ToF as shown in fig. 5.4e & fig. 5.4f.

4. **Beta ToF Efficiency ($Eff_{\beta ToF}$):** Efficiency loss as a result of quality selections on the ToF reconstructed beta as shown in fig. 5.5a & fig. 5.5b.

5. **Beta RICH Efficiency ($Eff_{\beta NaF}$&$Eff_{\beta Agl}$):** Efficiency loss as a result of quality selections on the RICH-NaF/Agl reconstructed beta as shown in fig. 5.5c & fig. 5.5d.

6. **Trigger Efficiency ϵ:** Efficiency loss arising from different treatment reserved to events passing the only unbiased trigger condition defined in Monte Carlo and in data.

5.1.2.4 Corrected Acceptance and Uncertainty

The final effective acceptances for ToF ($\tilde{A}_{\text{ToF}}$), RICH-NaF ($\tilde{A}_{\text{NaF}}$), and RICH-Agl ($\tilde{A}_{\text{Agl}}$) is obtained as follows :

$$\begin{aligned}
\tilde{A}_{\text{ToF}} &= A_{\text{ToF}} \times Eff_{\text{pickup}} \times Eff_{\text{tracking}} \times Eff_{\text{int}} \times Eff_{\beta\text{ToF}}, \\
\tilde{A}_{\text{NaF}} &= A_{\text{NaF}} \times Eff_{\text{pickup}} \times Eff_{\text{tracking}} \times Eff_{\text{int}} \times Eff_{\beta\text{NaF}}, \\
\tilde{A}_{\text{Agl}} &= A_{\text{Agl}} \times Eff_{\text{pickup}} \times Eff_{\text{tracking}} \times Eff_{\text{int}} \times Eff_{\beta\text{Agl}},
\end{aligned} \tag{5.27}$$

The Effective acceptance is shown in fig. 5.6 and we observe the following features:

- The plateau values for the three detectors are quite different, and this is related to the geometrical acceptance and relatively lower acceptance of RICH in general.
- Above the rigidity threshold, the acceptance absolute value seems inversely proportional to the isotope mass. This effect is anticipated as heavier isotopes possess larger nuclear cross-section and consequently higher probability of interaction with AMS material.

5.1.3 Unfolding

One of the prime impediment in unravelling nature's phenomena is that we don't have direct access to the probability distribution function (PDF) of an event. The true flux or the true PDF of CR species is distorted by our measurement apparatus, i.e., AMS-02 detector in our case. The following section describes the problem of folded fluxes, and the the D'Agostini iterative Bayesian unfolding used to retrieve the particle level fluxes.

5.1.3.1 Detector Smearing of True Spectrum

If the true value of an event is denoted by y, the true PDF, $f_{\text{true}}(y)$ is distorted by the detector through two ways:

- **Finite Resolution:** A measuring apparatus has a resolution that is finite. Any measured value x in an event given the true value is a random variable. In the trivial case, the measured PDF might be a Gaussian distribution ($\sim\ \mathcal{G}(x, y, \sigma)$) with the mean being

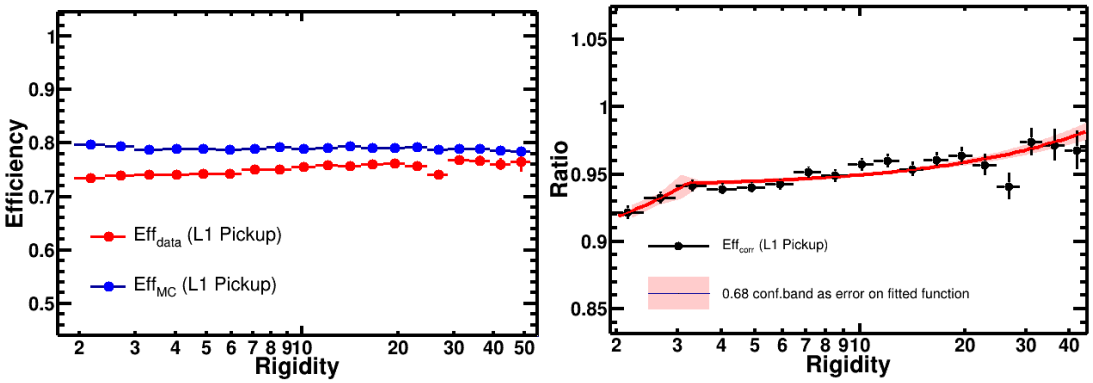

(a) Pickup Efficiency Curve

(b) Pickup Efficiency Correction

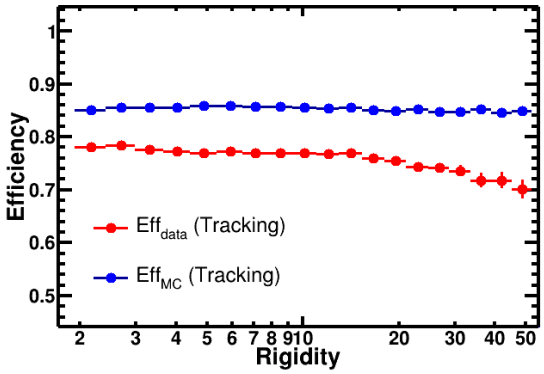

(c) Tracking Efficiency Curve

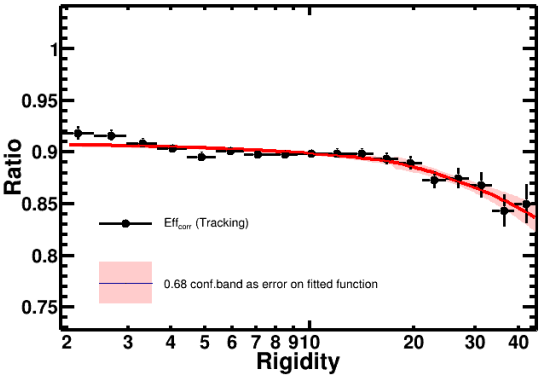

(d) Tracking Efficiency Correction

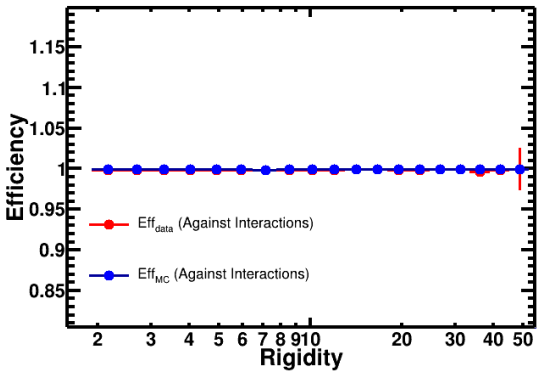

(e) Against Interactions Efficiency Curve

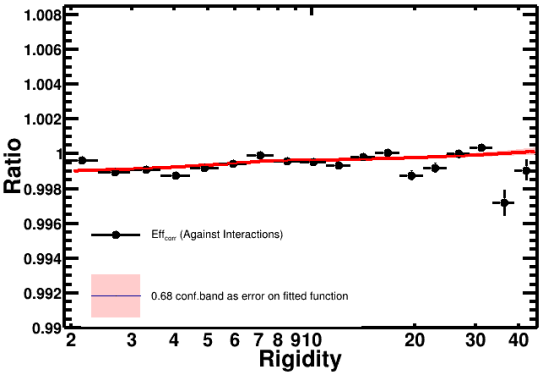

(f) Interactions Efficiency Correction

Figure 5.4: The efficiency curves and corrections for Be nuclei selections. On the left column of the figure, the red denotes the loss in efficiency in data, and the blue in Monte-Carlo. On the right side, the data/MC ratio is shown which forms the correction to be applied to the acceptance. They are fitted with a linear function with the 1σ confidence band shown.

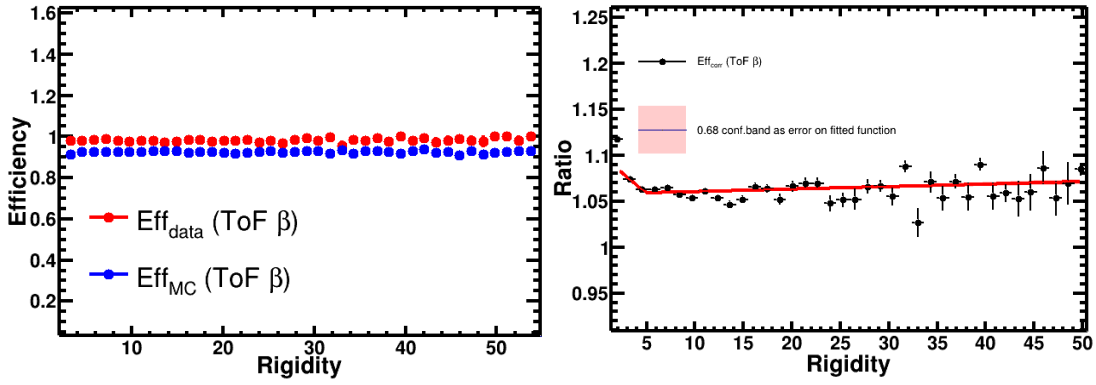

(a) ToF β Efficiency Curve

(b) ToF β Efficiency Correction

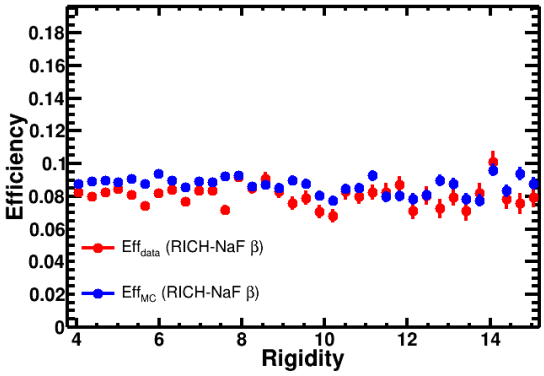

(c) RICH-NaF β Efficiency Curve

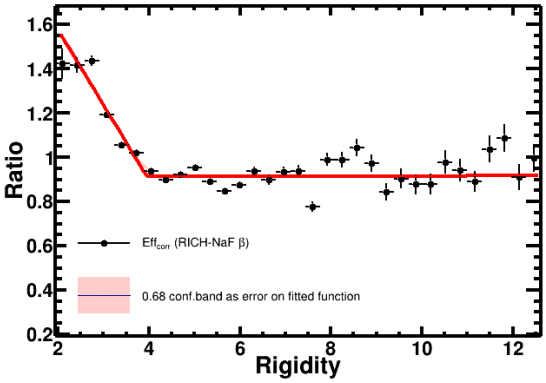

(d) RICH-NaF β Efficiency Correction

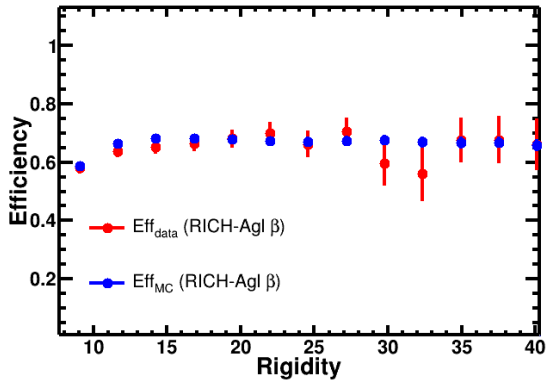

(e) RICH-Agl Efficiency Curve

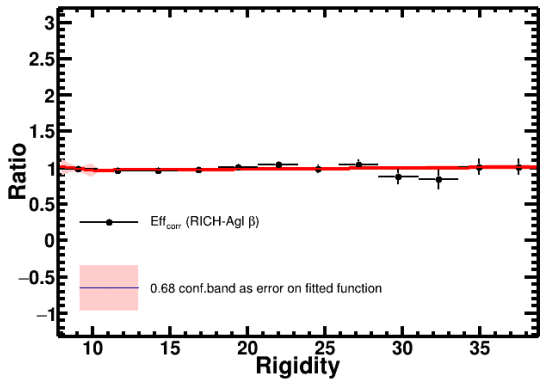

(f) RICH-Agl Efficiency Correction

Figure 5.5: The efficiency curves and corrections for Be velocity selections. On the left column of the figure, the red denotes the loss in efficiency in data, and the blue in Monte-Carlo. On the right side, the data/MC ratio is shown which forms the correction to be applied to the acceptance. They are fitted with a linear function with the 1σ confidence band shown.

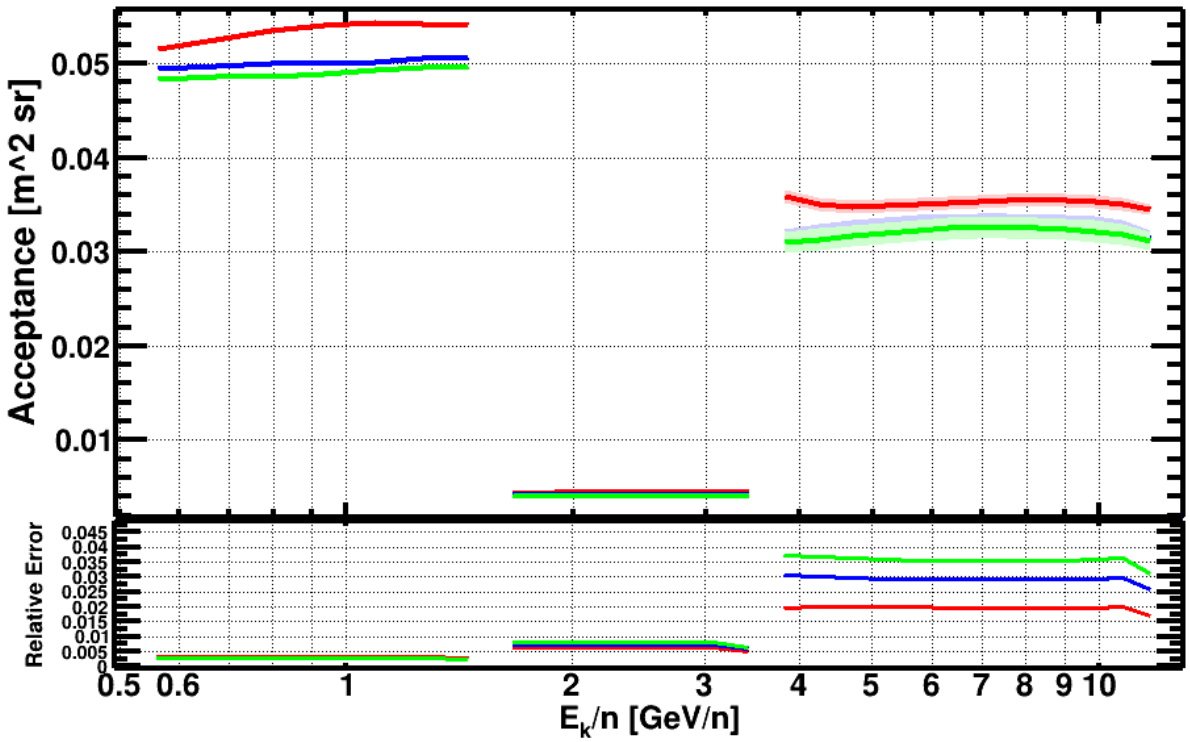

Figure 5.6: The MC acceptance corrected with the data-driven efficiency corrections with it's associated errors in the bottom panel. Here, the acceptance curves of ^{7}Be is shown in red, ^{9}Be in blue, and ^{10}Be in blue. Because of close values, some of the curves may not be clearly visible within the granularity of the plot's scale.

equal to the true value y and some non-zero variance σ. In essence, the true PDF is always smeared by the resolution function.

- **Finite Acceptance:** A detector cannot have 100 % acceptance. In our case, although CR flux is isotropic, AMS-02 is restricted by its field of view and geometry. Furthermore, there might be events below the minimum threshold of a particular sub-detector. For e.g., the RICH detectors won't be triggered below the beta threshold of the radiators. As such, AMS-02 or for that matter, any detector has event reconstruction efficiency lower than 1.

5.1.3.2 Mathematical Formalism of the Unfolding problem

As a consequence of the above effects, the true distribution of y gets convoluted and can be described by the following expression:

$$f(x) = \frac{1}{N} \int dy \mathcal{S}(x|y)\epsilon(y) f_{\textbf{true}(y)}, \tag{5.28}$$

where $\mathcal{S}(x|y)$ is the Resolution function, $\epsilon(y)$ is the reconstruction efficiency, and N is the normalisation factor. It is helpful to define the Response function $(\mathcal{R}(x|y))$ which is given by:

$$\mathcal{R}(x|y) = \mathcal{S}(x|y)\epsilon(y). \tag{5.29}$$

Mathematically, the true PDF is said to be folded with the response function. The inverse operation to reveal the true PDF is regarded as "Unfolding", which is also called as deconvolution or unsmearing. In principle, if we know the parametrisation of the true PDF along with the folded spectrum, we can estimate the true parameters using the maximum likelihood method. The folded spectrum is also called detector level spectrum or reco spectrum meanwhile the true PDF of unfolded data is called the truth or particle level spectrum. In principle, we can unfold to the parton level, but the latter would also include unfolding physics processes. Most often, we don't have an analytical expression for the response function. Instead, in experimental physics, the response function is encoded in a Monte-Carlo detector simulation, and accessed by a set of Monte-Carlo events.

The probability P_j of a true value y to fall in to a true bin j is given by:

$$P_j = \int_{\text{Bin j}} dy f_{\text{true}(y)}. \tag{5.30}$$

Let the number of bins of true distribution be M and the number of expected events in a true bin j be given by

$$\mu_j = \mu_{\text{total}} P_j, \tag{5.31}$$

where μ_{total} is the expected total number of events. The observed data is a distribution with N bins and it is not necessary that $N = M$. In each bin of the observed (or measured) histogram, there are n_i events and typically it is distributed according to Poissonian statistics, i.e. :

$$n_i \sim \text{Pois}(n_i, \nu_i), \tag{5.32}$$

where the expected value ν_i can be expressed in true quantities as:

$$\begin{aligned}
\nu_i &= \mu_{\text{total}} \int_{\text{bin i}} dx \int dy \mathcal{R}(x|y) f_{\text{true}}(y) \\
&= \mu_{\text{total}} \int_i dx \sum_j \int_j dy \mathcal{R}(x|y) f_{\text{true}}(y) \\
&= \sum_j \mu_j \frac{1}{P_j} \int_i dx \int_j dy \mathcal{R}(x|y) f_{\text{true}}(y) \quad \text{Using (5.31)} \\
&= \sum_j R_{ij} \mu_j,
\end{aligned} \tag{5.33}$$

where R_{ij} is the response matrix given by:

$$\begin{aligned}
R_{ij} &= \frac{\int_i dx \int_j dy \mathcal{R}(x|y) f_{\text{true}}(y)}{\int_j dy f_{\text{true}}(y)} \\
&= \frac{P(x \in \text{Bin i} \wedge y \in \text{Bin j})}{P(y \in \text{Bin j})} \\
&= P(x \in \text{Bin i} | y \in \text{Bin j}).
\end{aligned} \tag{5.34}$$

So, we see mathematically that the response matrix is nothing but the conditional probability that a measured value x belongs to a measured bin i given that a true value j belongs to a true bin j. However, the response matrix depends on $f_{\text{true}}(y)$ which is the distribution which we want to determine with the unfolding procedure in the first place.

The primary and unavoidable approximation in the unfolding procedure is the assumption that the response function is approximately constant in each true bin j. Given, this assumption, the response matrix doesn't depend on the true distribution within that interval. However, we have to assign a systematic uncertainty to the unfolding result as a consequence of this assumption.

Practically, the response matrix is a two-dimensional histogram and it is estimated by Monte-Carlo simulations. One can generate a true spectrum, and propagate the outgoing particles through the detector and fill bin ij. The MC simulation assumes some underlying true PDF which is some good assumption of $f_{\text{true}}(y)$. The response matrix normalisation is given by $\sum_i R_{ij} = \epsilon_i$, where ϵ_j is the average reconstruction efficiency in true bin j. The off-diagonal elements of R_{ij} are responsible for smearing of any fine structures of the true PDF.

5.1.3.3 D'Agostini's Iterative Bayesian Unfolding Method

In our analysis, we use the iterative Bayesian unfolding prescription by D'Agostini [129, 130]. It starts with building the unfolding matrix $\tilde{R}_{ij}$ given as the conditional probability that a true value y falls into a true bin j given that a measured value x falls into a measured bin i:

$$\begin{aligned}\tilde{R}_{ij} &= P(y \in \text{Bin j} | x \in \text{Bin i}) \\ &= \frac{P(x \in \text{Bin i}) | y \in \text{Bin j}) P(y \in \text{Bin j})}{P(x \in \text{Bin i})} \quad \text{(Using Bayes' Theorem)} \\ &= \frac{R_{ij} P(y \in \text{Bin j})}{\sum_i R_{ij} P(y \in \text{Bin j})}\end{aligned} \tag{5.35}$$

Hence, the expected number of events in true bin j is given by:

$$\hat{\mu}_j = \frac{1}{\epsilon_j} \sum_i \tilde{R}_{ij} n_i, \tag{5.36}$$

where ϵ_j is the average reconstruction efficiency in bin j and n_i is the measured data. We observed from (5.35) that the unfolding matrix again depends on the true spectrum. This calls for some iterative method to solve the equation. D'Agostini's method takes some first guess of the truth spectrum and follows the following algorithm:

- Build the version k of the unfolding matrix: $\tilde{R}^k_{ij}$
- Evaluate the $k+1$th version of the truth spectrum: $\hat{\mu}^{k+1}_j$, where the true spectrum is built as:

$$P(y \in \text{Bin j}) = \frac{\hat{\mu}_j}{\sum \hat{\mu}_j}. \tag{5.37}$$

- Then build a version $k+1$ of the unfolding matrix: $\tilde{R}_{ij}^{k+1}$
- The stopping criterion of this iterative procedure is found by evaluating the minimum of the χ^2 function:

$$\chi^2_{k+1,k} = \sum_j \left(\frac{\left(\hat{\mu}_j^{k+1} - \hat{\mu}_j^k\right)^2}{\hat{\mu}_j^k} \right) \tag{5.38}$$

5.1.3.4 Unfolding Factor for the Be isotope fluxes

The D'Agostini Bayesian iterative unfolding method is implemented in the *RooUnfold* package, and we use the same for our analysis. It requires the response matrices which as already mentioned is a two-dimensional migration matrix and for our purpose, we built them for the quantity: Energy per unit nucleon (E_k/n). The package also requires the true and measured normalisation distributions to normalise the migration matrix which are nothing but the one-dimensional projections of the migration matrix. The last ingredient are the counts that we extract from our fit method for each sub-detectors. After performing the unfolding on the counts, we take the ratio of the unfolded to the folded counts and define an Unfolding Factor.

The unfolding procedure is performed for ^7Be only since the mass resolution of all the isotopes are similar. As such, without any loss of generality, the same unfolding factor can be applied to other isotopes. As a cross-check, we indeed performed the unfolding on other isotopes and ended with comparable results. This unfolding factor is employed on the final fluxes to consequently obtain the unfolded fluxes. The response matrix, normalisation distributions, and the unfolding factor are show in fig. 5.7 for ToF, in fig. 5.8 for RICH-NaF, and in fig. 5.9 for RICH-Agl.

5.1.4 Systematic Uncertainties, Final Flux and Flux Ratios result

A ratio of the flux has the advantageous quality that most of the systematic uncertainties cancel out. However, there are few systematics that comes from individual isotopes that cannot be removed in a flux ratio. This includes differences in the isotopic efficiency in our selection, and the different survival probability among the Be isotopes. The systematic uncertainties that we need to take care are listed below:

- **Selection:** Systematic emerging from the different behaviour of Be isotopes with respect to our selection criterion.
- **Survival:** Systematic coming from the MC model of the different interaction probabilities for the three Be isotopes.
- **Detector Top:** Systematic coming from the MC modelisation of heavier nuclei fragmenting within AMS-02 to Be

The three sources of systematics correspond to the acceptance correction we described in the preceding section. Since these corrections have been determined using the MC simulation only,

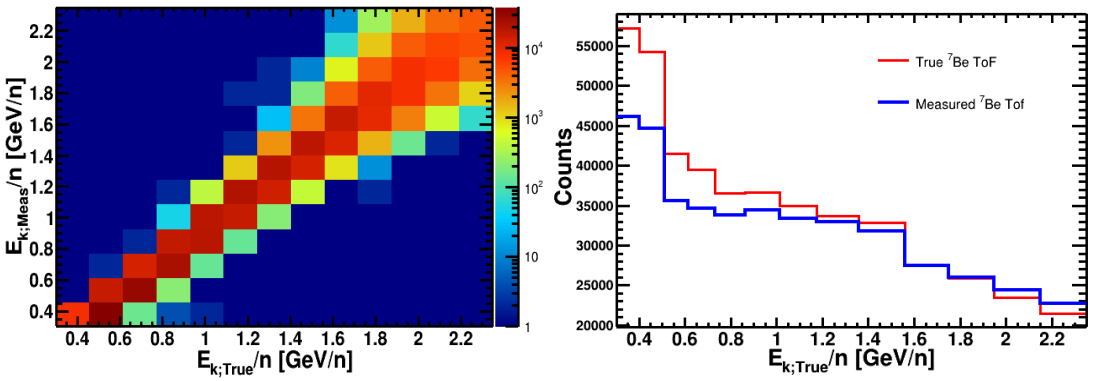

(a) ToF Response Matrix

(b) ToF normalisation distributions

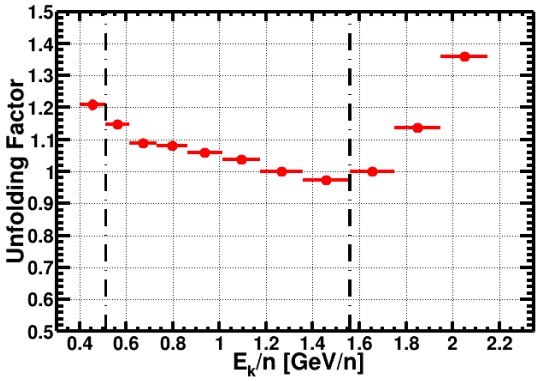

(c) ToF Unfolding Factor

Figure 5.7: (a) The response matrix for the ToF detector (b) The true and measured normalisation distributions (c) The unfolding factor for ToF detector. The analysis is performed for ^7Be counts and applied to other isotopes, taking advantage of similar mass resolution for all the three isotopes.

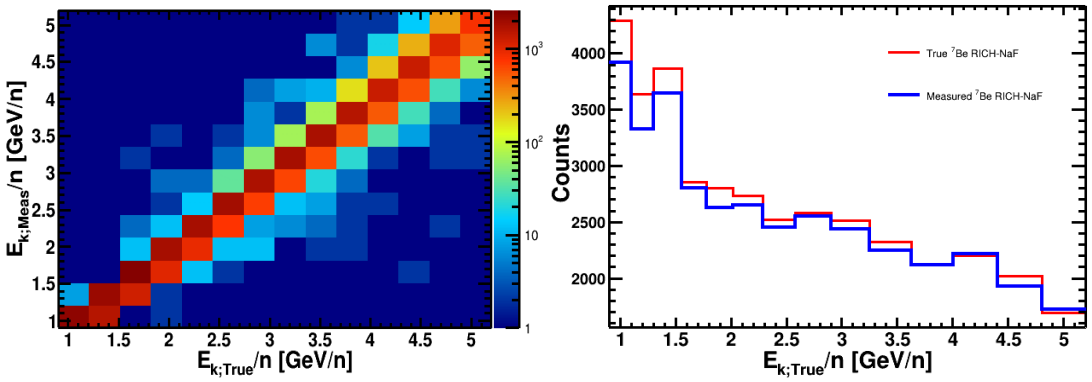

(a) RICH-NaF Response Matrix (b) RICH-NaF normalisation distributions

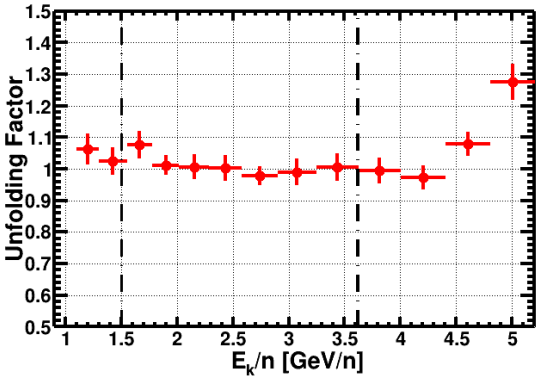

(c) RICH-NaF Unfolding Factor

Figure 5.8: (a) The response matrix for the RICH-NaF detector (b) The true and measured normalisation distributions (c) The unfolding factor for RICH-NaF detector. The analysis is performed for ^7Be counts and applied to other isotopes, taking advantage of similar mass resolution for all the three isotopes.

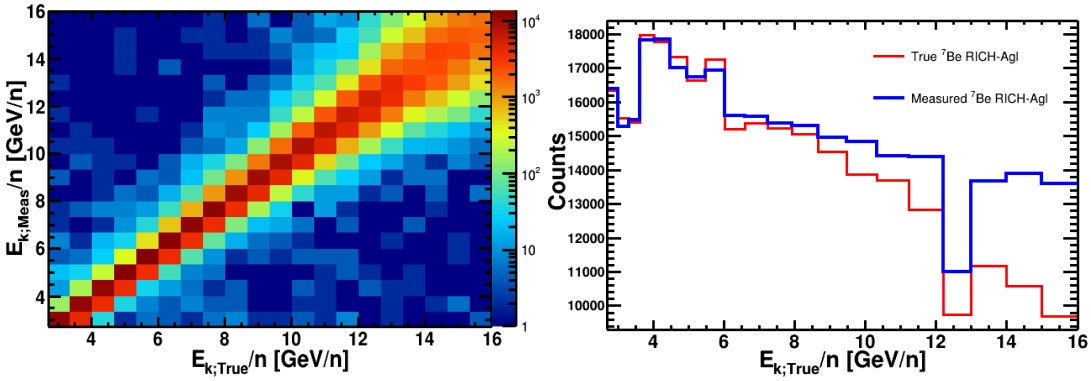

(a) RICH-Agl Response Matrix (b) RICH-Agl normalisation distributions

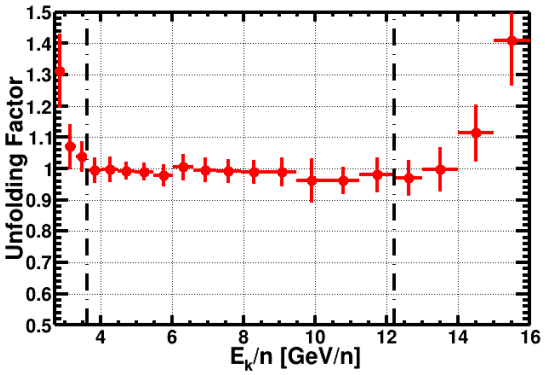

(c) RICH-Agl Unfolding Factor

Figure 5.9: (a) The response matrix for the RICH-Agl detector (b) The true and measured normalisation distributions (c) The unfolding factor for RICH-Agl detector. The analysis is performed for ^7Be counts and applied to other isotopes, taking advantage of similar mass resolution for all the three isotopes.

we decided to estimate a cautious systematic error of 5% added in quadrature to the overall error in the flux ratios.

In summary, now we have the counts of each of the isotopes from our fit model, the acceptance from the Monte-Carlo simulation which has been corrected for efficiency losses, and the exposure time calculated from the AMS-02 RTI information. This helps us to calculate the detector level flux or reconstructed spectra as explained in preceding section. Finally, the unfolding factor helps use to calculate the unfolded fluxes for the three isotopes and total Be flux as shown in fig. 5.10 and 5.11 with their respective relative errors. These individual fluxes can be divided to obtain the required flux ratios for $\Phi_{^{10}Be}/\Phi_{^{9}Be}$, and $\Phi_{^{7}Be}/\Phi_{\text{Total Be}}$, which are shown in fig. 5.12 and fig. 5.13 respectively. It was unanimously decided together with other analyses groups working on the Be isotope analysis to merge the original 27 bins of the analysis into 13 bins to reduce the statistical uncertainties and fluctuations. The similar scheme for bins is also instrumental in cross-checking the agreement of results between the different analysis groups. The ratio is plotted along with the measurement of previous 14 experiments in fig. 5.14 and fig. 5.15. Not only, AMS-02 extends the energy per unit nucleon range up to $\sim 12\ GeV/n$ but it also has significantly reduced uncertainties.

5.1.5 Comparison with theory and sensitivity to halo thickness parameter

The preliminary $\Phi_{^{10}Be}/\Phi_{^{9}Be}$ flux ratio measurements from AMS-02 is significant, in particular, the extension to relatively higher energy provides relevant information which combined with the complementary $\Phi_{^{7}Be}/\Phi_{\text{Total Be}}$ flux ratio will improve CR production/propagation models.

The other significant characteristics of the AMS-02 result is the relatively small uncertainty. As stated in previous chapters, the ratio $\Phi_{^{10}Be}/\Phi_{^{9}Be}$ will help us decouple the degeneracy in the H/D propagation parameters.

As an example, we give an estimation of the sensitivity of the AMS measurements to the H parameter, i.e., the halo thickness, of the models (DRAGON2 5.16a, GALPROP 5.16b, DERIVED 5.16c, & WEBBER 5.16d) discussed in [211]. The plot 5.17 shows the χ^2 of all the models discussed in the section. The fit is performed in the whole data range of the AMS-02 results. We conclude the following:

- A priori it seems that two models, i.e., GALPROP and DRAGON2 support a halo size greater than $8\ kpc$, with the exception of the DERIVED and WEBER model. However, the cross-section data of WEBBER are obsolete and last updated in the 2000s. While the first three models uses parametrisations supported by the most recent data.

- The cross sections of ^{10}Be suffer from ~ 20 % uncertainties. Therefore, also our predictions are uncertain by, at least, 20-40 % only from the cross section issue.

- The errors of the AMS-02 data might be correlated and hence underestimated.

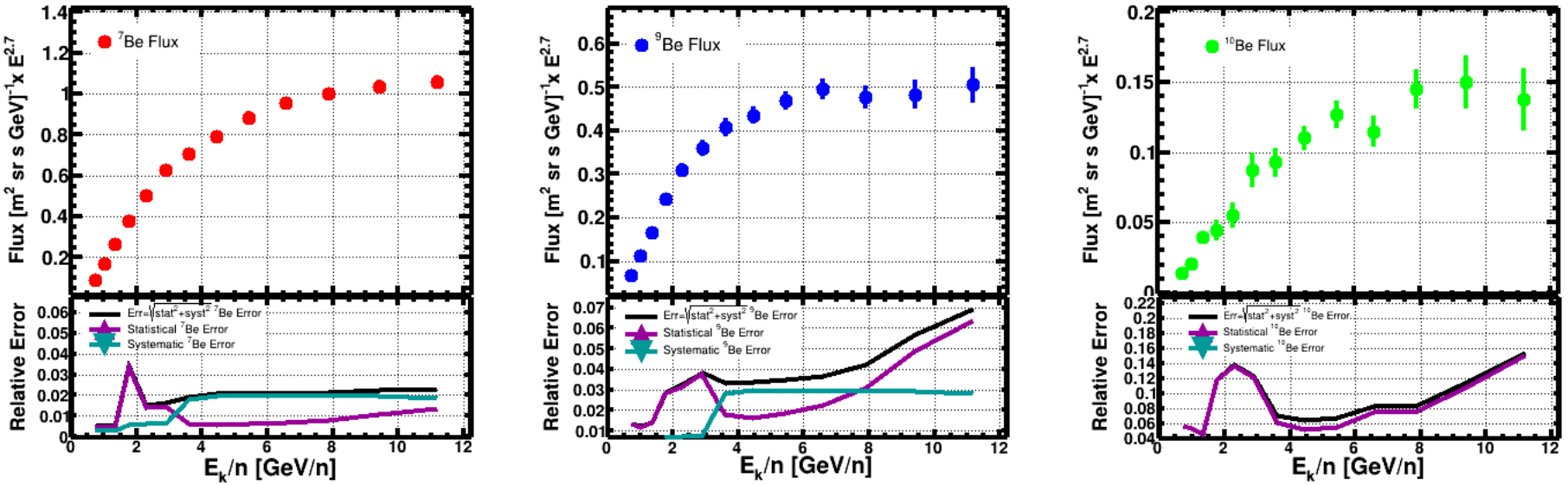

Figure 5.10: The fluxes for the isotopes ^{7}Be, ^{9}Be, and ^{10}Be with their relative error in the bottom panel. The Statistical errors are shown in magenta, Systematic errors in cyan, and Total errors in black.

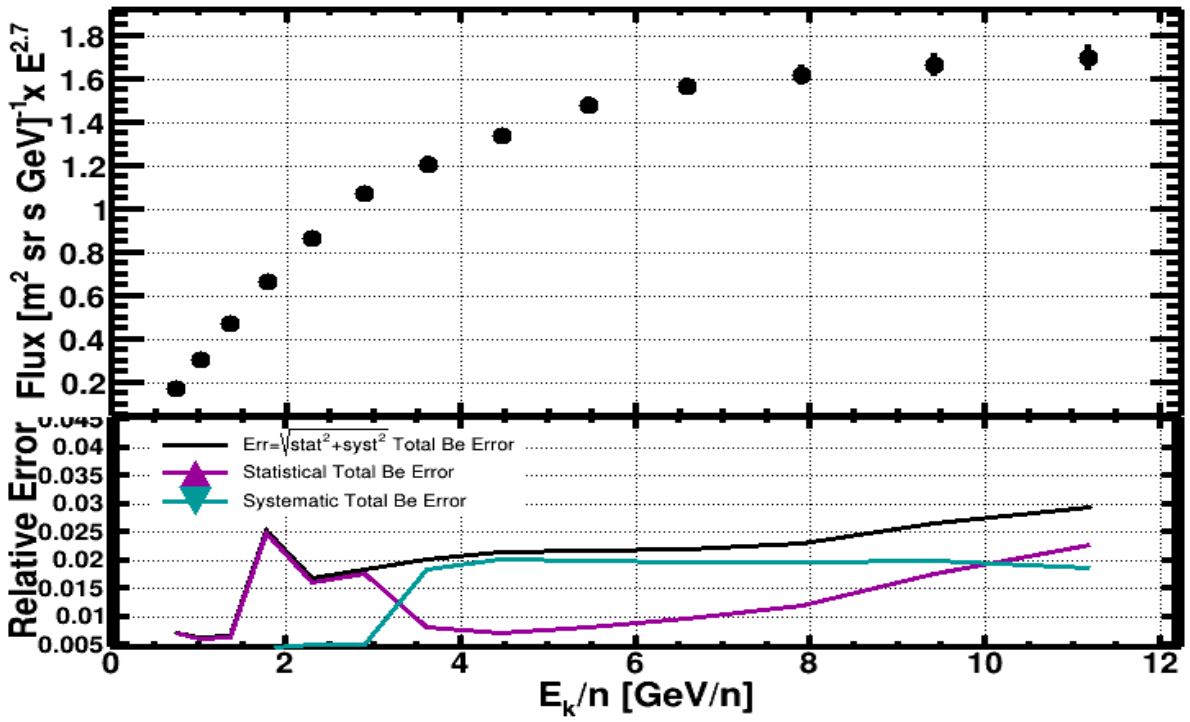

Figure 5.11: The total Be flux found by adding the individual fluxes of the three isotopes with their relative error. The Statistical errors is shown in magenta, Systematic errors in cyan, and Total errors in black.

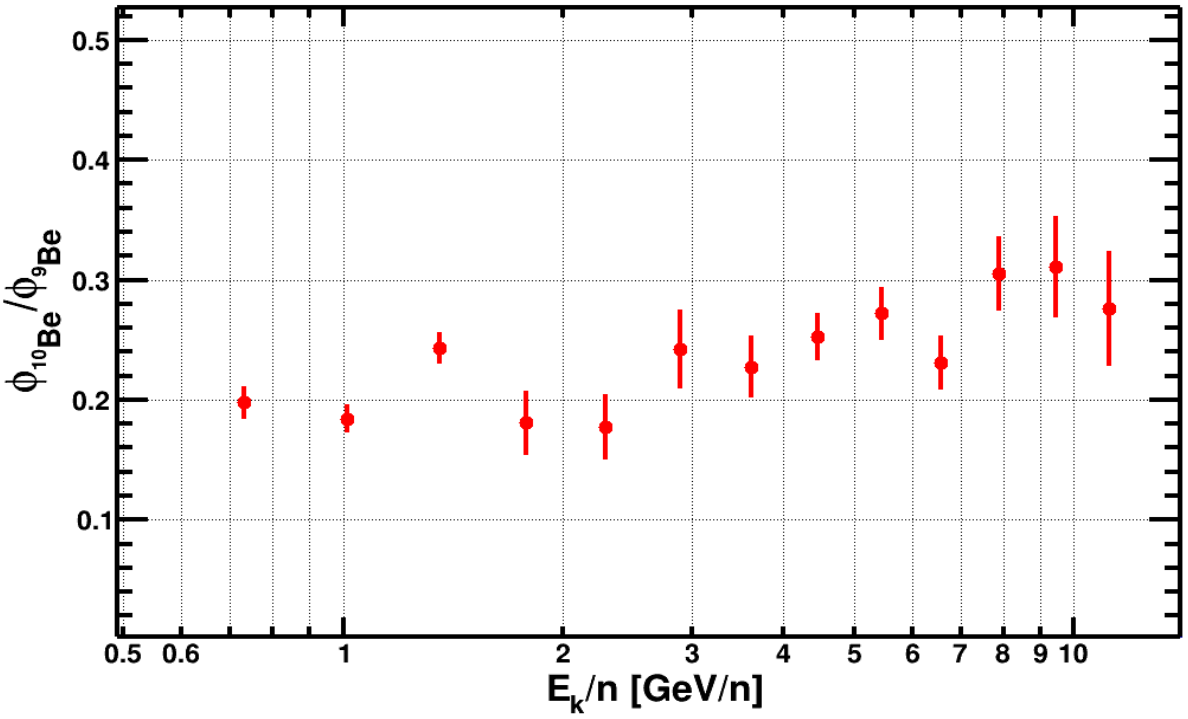

Figure 5.12: The flux ratio of $\Phi_{^{10}Be}/\Phi_{^{9}Be}$ from our analysis show in red.

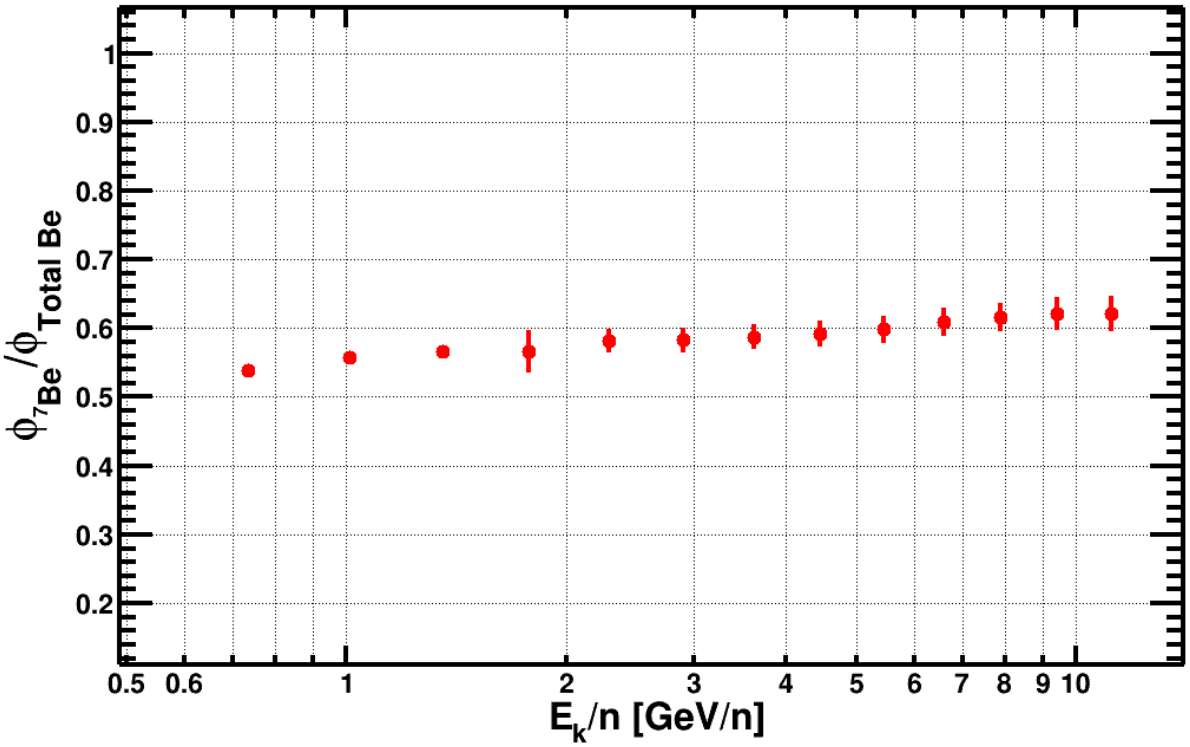

Figure 5.13: The flux ratio of $\Phi_{^7Be}/\Phi_{\text{Total Be}}$ from our analysis show in red.

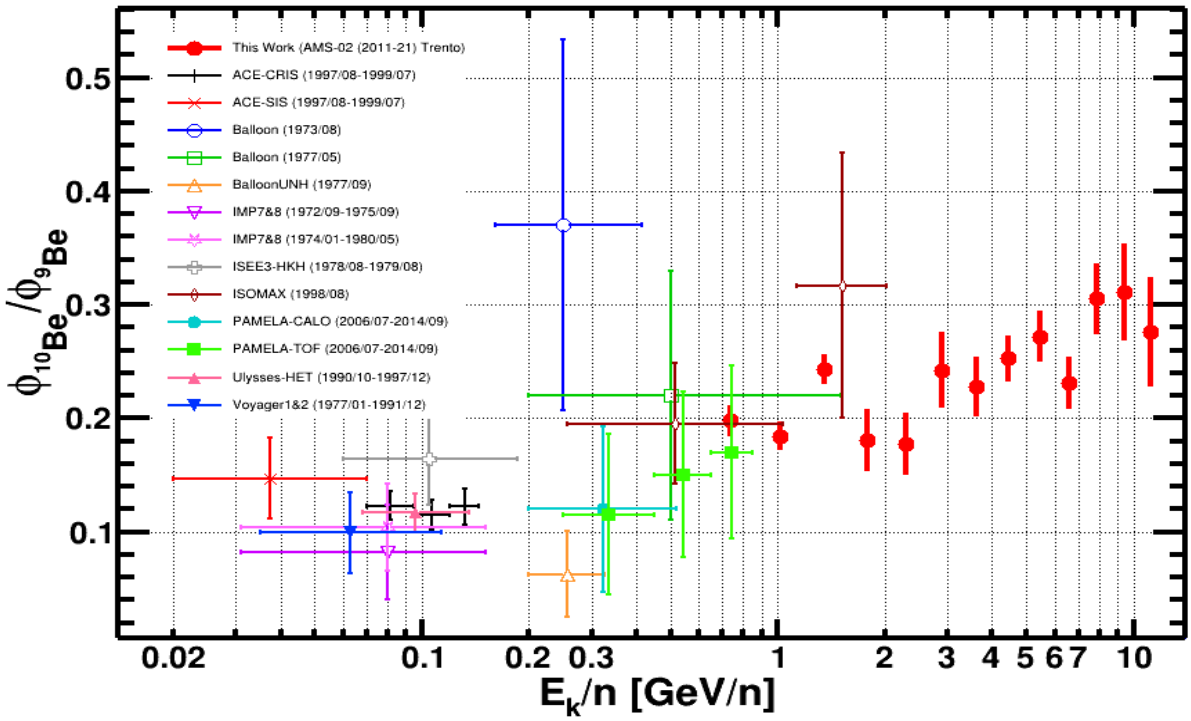

Figure 5.14: The flux ratio of $\Phi_{^{10}Be}/\Phi_{^9Be}$ from our analysis show in red, and plotted with previous measurements. ACE-CRIS (1997/08-1999/07) [279], ACE-SIS (1997/08-1999/07) [279], Balloon (1973/08) [176], Balloon (1977/05) [94], Balloon UNH (1977/09) [272], IMP7&8 (1972/09-1975/09) [163], IMP7&8 (1974/01-1980/05) [164], ISEE3-HKH (1978/08-1979/08) [277], ISOMAX (1998/08) [177], PAMELA-CALO (2006/07-2014/09) [225], PAMELA-TOF (2006/07-2014/09) [225], Ulysses-HET (1990/10-1997/12) [121], Voyager1&2 (1977/01-1991/12) [209], Voyager1&2 (1977/01-1998/12) [208]

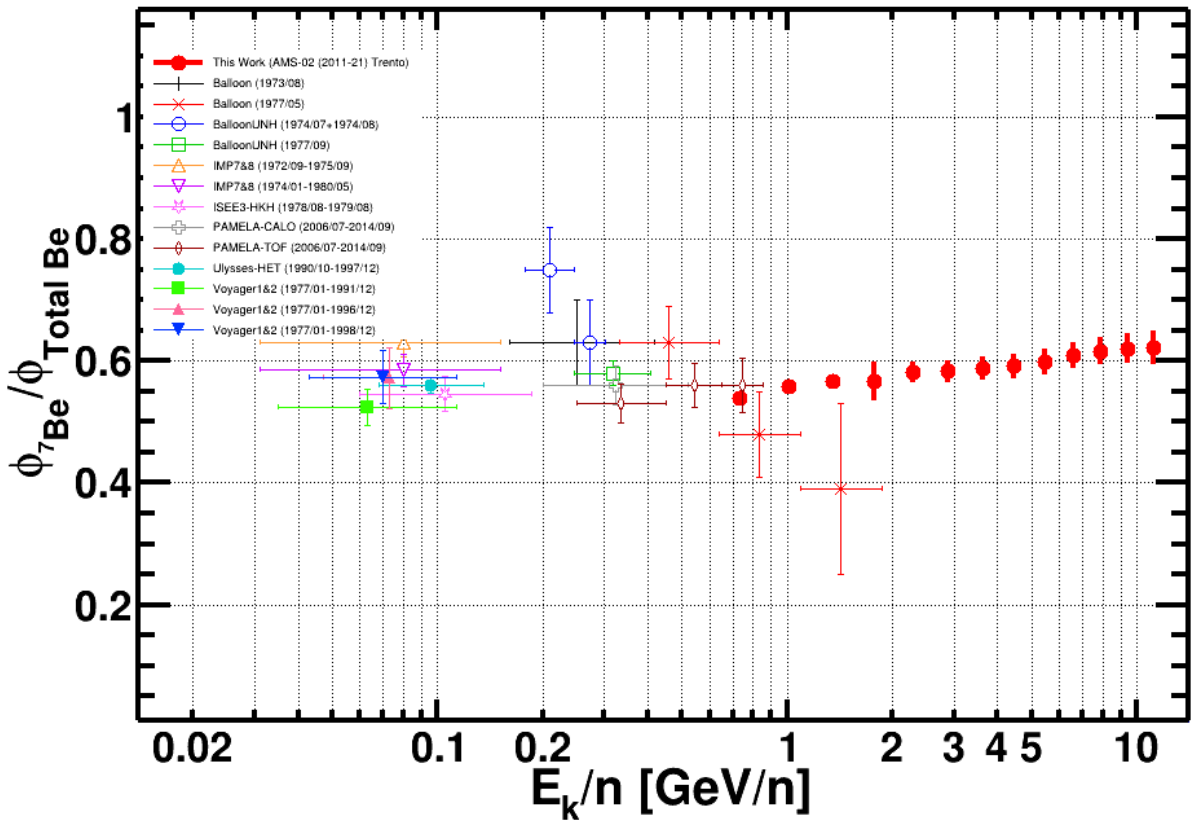

Figure 5.15: The flux ratio of $\Phi_{^7Be}/\Phi_{\text{Total Be}}$ from our analysis show in red, and plotted with previous measurements. Balloon (1973/08) [176], Balloon (1977/05) [94], Balloon UNH (1974/07+1974/08) [273], Balloon UNH (1977/09) [272], IMP7&8 (1972/09-1975/09) [163], IMP7&8 (1974/01-1980/05) [164], ISEE3-HKH (1978/08-1979/08) [277], PAMELA-CALO (2006/07-2014/09) [225], PAMELA-TOF (2006/07-2014/09) [225], Ulysses-HET (1990/10-1997/12) [121], Voyager1&2 (1977/01-1991/12) [209], Voyager1&2 (1977/01-1996/12) [210], Voyager1&2 (1977/01-1998/12) [208]

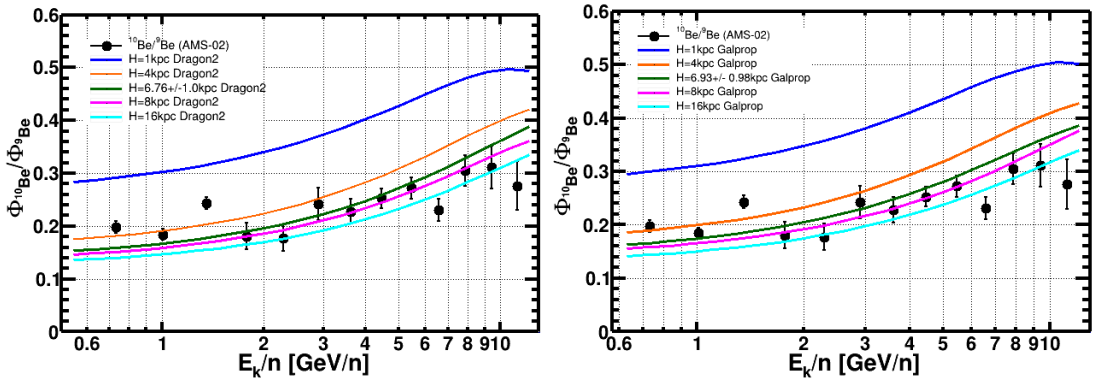

(a) Dragon Model

(b) Galprop Model

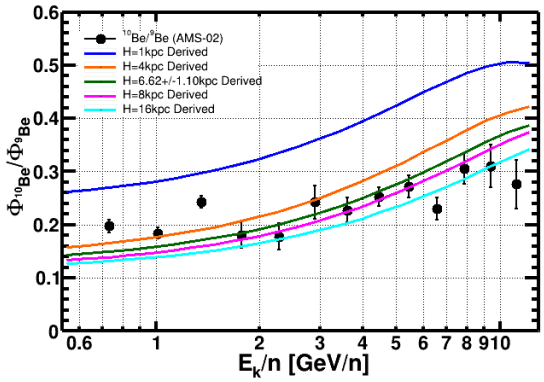

(c) Derived Model

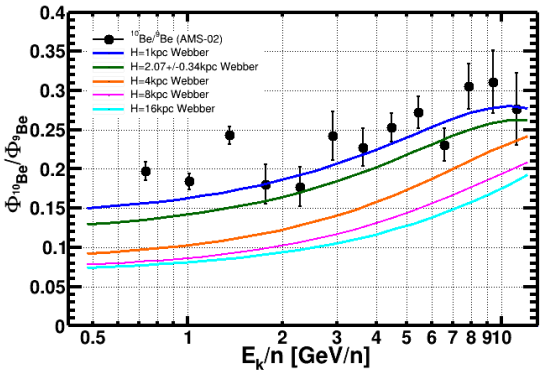

(d) WEBER Model

Figure 5.16: The model simulation [211] for various H sizes superimposed on the $^{10}Be/^{9}Be$ flux ratio from AMS-02. a)DRAGON2, b) GALPROP, c) DERIVED, d) WEBER

However, our analysis results suggest that our understanding of the Halo size is severely challenged by the AMS-02 data. Further in-depth investigation is necessary in this regards, and would be part of the future course of work.

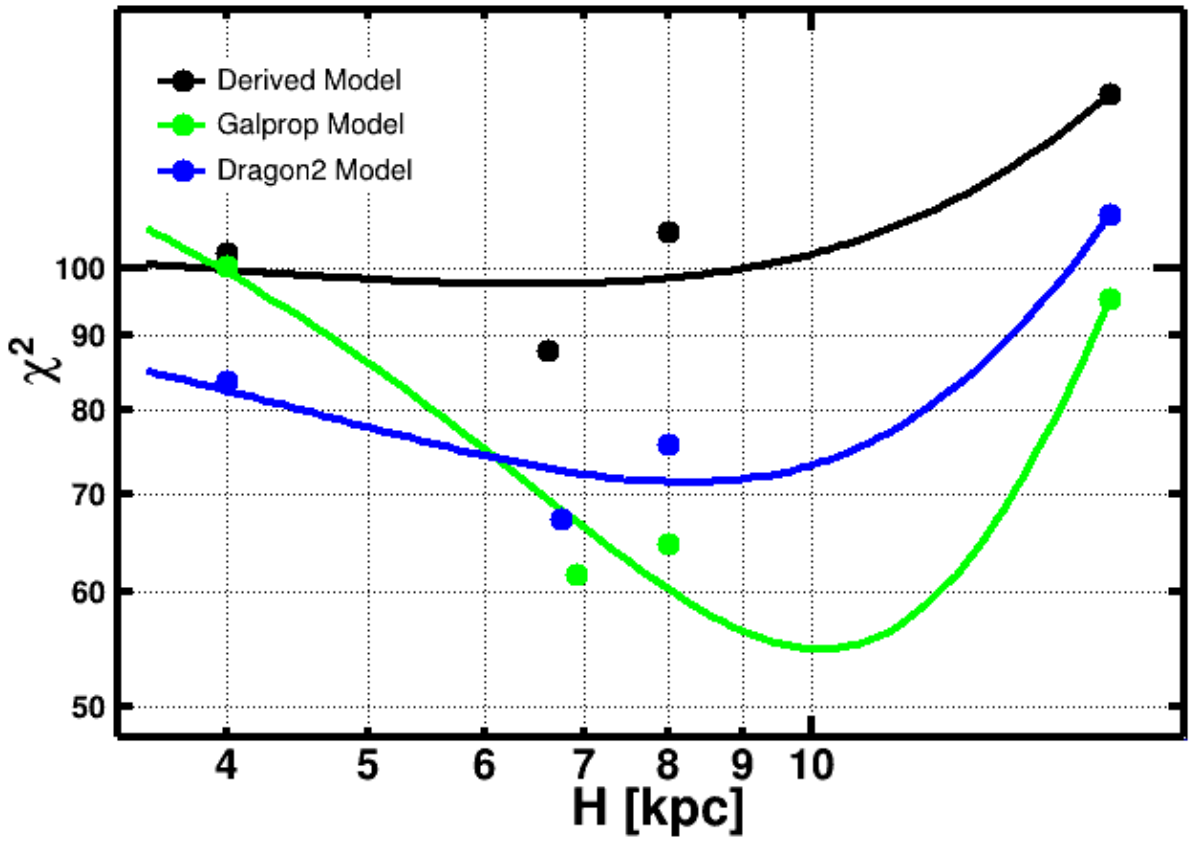

Figure 5.17: The χ^2 plot of the models fitted to the $^{10}Be/^{9}Be$ flux ratio in its entire energy per unit nucleon range. Three models, i.e., DRAGON2, GALPROP, & DERIVED suggest different halo sizes and calls for further investigation.

Chapter 6

Conclusion

Cosmic Rays have been at the forefront of accelerating high energy physics for more than a century, and this messenger of physics have time and again broken scientific knowledge plateaus. At a time, when production and direct detection of Dark Matter poses serious technological, and theoretical challenges; Cosmic Rays have again come to the rescue by providing us with a privileged channel of investigating DM through possible products of annihilation of WIMP like DM, which appears as excess in the rare component of Cosmic Rays. However, our ability to draw definite conclusion is limited by our knowledge of cosmic ray propagation model uncertainties, and cross-section uncertainties of production.

The excess in contention is that of anti-proton spectrum of cosmic rays. AMS-02 published high precision result of the $\bar{p}/p$ ratio which showed flattening above 60 GV rigidity. This is in conflict with theoretical predictions that expect the $\bar{p}$ component to decrease faster. Hence, the AMS-02 results showed an excess of $\bar{p}$ over standard astrophysical processes of $\bar{p}$ production, the latter primarily because of the interaction: $p+p/He \rightarrow \bar{p}+X$. However, to completely decouple the possible exotic component of $\bar{p}$ from standard production, we need accurate knowledge of cosmic ray propagation model parameters, and $\bar{p}$ production cross-section. This leads to two source of uncertainty: Astrophysical and Nuclear uncertainty. In order to reduce the astrophysical uncertainty, one of the important parameters is to constrain the ratio H^2/D, and for that purpose, we set on the endeavour to analyse the $^{10}Be/^{9}Be$ ratio. [1]

We performed the analysis of the Beryllium isotope ratio, $^{10}Be/^{9}Be$ to relatively higher energy $\sim$ 12 GeV/n as compared to existing measurements, along with necessary corrections required by detector systematics, and measurement methodology. Firstly, we prepared a sample of Beryllium $Z = 4$ events with high-quality measurements of speed, β, from the three sub-detectors: ToF, RICH-NaF, and RICH-Agl; and the Rigidity, R measured using the inner tracker through a series of selection based cuts on the data. A bi-Gaussian model with mass resolution modelled from AMS-02 Monte Carlo simulation was used to fit our data in 27 en-

[1] Along with that, to reduce the nuclear uncertainty, we conducted the measurement with proton beams at several energies directed at a liquid Helium target at the CERN M2 Beam line within the COMPASS++/AMBER facility. For this measurement, the COMPASS-RICH was used to detect the anti-protons. As such, we developed a Monte-Carlo simulation of the COMPASS-RICH, and also developed the preliminary scheme for the improvement of the reconstruction algorithm of the RICH rings.

ergy per unit nucleon bins. After agreement with AMS-02 collaborators, the final results were rebinned in 13 bins to reduce statistical uncertainty. We were able to extend the energy range by almost 500 % as compared to existing measurements, the latter being afflicted by huge uncertainties. Our analysis results would be a valuable tool to constrain cosmic ray propagation models by breaking the degeneracy of H^2/D parameter. As expected from theoretical consideration, we do see a flattening of the ratio at higher energies as a result of time dilation. This flattening also is majorly responsible for the severe challenge that our analysis provides to the understanding of Halo size. Our analysis results pose interesting challenge to phenomenologists, and would help us expand our knowledge of cosmic rays, dark matter, and universe in general.

As with previous publication of flux ratios, our knowledge about cosmic ray propagation models, and the universe have been increasing in incremental steps. Our work will be one component among all major efforts to help reduce the astrophysical and nuclear uncertainties required to have a definitive understanding of the exotic $\bar{p}$ component, and hence increase our signal sensitivity to Dark Matter.

Appendix A

AMBER experiment at CERN

A.1 Introduction

AMBER (*Apparatus for Meson and Baryon Experimental Research*) [13] is a newly proposed QCD facility at the M2 beam line of the CERN-SPS. It would use the COMPASS (*Common Muon and Proton Apparatus for Structure and Spectroscopy*) [9, 10] facility to conduct various experiments ranging from Proton-radius measurement, and Drell-Yan process, to antiproton production cross-section as its phase-1 physics programs. It consists of a two stage spectrometer, the stages being seperated by two spectrometer magnets. Both stages are equipped with a multitude of layers of trackers, electromagnetic and hadronic calorimeters, and particle identification detectors. The first stage of the spectrometer hosts a $3.3\ m$ long gaseous *Ring Imaging Cherenkov Counter* for hadron identification. The layout of the spectrometer is presented in fig. A.1

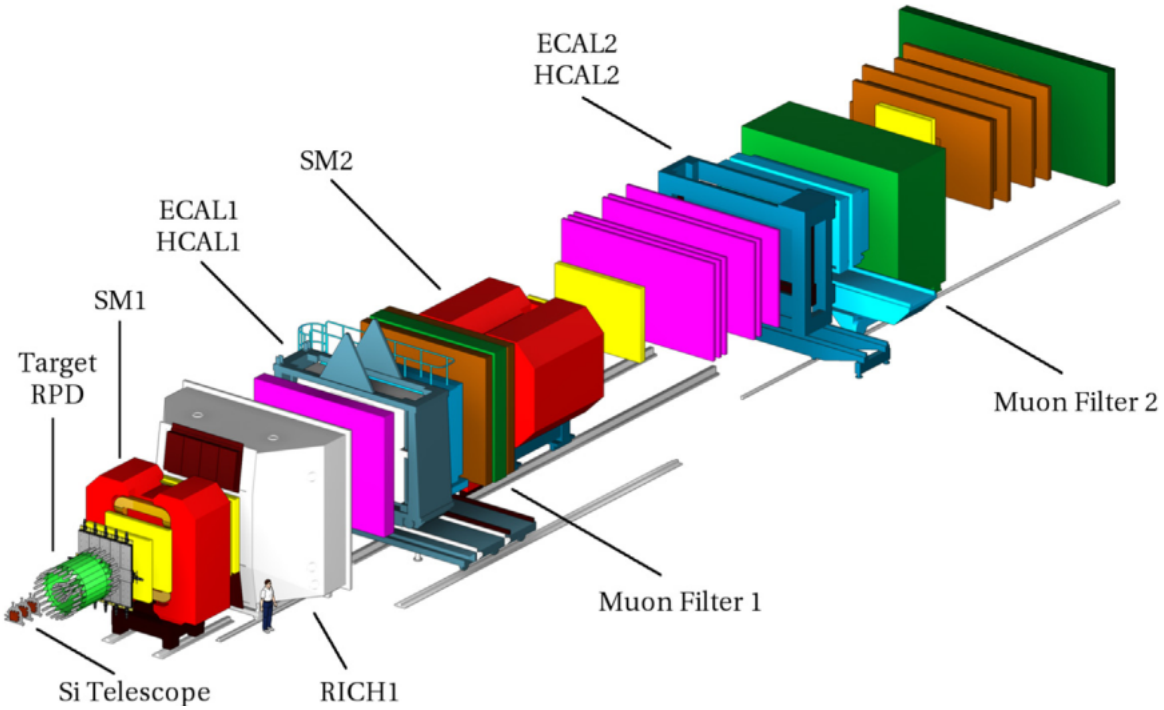

Figure A.1: The COMPASS setup for measurements with hadron beams. The beam arrives from the left side. Figure from [9]

At the relevant length scales probe of $\sim 10^{-15}\ m$ (low-energy regime), the strong coupling constant α_s approaches unity (becomes strong). The running coupling constant of QCD can be written as

$$\alpha_s(q^2) = \frac{\alpha_s(\mu^2)}{1 + B\alpha_s(\mu^2)\ln\left(\frac{q^2}{\mu^2}\right)}, \tag{A.1}$$

where, q^2 is the four-momentum squared, μ is some arbitrary scale at which the QCD charge is known, and $B = (11N_c - 2N_f)/12\pi$, where N_c, and N_f are the number of quark flavours and colours respectively. For $N_c = 3$ colours and $N_f \leq 6$ quarks, B is greater than zero and hence α_S decreases with increasing q^2 (energy). At $|q| \sim 1\ GeV$, α_S is of $\mathcal{O}(1)$ and perturbation theory breaks down, and we enter the domain of non-perturbative QCD regime.

Experiments with hadron beams for precision spectroscopy of light mesons and baryons with masses up to $3\ GeV/c^2$ require state-of-the-art spectrometer with high acceptance and resolution for charged and neutral particles, so as to perform precise measurements of the multi-particle final states over a wide kinematic range. The three different mechanisms that contribute towards the production of a system X are (see fig. A.2): *diffractive dissociation, central production* which proceeds via exchanging one or two *Reggeons* $\mathbb{R}$ (virtual particle involved in $t-$channel exchange of resonances for which the spin is bigger than 1) respectively between beam hadron and target nucleus N, and *photo-production* in the Coulomb field of a nucleus at very low values of momentum transfer.

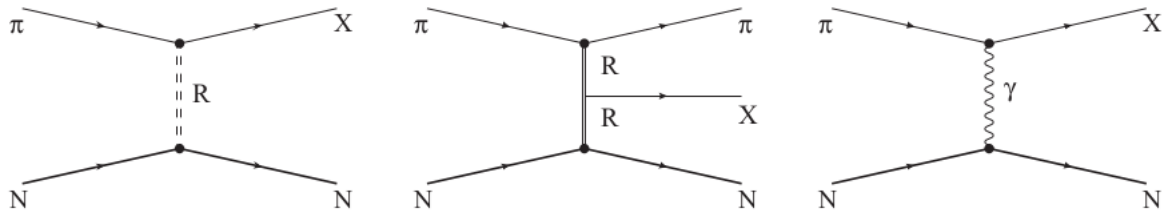

Figure A.2: Diffractive dissociation, central production, and photo-production by quasi-real photons γ, with π denoting the beam particle (can be also p, K), and N is the target nucleon or nucleus. These are the production mechanism in COMPASS [9].

A.2 Spectrometer for Hadron Physics

A.2.1 Beam line

The CERN SPS M2 beam line was originally built for high-intensity muon beam. Later the beam line was calibrated to include a high-intensity hadron beam, as well as, a low-intensity electron beam. Two CEDAR (*Cherenkov Detector with Achromatic Ring Focus*) detectors are added just before the spectromer for particle identification.

To produce secondary hadron or tertiary muon beam, $400\ GeV/c$ protons from the CERN SPS are slowly extracted onto a primary production target (T6). It takes $9.6\ s$ for these protons to arrive once evy $30 - 48\ s$ (depends on other users of the SPS). The primary target provides

the facility to select five positions: an empty target or one out of four Be targets. For e.g., a negative $190\ GeV/c$ hadron beam with a nominal intensity $5 \times 10^6\ s^{-1}$, is achieved by using 9×10^{12} protons/cycle on T6 and the $500\ mm\ Be$ target.

A.3 Beam particle identification

The beam particles are identified by two CEDAR detectors installed $30\ m$ before the COMPASS target region. These detectors are used for fast identification at high rates upto particle momenta of $300\ GeV/c$ [89].

A.3.1 CEDAR detector

The working principle is based on the fact that for a beam containing particles of different types but of the same momentum, the angles of the emitted Cherenkov photons are different in accordance with their masses. The photons are focused onto the photon detector using a mirror and a system of lenses. At the focal plane, we find rings of photons compensating for the chromatic aberration of the gas, which is essential for proper separation of the rings. A ring shaped diaphragm located at the focal plane perpendicular to the beam direction is used to select photon rings with a fixed radius. The radius of the diaphragm is regulated by manipulating the pressure of the helium gas in the vessel so as to match the radius of the photon ring. The photons are detected with PMTs (*Photo Multiplier Tubes*).

Each CEDAR detector of COMPASS consists of a $6\ m$ long vessel with pressurised He gas (see fig. A.3). The beam tracks have to be parallel for efficient working of the CEDARs. As such, a pair of scintillating fibre detectors (one horizontal, and one vertical) are installed upstream (FISC1,2) and downstream (FISC3,4) of the CEDARs. Also, two scintillating discs (TRIG 2) are installed as beam counters. They are used to normalise the CEDAR count during pressure scans. In a pressure scan, the CEDAR count rate normalised to the rate in the FISC counters is plotted as a function of the vessel pressure and PMT signal multiplicity. The refractive index is proprotional to p/T, and hence, during data taking, He pressure in the CEDARs is adjusted to compensate for He leakage and to keep p/T constant.

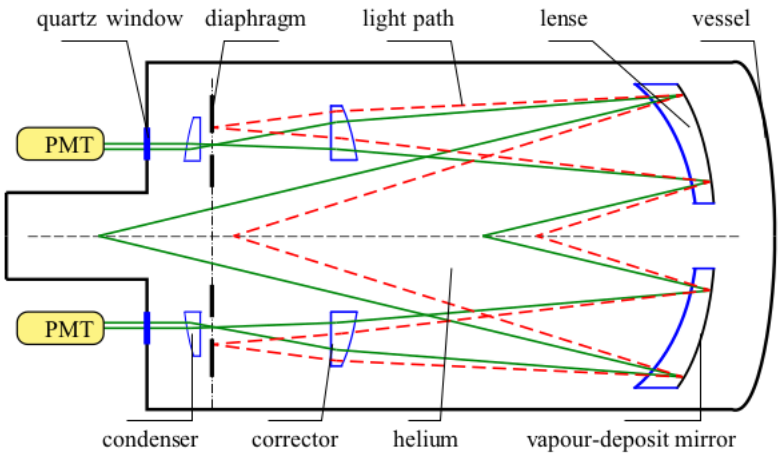

Figure A.3: Working principle of a CEDAR. Two particles with same momentum but different masses (full green and dashed red lines here) radiate Cherenkov photons at different angles, resulting in rings with different radii. A diaphragm adjusted to the photon ring radius selects a particle type. Figure from [9]

A.3.2 Positive Beam Separation

The proton component is dominant in the high-energy positive hadron beam. In CEDAR, a difference of 1 mm width is expected between protons and kaons at 190 GeV/c. Fig. A.4 shows a pressure scan for three different requirements on the minimum number of PMT hits (multiplicity). Pions and protons have a clear separation, while the kaon signal is hidden under the pion, and can't be distinguished here. Taking in consideration the measured rates, and the beam composition, a PID efficiency of 90% can be achieved for the protons using a multiplicity ≥ 4. One CEDAR is set to identify protons, the other to identify pions.

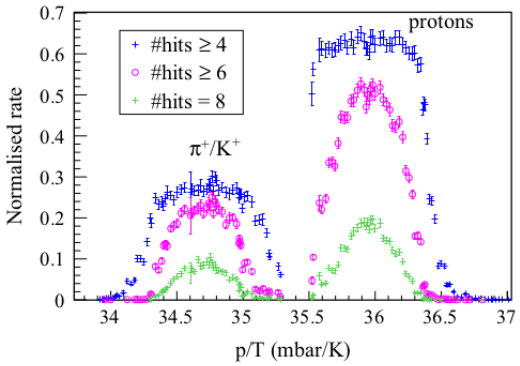

Figure A.4: CEDAR 1 pressure scan for a positive hadron beam with different multiplicities. The kaon peak cannot be distinguished from the pion peak.

A.4 Target Region

The target region consists of the target [89] systems, the *Recoil Proton Detector*, the *Sandwich Veto Detector* and the *Silicon Detectors* (see fig. A.5). Liquid hydrogen, liquid helium, and solid targets can be used for measurements with hadron beams.

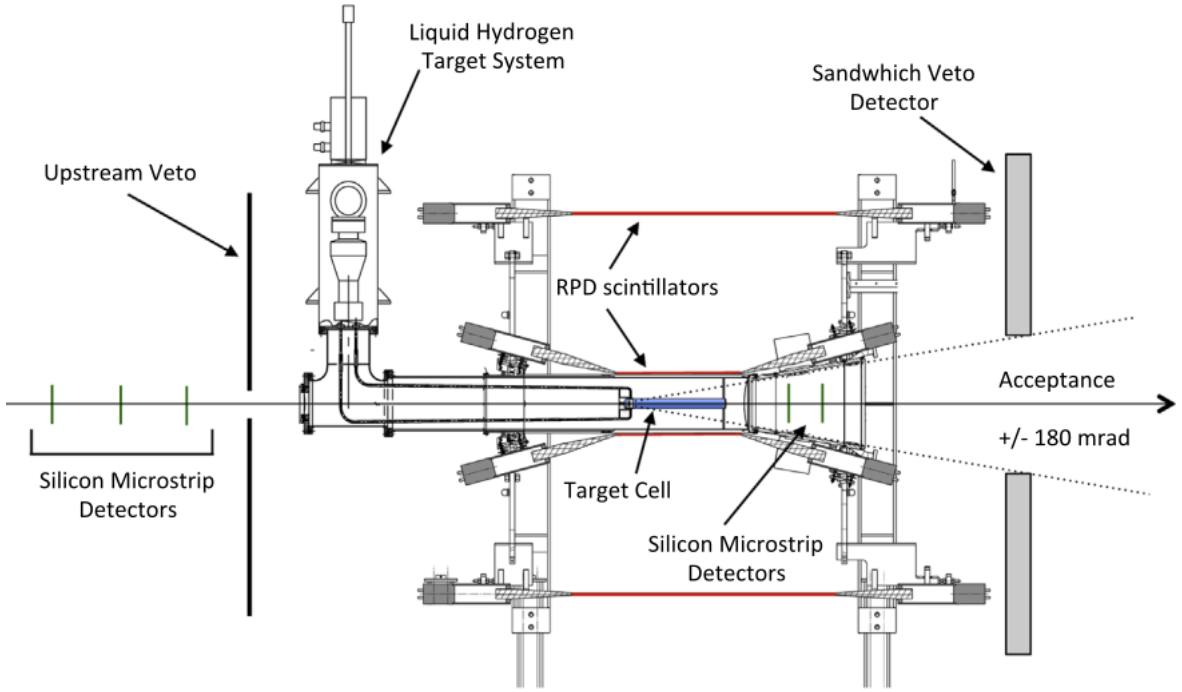

Figure A.5: Liquid hydrogen target system

A.4.1 Recoil Proton Detector

The target is surrounded by a time-of-flight and energy loss detector called Recoil Proton Detector (RPD). The RPD is made of two cylindrical layers of scintillator with diameter of 120 mm and 775 mm surrounding the target. The inner ring is composed by 12 scintillator slabs of $50 \times 6.6 \times 0.5\ cm^3$, while the outer ring of 24 slabs of $115 \times 20 \times 1\ cm^3$. The RPD helps us in fast particle identification and trigger on recoil proton via time-of-flight and energy loss measurement. The RPD measures times and hits of the track by a calculation of the effective speed of light in the scintillator slab. Combining measurements of time-of-flight and positions, one can measure the velocity of the particle. Each scintillator at both sides is read out by PMTs.

The momentum resolution as a function of proton momentum is evaluated though pion-proton elastic scattering events. The transverse momentum of the proton is measured in the RPD, and then it is compared to the value of momentum calculated from the kinematics of the pion detected in the spectrometer. The resulting width of the momentum distribution as a function of the proton momentum can be seen in fig. A.6.

Also, the energy loss in the outer ring as a function of the velocity measured by the RPD in elastic pp scattering is shown in fig. A.6. It can concluded that for velocities up to $\beta = 0.34$, the protons are stopped in the outer ring. Above this, the protons escape the scintillator, and deposit only a part of its energy. Therefore proton PID is reliable only upto $\beta < 0.4$.

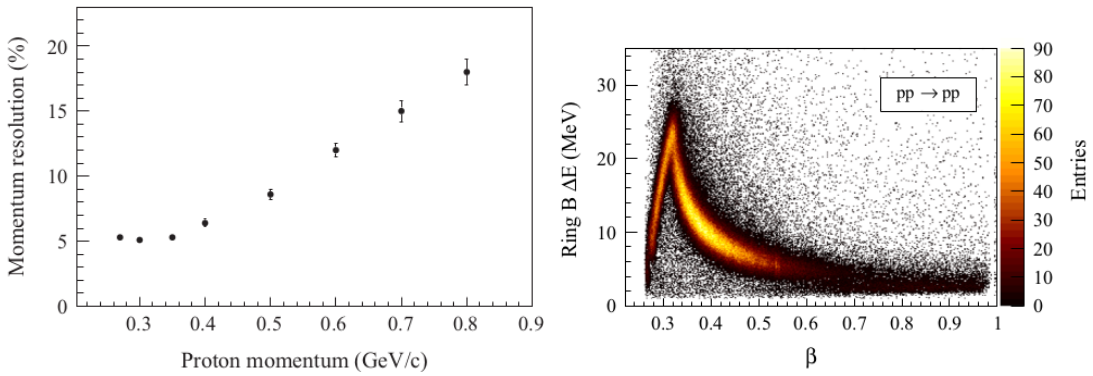

Figure A.6: Left: Momentum resolution of the RPD for protons detected at an angle of $70°$ with respect to the beam axis. Right: Energy loss ΔE in the outer ring of the RPD as a function of the velocity of the particle in elastic pp scattering. Figures taken from [9]

A.4.2 Sandwich Veto Detector

The Sandwich Veto Detector is used to veto events containing photons and charged particles that lies outside the acceptance gap of the RPD and Large Angle Spectrometer (LAS). It consists of a $2m \times 2m$ stack of five layers of steel-covered lead plates and scintillators with a total thickness of 5.1 radiation lengths. It is segmented into 12 elements and has central hole that matches the acceptance of the spectrometer (see fig. A.7). Each of the lead layer is composed of 5 $mm\ Pb$ plates with 1 mm steel plates on each side to ensure structural integrity. Each layer of scintillator is made of a pair of $80 \times 20\ cm^2$ scintillator bars lying side-by-side. Out of which, the first three layers have a thickness of 1 cm, while the last two is of $0.5\ cm$. The light is extracted from th scintillators using wavelength-shifting fibres connected to PMTs. The detector have a measured efficiency of 98 % for minimum ionising particles.

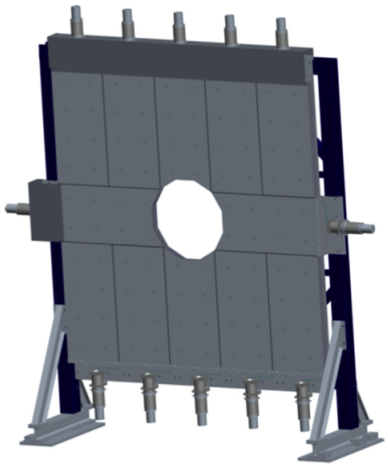

Figure A.7: Sandwich Veto Detector. Figure from [9]

A.5 Tracking Detectors

The tracking system is composed of several stations, each with a set of planar tracking detectors of the same type. Far downstream, to track low-momentum particles scattered at large angles, several variants of wire-based gas detectors like *Multiwire Proportional Chambers (MWPC)*,

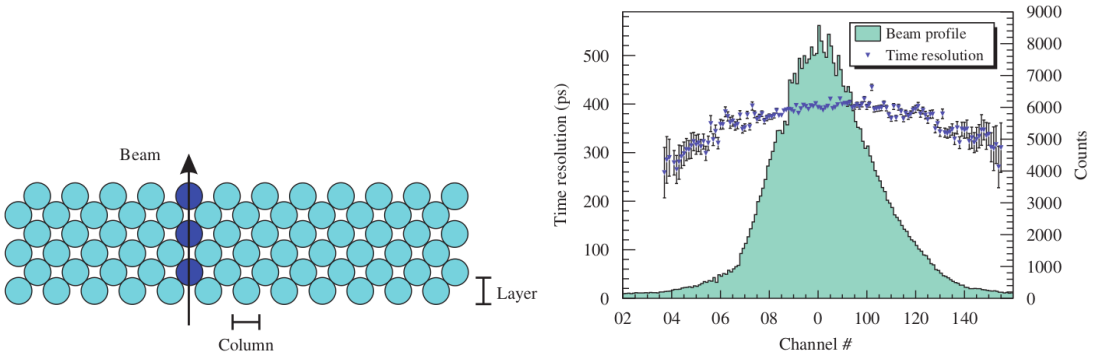

Figure A.8: Left: SciFi plane fibre configuration. The number of fibre layers per plane is 8,12 or 14, depending on the station. Right: Time resolution of a single SciFi plane across the beam region with the beam profile. Figures taken from [9]

Drift Chambers (DC), and *Straw Tube Chambers* are used. Near the beam, where the particle hit rate is high, fast detectors with a good resolution is required, micropattern gaseous detectors with strip readout, namely the *Micromegas* and *Gas Electron Multiplier (GEM)* are used. In the beam region, where rates are of the order of $10^5\ mm^{-2}s^{-1}$, *Scintillating Fibre Detectors* and novel GEM detectors with pixel readout *(PixelGEM)* are used. Tracking immediately upstream and downstream of the target is accomplished with the help of *Silicion Microstrip Detectors*.

A.5.1 Very Small Area Tracker

A.5.1.1 Scintillating Fibre Detectors (SciFi)

It was designed to provide tracking of incoming and scattered beam particles as well as of all other charged reaction products in the vicinity of the primary beam. As the hit rate is quite high, hits are assigned to the corresponding track by time correlation only, as spatial correlation would be ambigious. A total of eight SciFi detector stations are used. Two pair of stations are placed upstream (nos. 1,2) and downstream (nos. 3,4) of the target, two more pair upstream (nos. 5,6) and downstream (nos, 7,8) of the second spectrometer magnet (SM2). Each station consists of at least two projections, one vertical (Y), and one horizontal (X). Apart from these, three stations (nos, 3,4,6) have an additional inclined ($\sim 45°$) projections (U).

To provide enough photoelectrons for detection, several layers of fibres are stacked for each projection with an offset from one layer to another (see fig. A.8). The light output of a group of fibres lined up in beam direction (labelled ”coloumn” in fig. A.8) is collected by one *Photon Detector (PD)* channel.

The time resolution using one plane is nearly constant for all channels. R.M.S values between 350 and 450 ps is seen for the central regions of the various planes. In fig. A.8 , we can see that time resolution across the plane shows a smooth curve with slightly better values in the outside region, because of low intensity.

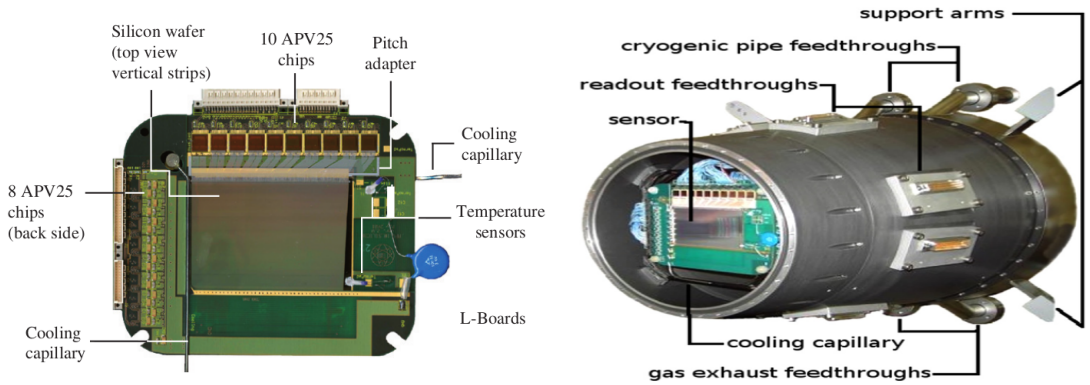

Figure A.9: Left: Front view of a Silicon Microstrip Detector. Figure from [10]. Right: The conical cryostat with the upstream beam window dismounted. The bent cooling capillary is fixed to the PCB close to the sensitive area of the detector. Inside the cryostat, the readout cables are directly soldered to the detector module and plugged to vacuum-sealed feedthrough connectors also visible on the outer surface of the cryostat. Figure taken from [9]

A.5.1.2 Silicon Microstrip Detectors

The Silicon Microstrip Detectors comprise of three stations upstream of the target used as a beam telescope, and two stations downstream of the target used for vertex reconstruction. The high beam intensity necessitates a radiation hard detector design with an excellent spatial and time resolution.

Each station has two silicon detectors with a stereo angle of 5° between their respective strip orientations to resolve multi-track ambiguities. Each detectors consist of a 300 μm thick silicon sensor with an active area of $50 \times 70\ mm^2$. The signals are read on both sides independently by 1280 strips on the n-side, and 1024 strips on the p-side oriented perpendicular with respect to the n-side.

The silicon wafer is glued with silicon glue to a frame consisting of two L-shaped printed circuit boards (L-board). The readout strips are tilted by 2.5° with respect to the wafer edge, and are connected with a 25 μm aluminium wire bonds and a glass pitch adapter to the front-end chips. Besides that, a capillary is soldered along two wafer edges onto the back side of the L-Board which is electrically insulated by a epoxy connector. The capillary is used to cool the front-end chips by flushing gaseous nitrogen through it. The analog signals induced on the microstrips are read out by a APV25 front-end chip. The whole setup can be seen in fig. A.9

These detectors are prone to radiation damage as they are traversed by the beam particles, and forward-boosted reaction products. The damage in the bulk material changes the doping, and damage to the surface leads to decrease of insulation, and consequent increase of depletion voltage and hence the leakage current. So, cooling is done using liquid nitrogen to minimise damage. The leakage current drops with temperature which consequently decreases the radiation damage noise. On top of that, cooling also ensures better spatial and time resolution. The cooling technology used relies on evapaoration of liquid nitrogen in thin capillaries on the PCBs. The downstream *Conical Cryostat* used for cooling can be seen in A.9. For more details

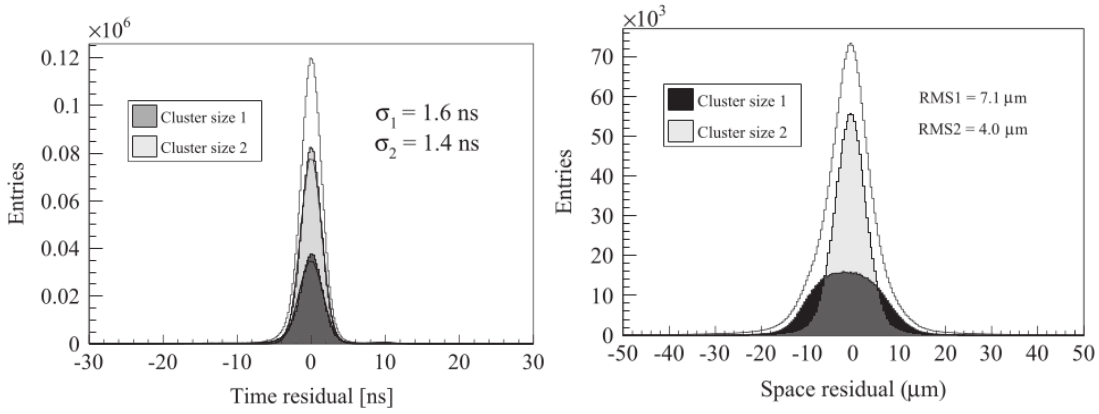

Figure A.10: Left: Spatial resolution of a single silicon detector plane. "RMS1" and "RMS2" refer to the cases of clusters with one and two hit strips, respectively. Right: Time resolution of a single silicion detector projection. Figure taken from [9]

on the cooling, one can refer [9].

The spatial resolution is in the range of $4 - 6\ \mu m$ for clusters when two strips are hit and a technique of amplitude weighting can be used to determine the track position [172]. If only one strip is hit, the resolution drops to $7 - 11\ \mu m$. The time and spatial resolution can be seen in fig. A.10

A.5.1.3 PixelGEM Detectors

To reduce the amount of detector material exposed to the hadron beam, some of the SciFi detectors were replaced with thinner detectors based on gas electrom multiplier (GEM) foils (See following section on small area tracker for its working principle). GEM detectors are able to cope with high particle fluxes in the beam centre, but the strip readout makes it impossible to separate individual hits close to the beam due to high occupancy. As such, a read-out method was realised using the GEM patterning and wet-etching printed-circuit board (PCB) technologies. As seen in fig. A.11 , the central area of $32 \times 32\ mm^2$ is patterned with 1024 pixels of $1 \times 1\ mm^2$ size of 50 μm thick polyimide foil. The rest of the total active area of 100×100 mm^2, where the occupancy is sufficiently low is covered by two orthogonal sets of 512 strips with a pitch of 400 μm, realised on a second $50\ \mu m$ thick polyimide foil. The spatial resolution is shown in fig. A.12, while the time resolution is shown in fig. A.13.

A.5.2 Small Area Trackers

A.5.2.1 Micromegas Detectors

The Micromegas *(Micromesh Gaseous Structure)* detector is based on a parallel plate electrode structure and a set of parallel microstrips for readout. The distinguishing feature of this detector is the presence of a metallic micromesh that separates the gaseous volume into two regions: a conversion gap where the ionisation takes place, and the resulting electrons drift in a moderate electric field (about 1 kV/cm over 3.2 mm), and an amplification gap with a higher field (50 kV/cm over 100 μm) which produces an *Townsend avalanche* which leads to production of

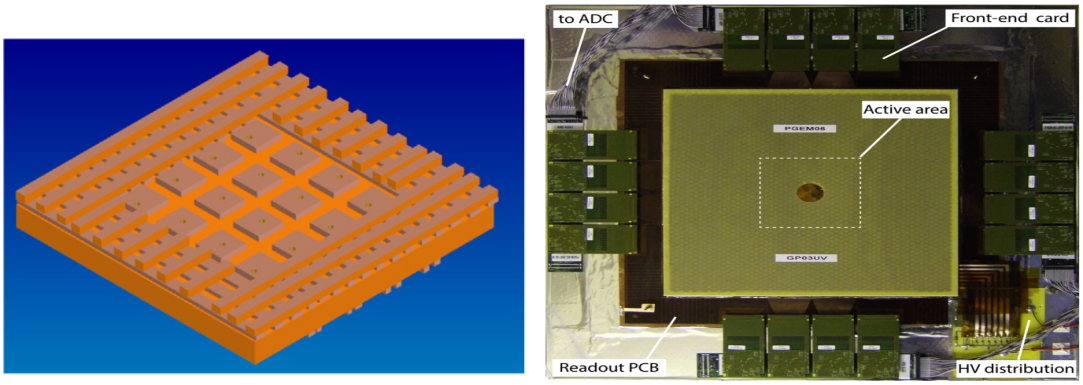

Figure A.11: Left: Schematic view of the pixel and strip region of the readout circuit. The pixel region consists of 32×32 pixels of 1 mm^2 size each, while only 4×4 are shown for clarity. Right: A fully assembled PixelGEM detector, equipped with 16 APV front-end cards. The digitisation of the analog signals from the APVs is done at an external ADC card, which is connected via the grey cables. Figure taken from [9]

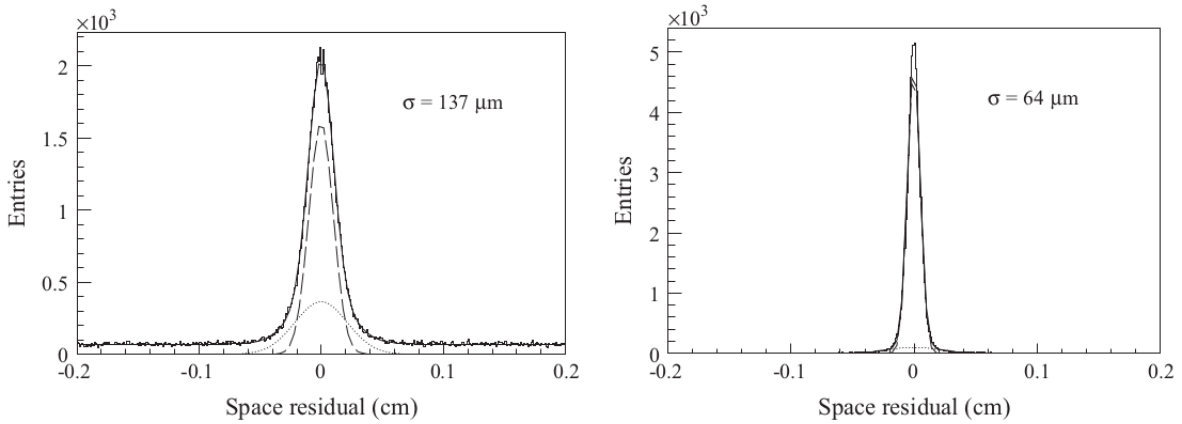

Figure A.12: The residual distribution, i.e., the difference between measured cluster position and track penetration point in $x-$ direction for the pixel (left) region, and the strip region (right) of a pixelGEM. The residulas are obtained by fitting a bi-gaussian with a constant background. After taking track uncertainty in consideration, spatial resolution of 106 μm (pixels) and 54 μm (strips) are obtained. Figure taken from [9]

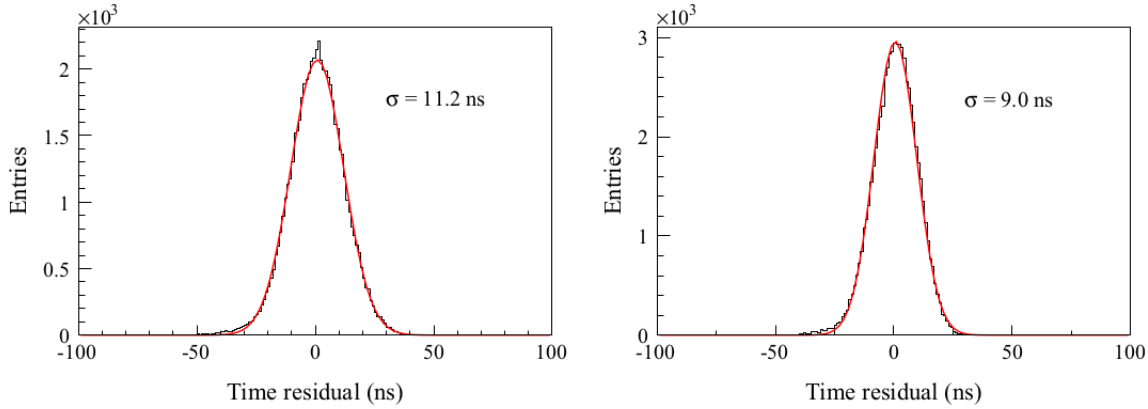

Figure A.13: The time residual distribution, i.e., the difference between measured cluster time and track time, for the pixel (left) region, and the strip (right) region in the $x-$ direction of a pixelGEM. Figures taken from [9]

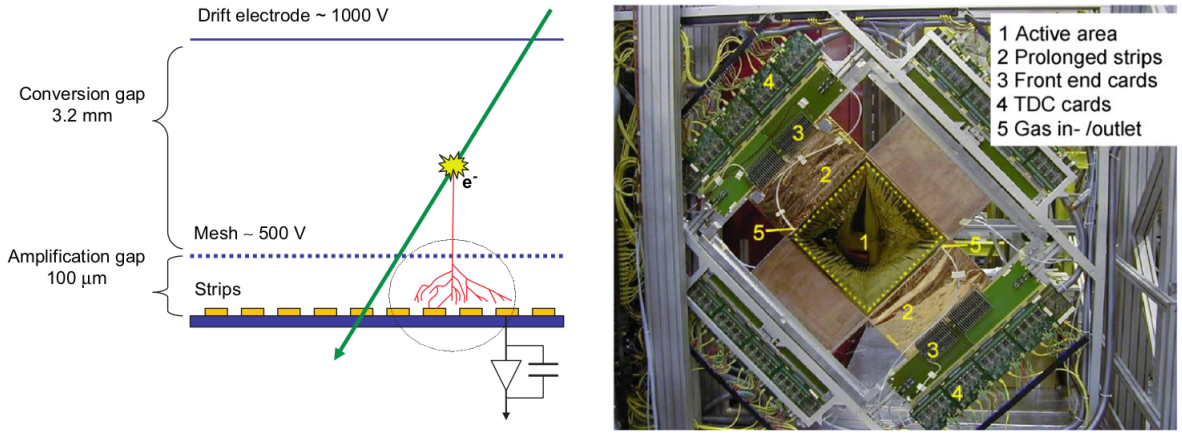

Figure A.14: Left: Principle of a Micromegas detector. Right: A Micromegas doublet (U and V projections) in the COMPASS setup. The active zone is the $40 \times 40\ cm^2$ internal square (1). Strips are extended (2) to keep the front-end electronics (3) outside the acceptance of the spectrometer.

large number of electron/ion pairs as shown in fig. A.14 . The electric field configuration in the vicinity of the mesh is such that most of the ions from the avalanche are captured by the mesh and do not drift back into the conversion gap. As such, the ion drift time over a maximum distance of 100 μm and the signal width induced by the ions do not exceed the ion drift time over that distance, which is around 100 ns. This results in a fast evacuation of positive ions which combined with reduced transverse diffusion of the electrons, and the higher granularity of the detector result in a high rate detection capability.

The experimental facility of AMBER has twelve Micromegas detectors, with 1024 strips each, assembled in 3 stations of four planes each (X, Y, U, V), that tracks particles in the 1 m long region between the polarised target solenoid and the first dipole magnet. The gas mixture used is $Ne/C_2H_6/CF_4$ $(80/10/10)$, which is optimised for good time resolution. It also minimised the discharge rate to 0.03 discharges per detector and per beam spill. The detector has an active area of $40 \times 40\ cm^2$ with a central dead zone of 5 cm in diameter. The strip pitch is 360 μm for the central part (512 strips), and 420 μm for the outer part (2×256 strips).

The mean time resolution has a value of 9.3 ns and is shown in fig. A.15 . To evaluate the spatial resolution, incident tracks are reconstructed using the hits in 11 Micromegas, and the residuals in the 12th one are evaluated as shown in fig. A.15 that shows the distribution of residuals for the full active area of one Micromegas. After that, deconvoluting the precession of the tracks, a spatial resolution of 90 μm is obained by averaging over all Micromegas at nominal beam intensity.

A.5.2.2 GEM Detectors

The GEM consists of a 50 μm thin Polyimide foil with Cu cladding on both sides. A large number of holes have been chemically etched on it using photolithography. On application of several hundreads of volts across the foil by inserting it between parallel plate electrodes of a

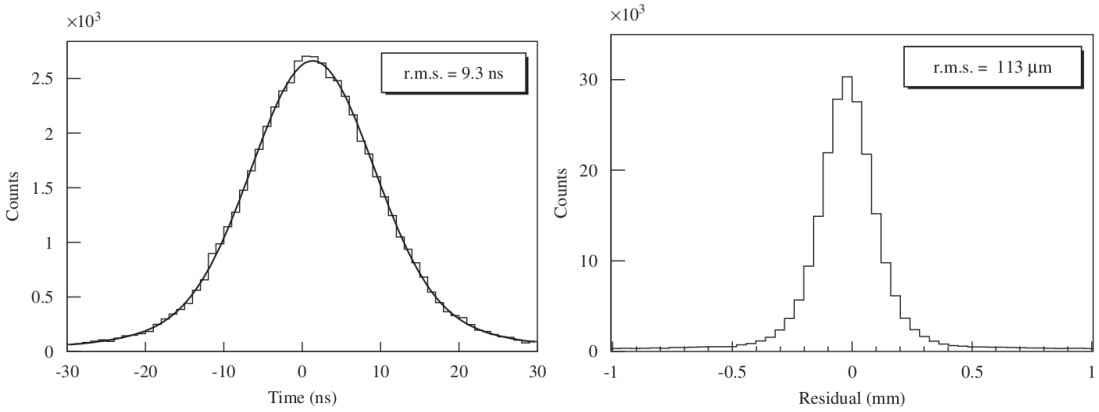

Figure A.15: Left: Distribution of the mean time measured by a Micromegas with respect to the track time for nominal intensity data. Right: Distribution of residuals of a Micromegas at high intensity. The r.m.s width is 113 μm to which the detector contributes 92 μm. Figures taken from [10]

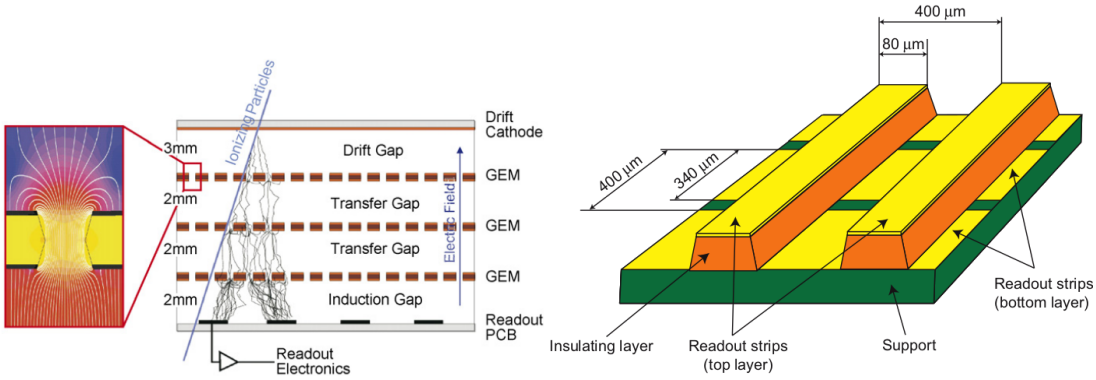

Figure A.16: Left: Triple GEM detector with its associated electric field configuration. Right: Two-dimensional readout structure of the GEMs. Figures taken from [10]

gas-filled chamber, avalanche multiplication of primary electrons is accomplished. Appropriate electric fields extract the electrons from the holes on the other side of the foil, and then guide them into the next amplification stage or to the readout anode. Fig.A.16 shows the working principle and the electric field configuration of a GEM.

The COMPASS GEM consists of three GEM amplification stages, stacked on top of each other, and separated by 2 mm height spacer grids. It consists of Ar/CO_2 $(70/30)$ gas mixture which is chosen for its large drift velocity, low diffusion, non-flammability, and non-polymerising properties.

The electron cloud emerging from the last GEM stage induces a fast signal on the readout anode. The latter is segmented in two sets of 768 strips with a pitch of 400 μm each, perpendicular to each other and separated by a thin insulating layer as seen in fig. A.16. The detector records two track projections with highly correlated amplitudes for each particle, and thus reduces multi-hit events amibguities. The spatial resolution can be seen in fig. A.17. It shows the distribution of residuals which is the difference along one corrdinate of expected track and measured cluster position, which is then plotted for all hits on one projection of a GEM detec-

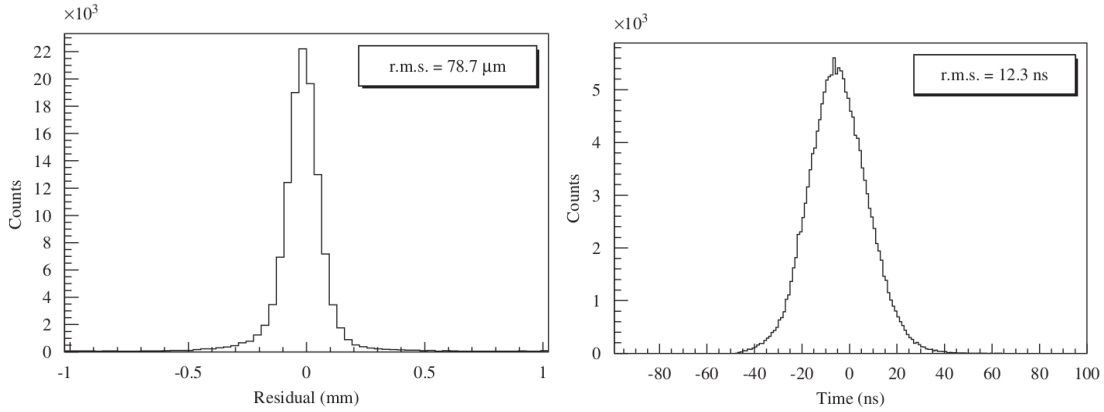

Figure A.17: Left: Residual distribution of one GEM projection in standard high intensity muon beam conditions. In this particular plane, the r.m.s width is 78.7 μm, out of which the detector contributes 66.4 μm. Right: Distribution of cluster time measured by a single GEM plane by sampling the analogue signal at 40 MHz, with respect to the track time. Figures taken from [10]

tor. After deconvolution of the track error, the resolution has an average value of 70 μm. The analog readout method also allows to extract time information by sampling the signal at three consecutive points in time. With the knowledge of the detector response to a minimum ionising potential, the hit time can be measured from the ratios of the three measured amplitudes. Using this method, an average time resolution of 12 ns is achieved for the GEM detectors for high intensity muon beam as shown in fig. A.17. For a better description, one can refer [191].

A.5.3 Large Area Tracker

A.5.3.1 Drift Chambers

Three identical Drift Chambers (DC) optimised for operations upstream of SM1, where the total particle flux is three times the flux on the downstream due to low-energy background which is bent away by the magnet are installed in the facility. One DC is installed upstream, and two DCs downstream of SM1. The three DCs have an active area of $180 \times 127\ cm^2$ that covers the whole acceptance of the SMC target magnet upstream as well as downstream of SM1.

Each DC is constructed out of eight layers of wires with four different inclinations: Vertical (X), horizontal (Y), and tilted by 20° (U), and -20° (V) with respect to the vertical direction. The tilt angles and the ordering of the planes ($XYUV$ along the beam) was selected to minimise the construction of fake tacks.

Each layer of wires is comprised of 176 *sensitive* wires of 20 μm diameter, alternated with a total of 177 *potential* wires with 100 μm diameter. These are enclosed by two Mylar® cathode foils of 25 μm thickness, coated with $\sim$ 10 μm graphite, which leads to a gas gap of 8 mm. Two consecutive layers of the same inclination are staggered by 3.5 mm (half a drift cell) in order to solve left-right ambiguities. During operation, the cathode foil is kept at -1700 V, the sensitive wires at 0 V, and the potential wires at 1700 V. The drift cell boundaries are defined

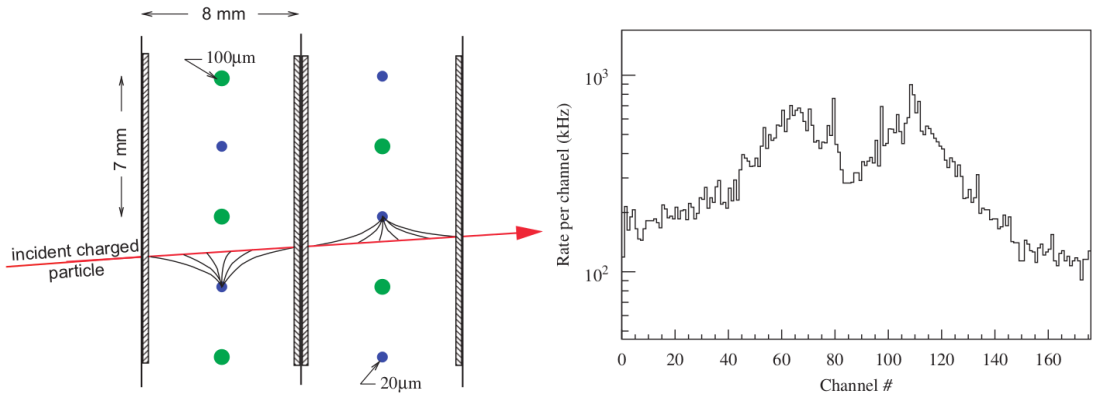

Figure A.18: Left: Drift cell geometry of the COMPASS Drift Chambers. Right: Hit rate versus wire number for one DC wire layer upstream of SM1 at nominal beam intensity with central zone deactivated. Figures taken from [10].

by the cathode foils, normal to the beam direction, and by two potential wires separated by 7 mm as shown in fig. A.18. The particle hit rate per wire at a distance of 15 cm from the beam reaches 800 kHz as shown in fig. **??**. Downstream of SM1, the maximum hit rate per wire comes down to 300 kHz. In order to avoid higher rates near the beam, a central dead zone of 30 cm diameter is implemented for all layers. This part is segmented from the whole cathode foil, and has an independent high voltage (HV) supply. During standard data taking, the central zone is deactivated by keeping the HV supply low, and hence decreasing the local efficiency. During alignment with low beam intensity, the dead zone is activated by setting HV to the nominal value of the potential wires, i.e., -1700 V.

The gas mixture of $Ar/C_2H_6/CF_4$ $(45/45/10)$ was chosen to ensure good spatial resolution, a linear time-vs-distance dependence (RT relation), minimisation of occupancy time, good efficiency, and a large HV plateau. Argon ensures high primary electron rate, C_2H_6 is used as a quencher, and CF_4 is used to increase drift velocity. Fig. A.19shows the RT relation for one layer of a DC, measured in low intensity beam. The spatial resolution is evaluated using the residuals of the fitted tracks for each wire layer. The residuals from two wire layers with same orientation are combined which allows us to separate the intrinsic layer resolution from the track fitting uncertainty. At nominal muon beam intensity, a resolution of 270 ± 20 μm was measured averaged over all layers and full active surface of DC as seen in fig A.19.

A.5.3.2 Straw Tube Chambers

Straw drift tubes are used for tracking of charged particles at large scattering angles (15-200 $mrad$) downstream of SM1.

They are made of two layers of thin plastic films. The inner layer is made of carbon loaded Kapton® foil with a thickness of 40 μm. The second layer consist of aluminised Kapton® foil of 12 μm thickness. The anode wires are made of gold-plated tungsten with 30 μm diameter, which are centered in the straw tubes by two end-plugs and four small plastic spacers positioned at intervals of 60 cm along each tube. The counting gas is supplied through the end-plugs and

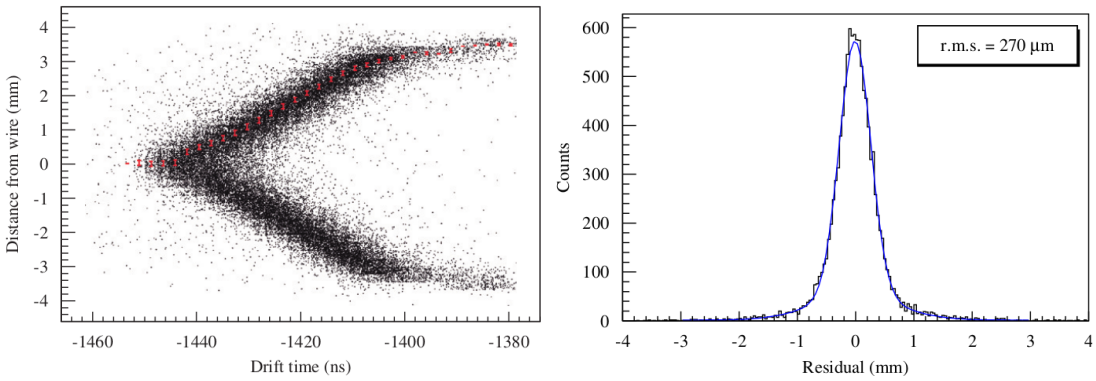

Figure A.19: Left: RT relation for one layer of a DC. Right: Residual distribution for a single DC layer (DC1 X) in high intensity beam. Figures taken from [10].

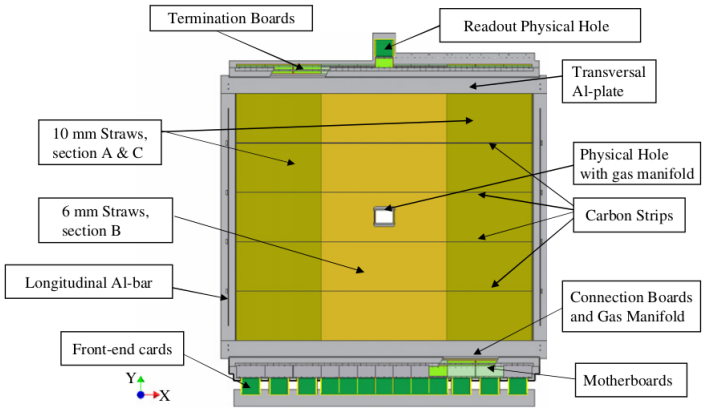

Figure A.20: Schematic view of a Straw Detector. Figure taken from [10]

a gas-manifold, which is integrated into the aluminium frame.

A total of 12440 straw tubes are brought together into 15 detectors. Each detector consists of two staggered layers of straws to resolve left-right ambiguity, they are glued together, and mounted onto an aluminium frame for stability. The detectors have an active area of 9 m^2 and is divided into three sections as shown in fig. A.20. The central part (section B) is close to the beam axis and is exposed to higher rates, and is made out of 190 long and 64 short straws per layer, with an outer diameter 6.14 mm, that forms a central dead zone of about 20×20 cm^2. It consist of a rectangular hole without material of about 20×10 cm^2 for the beam. The outer part, i.e., the section A and C, each have 96 straws with 9.65 mm outer diameter. A mixture of $Ar/CO_2/CF_4$ $(74/6/20)$ is used as a counting gas. The Straw Tubes operate at an HV of 1950 V.

One station consists of three detectors to measure three projections of a particle trajectory: one with vertical, one with horizontal, and one with inclined straw tubes. The inclined straw tube detector is rotated by 10° with respect to the vertical ones. The vertical and inclined straw detectors have the same geometry (called type X), while the horizontal one has a slightly different geometry.

The straw tubes increase lengthwise with humidity. The relative elongation was found to be

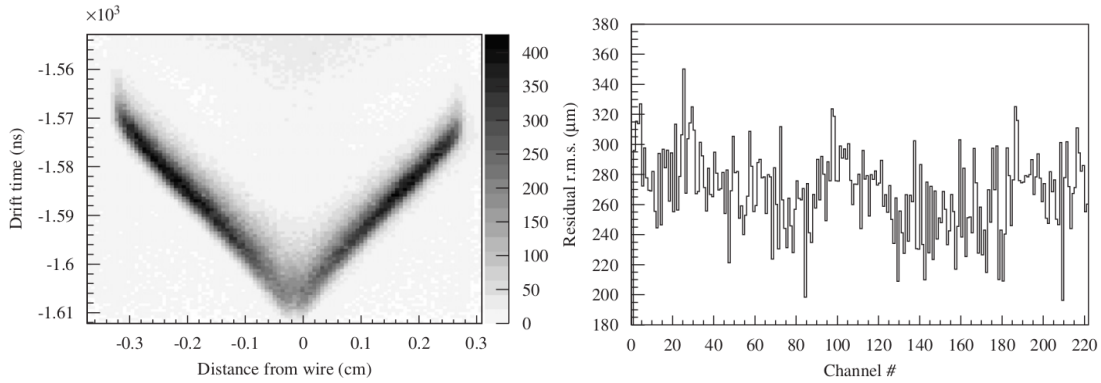

Figure A.21: Left: RT relation for a single 6 mm straw tube for particle tracks with the 160 GeV/c muon beam. Right: R.M.S widths of single-channel residual distributions versus channels number for all 6 mm straw tubes of one layer. Figures taken from [10].

$\sim 3 \times 10^{-5}$ for a 1 % humidity change that can result in increased tension on the frame, or even bending of the straws. In order to avoid this, the humidity is kept constant by surrounding each straw by a protective N_2 gas, enclosed by 12 μm thin Mylar® foils which are aluminised on both sides.

At nominal beam intensity, the relation between the measured drift times and the distance of the tracks to the anode wires were measured and is shown in fig. A.23 . Once the RT relation has been established, the resolution of a given straw can be determined from the R.M.S width of the distribution of the track residuals. Averaging over several layers of 6 mm straws, a mean value of 270 μm resolution is computed for one straw layer under nominal muon beam conditions as shown in fig. A.23.

A.5.3.3 Multiwire Proportional Chambers

At large radial distance to the beam, the tracking of particles in the SAS (Small Angle Spectrometer) is based on Multiwire Proportional Chambers (MWPCs). It consists of a total of 34 wire layers, which translates to 25000 detector channels. All layers have wire length of about 1 m with diameter of 20 μm and a wire pitch of 2 mm and anode/cathode gap of 8 mm.

COMPASS has three different types of MWPCs: Type-A, Type-A*, and Type-B. The Type-A detectors have three anode wire layers, one vertical (X) and two tilted by $\pm 10.14°$ with respect to the vertical axis (U, V) with an active area 178×120 cm^2. While Type-A* are similar to Type-A but has an additional horizontal wire layer (Y). On the other hand, Type-B detectors have only two wire layers, one vertical (X) and one tilted by $10.14°$ (U or V), with a smaller active area of 178×90 cm^2. All wire layers are enclosed from both sides by 10 μm thick graphite coated Mylar® cathode foils, which provides field symmetry and encloses the gas. It has a central dead zone of 16-22 mm diameter depending on the location of the chamber along the beam axis, and is realised by removing the graphite coating from the foils.

The MWPCs have a gas mixture of $Ar/CO_2/CF_4$ $(74/6/20)$. The CF_4 is fast gas crucial for

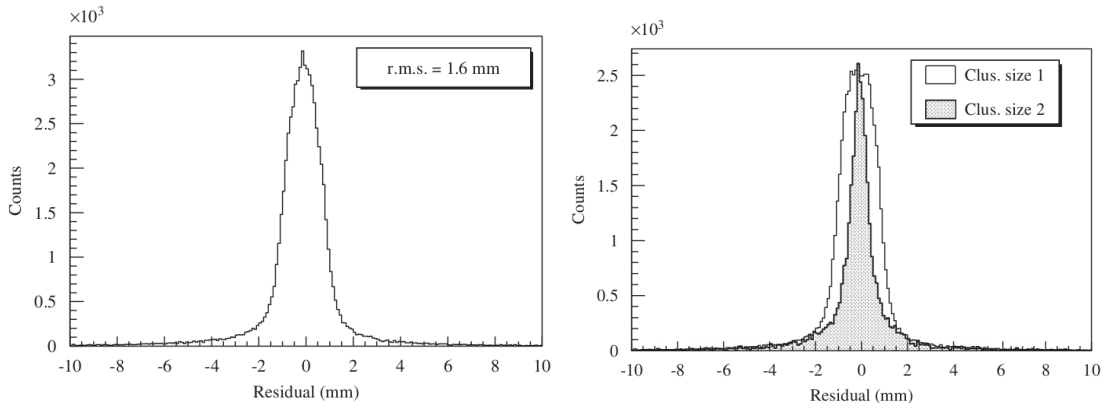

Figure A.22: Left: The MWPC residual distribution calculated as the difference between wire cluster postion and extrapolated track position along axis perpendicular to the wire layer. Right: MWPC residual distribution for cluster sizes 1 and 2. Figures taken from [10].

operation in high rate environment, with excessive dead time. An ionising particle may induce a signal on several neighbouring wires. The position of a hit is calculated from the wrighted mean of coordinates of the adjacent wires with signals (clusters). The residual distribution has an r.m.s width of 1.6 mm as shown in fig. The wire clusterisation improves spaital resolution as evident from the figure.

A.5.3.4 Large Area Drift Chamber

The tracking of charged particles deflected by a large-angle in the SAS is provided by a system of six large area DCs. Each chamber has an active area of $5 \times 2.5\ m^2$ consisting of four sensitive anode wire layers with a wire pitch of $4\ cm$, separated by layers of cathode wires with a pitch of 2 mm. All chambers have two planes, each plane consisting of two wire layers. Four of the chambers have X layers, coupled with Y (XY) type, V(+ 30° with respect to the X layer, XV type), or U (-30°, XU type) layers. The two other chambers are of $YV-$ type and $YU-$ type. The two wire layers with the same orientations in the same chamber are shifted by haf the wire pitch.

The anode wire has a diameter of 20 μm, while the cathode has 100 μm wires. The anode/cathode gap is 10 mm. The cathode wires have an inclination of 5° with respect to the vertical to provide better field homogeneity. The signal wires are separated by field wires of 200 μm diameter. A dead region with a diameter of 0.5 m and of 1 m is made in the centre of each layer of $XY-$ type, and of XV, XY, YV, and $YU-$ type chambers, respectively, as shown in fig. A.23 .

A gas mixture of $Ar/CF_4/CO_2$ $(85/10/5)$ is used to increase the drift velocity, which is important for track reconstruction. The signal wires are kept at an HV of 1925 V, while the field wire is at -800 V. The RT relation for one large area DC is shown in fig. A.23, and it has a mean spatial resolution of 0.5 mm.

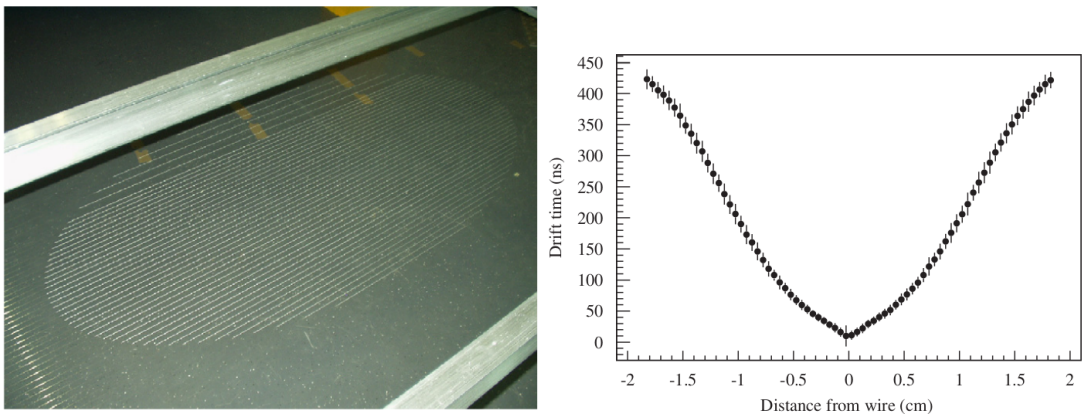

Figure A.23: Left: Large area Drift Chamber dead region. In the central part, the sensitive wire thickness is five times larger than in the active part. Right: RT relation for one Large Area Drift Chamber. Figures taken from [10].

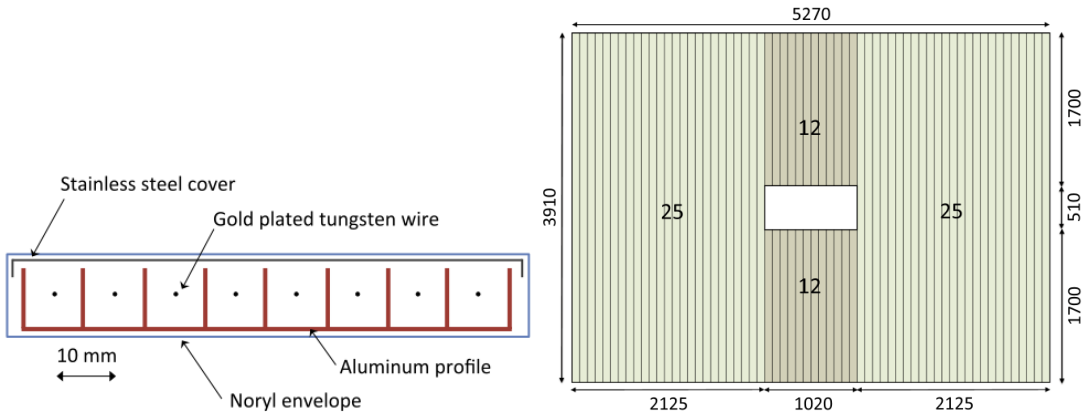

Figure A.24: Left: Mini Drift Tube module sketch. Right: Front view of an X-plane of the Rich Wall detector. The number of MDT modules in each sector is represented by the numbers outside, while the dimensions in mm are given by the numbers inside. Figures taken from [9].

A.5.3.5 Rich Wall

The Rich Wall detector was built to improve tracking accuracy at large angles ($150 < \theta < 300$ $mrad$) downstream of RICH-1. It is positioned between RICH-1 and ECAL1. The additional track points helps in better determination of large-angle particle trajectories through RICH-1, and hence helps in accuracy of Cherenkov Ring reconstruction.

The detector has dimensions of 5.27×3.91 m^2 with a central hole of 1.02×0.51 m^2. It is made out of eight planes of *Mini Drift Tubes (MDT)*. An MDT module consists of an eight-cell aluminium comb extrusion with a wall thickness of 0.44 mm, and covered on top with a 0.15 mm thick stainless steel foil. Gold plated tungsten wires of 50 μm diameter are strung in the centre of the cells. The wire pitch is 10 mm. A schematic representation of an MDT module can be seen in fig. A.24.

The gas mixture used is Ar/CO_2 $(70/30)$. The spatial resolution is shown in fig. A.25, and the improvement in Cherenkov Ring resolution is also shown in the same figure.

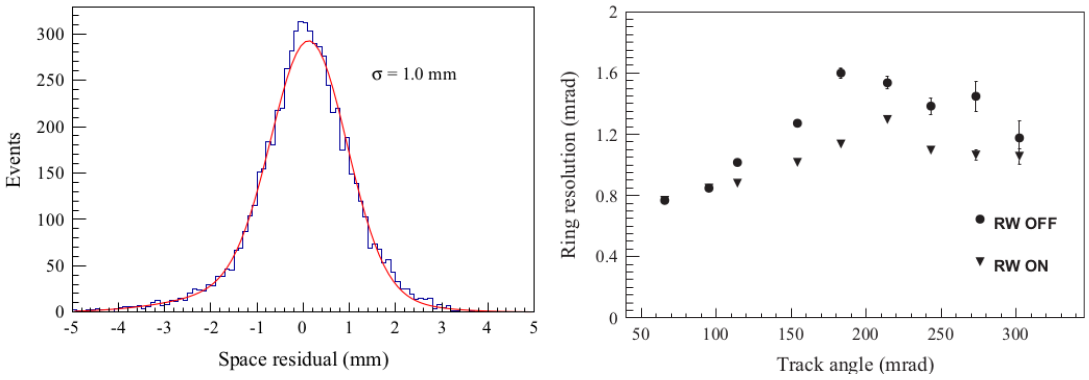

Figure A.25: Left: The Rich Wall residual distribution, i.e., the difference between reconstructed cluster position and extrapolated track position along the axis perpendicular to the wire layer is shown. The standard deviation is obtained by fitting a double gaussian. Right: Resolution of reconstructed Cherenkov rings for pions as a function of the track angle. The resolution improves by 20 % on an average. Figures taken from [9].

A.6 Particle Identification Detectors

The hadron physics programme requires the reconstruction of final states with charged and/or netural particles in a large angular bandwidth. Protons, charged pions and kaons, with momenta upto 50 GeV/c are identified in the RICH-1, and their energy is measured in two hadron calorimeters, HCAL1 and HCAL2. The photons emitted during interaction and decay photons are detected in two electromagnetic calorimeters, ECAL1 and ECAL2. The description of RICH-1 would be done in details in the following chapter. Hence, a brief description of calorimeteres are provided in the following sections.

A.6.1 Calorimeters

In each stages of the spectrometer, viz., LAS and SAS, the elctromagnetic calorimeter is upstream of the hadronic calorimeters (LAS: ECAL1, HCAL1, SAS: ECAL2, HCAL2). The hadronic calorimeters are sampling calorimeters, i.e., the materials for the generation of hadronic shower and scintillation by the particles of the shower are different. Meanwhile, the electromagnetic calorimeters are mostly homogeneous. To extend coverage at large angle, another electromagnetic calorimeter called the ECAL0 was installed downstream to the RPD in 2016-17 run.

A.6.1.1 Electromagnetic Calorimeter

The ECAL0 is constructed out of sampling *shashlik* structure. Each of them is mafe out of a lead/scintillator stack with the readout done by *Multipixel Avalanche Photo Diode (MAPD)* (15k pixels per mm^2).

The ECAL1 and ECAL2 are made of lead glass, where the EM shower is generated. The electrons and positrons from the shower emit Cherenkov light proportional to the energy deposited in each counter. There is a PMT which measures the light intensity at the end of each block.

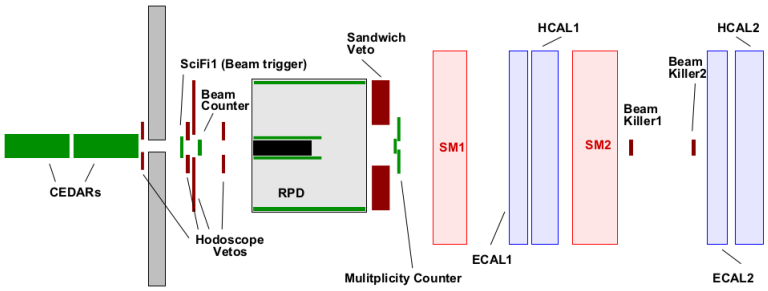

Figure A.26: Trigger elements in the Spectrometer. Figure taken from [9].

A.6.1.2 Hadronic Calorimeter

The hadronic calorimeters are built out of modules having a modular structure, as they are made out of alternating layers of iron and scintillators. The hadron shower is generated by the iron plates and it is detected by the scintillators. The hadronic calorimeters are larger in size than EM calorimeters, as the hadron showers are larger in size.

Each module of HCAL1 is composed of 40 layers of alternating iron and scintillators plates, which are 20 mm and 5 mm in thickness respectively, amounting to 4.8 nuclear interaction length. The HCAL2 is a matrix of 22×10 modules. Most of the modules consits of 36 plates of 25 mm thickness and inter-leaved with 5 mm thick scintillators. This makes the overall thickness to be 5 nuclear interaction length for the pions and 7 nuclear interaction length for the proton.

A.7 Trigger

A trigger system is required to select events that carries information for exclusive measurements. A fast response is necessary to provide a time reference for the readout of all detectors. A physics trigger can be broken down into three elements: selection of beam particles crossing the target, veto detectors for particles not produced in the target or outside spectrometer acceptance, and specific detector systems that takes in consideration particular physics case. The trigger elements can be visualised in fig.

A.7.1 Beam trigger

The beam trigger is used for the selection of incoming beam particles and to define event reference time. It also reduces the geometric acceptance of the beam in the transverse plane to match the target geometry. It consist of a coincidence of a SciFi with a beam counter.

A.7.2 Veto Detectors

A.7.2.1 Beam Killers

Beam killers are used to inhibit a trigger signal coming from non interacting beam particles. It introduces an angular cut-off of 0.97 $mrad$ with respect to the nominal beam axis. It consist of

two scintillating counters positioned along the beam axis. It reduces the trigger rate by half.

A.7.2.2 Sandwich Veto Detector

It is used to veto particles outside spectrometer angular acceptance and the RPD. It improves the purity of the physics trigger by 3.5 times.

A.7.2.3 Hodoscope Veto System

The *Hodoscope Veto System* remove events with large multiplicites in the RPD. For a detailed description, refer [10, 76].

A.7.3 Proton Trigger

The proton trigger is used to select events recoiling from the target. The RPD is used for target pointing and discrimination of protons from pions and delta-electrons with energy loss measurements in each RPD rings. The target pointing is executed by allowing for combinations in which hits in one scintillator of the inner ring is folllowed by a signal in one of the three corresponding outer ring scintillators as shown in fig. A.27

If a particle traversed the RPD, its energy losses in the inner and outer ring are highly correlated. This fact is used to reject electrons coming from the target as well as part of the low-energy pions. IN fig. A.27, we can see the energy losses for both protons and pions, for minumum and maximum polar angles of the RPD acceptance. The rejected area is defined using two levels of discriminator thresholds in both rings. The coincidence of low-threshold signals for upstream and downstream PMTs of the inner (outer) ring is denoted by $A_i^{Low}\ B_j^{Low}$, where i and j are respective scintillator elements. In a similar manner, the coincidence of two high-threshold signals is denoted by the superscript "High". The trigger logic for recoil prtons is given by

$$RPD = \bigvee_{i=1}^{12} A_{i,down}^{Low} \wedge \bigvee_{j=2i-1}^{2i+1} \left(A_i^{Low} B_j^{High} \vee A_i^{High} B_j^{Low} \right) \tag{A.2}$$

Here, the signals from the downstream PMTs of the inner ring denoted by $A_{i,down}^{low}$, are used to minimise the time jitter with respect to the beam trigger. The trigger logic rejects electrons that crosses both rings as well as pions that cross ring A but leaves few MeV in ring B. We can see the rejected region in fig. A.27 as the shaded region.

A.7.4 Multiplicity trigger

Multiplicity triggers were implemented to extend measurements to events with momentum transfer $-t$ smaller than $-t < 0.07\ GeV^2/c^2$ outside the acceptance of the proton trigger. It makes use of the multiplicity counter to estimate the charged-particle multiplicites in the beam region or tag events with at lease one track at large angles.

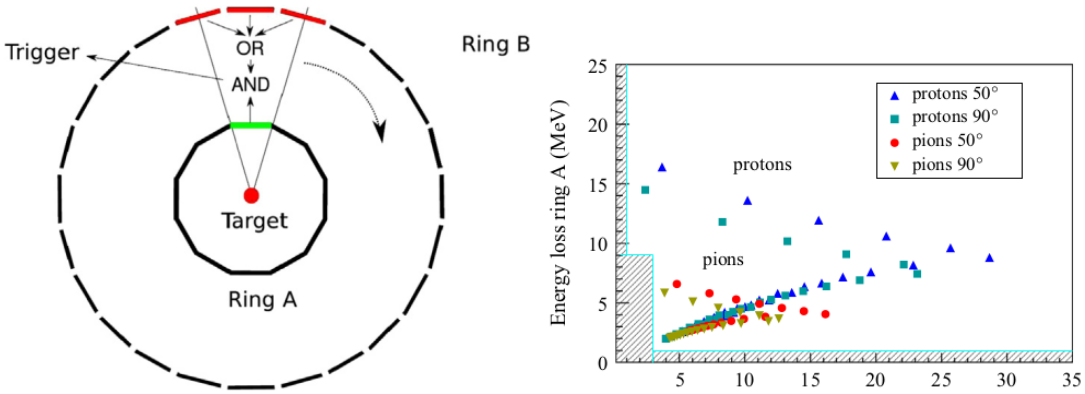

Figure A.27: Left: Target pointing logic description. Right: Energy loss correlation between protons and pions traversing ring A and stopping (or traversing) ring B of the RPD. Figures taken from [9].

A.7.5 Calorimeter Trigger

The calorimeter trigger is usd to select high-energy photons detected by ECAL2 within 12×12 cells, and eight cells surrounding the beam hole is excluded due to high rates.

A.8 Data Acquisition and Reconstruction

The *Data Acquistion (DAQ)* is responsible for the collection of data from the spectrometer. The logical steps for the DAQ are illustrated in fig. A.28. It is composed of several layers. The layer closest to the detectors have around 300k channels, and are called *Front End Electronics (FEE)*, which records signals directly from the detector and digitises them with the help of *Analog to Sampling Digital Converters (SADCs)* or *Time to Digital Converters (TDCs)*, depending on the detector type. The readout is done by *CATCH (COMPASS Accumulate, Transfer and Control Hardware)* or *GeSiCA (GEM and Silicon Control and Acquisition)* and *Gandalf concentrator* modules, based on VME standard and grouped into sub-events, that are read out, assembled and buffered by *FPGA (Field Programmable Gate Array)* based cards. The data taking is synchronised with the *Trigger Control System (TCS)*. The TCS trigger signals are transferred to all FEE via CATCH. The CATCH initialises all the FEE, the GeSiCA is similar but it has been optimised for GEMs and Silicon detectors and for RICH-1. Furthermore, the data is transferred to FPGA based multiplexers and then via a FPGA/Multiplexers switch it is connected to the 8 *Readout Buffer (ROB)* PCs, and are stored in 512 MB spill buffer cards. As part of further processing, the information of each sub-event in the ROB which doesn't contain the full information from all detectors, are transferred via three Gigabit Ethernet switches to the *Event Builder (EB)* computers. Each of the events are built by 12 EBs and then written to multiple 1 GB files (chunks) which are labelled by the run number and their associated chunk number. After which, the data is finally transferred to the *CERN central data recording facility (CASTOR)*.

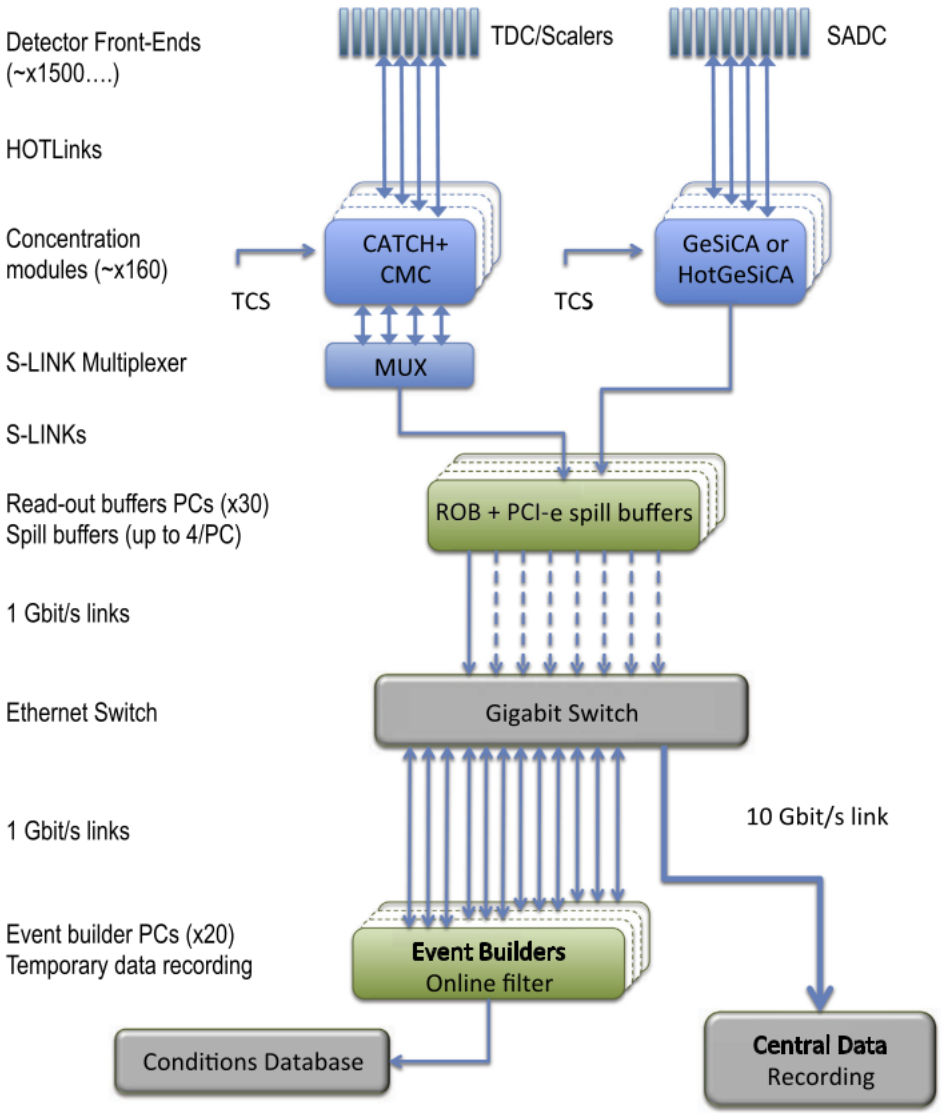

Figure A.28: Scheme of the COMPASS DAQ system. Data coming from the detectors are first digitised in the front-end cards and then merged in the concentrator modules, either CATCH or GeSiCA (HotGeSiCA). The data from the concentrator modules are first sent to the ROB and then transmitted to the EBs. The data are temporarily saved on disk, before being migrated to CASTOR. Figure taken from [9]

Appendix B

Ring Imaging Cherenkov Detector

B.1 Introduction

Primal to high energy particle physics is *Particle Identification (PID)* techniques. In the initial days of the field, several crude methods like bubble chambers, nuclear emlusion, and streamer chambers allowed one to kinematically reconstruct particle tracks and vertexes, in a pain staking and tedious process for e.g., as shown in fig. B.1. Couple with the time-consuming event reconstruction, it also had limited rate capability and triggerability, the latter two being of extreme relevance for modern day particle physics. To quantify this, we can look at the LHC with a centre-of-mass energy $\sqrt{s} = 13\ TeV$, the inelastic $p - p$ collisions have a cross-section of $\sim 78\ mbarn$ [3]. Considering nominal luminosity of the order of $10^{34}\ cm^{-2}s^{-1}$, the event rate measures to $7.8 \times 10^{8}\ Hz$. This has triggered the search for newer, faster and efficient PID techniques [203], out of which *Ring Imaging Cherenkov Detector (RICH)* [223] holds central relevance in almost all detector facilities.

One of the most important parameter to be determined throughout this thesis as we will see later in the analysis section, and also in general, in particle physics is that of the mass of the particle. However, mass of a subatomic particle cannot be determined directly, and rather we

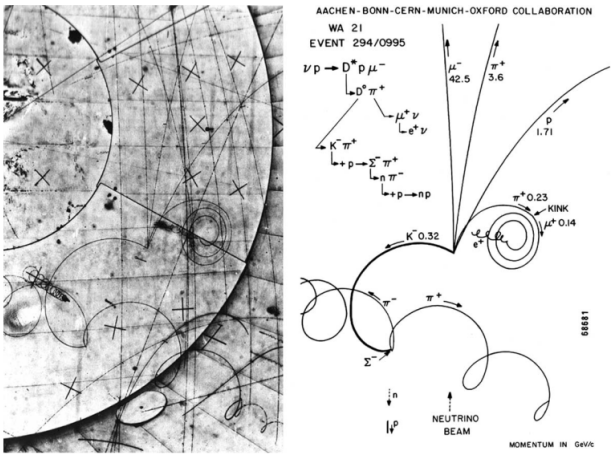

Figure B.1: Reconstruction of an event recorded with the BEBC hydrogen bubble chamber facility at CERN in 1978. Figure from [223].

have to rely on the particle momentum p, and the velocity normalised to the speed of light β, as both of them can be put in a trivial relativistic formula to give us the mass m of the particle as

$$m = \frac{p}{c\beta\gamma}, \tag{B.1}$$

where γ is the Lorentz factor. The value of momentum of a charged particle can be extracted by using a constant magnetic field which bends the tracks, and the curvature gives us a quantity called *Rigidity*, $R = p/Z$, where Z is the particle charge. The velocity can be measured in various ways: 1) Measuring the time-of-flight (TOF) of the charged particle over a known distance, ionisation energy loss, and through RICH detection techniques, as well as from transition radiation. Using error propagation formula for (B.1), we get

$$\left(\frac{dm}{m}\right)^2 = \left(\gamma^2\frac{d\beta}{\beta}\right)^2 + \left(\frac{dp}{p}\right). \tag{B.2}$$

It is evident from (B.2) that the proper estimation of the mass would be dependent on how accurately we measure the momentum and velocity. For argument purpose, if we consider the momentum to be accurately determined, and consider the second term in (B.2) to be negligible, we are left with the error on the velocity. The Lorentz factor coupled to the latter makes the situation more critical as this forces us to be more accurate in the velocity determination as we move up the momentum.

Assuming two particles with masses m_1, and m_2 that posseses the same momenta p, we can write using (B.1)

$$m_1^2 - m_2^2 = p^2\frac{\Delta\beta(\beta_1 + \beta_2)}{c^2(\beta_1 \cdot \beta_2)^2}, \tag{B.3}$$

where, $\Delta\beta = |\beta_1 - \beta_2|$. With the assumption that, $\beta_1, \beta_2 \sim \beta$, the above equation becomes

$$\frac{\Delta\beta}{\beta} = \frac{(m_1^2 - m_2^2)\cdot c^2}{2p^2}. \tag{B.4}$$

In fig. B.2, we can understand how the beta resolution decreases and hence become important with momentum. For an instance, above 40 GeV/c, if we want to separate pion and kaon, we need the beta resolution to be as good as of the order of 10^{-5}.

B.2 Theory of Cherenkov Radiation

When a charged particle travels through a refractive medium with a speed greater than the speed of light in that medium, it leads to the creation of an electromagnetic shock front in the medium, similar to a fighter jet breaching the sound barrier in the atmosphere. The shockwave leads to the emission of isotropic radiation called *Cherenkov Radiation* in the form of a cone. The mechanism can be visualised with the Huygens' construction of wavelets as show in fig. B.3. The Huygens' construction also helps us realise the classical radiation condition by trivial trigonometric relation, and given that each wavefront give rise to a coherent plane wave

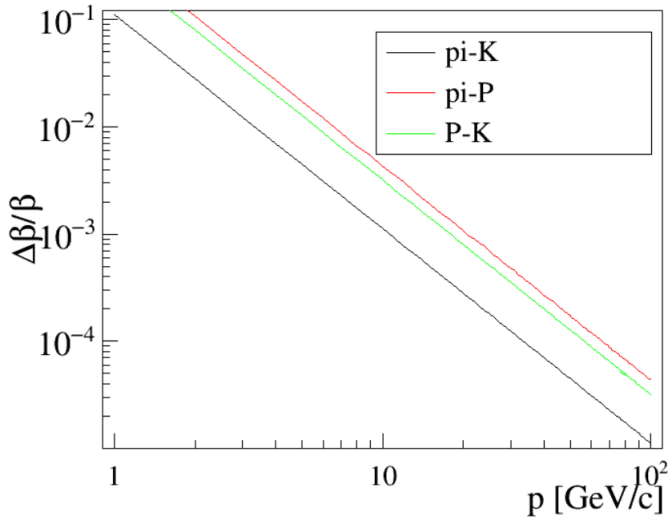

Figure B.2: Beta Resolution versus momentum. Figure taken from [102].

front. For a detailed description, refer [223]. However, the quantum theory gives us a more comprehensive picture, and is straightforward and hence explained below.

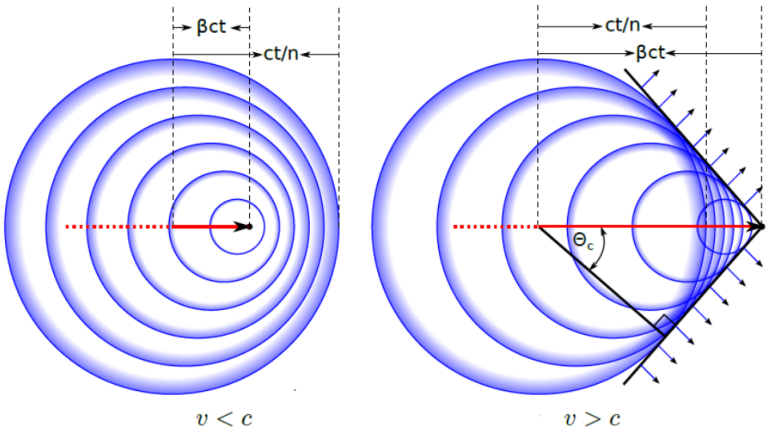

Figure B.3: Huygens' construction of Cherenkov Radiation. Figure from google.

B.2.1 Cherenkov Emission Angle

Consider a charged particle of rest mass m, travelling through a refractive medium of refractive index n with a constant velocity u. Assume that a certain point in its trajectory, it emits a photon of energy $\hbar\nu$ at an angle θ with respect to its original direction, where $\hbar$ is the planck's constant, and ν is the frequency of the photon. The ensuing energy loss of the particle leads to the particle changing its trajectory, and now it travels at an angle ϕ with respect to the original direction with velocity v, as shown in fig. B.4.

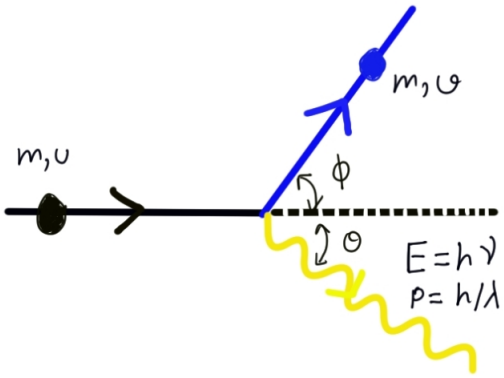

Figure B.4: A particle of mass travelling in a refractive medium with refractive index n. At some point in its trajectory, it emits a photon of energy $\hbar\nu$ and the particle itself scatters at an angle from the original direction.

Conservation of relativistic momentum in the longitudinal direction leads to

$$\frac{mv}{\sqrt{1-\frac{v^2}{c^2}}}\cos\phi + \frac{\hbar}{\lambda}\cos\theta = \frac{mu}{\sqrt{1-\frac{u^2}{c^2}}}, \tag{B.5}$$

where, λ is the wavelength of the wave associated with the emitted photon. The conservation of relativistic momentum in the transverse direction leads to

$$\frac{mv}{\sqrt{1-\frac{v^2}{c^2}}}\sin\phi = \frac{\hbar}{\lambda}\sin\theta. \tag{B.6}$$

Meanwhile, conservation of energy leads to

$$\frac{mc^2}{\sqrt{1-\frac{u^2}{c^2}}} = \frac{mc^2}{\sqrt{1-\frac{v^2}{c^2}}} + \hbar\nu. \tag{B.7}$$

Using the relation, $\nu = c/n\lambda$, and eliminating ϕ and v, we arrive at

$$\cos\theta = \frac{c}{nu} + \hbar\frac{\sqrt{1-\frac{u^2}{c^2}}\,(n^2-1)}{2mun^2\lambda}, \tag{B.8}$$

which can be repharased as

$$\cos\theta = \frac{1}{\beta n} + \left(\frac{\Lambda}{\lambda}\right)\left(\frac{n^2-1}{2n^2}\right), \tag{B.9}$$

where Λ is the *de Broglie* wavelength of the particle given by

$$\Lambda = \frac{\hbar\sqrt{1-\beta^2}}{mu} = \frac{\sqrt{1-\beta^2}}{\beta}\lambda_0, \tag{B.10}$$

where $\lambda_0 = \hbar/mc$ is the *Compton Wavelength* with a value of 0.024 $\mathring{A}$.

The second term in (B.9) is extremely small for all practical purposes. For e.g., for electrons with $\beta = 0.75$ in water, we can calculate $\Lambda \approx 0.021$ $\mathring{A}$, and $(\Lambda/\lambda) \approx 5 \times 10^{-6}$. So, the second term is suppressed and the dominating term is the classical radiation condition, $\cos\theta = 1/\beta n$.

B.2.2 Qualitative Description of the Cherenkov Process

To see the Cherenkov emission qualitatively, we can take the help of the fig. B.5. Consider this to be some refractive medium like water, and the approximately circular (spherical in 3-d) shape represents unpolarised atoms. In the ideal situation, there's a symmetry in the plane of the paper for any arbitrary point. In the left side, a negatively charged particle travels through the medium. At point P, it induces charges in the atoms which distorts its shape with the negative side facing away from the charged particle. Although locally, the symmetry breaks a little, the overall symmetry is conserved, and the dipoles generated cannot radiate electromagnetic waves coherently. However, in the right side, when the particle breaks the light speed barrier in the medium, the symmetry is broken axially (along the axis) about point P, the dipoles generated can radiate coherently and can give rise to a resultant field intensity at a given point at a distance.

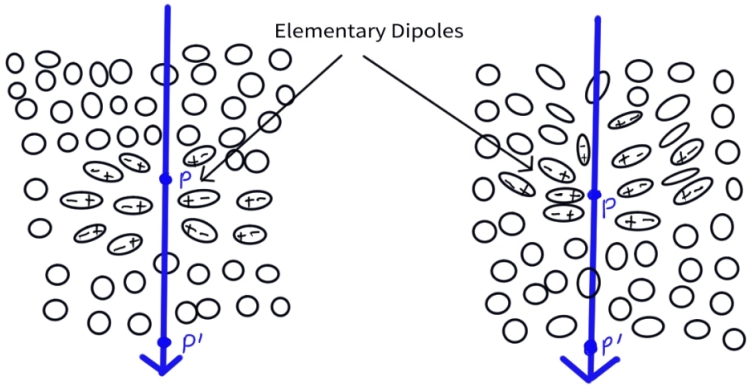

Figure B.5: The passage of a negatively charged particle in a refractive medium. At velocity lower than the speed of light, there is overall symmetry conservation. Breaching light speed barrier in the medium, results in a broken symmetry, and subsequent emission of coherent dipole radiation.

B.2.3 Cherenkov Energy Spectrum (Frank-Tamm Formula)

The *Frank-Tamm* formula gives us the Cherenkov radiation emitted at a given frequency when a charged particles travel through a refractive medium at superluminal velocity. The derivation of the relation relies on *Classical Electrodynamics* and one can refer [180] for relevant relations and notational clarity. The derivation relies on certain assumptions as illustrated in [183]:

- A continous media with a constant refractive index (or dielectric constant) is considered, and the microscopic structures are neglected
- At zeroth order, dispersion is neglected
- The chemical properties of the medium are unperturbed by the Cherenkov process

- The refractive medium is considered to be an isotropic dielectric with a macroscopic dielectric constant $\epsilon(\omega)$, and hence has zero conductivity and magnetic permeability $\mu = 1$.
- Multiple Coloumb scattering and ionisation processes are ignored, and the charged particle (electron in case of original Frank-Tamm derivation) is assumed to move with a constant velocity.
- the medium is considered to have no boundaries (hence no boundary effects), and the track length of the charged particle is considered to be infinite

We will determine the energy radiated in distant collisions, i.e, when the the impact parameter $b \leq a$, where a is the radius of the dielectric sphere. If we use the Fourier tansform for the vector potential $A_\mu(x)$, and source density $J_\mu(x)$, in the following general rule

$$F(\vec{x},t) = \frac{1}{(2\pi)^2}\int d^3k \int d\omega F(\vec{k},\omega)e^{i\vec{k}\cdot\vec{x}-i\omega t}, \tag{B.11}$$

we can show that the wave equations become

$$\begin{aligned}\left[k^2 - \frac{\omega^2}{c^2}\epsilon(\omega)\right]\Phi(\vec{k},\omega) &= \frac{4\pi}{\epsilon(\omega)}\rho(\vec{k},\omega),\\ \left[k^2 - \frac{\omega^2}{c^2}\epsilon(\omega)\right]\vec{A}(\vec{k},\omega) &= \frac{4\pi}{c}\vec{J}(\vec{k},\omega),\end{aligned} \tag{B.12}$$

where, $\rho(\vec{x},t)$, and $\Phi(\vec{k},w)$ are the charge density and scalar potential respectively. The charge and source density in coordinate space is given by

$$\begin{aligned}\rho(\vec{x},t) &= ze\delta(\vec{x}-\vec{v}t),\\ \vec{J}(\vec{x},t) &= \vec{v}\rho(\vec{x},t).\end{aligned} \tag{B.13}$$

The above equations can be Fourier transformed to give us the quantities in frequency-wave vector space as

$$\begin{aligned}\rho(\vec{k},\omega) &= \frac{ze}{2\pi}\delta(\omega-\vec{k}\cdot\vec{v}),\\ \vec{J}(\vec{k},\omega) &= \vec{v}\rho(\vec{k},\omega).\end{aligned} \tag{B.14}$$

Using (B.14) in (B.12), we can find out that the potentials are given by

$$\begin{aligned}\Phi(\vec{k},\omega) &= \frac{2ze}{\epsilon(\omega)}\frac{\delta(\omega-\vec{k}\cdot\vec{v})}{k^2-\frac{\omega^2}{c^2}\epsilon(\omega)},\\ \vec{A}(\vec{k},\omega) &= \epsilon(\omega)\frac{\vec{v}}{c}\Phi(\vec{k},\omega).\end{aligned} \tag{B.15}$$

If we write the electromagnetic fields in terms of the potentials, and do a Fourier transform, we get

$$\begin{aligned}\vec{E}(\vec{k},\omega) &= i\left[\frac{\omega\epsilon(\omega)}{c}\frac{v}{c}-\vec{k}\right]\Phi(\vec{k},\omega),\\ \vec{B}(\vec{k},\omega) &= i\epsilon(\omega)\vec{k}\times\frac{v}{c}\Phi(\vec{k},\omega).\end{aligned} \tag{B.16}$$

The energy loss by an electron in an atom at impact parameter b is given by

$$\Delta E = -e\int_{-\infty}^{\infty} \vec{v}\cdot\vec{E}dt = 2e\mathrm{Re}\int_{0}^{\infty} i\omega\vec{x}(\omega)\cdot\vec{E}^{*}(\omega)d\omega. \tag{B.17}$$

To find the electric field at a certain coordinate point $(0, b, 0)$, we can perform the inverse Fourier transform to go back to coordinate space as

$$\vec{E}(\omega) = \frac{1}{(2\pi)^{3/2}}\int d^3k\vec{E}(\vec{k},\omega)e^{ibk_2}. \tag{B.18}$$

Note that in the above equation, that we have only inverse Fourier transformed in one variable ($\vec{k}\rightarrow\vec{x}$), and we still have the field in frequency domain. Also, only the k_2 component of the wave vector $\vec{k}$ survives because we take the special coordinate $(0, b, 0)$, where b is the impact parameter as shown in fig. B.6

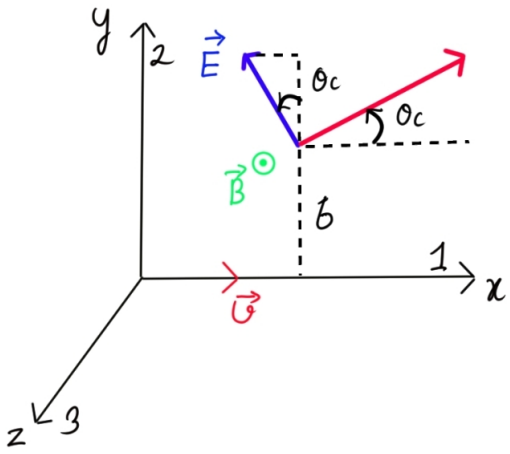

Figure B.6: The coordinate system considered for the Frank-Tamm formula

Now, inserting the equation (B.15) in (B.16) and using them in (B.18), and after that taking the component of $\vec{E}$ along the direction of velocity $\vec{v}$, we get

$$E_1(\omega) = \frac{2ize}{\epsilon(\omega)(2\pi)^{3/2}}\int d^3k e^{ibk_2}\left[\frac{\omega\epsilon(\omega)v}{c^2} - k_1\right]\frac{\delta(\omega - vk_1)}{k^2 - \frac{\omega^2}{c^2}\epsilon(\omega)}. \tag{B.19}$$

The integral over dk_1 is trivial because of the delta function and it gives us

$$E_1(\omega) = -\frac{2ize\omega}{(2\pi)^{3/2}v^2}\left[\frac{1}{\epsilon(\omega)} - \beta^2\right]\int_{-\infty}^{\infty} dk_2 e^{ibk_2}\int_{-\infty}^{\infty}\frac{dk_3}{k_2^2 + k_3^2 + \lambda^2}, \tag{B.20}$$

where,

$$\lambda^2 = \frac{\omega^2}{v^2} - \frac{\omega^2}{c^2}\epsilon(\omega) = \frac{\omega^2}{v^2}\left[1 - \beta^2\epsilon(\omega)\right]. \tag{B.21}$$

The integral over dk_3 yields the value $\pi/(\lambda^2 + k_2^2)^{1/2}$, so we can write $E_1(\omega)$ as

$$E_1(\omega) = -\frac{ize\omega}{\sqrt{2\pi}v^2}\left[\frac{1}{\epsilon(\omega)} - \beta^2\right]\int_{-\infty}^{\infty}\frac{e^{ibk_2}}{(\lambda^2 + k_2^2)^{1/2}}dk_2. \tag{B.22}$$

The remaining integral over k_2 is a representation of a *Modified Bessel function (Macdonald)* [66], which gives the result,

$$E_1(\omega) = -\frac{ize\omega}{v^2}\left(\frac{2}{\pi}\right)^{1/2}\left[\frac{1}{\epsilon(\omega)} - \beta^2\right]K_0(\lambda b). \tag{B.23}$$

Similarly, we can show that the other fields are given as

$$\begin{aligned} E_2(\omega) &= \frac{ze}{v}\left(\frac{2}{\pi}\right)^{1/2}\frac{\lambda}{\epsilon(\omega)}K_1(\lambda b), \\ B_3(\omega) &= \epsilon(\omega)\beta E_2(\omega). \end{aligned} \tag{B.24}$$

We now consider that the impact parameter to be much greater than the radius of the dielectric sphere, i.e., $b \gg a$, and consequently $|\lambda b| \gg 1$. This is the *Cherenkov Regime*, and here we can approximate the Bessel functions with their asymptotic forms. Hence, the fields in (B.23) and (B.24) become,

$$\begin{aligned} E_1(\omega, b) &\to i\frac{ze\omega}{c^2}\left[1 - \frac{1}{\beta^2\epsilon(\omega)}\right]\frac{e^{-\lambda b}}{\lambda b}, \\ E_2(\omega, b) &\to \frac{ze}{v\epsilon(\omega)}\sqrt{\frac{\lambda}{b}}e^{-\lambda b}, \\ B_3(\omega, b) &\to \beta\epsilon(\omega)E_2(\omega, b). \end{aligned} \tag{B.25}$$

To find the energy transferred to the atom at impact parameter b, we use the generalisation of (B.17)

$$\Delta E(b) = 2e\sum_j f_j \mathbf{Re}\int_0^\infty i\omega\vec{x}_j(\omega)\cdot\vec{E}^*(\omega)d\omega, \tag{B.26}$$

where $\vec{x}_j(\omega)$ is the amplitude of the jth type of electron in the atom. We express the sum of the dipole moments in terms of the molecular polarisability and the dielectric constant as:

$$-e\sum_j f_j\vec{x}_j(\omega) = \frac{1}{4\pi N}\left[\epsilon(\omega) - 1\right]\vec{E}(\omega), \tag{B.27}$$

where N is the number of atoms per unit volume. Thus the energy transfer can be expressed as

$$\Delta E(b) = \frac{1}{2\pi N}\mathbf{Re}\int_0^\infty -i\omega\epsilon(\omega)|\vec{E}(\omega)|^2 d\omega. \tag{B.28}$$

Hence the energy loss per unit distance in collisions with impact parameter $b \geq a$ is given by

$$\left(\frac{dE}{dx}\right)_{b>a} = 2\pi N\int_a^\infty \Delta E(b)bdb. \tag{B.29}$$

If the fields (B.23) and (B.24) are inserted into (B.28) and (B.29), we find

$$\left(\frac{dE}{dx}\right)_{b>a} = \frac{2}{\pi}\frac{(ze)^2}{v^2}\mathbf{Re}\int_0^\infty i\omega\lambda^* aK_1(\lambda^* a)K_0(\lambda a)\left(\frac{1}{\epsilon(\omega)} - \beta^2\right)d\omega, \tag{B.30}$$

where λ is given by (B.21). Alternatively, we can also consider a cylindrical cross-section of radius a around the path of the incident particle. Then, the electromagnetic energy flow can be found by conservation of energy, which gives the energy lost per unit time to be

$$\left(\frac{dE}{dx}\right)_{b>a} = \frac{1}{v}\frac{dE}{dt} = -\frac{c}{4\pi v}\int_{-\infty}^{\infty} 2\pi a B_3 E_1 dx. \tag{B.31}$$

Using, $dx = vdt$, we get

$$\left(\frac{dE}{dx}\right)_{b>a} = -\frac{ca}{2}\int_{-\infty}^{\infty} B_3(t)E_1(t)dt. \tag{B.32}$$

Fourier transforming the above to convert into a frequency integral yields

$$\left(\frac{dE}{dx}\right)_{b>a} = -ca\text{Re}\int_{0}^{\infty} B_3^*(\omega)E_1(\omega)d\omega. \tag{B.33}$$

Using (B.25) in (B.33) gives us for the integrand

$$-caB_3^*E_1 \to \frac{z^2e^2}{c^2}\left(-i\sqrt{\frac{\lambda^*}{\lambda}}\right)\omega\left[1-\frac{1}{\beta^2\epsilon(\omega)}\right]e^{-(\lambda+\lambda^*)a}. \tag{B.34}$$

Taking the real part of the above integrand, and then intergrating it over frequencies, yields the energy deposited far from the path of the particle. If λ has a positive real part, the exponential factor above would cause the expression to vanish rapidly at large distances. All the energy is deposited near the path. Only when λ is purely imaginary, this fact isn't true. In that case, the exponential becomes unity, and hence the dependence of the expression on 'a' vanishes, which further means that some of the energy escapes as radiation.

From (B.21), we can see that λ can be purely imaginary if $\epsilon(\omega)$ is real (no absorption) and $\beta^2\epsilon(\omega) > 1$. In reality, there would be mild absorption but for mathematical simplicity, we can consider $\epsilon(\omega)$ to be essentially real. We can write the condition, $\beta^2\epsilon(\omega)$ in a more convenient form as

$$v > \frac{c}{\sqrt{\epsilon(\omega)}}, \tag{B.35}$$

which shows that the speed of the particle must exceed the phase velocity of the electromagnetic fields at frequency ω in order to realise the emission of Cherenkov radiation of that frequency.

Again, from (B.21), if $\beta^2\epsilon(\omega) > 1$, and assuming that $\epsilon(\omega)$ has an infinitesimal positive imaginary part when $\omega > 0$, we have

$$\lambda = -i|\lambda| \quad \text{for} \quad \beta^2\epsilon > 1, \tag{B.36}$$

which means that $(\lambda^*/\lambda)^{1/2} = i$, and that turns (B.34) real and independent of 'a'. Then the (B.33) represents the energy radiated by Cherenkov radiation per unit distance along the path

of the particle as

$$\left(\frac{dE}{dx}\right) = \frac{(ze)^2}{c^2}\int_{\epsilon(\omega)>(1/\beta^2)} \omega\left(1 - \frac{1}{\beta^2\epsilon(\omega)}\right)d\omega. \tag{B.37}$$

The Cherenkov radiation is emitted in a region below anamolous dispersion, where $\epsilon(\omega) > \beta^{-2}$ as indicated in fig. B.7

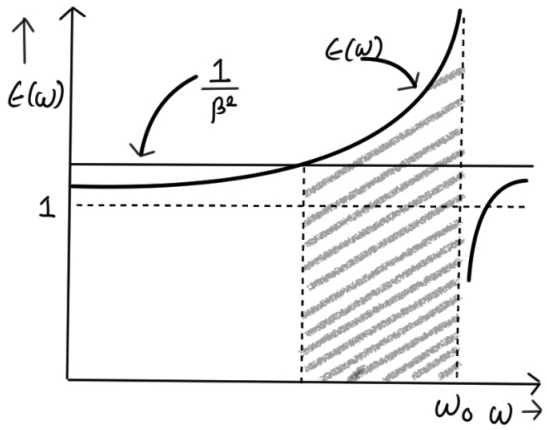

Figure B.7: Cherenkov band shown in shaded region

We can also realise the classical Cherenkov emission formula by noticing in fig. B.6 that

$$\tan\theta_C = -\frac{E_1}{E_2}. \tag{B.38}$$

From the asymptotic fields in (B.25), we arrive at

$$\cos\theta_C = \frac{1}{\beta\sqrt{\epsilon(\omega)}} = \frac{1}{\beta n(\omega)}. \tag{B.39}$$

For being complete, we also note that the *Frank-Tamm* relation (B.37) can be realised in a double-differential fashion, which gives us the differential energy radiation per unit length of a charged particle moving at superluminal speed in a medium as

$$\frac{d^2E}{dxd\omega} = \left(\frac{Ze}{c}\right)^2 \omega\left(1 - \frac{1}{\beta^2 n^2(\omega)}\right). \tag{B.40}$$

The number of photons produced by the charged particle can be obtained from the above equation, as a function of radiated photon wavelength ($\omega\lambda = 2\pi c/n(\lambda)$) as [223]

$$N = 2\pi LZ^2\alpha\int_{\beta n>1}\left(1 - \left(\frac{\beta_t(\lambda)}{\beta}\right)^2\right)\frac{d\lambda}{\lambda^2}, \tag{B.41}$$

where $\beta_t = 1/n(\lambda)$, and α is the fine structure constant. The particle traverses a distance L in the dielectric medium and has a photon wavelength λ. We can simplify the expression to write the number of emitted photons in $1cm$ of length in the spectral range of $1\ eV$ by a particle of

charge Ze with a $\beta \cong 1$ as

$$N(\text{cm}^{-1}\text{eV}^{-1}) \sim 370Z^2\left(1 - \frac{1}{n^2}\right). \tag{B.42}$$

From the above equation, we can derive the following conclusions,

- Cherenkov radiation causes a loss of energy at a rate of approximately keV/cm.
- The amount of Cherenkov radiation emitted is directly proportional to the square of the particle's charge. Eq. (B.41) shows that the particle charge can be generalized to Ze for particles with more than one electronic charge. The mass of the particle, however, does not affect the amount of Cherenkov radiation produced.
- The photon yield per unit wavelength interval $d\lambda$ is proportional to $d\lambda/\lambda^2$, which implies that most photons are emitted in the UV region.
- The number of photons emitted per unit length and per unit frequency remains constant.

B.2.4 Velocity Measurement from Cherenkov Angle

To construct a detector that measures the velocity of the particle, we can take help of the Cherenkov angle, in the following manner [102]

$$\begin{aligned}
\cos\theta_C &= \frac{1}{n\beta}, \\
\beta = \frac{p}{E} &= \frac{p}{\sqrt{p^2+m^2}}, \\
\cos\theta_C &= \frac{\sqrt{p^2+m^2}}{np}, \\
\Rightarrow m^2 &= p^2\left(n^2\cos^2\theta_C - 1\right).
\end{aligned} \tag{B.43}$$

We can further show that the error in velocity determination is given by

$$\left(\frac{\sigma_\beta}{\beta}\right)^2 = \left(\tan\theta_C\sigma_{\theta_C}\right)^2 + \left(\frac{\sigma_n}{n}\right)^2. \tag{B.44}$$

This error has irreducible parts since the refractive index of the gas is a function of temperature, pressure and photon wavelength. The latter fact is also important for the Geant4 simulation of the RICH detector that I would describe in the successive chapter. The error estimation can be done by extracting values of the refractive index at different temperatures and pressure, and interpolating it. The chromatic aberration of the refracting medium is quantified by the 2nd term in (B.44), σ_n/n, which is due to the variation of refractive index with the frequency of light, and is usually what determines the detector performance. In a small interval $\Delta\theta$, with a corresponding variation Δn, we can assume that the spread in Cherenkov angle due to dispersion is given by

$$\Delta\theta = \frac{\Delta n}{n\tan\theta}. \tag{B.45}$$

An effective way to reduce chromatic aberration is by constructing the detector to operate in the visible band. For an instance, in the case of a gas detector, the chromatic dispersion reduces by a factor of two in the visible region as compared to that of UV.

In a RICH detector, each of the photoelectrons that are detected offers a separate measurement. Hence, for N_{pe} photoelectrons, the Cherenkov angle resolution can be improved by minimising σ_θ in the single-photoelectron angle measurement and maximising the number of photoelectrons as

$$\sigma_{\theta_C} = \frac{\sigma_\theta}{\sqrt{N_{pe}}}. \tag{B.46}$$

For light gases, the refractive index is defined as $n-1$, which gives us its units in ppm. In the error estimation of the mass, we can ignore contributions of the order of $\sim 10^{-6}$, which yields the following expression [102]

$$\left(\frac{\sigma_{m^2}}{m^2}\right)^2 = \left(2m^2\frac{\sigma_p}{p}\right)^2 + \left(p^2\frac{2\theta_C\sigma_{\theta_C}}{(n-1)+1}\right)^2 + \left[\left(2p^2-(p\theta_C)^2\right)\frac{\sigma_{(n-1)}}{[(n-1)+1]^2}\right]^2. \tag{B.47}$$

The above expression shows that the mass resolution deteriorates with increasing momentum.

A RICH detector must take into account the transparency of the medium, and the photon detector inefficiences to reduce the losses in the number of detectable Cherenkov photons. Furthermore, the Cherenkov radiation is lineraly polarised with its electric vector lying in the plane defined by the particle and the photon direction as shown in fig. B.8. So, we must take in consideration the reflection losses, as well as ensure the the material is fully isotropic to polarised light.

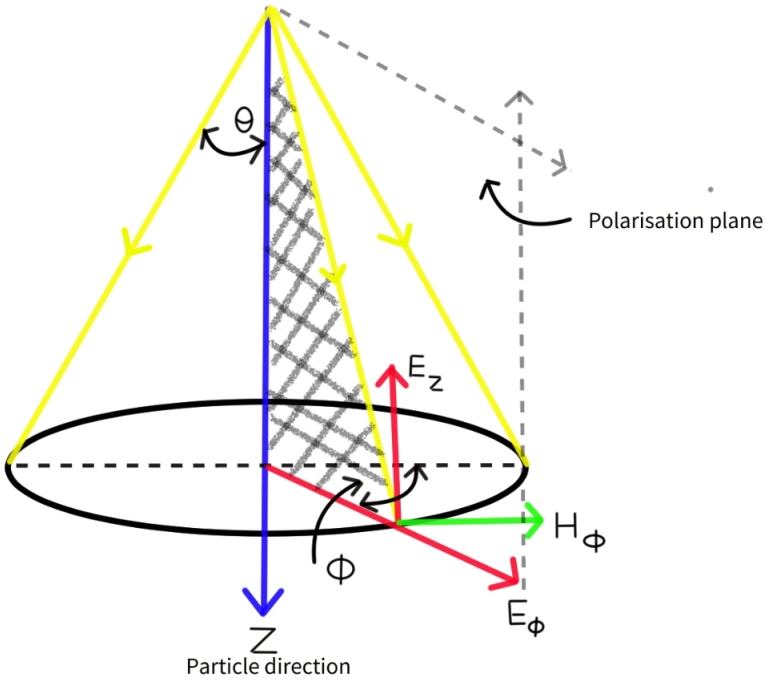

Figure B.8: Schematic representation of the Cherenkov light polarisation vectors. The electric field vector lies in the polarisation plane.

If we consider the case, where the Cherenkov photons are emitted in a frequency range where the refractive index is more or less constant away from the absorption bands, the resulting number of photoelectrons can N_{pe} can be written as

$$N_{pe} = N_0 L \sin^2 \theta_C, \tag{B.48}$$

where N_0 is called the *figure of merit* and is defined as

$$N_0 = \frac{2\pi\alpha}{h} \int \varepsilon \cdot \mathrm{QE} \cdot \mathrm{T} \cdot \mathrm{R} \cdot dE, \tag{B.49}$$

where QE is the photon detector quantum efficiency, ε is the single-electron detection efficiency, T is the total transmission of radiator and windows, and R is the mirror reflectivity. The lower limit of the integral is given by the photoionisation threshold and the top limit by the medium transparency. The perfomance of the detector scales with N_0. For, $\beta \to 1$, the Cherenkov angle tends to the asymptotic value θ_{max}, which is related to the threshold $\gamma_t = n/\sqrt{(n^2-1)}$ as

$$\sin^2 \theta_{max} = \frac{1}{\gamma_t}, \tag{B.50}$$

with a maximum expected number of detected Cherenkov photons given by

$$N_{max} = \frac{N_0 L}{\gamma_t^2}. \tag{B.51}$$

If we consider the fraction of Cherenkov photons at a given angle θ over the maximum yield, we get

$$\frac{N}{N_{max}} = \frac{\sin^2 \theta}{\sin^2 \theta_{max}}. \tag{B.52}$$

In the case of gas radiators, we find that

$$\frac{\sin^2 \theta}{\sin^2 \theta_{max}} \cong \frac{\theta}{\theta_{max}} \cong 1 - \frac{p_{th}^2}{p^2}, \tag{B.53}$$

where p and p_{th} are the actual particle's momentum and the threshold momentum for Cherenkov emission.

B.2.5 Upper Momentum limit for Separation of Two Particles

Let us consider two particles with masses m_1 and m_2. Then we can write the upper momentum limit $p_{up_{1,2}}$ for separation of the two particles. To accomplish that, we note the relation, $\beta = 1/n\cos\theta$, which we insert in (B.4). Since, we can derivate, $\Delta\beta = (\sin\theta\Delta\theta)/n\cos^2\theta$, we get,

$$\frac{\Delta\beta}{\beta} = \tan\theta\Delta\theta = \frac{\Delta m^2}{2p_{up_{1,2}}^2}. \tag{B.54}$$

So, we can express $p_{up_{1,2}}$ as

$$p_{up_{1,2}} = \left(\frac{\Delta m^2}{2\Delta\theta \tan\theta} \right)^{1/2} . \tag{B.55}$$

Defining the separation power in number of standard deviations such that $\Delta\theta = n_\sigma \sigma_\theta / \sqrt{N}$, we get,

$$p_{up_{1,2}} = \left(\frac{\Delta m^2 \sqrt{N}}{2 n_\sigma \sigma_\theta \tan\theta} \right) . \tag{B.56}$$

A well-designed detector aims to maximize the value of the upper momentum, given fixed values of n_σ, which are determined by the requirements for particle separation and contamination. The equation above indicates that the highest limit of momentum can be achieved by increasing N_0 and decreasing σ_θ. These two parameters are related and can be optimized by designing detectors that work in the visible light range. In fact, detectors that operate in this range offer advantages in terms of both operational efficiency and performance. This is because the figure of merit for the detector is higher at longer wavelengths due to the wider bandwidth for the relevant photoelectron yield and the angular uncertainty for a single photon is reduced due to the lower chromatic aberrations of materials in the visible region. On the other hand, the minimum limit of momentum is determined by the reduction in the number of detected photons as the momentum approaches the threshold, which has a direct impact on the efficiency of pattern recognition.

B.3 COMPASS-AMBER RICH-1

COMPASS-AMBER RICH-1 is a Ring Imaging Cherenkov Detector that uses a focusing technique with a spherical mirror (for RICH without focusing technique like the one in AMS-02 was discussed in a previous chapter [97], additionally one can also refer [224] for Belle-II aerogel RICH, as well as [165]). The RICH-1 has a 3 m long C_4F_{10} radiator [40], 21 m^2 VUV (Very Ultra-Violet) reflective mirror [41] system and 5.6 m^2 active detector surface. It is capable of identifying pions, kaons, and protons upto 55 GeV/c, and it is located in the first stage of the COMPASS-AMBER spectrometer.

B.3.1 RICH Vessel and the Radiator Gas

The RICH vessel is an aluminium structure, and has a length of 3 m, a width of 6 m and a height of 5 m. The size of the vessel can be appreciated in fig. B.9 which shows it being transported to the spectrometer hall. The front and back windows must withstand radiator gas hydrostatic pressure while minimizing material usage and staying within the spectrometer acceptance range. They are made up of two aluminum foils and a layer of rigid foam, creating a total material budget of 2% X_0. However, in the central region where the beam passes through, their material budget is reduced to 0.6% X_0 each.

Figure B.9: Transporting the RICH vessel in the 888 spectrometer hall at CERN

To minimize the amount of material in the beam region (which had more than 10% X_0 from the radiator gas) and to protect the RICH from the Cherenkov photons generated by the beam particles, a cylindrical pipe with a 100 mm diameter has been put in place and filled with helium. The original beam pipe was made of 150 μm thick stainless steel but was replaced in 2012 with a lighter pipe made of four layers of metalized BoPET (25 μm BoPET + 0.2 μm Al) as shown in fig.B.10. The new pipe, along with the helium, contributes 0.08% X_0 to the total material budget for beam particles (plus 0.06% due to helium).

Figure B.10: Beam pipe inside the RICH Vessel. Picture credits: [131]

However, for our physics requirement, the phase-space to explore anti-protons increases by a significant amount with the removal of the Beam pipe. As such, before data taking, a decision was made for the removal of beam pipe. The original beam pipe removal can be seen in fig. B.11.

The RICH-1 radiator gas was chosen to be C_4F_{10}, which is the heaviest fluorocarbon in gaseous phase at STP, in order to ensure low Cherenkov thresholds for different particle types (2.5, 9, 17 GeV/c for pions, kaons, and protons respectively) while maintaining low chromatic dispersion. The gas is kept at atmospheric pressure to prevent excessive stress on the vessel windows, with

Figure B.11: The beam pipe was removed in April, 2023 before the commencement of anti-proton XS data taking. The beam pipe can be seen lying in one of the ridges of the supporting structure below. The hexagonal structures are the VUV mirror, and the reflection of the beam hole can be seen in it towards the top-right of the picture.

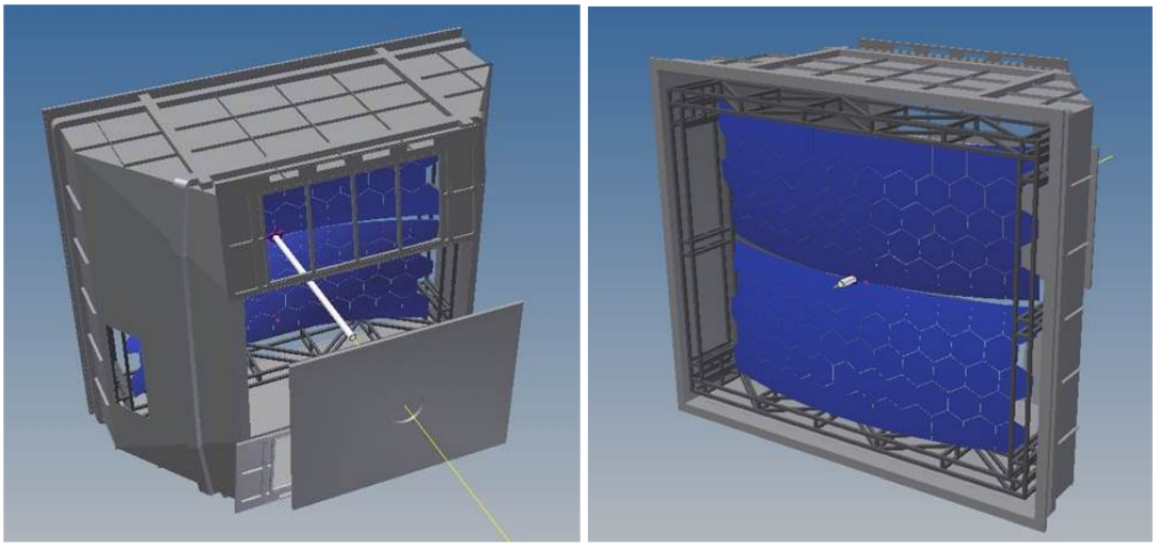

Figure B.12: A CAD rendition of the RICH-1 vessel with the mirrors in blue and the beam pipe in white. Figure taken from [131].

a maximum allowed deviation of 10 Pa at a reference point on the top of the vessel. A dedicated gas system continuously circulates the gas in a closed loop circuit at a rate of approximately 2 m^3/h. A CAD software rendition of RICH-1 can be seen in fig. B.12.

B.3.2 The Focusing Mirrors

A mirror wall with a surface area of 21 m^2 (as shown in fig. B.13) reflects the Cherenkov photons produced within the RICH-1 and focuses them onto the photon detectors located above and below the acceptance region. The mirror wall is made up of 116 spherical mirror units divided into two spherical surfaces with a radius of 6.6 m. These units consist of 68 regular hexagons with a diagonal length of 522 mm and 48 larger pentagons. The reflecting surface of each unit comprises an 80 nm thick layer of aluminum that is deposited on a 7 mm thick borosilicate glass substrate. Additionally, a 30 nm thick protective layer of MgF_2 covers the reflecting surface.

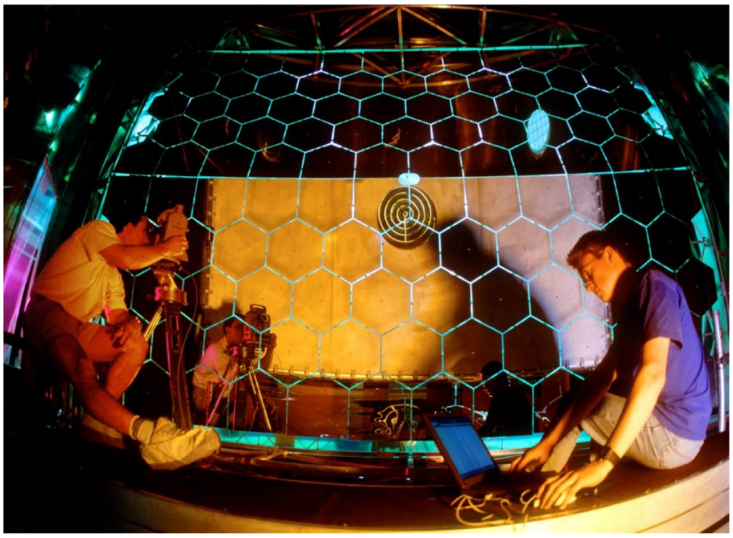

Figure B.13: Mirror alignment operation being conducted. Figure from [131].

Prior to installation, every mirror underwent complete characterization and offers a VUV reflectance that ranges from 83-87% within the 165-200 nm range. The reflectance of the mirrors has remained stable over time, except for some initial degradation in the smallest wavelengths. Fig. B.14 displays the mechanical structure that supports the mirrors. The design of the structure was aimed at minimizing the material within the acceptance region while maintaining the precise positioning of the mirrors. The structure is designed in a net-like configuration, with nodal points that are positioned on a sphere with an accuracy level of better than 1 mm.

Figure B.14: The mirror support structure; the nodal points are connected by light Al pipes. Picture taken from [131].

The mirrors are arranged in a mosaic-like formation, with minimal clearance between them that corresponds to only 4% of the total reflecting surface. They are suspended from the center of the nodal points of the support structure using a joint that permits slight angular adjustments by rotating two fine screws (as shown in fig. B.15).

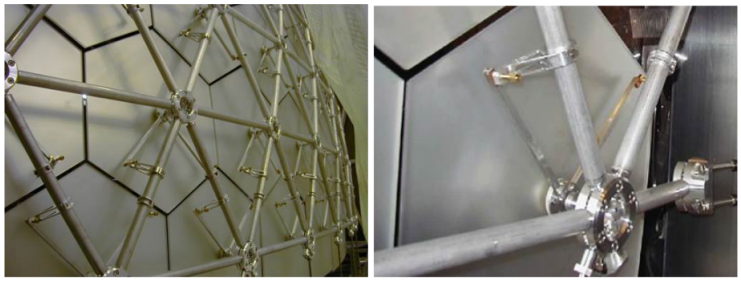

Figure B.15: The adjustments screws on the backside of the mirror. Picture taken from [131].

B.3.3 The CLAM System

In order to avoid the challenging and hazardous process of aligning the mirrors using the "theodolite auto-reflection" method (which involves opening the RICH-1 vessel, installing a scaffold structure inside it, and working in close proximity to the mirrors), as well as to regularly monitor the mirror alignment throughout data collection, a novel approach called CLAM [**lsteiger**] [47, 122] was created and introduced in 2007. This method employs four high-resolution cameras fixed at the vessel's corners and facing the mirror wall (as seen in fig. B.16).

The cameras capture the reflected image of a rectangular grid (can be seen in the photo of beam pipe B.10) placed close to the front wall of the vessel. To enhance the image contrast, the grid is made of retro-reflective material and equipped with optical targets. Moreover, LED light sources located near the camera positions provide illumination for each scene.

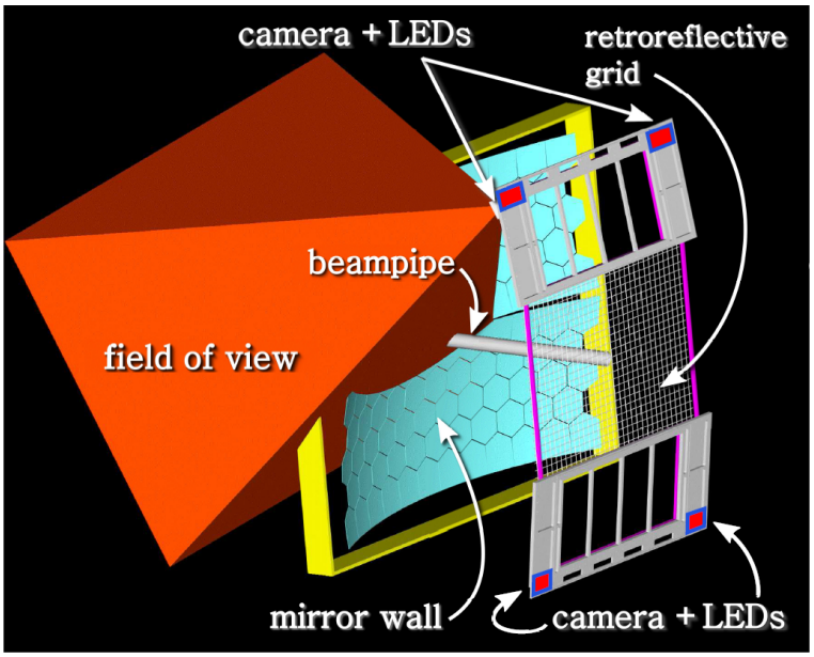

Figure B.16: The CLAM mirror alignment system. Figure taken from [122].

The camera observes the rectangular grid image as a group of intersecting conics (see fig. B.17). If two adjacent mirrors are misaligned, the conic lines appear disjointed, and the shift of the line images shows the direction and degree of the misalignment. To implement this method, separate calibration constants are necessary for each mirror position, which were determined beforehand through precise laboratory measurements.

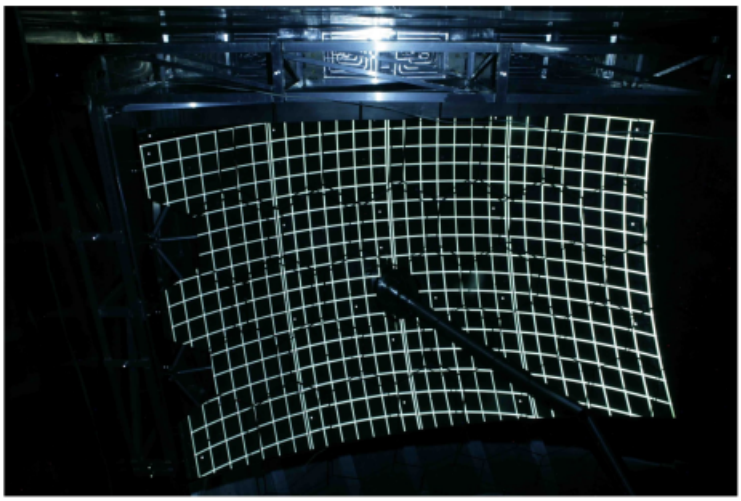

Figure B.17: Typical CLAM photo showing the image of the retro-reflective grid on the mirrors [131].

To ensure that the mirrors maintain their orientation during the operation period, the images

taken at various intervals are compared, and multiple slow and gradual movements have been identified. These movements have been found to cause tilts of up to maximum observed tilt value of 150 μrad.

Photogrammetry tools are utilized to extract the precise position of the center of curvature of each mirror by analyzing the images. This process involves a thorough characterization of each CLAM camera along with its optical system, as well as the geometrical position of each optical target inside the RICH.

B.4 Data Analysis and Reconstruction

The COMPASS-AMBER physics analysis is accomplished through a multi-layer data analysis package. They are listed as follows:

- **DDD:** Daq Data Decoding
- **CORAL:** COmpass Reconstruction and ALignment software package
- **PHAST:** PHysics Analysis Software Tools
- **COMGeant:** COMpass Geant Monte Carlo simulation program based on Geant 3.21
- **TGeant:** a Monte Carlo simulation program based on Geant4
- Time dependent inputs, like calibration and slow control data, are stored in a MySQL DataBase

Here, a brief description of CORAL is given, TGeant would be discussed briefly in a later chapter.

B.4.1 CORAL

CORAL is utilized primarily for data alignment and reconstruction purposes. It is a modular architecture object-oriented program written in C++. CORAL can process both raw data and data generated by COMPASS's Monte Carlo simulation software (COMGeant). The essential tasks performed by CORAL include:

- The decoding of all the data in order to extract the address of the fired channels (hits), the signal amplitudes and the time information.
- The reconstruction of the particle trajectories (tracking), the momentum analysis of the charged particles, and the reconstruction of the interaction and decay vertices.
- Identification of the muons utilising the information from the muon detectors.
- Accomplishing the RICH reconstruction and hadron PID, with the help of information from RICH-1.

- HCAL and ECAL detector response analysis.

B.4.2 RICHONE

RICHONE is the part of the CORAL package, and it is used for RICH reconstruction, characterisation, and analysis [8, 67, 247]. RICHONE, performs several crucial tasks. CORAL loops over the events and reconstructs the beam and tracks before proceeding to the RICH-1 data reconstruction. Once the RICH-1 data reconstruction is complete, the calorimeter reconstruction is done. RICHONE reads an option file where necessary options and initial values are stored.

B.4.2.1 Primary functions of the RICHONE package

RICHONE is a software package that handles standard PID tasks as well as additional tasks such as calibration and tuning. The type of data being processed by RICHONE is specified at the beginning of the reconstruction process, with options including raw data, simulated data, or a special file containing only RICH information. The code includes a monitoring function that allows the user to specify the data type and corresponding options stored in the option files. To match the photons emitted by a particle with that particle, RICHONE requires:

- CORAL uses a particle trajectory defined by its helix, which includes position, direction, and momentum, for the reconstruction of RICH-1 data. A helix is computed at the entrance window of RICH-1, and the trajectory is then extrapolated inside RICH-1, taking into account the spectrometer magnet's fringe field, which is located about 3 m upstream of RICH-1.

- Information recorded by the photon detectors of the RICH-1 and which is decoded by the DAQ decoder and transformed in the lab system.

The information that has been transformed into the lab system by the data acquisition decoder is referred to as digits. For RICHONE, digits consist of physical coordinates and signal amplitudes. The software executes four critical steps for successful completion, which are divided into different classes with numerous routines and subroutines within the RICHONE code. These four steps are:

- RICHONE reads the track information through other components of the CORAL software, which records essential parameters for PID, tuning, and characterization. These parameters include the momentum of the tracks multiplied by their charge, their position and direction at the entrance and exit planes of RICH.

- The RICH-1 photon detectors (PDs) measure photon hits, along with either their time information for the MAPMTs or three signal amplitudes for the gaseous detectors. The hit time information is utilized to reject out-of-time photons, while the hit amplitudes help reduce background from both the out-of-time photons and electronic noise. Regarding the gaseous detectors, a pad is chosen only if the signal amplitude is greater than 8 ADC channels, and the three signal samples (A_0, A_1, A_2) satisfy the condition: $A_0 < A_1 < A_2$.

- The clustering algorithm is used because photons may cause charge over multiple adjacent pads. The algorithm starts by searching for the pad with the highest signal amplitude, and then it includes adjacent pads in the cluster if their signal amplitude is less than a certain percentage of the highest signal amplitude (60% in the wire-plane direction and 30% in the transverse direction). The impact position, or cluster, is then determined by taking the mean of the hit positions weighted by their pulse height. The average cluster multiplicity is 1.1. However, for MAPMT, clustering is not used because the probability of having correlated hits in adjacent pads is negligible.

- Clusters of photons are reconstructed using their coordinates and the point at which they were emitted. The focusing RICH technique assumes that the mid-point of the photon trajectory inside the RICH volume is the emission point. Once the photons have been reconstructed, they are associated with particles. After this association, the rings are reconstructed and the likelihoods are computed. Ring angles are scaled to the UV refractive index for the ring recognition process.

The following flow-chart [102] depicts the algorithm executed by the code:

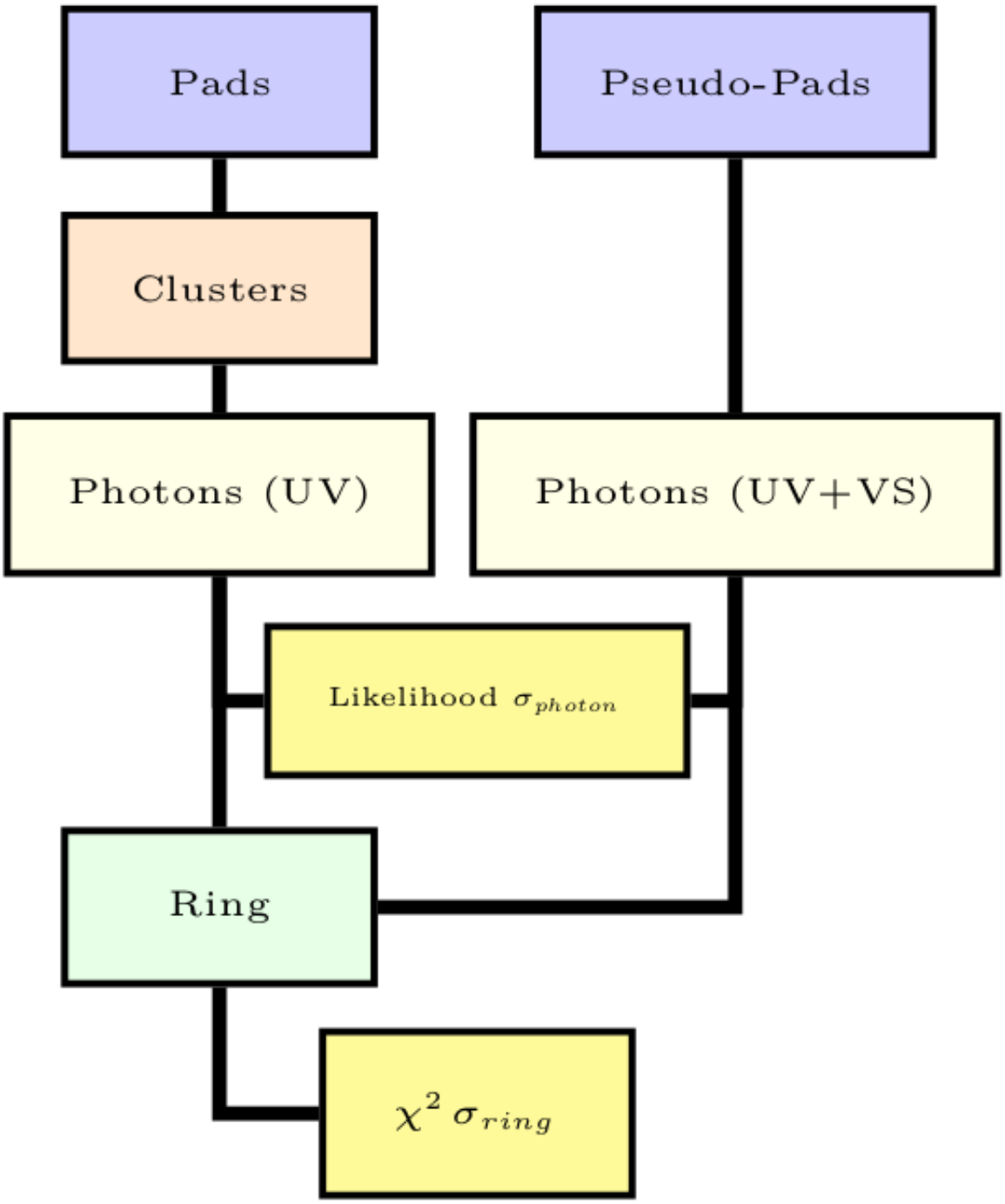

Figure B.18: RICHONE algorithm. Taken from [102].

Appendix C

Dark Matter: WIMP and Detection Channels

C.1 Introduction

This chapter will give a brief review of the state-of-the art of Dark Matter (DM), and the privileged anti-proton channel of detection. Although several models have been proposed to explain DM, some of which have been listed in the introduction chapter, *Weakly Interacting Massive Particle* (WIMP) provides one of the most interesting model and would be the one (without any particular consideration of the model candidate) considered henceforth for discussion. Cosmologist and Astrophysicist unanimously agree for the existence of DM as evident from different astrophysical messengers. So, an extensive discussion on the evidence is withheld in the chapter. Furthermore, an extensive discussion of DM candidates is beyond the scope of the thesis. However, a small section would be devoted to some interesting candidates that could be detected by AMS-02. Then, a discussion on why the anti-proton channel is a privileged channel for probing DM would be done. Since, there is a vociferous camp that proposes *Modified Newtonian Dynamics* (MOND), or, a modification to the *General Relativity* to explain DM, the chapter would end with a small critique of this argument.

C.1.1 Evidence of Dark Matter

The most promising evidence of DM emerges from the study of *Galaxy Rotation Curves*. Since the bulk motion of stars is dictated by their gravitation interactions, we can show that the circular velocity is given by

$$v_c(r) = \sqrt{\frac{GM}{r}}, \tag{C.1}$$

where M is the mass enclosed, r is the radial distance, and G is the gravitational constant. Considering Gauss's Law, distances beyond Galactic disk ($r > R_{disk}$), M would be constant which means that the velocity should decrease as square root of the inverse of the distance. However, in contrast, we find that the circular velocity flat lines at such distances, which implies that $M(r) \propto r$ (See fig. C.1). This suggests the presence of additional dark component of matter beyond the visible matter in the disk. Other strong evidence later emerged from *Gravi-*

tational Lensing, and studying the *Cosmic Microwave Background* which has led everyone to unanimously to conclude the existence of a dark component. The nature of this matter should be non-baryonic because baryonic matter as a result of strongly interacting among themselves tend to dissipate energy, and collapse into a disk. On the other hand, DM by assumption and observation forms spherical halos about the centre of galaxy.

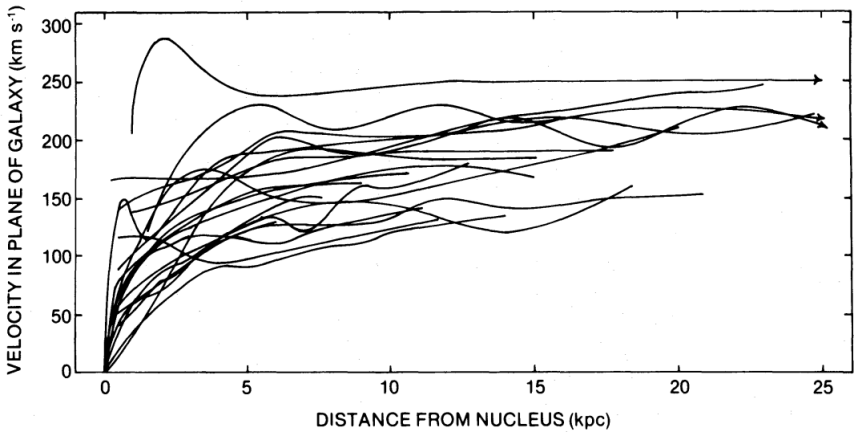

Figure C.1: Rotation curves of spiral galaxies from the original Rubin *et al.* paper [243] showing the flattening of the circular velocity at large radial distances.

C.1.2 Relic Abundance

We consider a situation in early universe when a DM particle (χ) is in thermal equilibrium via its interactions with Standard Model (SM) particles (X). There are two possible scenarios for $2 \to 2$ interaction diagrams: *Inelastic* ($\chi\chi \to XX$) and *Elastic* ($\chi X \to \chi X$) scattering (as shown in fig. C.2). When the former is in equilibrium, the DM particles are constantly being replenished. However with the expansion of the universe, it becomes difficult for DM particle to find another to annihilate and the forward reaction ceases, at which point, the DM density becomes frozen in time.

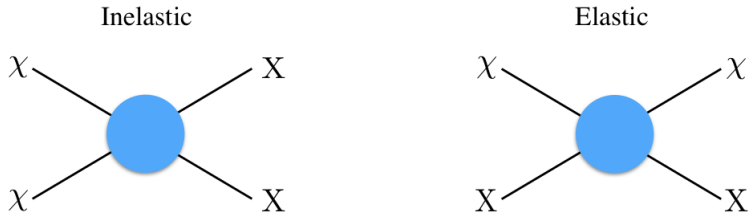

Figure C.2: Feynman Diagrams for inelastic and elastic scattering processes in early universe for DM particles. Figure from [204].

This *freeze-out* time is realised when the *annihilation rate*, $\Gamma_{inelastic}$ is of the order of *Hubble rate*, H:

$$\Gamma_{inelastic} = n_\chi \langle \sigma v \rangle \sim H, \tag{C.2}$$

where n_χ is the DM number density, and $\langle \sigma v \rangle$ is the velocity-averaged cross-section. *Cold DM* (CDM) is non-relativistic at freeze-out, with $n_\chi \sim T^{3/2} e^{-m_\chi/T}$, with T being the temperature of the DM species; meanwhile *Hot DM* is relativistic at freeze-out, with $n_\chi \sim T^3$. *Warm DM*

lies somewhere in between these two regimes.

Post freeze-out, the DM is no longer in chemical equilibrium, but remains in thermal equilibrium with the surrounding plasma via the elastic interaction as shown in fig. C.2. However, after a certain point, even this interaction decouples. The elastic interaction rate is given by [204],

$$\Gamma_{elastic} = n_X \langle \sigma v \rangle, \tag{C.3}$$

The above scales like T^3 as the X are relativistic. In the case of CDM, $\Gamma_{elastic}$ exceed the Hubble rate only after the DM ceases to be in chemical equilibrium which is referred to as *kinetic decoupling*, and DM is called to be in *free streaming*. For hot DM, kinetic decoupling happens earlier.

In order to calculate the DM number density, we track the evolution of the inelastic scattering process with time using the *Boltzmann equation* given by

$$\mathbf{L}[f] = \mathbf{C}[f], \tag{C.4}$$

where **L** and **C** are the *Liouville* and *Collision* operators, respectively. In the most general form, the Liouville operator is written as

$$\mathbf{L}[f] = p^\alpha \frac{\partial f}{\partial x^\alpha} - \Gamma^\alpha_{\beta\gamma} p^\beta p^\gamma \frac{\partial f}{\partial p^\alpha}, \tag{C.5}$$

where $\Gamma^\alpha_{\beta\gamma}$ is the *affine connection*. Given the *Friedmann–Lemaître–Robertson–Walker metric*, in the west-coast convention $(+---)$ (commonly used in quantum field theory and particle physics) i.e. , :

$$ds^2 = dt^2 - a^2(t)\left(\frac{dr^2}{1-kr^2} + r^2 d\theta^2 + r^2 \sin^2\theta d\phi^2\right), \tag{C.6}$$

we get for the covariant form of the Liouville operator:

$$\mathbf{L}[f] = E\frac{\partial f}{\partial t} - \frac{\dot{a}}{a}|\vec{p}|^2 \frac{\partial f}{\partial E}. \tag{C.7}$$

The number density of a given particle is related to its phase-space density, $f(E,t)$, via

$$n = g \int f(E,t) \frac{d^3p}{(2\pi)^3}. \tag{C.8}$$

We can compute using (C.7) and (C.8) that

$$g \int \mathbf{L}[f] \frac{d^3p}{(2\pi)^3} = \frac{1}{a^3}\frac{d}{dt}(na^3) = \frac{dn}{dt} + 3Hn, \tag{C.9}$$

where $H = \dot{a}/a$ is the expansion rate of the Universe, and a is the scale factor. In the absence of number-changing DM interactions (i.e., when **C**[f]=0), then (C.9) shows that the quantity na^3 is constant in time.

The collision operator $\mathbf{C}[f]$ comprises of the interactions between DM and other particles which includes self-interactions that may alter the phase-space density. In principle, this operator can be quite complex depending on the allowed interactions. Let us consider interactions of the form $1+2 \leftrightarrow 3+4$, which gives us for the collision term [171]:

$$g_1 \int \mathbf{C}[f_1] \frac{d^3p_1}{(2\pi)^3} = -\sum_{spins} \int \left[f_1 f_2 (1 \pm f_3)(1 \pm f_4) |\mathcal{M}_{12\to 34}|^2 - f_3 f_4 (1 \pm f_1)(1 \pm f_2) |\mathcal{M}_{34\to 12}|^2 \right] \times (2\pi)^4 \delta^4(p_1 + p_2 - p_3 - p_4) d\Pi_1 d\Pi_2 d\Pi_3 d\Pi_4, \tag{C.10}$$

where g_i and f_i are the spin degrees of freedom and phase-space densities, respectively, for particles i, and $\mathcal{M}_{x\to y}$ is the matrix element for the reaction $x \to y$. Whereas, factors of the form $(1 \pm f)$ represent *Pauli blocking* and *Bose enhancement*, where the minus sign applies to fermions and the plus sign to bosons. Qualitatively it means that it is easier/harder for a boson/fermion to transition to a state that already contains a boson/fermion. The delta function suggests that energy and momentum must be conserved, and the phase-space integration factors are given by

$$d\Pi_i = \frac{d^3p_i}{(2\pi)^3 2E_i}. \tag{C.11}$$

The complicated from in (C.10) can be reduced to a simpler form with the following assumptions

- Kinetic equilibrium is maintained, and hence the phase-space distributions either have the *Fermi-Dirac* or *Bose-Einstein* form.
- The temperature of each species satisfies $T_i \ll E_i - \mu_i$, where μ_i is its chemical potential. As such, they follow the *Maxwell-Boltzmann* distribution. In such a case, the statistical mechanical factors in the calculations can be neglected, and $(1 \pm f) \sim 1$.
- The SM particles are in thermal equilibrium with the photon bath.

Using the following relation between the cross-section and matrix element, we obtain

$$\sum_{spins} \int |\mathcal{M}_{ij\to kl}|^2 \times (2\pi)^4 \delta^4(p_i + p_j - p_k - p_l) d\Pi_k d\Pi_l = 4 g_i g_j \sigma_{ij} \sqrt{(p_i \cdot p_j)^2 - (m_i m_j)^2}, \tag{C.12}$$

where σ_{ij} is the cross-section for the scattering process. Substituting it back in (C.10) gives us

$$g_1 \int \mathbf{C}[f_1] \frac{d^3p_1}{(2\pi)^3} = -\int \left[(\sigma v_{M\o l})_{12} dn_1 dn_2 - (\sigma v_{M\o l})_{34} dn_3 dn_4 \right], \tag{C.13}$$

where the ***Møller velocity*** is given as

$$(v_{M\o l})_{ij} = \frac{\sqrt{(p_i \cdot p_j)^2 - (m_i m_j)^2}}{E_i \cdot E_j}, \tag{C.14}$$

for the $ij \to kl$ process. As $\sigma v_{M\o l}$ varies slowly with consequent changes in the number density

of the initial and final-state products, it can factored out of the integrand to yield

$$\dot{n}_1 + 3Hn_1 = -\langle \sigma v_{M\o l} \rangle_{12} n_1 n_2 + \langle \sigma v_{M\o l} \rangle_{34} n_3 n_4. \tag{C.15}$$

The Møller velocity multiplied by the species number density ($(v_{M\o l})_{ij} n_i n_j$)is Lorentz invariant quantity. We would henceforth denote $v_{M\o l} \to v$ for notational simplicity.

In fig. C.2, for the inelastic process, the particles 1 and 2 have identical number density n, and particles 3 and 4 are SM particles in thermal equilibrium with the photon bath. When the DM particles are also in equilibrium with the SM final states, the detailed balance yields:

$$\langle \sigma v \rangle_{12} n_{eq}^2 = \langle \sigma v \rangle_{34} n_3^{eq} n_4^{eq}, \tag{C.16}$$

which can be used in (C.15) to give

$$\dot{n} + 3Hn = \langle \sigma v \rangle \left(n_{eq}^2 - n^2 \right), \tag{C.17}$$

where $\langle \sigma v \rangle = \langle \sigma v \rangle_{12}$. We define a new variable, $Y = n/s$ to scale out the effect of decreasing DM number density with expansion of the universe, where s is the total entropy density of the Universe. Using this in (C.17), and making use of the fact that sa^3 is constant to obtain the relation $\dot{s} = -3sH$. Hence, (C.17) becomes

$$\frac{dY}{dt} = \langle \sigma v \rangle_s \left(Y_{eq}^2 - Y^2 \right) \to \frac{dY}{dx} = \frac{xs\langle \sigma v \rangle}{H(m)} \left(Y^2 - Y_{eq}^2 \right). \tag{C.18}$$

In above, the equation on the L.H.S is written in the usual time variable, and in the right in the rescaled time variable $x = m/T$, where m is the mass of the DM. We can observe that $dx/dt = H(x)x$, as $T \propto 1/a$ (the photon temperature is inversely proportional to its wavelength, which scales as a). For a precise definition of $H(m)$, one can refer [195].

So, we have an evolution equation in Y as the Universe cools, where Y is the DM number density, rescaled to remove the effects of the Universe's expansion. As such, the changes in Y encoded in the Boltzmann equation is purely an effect of DM interactions with states that are in thermal equilibrium with the photon bath. The evolution of Y is governed by the velocity-averaged cross-section:

$$\langle \sigma v \rangle = \frac{\int \sigma v dn_1^{eq} dn_2^{eq}}{\int dn_1^{eq} dn_2^{eq}} = \frac{\int \sigma v e^{-(E_1/T + E_2/T)} d^3p_1 d^3p_2}{\int e^{-(E_1/T + E_2/T)} d^3p_1 d^3p_2}. \tag{C.19}$$

The above equation can be further simplified by redefinition of the integration variables [171] to yield

$$\langle \sigma v \rangle = \frac{1}{8m^4 T K_2^2(m/T)} \int_{4m^2}^{\infty} \sigma(\tilde{s} - 4m^2) \sqrt{\tilde{s}} K_1(\sqrt{\tilde{s}}/T) ds \xrightarrow{\text{non-rel}} b_0 + \frac{3}{2} b_1 x^{-1} + \ldots, \tag{C.20}$$

where K_i are *modified Bessel functions* of the i^{th} order and $\tilde{s} = 2m^2 + 2E_1E_2 - 2p_1 \cdot p_2$. The

cross-section can be expanded in x in the non-relativistic limit with coefficients $b_{0,1}$. In the case, where b_0 dominates, it is referred to as *s-wave* annihilation. Whereas, the case where b_1 dominates, it is called *p-wave* annihilation.

There is no analytic solution for (C.18), so we resort to numerical solutions. However, we can consider the behaviour of solutions in the limiting case to have an idea about how DM number density evolves with time. As discussed before, when $\Gamma \gg H$, the annihilation process is efficient and equilibrium can be maintained between the DM and photon bath. However, when $\Gamma \ll H$, the annihilation process cease and it falls out of equilibrium. This can be reframed as

$$Y(x \lesssim x_f) \simeq Y_{eq}(x) \quad \text{and} \quad Y(x \geq x_f) \simeq Y_{eq}(x_f), \tag{C.21}$$

where x_f is the freeze-out time. For CDM, $Y(x)$ decreases exponentially before freeze-out. Post freeze-out, the abundance is larger than what its equilibrium value would have been if freeze-out had not occurred (as Y_{eq} is decreasing, $Y_{eq}(x_f) > Y_{eq}(x > x_f)$). Hence, (C.18) can be written as

$$\frac{dY}{dx} \simeq -\frac{\lambda}{x^{n+2}} Y^2, \quad \text{where} \quad \lambda = \frac{\langle \sigma v \rangle_0 s_0}{H(m)}, \tag{C.22}$$

where the x dependence has been pulled out of the cross-section and entropy to define λ. That is, $\langle \sigma v \rangle = \langle \sigma v \rangle_0 x^{-n}$ and $s = s_0 x^{-3}$. Considering $n = 0$, we can solve for the DM abundance today as

$$\frac{1}{Y_{today}} - \frac{1}{Y_f} = \frac{\lambda}{x_f} \rightarrow Y_{today} \simeq \frac{x_f}{\lambda}, \tag{C.23}$$

wherein, the last step entails the fact that the abundance at freeze-out, Y_f is typically greater than its value today. This result would change if the thermally averaged cross-section carries a dependence on x, which would depend on the particle physics model. If $n \neq 0$, then Y_{today} would have higher powers of x_f.

The fraction of the critical density, ρ_{cr}, contributed by the DM today is

$$\Omega_\chi = \frac{m \cdot s_{today} Y_{today}}{\rho_{cr}} \rightarrow \Omega_\chi h^2 \sim \frac{10^{-26} cm^3/s}{\langle \sigma v \rangle} \simeq 0.1 \left(\frac{0.01^2}{\alpha} \right) \left(\frac{m}{100 GeV} \right)^2, \tag{C.24}$$

taking $x_f \sim 10$ and $\langle \sigma v \rangle \sim \alpha^2/m^2$. If we assume, a weakly interacting DM particle with $\alpha \sim 0.01$ and mass $m_\chi \sim 100 GeV$, it gives us the correct abundance today as measured by Planck and WMAP. This fact that the weak-scale DM naturally gives the correct DM density today is known as the *WIMP Miracle*, and has henceforth became the dominant paradigm since many well-motivated models, such as supersymmetry, provides such candidates. Such kind of particles are called *Weakly Interacting Massive Particles* or WIMP.

C.2 Antiproton Excess as a Channel for Dark Matter Search

The indirect search of DM relies on the search for anomalous signals in CR spectrum that isn't expected from standard astrophysical anti-matter production mechanisms. It is theorised that

pairs of DM particles in the galactic halo can annihilate and give us particle anti-particle pairs as shown:

$$\chi + \bar{\chi} \rightarrow q\bar{q}, W^+W^-, \ldots \rightarrow \bar{p}, \bar{D}, e^+, \gamma, \nu_{e,\mu,\tau}. \tag{C.25}$$

These additional exotic components should appear as distortions in the expected standard anti-matter spectrum. This can be detected in principle by balloon or space born detectors, or by underground neutrino facilities. Indeed AMS-02 has published a precision measurement of anti-proton spectrum with a few percent uncertainty [27]. As such, it offers us the noble opportunity to explore this channel as a possible signal of DM. As explain in Chapter 2, the positron excess also instigated a series of discussion for its excess to be attributed to DM annihilation, however, the community more or less agrees that the excess can be fitted with a model of pulsars producing e^+e^- pairs with subsequent acceleration. So, the anti-proton channel is a privileged channel and the rest of the chapter would concentrate on the modus operandi to exploit it for indirect DM searches.

C.2.1 Anti-protons in Cosmic Rays

The transport equation for CRs as explained in chapter 2 has a source term, and in principle the following mechanism should contribute to the bulk of it:

- The interaction of high-energy primary nuclei i.e., spallation reactions with the ISM inside the galactic disc to produce secondary anti-protons
- The annihilation of WIMP DM candidate pairs throughout the *Milky Way* halo can generate anti-protons
- The spectral modifications are introduced at low energies during the propagation of $\bar{p}$ in the ISM due to ionization and loss of energy during deep-inelastic interactions (non-annihilating interactions). The latter one can lead to considerable loss of energy and a high energy $\bar{p}$ can emerge at low energies after the interaction with the production of pions, etc. This process is very effective in adding low energy $\bar{p}$ in the energy region, where it is kinematically very difficult to produce them. They are called tertiary antiprotons [255].

C.2.2 Secondary Anti-Protons

Secondary anti-protons represent the background against which we have to search for small signals for contributions of anti-protons coming from any exotic source like DM, since secondary anti-protons represent the dominant production mechanism.

The rate of production for secondary anti-protons gives the following source term for the transport equation [245]

$$q_{\bar{p}}^{sec}(r, E_{\bar{p}}) = \int_{E_{P,\alpha}^0}^{\infty} n_{H,\alpha} \times \beta_{p,\alpha}\psi_{p,\alpha}(r, E_{p,\alpha}) \times dE_{p,\alpha} \times \frac{d\sigma}{dE_{\bar{p}}}(E_{p,\alpha} \rightarrow E_{\bar{p}}), \tag{C.26}$$

that describes the interaction between cosmic ray anti-protons and α particles, hydrogen and helium nuclei in the ISM; where n represents the population of particles, and $\psi = dn/dE$ is the energy distribution function.

We can solve the transport equation with the above source term in the way it is done in [142]. Once the interstellar (IS) fluxes of anti-protons are calculated at the sun's position, it has to be further propagated in the heliosphere, where it is effected by the solar wind. The effect of solar modulation can be done with the force-field approximation as explained in the 2nd chapter. In this model, the top-of-atmosphere (TOA) flux for a cosmic species Φ^{TOA} is related to Φ^{IS} as

$$\frac{\Phi^{TOA}(E^{TOA})}{\Phi^{IS}(E^{IS})} = \left(\frac{p^{TOA}}{p^{IS}}\right), \tag{C.27}$$

where E and p denote the total energies and momenta of interstellar and TOA anti-protons, which are related by the energy shift

$$E^{TOA} = E^{IS} - \phi, \tag{C.28}$$

where ϕ is determined by fits on CR data. The secondary IS $\bar{p}$ flux is shown in the left panel of fig. C.3 alongside the solar demodulated data. The authors used DTUNUC (Monte Carlo dual parton model event generator) for the $\bar{p}$ production cross sections (solid line) or those discussed in [91,146]. The difference between the two curves points towards the uncertainty in production cross sections, where an analysis within the DTUNUC simulation gives an uncertainty of $\sim 25\%$ over the energy range 0.1-100 GeV. In the right panel, one can see the demodulated $\bar{p}/p$ data, where the curves bounding the propagation uncertainty on the $\bar{p}$ calculation either based on DTUNUC (solid lines) or those from [91] (dashed lines) are shown. The uncertainty arising from propagation are comparable to the nuclear one. It is manifest that the secondary contribution alone explains experimental data on the whole energy range, and there is no need to invoke an additional exotic component to the standard astrophysical one.

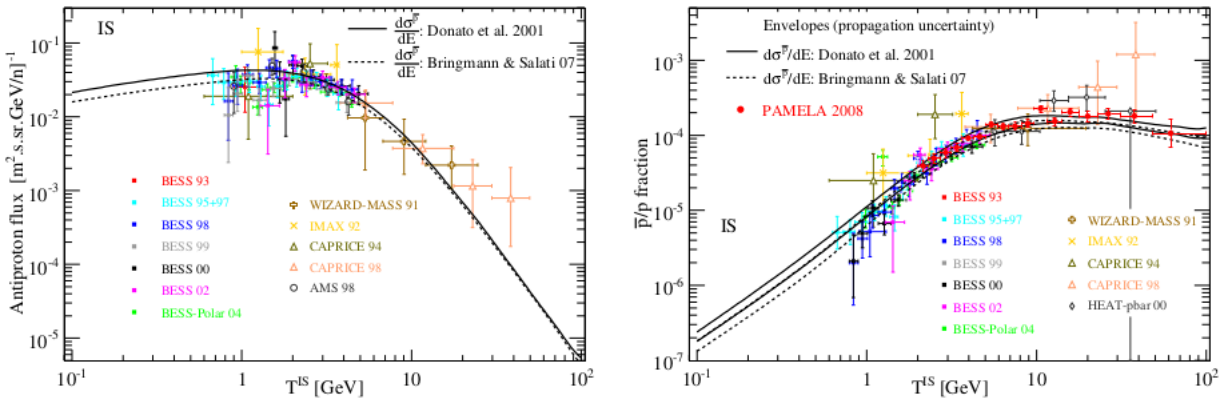

Figure C.3: Left: IS antiproton flux for the B/C best fit model and two parameterizations of the production cross-section. Right: propagation uncertainty envelopes of the IS $\bar{p}/p$ ratio for the same production cross sections as in the left [245].

C.2.3 Anti-protons from DM annihilation

The anti-proton signal from DM annihilation contributes as a primary component to the anti-proton spectrum. The differential rate of production per unit volume and time is a function of spatial coordinates and anti-proton kinetic energy $T_{\bar{p}}$ and can be written as [245]

$$q_{\bar{p}}^{DM}(r, z, T_{\bar{p}}) = \xi^2 \langle \sigma_{ann} v \rangle g(T_{\bar{p}}) \left(\frac{\rho_\chi(r, z)}{m_\chi} \right)^2, \tag{C.29}$$

where $\langle \sigma_{ann} v \rangle$ denotes the average over the Galactic velocity distribution function of the WIMP pair annihilation cross-section σ_{ann} multiplied by the relative velocity v. For any DM candidate, σ_{ann} is calculated from the model parameters. Here, the WIMP mass is represented by m_χ and the mass distribution function is denoted by $\rho_\chi(r, z)$. The quantity ξ parametrises the fact that the DM halo might not be totally constituted by the species under scrutiny. The quantity $g(T_{\bar{p}})$ represents the anti-proton differential spectrum per annihilation even and can be expounded as

$$\frac{dN_{\bar{p}}}{dE_{\bar{p}}} = \sum_{F,h} B_{\chi h}^{(F)} \frac{dN_{\bar{p}}^h}{dE_{\bar{p}}}. \tag{C.30}$$

The annihilation of DM into a quark or a gluon h is encoded into the different final states F with branching ratios $B_{\chi h}^{(F)}$. Quarks and gluons can either be produced directly from WIMP pair annihilation or might emerge from the intermediate production of Higgs boson or gauge bosons. After which, each quark or gluon generates a jet whose subsequent fragmentation and hadronisation results in an antiproton energy spectrum $dN_{\bar{p}}^h/dE_{\bar{p}}$. Generally, the single production spectra are calculated using Monte Carlo simulations of electroweak annihilation events (For e.g., see [143] for the calculation in a *Minimal Supersymmetric extension of the Standard Model* (MSSM)).

DM halo distribution function is highly debated and some detailed discussion can be found in [114]. However DM distribution is a crucial factor in the indirect detection through gamma-rays and neutrinos, while it is less relevant for anti-matter component, as the latter diffuses and the signal at Earth is more local, and weakly dependent on the inner structure of the galaxy [134, 143].

As an example, considering a spherical DM galactic distribution profile, the predicted anti-proton flux at kinetic energy $T_{\bar{p}} = 0.23\ GeV$, for two different SUSY models is shown in fig. C.4. The left panel shows a low-energy realisation of the MSSM, while the right represents a SUSY scheme where *gaugino* (superpartner of gauge bosons) non-universality is not assumed (SUSY considers unification of three gaugino masses at GUT scale), and therefore light *neutralinos* are present [87, 88]. In both the cases, the shaded yellow portion denotes the amount of anti-protons in excess of the secondary component, which can be accommodated at $T_{\bar{p}} = 0.23$ GeV so as to not exceed the observed flux measured by BESS. Therefore, all the points of the scatter plots that falls below the horizontal black line are compatible with observations [245].

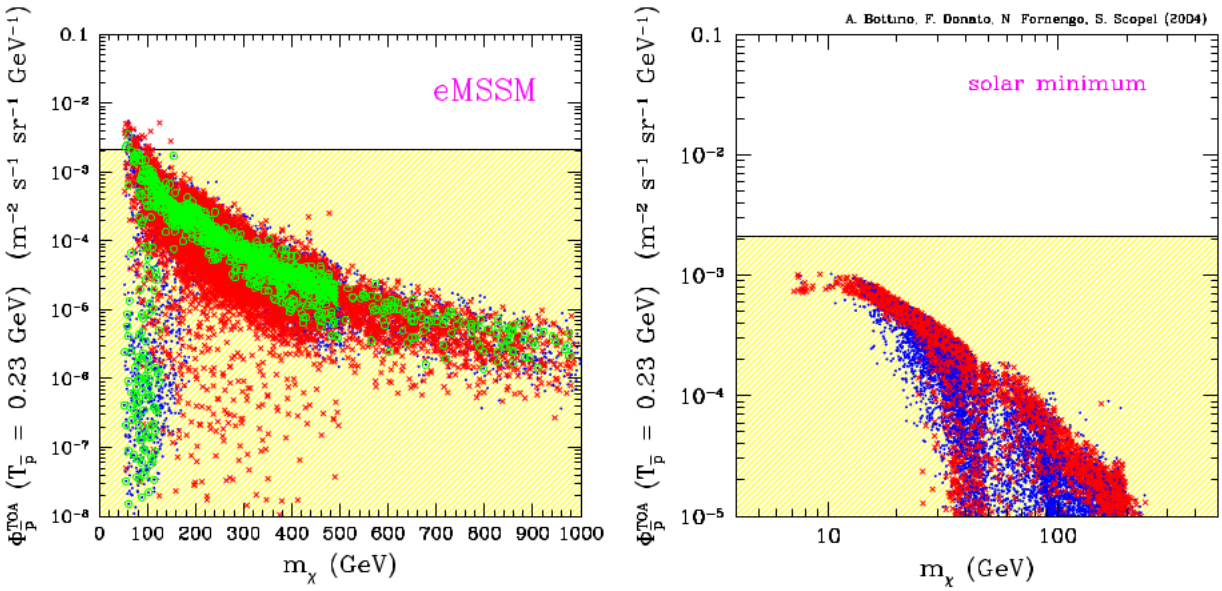

Figure C.4: Left: The scatter plot displays the $\bar{p}$ flux at solar minimum from neutralino annihilation calculated at $T_{\bar{p}} = 0.23\ GeV$ as a function of the neutralino mass for a generic scan in a low-energy MSSM and for MED set of astrophysical parameters [143]. Red crosses refer to cosmologically dominant neutralinos ($0.05 \leq \Omega_\chi h^2 \leq 0.3$), blue dots refer to sub dominant relic neutralinos ($\Omega_\chi < 0.05$). Right: Similar to the left panel, but calculated for in scan of SUSY framework where gaugino non-universality is not assumed, and therefore light neutralinos are present. [245].

C.2.4 AMS-02 Anti-Proton to Proton Ratio

AMS-02 published precession measurement for the anti-proton to proton ratio (See fig. C.5), and it shows that ratio above 60 GV rigidity is practically flat. This is in contrast to theoretical predictions because progenitor protons have a power law spectrum that decreases at higher rigidity, and since the source term that includes anti-protons coming from protons would be dictated by this power law too; the overall effect should be a decrease in this ratio. So, the observed excess presents us an interesting channel to investigate dark matter channels. As to why it is privileged over the positron spectrum is explained in chapter 2.

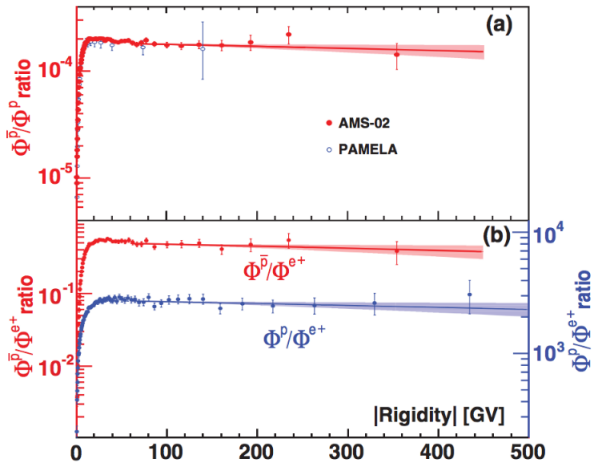

Figure C.5: a) The measured $\bar{p}/p$ flux ratio of AMS-02 as a function of rigidity compared with PAMELA. b) $\bar{p}/e^+$ (red, left axis) and p/e^+ (blue, right axis) flux ratios [27].

C.3 Theoretical Uncertainties in DM Interpretation from Anti-Proton Spectrum

The never reached before precision of the measurement provided by AMS-02 poses the challenge of a theoretical interpretation with an uncertainty at a similar level. As already discussed, the secondary anti-protons are provided by the interaction of CR p and He with that of ISM which again mostly consist of H and He. Hence, the number of anti-protons produced depends on the correct modelling of the production cross-section $d\sigma(p + p \rightarrow \bar{p} + X)/dT_{\bar{p}}$ and the equivalent reactions with He instead of p. It has been shown that the production cross-section produces a non-negligible uncertainty in the predictions of the secondary anti-protons [91, 141, 142]. A number of approaches have been put forth to describe the $\bar{p}$ production: the earliest parametrisation for pp scattering was done in [263], after which MC predictions were employed, in particular for He channels using the DTUNUC code [142,251]. LHCb published an analysis of anti-protons in collisions of $6.5\ TeV$ protons on a fixed helium target at the LHC [173]. Another parametrisation deduced from large pp and pA (proton-nuclei) data set was proposed in [147]. After publication of NA49 data [118], new parametrisations have been proposed in [137, 189], along with predictions from MC generators were tuned with LHC data [187]. In spite of these, the theoretical uncertainty introduced by the modeling of the fundamental interactions on the anti-proton spectrum is non-negligible, upto the order of few ten percent.

C.3.1 Astrophysical Uncertainties

Propagation of CRs in the galaxy is modeled using transport equations as discussed in Chapter 2, and the diffusive models used to understand them depends on several input parameters, which in turn are derived from the data analysis of CR primary and secondary species. These models introduce what we call astrophysical uncertainty on the anti-proton spectrum from theoretical prediction. As seen in fig. C.6, as of now, the theoretical astrophysical uncertainty are smaller than the nuclear physics one. AMS-02 data and subsequent analysis, for an example, the analysis of the $^{10}Be/^{9}Be$ which is sensitive to the astrophysically important ratio H^2/D (see chapter 2), and forms a major component of this thesis; will help us to keep on reducing the astrophysical uncertainty.

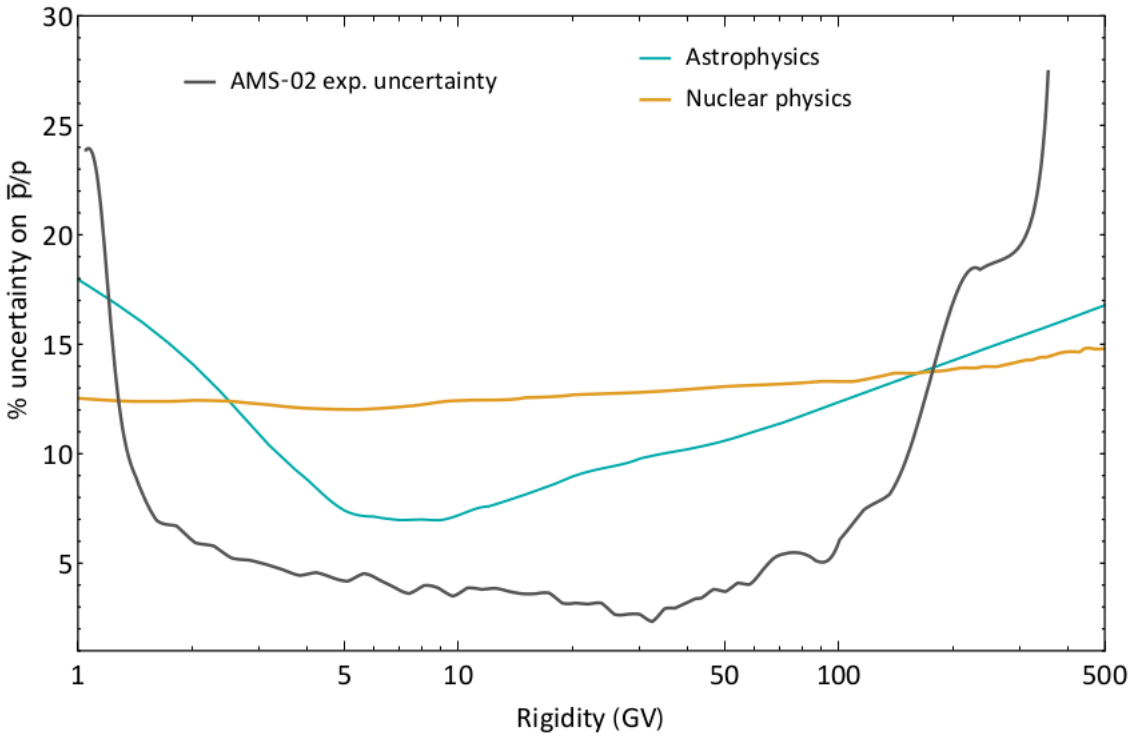

Figure C.6: Relative uncertainty on the prediction for the $\bar{p}/p$ ratio, with respect to rigidity: the astrophysical uncertainty derived from AMS-02 data is shown in light blue [84–86], and the mean of uncertainties introduced by nuclear physics is shown in dark yellow [137, 197]. The AMS-02 measurement uncertainties as reported in [27] is shown in black.

C.3.2 Nuclear Uncertainties

As we already know that anti-protons in galaxy are produced predominantly by primary CR nuclei interaction with the ISM, so to calculate the $\bar{p}$ source term, i.e., the number of anti-protons per volume, time, and energy; we need the flux of the incident CR species i, ϕ_i, and the density of the ISM component j. In practical terms, i and j refers to both p and He. The source term is written as an integral of the CR flux, the ISM targets, and the relevant cross-sections [140]:

$$q_{ij}(T_{\bar{p}}) = \int_{T_{th}}^{\infty} dT_i 4\pi n_{ISM,j} \phi_i(T_i) \frac{d\sigma_{ij}}{dT_{\bar{p}}}(T_i, T_{\bar{p}}). \tag{C.31}$$

Where n_{ISM} is the ISM density and T_{th} is the production energy threshold to produce a $\bar{p}$. The factor 4π comes from the angular integration of the isotropic flux ϕ. $T_{\bar{p}}$ is the anti-proton kinetic energy, and $\phi_i(T_i)$ is the CR flux of i species at kinetic energy T_i. The fluxes are known precisely at the top of the Earth's atmosphere (TOA) because of AMS-02 [22, 34], PAMELA [19, 20] and CREAM [282] as shown in fig.C.7. The $\bar{p}$ production threshold in pp and pHe collisions is around $E_p > 7m_p \sim 6.6\ GeV$ and $E_p > 4m_p \sim 3.8\ GeV$ respectively. The p and He IS fluxes can be obtained from demodulated AMS-02 data within the force-field approximation, as the solar modulation becomes negligible above a few $10\ GeV$. The scattering sights are the ISM components H and He with density 1 and $0.1\ cm^{-3}$ respectively in the Galactic disk.

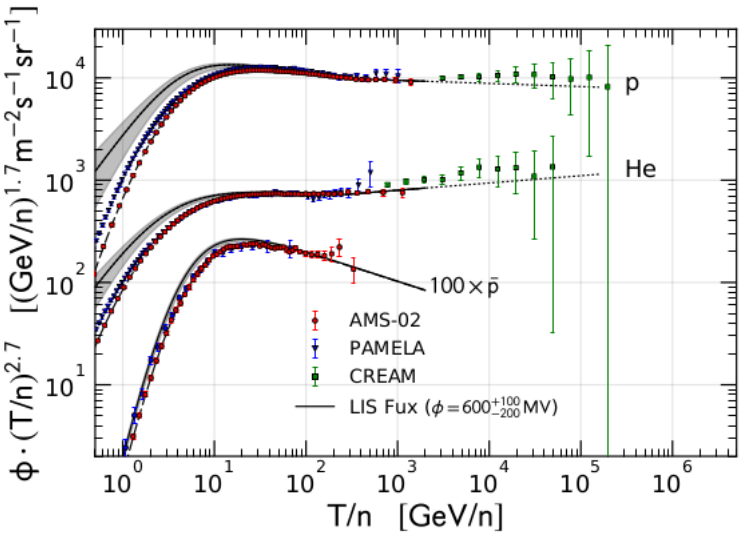

Figure C.7: Fluxes of CR p, He, and $\bar{p}$ by AMS-02, PAMELA, and CREAM with respect to energy per nucleon. The IS fluxes are demodulated with an average Fisk potential $\phi_\odot = 600^{+100}_{-200}\ MV$. Figure taken from [140].

The last essential ingredient to compute the source term is the cross-section corresponding to the production reaction $CR_i + ISM_j \to \bar{p} + X$:

$$\frac{d\sigma_{ij}}{dT_{\bar{p}}}(T_i, T_{\bar{p}}). \tag{C.32}$$

The quantity above in (C.32) is referred to as the *energy-differential cross section* (in particular, $dT \equiv dE$, and hence $d\sigma/dE \equiv d\sigma/dT$). An example based on the cross-section parametrisation in [137] for the pp channel is shown in fig. C.8 as a function of T_p and $T_{\bar{p}}$. The kinetic energy threshold can be seen at $T_p = 6m_p$.

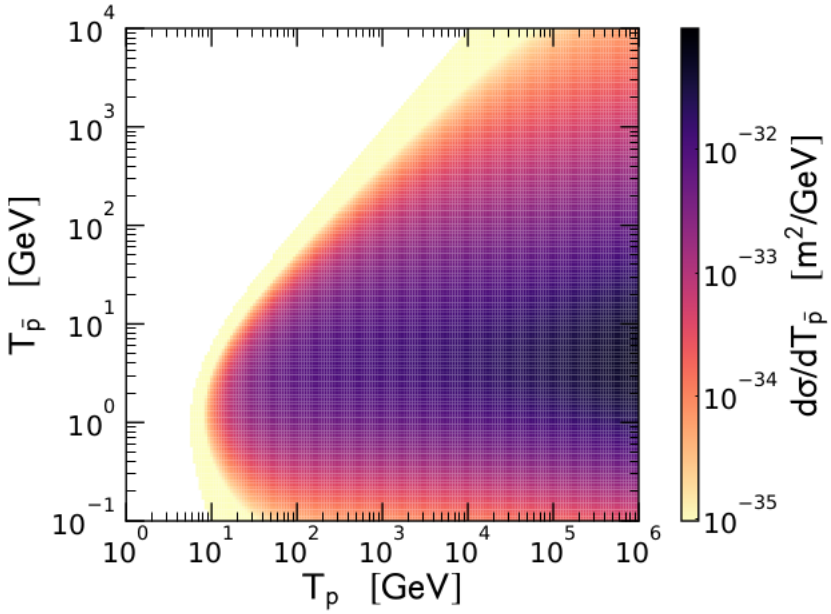

Figure C.8: Energy-differential $\bar{p}$ cross-section from pp collisions in the LAB frame as a function of T_p and $T_{\bar{p}}$. Figure taken from [140].

However, in experiments the production cross-section is not measured in the form of (C.32).

Instead, experiments measure the angular distribution on top of the energy-differential cross-sections and then present the Lorentz invariant (LI) form

$$\sigma_{inv}(\sqrt{s}, x_R, p_T) \equiv E\frac{d^3\sigma}{dp^3}(\sqrt{s}, x_R, p_T), \tag{C.33}$$

where E and p are the total $\bar{p}$ energy and momentum respectively, $\sqrt{s}$ is the center-of-mass (CM) energy of the colliding nucleons, $x_R = E^*_{\bar{p}}/E^*_{\bar{p},max}$ ($*$ refers to CM quantities) is the ratio of the $\bar{p}$ energy to the maximum possible energy in the CM frame, and p_T is the transverse momentum of the produced $\bar{p}$. The three quantities are LI ones, and the subscript i and j are witheld for notational simplicity. The (C.33) is valid for all combinations of projectile and target, within the context of nucleon-nucleon system.

C.3.2.1 Maximal Energy of Product Particles

Assuming a generic process $a + b \to c + X$ in the centre-of-mass frame, we get for the mass of X

$$\begin{aligned} m_X^2 = p_X^2 &= (p_a + p_b - p_c)^2 \\ &= s + m_c^2 - 2(p_a + p_b).p_c \quad \text{since} \quad p_a + p_b \equiv (\sqrt{s}, 0) \quad \text{and} \quad p_c \equiv (E_c, \vec{p}_c) \\ &= s + m_c^2 - 2\sqrt{s}E_c \\ \implies E_c &= \frac{s + m_c^2 - m_X^2}{2\sqrt{s}}. \end{aligned} \tag{C.34}$$

Here, p_i are the 4-momenta of particle i. For $\bar{p}$ production in pp scattering, we have $m_c = m_p$ and to be consistent with baryon number conservation, $m_{X,min} = 3m_p$. Hence, the maximal energy allowed for the produced anti-proton that enters the definition of x_R is

$$E_{\bar{p},max} = \frac{s - 8m_p^2}{2\sqrt{s}}. \tag{C.35}$$

C.3.2.2 Relation between LAB and CM frame for the energy-differential cross-section

We have two frames; in the CM frame, we have $p - p$ or in the more general case, nucleon-nucleon scattering, and we denote variables in this frame with the $*$ superscript. On the other hand, we have the LAB frame where one of the particles is at rest. As we know the CM energy is given by

$$s = (p_a + p_b)^2, \tag{C.36}$$

where the square of 4-momenta gives us the energy because in CM frame, the total 3-momentum is zero. And since they are 4-momenta, squaring them gives us a LI quantity s. Now, since in CM frame, we have $\vec{p}_a = -\vec{p}_b$, the CM energy is

$$s = (p_a + p_b)^2 = (E_a + E_b)^2 = (E^* + E^*)^2 = 4(E^*)^2, \tag{C.37}$$

where E^* is the energy of a proton in the CM frame. Whereas, in the lab frame, we have an incident proton and one at rest. Let E be the energy of incident proton, and m the mass of proton. Hence

$$\begin{aligned} s &= (p_a + p_b)^2 \\ &= (E + m, \vec{p} + \vec{0})^2 \\ &= (E + m)^2 - p^2 \quad \text{considering} \quad (+ - - -) \quad \text{west coast/timelike metric} \\ &= (E^2 - p^2) + m^2 + 2Em \\ s &= 2Em + 2m^2 \quad \text{since} \quad E^2 = p^2 + m^2, \end{aligned} \tag{C.38}$$

So, we have that

$$s = 4(E^*)^2 = 2Em + 2m^2. \tag{C.39}$$

The relation between E and p between the two frames is given by Lorentz transformation as

$$E = \gamma^* E^* + \gamma^* \beta^* p^*, \tag{C.40}$$

$$p = \gamma^* \beta^* E^* + \gamma^* p^*, \tag{C.41}$$

where β^* is the particle velocity normalised to light speed, and $\gamma^* = \sqrt{1 - (\beta^*)^2}$ is the corresponding Lorentz factor. All the relevant relations are as follows:

$$\beta^* = p^*/E^* = \sqrt{\frac{E - m}{E + m}} = \sqrt{\frac{s - 4m^2}{s}}, \tag{C.42}$$

$$\gamma^* = E^*/m = \sqrt{\frac{E + m}{2m}} = \frac{\sqrt{s}}{2m_p}, \tag{C.43}$$

$$\gamma^* \beta^* = p^*/m = \sqrt{\frac{E - m}{2m}} = \frac{\sqrt{s - 4m^2}}{2m}. \tag{C.44}$$

In order to relate the LI cross-section to the energy-differential one in (C.32), we first need to link the LI kinetic variables $\{\sqrt{s}, x_R, p_T\}$ to that of an equivalent set in the LAB frame, where the target is at rest. One such set is given by the projectile and the $\bar{p}$ kinetic energies, and the scattering angle $\{T, T_{\bar{p}}, \cos(\theta)\}$.

From C.39, we can write that

$$s = 2Tm + 2m^2. \tag{C.45}$$

The transverse momentum is invariant under Lorentz transformation

$$p_T = p \sin\theta = \sqrt{2m^2 + 2Tm}/\cosh(\eta) \quad \text{where} \quad \sin(\theta) = 1/\cosh(\eta) \quad \text{for} \quad \theta \in [0, \pi]. \tag{C.46}$$

Finally, we get:

$$\begin{aligned} x_R &= \frac{E^*_{\bar{p}}}{E^*_{\bar{p},max}} = \frac{2\sqrt{s}E_{\bar{p}}}{s - 8m_p} \quad \text{with} \\ E^*_{\bar{p}} &= \gamma^* E_{\bar{p}} - \gamma^* \beta^* p_{L_{\bar{p}}} \quad \text{and} \\ p_{L_{\bar{p}}} &= \cos(\theta) p_{\bar{p}} = \tanh(\eta) p_{\bar{p}}. \end{aligned} \tag{C.47}$$

So, the energy-differential invariant cross-section becomes

$$\begin{aligned} \frac{d\sigma}{dT_{\bar{p}}}(T, T_{\bar{p}}) &= \int d\Omega \frac{d^3\sigma}{dE_{\bar{p}} d\Omega} \\ &= \int_0^{2\pi} d\phi \int_{-1}^{1} d\cos(\theta) p_{\bar{p}}^2 \frac{dp_{\bar{p}}}{dE_{\bar{p}}} \frac{d^3\sigma}{p_{\bar{p}}^2 dp_{\bar{p}} d\Omega} \\ &= 2\pi \int_{-1}^{1} d\cos(\theta) p_{\bar{p}}^2 \frac{E_{\bar{p}}}{p_{\bar{p}}} \frac{1}{E_{\bar{p}}} \sigma_{inv} \\ &= 2\pi p_{\bar{p}} \int_{-1}^{1} d\cos(\theta) \sigma_{inv} \\ &= 2\pi p_{\bar{p}} \int_{-\infty}^{\infty} d\eta \frac{1}{\cosh^2(\eta)} \sigma_{inv}, \end{aligned} \tag{C.48}$$

So, we finally have

$$\frac{d\sigma}{dT_{\bar{p}}}(T, T_{\bar{p}}) = 2\pi p_{\bar{p}} \int_{-\infty}^{\infty} d\eta \frac{1}{\cosh^2(\eta)} \sigma_{inv}, \tag{C.49}$$

where $\cos(\theta) = \tanh(\eta)$ was used in the last line. Here θ is the angle between incident projectile and the produced anti-proton in the LAB frame. In the last line, the angular integration is transformed to that of one with pseudorapidity defined as

$$\eta = -\ln\left(\tan\left(\frac{\theta}{2}\right)\right). \tag{C.50}$$

This transformation provides us with an advantage because the invariant cross-section is very peaked in the forward direction at small angles.

In fig. C.9, we can see the three different parametrisation of the $p + p \rightarrow \bar{p} + X$ cross-section [140]. The figure displays the profile of energy differential cross-section for either fixed T_p or $T_{\bar{p}}$. At anti-proton energies of few 10 GeV, which are dominantly produced by protons with an energy of a couple of 100 GeV, all approaches are in agreement. However, at lower and higher energies, the agreement starts getting diffused. In particular, for anti-proton energies below 10 GeV, the disagreement is non-negligible. For more information, one can refer [140].

C.4 Determination of Precision on the Cross-Section

To determine the uncertainty requirements on the $\bar{p}$ cross-section measurements for a given cosmic anti-proton flux accuracy, the contribution to the source term from each point in the parameter space of the fully differential LI cross-section is determined, and then two principles

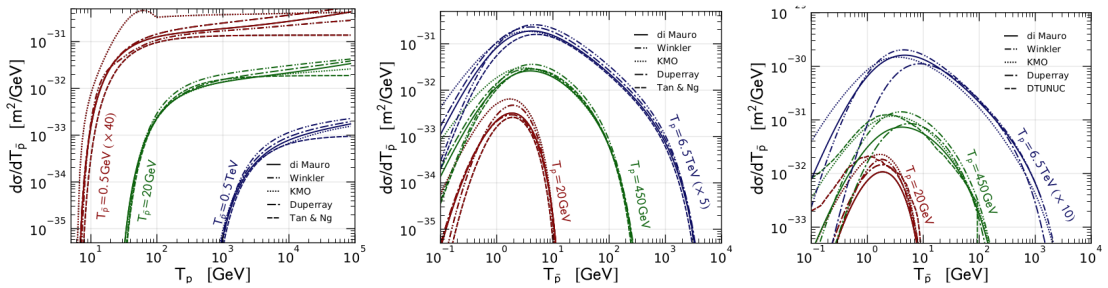

(a) (b) (c)

Figure C.9: Panel a) and b) shows the energy-differential cross-sections for the interaction $p + p \rightarrow \bar{p} + X$ in the LAB frame for fixed anti-proton and proton kinetic energy respectively. Panel c) is similar to b) but for the interaction $p + He \rightarrow \bar{p} + X$. Plots taken from [140].

are followed [140]

- The total uncertainty should be compatible with the experimental flux accuracy provided by AMS-02.

- Higher accuracy is required in the parameter space where the cross-section provides a dominant contribution to the source term.

The uncertainty level in the anti-proton flux measurement is taken as the starting point with AMS-02 data as a prior, as the latter provides us with the most accurate determination over the widest energy range. The relate the TOA spectrum to the $\bar{p}$ source spectrum, the local IS fluxes are extracted from the TOA one. The solar modulation effect is corrected by using a force-field approximation, which dictates a simple shift of all data points by $\Delta E = |Z|\phi_{\odot}$, where $\phi_{\odot}$ is fixed at 600 MV. After that, the relation between the IS flux and the source spectrum is obtained by the diffusion equation dictating the propagation of CR, as discussed in chapter 2.

In a first order approximation, we can assume that the relative uncertainties of IS flux and the source term are equal above $\sim 1\ GeV$. As flux and source term are linked by linear differential equation, the diffusion term keeps the ratio unaffected. The only possibility of affecting the ratio comes from energy distortions between the propagated flux and the source spectrum that can arise because of reacceleration at very low energies. However, in [140], several strongly peaked toy-source term spectra were propagated using GALPROP, and compared with the resulting propagated flux, and it was concluded that the energy distortion is negligible down to 1 GeV. Hence, the relative flux uncertainty $\sigma_{\phi_{\bar{p}}}$ is used as a proxy for source term uncertainties σ_q:

$$\sigma_q^{rel}(T_{\bar{p}}) \equiv \frac{\sigma_q(T_{\bar{p}})}{q(T_{\bar{p}})} \approx \frac{\sigma_{\phi_{\bar{p}}}(T_{\bar{p}})}{\phi_{\bar{p}}(T_{\bar{p}})}. \tag{C.51}$$

The quantity $\sigma_q^{rel}(T_{\bar{p}})$ can be inferred from fig. C.10, which has been derived from the AMS-02 $\bar{p}$ measurements [27]. And we see that between 1 and 100 GeV, the uncertainty is below 5 %. Hence this is the minimum level of accuracy which is required for any prediction. The uncertainty of the source term has to be distributed among each production channels. It is

assumed that the relative uncertainties in all the p and He channels are equal, hence

$$\sigma_q^{rel}(T_{\bar{p}}) = \sigma_{q_{ij}}^{rel}(T_{\bar{p}}). \tag{C.52}$$

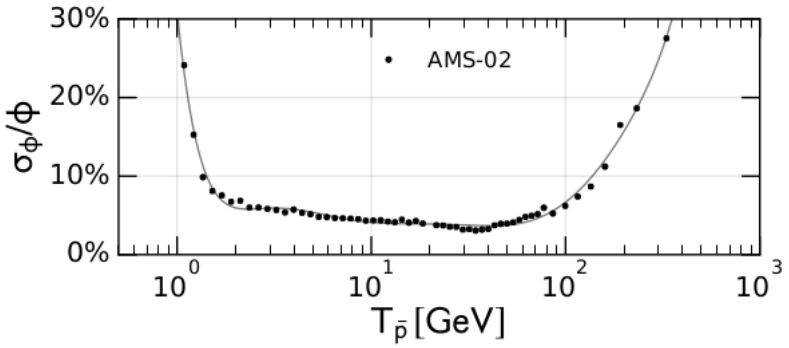

Figure C.10: Relative uncertainty of the AMS-02 anti-proton flux measurements. The demodulated IS flux is shown, i.e., each data points are shifted by 600 MeV. Plot taken from [140].

In order to determine the contribution from each parameter point of the invariant cross-section, we insert (C.49) in (C.31), and changing the energy integration to $log(T)$ to work with the full expression of the source term, to obtain:

$$q(T_{\bar{p}}) = \int_{log(E_{th})}^{\infty} d\log(T) \int_0^{\infty} d\eta \underbrace{\frac{8\pi^2 p_{\bar{p}} n_{ISM} T \phi(T) \sigma_{inv}(T_{\bar{p}}, T, \eta)}{\cosh^2 \eta}}_{\equiv I(T_{\bar{p}}, T, \eta)}. \tag{C.53}$$

where the labels i and j has been dropped. The containment function is defined as

$$x(T_{\bar{p}}, T, \eta) = \frac{1}{q(T_{\bar{p}})} \int_{I(T_{\bar{p}}, T', \eta') > I(T_{\bar{p}}, T, \eta)} d\log(T') d\eta' I(T_{\bar{p}}, T', \eta'). \tag{C.54}$$

The containment function varies between $[0, 1]$. For e.g., if $x < 0.9$, it means that at a given anti-proton energy, we have experimentally explored 90 % of the source term. More details on the calculation procedure can be read in [140].

In fig. C.11, we can see the containment parameter space for the pp channel when $x(T_{\bar{p}}, T, \eta) = 0.90, 0.99,$ and 0.999, as a function of pseudorapidity η and proton kinetic energy T_p at fixed anti-proton kinetic energy $T_{\bar{p}} = 50\ GeV$. Here we can see that 90 % of the anti-protons are produced by protons with energies spanning about 90 GeV - 3 TeV and η between 2 and 7. If we want to explore 99.9 % of the pp source spectrum, one has to consider protons with energies up to 70 TeV with pseudorapidity values around 5.

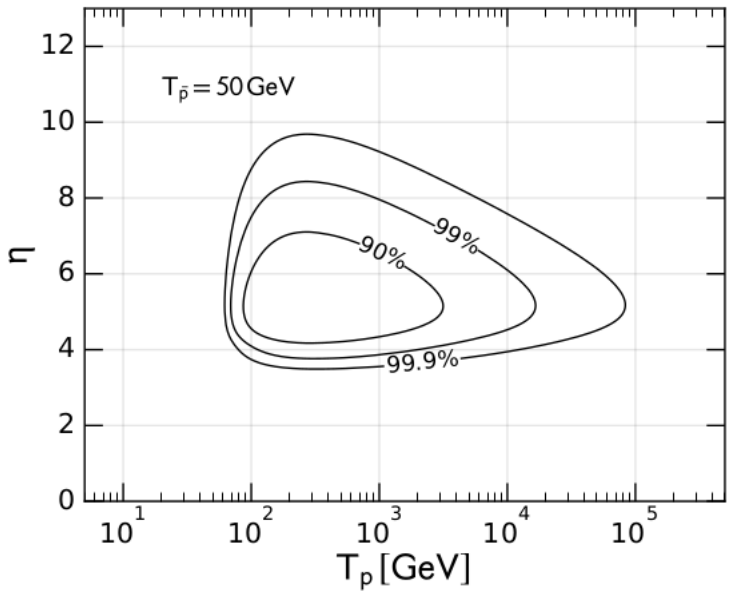

Figure C.11: Isocontours for the containment function $x(T_{\bar{p}}, T, \eta)$ for the contribution of the pp channel to the anti-proton source term as a function of kinetic variables, incident proton kinetic energy T_p and pseudorapidity η in the LAB frame, at a fixed anti-proton kinetic energy $T_{\bar{p}} = 50$ GeV. Here 90 % level corresponds to $x = 0.9$. Plot taken from [140].

The relative uncertainty on the invariant cross-section is represented as $\sigma^{rel}_{\sigma_{inv}}$, and it should increase as x varies from 0 to 1. By increasing x, one increases the spanned kinematical parameter space. In calculation, a precision level has to fixed for the relative uncertainties on the LI cross-sections for $\bar{p}$ production. One such choice was made in [140] as step function:

$$\sigma^{rel}_{\sigma_{inv}} = \begin{cases} 3\% & \text{if } x < x_t(T_{\bar{p}}) \\ 0 & \text{if elsewhere} \end{cases} . \tag{C.55}$$

It should be noted that the choice is free but based on most precise measurements of cross-section and spread of various paremetrisations in the energy regime of interest. Here $x_t(T_{\bar{p}})$ is a threshold value for containment function and is fixed by the requirement to match AMS-02 accuracy, which is found by solving

$$\int_0^1 dx \sigma^{rel}_{\sigma_{inv}}(x, T_{\bar{p}}) = \sigma^{rel}_q(T_{\bar{p}}). \tag{C.56}$$

The R.H.S of the above equation is taken from the parametrisation of the uncertainties on the $\bar{p}$ data as shown in fig. C.10.

The parameter space of the inclusive $\bar{p}$ cross-section is determined in accordance with the accuracy dictated by recent AMS-02 measurements. Fig. C.12 displays the parameter space that has to be covered by experiment to guarantee the AMS-02 precision level on the $\bar{p}$ source term, if the the $p + p \to \bar{p} + X$ cross-section is determined with 3 % uncertainty within the blue shaded regions and by 30 % outside the contours. The plot is done for both the LAB (kinetic energy of the proton and anti-proton T_p, and $T_{\bar{p}}$ respectively, and the pseudorapidity of the anti-

proton η)and CM (CM energy $\sqrt{s}$, ratio between anti-proton energy and its maximal energy x_R, and the transverse momentum of the anti-proton p_T) frame reference variables. So, for the LAB frame, the contours are shown as a function of η and T, for selected values of $T_{\bar{p}}$ from 1.1 GeV i.e the lowest energy below 30% uncertainty in the CR $\bar{p}$ flux as seen in fig. C.10 to 300 GeV. As expected, the contour decreases when $T_{\bar{p}}$ approaches to 1 GeV, as the AMS-02 uncertainty on the anti-proton flux there reaches 30 %. Similarly for the case of higher values of $T_{\bar{p}}$. The coverage of η values increases with anti-protons of increasing energy. For the whole AMS-02 energy range, one should collect the cross-section data with proton beams from 10 GeV to 6 TeV, and η increasing from 2 to nearly 8. The right panel of fig. C.12 displays the contours in the CM reference frame. The $\sqrt{s}$ is fixed to representative values from 5 to 110 GeV. A full coverage of the parameter space should span p_T from 0.04 to 2 GeV, and x_R from 0.02 to 0.7.

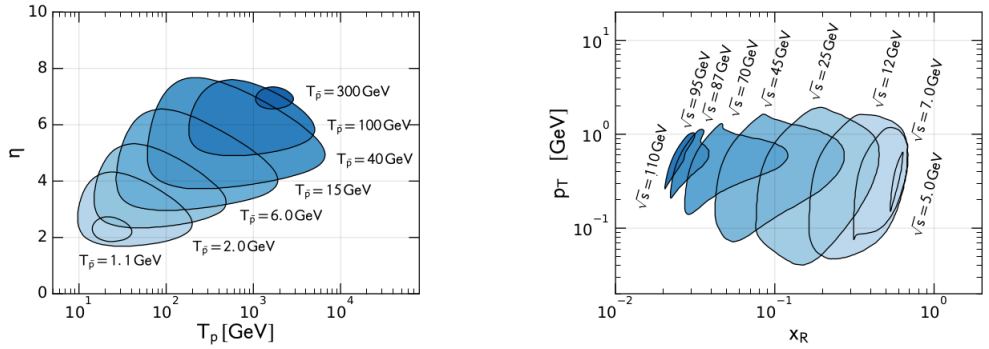

(a) LAB frame

(b) CM frame

Figure C.12: Contour plot of the parameter space for $pp \rightarrow \bar{p}X$ cross-section required to determine the anti-proton source term with accuracy similar to AMS-02 measurements. Here, within the blue shades regions, the cross-section has to be known with an accuracy of 3% and 30 % outside. Plots taken from [140].

The parameter space at first approximation, for pp and pHe channels are related by a rescaling, however this rescaling depends non linearly on the atomic mass number, CM energy, and the Feynman scaling variable. As such, the only way to obtain the rescaling is through an empirical fit on the data. Hence along with pp channel, it is of prime importance to obtain the cross-section measurements in the pHe channel. Using high-energy protons scattering off a fixed helium target, in order to have the 3% - 30 % accuracy requirement, to reach the AMS-02 precision of the $\bar{p}$ spectrum, we need the following span of parameter space as shown in fig. C.13, where the contours are displayed for anti-proton momentum and transverse momentum. The parameter space spans from below 10 GeV to more than 6.5 TeV, while the required $\bar{p}$ momentum tracks the AMS-02 measurement range from about 1 to 350 GeV. The LI transverse momentum lies between 0.04 to 2 GeV. Similarly to pp channel, at T_p below 10 GeV or above 2 TeV, the contour size shrinks as the dominant production of anti-proton is below or above the AMS-02 measurement range, respectively.

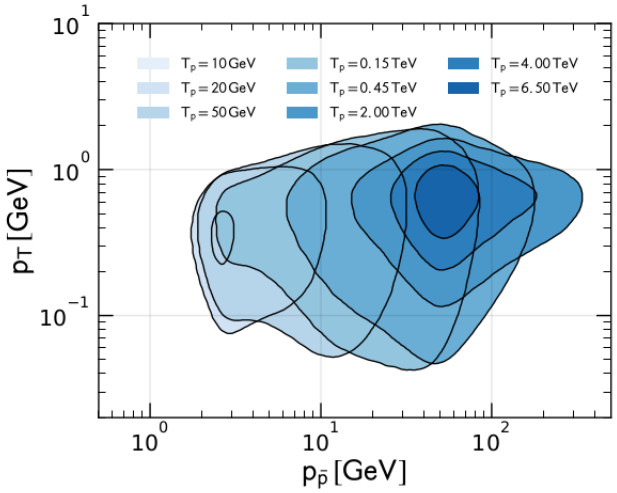

Figure C.13: Parameter space for the pHe channel for a fixed He target experiment. The different shaded areas corresponds to different proton beam energies. Plot taken from [140].

Nuclei that are heavier than helium contributes to a small amount of secondary anti-proton production [197]. The dominant reactions are those involving protons and helium ($p + p$, $p +^4 He$, $^4He + p$, $^4He +^4 He$). As can be seen in fig. C.14 , the interactions involving ^4He either as a target or projectile represents 40 % of the $\bar{p}$ production.

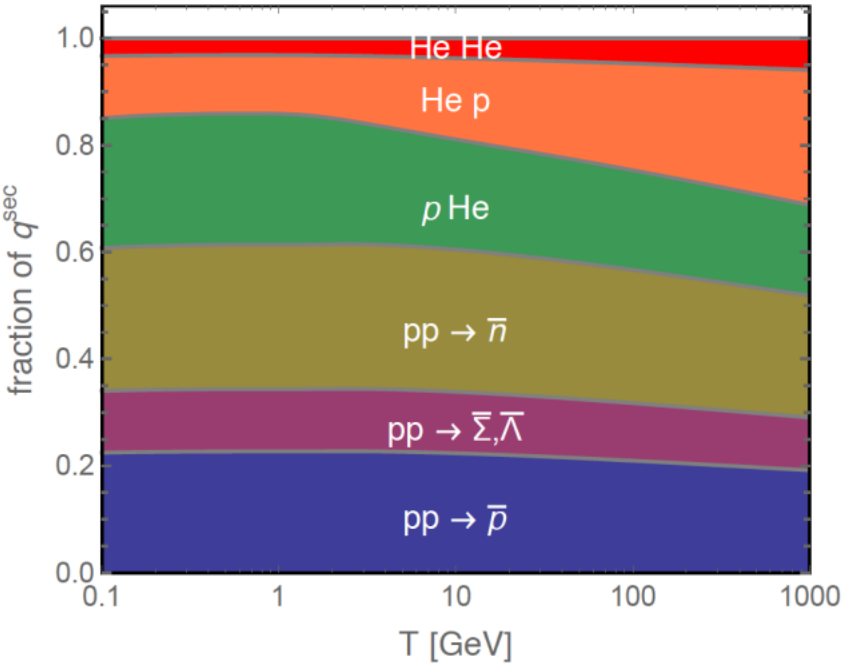

Figure C.14: Fractional contribution to $\bar{p}$ production from different interactions on the ISM as a function of $T_{\bar{p}}$. Plot taken from [13].

In principle *anti-neutrons* and *anti-hyperons* can decay into anti-protons, however, their total $\bar{p}$ production can be obtained by rescaling the prompt production i.e.,

$$\sigma_{tot} = \sigma_{prompt}(2 + \Delta_{IS} + 2\Delta_{\Lambda}), \tag{C.57}$$

where Δ_{IS} is the enhancement factor of anti-neutron-over-anti-proton due to isopsin effects,

and Δ_Λ is the hyperon factor, which assumes that the anti-proton and anti-neutron production from hyperons are equally abundant. It was found that the combined uncertainty arising from anti-neutron and hyperon induced production didn't exceed 5% and to be energy dependent [278].

The AMS-02 precession measurement of $\bar{p}/p$ ratio offers two promising momentum ranges for DM discovery: $10 - 20\ GeV/c$, and $200 - 300\ GeV/c$. The first window was studied in [110, 123–126], and alludes towards the existence of WIMP candidates in the mass range 50-90 GeV/c^2. In addition to that, the discrepancy observed in the high energy window could result from the annihilation of a heavy, TeV-scale WIMP candidate, as suggested by combing positron and anti-proton production measurements [217].

In case of $p + p$ collisions, a few experimental data sets are available [117–119] , and the first data set on $p +^4 He$ collisions was collected towards the end of 2015 by the LHCb experiment using 4 TeV and 7 TeV protons and a ^4He target [6].

In the light of above, the collection of new data using a proton beam with energies ranging between 50 to 280 GeV with a ^4He (or H) target would allow us to extensively characterise the $\bar{p}$ production spectrum, which can be further used to derive and/or constrain $\bar{p}$ production models, and would help us to decrease the overall uncertainty on the $\bar{p}$ production cross-section.

As such, we perform the aforementioned measurement in the COMPASS++/AMBER facility at the M2 beam line of the CERN SPS, with data taking starting from mid of May, 2023 till the last week of June.

C.5 Dark Matter Candidates for AMS-02 and criticism of MOND theories

Several possible DM candidates have been put forth in literature. A theoretical exposition of DM candidates is not the purpose of the present work. However, for completeness, following is a very brief qualitative description of the same based on the work done in [216].

- **SUSY particles :** The challenge of gauge hierarchy problem (i.e. massive discrepancy between various aspects of weak forces and gravity) is elegantly addressed through the implementation of supersymmetry [157, 161, 236]. Within supersymmetric extensions of the Standard Model, each particle in the Standard Model is accompanied by an unexplored partner particle, sharing identical quantum properties and gauge interactions but differing in spin by $1/2$.

  For DM, we look at neutral spin $1/2$ supersymmetric particles which are given by

$$\text{spin 1/2 fermions} : \widetilde{B}, \widetilde{W}, \widetilde{H_1}, \widetilde{H_2} \rightarrow \text{Neutralinos } \chi_1, \chi_2, \chi_2, \chi_4 \tag{C.58}$$

The neutral spin $1/2$ femions mix to form four mass eigenstates, called the *Neutralinos*, where $\widetilde{B}$ is called *Bino*, $\widetilde{W}$ is called *Wino*; and $\widetilde{H_1}$ and $\tilde{H}_2$ are called *Higgsinos*, and a neutralino can be written as the following linear combination

$$\chi = \alpha\widetilde{B} + \beta\widetilde{W}^3 + \gamma\widetilde{H_1} + \delta\widetilde{H_2}. \tag{C.59}$$

Then a mixing matrix is constructed similar to one of the Higgs sector, which mix the mass and the electroweak/supersymmetric states. Based on the amount of Bino, Wino and Higgsino fraction, models are created out of which AMSB (Anomaly Mediated Symmetry Breaking) Wino MSSM seems to be most suitable for AMS-02, both in anti-protons and positron channel [216].

- **Little Higgs Particle:** As a substitute approach to SUSY for ensuring the stability of the weak scale, the "Little Higgs" model has been suggested and advanced. Within these models, the Higgs of the SM assumes the role of a pseudo-Goldstone boson, with its mass safeguarded through approximate nonlinear global symmetries. In these particular theories, the gauge group takes the shape of a direct combination of multiple identical factors, such as $SU(3) \times SU(3)$. Each individual $SU(3)$ factor can be envisioned as the $SU(2)$ group existing at a specific location within an additional spatial dimension. As a result, numerous advantages associated with theories involving extra dimensions can be replicated, despite the fact that the little Higgs theory is confined to three spatial dimensions plus one temporal dimension. One of the classes of this model includes the "theory space" Little Higgs model, and can provide a stable, scalar particle that can give us the measured density of dark matter. AMS-02 can explore the parameter space of this theory [60, 235].

- **Scalar Singlet:** A minimalistic approach to extend the SM to provide an explanation for DM involves introducing a real scalar singlet and preserving an unbroken Z_2 symmetry [175, 237]. Under this symmetry, the singlet is assigned an odd value while all other fields possess even values. The singlet model consists of just one additional field, the singlet scalar, along with two new parameters: the mass of the singlet and the coupling between the singlet and the Higgs which is the only field in the SM that interacts with it. The relic density of the singlet, as well as its rates of direct and indirect detection, are further influenced by the mass of the Higgs. By imposing the constraint of DM, the viable parameter space is simplified to solely the singlet mass and the Higgs mass. The renormalisable Lagrangian can be realised as:

$$\mathcal{L} = \mathcal{L}_{\mathcal{SM}} + \frac{1}{2}\partial_\mu S \partial^\mu S - \frac{m_0^2}{2}S^2 - \frac{\lambda_s}{4}S^4 - \lambda S^2 H^\dagger H, \tag{C.60}$$

where $\mathcal{L}_{\mathcal{SM}}$ is the SM lagrangian, H is the Higgs doublet, and S is the singlet scalar field. AMS-02 measurements can put constraints on these theories in the anti-proton channel.

- **Primordial Black Holes:** Micro black holes are anticipated as minuscule black holes, also referred to as quantum mechanical or mini black holes, where quantum effects play

a significant role. These quantum primordial black holes could have emerged during the high-density conditions of the Early Universe or potentially during subsequent phase transitions. Astrophysicists may have the opportunity to detect them in the foreseeable future through the particles they are expected to emit via Hawking radiation. Certain theories that incorporate extra dimensions suggest that micro black holes could be generated at relatively low energy levels, such as in the TeV range achievable in particle accelerators like the LHC. However, these quantum black holes would rapidly dissipate, either completely or leaving behind an extremely weakly interacting residue. Regarding their detectability, numerous challenges arise. Micro black holes primarily generate low energy hadrons. The production of anti-protons contradicts the data obtained from PAMELA, and the production of anti-deuterons is just on the cusp of AMS-02's sensitivity limit.

- **Kaluza-Klein Particle:** Kaluza-Klein theory was originally developed as an extension of General Relativity in 5-dimensions, and the field equations naturally accommodated the GR equations along with that of electrodynamics. One of its modern descendants is Universal Extra Dimension (UED). The simplest of UED models preserve a discrete parity called KK-parity, which implies that the Lightest KK particle (LKP) is stable and a possible DM candidate [78, 106, 249]. Another particle within the KK theory spectrum is the LZP, i.e., a right-handed neutrino which might account for DM observations. Both the predicted particles can be detected by AMS-02 in all the particle channels: positrons, anti-protons and anti-deuterons. Especially, a sharp bump in the high energy spectrum of anti-protons could allude to DM existence. However for this theory to be valid, extra-dimensions are a requirement and there's no evidence of it.

- **Axions:** The Axion is a pseudo Nambu-Goldstone of the spontaneously broken *Peccei-Quinn* symmetry, and was introduced as an attempt to solve the *strong CP problem*. The CP violating term in the QCD Lagrangian is given by:

$$\mathcal{L}_{\mathcal{CP}} = \Theta \frac{g^2}{32\pi^2} G^a_{\mu\nu} \widetilde{G}^{a\mu\nu}, \tag{C.61}$$

  where $G^a_{\mu\nu}$ and $\widetilde{G}^{a\mu\nu}$ are the gluon field strength and its dual respectively, Θ is a dimensionless parameter, whose value dictates the magnitude of the effective term of the Lagrangian. When the symmetry breaks, the axions accquire an effective coupling to gluons that cancels the Θ parameter, and solves the problem. The Axion has been discussed as a possible DM candidate [77, 200], however they aren't detectable through AMS-02.

- Other possible DM candidates but that cannot be (or most likely cannot be) detected by AMS-02 are ***Sterile Neutrinos*** [138], ***Singlino*** [215], ***4th SM generation Minimal Dark Matter*** [113], and ***Tulin Anti-baryonic Dark Matter*** [188].

C.6 Non-Particle Description of Dark Matter

The inability to find a suitable particle DM candidate also triggered the growth of non-particle description of DM. Even before theoretical DM landscape reached its full glory, attempts were made to explain observations not in line with GR with alternative theories. The simplest of which involves the modification of Newtonian gravity at large scale also called *Modified Newtonian Dynamics* (MOND). Another direct attempts include generalisation of the *Einstein-Hilbert action* to include higher order terms, or to introduce new fields in addition to the tensor-field of ordinary GR. A quick and short description of popular alternative theories of gravity can be found in [132]. However all these theories pose the following problems:

- MOND models aren't able to explain multiple cosmological observations. Although recently in 2021, relativistic MOND theories have been able to reproduce the CMB spectrum [253]. However from a pure philosophical perspective, they just add a new degree of freedom (a field ϕ) to explain the DM component, while the particle physics community presses for a new particle, and hence both the contrasting pictures could be just manifestation of the same underlying theory. Another pespective might be that we have a combination of modified gravity and dark matter.

- Higher derivative theories like Hořava-Lifshitz gravity explains DM as an integration constant and are ghost-free [222]. Although it is power-counting renormalisable, it is not clear if it produces GR in the infrared limit (the RG flow studies of various couplings are still an area of research). Other higher derivative theories that includes higher order time derivative terms have the problem of ghost degrees of freedom.

- Scalar-Tensor-Vector Gravity (STVG) has been able to reproduce even the bullet cluster gravitational lensing but it adds a fifth force and several bosonic massive fields. Also, it is yet to be seen if STVG is also consistent with the invisible dark matter filament (cosmic thread) connecting the galaxy clusters Abell 222 and Abell 223.

In the light of above, a consistent particle landscape of Dark Matter seems exponentially more probable than a modification of classical gravity.

Appendix D

Monte Carlo Simulation of the AMBER-RICH Detector and RICH Ring Reconstruction Algorithm

D.1 Introduction

The RICH-1 constitutes a gaseous detector situated in the COMPASS facility at the M2 beam line of the CERN-SPS. It represents one of the pioneering RICH detectors in terms of its scale. A comprehensive account of the detector's construction is available in Appendix B, and therefore, further details are omitted in this section. The primary purpose of RICH-1 is to identify anti-protons for the pbar production cross-section measurement. To achieve this, an accurate Monte Carlo simulation of the detector was developed to facilitate various studies. Geant4, a powerful MC simulation toolkit, was employed in conjunction with the QT Graphical Interface for this simulation. While a detailed explanation of Geant4 and the code structure falls outside the scope of this thesis, the simulation results are presented and discussed.

The chapter commences with a description of a MC simulation of an ideal toy RICH detector using a solid radiator (NaF). Subsequent section focuses on the analysis of the Cherenkov rings, reconstruction of the ring, and extraction of event data; and relevant theoretical aspects. Following that, we conduct a basic MC simulation of a toy Gaseous RICH detector (C_4F_{10}); the physics analysis is not discussed in this case as it is similar to the former. The motivation behind starting from scratch was to validate our simulation from the ground up and to ensure the appropriate utilisation of Geant4 physics processes.

After confirming the robustness of our simulation, we proceed with employing the exact AMBER RICH-1 geometry in the MC simulation. Subsequent analysis entails developing statistical models to fit the RICH rings based on an elliptical geometry. The consistency of our MC simulation is scrutinized up to 50 GeV proton hits. Finally, in a step towards improving the RICH ring Reconstruction, we utilize the ROOT toolkit to simulate the physics processes and geometry of RICH-1. Further progress on the reconstruction algorithm is currently underway

as of the writing of this thesis.

D.2 NaF Radiator RICH MC simulation

The detector has been constructed with the following components:

- **NaF radiator:** NaF has one of the lowest refractive index among optical materials. Hence, it is a good material of choice for Cherenkov radiation based detectors. It has a refractive index of 1.3255 at 0.6 μm wavelength at 300 K. Another great option is that of Aerogel, however, the latter is difficult to handle structurally because of its brittle nature. It was decided to proceed with NaF because it is the most commonly discussed material for radiator in literature (for e.g., [59]). A very thin NaF disc of 5 mm thickness is used, to reduce the number of optical photons produced in the event generation; which further helps in reducing the computation time, as well as, facilitates in formation of thin Cherenkov Rings ultimately increasing the precision of our measurement.

  Geant4 allows the user to construct their own element, compounds and isotopes. As such, The NaF material was constructed using the following parameters in table D.1 with density: 2.56 g/cm^3.

NaF material construction		
Element eV	**Atomic Number**	**Atomic Mass** $g/mole$
Nitrogen (N)	11	22.989769
Flourine (F)	9	18.998403

Table D.1: NaF material parameters.

  In Geant4, for a realistic simulation, a vector array of the refractive index as a function of the photon energy needs to be instantiated D.2. This was achieved through the empirical *Sellmeier* single-resonance formula [59] fitting the NaF refractive index vs photon energy plot D.1:

$$\frac{n^2-1}{n^2+2} = \frac{F_A}{E_A^2 - E^2}, \tag{D.1}$$

  with $F_A = 48.76\ eV^2$, and $E_A = 15.78\ eV$, where E is the photon energy, and n is the refractive index.

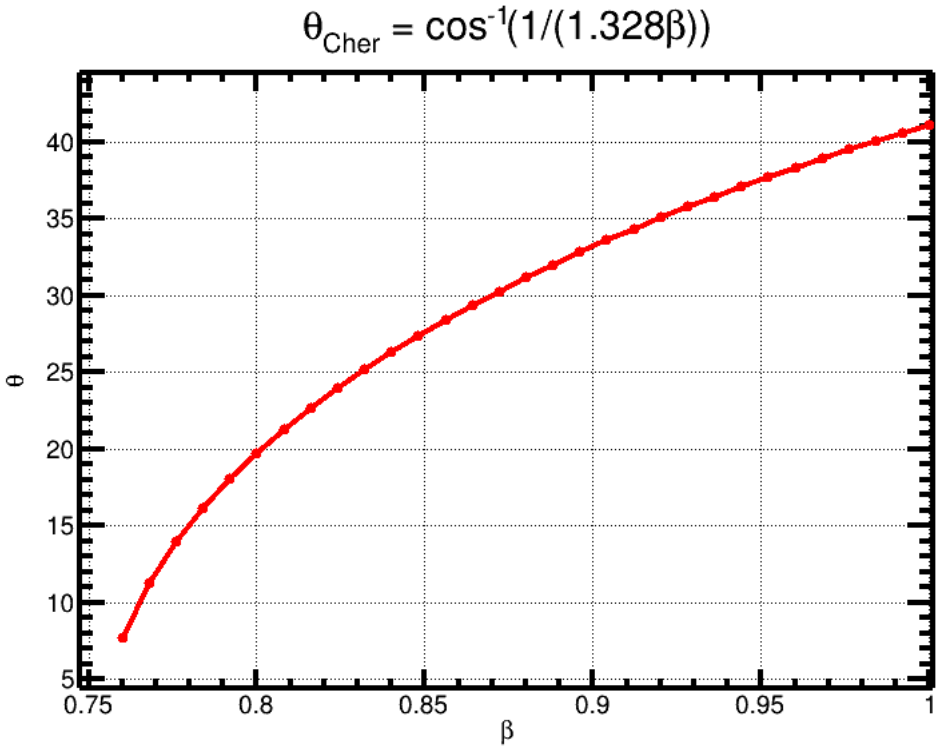

Figure D.2: Characteristic β vs θ curve in the RICH-NaF MC simulation for the refractive index 1.328 corresponding to photon energy 3.026 eV.

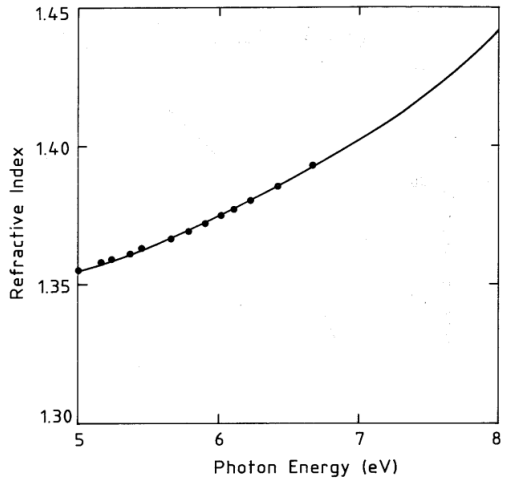

Figure D.1: Refractive index vs Photon Energy for NaF as reported in [59].

The refractive index is sufficiently small to let most of the Cherenkov photons to refract out and not be trapped by total internal reflection. At 3.026 eV, the refractive index is 1.328, which give the threshold $\beta = 0.75$, and $\beta\gamma = 1.33$, and maximum Cherenkov angle ($\beta = 1$) of 717 $mrad$. The variation of the Cherenkov angle with β is displayed in fig. D.2.

- **Photon Detector panel:** The detector to detect the optical photons is considered to be an ideal one without any quantum efficiency and photon collection efficiency loss. The detector has an area of 250×250 cm^2 and a thickness of 0.1 cm. No underlying optical physics has been considered for the photon detectors. The detector measures the

NaF Refractive Index Characterisation	
Photon Energy eV	**Refractive Index**
2.034	1.32133
2.068	1.32153
2.103	1.32174
2.139	1.32196
2.177	1.3222
2.216	1.32244
2.256	1.3227
2.298	1.32298
2.341	1.32327
2.386	1.32358
2.433	1.32391
2.481	1.32426
2.532	1.32463
2.585	1.32503
2.64	1.32546
2.697	1.32591
2.757	1.32639
2.82	1.32691
2.885	1.32747
2.954	1.32807
3.026	1.32872
3.102	1.32942
3.181	1.33018
3.265	1.331
3.353	1.3319
3.446	1.33287
3.545	1.33394
3.649	1.33511
3.76e	1.33641
3.877	1.33782
4.002	1.3394
4.136e	1.34117

Table D.2: The refractive index asa a functon of Photon Energy incorporated in the MC simulation.

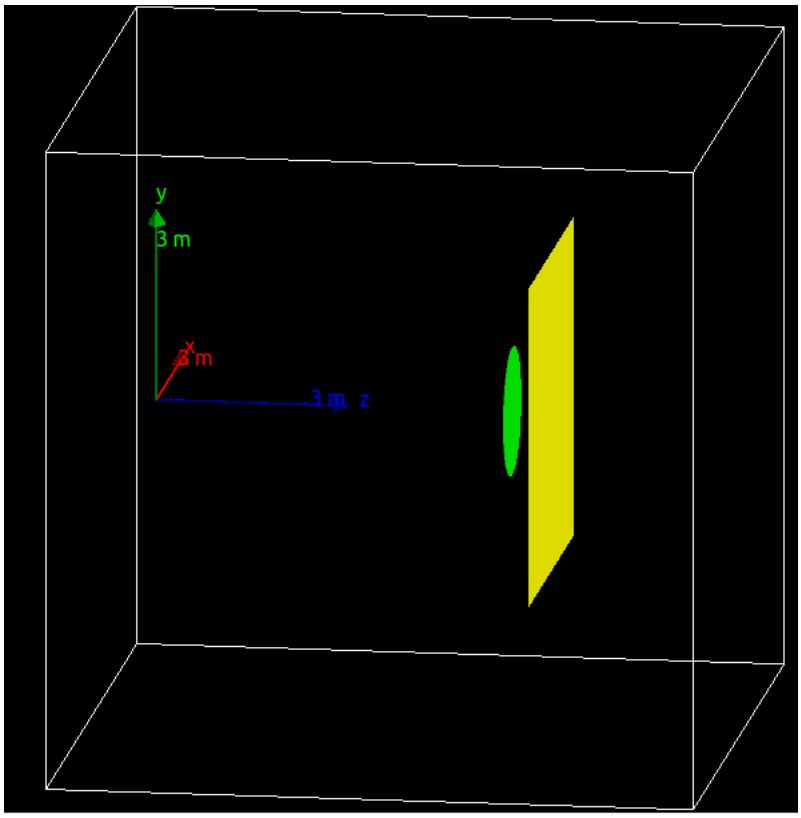

Figure D.3: The detector geometry of the RICH-NaF simulation. The circular disc is the **NaF radiator**, and the rectangular screen is the **photon detector**. The Geant4 simulation has been rendered with the QT GUI.

hit positions of the individual optical photons arriving on it, as well as the momentum, energy deposition, azimuthal and polar angles of the incoming particles, as well as the PDG (Particle Data Group) code.

- **Vacuum:** The vacuum is simulated in our case with a very low density gas with a characteristic refractive index of unity for all wavelengths.

Everything is placed in a chamber of $10 \times 10 \times 10\ m^3$ consisting of vacuum. While the Geant4 code is written in c++, a graphical interface called QT helps us to render the geometry as shown in fig. D.3.

In the MC simulation, the radiator and the photon detector is centered at $(x, y) \equiv (0, 0)$. The NaF radiator is centered at a distance of 150.25 cm along the z-axis, and the detector screen at a distance of 210.05 cm (Note that the NaF radiator and the detector has a thickness of 5 mm and $1mm$ respectively). The polar and azimuthal angles are measured with respect to z-axis (towards the right of the page here). Phenomena such a multiple scattering of the incident particle, reflection losses at the boundaries, and absorption losses in the bulk is taken in consideration by the physics processes in this particular simulation. Furthermore, the quantum efficiency and photon collection efficiency is considered to be unity. The event simulation with a 10 GeV proton has been shown in fig. D.4.

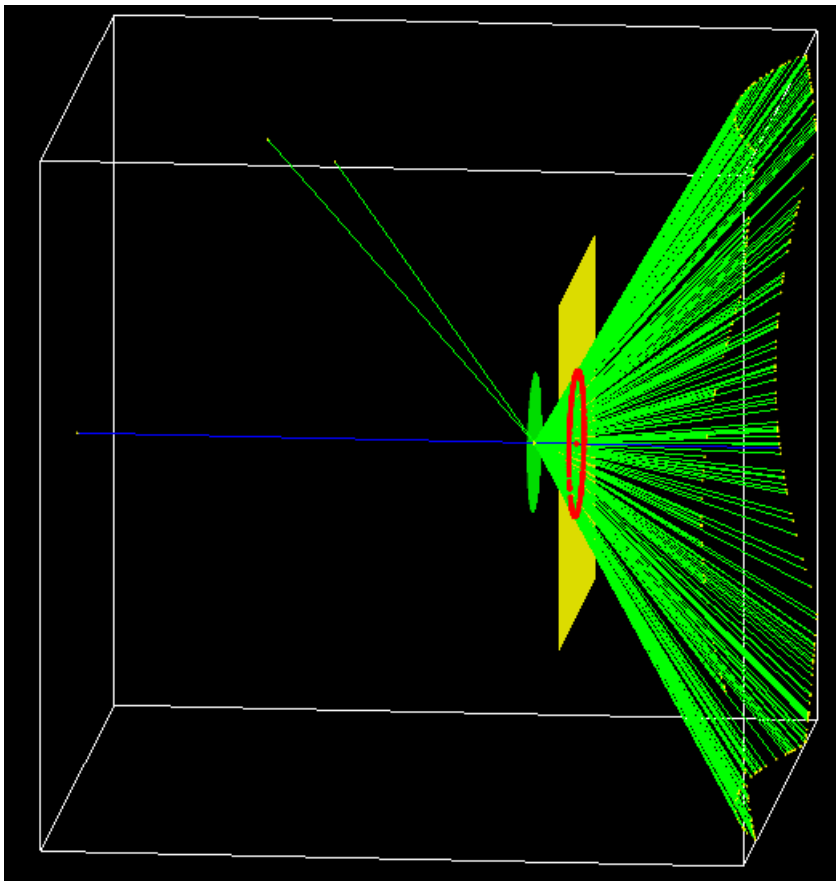

Figure D.4: A 10 GeV proton $\beta = 0.995$ perpendicular to radiator surface generates a cone of Cherenkov light which forms a Cherenkov Ring on the Detector screen.

D.2.1 RICH-NaF Ring Analysis

The result of the simulation with various particles and momentum are stored in a ROOT tree, from which various kinematical parameters like position, momentum, energy depostion can be retrieved to do data analysis. Plotting a 2-d histogram with x and y positions of the hit should give the Cherenkov Rings. To further extract the velocity from the rings, one need to have a Reconstruction Algorithm. In the first order approximation, a chi-square function to fit the circular rings were developed, and then utilising the geometrical, and optical parameters; the velocity (β) of the particle can be obtained.

D.2.1.1 Model to Fit Cherenkov Rings

To come up with a fitting algorithm, we utilise the property of a circle. We note that the distance from the centre to the a point in the circumference of the circle should be equal o the radius of the circle. So, a function that minimises the difference between the radius of the circle, and the distance from the centre to any point on the circumference should help us provide a good fit method. So, we write a function as

$$f(x, y; x_0, y_0, R) = R - \sqrt{(x - x_0)^2 + (y - y_0)^2}, \tag{D.2}$$

where x, y are the variables, and $x_0, y_0,\ R$ represents the free parameters ascribing the x-centre, y-centre, and radius of the ring respectively. The TMinuit ROOT class is utilised to achieve the fit; some of the fit results are displayed in fig. D.5.

D.2.1.2 β Reconstruction from Fit Model

The geometry of the simulation is shown fig. D.6a. The angle subtended by the circumference of the ring at the centre of the NaF disc can be determined easily with help of trignonometry such that

$$\sin(\theta_{out}) = \frac{R}{\sqrt{R^2 + d^2}}, \tag{D.3}$$

where d is the distance between the centre of the NaF disc and the centre of the detector plane, and R is the radius of the Cherenkov Ring. However, we note that the radiation changes medium from NaF to vacuum on its way towards the detector plane as shown in fig.D.6b. As such using the Snell's law

$$\begin{aligned} \frac{\sin(\theta_1)}{\sin(\theta_2)} &= \frac{n_2}{n_1} \\ \frac{\sin(\theta_{cher})}{\sin(\theta_{out})} &= \frac{1}{n(NaF)}, \end{aligned} \tag{D.4}$$

Using (D.4) in (D.3), we get for the actual Cherenkov angle θ_{cher}:

$$\sin(\theta_{cher}) = \frac{\sin(\theta_{out})}{n} = \frac{R}{n\sqrt{R^2 + d^2}}. \tag{D.5}$$

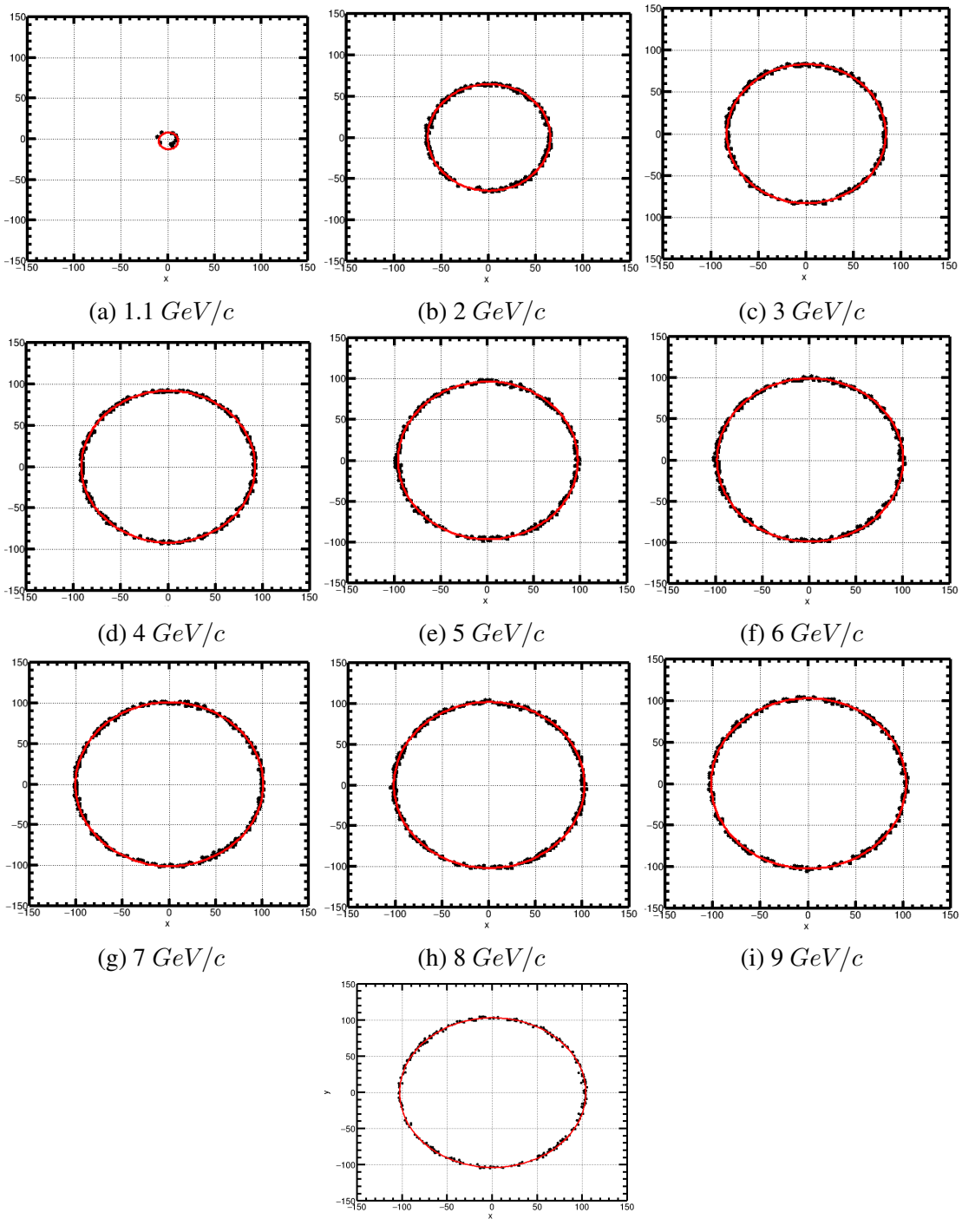

(a) 1.1 GeV/c (b) 2 GeV/c (c) 3 GeV/c

(d) 4 GeV/c (e) 5 GeV/c (f) 6 GeV/c

(g) 7 GeV/c (h) 8 GeV/c (i) 9 GeV/c

(j) 10 GeV/c

Figure D.5: The resultant Cherenkov Ring for a proton from the MC simulation with the fitted function on it, in increasing order of proton momentum. The arbitrary choice of 1.1 GeV/c as the first momentum for this representation is to be above the β threshold of NaF.

Using the Cherenkov expression, $\cos\theta = 1/n\beta$, we get for the β:

$$\beta = \frac{1}{n\cos\left(\sin^{-1}\left(\frac{R}{n\sqrt{R^2+d^2}}\right)\right)}. \tag{D.6}$$

And the error on beta is given as:

$$\sigma_\beta = \frac{Rd^2}{\sqrt{d^2+R^2}\left[[n^2(d^2+R^2)-R^2)\right]^{3/2}}\sigma_R. \tag{D.7}$$

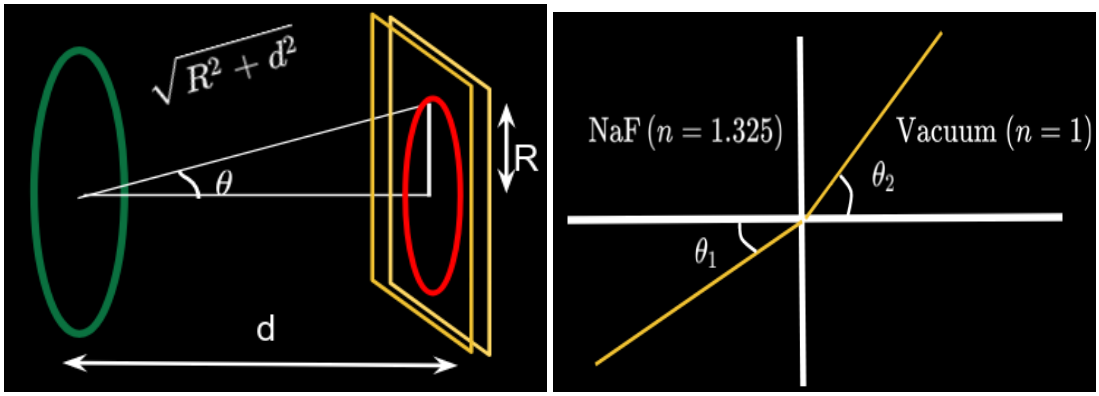

(a) 1.1 GeV/c (b) 2 GeV/c

Figure D.6: Left: The geometry of the MC simulation, the one in green is the NaF radiator, the Cherenkov Ring is in red, and the Detector plane is in yellow. Right: The refraction of the Cherenkov radiation at the interface of NaF radiator and vacuum.

The table D.3 shows the comparison between the theoretical β values for the momentum range $[1.1, 10]$ GeV/c for a proton and the associated error from the reconstruction algorithm. The range starts at 1.1 GeV/c to be above the β threshold for NaF. Meanwhile the table D.4 shows the same comparsion for the Cherenkov angle. The plot D.7 shows the θ-β curve for the MC β, and theoretical β at the measured momentum as depicted; which is superimposed on the theoretical curve, $\theta = \cos^{-1}(1/n\beta)$.

The successful simulation and good agreement with theory enables one to trust the physics processes and simulation procedures, which can be used to build upon and move towards further complexities, which in our case is the simulation of the AMBER-RICH detector.

Comparsion between Theory and Simulation for β					
Momentum (GeV/c)	**Energy** GeV	β_{theory}	$\beta_{measured}$	$\sigma(\beta_{meas})$	$\lvert\beta_{th} - \beta_{mes}\rvert/\beta_{th}$
1.1	1.44580	0.76082	0.76091	0.00015	0.00011
2	2.20915	0.90532	0.90535	0.00005	0.28784
3	3.14330	0.95441	0.95412	0.00003	0.00030
4	4.10857	0.97357	0.97313	0.00003	0.00045
5	5.08727	0.98284	0.98266	0.00002	0.00018
6	6.07292	0.98799	0.98784	0.00002	0.00015
7	7.06260	0.99114	0.99113	0.00002	0.61469
8	8.05483	0.99319	0.99282	0.00002	0.00038
9	9.04878	0.99461	0.99400	0.00002	0.00061
10	10.04392	0.99563	0.99559	0.00002	0.33244

Table D.3: Table comparing the theoretical and simulation values of velocity if a proton for different momentum

Comparsion between Theory and Simulation for θ (Degrees)				
Momentum (GeV/c)	**Energy** GeV	θ_{theory}	$\theta_{measured}$	$\lvert\theta_{th} - \theta_{mes}\rvert/\theta_{th}$
1.1	1.44580	7.3146	7.2633	0.00706
2	2.20915	33.5278	33.5253	0.00007
3	3.14330	37.7203	37.7427	0.00059
4	4.10857	39.1448	39.1767	0.00081
5	5.08727	39.8222	39.8352	0.00033
6	6.07292	40.1815	40.1917	0.00025
7	7.06260	40.4059	40.4063	0.00001
8	8.05483	40.5201	40.5455	0.00063
9	9.04878	40.6001	40.6408	0.00100
10	10.04392	40.7068	40.7090	0.00005

Table D.4: Table comparing the theoretical and simulation values of $\theta_{cherenkov}$ of a proton for different momentum

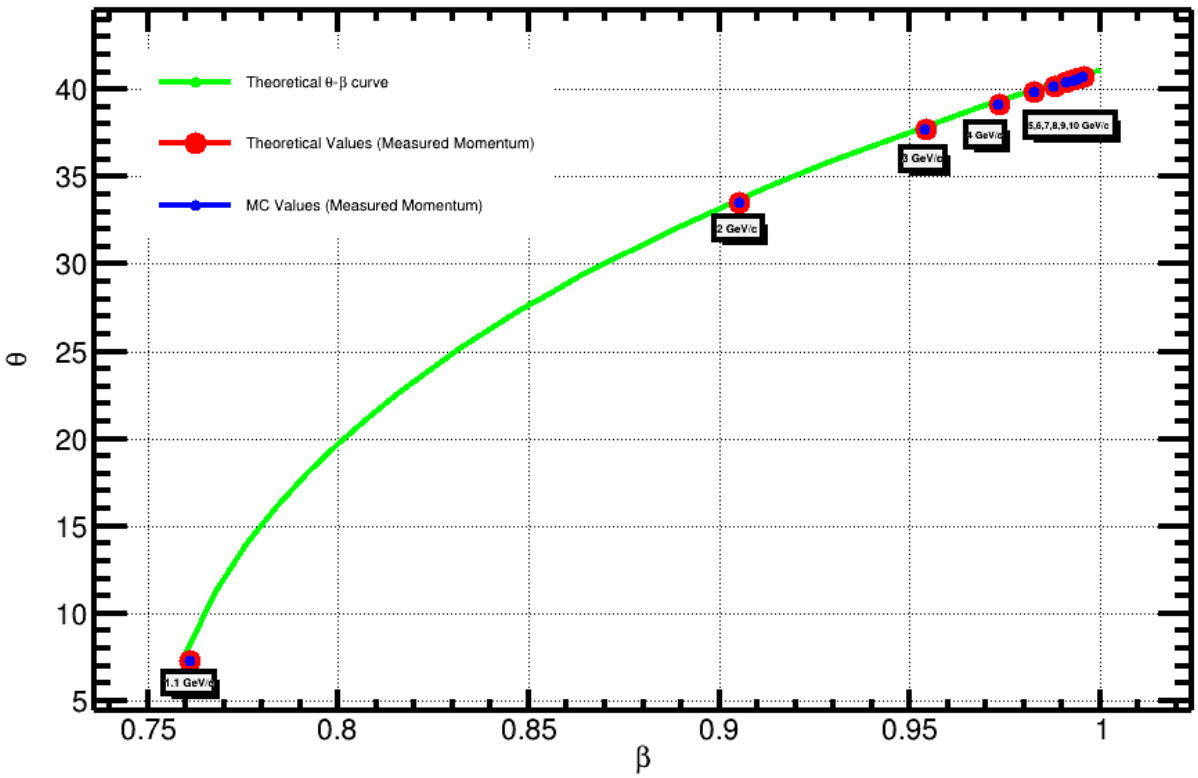

Figure D.7: The measured θ and β values at the simulated proton momenta as labelled. The plot clearly shows that the MC simulation is robust. Note that the marker size has been selected to be such that each of the partly (or partially) superimposed points are distinguishable.

D.3 Proximity Focussing Gas-RICH Detector

The main motive of this next step of simulation is to demonstrate the reliability of the supplementary physics processes required in addition to one already utilised in the simulation before. A discussion on the Cherenkov Rings and its analysis follows the same procedure as discussed in the previous section, and hence not done here. In this case, we replace the NaF radiator with a compartment filled with a suitable gas for the Cherenkov process. Since the gas present in the AMBER-RICH detector is C_4F_{10}, we use the same one for this simulation. The problem with gaseous RICH is that the emission of Cherenkov light is continuous, and we need to use a mirror to focus the light for the formation of a ring. As such, a spherical mirror with a high radius of curvature is also constructed to accomplish the purpose. We construct the detector with the following components:

- C_4F_{10} **gas:** This gas has a very low refractive index of ~ 1.0014 making it suitable for Cherenkov detection of highly energetic particles. The threshold β value is 0.9986 and maximum Cherenkov angle of 52.99 $mrad$. The variation of the Cherenkov angle with β is displayed in fig. D.8. We need to take in consideration that since it is a gas, the refractive index is a function of temperature and pressure. As such, we consider a temperature of 298.15 K and a pressure of 1 atm and a density of 11.2 kg/m^3. The gas was built in Geant4 with the parameters written in table D.5. We also consider a radiator volume of $500 \times 500 \times 300$ cm^3.

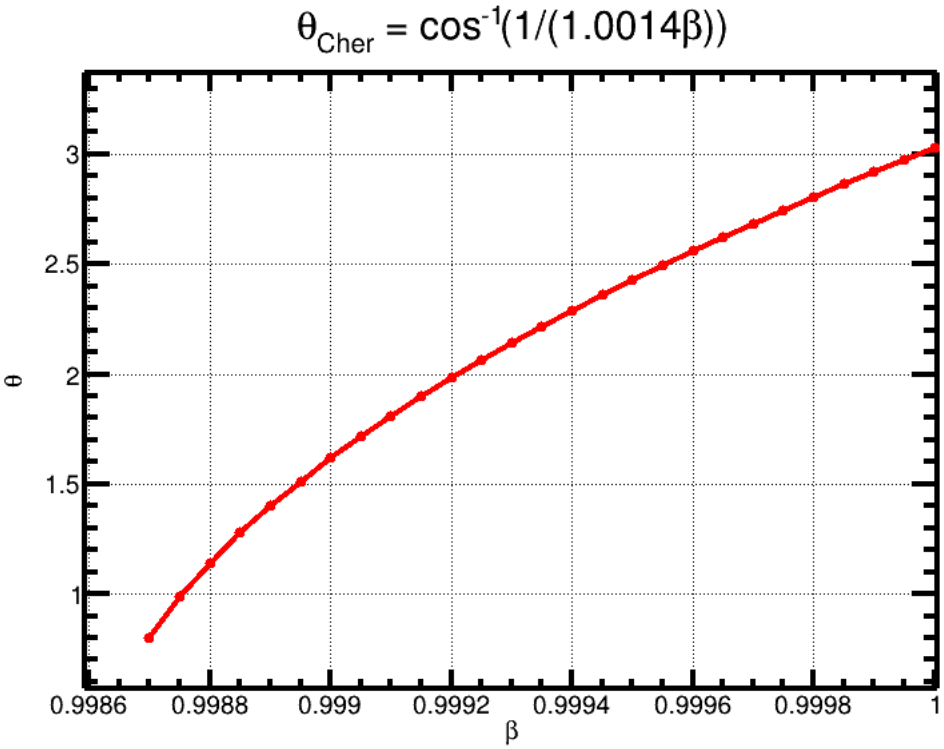

Figure D.8: Characteristic β vs θ curve in the RICH-C_4F_{10} MC simulation for the refractive index 1.0014.

C_4F_{10} **material construction**		
Element eV	**Atomic Number**	**Atomic Mass** $g/mole$
Carbon (C)	6	12.0107
Flourine (F)	9	18.998403

Table D.5: C_4F_{10} material parameters.

- **Focussing Mirror:** A paraboloid mirror of radius of curvature $500\ cm$ and depth $1\ cm$ is employed to focus the Cherenkov photons onto the detector screen with the following parametrisation
  - **Equation of Surface:** $z = a(x^2 + y^2) + b$, where a and b are some arbitrary parameters.
  - **Material:** Pyrex Glass.
  - **Surface finish:** Fully Polished with a top layer of paint with perfect specular reflection with angular width of the specular spike (see fig. D.9) set to 0. The reflectivity is also considered to be 1.
  - **Photon Detector Panel:** It is same as the NaF-RICH, except that the dimensions are $500 \times 500 \times 0.1\ cm^3$.

In the MC simulation, the gas volume and the Detector are centered at $(x, y) \equiv (0, 0)$. The Gas vessel is centered at a distance of 150 cm along the z-axis, and the detector screen at a distance of $-150\ cm$. The mirror is placed at a distance of 451 cm along the z-axis. It is to

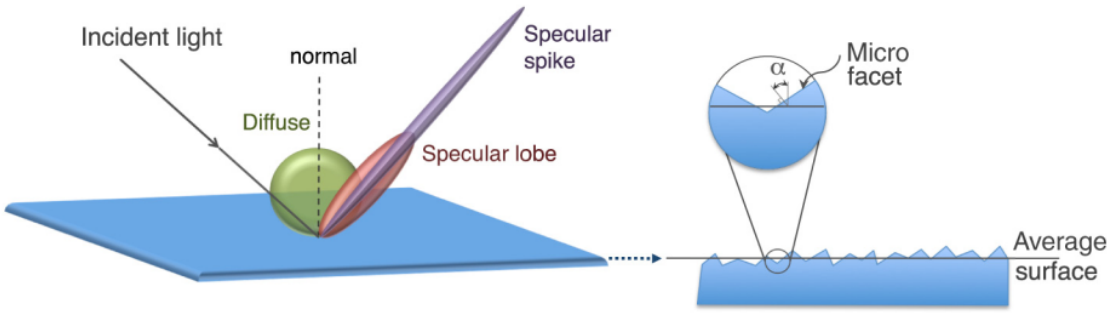

Figure D.9: Light reflection types: Specular spike (i.e., perfect mirror), specular lobe, and diffuse (Lambertian). A ground surface is composed of micro-facets where α is the angle between a microfacet normal and the average surface normal. Figure from [127].

be noted in Geant4 simulations, it is important to check overlaps between geometrical objects; in particular, for this case, the mirror geometry placement is important to avoid overlap with the gas vessel (else the reflection doesn't take place). Also, it is important to specify the type of interface which is *dielectric-dielectric* in our specific case. Physics processes to take in consideration the relevant optical physics for interaction between boundaries and interfaces have been implemented. The event simulation with a 100 GeV proton has been shown in fig. D.10. The data analysis of the resultant Cherenkov rings follow the same principle as the preceding analysis in the case of NaF-RICH, and is not discussed here further.

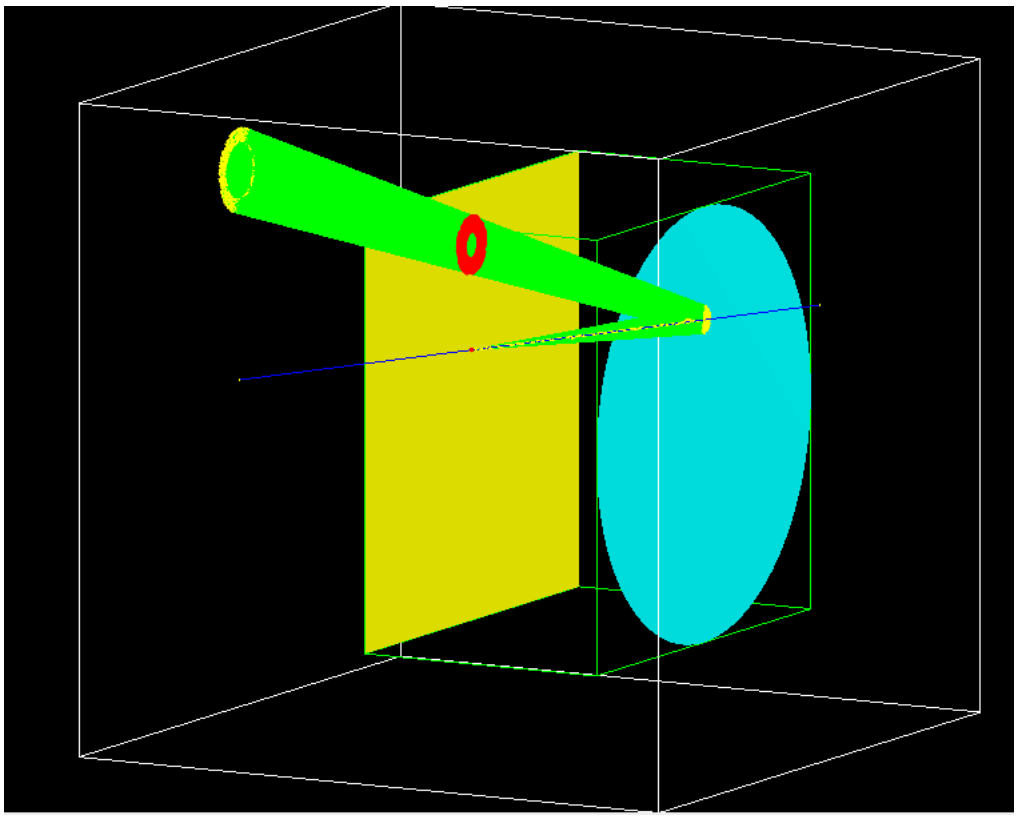

Figure D.10: A 100 GeV Proton $\beta = 0.99996$ fired at an angle of 197 $mrad$ with respect to the z-axis generates a cone of Cherenkov Light which forms a Cherenkov Ring on the detector screen after being reflected from the Paraboloid Mirror.

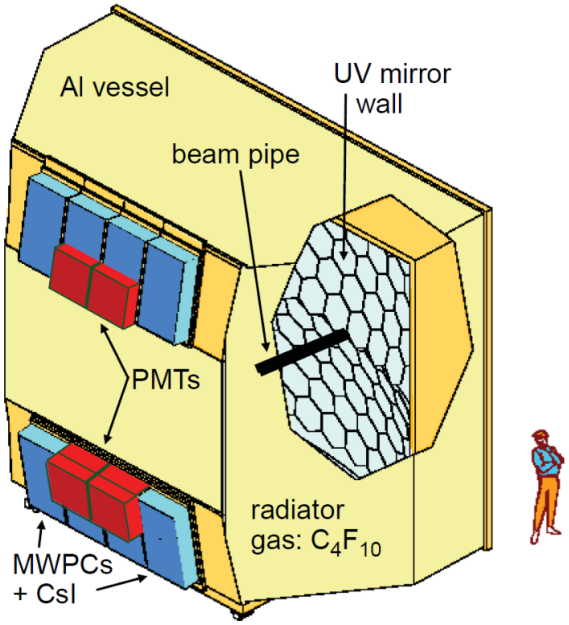

Figure D.11: Artistic rendition of RICH-1 detector. The person standing next to it helps one appreciate the size of the detector. Figure taken from [131]

.

D.4 AMBER-RICH

The Detector construction has been explained in details in Chapter 5, and one can refer to the references therein for further details. As such, an extensive discussion on the Detector Geometry (see fig. D.11) is not done in this section. However, for completeness, the main components of the Detector is summarised below:

- C_4F_{10} **Gaseous Radiator:** A $3 \times 6 \times 5\ m^3$ vessel consisting of high purity C_4F_{10}. The hydro-static pressure of the radiator gas are held by the front and rear windows, which are built with minimum material budget due to their presence in the spectrometer acceptance.

- **Beam Pipe:** A cylindrical pipe of 100 mm diameter on nominal beam axis had been installed to shadow the Cherenkov photons generated by the beam particles. This pipe is filled with helium to reduce the material budget.

- **Mirror:** The RICH-1 optical configuration consists of a pair of spherical VUV reflecting surfaces. These surfaces have a combined area exceeding 21 m^2 and are positioned with a vertical displacement of 1600 mm relative to the beam axis. This displacement serves the purpose of focusing the image outside the range accepted by the spectrometer. The main geometrical parameters of the mirror are shown in fig. D.12.

  The two surfaces are constructed using a mosaic pattern of spherical mirror units. The majority of these units are regular hexagons with sides measuring 261 mm. Additionally, there are 48 pentagons of six distinct sizes incorporated into the pattern. This variety helps prevent the formation of jagged patterns at the edges of the surface. Due to the

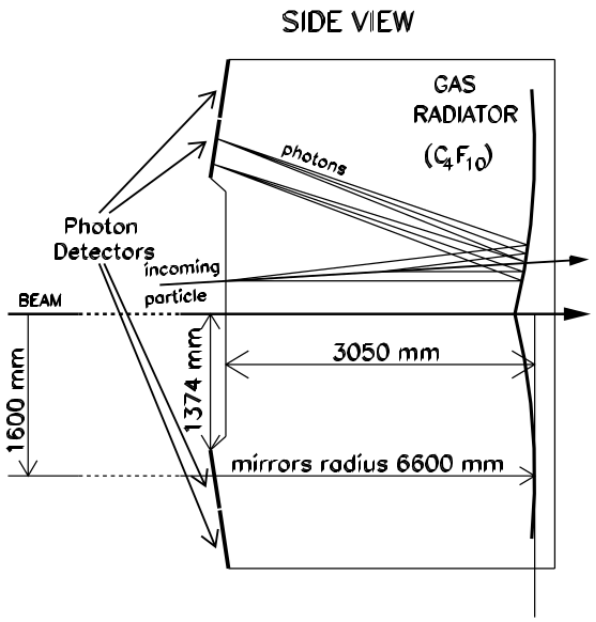

Figure D.12: The geometrical parameters of RICH-1. Figure taken from [41].

gaps left between adjacent mirrors, there is a loss of 4% in the overall reflective surface area. The main parameters of the mirros are

- **Radius of Curvature:** 6600 $mm \pm 1\%$.
- **Roughness:** R.M.S $< 1.6\ nm$.
- **Reflectance:** $r > 80\%$; for wavelengths in the interval 160–200 nm.
- **Substrate Thickness:** $<6\%$ of radiation length (minimum material is required also for the mechanical integrity of the mirror wall).

- **Photon Detectors (PD):** Vacuum based MAPMT dettectors, MWPC with CsI photocathodes as VUV (165–200 nm) PDs, and THGEM-MM based hybrid PDs. One can refer to [102] and [131] for complete details. The scheme of the PDs are shown in fig D.13. However for this simulation, we won't consider the optical physics of the PDs which is a non-trivial exercise and consider 100 % efficiency (quantum and photon collection, and photon to electron conversion). However we are also working on developing the reconstruction algorithm for the Cherenkov rings (See later sections), and for that purpose we would take all these non-trivial technicalities in consideration.

Owing to the geometry of the Detector, Cherenkov Rings can form in different ways, which we name in following categories, assuming we have a minimum number of photons to distinguish:

- **a) Semi-circular Upper Half Ring and Lower Half Ring:** This can happen if the incident particle is perfectly collinear with the Beam axis. This is a very unlikely event even though we decided to remove the Beam pipe while taking measurement.

- **b) Positively offset Upper half ring (Negatively offset lower half ring):** If the particle track is above the beam axis such that most of the Cherenkov light falls on the upper half mirror, than the lower ones

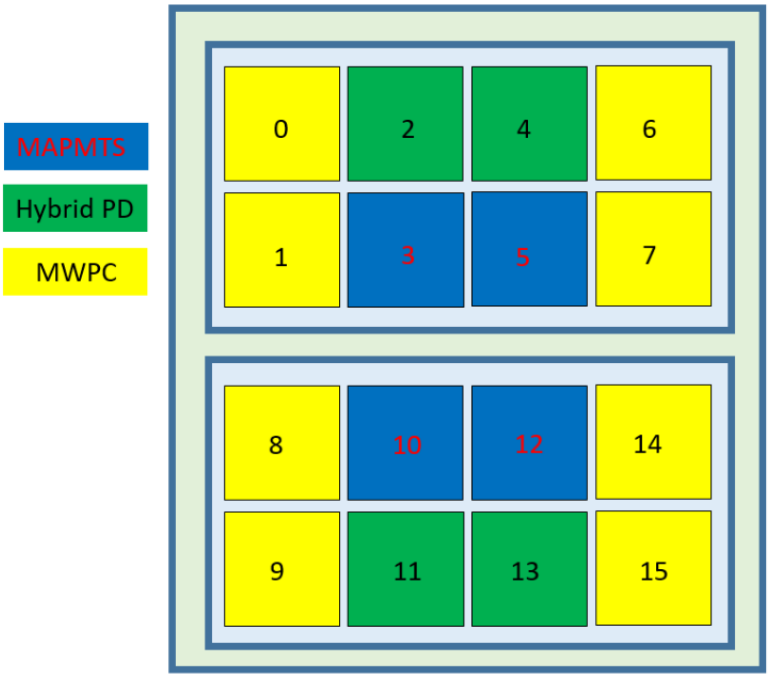

Figure D.13: The photon detectors present in RICH-1. The PDs are divided into two panels, upper and lower eaching consisting of 8 PDs. The nomenclature of each PDs is as depicted. Figure taken from [102].

- **c) Positively offset Lower half ring (Negatively offset Upper half ring):** If the particle track is below the beam axis such that most of the Cherenkov light falls on the lower half mirror, than the upper ones.
- **d) Full Upper or Lower rings:** These are the most probable cases, and happens when the particle track is sufficiently above or below the beam axis such that the Cherenkov light falls and is reflected by only one half of the mirror.
- **e) Multiple Rings:** When there are multiple particles like pions, kaons and protons traversing the expansion length which forms Cherenkov rings. In this case, the PID is extremely important, and for this purpose the reconstruction algorithm needs to be enhanced.
- **f) Fringe Cases (The case of two photons):** The minimum number of photons required to reconstruct the ring is theoretically two photons. However, if we have fringe cases, where one photon is detected in the lower PD, and one in the upper, we have to discard such cases. An estimate of such fringe cases is not possible in the present simulation because of non consideration of PD Physics, but can be implemented in the future.

Some typical examples exemplifying the above cases (except the case (f) as it requires PD physics simulation) are shown in fig. D.14 and D.15.

D.4.1 Model to Fit the Cherenkov Rings

A model similar to the one employed in the preceding section for NaF-RICH, based on fitting a circle will not work in this case. This is because the photon detector containers are placed at an

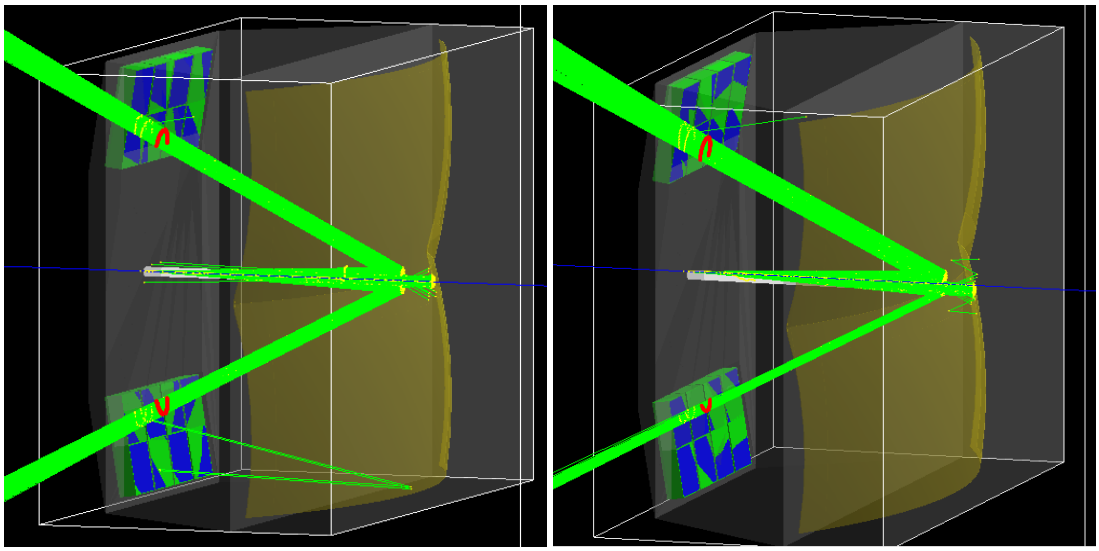

(a) Semi-circular Upper and Lower Half Ring formed by a 48 GeV/c proton)

(b) Positively offset upper half ring formed by a 48 GeV/c proton

Figure D.14: Examples of the MC simulation of AMBER-RICH rendere in QT GUI for different configuration of the momentum direction and species of particles as described.

angle with respect to the vertical, so as to remain in the focal plane of the mirrors, and reduce spherical aberration. However, we use a global coordinate system for the analysis, and hence the recorded hits are projection of the hits on the PDs. A projection of the circle is an Ellipse. Hence, an Elliptical fitting algorithm is developed for the purpose of data analysis.

As a starting point, we exploit the property of an ellipse that sum of the distances from both the focus to a point on the circumference of the ellipse is a constant and is equal to twice the radius of the semi-major axis. As shown in fig. D.16, let this point be $P(x, y)$, and the focii be described by $O(x_0, y_0)$, and $O'(x_1, y_1)$. Let the semi major axis has a radius a, and the semi-minor axis has a radius b. Also, let the distance between the two focii be c. Finally, Let the distance $OP \equiv d_1$, and $O'P \equiv d_2$. Then the distance d_1 and d_2 can be written as

$$\begin{aligned} d_1 &= \sqrt{(x - x_0)^2 + (y - y_0)^2} \\ d_2 &= \sqrt{(x - x_1)^2 + (y - y_1)^2}. \end{aligned} \tag{D.8}$$

Also, the distance c can be written as

$$c = \sqrt{(x_0 - x_1)^2 + (y_0 - y_1)^2}. \tag{D.9}$$

Furthemore, geometry tells us that the quantity a, b, and c are related as

$$a = \sqrt{b^2 + c^2}. \tag{D.10}$$

Taking all these in consideration, we can write a χ^2 function:

$$f(x, y; x_0, y_0, x_1, y_1, b) = 2a(x, y; b, x_0, y_0, x_1, y_1) - \left[d_1(x, y; x_0, y_0) + d_2(x, y; x_1, y_1)\right]. \tag{D.11}$$

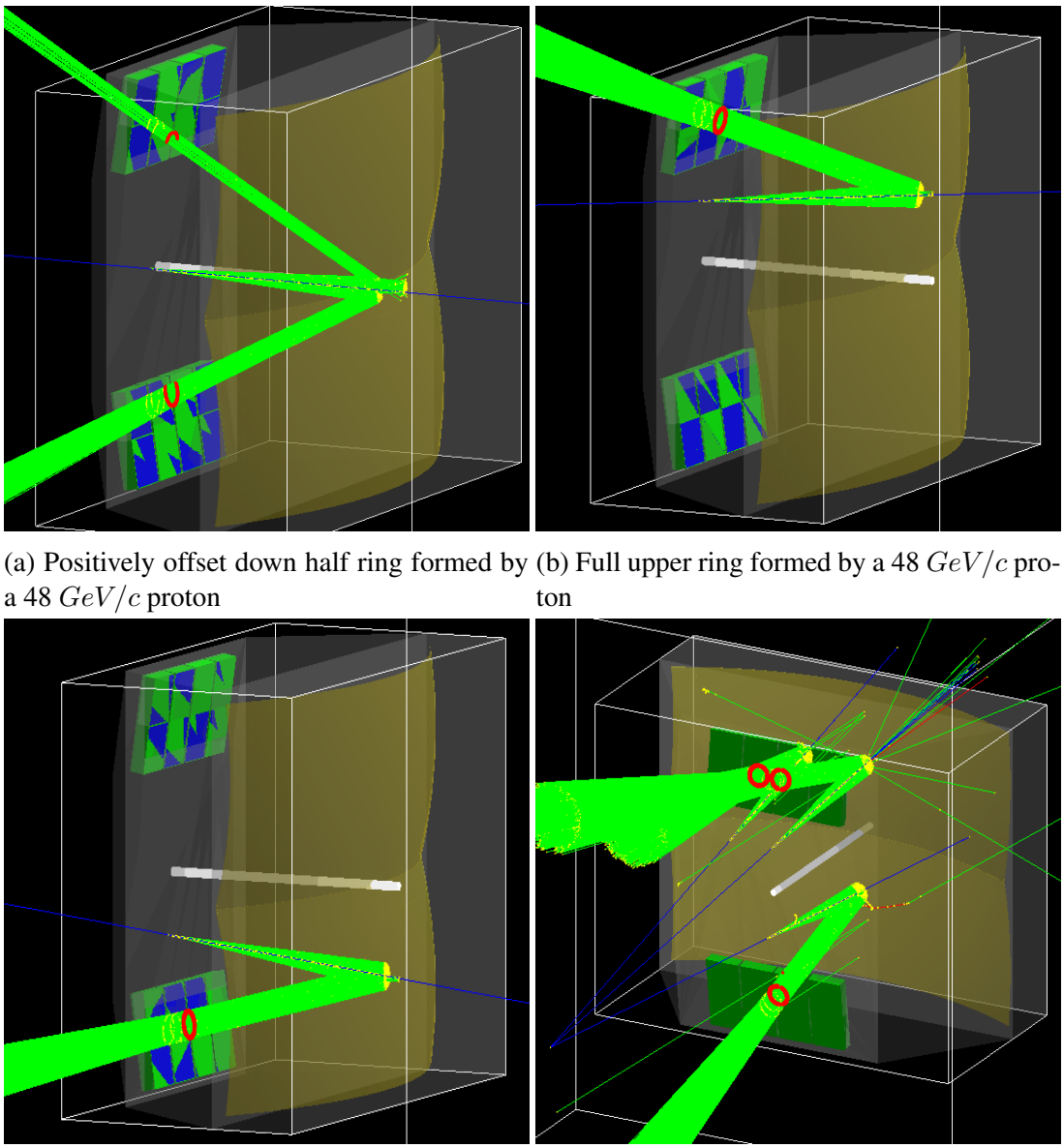

(a) Positively offset down half ring formed by a 48 GeV/c proton

(b) Full upper ring formed by a 48 GeV/c proton

(c) Full down ring formed by a 48 GeV/c proton

(d) Multiple Rings formmed by 100 GeV/c p, and $\pi^{\pm}$.

Figure D.15: Examples of the MC simulation of AMBER-RICH rendere in QT GUI for different configuration of the momentum direction and species of particles as described.

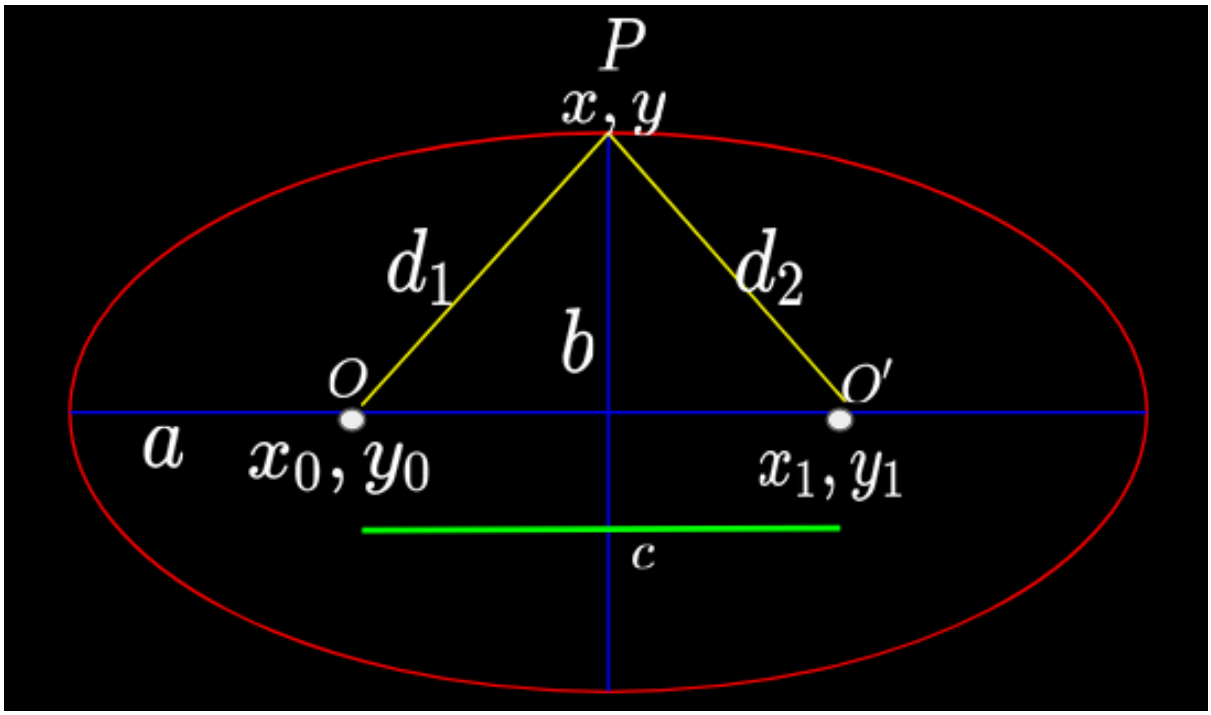

Figure D.16: $P(x, y)$ is an arbitrary point on the circumerence of the ellipse, and the focii are denoted by $O(x_0, y_0)$, and $O'(x_1, y_1)$. The semi major axis has a radius a, and the semi-minor axis has a radius b. The distance between the two focii be c. The distance $OP \equiv d_1$, and $O'P \equiv d_2$.

Hence we have 5 parameters for the fit model. One of the primal rule while doing a chi-square fit is to minimise the dimensions of the parameter space. To that purpose, we exploit the fact that the detector is structurally rigid, and hence, we consider an absence of any rotation degree of freedom in the $x - y$ plane. With this in consideration, we have that, $y_0 = y_1 = y_c$, which reduces the parameters to 4. Hence, the final χ^2 function becomes

$$f(x, y; x_0, x_1, y_c, b) = 2a(x, y; b, x_0, x_1, y_c) - [d_1(x, y; x_0, y_c) + d_2(x, y; x_1, y_c)]\,. \quad \text{(D.12)}$$

As usual, we use the TMinuit class of ROOT tookit to achieve the fit. As a demonstrative example, a 48 GeV proton forms a Cherenkov Ring as shown in fig. D.17 which is fitted with the algorithm described above

D.4.2 Naive β Reconstruction from Fit Model

As a first approximation test of the validity of our MC simulation, we test the validity of the measured β against theoretical β. The velocity can be obtained easily following the same geometrical and optical arguments similar to NaF-RICH. As such, the β is given by

$$\beta = \frac{\sqrt{R^2 + L^2}}{nL}, \quad \text{(D.13)}$$

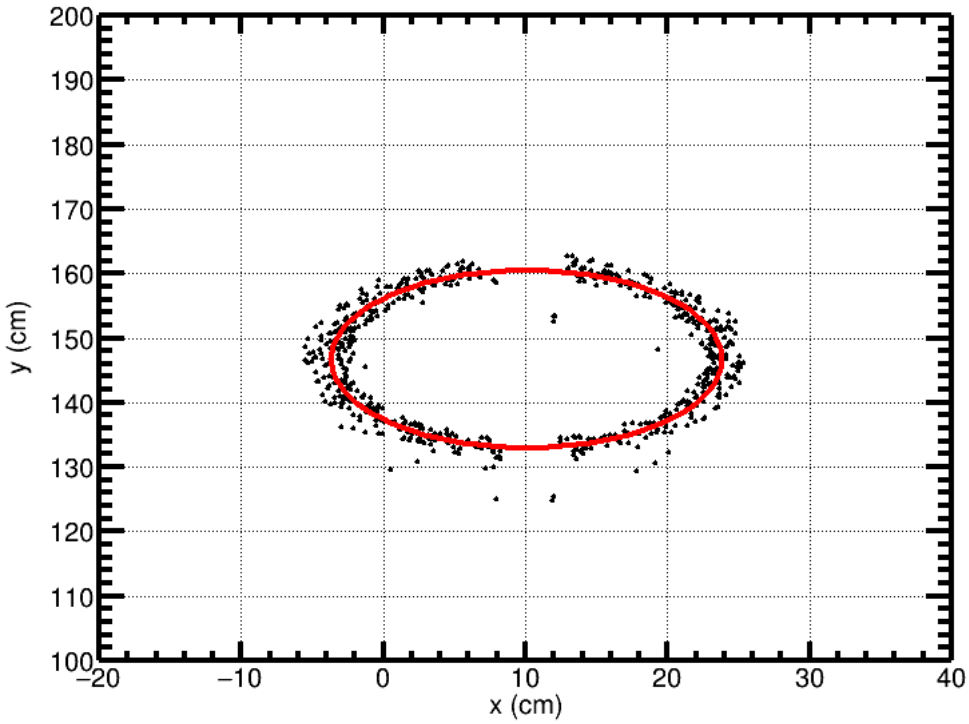

Figure D.17: A Cherenkov Ring formed on the PD by a 48 GeV/c proton fired from (0,15 cm,0) with a momentum direction vector (0,0,1). The fitted ring is displayed in red.

and the uncertainty is given by

$$\sigma_\beta = \frac{R}{nL\sqrt{R^2 + L^2}}\sigma_R, \tag{D.14}$$

where R is the radius obtained from the fit model, L is the expansion length inside the gas vessel, and n is the refractive index of C_4F_{10}. To calculate the β, we proceed as follows:

1. Simulate 1000 events of a particular species with a particular momentum.
2. Fit the resultant 1000 Cherenkov Rings using the elliptical fit algorithm described above
3. Plot a distribution of the semi-major axis radius. Fit it with a gaussian function, and obtain the mean. Since the rotation of the PD is in the $y - z$ plane, the semi-major axis radius is also the real radius of the Cherenkov Ring.

As a demonstrative example, for a 48 GeV/c proton, for a simulation of 1000 events, the resultant distribution of the Cherenkov Ring radius is shown in fig. D.18.

The problem with this β reconstruction is the value of the expansion length which slightly differs from the maximum horizontal expansion length of 305 cm (see fig. D.12) based on the position of the centre of the Cherenkov Ring. One can in principle, extrapolate the track of the primary particle and calculate the hit position on the PD, and easily calculate the expansion length by projecting it along the beam axis. However, a straight forward first order approximation technique which would be sufficient for our purpose of validating the MC simulation, is to reverse engineer it from the theoretical value of β. In the simulation, we know the momentum

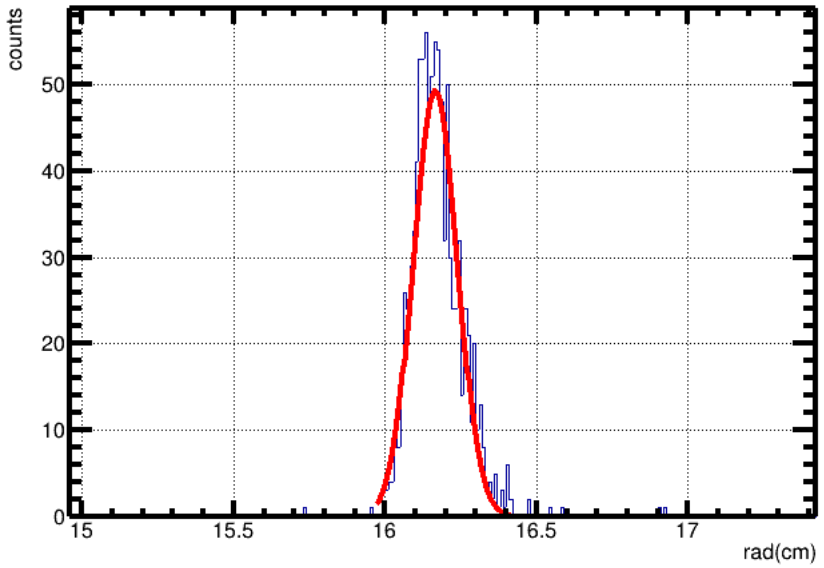

Figure D.18: The distribution of the Cherenkov Ring radius for a simulation of 1000 events of a 48 GeV/c proton. The gaussian fit is shown in red with a mean of 16.16 cm.

(or energy) of the primary particle, and hence the theoretical velocity β_{theo} can be known a priori as an MC truth. As such, we can find the expansion length with the expression

$$L = \sqrt{\frac{R^2}{n^2\beta_{theo}^2 - 1}}. \tag{D.15}$$

After that, the simulation is run for same momentum again, and with the previously calculated expansion length, the β is measured. A better and full proof reconstruction algorithm is being developed, a part of which, would be disccused later in the chapter. As a test for validation of the MC, table D.6 tabulates the velocity calculated for various ranges of momentum of a proton primary particle.

D.5 Work Towards an Exact β Reconstruction Algorithm

For an exact β reconstruction, we need to encode the entire physics of the RICH detector. For that purpose, a code is written in c++ language, with the help of classes from ROOT toolkit to display the resulting simulation result. We do not opt for a Monte-Carlo based method here, as we have known classical physics that is tractable. Hence, we can avoid the inherent uncertainty associated with a Monte Carlo process. A discussion on the structure of the code is not done in the thesis, however, a gitlab link would be made available on request to the authors.

Before proceeding, it is prudent to revise some basics of 3-D coordinate geometry. As such, the equation of a ray in three dimensions can be conveniently written in a vector form as

$$\vec{P} = \vec{P_0} + t \cdot \vec{D} \tag{D.16}$$

where, $P_0 \equiv (P_{0x}, P_{0y}, P_{0z})$ is the coordinate of the origin of the ray, t is some parameter that

Comparison between Theory and Simulation for β						
Momentum (GeV/c)	**Energy** (GeV)	**Radius** (cm)	β_{theory}	**Expansion Length** (cm)	$\beta_{measured}$	$\sigma_\beta \times 10^{-6}$
30	30.01467	13.90000	0.99951	325.64122	0.99951	1.65694
33	33.01334	14.58000	0.99960	326.67706	0.99960	2.24952
35	35.01257	14.93000	0.99964	327.21954	0.99964	2.55923
38	38.01158	15.34000	0.99970	327.72368	0.99970	2.06498
40	40.01100	15.56000	0.99973	327.99697	0.99973	2.60069
43	43.01024	15.83000	0.99976	328.31793	0.99976	2.99438
45	45.00978	15.98000	0.99978	328.51253	0.99978	2.83763
48	48.00917	16.16000	0.99981	328.57074	0.99981	1.98573
50	50.00880	16.27000	0.99982	328.77360	0.99982	1.23767

Table D.6: Table comparing the theoretical and simulation values of velocity of a proton for different momenta. Since it is a first order approximation validation, we are not interested in the uncertainties.

can be computed with the knowledge of another point through which the ray passes through. While, the $\vec{D}$ is the direction vector of the ray, which can be written in Cartesian coordinates as

$$D_x = \frac{x - P_{0x}}{r}, D_y = \frac{y - P_{0y}}{r}, D_z = \frac{z - P_{0z}}{r}. \tag{D.17}$$

where, r is the magnitude of the vector, and is given by $r = \sqrt{(x - P_{0x})^2 + (y - P_{oy})^2 + (z - P_{0z})^2}$.

In spherical polar coordinates, we have the relation

$$x - P_{0x} = r \sin\theta \cos\phi \tag{D.18}$$

$$y - P_{0y} = r \sin\theta \sin\phi, \tag{D.19}$$

$$z - P_{0z} = r \cos\theta, \tag{D.20}$$

where, θ, and ϕ are the azimuthal and polar angles respectively as shown in fig.D.19. So, the direction vector in spherical polar coordinates after dividing by r will be

$$\vec{D} = \sin\theta \cos\phi \hat{x} + \sin\theta \sin\phi \hat{y} + r \cos\theta \hat{z}. \tag{D.21}$$

The equation of a sphere in three dimensions considering that the center is at $(0, 0, 0)$ is

$$x^2 + y^2 + z^2 = R^2; \tag{D.22}$$

where R is the radius of the sphere.

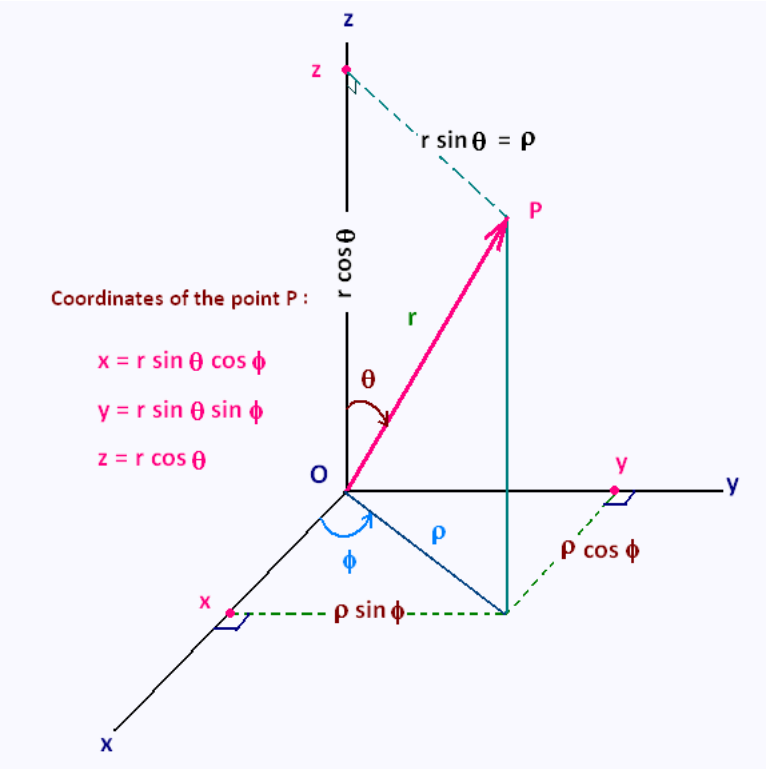

Figure D.19: The spherical polar coordinate system used throughout the code. Remaining consistent with this scheme of reference is important for valid simulation results.

D.5.1 The Mother equation

We substitute the the ray equation (D.16) in mirror equation (D.22). To do that, we decompose vector equation (D.16) into its components and substitute in (D.22) as follows:

$$\begin{aligned}&(P_{0x}+t\cdot D_x)^2+(P_{0y}+t\cdot D_y)^2+(P_{0z}+t\cdot D_z)^2=R^2 \\ &(P_{0x})^2+2\cdot t\cdot (P_{0x})(D_x)+(t\cdot D_x)^2+(P_{0y})^2+2\cdot t\cdot (P_{0y})(D_y) \\ &+(t\cdot D_y)^2+(P_{0z})^2+2\cdot t\cdot (P_{0z})(D_z)+(t\cdot D_z)^2=R^2.\end{aligned} \tag{D.23}$$

Rearranging the above, we get:

$$\begin{aligned}\left[(D_x)^2+(D_y)^2+(D_z)^2\right]t^2+2\left[(P_{0x})(D_x)+(P_{0y})(D_y)+(P_{0z})(D_z)\right]t \\ +(P_{0x})^2+(P_{0y})^2+(P_{0z})^2-R^2=0.\end{aligned} \tag{D.24}$$

The above equation can be conveniently written as

$$at^2+bt+c=0, \tag{D.25}$$

where,

$$\begin{aligned}a&=\left[(D_x)^2+(D_y)^2+(D_z)^2\right], \\ b&=2\left[(P_{0x})(D_x)+(P_{0y})(D_y)+(P_{0z})(D_z)\right], \\ c&=(P_{0x})^2+(P_{0y})^2+(P_{0z})^2-R^2.\end{aligned} \tag{D.26}$$

We name this equation the mother equation. Solving this equation should give us the intersection point of the ray with that of the mirror. We have to define a physical condition to reject one of the intersection points so as to leave us with only the intersection point with the mirror.

D.5.2 Final incident ray equation and mirror intersection values

In this section, we will derive the expressions for the incident ray taking in consideration the direction vectors in a spherical polar coordinates and the resultant intersection points of the ray with the mirror.

D.5.2.1 Mirror Intersection Points Expression

Taking in cosideration, the form of the direction vector in (D.21), we get for the equation of ray:

$$\vec{P} = \vec{P_0} + t \cdot \left[(\sin\theta\cos\phi)\hat{x} + (\sin\theta\sin\phi)\hat{j} + \cos\theta\hat{k}\right]. \tag{D.27}$$

Considering, $\vec{P} \equiv (x, y, z)$ and $\vec{P_0} \equiv (x_0, y_0, z_0)$, decomposing the above in components gives us

$$\begin{aligned} x &= x_0 + t\sin\theta\cos\phi, \\ y &= y_0 + t\sin\theta\sin\phi, \\ z &= z_0 + t\cos\theta. \end{aligned} \tag{D.28}$$

So, from (D.26), we get

$$\begin{aligned} a &= (\sin\theta\cos\phi)^2 + (\sin\theta\sin\phi)^2 + (\cos\theta)^2, \\ b &= 2(x_0\sin\theta\cos\phi + y_0\sin\theta\sin\phi + z_0\cos\theta) \\ c &= x_0^2 + y_0^2 + z_0^2 - R^2. \end{aligned} \tag{D.29}$$

The solution to the equation $at^2 + bt + c = 0$, can be found out by the following formula

$$t = \frac{-b \pm \sqrt{b^2 - 4ac}}{2a}. \tag{D.30}$$

where we have to put the values of (D.29).

We have two values for t because there would be two values of intersection $t_1,\ t_2$ as shown in the fig. D.20.

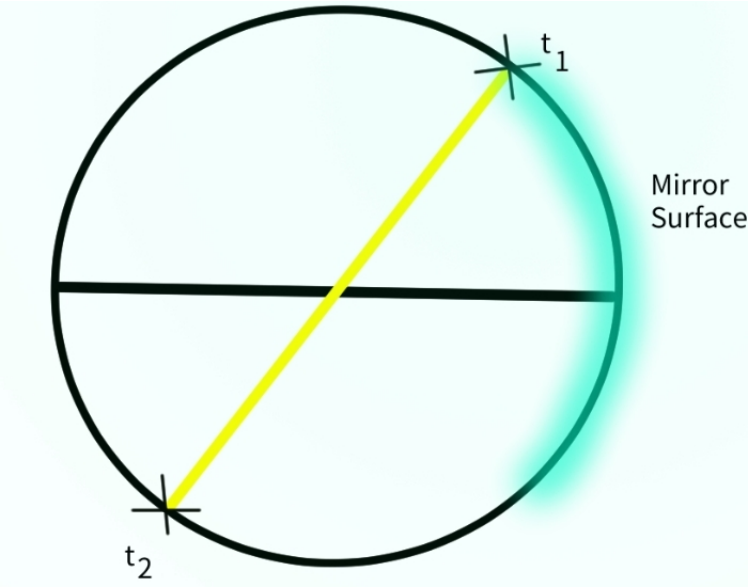

Figure D.20: Intersection of a straight line with a sphere.

As such, we have to implement a Boolean condition to gaue which t is the suitable one for our purpose. We accomplish that by asking if the intersection points lie within the aperture of the mirror. After one of t is chosen, we can write the (x, y, z) coordinates by replacing it in the ray equation. We choose the Boolean condition that the intersection point with the mirror should be $z > 0$.

D.5.2.2 Normal at the point of Intersection

Let the intersection points be represented by $\vec{P_c}$, then the normal at that point is given by

$$\vec{N} = \frac{\vec{P_c} - \vec{O}}{R}, \tag{D.31}$$

where $\vec{O}$ is the centre of the spherical surface which is at $(0, 0, 0)$ with our consideration, and R is the radius of curvature (radius) of the mirror. Hence, the normal vector can be written as

$$\vec{N} = \frac{\vec{P_c}}{R} \tag{D.32}$$

We can then write the normalised normal vector as

$$\hat{N} = \frac{\vec{N}}{\sqrt{N_x^2 + N_y^2 + N_z^2}}. \tag{D.33}$$

D.5.2.3 Reflected Ray Formula

Here we will describe the vector formula for the reflected ray with the help of the construction in fig. D.21, where $\vec{D}$ is the direction vector for the incident ray, and $\vec{R}$ is the direction vector for the reflected ray, and $\vec{N}$ is the normal at the point of intersection. We decompose the $\vec{D}$ into a parallel and perpendicular component, $\vec{D_n}$ and $\vec{D_p}$ respectively, and do the same for $\vec{R}$ into $\vec{R_n}$ and $\vec{R_p}$.

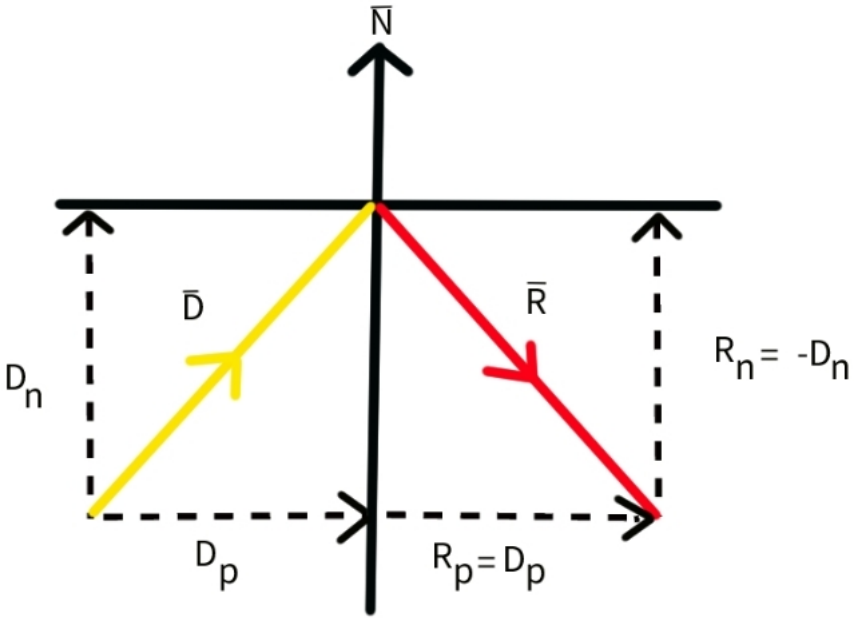

Figure D.21: Geometry of reflection. Here the vectors are written in latex code format

The parallel component of incident direction vector D_n can be written as a dot product with the normal vector, with the direction given by the unit normal vector. Hence,

$$\vec{D_n} = (\vec{D} \cdot \hat{N})\hat{N}. \tag{D.34}$$

The perpendicular component $\vec{D_p}$ can be found by subtracting the parallel component from the total vector as

$$\vec{D_p} = \vec{D} - \vec{D_n}. \tag{D.35}$$

The reflected direction vector can be written by reversing the direction of the parallel vector $\vec{D_n}$ and adding it to the perpendicular component $\vec{D_p}$ which remains the same. So,

$$\begin{aligned} \vec{R} &= \vec{R_n} + \vec{R_p}, \\ &= -\vec{D_n} + \vec{D_p}, \\ &= -(\vec{D} \cdot \hat{N})\hat{N} + \hat{D_p} \text{ using (D.34)} \\ &= -(\vec{D} \cdot \hat{N})\hat{N} + (\vec{D} - (\vec{D} \cdot \hat{N})\hat{N}) \text{ using (D.35)} \\ \vec{R} &= \vec{D} - 2(\vec{D} \cdot \hat{N})\hat{N}. \end{aligned} \tag{D.36}$$

We can substitute in the above, the expressions for the incident direction vector (D.21), and the normal vector (D.32).

Now, the reflected ray can be written as

$$\vec{R_r}(t) = \vec{P_c} + t\vec{R}. \tag{D.37}$$

Let a screen surface be parametrised by

$$z = \tan(\theta_{in})y + h, \tag{D.38}$$

where h is the distance from the origin, and θ_{in} is the inclination of the photon detector panel with respect to the y-axis as shown in fig. D.22.

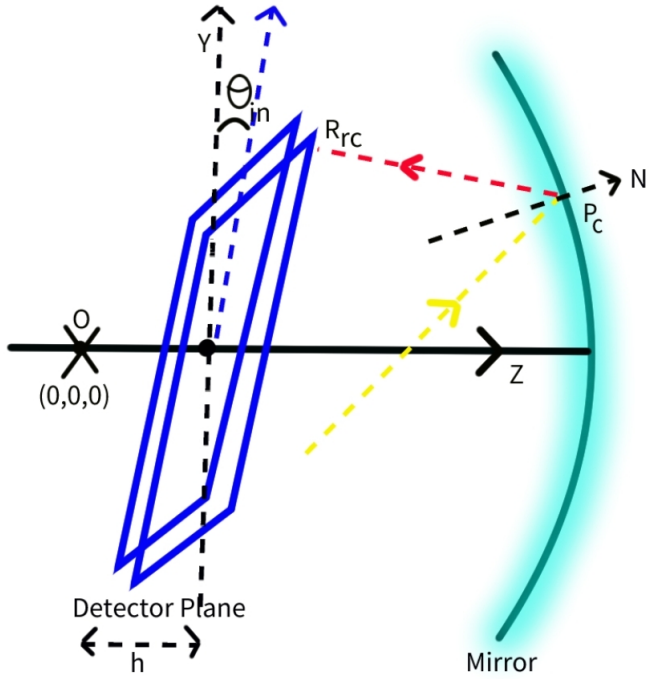

Figure D.22: Diagram to illustrate the process of reflection from the mirror, and subsequent reflection and hit on the photon detector. The photon detector is in blue, the incident ray is in yellow, and reflected ray is in red.

Now putting (D.38) in (D.37) ($R_r(t) = z$), and considering the point of intersection with the mirror to be $\vec{P_c} = (P_{cx}, P_{cy}, P_{cz})$, and the point of intersection with the photon detector to be $\vec{R_c} \equiv (R_x, R_y, R_z)$ we get

$$P_{cz} + tR_z = \tan(\theta_{in})P_{cy} + h, \tag{D.39}$$

so, t becomes

$$t = \frac{\tan(\theta_{in})P_{cy} + h - P_{cz}}{R_z}. \tag{D.40}$$

We can now find the point of intersection with the screen (Photon hits) by putting in the ray formula

$$\vec{R_r}(t) = \vec{P_c} + \left(\frac{\tan(\theta_{in})P_{cy} + h - P_z}{R_z}\right)\vec{R}, \tag{D.41}$$

which will give three values for the coordinates. In reality, θ_{in} and h aren't free parameters of the model but fixed because of how the detector was constructed. As per the detector construction, the values are $\theta_{in} = 8°$, and $h = 305\ cm$.

We extract the detector component dimensions from the engineering drawings in consultation with the University of Trieste, COMPASS-AMBER group for the code.

One can pose the question, why the Cherenkov cone and the mirror can be considered within the same reference frame? Let us take help of the diagram D.23. Here, the blue hue is the mirror screen, considered along the z-axis for the simulation. Consider a particle track from point B that emits a cherenkov photon at point A with a cherenkov angle θ_c. We can see that the polar angle of the particle track is θ. We can extend the the cherenkov ray backwards to meet the z=0 line segment.

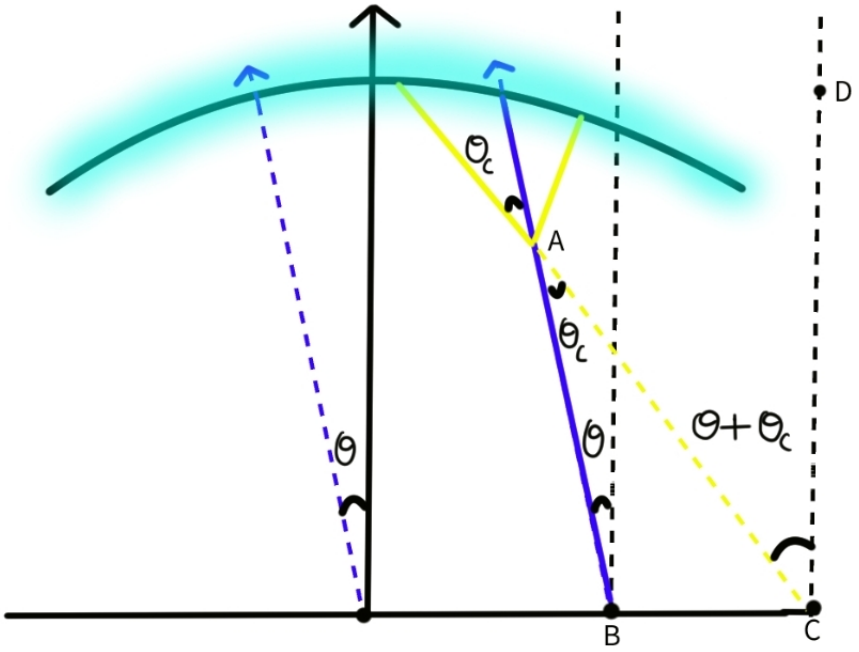

Figure D.23: Diagram to see the cherenkov photon ray angle

Here $\angle ABC = \dfrac{\pi}{2} + \theta$.
So, $\angle ACB = \pi - \left(\dfrac{\pi}{2} + \theta\right) - \theta_c = \dfrac{\pi}{2} - \theta - \theta_c$.
Hence, $\angle ACD = \dfrac{\pi}{2} - \left(\dfrac{\pi}{2} - \theta - \theta_c\right) = \theta + \theta_c$.

As is evident from the above construction, if we consider a particle track from point B, and the cherenkov emission point to be A; the polar angle of the particle track can be considered in the same reference frame of the mirror, and the photon ray after emission can be considered with respect to the mirror frame by just considering $\theta + \theta_c$, where θ and θ_c, are the polar angle with respect to the polar axis (z-axis).

Based on this, a c++ code was written with the following input parameters:

1. **Particle Track Origin Parameters:**
   (a) x_0**:** X-coordinate of the origin of the track
   (b) y_0**:** Y-coordinate of the origin of the track
   (c) z_0**:** Z-coordinate of the origin of the track
   (d) θ_{deg}**:** Incident particle track theta angle in degrees

(e) ϕ_{deg}**:** Incident particle track phi angle in degrees

(f) $\theta_{cherenkov_{deg}}$**:** Cherenkov angle in degrees

2. **Mirror Dimensions Parameters:**

(a) $radius_{mirror}$**:** Radius of curvature of the mirror

(b) $\theta_{max_{deg}}$**:** Maximum polar angle of mirror's aperture in degrees for x projection only.

3. **Photon Detector (PD) Dimensions:**

(a) $x_{screen_{min}}$**:** Minimum X-coordinate of the PD

(b) $x_{screen_{max}}$**:** Maximum X-coordinate of the PD

(c) $y_{screen_{min}}$**:** Minimum Y-coordinate of the PD

(d) $y_{screen_{max}}$**:** Maximum Y-coordinate of the PD

(e) z_{screen}**:** Z-coordinate intercept of the PD

(f) θ_{in}**:** Inclination of the PD with respect to the vertical axis

In practise, the only input variables are the 1. a)-f). The parameters in 2. and 3. are fixed by the detector construction dimensions.

Based on the above parameters, figures D.24, and D.25 show one typical example for the following parametrisation:

1. **Particle Track Origin Parameters:**

(a) x_0**:** 120 cm

(b) y_0**:** 40 cm

(c) z_0**:** 380 cm

(d) θ_{deg}**:** 0.08°

(e) ϕ_{deg}**:** 10°

(f) $\theta_{cherenkov_{deg}}$**:** 1.5°

2. **Mirror Dimensions Parameters:**

(a) $radius_{mirror}$**:** 660 cm

(b) $\theta_{max_{deg}}$**:** 30°

3. **Photon Detector (PD) Dimensions:**

(a) $x_{screen_{min}}$**:** -288 cm

(b) $x_{screen_{max}}$**:** 288 cm

(c) $y_{screen_{min}}$**:** -22.6 cm

(d) $y_{screen_{max}}$: 92.6 cm

(e) z_{screen}: 305 cm

(f) θ_{in}: 8°

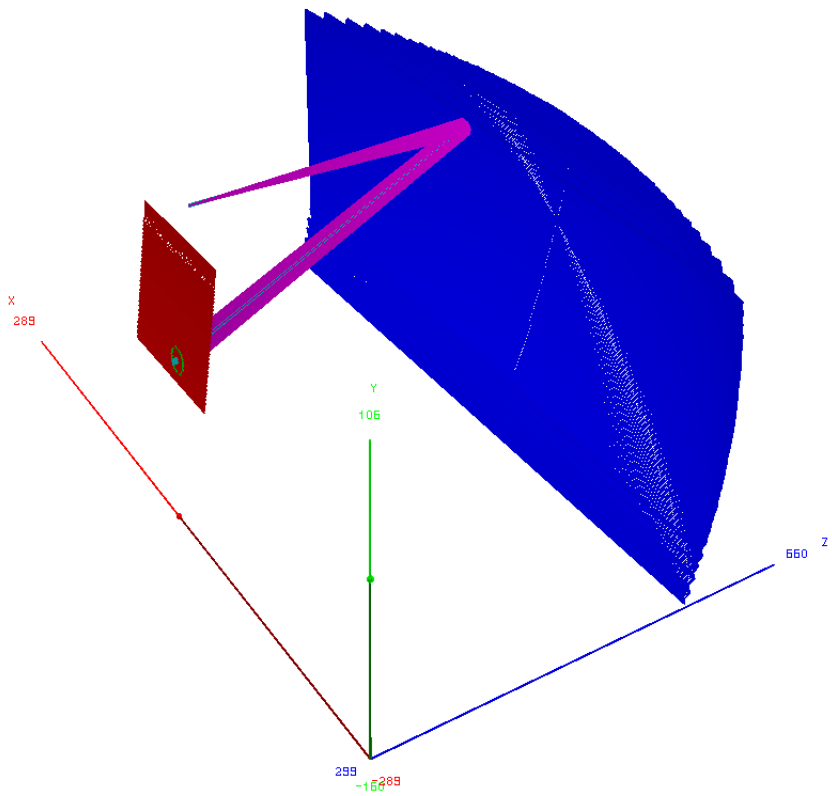

Figure D.24: Representation of the beta reconstruction simulation code using ROOT classes. The graphics has been rendered in OpenGL GUI. The emitted Cherenkov cone, and the reflected ones are shown in magenta. The mirror is in blue, and the Photon Detector is in red.

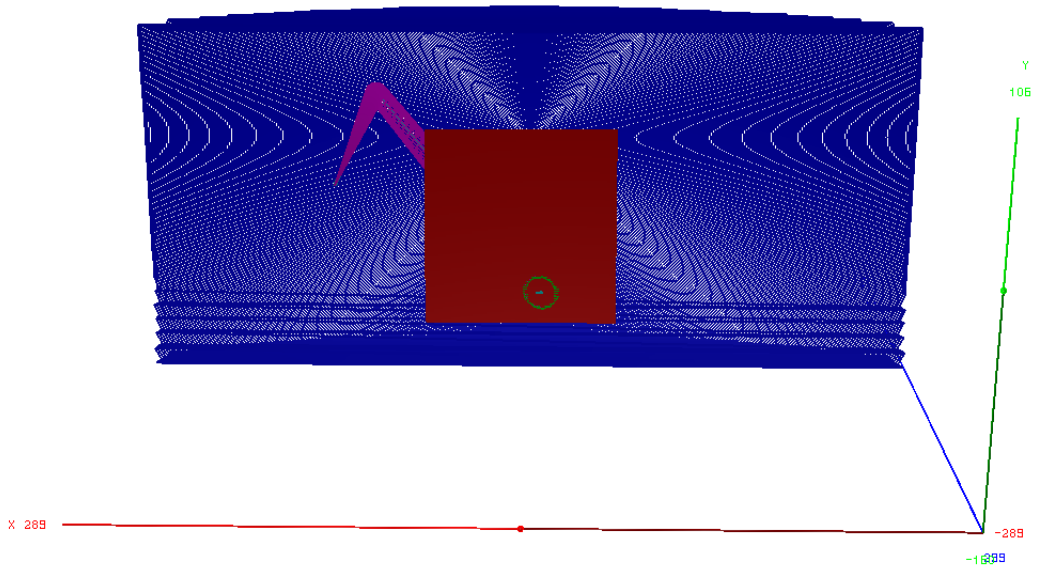

Figure D.25: Representation of the beta reconstruction simulation code using ROOT classes. The graphics has been rendered in OpenGL GUI. The Cherenkov cone is shown in green, and the extrapolated track position to give us the centre of the ring is shown in cyan.

Bibliography

[1] Anatomy of the milky way, https://www.esa.int.

[2] Direct detection of a break in the teraelectronvolt cosmic-ray spectrum of electrons and positrons. *Nature*, 552(7683):63–66, 2017.

[3] Morad Aaboud, G Aad, B Abbott, J Abdallah, Baptiste Abeloos, Rosemarie Aben, OS AbouZeid, NL Abraham, Halina Abramowicz, Henso Abreu, et al. Measurement of the inelastic proton-proton cross section at s= 13 tev with the atlas detector at the lhc. *Physical review letters*, 117(18):182002, 2016.

[4] Morad Aaboud, Georges Aad, Brad Abbott, B Abeloos, SH Abidi, OS AbouZeid, Nadine L Abraham, Halina Abramowicz, Henso Abreu, R Abreu, et al. Search for dark matter and other new phenomena in events with an energetic jet and large missing transverse momentum using the atlas detector. *Journal of High Energy Physics*, 2018(1):1–53, 2018.

[5] Roel Aaij, Bernardo Adeva, Marco Adinolfi, Ziad Ajaltouni, Simon Akar, Johannes Albrecht, Federico Alessio, Michael Alexander, Suvayu Ali, Georgy Alkhazov, et al. Search for higgs-like bosons decaying into long-lived exotic particles. *The European Physical Journal C*, 76:1–15, 2016.

[6] Roel Aaij, C Abellán Beteta, Bernardo Adeva, Marco Adinolfi, Christine Angela Aidala, Ziad Ajaltouni, Simon Akar, Pietro Albicocco, Johannes Albrecht, Federico Alessio, et al. Measurement of antiproton production in p- he collisions at s nn= 110 gev. *Physical Review Letters*, 121(22):222001, 2018.

[7] Craig E Aalseth, PS Barbeau, NS Bowden, B Cabrera-Palmer, J Colaresi, JI Collar, S Dazeley, P De Lurgio, James E Fast,

N Fields, et al. Results from a search for light-mass dark matter with a p-type point contact germanium detector. *Physical Review Letters*, 106(13):131301, 2011.

[8] P Abbon, Maxim Alexeev, H Angerer, Günter Baum, R Birsa, P Bordalo, Franco Bradamante, Andrea Bressan, Michela Chiosso, Piero Ciliberti, et al. The experience of building and operating compass rich-1. *Nuclear Instruments and Methods in Physics Research Section A: Accelerators, Spectrometers, Detectors and Associated Equipment*, 639(1):15–19, 2011.

[9] Philippe Abbon, C Adolph, R Akhunzyanov, Yu Alexandrov, MG Alexeev, GD Alexeev, A Amoroso, V Andrieux, V Anosov, A Austregesilo, et al. The compass setup for physics with hadron beams. *Nuclear Instruments and Methods in Physics Research Section A: Accelerators, Spectrometers, Detectors and Associated Equipment*, 779:69–115, 2015.

[10] Philippe Abbon, E Albrecht, V Yu Alexakhin, Yu Alexandrov, GD Alexeev, MG Alekseev, Antonio Amoroso, H Angerer, VA Anosov, B Badełek, et al. The compass experiment at cern. *Nuclear Instruments and Methods in Physics Research Section A: Accelerators, Spectrometers, Detectors and Associated Equipment*, 577(3):455–518, 2007.

[11] L Accardo, M Aguilar, D Aisa, B Alpat, A Alvino, G Ambrosi, K Andeen, L Arruda, N Attig, P Azzarello, et al. High statistics measurement of the positron fraction in primary cosmic rays of 0.5–500 gev with the alpha magnetic spectrometer on the international space station. *Physical review letters*, 113(12):121101, 2014.

[12] Markus Ackermann, Marco Ajello, A Allafort, Luca Baldini, Jean Ballet, Guido Barbiellini, MG Baring, D Bastieri, K Bechtol, R Bellazzini, et al. Detection of the characteristic pion-decay signature in supernova remnants. *Science*, 339(6121):807–811, 2013.

[13] B Adams, V Anosov, N Zhuravlev, GV Meshcheryakov, OM Kouznetsov, K Kondo, RR Dusaev, S Wallner, A Kveton, D Keller, et al. Compass++/amber: Proposal for measurements at the m2 beam line of the cern sps phase-1: 2022-2024. Technical report, 2019.

[14] Catherine Adloff, L Basara, G Bigongiari, F Bosi, P Brun, F Cadoux, F Cervelli, V Chambert, G Chen, GM Chen, et al. The ams-02 lead-scintillating fibres electromagnetic calorimeter. *Nuclear Instruments and Methods in Physics Research Section A: Accelerators, Spectrometers, Detectors and Associated Equipment*, 714:147–154, 2013.

[15] O Adriani, Y Akaike, K Asano, Y Asaoka, MG Bagliesi, G Bigongiari, WR Binns, S Bonechi, M Bongi, P Brogi, et al. Energy spectrum of cosmic-ray electron and positron from 10 gev to 3 tev observed with the calorimetric electron telescope on the international space station. *Physical review letters*, 119(18):181101, 2017.

[16] O Adriani, GC Barbarino, GA Bazilevskaya, R Bellotti, A Bianco, M Boezio, EA Bogomolov, M Bongi, V Bonvicini, S Bottai, et al. Cosmic-ray positron energy spectrum measured by pamela. *Physical review letters*, 111(8):081102, 2013.

[17] O Adriani, GC Barbarino, GA Bazilevskaya, R Bellotti, M Boezio, EA Bogomolov, M Bongi, V Bonvicini, S Borisov, S Bottai, et al. Time dependence of the proton flux measured by pamela during the 2006 july–2009 december solar minimum. *The Astrophysical Journal*, 765(2):91, 2013.

[18] O Adriani, GC Barbarino, GA Bazilevskaya, R Bellotti, M Boezio, EA Bogomolov, M Bongi, V Bonvicini, S Bottai, A Bruno, et al. Measurement of boron and carbon fluxes in cosmic rays with the pamela experiment. *The Astrophysical Journal*, 791(2):93, 2014.

[19] O Adriani, GC Barbarino, GA Bazilevskaya, M Boezio, EA Bogomolov, L Bonechi, M Bongi, V Bonvicini, SV Borisov, S Bottai, et al. Measurements of cosmic-ray proton and helium spectra with the pamela calorimeter. *Advances in Space Research*, 51(2):219–226, 2013.

[20] O Adriani, GA Bazilevskaya, GC Barbarino, R Bellotti, M Boezio, EA Bogomolov, V Bonvicini, M Bongi, L Bonechi, SV Borisov, et al. Measurement of the flux of primary cosmic ray antiprotons with energies of 60 mev to 350 gev in the pamela experiment. *JETP letters*, 96:621–627, 2013.

[21] Oea Adriani, GC Barbarino, GA Bazilevskaya, R Bellotti, M Boezio, EA Bogomolov, L Bonechi, M Bongi, V Bonvicini, S Borisov, et al. Pamela measurements of cosmic-ray proton and helium spectra. *Science*, 332(6025):69–72, 2011.

[22] M Aguilar, D Aisa, B Alpat, A Alvino, G Ambrosi, K Andeen, L Arruda, N Attig, P Azzarello, A Bachlechner, et al. Precision measurement of the proton flux in primary cosmic rays from rigidity 1 gv to 1.8 tv with the alpha magnetic spectrometer on the international space station. *Physical review letters*, 114(17):171103, 2015.

[23] M Aguilar, J Alcaraz, J Allaby, B Alpat, G Ambrosi, H Anderhub, L Ao, A Arefiev, L Arruda, P Azzarello, et al. Relative composition and energy spectra of light nuclei in cosmic rays: results from ams-01. *The Astrophysical Journal*, 724(1):329, 2010.

[24] M Aguilar, J Alcaraz, J Allaby, B Alpat, G Ambrosi, H Anderhub, L Ao, A Arefiev, P Azzarello, E Babucci, et al. The alpha magnetic spectrometer (ams) on the international space station: Part i–results from the test flight on the space shuttle. *Physics reports*, 366(6):331–405, 2002.

[25] M Aguilar, J Alcaraz, J Allaby, B Alpat, G Ambrosi, H Anderhub, L Ao, A Arefiev, P Azzarello, E Babucci, et al. A study of cosmic ray secondaries induced by the mir space station using ams-01. *Nuclear Instruments and Methods in Physics Research Section B: Beam Interactions with Materials and Atoms*, 234(3):321–332, 2005.

[26] M Aguilar, J Alcaraz, J Allaby, B Alpat, G Ambrosi, H Anderhub, L Ao, A Arefiev, P Azzarello, Luca Baldini, et al. Cosmic-ray positron fraction measurement from 1 to 30 gev with ams-01. *Physics Letters B*, 646(4):145–154, 2007.

[27] M Aguilar, L Ali Cavasonza, B Alpat, G Ambrosi, L Arruda, N Attig, S Aupetit, P Azzarello, A Bachlechner, F Barao, et al. Antiproton flux, antiproton-to-proton flux ratio, and properties of elementary particle fluxes in primary cosmic rays measured with the alpha magnetic spectrometer on the international space station. *Physical Review Letters*, 117(9):091103, 2016.

[28] M Aguilar, L Ali Cavasonza, B Alpat, G Ambrosi, L Arruda, N Attig, S Aupetit, P Azzarello, A Bachlechner, F Barao, et al. Observation of the identical rigidity dependence of he, c, and o cosmic rays at high rigidities by the alpha magnetic spectrometer on the international space station. *Physical review letters*, 119(25):251101, 2017.

[29] M Aguilar, L Ali Cavasonza, B Alpat, G Ambrosi, L Arruda, N Attig, C Bagwell, F Barao, L Barrin, A Bartoloni, et al. Properties of cosmic-ray sulfur and determination of the composition of primary

cosmic-ray carbon, neon, magnesium, and sulfur: Ten-year results from the alpha magnetic spectrometer. *Physical review letters*, 130(21):211002, 2023.

[30] M Aguilar, L Ali Cavasonza, G Ambrosi, L Arruda, N Attig, S Aupetit, P Azzarello, A Bachlechner, F Barao, A Barrau, et al. Precision measurement of the boron to carbon flux ratio in cosmic rays from 1.9 gv to 2.6 tv with the alpha magnetic spectrometer on the international space station. *Physical review letters*, 117(23):231102, 2016.

[31] M Aguilar, L Ali Cavasonza, G Ambrosi, L Arruda, N Attig, S Aupetit, P Azzarello, A Bachlechner, F Barao, A Barrau, et al. Observation of new properties of secondary cosmic rays lithium, beryllium, and boron by the alpha magnetic spectrometer on the international space station. *Physical review letters*, 120(2):021101, 2018.

[32] M Aguilar, L Ali Cavasonza, G Ambrosi, L Arruda, N Attig, P Azzarello, A Bachlechner, F Barao, A Barrau, L Barrin, et al. Towards understanding the origin of cosmic-ray positrons. *Physical review letters*, 122(4):041102, 2019.

[33] M Aguilar, L Ali Cavasonza, G Ambrosi, L Arruda, N Attig, F Barao, L Barrin, A Bartoloni, S Başeğmez-du Pree, J Bates, et al. The alpha magnetic spectrometer (ams) on the international space station: Part ii—results from the first seven years. *Physics reports*, 894:1–116, 2021.

[34] Mea Aguilar, D Aisa, B Alpat, A Alvino, G Ambrosi, K Andeen, L Arruda, N Attig, P Azzarello, A Bachlechner, et al. Precision measurement of the helium flux in primary cosmic rays of rigidities 1.9 gv to 3 tv with the alpha magnetic spectrometer on the international space station. *Physical review letters*, 115(21):211101, 2015.

[35] AA Aguilar-Arevalo, M Backfish, A Bashyal, B Batell, BC Brown, R Carr, A Chatterjee, RL Cooper, P deNiverville, R Dharmapalan, et al. Dark matter search in nucleon, pion, and electron channels from a proton beam dump with miniboone. *Physical Review D*, 98(11):112004, 2018.

[36] S Ahlen, VM Balebanov, R Battiston, U Becker, J Burger, M Capell, HF Chen, HS Chen, M Chen, N Chernoplekov, et al. An antimatter spectrometer in space. *Nuclear Instruments and Methods in Physics Research Section A: Accelerators, Spectrometers, Detectors and Associated Equipment*, 350(1-2):351–367, 1994.

[37] HS Ahn, P Allison, MG Bagliesi, L Barbier, JJ Beatty, G Bigongiari, TJ Brandt, JT Childers, NB Conklin, S Coutu, et al. Energy spectra of cosmic-ray nuclei at high energies. *The Astrophysical Journal*, 707(1):593, 2009.

[38] HS Ahn, PS Allison, MG Bagliesi, JJ Beatty, G Bigongiari, PJ Boyle, TJ Brandt, JT Childers, NB Conklin, Stephane Coutu, et al. Measurements of cosmic-ray secondary nuclei at high energies with the first flight of the cream balloon-borne experiment. *Astroparticle Physics*, 30(3):133–141, 2008.

[39] DS Akerib, S Alsum, HM Araújo, X Bai, AJ Bailey, J Balajthy, P Beltrame, EP Bernard, A Bernstein, TP Biesiadzinski, et al. Results from a search for dark matter in the complete lux exposure. *Physical review letters*, 118(2):021303, 2017.

[40] E Albrecht, Günter Baum, T Bellunato, Renato Birsa, M Bosteels, Franco Bradamante, Andrea Bressan, A Chapiro, A Cicuttin, A Colavita, et al. The radiator gas and the gas system of compass rich-1. *Nuclear Instruments and Methods in Physics Re-*

search Section A: Accelerators, Spectrometers, Detectors and Associated Equipment, 502(1):266–269, 2003.

[41] E Albrecht, Günter Baum, R Birsa, F Borotto, F Bradamante, A Braem, Andrea Bressan, A Chapiro, A Cicuttin, C D'Ambrosio, et al. The mirror system of compass rich-1. *Nuclear Instruments and Methods in Physics Research Section A: Accelerators, Spectrometers, Detectors and Associated Equipment*, 502(1):236–240, 2003.

[42] J Alcaraz, B Alpat, G Ambrosi, H Anderhub, L Ao, A Arefiev, P Azzarello, E Babucci, Luca Baldini, M Basile, et al. Cosmic protons. *Physics Letters B*, 490(1-2):27–35, 2000.

[43] J Alcaraz, B Alpat, G Ambrosi, H Anderhub, L Ao, A Arefiev, P Azzarello, E Babucci, Luca Baldini, M Basile, et al. Helium in near earth orbit. *Physics Letters B*, 494(3-4):193–202, 2000.

[44] J Alcaraz, B Alpat, G Ambrosi, H Anderhub, L Ao, A Arefiev, P Azzarello, E Babucci, Luca Baldini, M Basile, et al. Leptons in near earth orbit. *Physics Letters B*, 484(1-2):10–22, 2000.

[45] J Alcaraz, D Alvisi, B Alpat, G Ambrosi, H Anderhub, L Ao, A Arefiev, P Azzarello, E Babucci, Luca Baldini, et al. Search for antihelium in cosmic rays. *Physics Letters B*, 461(4):387–396, 1999.

[46] J Alcaraz, D Alvisi, B Alpat, G Ambrosi, H Anderhub, L Ao, A Arefiev, P Azzarello, E Babucci, Luca Baldini, et al. Protons in near earth orbit. *Physics Letters B*, 472(1-2):215–226, 2000.

[47] M Alexeev, R Birsa, F Bradamante, Andrea Bressan, Michela Chiosso, Piero Ciliberti, ML Colantoni, S Dalla Torre, O Denisov, V Diaz, et al. On-line mirror alignment monitoring method for compass rich-1. *Nuclear Instruments and Methods in Physics Research Section A: Accelerators, Spectrometers, Detectors and Associated Equipment*, 595(1):194–196, 2008.

[48] Patrick Alken, Erwan Thébault, Ciarán D Beggan, Hagay Amit, J Aubert, J Baerenzung, TN Bondar, WJ Brown, S Califf, A Chambodut, et al. International geomagnetic reference field: the thirteenth generation. *Earth, Planets and Space*, 73(1):1–25, 2021.

[49] John Allison, Katsuya Amako, JEA Apostolakis, HAAH Araujo, P Arce Dubois, MAAM Asai, GABG Barrand, RACR Capra, SACS Chauvie, RACR Chytracek, et al. Geant4 developments and applications. *IEEE Transactions on nuclear science*, 53(1):270–278, 2006.

[50] John Allison, Katsuya Amako, John Apostolakis, Pedro Arce, Makoto Asai, Tsukasa Aso, Enrico Bagli, A Bagulya, S Banerjee, GJNI Barrand, et al. Recent developments in geant4. *Nuclear instruments and methods in physics research section A: Accelerators, Spectrometers, Detectors and Associated Equipment*, 835:186–225, 2016.

[51] Roberto Aloisio and Pasquale Blasi. Propagation of galactic cosmic rays in the presence of self-generated turbulence. *Journal of Cosmology and Astroparticle Physics*, 2013(07):001, 2013.

[52] Roberto Aloisio, Pasquale Blasi, and PD Serpico. Nonlinear cosmic ray galactic transport in the light of ams-02 and voyager data. *Astronomy & Astrophysics*, 583:A95, 2015.

[53] B Alpat, G Ambrosi, Ph Azzarello, R Battiston, B Bertucci, M Bourquin, WILLIAM J Burger, F Cadoux, CF da Silva Costa, V Choutko, et al. The internal alignment

and position resolution of the ams-02 silicon tracker determined with cosmic-ray muons. *Nuclear Instruments and Methods in Physics Research Section A: Accelerators, Spectrometers, Detectors and Associated Equipment*, 613(2):207–217, 2010.

[54] G Ambrosi, V Choutko, C Delgado, A Oliva, Q Yan, and Yang Li. The spatial resolution of the silicon tracker of the alpha magnetic spectrometer. *Nuclear Instruments and Methods in Physics Research Section A: Accelerators, Spectrometers, Detectors and Associated Equipment*, 869:29–37, 2017.

[55] Carl D Anderson. The positive electron. *Physical Review*, 43(6):491, 1933.

[56] Anton Andronic and Johannes P Wessels. Transition radiation detectors. *Nuclear Instruments and Methods in Physics Research Section A: Accelerators, Spectrometers, Detectors and Associated Equipment*, 666:130–147, 2012.

[57] Godehard Angloher, M Bauer, I Bavykina, A Bento, C Bucci, C Ciemniak, G Deuter, F von Feilitzsch, D Hauff, P Huff, et al. Results from 730 kg days of the cresst-ii dark matter search. *The European Physical Journal C*, 72:1–22, 2012.

[58] Elena Aprile, Jasper Aalbers, F Agostini, M Alfonsi, FD Amaro, M Anthony, F Arneodo, P Barrow, L Baudis, Boris Bauermeister, et al. First dark matter search results from the xenon1t experiment. *Physical review letters*, 119(18):181301, 2017.

[59] R Arnold, JL Guyonnet, Y Giomataris, P Petroff, J Seguinot, J Tocqueville, and T Ypsilantis. A rich detector with a sodium fluoride radiator: πk identification up to 3 gev/c. *Nuclear Instruments and Methods in Physics Research Section A: Accelerators, Spectrometers, Detectors and Associated Equipment*, 273(2-3):466–470, 1988.

[60] Masaki Asano, Shigeki Matsumoto, Nobuchika Okada, and Yasuhiro Okada. Cosmic positron signature from dark matter in the littlest higgs model with t parity. *Physical Review D*, 75(6):063506, 2007.

[61] E Atkin, V Bulatov, V Dorokhov, N Gorbunov, S Filippov, V Grebenyuk, D Karmanov, I Kovalev, I Kudryashov, A Kurganov, et al. First results of the cosmic ray nucleon experiment. *Journal of cosmology and astroparticle physics*, 2017(07):020, 2017.

[62] Walter Baade and Fritz Zwicky. Cosmic rays from super-novae. *Proceedings of the National Academy of Sciences*, 20(5):259–263, 1934.

[63] Yang Bai, Joshua Berger, and Sida Lu. Supersymmetric resonant dark matter: A thermal model for the ams-02 positron excess. *Physical Review D*, 97(11):115012, 2018.

[64] Luca Baldini. Space-based cosmic-ray and gamma-ray detectors: a review. *arXiv preprint arXiv:1407.7631*, 2014.

[65] A Basili, V Bindi, D Casadei, G Castellini, A Contin, A Kounine, M Lolli, F Palmonari, and L Quadrani. The tof-acc flight electronics for the fast trigger and time of flight of the ams-02 cosmic ray spectrometer. *Nuclear Instruments and Methods in Physics Research Section A: Accelerators, Spectrometers, Detectors and Associated Equipment*, 707:99–113, 2013.

[66] Harry Bateman. *Tables of integral transforms*, volume 1. McGraw-Hill book company, 1954.

[67] Guenter Baum, R Birsa, F Bradamante, Andrea Bressan, A Chapiro, A Cicuttin, A Colavita, S Costa, M Crespo, S Dalla Torre, et al. Richone: a software package for the analysis of compass rich-1 data. *Nuclear Instruments and Methods*

in Physics Research Section A: Accelerators, Spectrometers, Detectors and Associated Equipment, 502(1):315–317, 2003.

[68] Rainer Beck. Galactic and extragalactic magnetic fields. In *AIP Conference Proceedings*, volume 1085, pages 83–96. American Institute of Physics, 2008.

[69] Rainer Beck. Measuring interstellar magnetic fields by radio synchrotron emission. *Proceedings of the International Astronomical Union*, 4(S259):3–14, 2008.

[70] AR Bell. The acceleration of cosmic rays in shock fronts–i. *Monthly Notices of the Royal Astronomical Society*, 182(2):147–156, 1978.

[71] AR Bell. The acceleration of cosmic rays in shock fronts–ii. *Monthly Notices of the Royal Astronomical Society*, 182(3):443–455, 1978.

[72] J Berdugo, V Choutko, C Delgado, and Q Yan. Determination of the rigidity scale of the alpha magnetic spectrometer. *Nuclear Instruments and Methods in Physics Research Section A: Accelerators, Spectrometers, Detectors and Associated Equipment*, 869:10–14, 2017.

[73] V Berezinsky. Ultra high energy cosmic rays. *Nuclear Physics B-Proceedings Supplements*, 70(1-3):419–430, 1999.

[74] R Bernabei, P Belli, F Cappella, R Cerulli, CJ Dai, A d'Angelo, HL He, A Incicchitti, HH Kuang, JM Ma, et al. First results from dama/libra and the combined results with dama/nai. *The European Physical Journal C*, 56:333–355, 2008.

[75] Rita Bernabei, Pierluigi Belli, Andrea Bussolotti, Fabio Cappella, Vincenzo Caracciolo, Riccardo Cerulli, Chang-Jiang Dai, Annelisa d'Angelo, Alessandro Di Marco, Hui-Lin He, et al. First model independent results from dama/libra–phase2. *Universe*, 4(11):116, 2018.

[76] C Bernet, A Bravar, J Hannappel, Dv Harrach, R Hermann, E Kabuss, F Klein, A Korzenev, M Leberig, M Ostrick, et al. The compass trigger system for muon scattering. *Nuclear Instruments and Methods in Physics Research Section A: Accelerators, Spectrometers, Detectors and Associated Equipment*, 550(1-2):217–240, 2005.

[77] Gianfranco Bertone, Dan Hooper, and Joseph Silk. Particle dark matter: Evidence, candidates and constraints. *Physics reports*, 405(5-6):279–390, 2005.

[78] Gianfranco Bertone, Geraldine Servant, and Guenter Sigl. Indirect detection of kaluza-klein dark matter. *Physical Review D*, 68(4):044008, 2003.

[79] Wolfgang Bietenholz. The most powerful particles in the universe: a cosmic smash. *arXiv preprint arXiv:1305.1346*, 2013.

[80] V Bindi, D Casadei, G Castellini, F Cindolo, A Contin, F Giovacchini, C Guandalini, G Laurenti, G Levi, M Lolli, et al. The scintillator detector for the fast trigger and time-of-flight (tof) measurement of the space experiment ams-02. *Nuclear Instruments and Methods in Physics Research Section A: Accelerators, Spectrometers, Detectors and Associated Equipment*, 623(3):968–981, 2010.

[81] V Bindi, GM Chen, HS Chen, E Choumilov, V Choutko, A Contin, A Lebedev, YS Lu, N Masi, A Oliva, et al. Calibration and performance of the ams-02 time of flight detector in space. *Nuclear Instruments and Methods in Physics Research Section A: Accelerators, Spectrometers, Detectors and Associated Equipment*, 743:22–29, 2014.

[82] V Bindi, E Choumilov, A Contin, N Masi, A Oliva, F Palmonari, L Quadrani, and

Q Yan. The ams-02 time of flight (tof) system: construction and overall performances in space. In *Proceedings of the 33rd International Cosmic Rays Conference, Rio Janeiro, Brazil*. Citeseer, 2013.

[83] Matteo Jerome Boschini, Stefano Della Torre, Massimo Gervasi, Giuseppe La Vacca, and Pier Giorgio Rancoita. The helmod model in the works for inner and outer heliosphere: from ams to voyager probes observations. *Advances in Space Research*, 64(12):2459–2476, 2019.

[84] MJ Boschini, S Della Torre, M Gervasi, D Grandi, Gulaugur Jóhannesson, G La Vacca, N Masi, IV Moskalenko, S Pensotti, TA Porter, et al. Deciphering the local interstellar spectra of primary cosmic-ray species with helmod. *The Astrophysical Journal*, 858(1):61, 2018.

[85] MJ Boschini, S Della Torre, M Gervasi, D Grandi, Gulaugur Jóhannesson, G La Vacca, N Masi, IV Moskalenko, S Pensotti, TA Porter, et al. Helmod in the works: from direct observations to the local interstellar spectrum of cosmic-ray electrons. *The Astrophysical Journal*, 854(2):94, 2018.

[86] MJ Boschini, Stefano Della Torre, Massimo Gervasi, D Grandi, Gulaugur Jóhannesson, M Kachelriess, G La Vacca, N Masi, IV Moskalenko, E Orlando, et al. Solution of heliospheric propagation: Unveiling the local interstellar spectra of cosmic-ray species. *The Astrophysical Journal*, 840(2):115, 2017.

[87] A Bottino, F Donato, N Fornengo, and S Scopel. Lower bound on the neutralino mass from new data on cmb and implications for relic neutralinos. *Physical Review D*, 68(4):043506, 2003.

[88] A Bottino, N Fornengo, and S Scopel. Light relic neutralinos. *Physical Review D*, 67(6):063519, 2003.

[89] Claude Bovet, Réne Maleyran, L Piemontese, Alfredo Placci, and Massimo Placidi. The cedar counters for particle identification in the sps secondary beams: a description and an operation manual. Technical report, European Organization for Nuclear Research, 1982.

[90] Virginia Bresci, Elena Amato, Pasquale Blasi, and Giovanni Morlino. Effects of re-acceleration and source grammage on secondary cosmic rays spectra. *Monthly Notices of the Royal Astronomical Society*, 488(2):2068–2078, 2019.

[91] Torsten Bringmann and Pierre Salati. Galactic antiproton spectrum at high energies: Background expectation versus exotic contributions. *Physical Review D*, 75(8):083006, 2007.

[92] T Bruch and W Wallraff. The anti-coincidence counter shield of the ams tracker. *Nuclear Instruments and Methods in Physics Research Section A: Accelerators, Spectrometers, Detectors and Associated Equipment*, 572(1):505–507, 2007.

[93] Gianfranco Brunetti, Pasquale Blasi, Rossella Cassano, and Stefano Gabici. Alfvénic reacceleration of relativistic particles in galaxy clusters: Mhd waves, leptons and hadrons. *Monthly Notices of the Royal Astronomical Society*, 350(4):1174–1194, 2004.

[94] A. Buffington, C. D. Orth, and T. S. Mast. A measurement of cosmic-ray beryllium isotopes from 200 to 1500 MeV per nucleon. , 226:355–371, November 1978.

[95] F Cadoux, F Cervelli, V Chambert-Hermel, G Chen, H Chen, G Coignet, S Di Falco, JM Dubois, E Falchini, A Franzoso, et al.

The ams-02 electromagnetic calorimeter. *Nuclear Physics B-Proceedings Supplements*, 113(1-3):159–165, 2002.

[96] X Cai. On board computing system for ams-02 mission. 2005.

[97] D. Casadei. Design and test results of the AMS RICH detector. *Nucl. Phys. B Proc. Suppl.*, 125:303–307, 2003.

[98] Pavel Alekseevič Čerenkov. Visible radiation produced by electrons moving in a medium with velocities exceeding that of light. *Physical Review*, 52(4):378, 1937.

[99] Cinzia Cernetti and Francesco Nozzoli. A data driven approach to the measurement of 10be/9be in cosmic rays with magnetic spectrometers. In *Physical Sciences Forum*, volume 2, page 13. MDPI, 2021.

[100] F Cervelli, G Chen, G Coignet, S Di Falco, E Falchini, T Lomtadze, Z Liu, P Maestro, PS Marrocchesi, R Paoletti, et al. A reduced scale em calorimeter prototype for the ams-02 experiment. *Nuclear Instruments and Methods in Physics Research Section A: Accelerators, Spectrometers, Detectors and Associated Equipment*, 490(1-2):132–139, 2002.

[101] Jin Chang, JH Adams, HS Ahn, GL Bashindzhagyan, M Christl, O Ganel, TG Guzik, J Isbert, KC Kim, EN Kuznetsov, et al. An excess of cosmic ray electrons at energies of 300–800 gev. *Nature*, 456(7220):362–365, 2008.

[102] Chandradoy Chatterjee. Performance study of the RICH at COMPASS experiment for hadron identification in SIDIS physics, 2020. Presented 05 Mar 2020.

[103] H Che and GP Zank. A brief review on particle acceleration in multi-island magnetic reconnection. In *Journal of Physics: Conference Series*, volume 1332, page 012003. IOP Publishing, 2019.

[104] Chuan-Hung Chen, Cheng-Wei Chiang, and Takaaki Nomura. Dark matter for excess of ams-02 positrons and antiprotons. *Physics Letters B*, 747:495–499, 2015.

[105] Hesheng Chen. Permanent magnet system of alpha magnetic spectrometer. *Science in China Series A: Mathematics*, 43:996–1008, 2000.

[106] Hsin-Chia Cheng, Jonathan L Feng, and Konstantin T Matchev. Kaluza-klein dark matter. *Physical review letters*, 89(21):211301, 2002.

[107] Michael L Cherry, Gernot Hartmann, Dietrich Müller, and Thomas A Prince. Transition radiation from relativistic electrons in periodic radiators. *Physical Review D*, 10(11):3594, 1974.

[108] Michael L Cherry and Dietrich Müller. Measurements of the frequency spectrum of transition radiation. *Physical Review Letters*, 38(1):5, 1977.

[109] Ilias Cholis, Dan Hooper, and Tim Linden. A predictive analytic model for the solar modulation of cosmic rays. *Physical Review D*, 93(4):043016, 2016.

[110] Ilias Cholis, Tim Linden, and Dan Hooper. A robust excess in the cosmic-ray antiproton spectrum: implications for annihilating dark matter. *Physical Review D*, 99(10):103026, 2019.

[111] Vitali Choutko, A Egorov, A Eline, and BS Shan. Computing strategy of the ams experiment. In *Journal of Physics: Conference Series*, volume 664, page 032029. IOP Publishing, 2015.

[112] Vitali Choutko, on behalf ofthe Ams Collaboration, et al. Parallelization of the event processing in the ams experiment. In *Journal of Physics: conference series*, volume 219, page 032032. IOP Publishing, 2010.

[113] Marco Cirelli and Alessandro Strumia. Minimal dark matter: model and results. *New Journal of Physics*, 11(10):105005, 2009.

[114] Dan Coe. Dark matter halo mass profiles, 2010.

[115] DAMPE collaboration, Q An, R Asfandiyarov, P Azzarello, P Bernardini, XJ Bi, MS Cai, J Chang, DY Chen, HF Chen, et al. Measurement of the cosmic ray proton spectrum from 40 gev to 100 tev with the dampe satellite. *Science advances*, 5(9):eaax3793, 2019.

[116] KIMS collaboration et al. Limits on wimp-nucleon cross section with csi (tl) crystal detectors. *Phys. Rev. Lett*, 99:091301, 2007.

[117] NA49 Collaboration. Inclusive production of charged pions in p+ p collisions at 158 gev/c beam momentum. *The European Physical Journal C-Particles and Fields*, 45(2):343–381, 2006.

[118] NA49 Collaboration, T Anticic, B Baatar, J Bartke, L Betev, H Białkowska, C Blume, B Boimska, J Bracinik, V Cerny, et al. Inclusive production of protons, anti-protons and neutrons in p+ p collisions at 158 gev/c beam momentum. *The European Physical Journal C*, 65:9–63, 2010.

[119] NA61/SHINE collaboration et al. Measurements of $\pi\pm$, k$\pm$, p and p spectra in proton-proton interactions at 20, 31, 40, 80 and 158 gev/c with the na61/shine spectrometer at the cern sps. *Eur. Phys. J. C*, 77:671, 2017.

[120] Pierre Auger Collaboration, Alexander Aab, P Abreu, M Aglietta, I Al Samarai, IFM Albuquerque, I Allekotte, A Almela, J Alvarez Castillo, J Alvarez-Muñiz, et al. Observation of a large-scale anisotropy in the arrival directions of cosmic rays above $8\times$ 1018 ev. *Science*, 357(6357):1266–1270, 2017.

[121] J. J. Connell. Galactic Cosmic-Ray Confinement Time: ULYSSES High Energy Telescope Measurements of the Secondary Radionuclide 10Be. , 501:L59, July 1998.

[122] S Costa, S Dalla Torre, D Faso, J-Ch Gayde, A Latina, and F Tessarotto. Clam, a continuous line alignment and monitoring method for rich mirrors. *Nuclear Instruments and Methods in Physics Research Section A: Accelerators, Spectrometers, Detectors and Associated Equipment*, 553(1-2):135–139, 2005.

[123] Ming-Yang Cui, Xu Pan, Qiang Yuan, Yi-Zhong Fan, and Hong-Shi Zong. Revisit of cosmic ray antiprotons from dark matter annihilation with updated constraints on the background model from ams-02 and collider data. *Journal of Cosmology and Astroparticle Physics*, 2018(06):024, 2018.

[124] Alessandro Cuoco, Jan Heisig, Lukas Klamt, Michael Korsmeier, and Michael Krämer. Scrutinizing the evidence for dark matter in cosmic-ray antiprotons. *Physical Review D*, 99(10):103014, 2019.

[125] Alessandro Cuoco, Jan Heisig, Michael Korsmeier, and Michael Krämer. Constraining heavy dark matter with cosmic-ray antiprotons. *Journal of Cosmology and Astroparticle Physics*, 2018(04):004, 2018.

[126] Alessandro Cuoco, Michael Krämer, and Michael Korsmeier. Novel dark matter constraints from antiprotons in light of ams-02. *Physical Review Letters*, 118(19):191102, 2017.

[127] Vesna Cuplov, Iréne Buvat, Frédéric Pain, and Sébastien Jan. Extension of the gate monte-carlo simulation package to model bioluminescence and fluorescence imaging. *Journal of biomedical optics*, 19(2):026004–026004, 2014.

[128] Henryk Czyż, E Kou, P Urquijo, W Altmannshofer, F Beaujean, G Bell, M Beneke,

II Bigi, F Bishara, M Blanke, et al. The belle ii physics book. 2019.

[129] Giulio D'Agostini. A multidimensional unfolding method based on bayes' theorem. *Nuclear Instruments and Methods in Physics Research Section A: Accelerators, Spectrometers, Detectors and Associated Equipment*, 362(2-3):487–498, 1995.

[130] Giulio D'Agostini. Improved iterative bayesian unfolding. *arXiv preprint arXiv:1010.0632*, 2010.

[131] Shuddha Shankar Dasgupta. Particle Identification with the Cherenkov imaging technique using MPGD based Photon Detectors for Physics at COMPASS Experiment at CERN, 2017. Presented 13 Apr 2017.

[132] Abhinandan Dass. Gravitation beyond general relativity with gravity probe-b.

[133] Alessandro De Angelis. *L'enigma dei raggi cosmici: le più grandi energie dell'universo*. Springer Science & Business Media, 2011.

[134] T Delahaye, R Lineros, Fiorenza Donato, Nicolao Fornengo, and P Salati. Positrons from dark matter annihilation in the galactic halo: theoretical uncertainties. *Physical Review D*, 77(6):063527, 2008.

[135] S Della Torre, M Gervasi, PG Rancoita, D Rozza, and A Treves. Pulsar wind nebulae as a source of the observed electron and positron excess at high energy: The case of vela-x. *Journal of High Energy Astrophysics*, 8:27–34, 2015.

[136] Mattia Di Mauro, Fiorenza Donato, Nicolao Fornengo, and Andrea Vittino. Dark matter vs. astrophysics in the interpretation of ams-02 electron and positron data. *Journal of Cosmology and Astroparticle Physics*, 2016(05):031, 2016.

[137] Mattia Di Mauro, Fiorenza Donato, Andreas Goudelis, and Pasquale Dario Serpico. New evaluation of the antiproton production cross section for cosmic ray studies. *Physical Review D*, 90(8):085017, 2014.

[138] Scott Dodelson and Lawrence M Widrow. Sterile neutrinos as dark matter. *Physical Review Letters*, 72(1):17, 1994.

[139] Ph v Doetinchem, S Fopp, W Karpinski, Th Kirn, K Lübelsmeyer, J Orboeck, S Schael, A Schultz von Dratzig, G Schwering, Th Siedenburg, et al. Performance of the ams-02 transition radiation detector. *Nuclear Instruments and Methods in Physics Research Section A: Accelerators, Spectrometers, Detectors and Associated Equipment*, 558(2):526–535, 2006.

[140] Fiorenza Donato, Michael Korsmeier, and Mattia Di Mauro. Prescriptions on antiproton cross section data for precise theoretical antiproton flux predictions. *Physical Review D*, 96(4):043007, 2017.

[141] Fiorenza Donato, D Maurin, P Brun, T Delahaye, and P Salati. Constraints on wimp dark matter from the high energy pamela p/p data. *Physical review letters*, 102(7):071301, 2009.

[142] Fiorenza Donato, D Maurin, P Salati, A Barrau, G Boudoul, and Richard Taillet. Antiprotons from spallations of cosmic rays on interstellar matter. *The Astrophysical Journal*, 563(1):172, 2001.

[143] Fornengo Donato, Nicolao Fornengo, D Maurin, P Salati, and R Taillet. Antiprotons in cosmic rays from neutralino annihilation. *Physical Review D*, 69(6):063501, 2004.

[144] F Donnini. Time-dependent geomagnetic cutoff estimation along the iss orbit. *Il nuovo cimento C*, 39(1):1–2, 2016.

[145] Federico Donnini. *Flux measurement of light nuclei in Cosmic Rays with the AMS-*

02 experiment. PhD thesis, Perugia U., 2018.

[146] R Duperray, B Baret, D Maurin, G Boudoul, A Barrau, L Derome, K Protasov, and M Buenerd. Flux of light antimatter nuclei near earth, induced by cosmic rays in the galaxy and in the atmosphere. *Physical Review D*, 71(8):083013, 2005.

[147] RP Duperray, C-Y Huang, KV Protasov, and M Buenerd. Parametrization of the antiproton inclusive production cross section on nuclei. *Physical Review D*, 68(9):094017, 2003.

[148] JJ Engelmann, P Ferrando, A Soutoul, Ph Goret, E Juliusson, L Koch-Miramond, N Lund, P Masse, B Peters, N Petrou, et al. Charge composition and energy spectra of cosmic-ray nuclei for elements from be to ni-results from heao-3-c2. *Astronomy and Astrophysics*, 233:96–111, 1990.

[149] Carmelo Evoli. Phenomenological models of Cosmic Ray transport in Galaxies, June 2022.

[150] Carmelo Evoli, Roberto Aloisio, and Pasquale Blasi. Galactic cosmic rays after the ams-02 observations. *Physical Review D*, 99(10):103023, 2019.

[151] Carmelo Evoli, Pasquale Blasi, Giovanni Morlino, and Roberto Aloisio. Origin of the cosmic ray galactic halo driven by advected turbulence and self-generated waves. *Physical Review Letters*, 121(2):021102, 2018.

[152] Carmelo Evoli, Daniele Gaggero, Andrea Vittino, Giuseppe Di Bernardo, Mattia Di Mauro, Arianna Ligorini, Piero Ullio, and Dario Grasso. Cosmic-ray propagation with dragon2: I. numerical solver and astrophysical ingredients. *Journal of Cosmology and Astroparticle Physics*, 2017(02):015, 2017.

[153] Carmelo Evoli, Giovanni Morlino, Pasquale Blasi, and Roberto Aloisio. Ams-02 beryllium data and its implication for cosmic ray transport. *Physical Review D*, 101(2):023013, 2020.

[154] Kun Fang, Xiao-Jun Bi, and Peng-Fei Yin. Reanalysis of the pulsar scenario to explain the cosmic positron excess considering the recent developments. *The Astrophysical Journal*, 884(2):124, 2019.

[155] Yasaman Farzan and Meshkat Rajaee. Dark matter decaying into millicharged particles as a solution to ams-02 positron excess. *Journal of Cosmology and Astroparticle Physics*, 2019(04):040, 2019.

[156] Jie Feng, Nicola Tomassetti, and Alberto Oliva. Bayesian analysis of spatial-dependent cosmic-ray propagation: astrophysical background of antiprotons and positrons. *Physical Review D*, 94(12):123007, 2016.

[157] Jonathan L Feng. Dark matter candidates from particle physics and methods of detection. *Annual Review of Astronomy and Astrophysics*, 48:495–545, 2010.

[158] Enrico Fermi. On the origin of the cosmic radiation. *Physical review*, 75(8):1169, 1949.

[159] Katia M Ferriere. The interstellar environment of our galaxy. *Reviews of Modern Physics*, 73(4):1031, 2001.

[160] E Fiandrini, G Esposito, B Bertucci, B Alpat, G Ambrosi, R Battiston, WJ Burger, D Caraffini, L Di Masso, N Dinu, et al. Protons with kinetic energy e¿ 70 mev trapped in the earth's radiation belts. *Journal of Geophysical Research: Space Physics*, 109(A10), 2004.

[161] Nicolao Fornengo. Status and perspectives of indirect and direct dark matter searches.

Advances in Space Research, 41(12):2010–2018, 2008.

[162] Giovanni Gallucci et al. Performance of the ams-02 electromagnetic calorimeter in space. In *Journal of Physics: Conference Series*, volume 587, page 012028. IOP Publishing, 2015.

[163] M. Garcia-Munoz, G. M. Mason, and J. A. Simpson. The age of the galactic cosmic rays derived from the abundance of Be-10. , 217:859–877, November 1977.

[164] M. Garcia-Munoz, J. A. Simpson, and J. P. Wefel. The propagation lifetime of galactic cosmic rays determined from the measurement of the beryllium isotopes. In *International Cosmic Ray Conference*, volume 2 of *International Cosmic Ray Conference*, pages 72–75, 1981.

[165] F Garibaldi, E Cisbani, S Colilli, F Cusanno, S Frullani, R Fratoni, F Giuliani, M Gricia, M Iodice, M Lucentini, et al. A proximity focusing rich detector for kaon physics at jefferson lab hall a. *Nuclear Instruments and Methods in Physics Research Section A: Accelerators, Spectrometers, Detectors and Associated Equipment*, 502(1):117–122, 2003.

[166] H Gast, K Andeen, A Bachlechner, A Bartoloni, U Becker, B Beischer, B Borgia, CH Chung, W De Boer, I Gebauer, et al. Identification of cosmic-ray positrons with the transition radiation detector of the ams experiment on the international space station. *33rd*, 2013.

[167] Yoann Genolini, Mathieu Boudaud, P-I Batista, Sami Caroff, Laurent Derome, Julien Lavalle, Alexandre Marcowith, David Maurin, Vincent Poireau, Vivian Poulin, et al. Cosmic-ray transport from ams-02 boron to carbon ratio data: Benchmark models and interpretation. *Physical Review D*, 99(12):123028, 2019.

[168] W Gillard et al. High precision measurement of the ams-rich aerogel refractive index with cosmic ray. In *33rd International Cosmic Ray Conference*, number 742, 2013.

[169] F Giovacchini, AMS02-RICH Collaboration, et al. Performance in space of the ams-02 rich detector. *Nuclear Instruments and Methods in Physics Research Section A: Accelerators, Spectrometers, Detectors and Associated Equipment*, 766:57–60, 2014.

[170] LJ Gleeson and WI Axford. Solar modulation of galactic cosmic rays. *Astrophysical Journal, vol. 154, p. 1011*, 154:1011, 1968.

[171] Paolo Gondolo and Graciela Gelmini. Cosmic abundances of stable particles: Improved analysis. *Nuclear Physics B*, 360(1):145–179, 1991.

[172] Stefanie Grabmüller. Cryogenic Silicon Detectors and Analysis of Primakoff Contributions to the Reaction $\pi^- Pb \to \pi^-\pi^-\pi^+ Pb$ at COMPASS, 2012. Presented 27 Sep 2012.

[173] Giacomo Graziani and LHCb collaboration. Measurement of antiproton production in p–he collisions at lhcb to constrain the secondary cosmic antiproton flux. *Astronomische Nachrichten*, 338(9-10):1113–1117, 2017.

[174] Kenneth Greisen. End to the cosmic-ray spectrum? *Physical Review Letters*, 16(17):748, 1966.

[175] Wan-Lei Guo and Yue-Liang Wu. The real singlet scalar dark matter model. *Journal of High Energy Physics*, 2010(10):1–13, 2010.

[176] F. A. Hagen, A. J. Fisher, and J. F. Ormes. Be-10 abundance and the age of cosmic rays - A balloon measurement. , 212:262–277, February 1977.

[177] T. Hams, L. M. Barbier, M. Bremerich, E. R. Christian, G. A. de Nolfo, S. Geier,

H. Göbel, S. K. Gupta, M. Hof, W. Menn, R. A. Mewaldt, J. W. Mitchell, S. M. Schindler, M. Simon, and R. E. Streitmatter. Measurement of the Abundance of Radioactive ^{10}Be and Other Light Isotopes in Cosmic Radiation up to 2 GeV Nucleon^{-1} with the Balloon-borne Instrument ISOMAX. , 611:892–905, August 2004.

[178] VF HESS. The highest-energy cosmic rays. *Physikalische Zeitschrift*, 13:1084, 1912.

[179] C Höppner, S Neubert, B Ketzer, and S Paul. A novel generic framework for track fitting in complex detector systems. *Nuclear Instruments and Methods in Physics Research Section A: Accelerators, Spectrometers, Detectors and Associated Equipment*, 620(2-3):518–525, 2010.

[180] John David Jackson. Classical electrodynamics, 1999.

[181] TR Jaffe, JP Leahy, AJ Banday, Samuel M Leach, SR Lowe, and A Wilkinson. Modelling the galactic magnetic field on the plane in two dimensions. *Monthly Notices of the Royal Astronomical Society*, 401(2):1013–1028, 2010.

[182] Ronnie Jansson, Glennys R Farrar, Andre H Waelkens, and Torsten A Enßlin. Constraining models of the large scale galactic magnetic field with wmap5 polarization data and extragalactic rotation measure sources. *Journal of Cosmology and Astroparticle Physics*, 2009(07):021, 2009.

[183] John Vernon Jelley. *Cherenkov Radiation: And Its Applications*. pergamon press, 1958.

[184] Y Jia, Q Yan, V Choutko, H Liu, and A Oliva. Nuclei charge measurement by the alpha magnetic spectrometer silicon tracker. *Nuclear Instruments and Methods in Physics Research Section A: Accelerators, Spectrometers, Detectors and Associated Equipment*, 972:164169, 2020.

[185] Frank C Jones, Andrew Lukasiak, Vladimir Ptuskin, and William Webber. The modified weighted slab technique: models and results. *The Astrophysical Journal*, 547(1):264, 2001.

[186] M Kachelriess. Lecture notes on high energy cosmic rays. *arXiv preprint arXiv:0801.4376*, 2008.

[187] Michael Kachelriess, Igor V Moskalenko, and Sergey S Ostapchenko. New calculation of antiproton production by cosmic ray protons and nuclei. *The Astrophysical Journal*, 803(2):54, 2015.

[188] David E Kaplan, Markus A Luty, and Kathryn M Zurek. Asymmetric dark matter. *Physical Review D*, 79(11):115016, 2009.

[189] Rolf Kappl and Martin Wolfgang Winkler. The cosmic ray antiproton background for ams-02. *Journal of Cosmology and Astroparticle Physics*, 2014(09):051, 2014.

[190] Chris Kelso, Dan Hooper, and Matthew R Buckley. Toward a consistent picture for cresst, cogent, and dama. *Physical Review D*, 85(4):043515, 2012.

[191] B Ketzer, Q Weitzel, S Paul, F Sauli, and L Ropelewski. Performance of triple gem tracking detectors in the compass experiment. *Nuclear Instruments and Methods in Physics Research Section A: Accelerators, Spectrometers, Detectors and Associated Equipment*, 535(1-2):314–318, 2004.

[192] Th Kirn. Threshold transition radiation detectors in astroparticle physics. *Nuclear Instruments and Methods in Physics Research Section A: Accelerators, Spectrometers, Detectors and Associated Equipment*, 563(2):338–342, 2006.

[193] Th Kirn and Th Siedenburg. The ams-02 transition radiation detector. *Nuclear Instruments and Methods in Physics Research*

Section A: Accelerators, Spectrometers, Detectors and Associated Equipment, 535(1-2):165–170, 2004.

[194] Gary H Kitmacher. *Reference guide to the international space station*. Number NASA/SP-2006-557. 2006.

[195] EW Kolb and MS Turner. The early universe westview press, 1994.

[196] Michael Korsmeier and Alessandro Cuoco. Galactic cosmic-ray propagation in the light of ams-02: Analysis of protons, helium, and antiprotons. *Physical Review D*, 94(12):123019, 2016.

[197] Michael Korsmeier, Fiorenza Donato, and Mattia Di Mauro. Production cross sections of cosmic antiprotons in the light of new data from the na61 and lhcb experiments. *Physical Review D*, 97(10):103019, 2018.

[198] A Kounine and V Koutsenko. Flight software for xdr and jinx nodes in ams-02. *AMS internal notes*, 2011.

[199] A Kounine, Z Weng, W Xu, and C Zhang. Precision measurement of 0.5 gev–3 tev electrons and positrons using the ams electromagnetic calorimeter. *Nuclear Instruments and Methods in Physics Research Section A: Accelerators, Spectrometers, Detectors and Associated Equipment*, 869:110–117, 2017.

[200] Markus Kuster, Georg Raffelt, and Berta Beltrán. *Axions: Theory, cosmology, and experimental searches*, volume 741. Springer, 2007.

[201] Ruixing Liang. Contribution of pulsars to the ams-02 positron excess. In *Journal of Physics: Conference Series*, volume 2346, page 012008. IOP Publishing, 2022.

[202] Tim Linden and Stefano Profumo. Probing the pulsar origin of the anomalous positron fraction with ams-02 and atmospheric cherenkov telescopes. *The Astrophysical Journal*, 772(1):18, 2013.

[203] Christian Lippmann. Particle identification. *Nuclear Instruments and Methods in Physics Research Section A: Accelerators, Spectrometers, Detectors and Associated Equipment*, 666:148–172, 2012.

[204] Mariangela Lisanti. Lectures on dark matter physics. In *New Frontiers in Fields and Strings: TASI 2015 Proceedings of the 2015 Theoretical Advanced Study Institute in Elementary Particle Physics*, pages 399–446. World Scientific, 2017.

[205] Hu Liu, J Casaus, F Giovacchini, A Oliva, X Xia, AMS02-RICH Collaboration, et al. The rich detector of ams-02: 5 years of operation in space. *Nuclear Instruments and Methods in Physics Research Section A: Accelerators, Spectrometers, Detectors and Associated Equipment*, 876:5–8, 2017.

[206] Malcolm S Longair. *High energy astrophysics*. Cambridge university press, 2010.

[207] K Lübelsmeyer, A Schultz von Dratzig, M Wlochal, G Ambrosi, P Azzarello, R Battiston, R Becker, U Becker, B Bertucci, K Bollweg, et al. Upgrade of the alpha magnetic spectrometer (ams-02) for long term operation on the international space station (iss). *Nuclear Instruments and Methods in Physics Research Section A: Accelerators, Spectrometers, Detectors and Associated Equipment*, 654(1):639–648, 2011.

[208] A. Lukasiak. Voyager Measurements of the Charge and Isotopic Composition of Cosmic Ray Li, Be and B Nuclei and Implications for Their Production in the Galaxy. In *International Cosmic Ray Conference*, volume 3 of *International Cosmic Ray Conference*, page 41, August 1999.

[209] A. Lukasiak, P. Ferrando, F. B. McDonald, and W. R. Webber. The isotopic composi-

tion of cosmic-ray beryllium and its implication for the cosmic ray's age. , 423:426–431, March 1994.

[210] A. Lukasiak, F. B. McDonald, and W. R. Webber. Voyager Measurements of the Isotopic Composition of Li, Be and B Nuclei. In *International Cosmic Ray Conference*, volume 3 of *International Cosmic Ray Conference*, page 389, 1997.

[211] P De La Torre Luque, Mario Nicola Mazziotta, Francesco Loparco, Fabio Gargano, and Davide Serini. Implications of current nuclear cross sections on secondary cosmic rays with the upcoming dragon2 code. *Journal of Cosmology and Astroparticle Physics*, 2021(03):099, 2021.

[212] Dmitry Malyshev, Ilias Cholis, and Joseph Gelfand. Pulsars versus dark matter interpretation of atic/pamela. *Physical Review D*, 80(6):063005, 2009.

[213] Silvia Manconi, Mattia Di Mauro, and Fiorenza Donato. Dipole anisotropy in cosmic electrons and positrons: inspection on local sources. *Journal of Cosmology and Astroparticle Physics*, 2017(01):006, 2017.

[214] Silvia Manconi, Mattia Di Mauro, and Fiorenza Donato. Multi-messenger constraints to the local emission of cosmic-ray electrons. *Journal of Cosmology and Astroparticle Physics*, 2019(04):024, 2019.

[215] MJIJoMPA Maniatis. The next-to-minimal supersymmetric extension of the standard model reviewed. *International Journal of Modern Physics A*, 25(18n19):3505–3602, 2010.

[216] Nicoló Masi. The ams-02 experiment and the dark matter search, dottorato di ricerca in fisica. *Alma Mater Studiorum–Università di Bologna, Bologna, Italia*, 2013.

[217] Nicolò Masi and Mario Ballardini. A conservative assessment of the current constraints on dark matter annihilation from cosmic rays and cmb observations. *International Journal of Modern Physics D*, 26(06):1750041, 2017.

[218] D Maurin, F Melot, and Richard Taillet. A database of charged cosmic rays. *Astronomy & Astrophysics*, 569:A32, 2014.

[219] PETER Meyer, DIETRICH Muller, JACQUES Lheureux, and SIMON Swordy. Cosmic ray nuclei (crn) detector investigation. final report. Technical report, Chicago Univ., IL (United States), 1991.

[220] John W Mitchell, Ko Abe, Hideyuki Fuke, Sadakazu Haino, Thomas Hams, M Hasegawa, A Horikoshi, KC Kim, MH Lee, Y Makida, et al. Solar modulation of low-energy antiproton and proton spectra measured by bess. In *International Cosmic Ray Conference*, volume 1, pages 455–458, 2008.

[221] Miguel Molero Gonzalez. Measurement of the Cosmic Ray Anisotropy with AMS-02 on the International Space Station, 2021. Presented 14 Jul 2021.

[222] Shinji Mukohyama. Dark matter as integration constant in hoř ava-lifshitz gravity. *Physical Review D*, 80(6), sep 2009.

[223] E Nappi and J Seguinot. Ring imaging cherenkov detectors: The state of the art and perspectives. *La Rivista del Nuovo Cimento*, 28:1–130, 2005.

[224] S Nishida, I Adachi, N Hamada, K Hara, T Iijima, S Iwata, H Kakuno, H Kawai, S Korpar, P Kriz, et al. Aerogel rich for the belle ii forward pid. *Nuclear Instruments and Methods in Physics Research Section A: Accelerators, Spectrometers, Detectors and Associated Equipment*, 766:28–31, 2014.

[225] Francesco Nozzoli and Cinzia Cernetti.

[226] A Obermeier, M Ave, P Boyle, Ch Höppner, J Hörandel, and D Müller. Energy spectra of primary and secondary cosmic-ray nuclei measured with tracer. *The Astrophysical Journal*, 742(1):14, 2011.

[227] Giuseppe PS Occhialini and CF Powell. Nuclear disintegrations produced by slow charged particles of small mass. *Nature*, 159(4032):186–190, 1947.

[228] Nils Olsen, R Holme, G Hulot, T Sabaka, Torsten Neubert, L Tøffner-Clausen, Fritz Primdahl, J Jørgensen, J-M Léger, D Barraclough, et al. Ørsted initial field model. *Geophysical Research Letters*, 27(22):3607–3610, 2000.

[229] Domenico Pacini. La radiazione penetrante alla superficie ed in seno alle acque. *Il Nuovo Cimento (1911-1923)*, 3(1):93–100, 1912.

[230] AD Panov, Jr H Adams, HS Ahn, GL Bashinzhagyan, JW Watts, JP Wefel, J Wu, O Ganel, TG Guzik, VI Zatsepin, et al. Energy spectra of abundant nuclei of primary cosmic rays from the data of atic-2 experiment: Final results. *Bulletin of the Russian Academy of Sciences: Physics*, 73:564–567, 2009.

[231] AD Panov, NV Sokolskaya, JH Adams Jr, HS Ahn, GL Bashindzhagyan, KE Batkov, J Chang, M Christl, AR Fazely, O Ganel, et al. Relative abundances of cosmic ray nuclei bcno in the energy region from 10 gev/n to 300 gev/n. results from atic-2 (the science flight of atic). *arXiv preprint arXiv:0707.4415*, 2007.

[232] En N Parker. The passage of energetic charged particles through interplanetary space. *Planetary and Space Science*, 13(1):9–49, 1965.

[233] Claudia Patrignani, K Agashe, G Aielli, C Amsler, M Antonelli, DM Asner, H Baer, Sw Banerjee, RM Barnett, T Basaglia, et al. Review of particle physics. 2016.

[234] R Pereira, AMS Rich Collaboration, et al. The ams-02 rich detector: Performance during ground-based data taking at cern. *Nuclear Instruments and Methods in Physics Research Section A: Accelerators, Spectrometers, Detectors and Associated Equipment*, 639(1):37–41, 2011.

[235] Maxim Perelstein and Andrew Spray. Indirect detection of little higgs dark matter. *Physical Review D*, 75(8):083519, 2007.

[236] Daniel James Phalen. *Searches for dark matter*. University of Michigan, 2010.

[237] Stefano Profumo, Lorenzo Ubaldi, and Carroll Wainwright. Singlet scalar dark matter: monochromatic gamma rays and metastable vacua. *Physical Review D*, 82(12):123514, 2010.

[238] Tomi Räihä, Andreas Bachlechner, Bastian Beischer, Chan Hoon Chung, Henning Gast, Stefan Schael, and Thorsten Siedenburg. Monte carlo simulations of the transition radiation detector of the ams-02 experiment. *Nuclear Instruments and Methods in Physics Research Section A: Accelerators, Spectrometers, Detectors and Associated Equipment*, 868:10–14, 2017.

[239] Annika Reinert and Martin Wolfgang Winkler. A precision search for wimps with charged cosmic rays. *Journal of Cosmology and Astroparticle Physics*, 2018(01):055, 2018.

[240] GD ROCHESTERDr and CC BUTLERDr. Evidence for the existence of new unstable elementary particles. *Nature*, 160(4077):855–857, 1947.

[241] Bruno Rossi. Method of registering multiple simultaneous impulses of several geiger's counters. *Nature*, 125(3156):636–636, 1930.

[242] Bruno Rossi. On the magnetic deflection of cosmic rays. *Physical Review*, 36(3):606, 1930.

[243] Vera C Rubin, W Kent Ford Jr, and Norbert Thonnard. Rotational properties of 21 sc galaxies with a large range of luminosities and radii, from ngc 4605/r= 4kpc/to ugc 2885/r= 122 kpc. *Astrophysical Journal, Part 1, vol. 238, June 1, 1980, p. 471-487.*, 238:471–487, 1980.

[244] A Sabellek. *The Space Qualified Data Acquisition for the Transition Radiation Detector of the AMS-02 Experiment on the International Space Station*. PhD thesis, PhD thesis. Karlsruhe Institute of Technology, 2009.

[245] Pierre Salati, Fiorenza Donato, and Nicolao Fornengo. Indirect dark matter detection with cosmic antimatter. *arXiv preprint arXiv:1003.4124*, 2010.

[246] Christopher Savage, Graciela Gelmini, Paolo Gondolo, and Katherine Freese. Compatibility of dama/libra dark matter detection with other searches. *Journal of Cosmology and Astroparticle Physics*, 2009(04):010, 2009.

[247] P Schiavon. Particle identification in compass rich-1. *Progress Report. September*, pages 2001–12, 2001.

[248] Thomas Schwetz and Jure Zupan. Dark matter attempts for cogent and dama. *Journal of Cosmology and Astroparticle Physics*, 2011(08):008, 2011.

[249] Geraldine Servant and Tim MP Tait. Is the lightest kaluza–klein particle a viable dark matter candidate? *Nuclear Physics B*, 650(1-2):391–419, 2003.

[250] R Silberberg, CH Tsao, and AF Barghouty. Updated partial cross sections of proton-nucleus reactions. *The Astrophysical Journal*, 501(2):911, 1998.

[251] M Simon, A Molnar, and S Roesler. A new calculation of the interstellar secondary cosmic-ray antiprotons. *The Astrophysical Journal*, 499(1):250, 1998.

[252] Albert M Sirunyan, Armen Tumasyan, Wolfgang Adam, Federico Ambrogi, Ece Asilar, Thomas Bergauer, Johannes Brandstetter, Erica Brondolin, Marko Dragicevic, Janos Erö, et al. Search for new physics in events with a leptonically decaying z boson and a large transverse momentum imbalance in proton–proton collisions at s s= 13\, tev tev. *The European Physical Journal C*, 78:1–32, 2018.

[253] Constantinos Skordis and Tom Złośnik. New relativistic theory for modified newtonian dynamics. *Physical review letters*, 127(16):161302, 2021.

[254] Todor Stanev. Ultra-high-energy cosmic rays and the large-scale structure of the galactic magnetic field. *The Astrophysical Journal*, 479(1):290, 1997.

[255] SA Stephens. A closer look at the tertiary production of antiprotons in the galaxy. *Advances in Space Research*, 35(1):142–146, 2005.

[256] Carl Störmer. *The polar aurora*. Clarendon Press, 1955.

[257] J Curry Street and EC Stevenson. New evidence for the existence of a particle of mass intermediate between the proton and electron. *Physical Review*, 52(9):1003, 1937.

[258] AW Strong, IV Moskalenko, TA Porter, G Jóhannesson, E Orlando, and SW Digel. The galprop cosmic-ray propagation code. *arXiv preprint arXiv:0907.0559*, 2009.

[259] Keith Strong, Nicholeen Viall, Joan Schmelz, and Julia Saba. Understanding space weather: Part iii: The sun's domain. *Bulletin of the American Meteorological Society*, 98(12):2593–2602, 2017.

[260] XH Sun, W Reich, A Waelkens, and TA Enßlin. Radio observational constraints on galactic 3d-emission models. *Astronomy & Astrophysics*, 477(2):573–592, 2008.

[261] IE Tamm, I Frank, and Ig Tamm. Coherent visible radiation of fast electrons passing through matter. *Selected Papers*, pages 29–35, 1991.

[262] Andi Tan, Mengjiao Xiao, Xiangyi Cui, Xun Chen, Yunhua Chen, Deqing Fang, Changbo Fu, Karl Giboni, Franco Giuliani, Haowei Gong, et al. Dark matter results from first 98.7 days of data from the pandax-ii experiment. *Physical review letters*, 117(12):121303, 2016.

[263] LC Tan and LK Ng. Calculation of the equilibrium antiproton spectrum. *Journal of Physics G: Nuclear Physics*, 9(2):227, 1983.

[264] Erwan Thébault, Christopher C Finlay, Ciarán D Beggan, Patrick Alken, Julien Aubert, Olivier Barrois, Francois Bertrand, Tatiana Bondar, Axel Boness, Laura Brocco, et al. International geomagnetic reference field: the 12th generation. *Earth, Planets and Space*, 67:1–19, 2015.

[265] CH Tsao, R Silberberg, and AF Barghouty. Partial cross sections of nucleus-nucleus reactions. *The Astrophysical Journal*, 501(2):920, 1998.

[266] Manuela Vecchi, L Basara, G Bigongiari, F Cervelli, G Chen, GM Chen, HS Chen, G Coignet, S Di Falco, S Elles, et al. The electromagnetic calorimeter of the ams-02 experiment. *arXiv preprint arXiv:1210.0316*, 2012.

[267] Jacco Vink and Jacco Vink. Cosmic-ray acceleration by supernova remnants: Introduction and theory. *Physics and Evolution of Supernova Remnants*, pages 277–321, 2020.

[268] Andrey E Vladimirov, Seth W Digel, Gudlaugur Johannesson, Peter F Michelson, Igor V Moskalenko, Patrick L Nolan, Elena Orlando, Troy A Porter, and Andrew W Strong. Galprop webrun: an internet-based service for calculating galactic cosmic ray propagation and associated photon emissions. *Computer Physics Communications*, 182(5):1156–1161, 2011.

[269] Ph von Doetinchem, W Karpinski, Th Kirn, K Lübelsmeyer, St Schael, and M Wlochal. The ams-02 anticoincidence counter. *arXiv preprint arXiv:0811.4314*, 2008.

[270] Ph von Doetinchem, Th Kirn, K Lübelsmeyer, and St Schael. The anticoincidence counter system of ams-02. *arXiv preprint arXiv:0906.1068*, 2009.

[271] Bing-Bing Wang, Xiao-Jun Bi, Su-Jie Lin, and Peng-fei Yin. Explanations of the dampe high energy electron/positron spectrum in the dark matter annihilation and pulsar scenarios. *arXiv preprint arXiv:1707.05664*, 2017.

[272] W. R. Webber and J. Kish. Further Studies of the Isotopic Composition of Cosmic Ray li, BE and B Nuclei - Implications for the Cosmic Ray Age. In *International Cosmic Ray Conference*, volume 1 of *International Cosmic Ray Conference*, page 389, 1979.

[273] W. R. Webber, J. A. Lezniak, J. C. Kish, and G. A. Simpson.

[274] WR Webber, JC Kish, and DA Schrier. Formula for calculating partial cross sections for nuclear reactions of nuclei with e 200 mev/nucleon in hydrogen targets. *Physical Review C*, 41(2):566, 1990.

[275] WR Webber, A Soutoul, JC Kish, and JM Rockstroh. Updated formula for calculating partial cross sections for nuclear reactions of nuclei with z 28 and e¿ 150 mev nucleon–1 in hydrogen targets. *The*

Astrophysical Journal Supplement Series, 144(1):153, 2003.

[276] Nathanael Weinrich, Mathieu Boudaud, Laurent Derome, Yoann Génolini, Julien Lavalle, David Maurin, Pierre Salati, P Serpico, and Gilles Weymann-Despres. Galactic halo size in the light of recent ams-02 data. *Astronomy & Astrophysics*, 639:A74, 2020.

[277] M. E. Wiedenbeck and D. E. Greiner. A cosmic-ray age based on the abundance of Be-10. , 239:L139–L142, August 1980.

[278] Martin Wolfgang Winkler. Cosmic ray antiprotons at high energies. *Journal of Cosmology and Astroparticle Physics*, 2017(02):048, 2017.

[279] N. E. Yanasak, M. E. Wiedenbeck, R. A. Mewaldt, A. J. Davis, A. C. Cummings, J. S. George, R. A. Leske, E. C. Stone, E. R. Christian, T. T. von Rosenvinge, W. R. Binns, P. L. Hink, and M. H. Israel. Measurement of the Secondary Radionuclides ^{10}Be, ^{26}Al, ^{36}Cl, ^{54}Mn, and ^{14}C and Implications for the Galactic Cosmic-Ray Age. , 563:768–792, December 2001.

[280] Peng-Fei Yin, Zhao-Huan Yu, Qiang Yuan, and Xiao-Jun Bi. Pulsar interpretation for the ams-02 result. *Physical Review D*, 88(2):023001, 2013.

[281] Young Soo Yoon, T Anderson, A Barrau, NB Conklin, S Coutu, L Derome, JH Han, JA Jeon, KC Kim, MH Kim, et al. Proton and helium spectra from the cream-iii flight. *The Astrophysical Journal*, 839(1):5, 2017.

[282] YS Yoon, HS Ahn, PS Allison, MG Bagliesi, JJ Beatty, G Bigongiari, PJ Boyle, JT Childers, NB Conklin, Stephane Coutu, et al. Cosmic-ray proton and helium spectra from the first cream flight. *The Astrophysical Journal*, 728(2):122, 2011.

[283] Paolo Zuccon. A monte carlo simulation of the cosmic rays interactions with the near earth environment. *Ph. D. Thesis*, 2002.

[284] Paolo Zuccon, G Ambrosi, P Azzarello, et al. Ams-02 track reconstruction and rigidity measurement. In *Proceedings of the 33rd International Cosmic Ray Conference (Rio de Janeiro)*, 2013.